UNIVERSITY OF ADELAIDE LIBRARY
20-9-96

Dispersion Modelling using Finite-Difference Methods with Application to Larval Western King Prawn (*Penaeus latisulcatus*) in Spencer Gulf, South Australia

John Bruce Nixon, B.Sc (Hons) (Adelaide)

Thesis submitted for the degree of
Doctor of Philosophy
in
Applied Mathematics
at
The University of Adelaide
(Faculty of Mathematical and Computer Sciences)

Department of Applied Mathematics

Submitted: March 29, 1996
Qualified: July 17, 1996
Conferred: October 14, 1996

Contents

List of Tables vii

List of Figures ix

Abstract xiii

Signed Statement xv

Acknowledgements xvii

1 Introduction 1
- 1.1 Pelagic Fisheries Research . . . 4
- 1.2 *Penaeus latisulcatus* in Spencer Gulf . . . 6
  - 1.2.1 The Cray Collaborative Research Grant . . . 7
  - 1.2.2 The Fisheries Research and Development Corporation Project . . . 8
- 1.3 Chapter Synopses . . . 8

2 Penaeid Prawn Biology 11
- 2.1 Larval Spawning . . . 12
  - 2.1.1 Spawning Grounds . . . 13
  - 2.1.2 Spawning Periods . . . 14
  - 2.1.3 Spawn Concentrations Measured . . . 14
  - 2.1.4 Spawn Concentrations Derived . . . 17
  - 2.1.5 Spawning Initial Conditions . . . 21
  - 2.1.6 Discussion . . . 30
- 2.2 The Larval Phase . . . 31
  - 2.2.1 Larval Dispersion . . . 31
  - 2.2.2 Postlarval Settlement . . . 32
  - 2.2.3 Conclusions . . . 33
- 2.3 Juvenile Settlement . . . 33
  - 2.3.1 Temperature, Salinity, and *Penaeus* Species Abundance . . . 33
  - 2.3.2 Juvenile *Penaeus latisulcatus* Habitats . . . 33
  - 2.3.3 Juvenile *Penaeus latisulcatus* in South Australia . . . 34
  - 2.3.4 Juvenile *Penaeus latisulcatus* in Spencer Gulf . . . 35
  - 2.3.5 Conclusions . . . 37
- 2.4 Vertical Migration . . . 38
  - 2.4.1 Observational Evidence . . . 38
  - 2.4.2 Modelling Simulations . . . 40
  - 2.4.3 Conclusions . . . 42

3 The Tidal Model 45
3.1 The Mathematical Model . . . 45
3.1.1 The Three-Dimensional Equations . . . 46
3.1.2 The Boundary and Initial Conditions . . . 50
3.2 The Computational Model . . . 53
3.2.1 The Horizontal Grid . . . 53
3.2.2 The Vertical Grid . . . 54
3.2.3 The Finite-Difference Scheme . . . 55
3.2.4 The Grid Element Classification Scheme . . . 57
3.2.5 The Finite-Difference Approximations . . . 58
3.2.6 The Neighbourhood Configuration Scheme . . . 59
3.3 Calibration . . . 59
3.3.1 Spencer Gulf Field Observations . . . 60
3.3.2 Error Measures for Simulation Comparisons . . . 61
3.3.3 Specifying the Horizontal Grid . . . 63
3.3.4 Specifying the Horizontal Eddy Viscosity . . . 64
3.3.5 Specifying the Vertical Grid . . . 64
3.3.6 Specifying the Vertical Eddy Viscosity . . . 64
3.3.7 Determining Mean Sea Level from Indian Spring Low Water . . . 66
3.3.8 Determining the Optimal Time–Step . . . 67
3.4 The Coarse Grid Spencer Gulf Model . . . 67
3.5 Summary . . . 76

4 The Wind Model 77
4.1 Available Wind Data . . . 77
4.1.1 Surface Wind Stations . . . 77
4.1.2 Upper Wind Stations . . . 78
4.2 Specifying the Wind Field in Spencer Gulf . . . 86
4.3 Wind Field Specification Validity . . . 86
4.4 Historical Wind Data . . . 87
4.4.1 "The Stony Point Summer Investigations" . . . 87
4.4.2 Measured/Derived Surface Wind Correlations . . . 92
4.4.3 Measured Upper Wind Correlations . . . 95
4.4.4 "Stony Point—South Australia" . . . 96
4.4.5 "Stony Point and Port Stanvac" . . . 98
4.4.6 Conclusions . . . 99
4.5 Summary . . . 99

5 The Supercomputer Model 101
5.1 The Test Problem . . . 101
5.2 Porting to a SPARC Workstation . . . 102
5.3 Porting to a CRAY Supercomputer . . . 103
5.4 Use of Automatic Vectorisation . . . 103
5.5 Use of Compiler Directives . . . 103
5.6 Removal of Time–Centring . . . 104
5.7 Modification of FORTRAN Code . . . 105
5.7.1 Vectorising the `thomas` Subroutine . . . 106
5.7.2 Vectorising the `ucalcn` and `vcalcn` Subroutines . . . 107
5.7.3 Discussion . . . 108
5.8 Removal of Memory Bank Conflicts . . . 111
5.9 Removal of Obvious Bottlenecks . . . 113
5.10 Discussion . . . 114
5.10.1 "See `ted` Run a Four-Minute Mile" . . . 117

5.10.2 Further Optimisation . . . 117
5.11 Summary . . . 117

6 The Fine Grid Spencer Gulf Model **119**
6.1 Specifying the Horizontal Grid . . . 119
6.2 Specifying the Vertical Grid . . . 121
6.3 Determining the Optimal Time–Step . . . 121
6.4 Spencer Gulf Field Observations . . . 122
6.5 Determining Mean Sea Level . . . 122
6.5.1 Determining Indian Spring Low Water from Chart Datum . . . 122
6.5.2 Determining Mean Sea Level from Indian Spring Low Water . . . 126
6.6 Specifying the Vertical Eddy Viscosity . . . 128
6.7 Tidal Model Prediction Validity . . . 130
6.7.1 Sea–Surface Elevation Prediction Validity . . . 130
6.7.2 Horizontal Current Prediction Validity . . . 130
6.7.3 Discussion . . . 131
6.8 Summary . . . 131

7 The Larval Dispersion Model **133**
7.1 Larval Dispersion Modelling . . . 133
7.2 Analytical Dispersion Models . . . 134
7.2.1 Jackson and Strathmann . . . 134
7.2.2 Hill . . . 135
7.2.3 Richards, Possingham, and Noye . . . 138
7.2.4 Summary . . . 139
7.3 Vertical Migration . . . 139
7.4 Larval Advection . . . 140
7.4.1 Tidal Ellipses . . . 141
7.4.2 Residual Currents . . . 142
7.4.3 Tidal Ellipses of Spencer Gulf Major Constituents . . . 144
7.4.4 Residual Currents for Spencer Gulf Major Constituents . . . 148
7.4.5 Summary . . . 150
7.5 Diffusion: Eddy, Molecular, and Shear . . . 151
7.5.1 Diffusion Coefficients in Mathematical Models . . . 153
7.5.2 Diffusion Coefficients in the Larval Dispersion Model . . . 153
7.6 Eddy Diffusion in Spencer Gulf . . . 153
7.6.1 Horizontal Eddy Diffusion in Spencer Gulf . . . 153
7.6.2 Eddy Diffusion Coefficient Empirical Data . . . 156
7.6.3 Eddy Diffusion Coefficient Upper Bounds . . . 156
7.6.4 Spatially Variable Horizontal Eddy Diffusion . . . 157
7.6.5 Constant Eddy Diffusion . . . 158
7.6.6 Discussion . . . 160
7.6.7 Conclusions . . . 160
7.7 Larval Mortality . . . 161
7.7.1 Mortality Variability with Density . . . 161
7.7.2 Mortality Variability with Time . . . 162
7.7.3 Estimating Larval Mortality . . . 162
7.7.4 Conclusions . . . 163
7.7.5 Mortality Estimates . . . 163
7.7.6 Variable Mortality . . . 164
7.7.7 Mortality Variability . . . 164
7.7.8 Summary . . . 166
7.8 The Advection–Diffusion–Mortality Model . . . 167

7.9 Summary . . . 168

8 The Advection–Diffusion Model **169**
8.1 One-Dimensional Advection–Diffusion . . . 169
8.1.1 Equivalent and Modified Equivalent Partial Differential Equations . . . 169
8.1.2 Convergence, Consistency, Stability, and Non-Negativity . . . 171
8.1.3 Wave Propagation Characteristics . . . 172
8.2 One-Dimensional Advection–Diffusion Methods . . . 173
8.2.1 The Lax–Wendroff Type (1,3) Method . . . 173
8.3 One-Dimensional Advection . . . 176
8.4 One-Dimensional Advection Methods . . . 177
8.4.1 The "Box" Type (2,2) Method . . . 177
8.5 Two-Dimensional Advection–Diffusion . . . 178
8.6 Finite-Difference Method Criteria . . . 179
8.7 Two-Dimensional Advection–Diffusion Methods . . . 181
8.7.1 The "Leapfrog"/Du Fort–Frankel Type (1,4,1) Method . . . 181
8.7.2 The Forward-Time Centred-Space (1,5) Method . . . 182
8.7.3 The "Modified" Forward-Time Centred-Space (1,5) Method . . . 183
8.7.4 The Lax–Wendroff Type 2(1,3) Method . . . 185
8.7.5 Discussion . . . 185
8.8 The Finite-Difference Scheme . . . 187
8.8.1 Initial and Boundary Conditions . . . 187
8.8.2 Discussion . . . 190
8.9 The Finite-Difference Method Tests . . . 191
8.9.1 The Numerical Tests . . . 191
8.9.2 The "Oscillating Tide" Test . . . 192
8.9.3 The "Constant Current" Test . . . 196
8.9.4 The "Cowell Spawning Ground, Spencer Gulf" Test . . . 203
8.9.5 Discussion . . . 214
8.9.6 Tidal Model and Dispersion Model Coupling . . . 215
8.10 Summary . . . 215

9 Numerical Larval Dispersion Models **217**
9.1 Penn . . . 217
9.2 Bartsch, Brander, Heath, Munk, Richardson, and Svendsen . . . 218
9.3 Johnson and Hess . . . 218
9.3.1 The Hydrodynamic Model . . . 219
9.3.2 The Dispersion Model . . . 220
9.3.3 Simulations and Results . . . 220
9.4 Noye, Bills, I'Anson, and Wong . . . 220
9.5 Possingham and Roughgarden . . . 221
9.6 Church, Forbes, Jackson, Pendrey, and Rothlisberg . . . 221
9.6.1 Models and Methods . . . 221
9.6.2 Experiments and Results . . . 222
9.7 Andrews, Black, Gay, McShane, Moran, and Smith . . . 224
9.7.1 The Hydrodynamic Model . . . 224
9.7.2 The Dispersion Model . . . 224
9.7.3 Black and Gay (1987) . . . 225
9.7.4 Black (1989) . . . 225
9.7.5 McShane, Black, and Smith (1988) . . . 226
9.7.6 Black, Gay, and Andrews (1990) . . . 226
9.7.7 Black and Moran (1991) . . . 226
9.8 Bode, Dight, James, and Scandol . . . 227

9.8.1 The Hydrodynamic Model . . . 227
9.8.2 The Dispersion Model . . . 228
9.8.3 Dight, Bode, and James (1990a) . . . 228
9.8.4 Dight, Bode, and James (1990b) . . . 229
9.8.5 James and Scandol (1992) . . . 229
9.8.6 Scandol and James (1992) . . . 230
9.9 Babcock, King, Oliver, Willis, and Wolanski . . . 230
9.9.1 Bode, Dight, James, and Scandol . . . 231
9.9.2 Andrews, Black, Gay, McShane, Moran, and Smith . . . 231
9.9.3 Model Realism . . . 234
9.10 Summary . . . 234

10 Larval Dispersion Simulations **235**
10.1 Wind–Stress Sensitivity . . . 236
10.1.1 Space and Time Independent Wind–Stress . . . 236
10.1.2 Space and Time Dependent Wind–Stress . . . 244
10.1.3 Conclusions . . . 251
10.2 Initial Condition Sensitivity . . . 251
10.2.1 Tidal Currents . . . 252
10.2.2 Larval Dispersion . . . 252
10.2.3 Conclusions . . . 261
10.3 Postlarval Settlement . . . 261
10.3.1 Postlarval Transect Trends . . . 261
10.3.2 Conclusions . . . 266
10.4 Dispersion Period Sensitivity . . . 266
10.4.1 Fixed Dispersion Periods . . . 266
10.4.2 Variable Dispersion Periods . . . 279
10.4.3 Transect Trends . . . 284
10.4.4 Conclusions . . . 288
10.5 Summary . . . 288

11 Conclusions and Recommendations **291**
11.1 The Biological Model . . . 291
11.1.1 Observational Mortality Data . . . 291
11.1.2 Observational Spawning Data . . . 292
11.1.3 Observational Dispersal Data . . . 292
11.1.4 Observational Settlement Data . . . 292
11.2 The Dispersion Model . . . 292
11.2.1 Three-Dimensional Dispersion Modelling . . . 293
11.2.2 Eddy Diffusion Specification . . . 293
11.3 The Hydrodynamic Model . . . 293
11.3.1 Fine Grid Spencer Gulf Model Validation . . . 293
11.3.2 Surface Wind Specification . . . 293
11.3.3 Tidal-Flats Representation . . . 293
11.3.4 Spherical Coordinate Representation . . . 294
11.3.5 Coastal Boundary Representation . . . 294
11.4 Recruitment Forecasting . . . 294

12 Summary **295**

Bibliography **297**

Glossary of Notation **313**

Glossary of Terms 325

List of Tables

2.1 Major *Penaeus latisulcatus* spawning grounds in Spencer Gulf. 13

3.1 Major tidal constituents observed in Spencer Gulf. 61
3.2 Spencer Gulf tidal observation station locations and location errors. 62
3.3 Vertical grid-spacing variation. 65
3.4 Coarse grid Spencer Gulf model open boundary tidal constituents. 71

4.1 Spencer Gulf meteorological observation station locations and elevations 78
4.2 Summary of wind statistics over Spencer Gulf. 99

5.1 Coarse grid Spencer Gulf tidal model execution times. 114

6.1 Fine grid Spencer Gulf model open boundary tidal constituents. 124
6.2 Major tidal constituents in Spencer Gulf. 128

7.1 Horizontal eddy diffusion coefficient measurements in Spencer Gulf. 156
7.2 Time-independent larval mortality rates. 165
7.3 Time-dependent larval mortality rates. 165

8.1 The "oscillating tide" test statistics for the final time–step. 194
8.2 The "oscillating tide" test statistics over all time–steps. 194
8.3 The "constant current" test statistics for the final time–step. 197
8.4 The "constant current" test statistics over all time–steps. 197
8.5 The "Cowell Spawning Ground" test statistics for the final time–step. 212
8.6 The "Cowell Spawning Ground" test statistics over all time–steps. 212

10.1 The constant wind–stress simulation statistics for the final time–step. 240
10.2 The constant wind–stress simulation statistics over all time–steps. 240
10.3 The variable wind–stress simulation statistics for the final time–step. 244
10.4 The variable wind–stress simulation statistics over all time–steps. 244
10.5 The initial condition simulation statistics for the final time–step. 252
10.6 The initial condition simulation statistics over all time–steps. 259
10.7 Spencer Gulf prawn larvae sampling site locations. 265
10.8 The dispersion period simulation statistics for the final time–step. 270
10.9 The dispersion period simulation statistics over all time–steps. 270

List of Figures

1.1 The distribution of *Penaeus latisulcatus* in Australian waters. 1
1.2 Important geographical features and places of interest in Spencer Gulf. 2
1.3 Tide–height and tidal current observation stations in Spencer Gulf. 3
1.4 A typical penaeid prawn life cycle (schematic). 6
1.5 A typical prawn life cycle (to scale). 7

2.1 The northern Spencer Gulf spawning grounds trawl locations. 15
2.2 The southern Spencer Gulf spawning grounds trawl locations. 16
2.3 Measured and smoothed egg production for the Wallaroo spawning ground. . . . 17
2.4 Measured and smoothed egg production for the Gutter spawning ground. 18
2.5 Measured and derived egg production for the Wallaroo spawning ground. 19
2.6 Measured and derived egg production for the Gutter spawning ground. 20
2.7 Measured and derived egg production in data sparse regions. 21
2.8 Measured and smoothed egg production data, without further derivation. 22
2.9 Measured and smoothed egg production data, with further derivation. 23
2.10 The 1988 egg production initial condition. 24
2.11 The 1991 egg production initial condition. 25
2.12 The 1992 egg production initial condition. 26
2.13 The 1993 egg production initial condition. 27
2.14 The 1994 egg production initial condition. 28
2.15 The "average" egg production initial condition. 29
2.16 The *Penaeus latisulcatus* life cycle (schematic). 32
2.17 Nursery areas of juvenile *Penaeus latisulcatus* in South Australian waters. . . . 35
2.18 The fine grid Spencer Gulf model 10 m (mean sea level) depth contour. 36

3.1 Cartesian and transformed vertical coordinate system cross–sections. 48
3.2 Functional forms for vertical variation of the vertical eddy viscosity coefficient. . 50
3.3 A grid element plan view, indicating elevation and horizontal velocity grid–points. 54
3.4 A transformed vertical grid depth–interval cross–section. 55
3.5 A grid element plan view, indicating the immediate neighbour indexing scheme. 56
3.6 Schematic of the tidal model finite-difference scheme. 56
3.7 Coordinate grids generated using different vertical grid–spacing parameter values. 65
3.8 The coarse grid Spencer Gulf model grid element Type input matrix. 68
3.9 The coarse grid Spencer Gulf model. 69
3.10 The coarse grid Spencer Gulf model open boundary. 70
3.11 The coarse grid Spencer Gulf model Indian Spring Low Water depths. 72
3.12 The coarse grid Spencer Gulf model mean sea level depths. 73
3.13 The coarse grid Spencer Gulf model mean sea level depth contours. 74
3.14 The coarse grid Spencer Gulf model ISLW to MSL depth correction contours. . . 75

4.1 Surface wind and upper wind observation stations in the Spencer Gulf region. . 79
4.2 Measured vector time–series at surface wind stations during December 1987. . . 80
4.3 Measured vector time–series at surface wind stations during January 1988. . . . 81
4.4 Measured vector time–series at surface wind stations during February 1988. . . 82

4.5 Measured vector time–series at upper wind stations during December 1987. . . . 83
4.6 Measured vector time–series at upper wind stations during January 1988. 84
4.7 Measured vector time–series at upper wind stations during February 1988. . . . 85
4.8 Derived vector time–series at surface wind stations for December 1987. 88
4.9 Derived vector time–series at surface wind stations for January 1988. 89
4.10 Derived vector time–series at surface wind stations for February 1988. 90
4.11 Auto-correlations of measured and derived surface wind data at Port Augusta. . 92
4.12 Auto-correlations of measured and derived surface wind data at Whyalla. 93
4.13 Auto-correlations of measured and derived surface wind data at Port Lincoln. . 94
4.14 Auto-correlations of measured upper wind data at Adelaide Airport. 95
4.15 Auto-correlations of measured upper wind data at Ceduna. 96
4.16 Auto-correlations of measured upper wind data at Woomera. 97

5.1 Idealised FORTRAN code illustrating the use of the SHORTLOOP compiler directive. 103
5.2 Idealised FORTRAN code illustrating the use of the UNROLL compiler directive. . . 104
5.3 Idealised FORTRAN code illustrating the poorly vectorised subroutine thomas. . . 107
5.4 Idealised FORTRAN code illustrating the well vectorised subroutine thomas. . . . 107
5.5 Idealised FORTRAN code illustrating the poorly vectorised subroutines u/vcalcn. 109
5.6 Idealised FORTRAN code illustrating the well vectorised subroutines u/vcalcn. . . 110
5.7 Memory access sequence for well optimised FORTRAN array operations. 111
5.8 Idealised FORTRAN code illustrating a poorly optimised nested loop structure. . . 112
5.9 Memory access sequence for poorly optimised FORTRAN array operations. 112
5.10 Idealised FORTRAN code illustrating a well optimised nested loop structure. . . . 113
5.11 Absolute processing time against optimisation stage. 115
5.12 Percentage processing time against optimisation stage. 115

6.1 The fine grid Spencer Gulf model. 120
6.2 The fine grid Spencer Gulf model open boundary. 123
6.3 The fine grid Spencer Gulf model open boundary tide–height forcing. 125
6.4 The fine grid Spencer Gulf model mean sea level depth contours. 127
6.5 The fine grid Spencer Gulf model ISLW to MSL depth correction contours. 129

7.1 Spencer Gulf O_1 tidal ellipses for the period 01/02/88–01/03/88. 142
7.2 Spencer Gulf K_1 tidal ellipses for the period 01/02/88–01/03/88. 143
7.3 Spencer Gulf M_2 tidal ellipses for the period 01/02/88–01/03/88. 144
7.4 Spencer Gulf S_2 tidal ellipses for the period 01/02/88–01/03/88. 145
7.5 Mid-northern Spencer Gulf mean sea level depth contours. 146
7.6 Mid-northern Spencer Gulf O_1 tidal ellipses for the period 01/02/88–01/03/88. . 147
7.7 Mid-northern Spencer Gulf K_1 tidal ellipses for the period 01/02/88–01/03/88. . 148
7.8 Mid-northern Spencer Gulf M_2 tidal ellipses for the period 01/02/88–01/03/88. 149
7.9 Mid-northern Spencer Gulf S_2 tidal ellipses for the period 01/02/88–01/03/88. . 150
7.10 Spencer Gulf residual current vectors for 01/02/88–01/03/88. 151
7.11 Mid-northern Spencer Gulf residual current vectors for 01/02/88–01/03/88. . . . 152
7.12 Horizontal eddy diffusion coefficient measurements in Spencer Gulf. 155
7.13 Horizontal eddy diffusion coefficient approximations in Spencer Gulf. 159
7.14 Larval mortality rates and resulting abundances. 166

8.1 The Lax–Wendroff type scheme computational stencil and stability regions. . . . 174
8.2 The Lax–Wendroff type scheme wave propagation characteristics. 175
8.3 The Lax–Wendroff type scheme wave propagation trends. 176
8.4 The "box" type scheme computational stencil. 177
8.5 The "box" type scheme wave propagation characteristics and trends. 178
8.6 The Du Fort–Frankel type scheme computational stencil and stability regions. . 181
8.7 The Du Fort–Frankel type scheme stability regions. 182

8.8 The FTCS scheme computational stencil and stability regions. 183
8.9 The FTCS scheme stability regions. 184
8.10 The "modified" FTCS scheme computational stencil and stability regions. 185
8.11 The "modified" FTCS scheme stability regions. 186
8.12 The Lax–Wendroff type scheme computational stencils. 186
8.13 The Lax–Wendroff type scheme stability regions. 187
8.14 A coastal boundary plan view, indicating the reflecting boundary condition. . . 188
8.15 An open boundary plan view, indicating the open boundary condition. 189
8.16 The "oscillating tide" test initial condition and analytical solution. 193
8.17 The Du Fort–Frankel type scheme "oscillating tide" test approximation. 194
8.18 The "modified" FTCS scheme "oscillating tide" test approximation. 195
8.19 The Lax–Wendroff type scheme "oscillating tide" test approximation. 196
8.20 The "constant current" test initial condition and analytical solution. 198
8.21 The Du Fort–Frankel type scheme "constant current" test approximation. . . . 199
8.22 The FTCS scheme "constant current" test approximation. 200
8.23 The "modified" FTCS scheme "constant current" test approximation. 201
8.24 The Lax–Wendroff type scheme "constant current" test approximation. 202
8.25 The Du Fort–Frankel "Cowell spawning ground" approximation, not clipped. . . 204
8.26 The Du Fort–Frankel "Cowell spawning ground" approximation, clipped. 205
8.27 The FTCS "Cowell spawning ground" approximation, not clipped. 206
8.28 The FTCS "Cowell spawning ground" approximation, clipped. 207
8.29 The "modified" FTCS "Cowell spawning ground" approximation, not clipped. . . 208
8.30 The "modified" FTCS "Cowell spawning ground" approximation, clipped. 209
8.31 The Lax–Wendroff "Cowell spawning ground" approximation, not clipped. . . . 210
8.32 The Lax–Wendroff "Cowell spawning ground" approximation, clipped. 211
8.33 The "Cowell spawning ground" test initial condition. 213

10.1 Zero (constant) wind–stress simulation larval concentrations. 237
10.2 Constant SSE wind–stress simulation larval concentrations. 238
10.3 Constant NNE wind–stress simulation larval concentrations. 239
10.4 Spencer Gulf residual current vectors for 12/12/88–10/01/89 with zero wind. . . 241
10.5 Spencer Gulf residual current vectors for 12/12/88–10/01/89 with SSE wind. . . 242
10.6 Spencer Gulf residual current vectors for 12/12/88–10/01/89 with NNE wind. . . 243
10.7 Zero (variable) wind–stress simulation larval concentrations. 245
10.8 Non-zero variable wind–stress simulation larval concentrations. 246
10.9 Spencer Gulf near sea–surface residual current vectors for 01/02/88–01/03/88. . 247
10.10 Spencer Gulf near sea–bed residual current vectors for 01/02/88–01/03/88. . . . 248
10.11 Mid-northern Spencer Gulf sea–surface residuals for 01/02/88–01/03/88. 249
10.12 Mid-northern Spencer Gulf sea–bed residuals for 01/02/88–01/03/88. 249
10.13 The 1988 initial condition simulation larval concentrations. 253
10.14 The 1991 initial condition simulation larval concentrations. 254
10.15 The 1992 initial condition simulation larval concentrations. 255
10.16 The 1993 initial condition simulation larval concentrations. 256
10.17 The 1994 initial condition simulation larval concentrations. 257
10.18 The "average" initial condition simulation larval concentrations. 258
10.19 Prawn larvae observation stations in Spencer Gulf. 262
10.20 The fine grid Spencer Gulf model prawn larvae station locations. 263
10.21 The east-west dispersion period simulation final larval concentration trends. . . 264
10.22 The north-south dispersion period simulation final larval concentration trends. . 267
10.23 The 15/12/87–13/01/88 dispersion period simulation larval concentrations. . . . 268
10.24 The 01/02/88–01/03/88 dispersion period simulation larval concentrations. . . . 269
10.25 Spencer Gulf near sea–surface depth–level residuals for two 29 d periods. 271
10.26 Spencer Gulf near sea–bed depth–level residuals for two 29 d periods. 272

10.27 Mid-northern Spencer Gulf near sea–surface residuals for two 29 d periods. . . . 273
10.28 Mid-northern Spencer Gulf near sea–bed residuals for two 29 d periods. 274
10.29 Mid-northern Spencer Gulf O_1 tidal ellipses for two 29 d periods. 275
10.30 Mid-northern Spencer Gulf K_1 tidal ellipses for two 29 d periods. 276
10.31 Mid-northern Spencer Gulf M_2 tidal ellipses for two 29 d periods. 277
10.32 Mid-northern Spencer Gulf S_2 tidal ellipses for two 29 d periods. 278
10.33 Predicted larval concentration time–series for 7 d at Transect 1. 280
10.34 Predicted larval concentration time–series for 29 d at Stations 2 and 4, Transect 1. 280
10.35 Predicted larval concentration time–series for Transects 1–4 at Station 1. 281
10.36 Predicted larval concentration time–series for Transects 1–4 at Station 2. 282
10.37 Predicted larval concentration time–series for Transects 1–4 at Station 3. 283
10.38 Predicted larval concentration time–series for Transects 1–4 at Station 4. 284
10.39 Predicted larval concentration time–series for Transects 1–4 at Station 5. 285
10.40 The east-west initial, intermediate, and final larval concentration trends. 286
10.41 The north-south initial, intermediate, and final larval concentration trends. . . . 287

Abstract

This thesis reports the development, testing, and application of computer programs for simulating dispersion in coastal seas, with particular application to larvae of the western king prawn (*Penaeus latisulcatus*) in Spencer Gulf, South Australia.

Theoretical discussions of, and experimental evidence for, larval dispersion processes are distilled from the literature concerning the determination and measurement of larval behaviour. Simplifications and approximations are made according to the manner in which these processes may be qualified in mathematical models and then quantified in numerical models.

A numerical hydrodynamical model is required to approximate tidal currents over a period of time, at more than one depth, at many locations in the region of interest. Approximations are computed of different hindcast scenarios with respect to the period of the tidal simulation and the associated meteorological events. Information parameterising the significant tidal and meteorological forcings during the periods of interest is derived from the available observational data and then compared with the historical records. An existing three-dimensional numerical tidal model is modified and optimised for a vector supercomputer in order to achieve the spatial and temporal extent and resolution required of the simulations, within imposed computational resource constraints. The tidal model is then calibrated for a greater resolution application than ever before attempted for the physical region of interest.

A numerical dispersion model is required to approximate larval concentrations at gulf interior and coastal region locations up to a specified time after an initial larval spawning. Approximations are computed for different experimental scenarios with respect to the dates of the spawning events, the initial conditions at those dates, and the tidal currents as determined by the tidal model and associated forcings. An advection–diffusion–mortality model is derived using an underlying two-dimensional numerical transport scheme chosen from among many alternative finite-difference schemes.

The dispersion model hindcasts of specific periods of interest are presented, and analysed with respect to field observations of larvae in Spencer Gulf. The paucity of available observational data deems quantitative error measures indefinable. Rather, sensitivity analyses are carried out to determine relative effects of model parameter variation. The choice of the dispersion model finite-difference scheme is shown to have greater effect on the simulation results than any alteration, within realistic bounds, of model input parameters. Simulation results presented are found to adequately approximate dispersion processes observed in the field by workers studying larval movements within the modelled region.

Signed Statement

This work contains no material which has been accepted for the award of any other degree or diploma in any university or other tertiary institution and, to the best of my knowledge and belief, contains no material previously published or written by another person, except where due reference has been made in the text.

I give consent to this copy of my thesis, when deposited in the University Library, being available for loan and photocopying.

SIGNED: DATE: 20/8/96

Acknowledgements

I thank my supervisor, Assoc. Prof. John Noye, for his support, encouragement, and enthusiasm throughout the development of this work and for the hours spent in discussion and proof-reading. Thanks also to Dr. Peter Bills for expert and thorough proof-reading and the many hours spent discussing tidal modelling in general and the `ted` computer program suite in particular, and to Karyn "once-was Ms. I'Anson/now-is Dr. Matthews" for the time spent discussing just about everything else! Many thanks to David Beard for extraordinary computing support, and to Dr. Peter Gill, Marcus Grzechnik, Don Oats, Dr. Shane Richards, Alice von Trojan, and all at the Department of Applied Mathematics of The University of Adelaide.

I thank Neil Carrick of the South Australian Research and Development Institute, and Mick Puglisi and members of the Spencer Gulf and West Coast Prawn Fishermen's Association for the prawns—they were delicious!

Thanks to Roger Brown, Peter Edwards, Peter Grimes, Andy Whyatt, and all at Cray Research (Australia) Pty. Ltd. for providing time on `cherax`[1], the CRAY Y-MP 2D 2-16 at Leading Edge Technologies Ltd. and on `maloo`[2], the CRAY Y-MP 2E 2-32 at the Bureau of Meteorology. For advice on vector supercomputing techniques, and for service above and beyond the call of duty, special thanks go to Dave Micklethwaite, Supercomputer Consultant at Cray and all around nice guy. I thank Eva Hatzi, "the keepers of the tapes", and all on the Help Desk at Leading Edge for managing with my excessive resource requirements and allowing me to somewhat overstay my welcome on `cherax`, and Hank Kloppenborg, Rob Thurling, and all in system administration at the Bureau of Meteorology for placing me in "the express lane" and allowing me to complete my final runs on `maloo`.

Thanks to Prof. Geoff Lennon, Bill Mitchell, and all at the National Tidal Facility, the Flinders Institute for Atmospheric and Marine Sciences, and The Flinders University of South Australia for the provision of tidal constituent constants used throughout this work.

I thank Nick Cundell, Dave Goodwins, and all at the Information Services Division of the South Australian Department of Environment and Planning for providing Spencer Gulf bathymetry data and Anne Brewster, Sue Duckmanton, Robin Hicks, and all at the National Climate Centre of the Bureau of Meteorology for providing Spencer Gulf wind data.

I would like to acknowledge the financial assistance of The University of Adelaide through a University of Adelaide Scholarship for Postgraduate Research (27/3/87–27/11/90), the High Frequency Radar Division of the Surveillance Research Laboratory at the Defence Science Technology Organisation through a Cadet Research Scientist position (17/1/91–26/5/92), Cray Research (Australia) Pty. Ltd. for free time on CRAY Y-MP supercomputers through a Cray Collaborative Research Grant of over 200 h on `cherax` and `maloo`, and the Fisheries Research and Development Corporation through a Research Officer position in the Department of Applied Mathematics at The University of Adelaide (22/6/92–1/7/95).

This document was produced using the $\mathcal{AMS}$-LaTeX (Anonymous 1991), BibTeX (Patashnik 1988a, 1988b), `draw` (Beard and Nixon 1990), `dvips` (Rokicki 1993), `ghostview` (Theisen 1992), LaTeX (Lamport 1994), and PiCTeX (Wichura 1987), software tools. I give thanks for their efforts to the people responsible.

Extra special thanks go to Patricia and Gordon Nixon, and Helen Vaughan.

[1] The zoological name for the freshwater crustacean more commonly known (locally) as a "yabby".

[2] The Aboriginal name for the meteorological phenomenon more commonly known (globally) as thunder.

UNIVERSITY OF ADELAIDE LIBRARY

Chapter 1

Introduction

To the taxonomist, shrimps and prawns belong to the swimming or natantian decapod Crustacea. It is generally accepted that no systematic distinction can be made between the two common names. In Great Britain small carideans (e.g., *Pandalus montagui*) are called shrimp, larger species (*P. borealis*), prawns. Marine species of penaeid are called "shrimp" in the USA, "prawns" in Australia, India, and South Africa, while either term may be used in Japan (Wickins 1976, p. 435). In this thesis the term "prawn" will be used exclusively.

The western king prawn (*Penaeus latisulcatus*) is a commercially trawled pelagic species in Spencer Gulf (SG), South Australia (SA). The location of this region relative to the Australian continent is depicted in Figures 1.1, 1.2, and 1.3. In Figure 1.1 the names and locations

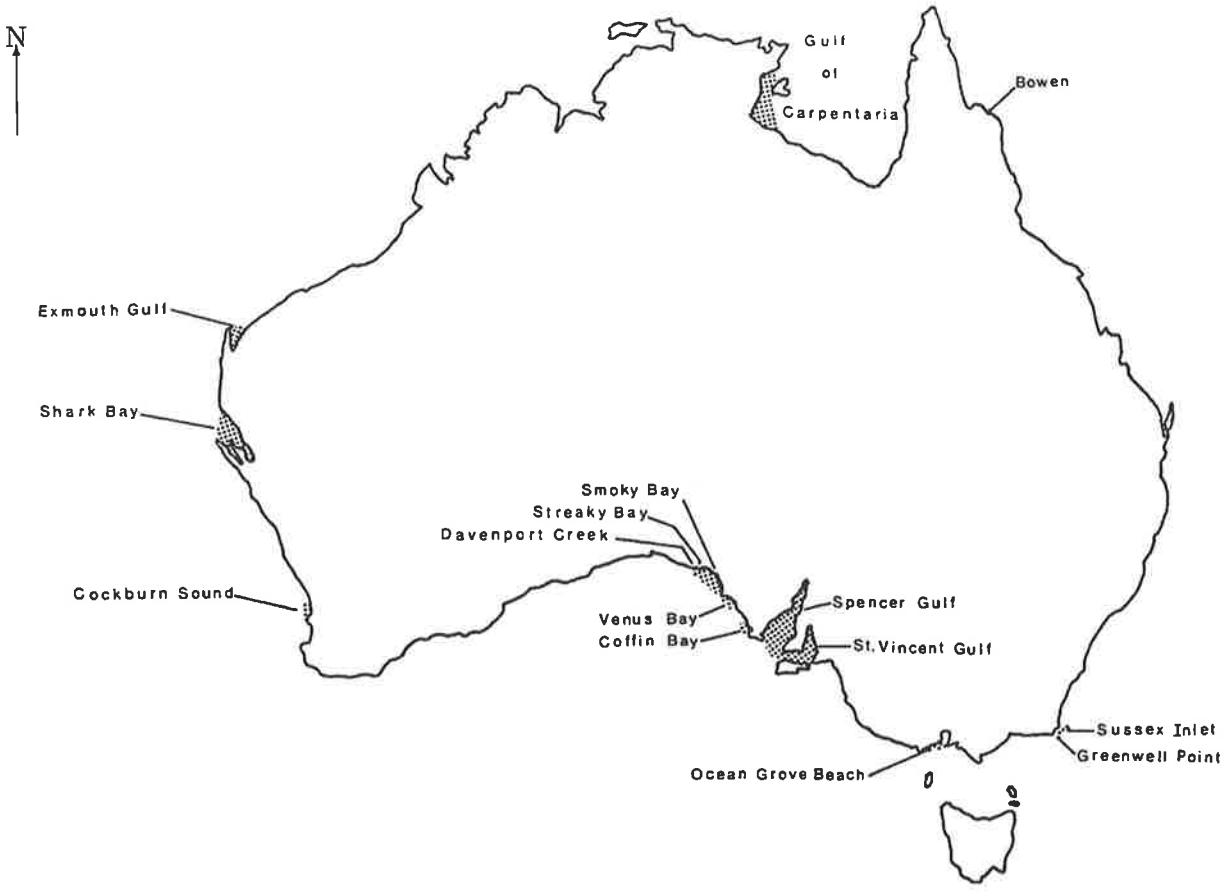

Figure 1.1: The distribution of *Penaeus latisulcatus* in Australian waters (from Zed 1980, Figure 1). Shading indicates regions in which the species is abundant.

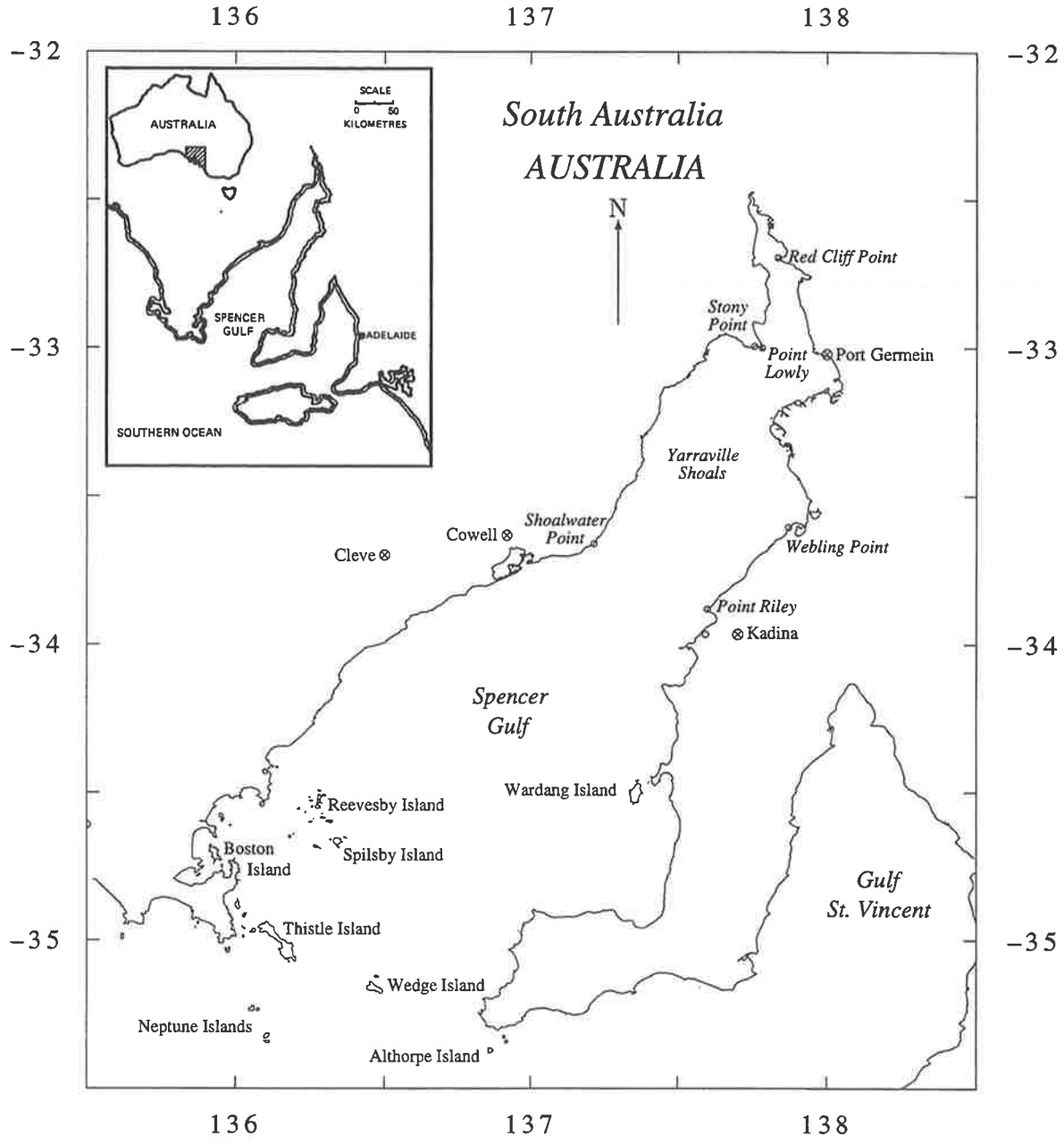

Figure 1.2: Important geographical features (italics) and places of interest (roman) in Spencer Gulf. Population centres (larger crossed circles) and physical features (smaller uncrossed circles) are indicated. The x and y axes indicate longitude (°E) and latitude (°N), respectively.

of areas in which *P. latisulcatus* is distributed are shown. In Figure 1.2 the names and locations of important geographical features and places of interest in this region are shown. In Figure 1.3 the names and locations of observation stations, many corresponding to important population centres and geographical features, are also shown. These figures should be consulted to determine the position of places, features, or stations named in this thesis.

Within Australian waters *P. latisulcatus* is found from South Australia around through west and tropical Australia, as shown in Figure 1.1. The species has a scattered distribution down the east coast and has been reported as far south as Ocean Grove at the entrance to Port Philip Bay, in central Victoria (Winstanley 1975). The major fisheries for *P. latisulcatus* are in Spencer Gulf in South Australia and Shark Bay in Western Australia (King 1980, p. 4). Small prawns

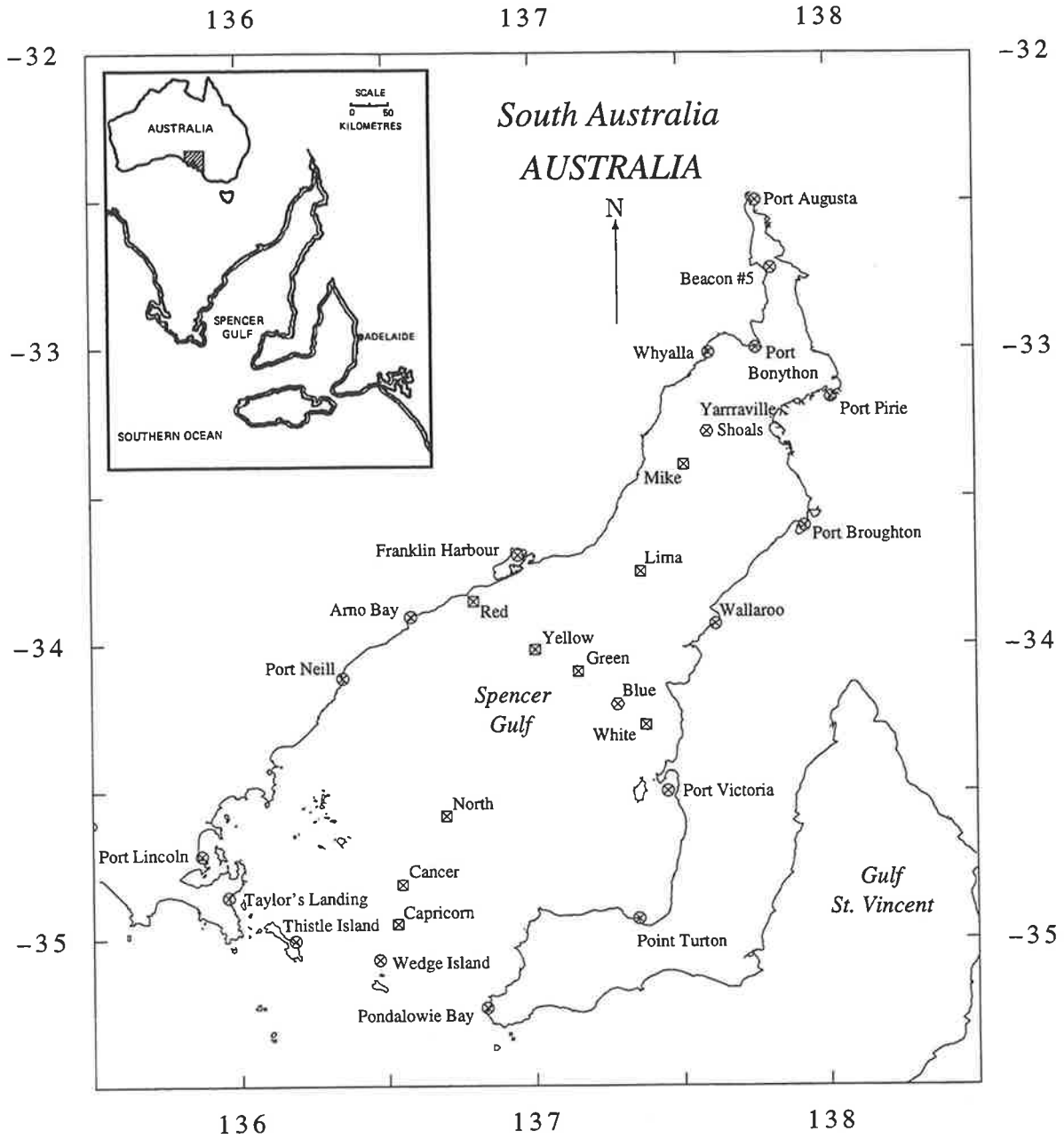

Figure 1.3: Observation stations for tide–height only (crossed circles), tidal current only (crossed squares), and both (crossed hexagons) in Spencer Gulf. Important geographical features (italics) are also shown. The x and y axes indicate longitude (°E) and latitude (°N), respectively.

have been caught in shallow water areas of Spencer Gulf and Gulf St. Vincent for perhaps one hundred years (King 1980, p. 41). The Spencer Gulf prawn fishery is, however, a relatively new fishery (Carrick 1982, p. 3) and is based on this single penaeid species (Carrick 1988, p. 4). On a world-wide basis, this fishery is the major producer of western king prawns (Carrick 1982, p. 3). It has been valued at approximately \$AUD40 million per annum (Carrick 1992a, p. 1), and approximately 90% of the catch is exported (Carrick 1982, p. 3). Trawlers manned by members of the Spencer Gulf and West Coast Prawn Fishermen's Association (SGWCPFA) operate on days of the year predetermined by fisheries management at the South Australian Research and Development Institute (SARDI). They are restricted in their efforts in terms of periods open to fishing, numbers of vessels trawling, maximum haul sizes taken, ship and equipment

types used, and individual prawn lengths allowed, etc. The prawn fishery in South Australia is unique in that sensible management measures were taken at its very inception in 1968, and these measurements have served the fishery well in its development (King 1980, p. (*i*)).

In order to set these restrictions so as to successfully manage such an economically significant resource, management needs an in-depth understanding of the factors which structure recruitment to nurseries and the fishery (Carrick 1992a, p. 1). Here the term *recruitment* refers to transition from larval to juvenile phases (Hill 1991a, p. 118). Detailed investigation of juvenile prawn populations in the nursery areas is thought to be the key to understanding the dynamics of the prawn population in Spencer Gulf (Carrick 1982, p. 23).

Larval advection and the level of reproductive depletion of key spawning areas by fishing are considered by SARDI to be important factors which affect recruitment to the Spencer Gulf fishery (Carrick 1991, p. 2). It should be noted that the term *larvae* will be used a little loosely in this thesis. This is because there is a range of points in the very early parts of the life cycle when pelagic dispersal commences (Hill 1991a, p. 118). The term larvae will, following Hill (1991a), henceforth be used to describe all planktonic early life–stages released into the water column.

At some point in each prawn's life expectancy, it will reach a maximum biovalue. The regime developed by SARDI of sampling and stock harvesting at key areas in Spencer Gulf and during key times of the year has aimed at achieving as close to this maximum as possible. The management of a fish resource becomes in this sense closer to crop or forest husbandry, whereby the producer waits for the best biological and economic conditions to reap the benefits (Carrick 1985, p. 6). Strategies can be designed to target best market periods provided that an understanding of the fundamental processes which structure recruitment to the fishery are better understood (Carrick 1992a, p. 1). Significant economic benefits can thus accrue by allowing prawns to grow to a more valued size (Carrick 1982, p. 10), but there is a need to develop harvesting strategies which have stronger biological basis (Carrick 1992a, p. 1).

A depletion study, to estimate catchability, has indicated that natural adult mortality (from April to June) is less than $5\%\,\mathrm{mo}^{-1}$. The depletion effects of fishing, on the other hand, are indicated in the fact that the fleet reduced the experimental population by at least 70% during the same period (Carrick 1988, p. 6). The potential for *growth overfishing*—which occurs when the fishing effort significantly reduces the average size of individuals in the population (Carrick 1982, p. 5)—is thus obvious. This potential is enhanced by the fact that the prawn fishing grounds are relatively small compared to the overall size of the Gulf (Carrick 1982, p. 4) and the efficiency of the trawling fleet is so great (Carrick 1982, 1988).

Subsequent analyses of results indicated that the best period to fish the main cohort was from late May–June, when biovalue was at a maximum and there was minimal mixing with smaller recruits (Carrick 1988, p. 8). Here the terms *recruit* and *cohort* refer to: transition from juvenile to adult phases with the ingress of small prawns from the coastal nursery areas to the open Gulf fishing grounds; and a statistically significant size group, respectively (Carrick 1988, p. 4).

The coupling of modelling studies of larval advection with empirical field testing will provide a better understanding of the importance of advection and other factors which structure recruitment to fisheries (Carrick 1992a, p. 2).

1.1 Pelagic Fisheries Research

The number of fish at the age of first capture in a fishery (recruitment) is dependent on the production of eggs by the parent stock and the survival of early life stages (eggs, larvae, and juveniles). In many pelagic species the survival of larvae depends on transport from spawning to nursery areas (Bartsch et al. 1989, p. 632). Predicting variations in recruitment in advance of fishery legislation has always been difficult, and the collapse of the North Sea herring populations during the mid-1970s is believed to have been due to a period of several years of low recruitment

coupled with high fishing activity (Bartsch et al. 1989, p. 632). Bartsch et al. (1989) suggested that a better understanding could be achieved with the aid of environmental modelling.

One of the major determinants of commercial abundance for species with planktonic larvae is the degree to which dispersal by water currents diminishes or enhances larval recruitment (Johnson and Hess 1990, p. 195), however "favourable circulation" is a necessary, but not sufficient, prerequisite for good recruitment (Bartsch et al. 1989, p. 635). In addition to being influenced by circulation patterns, the dispersal of planktonic larvae is also a function of: (*a*) the location and timing of egg hatching; (*b*) the individual larva's vertical position; and (*c*) the duration of the planktonic phase (Johnson and Hess 1990, p. 195). Residual tidal currents, resulting from nonlinear effects, may also strongly influence the net displacement of larvae (Johnson and Hess 1990, p. 196).

Forbes and Church (1982) point out that the biological and physical factors affecting larval survival have long been recognised as important in establishing year class strength in many fisheries. Most studies, however, have been either descriptive or correlative, with little knowledge of mechanisms that affect larval survival or distribution. The larval ecology of penaeid prawns is no exception. Several hypotheses of how larvae and postlarvae are moved from offshore spawning grounds to nearshore or estuarine nursery grounds have been put forward with very little understanding of the underlying physical and biological mechanisms (Forbes and Church 1982, p. 21). Interannual differences in rates and direction of larval drift, induced by changes in current direction and speed, are known to have significant influences on larval survival and ultimately on recruitment to adult stocks of marine fishes (Leggett 1984, p. 168). It is clear that a detailed knowledge of both larval behaviour and current regimes will be necessary to understand the larval movements from the offshore spawning grounds to the nearshore nursery grounds, and to explain the year to year variation in recruitment strength to the juvenile and adult stocks (Forbes and Church 1982, p. 22). Knowledge of dispersal pathways, mechanisms, and distances would also help define geographic management boundaries and measures (Rothlisberg et al. 1985, p. 23).

The biological value of knowing the circulation of offshore waters is that a predictive model for population dynamics could be developed that combines both ecological and physical-oceanographic information (Roughgarden et al. 1988, p. 1465). It follows from the above arguments that this value could also be extended from one measured in scientific terms to one realised in economic terms. Such a model would be more realistic than the "*stock-recruitment*" approach routinely applied to marine population dynamics. In this approach the larval input rate is regressed against the stock size with a second-degree polynomial, the coefficients of which are interpreted in terms of density-dependent mechanisms affecting fecundity, growth, and mortality. Such an approach would seem appropriate only if the larvae are confined to some small neighbourhood of the adult habitat (Roughgarden et al. 1988, p. 1466). An *analysis of variance* or a *multiple regression* type approach may also not be appropriate due to the dangers in applying such analyses to short series of data, and since the independent variable is not under the control of the experimenter (Zed 1980, p. 58). More fundamentally, if one looks extensively enough, a statistically significant correlation is sure to be found, but its biological relevance may be difficult to assess. This is because the factor found to correlate significantly with recruitment may have no direct role in determining recruitment but may be itself correlated to some other variable that does determine recruitment but which was overlooked by the investigator (Zed 1980, p. 59). In short, studies carried out at only one of the habitats tell no more than half the story. Study of both habitats involved in a two-phase life cycle—such as that of *P. latisulcatus* in Spencer Gulf—is, however, feasible both theoretically and in the field (Roughgarden et al. 1988, p. 1466).

1.2 *Penaeus latisulcatus* in Spencer Gulf

The physical processes of advection and diffusion play an important role in determining which organisms reach the recruitment site. In contrast, return of adults to the release site is probably influenced to a greater degree by biological processes (Hill 1991a, p. 127). This thesis, however, is not concerned with the return phase of the *P. latisulcatus* life cycle in Spencer Gulf.

The juveniles and adults exist in separate geographic areas (King 1980, p. (*ii*)), here labelled *inshore* and *offshore* for convenience, as shown in Figure 1.4. Little detail is known about the

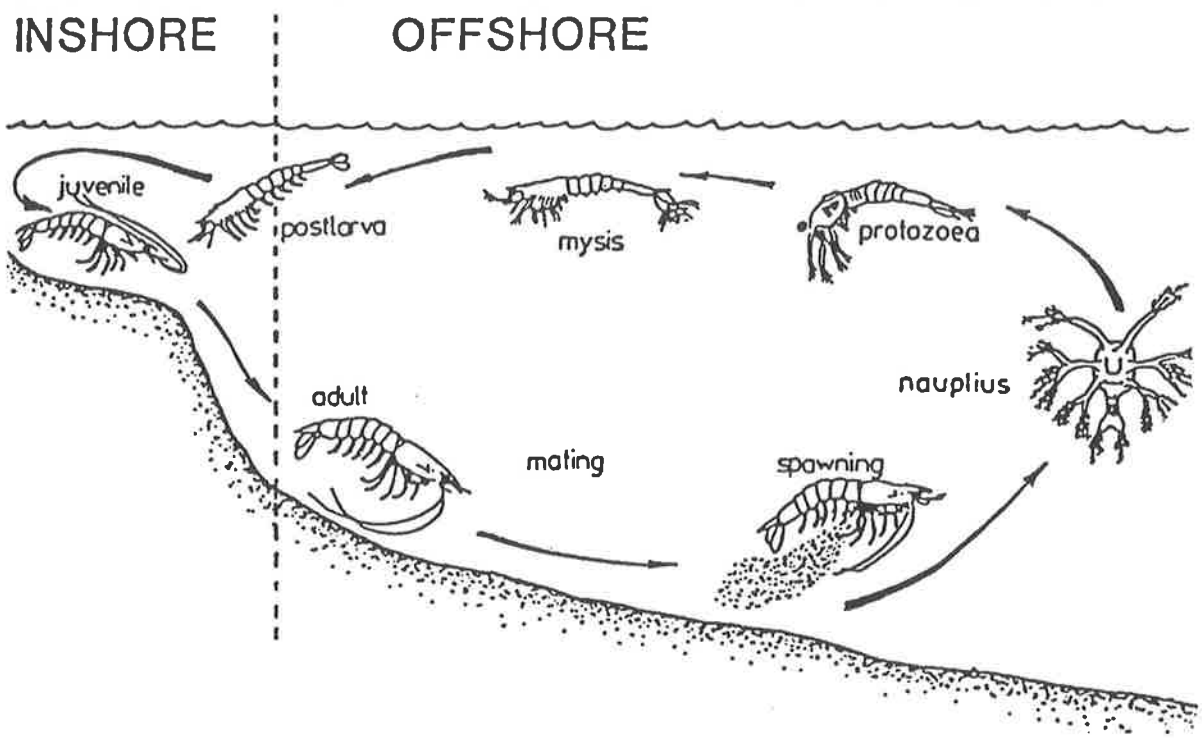

Figure 1.4: A typical penaeid prawn life cycle, showing three larval development stages: (1) nauplius, (2) protozoea, and (3) mysis (original source unknown). The dispersal period with which this thesis is concerned is depicted by the five arrows between the spawning–larval, larval–postlarva, and postlarva–juvenile stages. Note that this schematic is not to scale.

strictly larval and assumed pelagic phase of the penaeid life cycle (Kirkegaard 1975; Zed 1980), as individuals develop from fertilised eggs in open-water (i.e. offshore) spawning grounds to juvenile prawns settling, hopefully, in suitable coastal-water (i.e. inshore) nurseries. During this 3–4 wk period of their life cycle (Kirkegaard 1975, p. 55), the larvae are of such minute size (see Figure 1.5(a)) and limited horizontal locomotive ability (see Section 2.4) that they can essentially be considered buoyant passive particles subject to tidal currents, predators, and meteorological conditions (see Chapter 2). They are, however, of such large spatial distribution and low density that physical tracking or capture is usually difficult (John 1984; Fairweather 1991), and often expensive (Kirkegaard 1975, p. 57). Thus, rather than attempt a statistical regression type analysis of field data to determine larval spread from spawning grounds to nurseries in a particular breeding season, a more general deterministic mathematical modelling approach is used in this thesis. The model is based on larval transport in currents produced by tides and winds, dispersion due to small-scale eddy turbulence, and mortality due to predation, etc.

Larvae are found near the sea–surface at night and near the sea–bed during the day (see Section 2.4). Thus, sea current data is required from at least these two depth–levels for input to

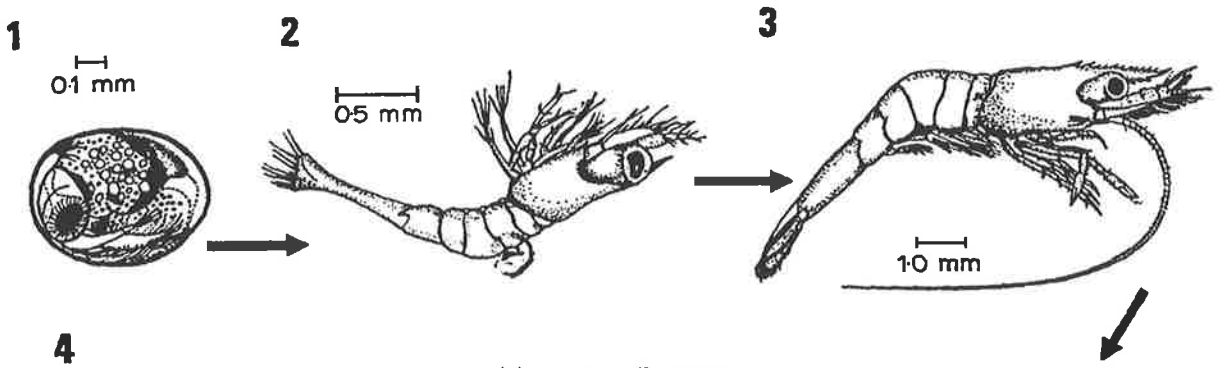

(a) pre-juvenile stages

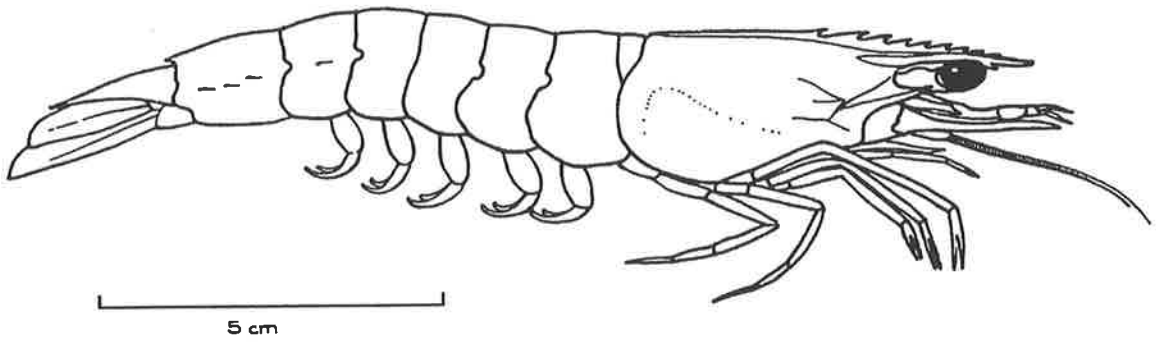

(b) post-juvenile stage

Figure 1.5: A typical prawn life cycle. (a) Pre-juvenile: **1** egg; **2** larva; and **3** postlarva (from Wickins 1976, Figure 4, of a cridean prawn, *Macrobrachium* sp.), and (b) Post-juvenile: **4** adult (from King 1980, Frontispiece, of the western king prawn, *Penaeus latisulcatus*).

an advection–diffusion–mortality model (see Chapter 7), which is applied at the near surface or near bed depth–level during the appropriate time interval. A three-dimensional hydrodynamic-numeric tidal model (see Chapter 3) incorporating spatially and temporally variable wind–stress (see Chapter 4), computes currents at the required depth–levels. A two-dimensional advection–diffusion–mortality model (see Chapter 8) is then sufficient to compute larval dispersion because: the details of larval traversal through the water column are uncertain (see Section 2.4); horizontal advection in Spencer Gulf is several orders of magnitude greater than vertical advection (Bills 1991, p. 288); and horizontal eddy diffusion in the Gulf is approximately 30 times that in the vertical (see Section 7.6).

1.2.1 The Cray Collaborative Research Grant

Under normal university or industry research conditions in Australia, projects of this nature could not progress beyond feasibility studies due to the enormous computational resources required by a complete study. Bills (1991) developed a numerical tidal model which predicted currents caused by winds and tides at approximately 800 locations in Spencer Gulf. Each prediction required the calculation of currents at ten depth–levels at each of these locations every 3 min for 1 mo of simulated time. This took over 15 h on a VAX 11/785 minicomputer (the machine available at the time at which Bills's (1991) work was commenced), nearly 4 h on a SPARCstation 1+ workstation (routinely used for research in the Department of Applied Mathematics at The University of Adelaide), but under 4 min on a CRAY Y-MP supercomputer (made available for the present work by Cray Research, Australia). The Bills (1991) tidal model

is the basis of the advection simulations in this thesis, but it has been significantly modified by Nixon (1992) to provide this level of performance on vector processor supercomputers. The new model predicts currents at ten depth–levels at approximately 6,000 locations every 1 min for 6 mo of simulated advection in approximately 9 h of supercomputer time.

1.2.2 The Fisheries Research and Development Corporation Project

Only two major research projects similar to this Fisheries Research and Development Corporation (FRDC) funded project (Nixon and Noye 1993a) have been described in the scientific literature, namely Bartsch et al. (1989) and Johnson and Hess (1990). This project is the first full-scale predictive study of the spread of prawn larvae based on field measurements of adult spawning to use a fully nonlinear and three-dimensional tidal model driven by field measurements of tide–heights and of surface wind velocities to compute currents at multiple depths, and to use these in a layered two-dimensional advection–diffusion model incorporating vertical larval migration. Preliminary studies to illustrate the feasibility of this project were carried out by I'Anson (1989), Wong (1990), and Noye et al. (1992). Results obtained from these tests were in qualitative agreement with Carrick's (1994) personal observations.

Results of this project (FRDC Project 91/004) were made available to FRDC personnel, SARDI fisheries officers, and SGWCPFA members, to assist in the development of resource management strategies for the Spencer Gulf prawn industry (Nixon 1993a, 1993b, 1994a, 1994b, 1995a, 1995b, 1995c; Nixon and Noye 1996a). Colour animated computer graphics displays (Doty 1992) were also used to present these results (Nixon and Noye 1993b), thus enabling these prawn fishing research and industry groups to quickly assess the enormous quantity of data produced, and to devise management strategies for the sustainable harvesting of this resource. Comparing model results with the results of SARDI field studies presently under statistical analysis will, it is hoped, assist in fine-tuning model input parameter specifications, which in turn should lead to more accurate modelling.

It is with the background of environmental and scientific interest that the modelling of prawn larvae dispersion has been approached. Could the observed features of *Penaeus latisulcatus* larvae dispersion in Spencer Gulf be reproduced by a new numerical approach? If so, perhaps new features might be predicted, leading to a greater understanding of larval transport in this region. With enhanced understanding there might emerge a firmer basis for the more informed management of, and greater concern and respect for, the Spencer Gulf prawn fishery.

The models developed ought also to be stable and flexible. As the need arises to investigate different aspects of the Gulf's transport dynamics, the models should be able to be extended and applied easily. The computer programs should also be able to be used to model other coastal regions. It is felt that these criteria have been successfully fulfilled by the models described and developed in this thesis.

1.3 Chapter Synopses

Chapter 2 describes aspects of the biology of the western king prawn that have a direct bearing on the manner in which the determination of prawn larvae dispersion by mathematical and/or numerical models must be approached.

Chapter 3 contains the mathematical formulations of the tidal equations solved in order to provide advection velocities to a numerical model of larval dispersion. These equations are well known and standard throughout tidal modelling literature. The tidal model is, however, described in sufficient detail to enable certain aspects of its construction to be discussed in the remainder of this thesis, in particular within Chapters 5 and 7. Surface stress terms are included in the equations to incorporate wind effects since, in the case of the movement of prawn larvae, these are deemed to be of great importance.

Chapter 4 describes the nature of the available wind data pertaining to the Spencer Gulf region, and the scheme used to interpret these data and provide them in a suitable form as

input to the tidal model.

Chapter 5 describes the optimisation of the tidal model for a supercomputer architecture. The numerical scheme of the three-dimensional program is modified to run efficiently on the vector processors of a CRAY Y-MP. Six-month tide and tide and wind forced simulations of the entire prawn larvae dispersion period, spanning peak spawning and settlement periods, are required to be conducted as part of developing sound management strategies for the prawn fishery in Spencer Gulf. Efficient supercomputer-class performance is thus required.

Chapter 6 describes a high resolution application of the numerical model to predict tide and tide and wind induced currents at over 6,000 locations in Spencer Gulf. The calibration of the high resolution model, and other interesting aspects of carrying out such large scale computations, are also discussed.

Chapter 7 describes the advection–diffusion–mortality scheme used to model prawn larvae movement in Spencer Gulf. Aspects of the scheme required to adequately model the biological behaviour of prawn larvae are discussed. A review of the literature concerning analytical models previously used to represent similar biological advection, diffusion, and mortality processes is also presented.

Chapter 8 describes in detail one- and two-dimensional equations governing advection and diffusion, and presents specific finite-difference methods for the solution of these equations to a collection of advection–diffusion problems. Alternative methods are discussed in terms of numerical stability, theoretical accuracy, and experimental accuracy of solution with respect to an idealised problem. A "best" method for the approximation of larval dispersion is chosen from the alternative methods, taking into account the properties and performance of each, and the desired characteristics of a hypothetical "ideal" method.

Chapter 9 presents a review of the literature concerning numerical models previously used to represent similar biological advection, diffusion, and mortality processes. The methods of solution associated with these models are analysed with respect to that of the larval dispersion model developed in this thesis.

Chapter 10 describes the simulations performed to predict prawn larvae dispersion during spawning seasons corresponding to periods in the past. The relationship between predictions made by the numerical model, parameters input to the model, and observations made by field researchers is discussed.

Chapter 11 describes the possible future extensions of the present prawn larvae dispersion model as more quantitative information concerning larval biology, more reliable estimates of input parameters, and greater computing power become available.

Chapter 12 summarises what has been achieved in this thesis, and what the author feels could be achieved in the future, with respect to numerical prawn larvae dispersion modelling.

Chapter 2

Penaeid Prawn Biology

Three types of prawn life cycle have been distinguished: ocean prawns, which spend both their larval and adult phases offshore; estuarine prawns, which spend their entire life cycle in estuaries or creeks; and prawns which spend their juvenile phase inshore and their adult phase offshore in deeper water, with migrations between. The most prolific species of prawns, and therefore the most commercially exploited species, belong to the third category (Kirkegaard 1975, p. 54). In these species spawning takes place offshore, fertilisation is external, and the eggs are shed near the sea–bottom. The important commercial species with the mixed life cycle and high levels of abundance are king prawns, banana prawns, and greasyback or greentail prawns.

Penaeid prawns are distributed worldwide in tropical to temperate latitudes (Rothlisberg et al. 1987, p. 1). Distribution of *Penaeus latisulcatus* within Australian waters is shown in Figure 1.1. The *Penaeus* family is arguably the most valuable group of marine species in the world (Rothlisberg et al. 1987, p. 1). The primary reason the larval ecology of penaeids has not been pursued in Australia, and indeed world-wide, is the lack of taxonomic resolution of the early larval stages (Rothlisberg et al. 1985, p. 23). It is, however, known that *P. latisulcatus* larvae exist in nauplius, zoea (possibly three sub-stages), mysis (possibly three sub-stages), and postlarva stages (Rothlisberg et al. 1985, Table 1). *P. latisulcatus* larvae have been reared at a commercial prawn culture enterprise at Port Broughton (see Figure 1.3), where up to six naupliar sub-stages have been observed (Zed 1980, p. 12). The four main stages are illustrated in Figure 1.4 (not to scale). The relative size of a prawn egg, larva, and postlarva is illustrated in Figure 1.5(a) (with appropriate scales). Typically, penaeid nauplii hatch from the eggs 10–15 h after spawning and subsist on yolk reserves for 2–3 d until active feeding occurs in the first protozoeal stage. The larva moults to the mysis stage after 3–4 d and to the postlarva after a further 3–5 d. During this time it may pass through as many as 11–14 moults (Zed 1980, p. 12). The rate of development is dependent on temperature, food, and water quality, but in good conditions development to the postlarval stage occurs within 11–21 days (Wickins 1976). Following the nauplius, protozoae, and mysis larval stages, the postlarvae reach and settle in shallow "nursery" areas on the coast. Here, the juveniles grow to sub-adults before migrating offshore to join the adult stock. Penaeid fisheries are therefore based on "annual crops" of newly recruited prawns. The fishing and natural mortality in most prawn fisheries is generally thought to be high enough to allow only a small number of individuals to reach their second year offshore (King 1980, p. 3).

Although annual stock sizes fluctuate widely, few stock-recruitment relationships have been demonstrated, and the role of the environment in larval and postlarval mortality is poorly known. These relationships are likely to be complex, given that most species complete their life cycles in a variety of coastal habitats, and have high growth rates and short life spans. In addition they are highly fecund and the larvae hatch at a primitive stage of development, undergoing marked changes in morphology, behaviour, food requirements, and habitats during their short planktonic life (Rothlisberg et al. 1987, p. 1). Some of these points are depicted in Figure 1.4 (schematically) and Figure 1.5 (in detail).

Most biologists assume that marine population fluctuations are somehow caused by events in the offshore waters, since the dynamics of a two-phase (larval and adult) species can, in principle, be affected at either phase (Roughgarden et al. 1988, p. 1460). Because of the number of biological and physical linkages between the life history stages in their different habitats, only multidisciplinary studies, over extended periods, will explain the complex factors that affect recruitment at each stage. Recruitment dynamics at each life history stage are, however, controlled by the complex interaction of seasonal hydrological and meteorological events (Rothlisberg et al. 1987, p. 14). The hydrographical environment in which the larvae are found may account, in part, for the patterns of larval distribution and ultimately for the distribution of the species (Rothlisberg and Jackson 1987, p. 20).

Because most coastal marine populations have a two-phase life cycle, the reason why such populations fluctuate is a general question in biology, and one whose answer affects thousands of species many of which have commercial, recreational, or conservation value. To ascertain whether larvae are bound to return to their adult habitat requires analysing the circulation pattern in the offshore water column (Roughgarden et al. 1988, p. 1461). Whether the community ecology at a site is governed by adult-adult interactions within the site, or by limitations to the supply of larvae reaching the site, is determined by the regional pattern of circulation in the coastal waters. Models combining larval circulation with adult interactions can thus potentially forecast population fluctuations (Roughgarden et al. 1988, p. 1460).

In this chapter, aspects of the biology of penaeid prawns in general, and *Penaeus latisulcatus* in particular, that have a direct bearing on the manner in which prawn larvae dispersion may be determined by mathematical and/or numerical models will be discussed. Since the portion of life cycle with which the proposed model is concerned does not include juvenile and adult behaviours, these discussions will be limited to theoretical models of, and experimental evidence for, processes pertinent to larvae dispersal, as distilled from the literature. Simplifications and approximations will be made according to the manner in which these processes may be further qualified in mathematical models and then quantified in numerical models.

2.1 Larval Spawning

Marine species commonly have broadly dispersing life stages collectively called larvae. Their return to the adult populations is highly variable, often generating large fluctuations in population size, and the causes of the variation are poorly understood. Historically, attention has been focussed on large fluctuations in population size being due to variable reproductive output by adults and variable mortality during larval development (Gaines and Bertness 1992, p. 579).

In this section, qualitative information concerning spawning behaviour, which is considered applicable to numerical models of larval dispersion, is gleaned from the literature. Quantitative information concerning *Penaeus latisulcatus* spawning in the Spencer Gulf region is also presented. In Section 2.1.1 spatial variability of larval concentrations corresponding to particular spawning seasons is illustrated. This is only possible for the fact that detailed spatial surveys have recently been taken. In Section 2.1.2 temporal variations in observed spawning behaviour are discussed. Detailed temporal surveys of this species in this region are, in contrast, less abundant. The paucity of available data approaches that for *Acanthaster* larvae in the Great Barrier Reef (off the north-eastern coast of Australia, in the vicinity of Bowen indicated in Figure 1.1) where, within each season, there is no knowledge of the timings of spawning events (Scandol and James 1992, p. 573).

It is known, however, that *Penaeus* species generally reach maturity within one year of hatching and are probably capable of spawning three to five times during their life (Wickins 1976). Penaeids are also among the most fecund of the Natantia and can release 100,000 to 1,000,000 eggs at a single spawning (Zed 1980, p. 11). The spawning data presented in this section, and particularly the units used to described those data, will reflect this observation.

2.1.1 Spawning Grounds

In a study assessing the reproductive activity of five species of *Penaeus* in the Gulf of Carpentaria (indicated in Figure 1.1), it was found that reproductive output varied geographically and from year to year within and between species (Rothlisberg et al. 1987, p. 14). However, in a study of the *Penaeus latisulcatus* species in Spencer Gulf, it was found that females with well developed ovaries appeared to be widely distributed over the fishing grounds and that there was no evidence to suggest the existence of particular or well defined spawning areas (King 1980, p. 95).

The major prawn grounds of the Spencer Gulf *P. latisulcatus* fishery are restricted in depth ranging from 15 to 40 m (Carrick 1982, p. 3). The fishing grounds form two broad regions:

1. The southern grounds situated south of a line extending from Shoalwater Point Beacon to Webling Point. The major grounds are known as the Gutter, the Western Gutter, Wallaroo, and Cowell (now closed to fishing).

2. The northern region, situated north of a line from Shoalwater Point Beacon to Webling Point and bound in the north by a line extending from Point Lowly to the northern light at Eastern Shoal, thence to Port Germein. The main grounds are called Middlebank, Yarraville Basin, Stones, Teardrops, Musgrave Shoal, Port Broughton (now closed to fishing), and the Eastern Shoal–Lowly Channel.

as defined by Carrick (1982). The locations of many of these places are depicted in Figures 1.2–1.3 above. Others are indicated, indirectly, in the spawning grounds of Figures 2.1–2.2 below, as derived from SARDI spawning data (Carrick 1989 and 1994, personal communications) and the information listed in Table 2.1. As can be seen from these figures, the prawn fishing grounds of

Spencer Gulf Major Spawning Grounds	
Region (number)	Ground (name)
?	Port Broughton
1	*unnamed*
2	Eastern Shoal–Lowly Channel
3	Musgrave Shoal
3	Teardrops
4	Stones
5, 6	Yarraville Basin
7	Middle Bank
8	Wallaroo
9, 13	Gutter
10–12	Cowell
14	Western Gutter
(11)–(12)	Southern Gutter

Table 2.1: The major *Penaeus latisulcatus* spawning grounds in Spencer Gulf, South Australia. Listed for each is its region number (see Figures 2.1–2.2) and ground name (from Carrick 1982).

Spencer Gulf are relatively small compared to the overall size of the Gulf (Carrick 1982, p. 4). The extent of the fishery appears to be restricted to the relatively consistent fishing grounds described above. However, periods of unusual hydrological conditions could result in irregular occurrences of the species in areas beyond the limits of the present fishery (King 1980, p. 59). It has been reported (Noye et al. 1992, p. 389) that statistical f-tests on the spawning capacity of female adults indicate that, in general, prawns in the Yarraville Shoals spawning ground of

the northern Spencer Gulf region were able to produce more eggs compared to those in other spawning grounds (Carrick 1990, personal communications).

More recently, in an annual report for 1994 on the research and management of the Spencer Gulf prawn fishery, Carrick noted that the northern regions in the vicinity of Whyalla and Port Pirie are important spawning areas (Anonymous 1994, p. 12). In Sections 2.1.3–2.1.5, data supplied by Carrick (1989 and 1994, personal communications) is used to define quantitative spawning initial conditions, geographically defined by trawls for spawning adults carried out by SARDI research officers.

2.1.2 Spawning Periods

In a study assessing the reproductive activity of five species of *Penaeus*, it was found that two seasonal peaks of reproduction were common in *Penaeus latisulcatus* in most areas of the Gulf of Carpentaria (Rothlisberg et al. 1987, p. 1). Early studies of fertility determined that a peak in ovary development occurred around November for *P. latisulcatus* in Spencer Gulf (King 1980, p. 2), and suggested that there was a second peak in the early months of the following year. The data indicated that older prawns contributed to the spawning stock in November, and that from December to March newly recruited prawns were added to form a second peak in ovary development (King 1980, p. 95). More recently, it has been observed that spawning activity of *P. latisulcatus* in Spencer Gulf takes place from October to March with an indication of two peaks—one in mid-December and another in January/February (Carrick 1991, p. 4 and Figure 2). It has also been shown that intensive spawning activity is generally related to a rise in water temperature (Zed 1980, p. 11).

2.1.3 Spawn Concentrations Measured

Data supplied by Carrick (1989 and 1994, personal communications) can be used to derive quantitative spawning initial conditions for prawn larvae dispersion simulations, geographically defined by trawls for spawning adults carried out by SARDI research officers. This derivation makes use of the finite-difference grid defined for the fine resolution Spencer Gulf numerical models, as described in Chapter 6 below.

Missing data could not, of course, be used in deriving these initial conditions. Some entries were marked "*", " ", and "CK" in the supplied data. Such entries, as well as entries for which a value of 0.0 was listed, were treated as missing data. Some trawl location coordinates were derived from the coordinates of nearby trawls, due to insufficient information supplied. All spawning trawl location coordinates were approximated from hydrographic maps (Royal Australian Survey Corps 1982a, 1989), since the trawl coordinates themselves were not supplied. These approximations thus introduced small errors in trawl location positioning.

Some years for which egg production data were supplied, were not used in deriving initial conditions for the corresponding trawl location regions, since there were insufficient data for these years at these regions. Some trawl locations were also not used in deriving *any* initial conditions since there were insufficient data at these locations.

All spawning trawl locations derived from data supplied are illustrated in Figures 2.1–2.2. Trawl locations are indicated by solid straight line segments between the northern and southern endpoint coordinates. Locations used in deriving initial conditions have the trawl midpoint indicated, with a crossed circle for location coordinates supplied, and with a crossed square for location coordinates derived from location coordinates supplied. Locations not used in deriving *any* initial conditions have the trawl midpoint indicated with an uncrossed circle. Trawl regions are indicated with closed curves enclosing the appropriate locations. These curves are defined by grid–points associated with the fine resolution Spencer Gulf model grid (see Chapter 6 below) which result in trawl region boundaries approximately enclosing the appropriate regional set of trawl location endpoints. Those regions not used in deriving *any* initial conditions have dashed curves as boundaries, and those used have solid curves as boundaries.

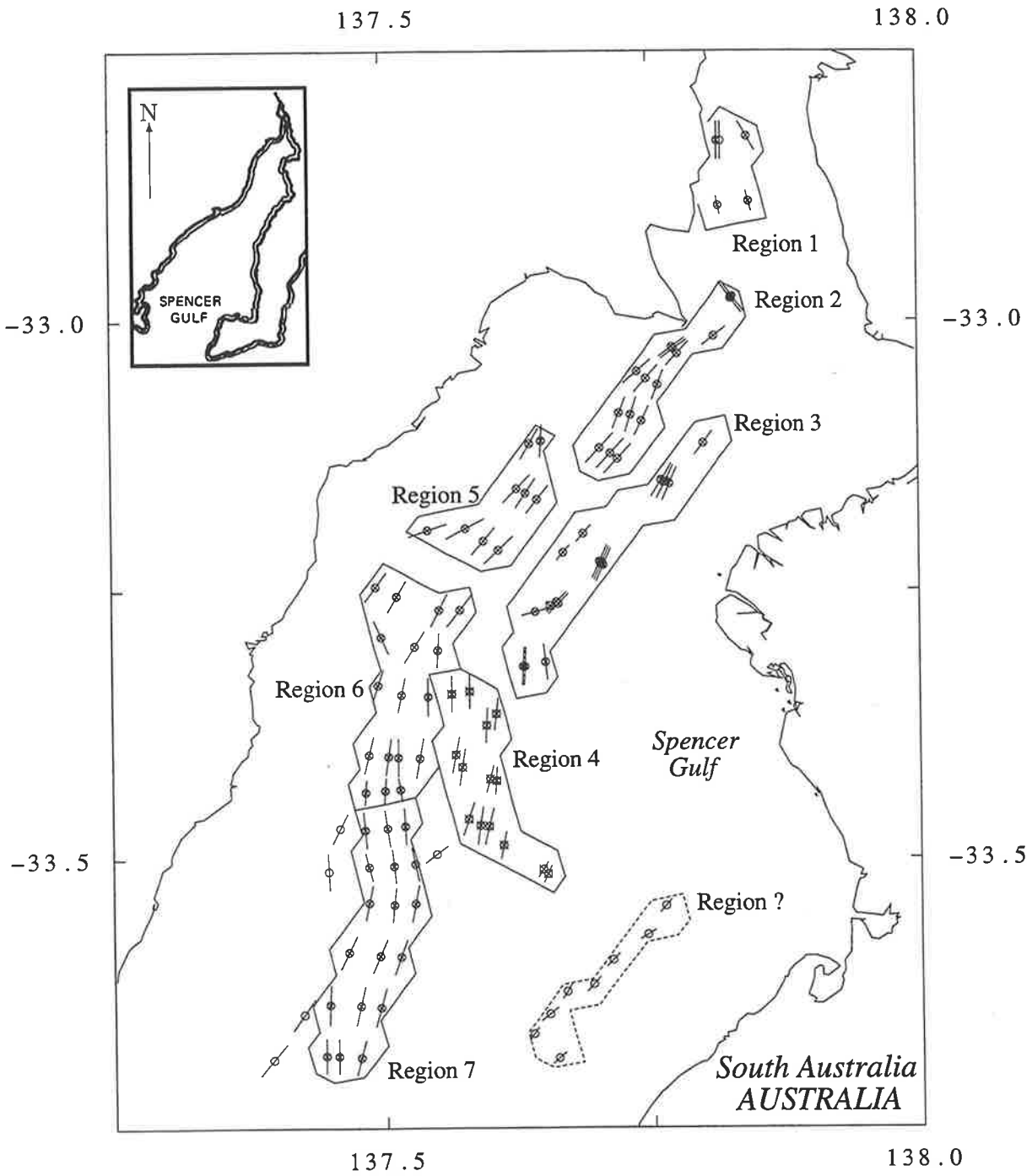

Figure 2.1: Spawning trawl locations in northern Spencer Gulf, South Australia. Coordinates for locations at which spawning data were supplied, calculated as midpoints of associated endpoints (circles), and derived from midpoints of known locations (squares) are shown. Trawl locations for which data were supplied (crossed midpoints), and for which data were not supplied (hollow midpoints) are differentiated. Region boundaries determined by data availability and fine resolution Spencer Gulf model grid location, as discussed in the text, are also shown. The x and y axes indicate longitude (°E) and latitude (°N), respectively.

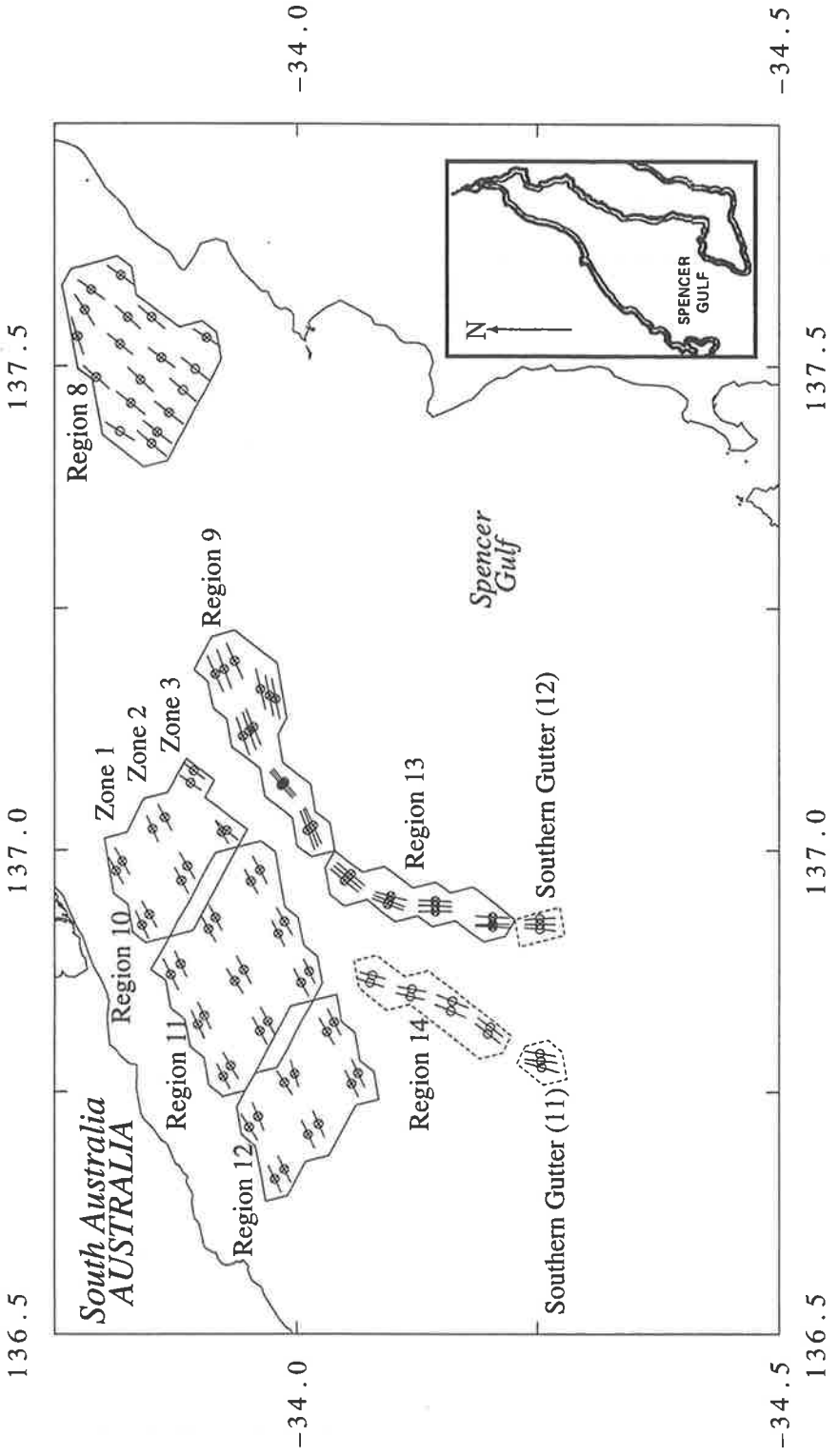

Figure 2.2: Spawning trawl locations in southern Spencer Gulf, South Australia. Coordinates for locations at which spawning data were supplied, calculated as midpoints of associated endpoints (circles), and derived from midpoints of known locations (squares) are shown. Trawl locations for which data were supplied (crossed midpoints), and for which data were not supplied (hollow midpoints) are differentiated. Region boundaries determined by data availability and fine resolution Spencer Gulf model grid location, as discussed in the text, are also shown. The x and y axes indicate longitude (°E) and latitude (°N), respectively.

2.1.4 Spawn Concentrations Derived

To determine, from the available egg production data, initial conditions for prawn larvae dispersion, these data were augmented by fitting a thin-plate smoothing spline to a set of control points. The data were then interpolated/extrapolated by evaluating this spline on a regular grid (as in Figures 2.3–2.9 depicting gridded surfaces), or at a set of grid–points (as in Figures 2.10–2.15 depicting level curves). This was achieved using `rkpack` (Gu 1989), a minipackage which forms a core for fitting various kinds of smoothing spline models, in which the smoothing parameters are chosen by a practical data-driven method for selecting them, known as generalised cross validation (GCV).

In the following figures measured data, as supplied by SARDI, are depicted using vertical lines from the datum coordinate to a diamond ($\diamond$) at the datum value. A plus (+) depicts the interpolated value. This gives both an indication of the datum location and of the difference between the measured and interpolated values at that location. Surfaces are depicted to indicate the overall "shape" of the interpolated data.

Smoothed Data

The GCV procedure results in what is essentially a compromise between data smoothing and data fitting. As can be seen from Figure 2.3, calculated using 1991–1994 egg production data from the

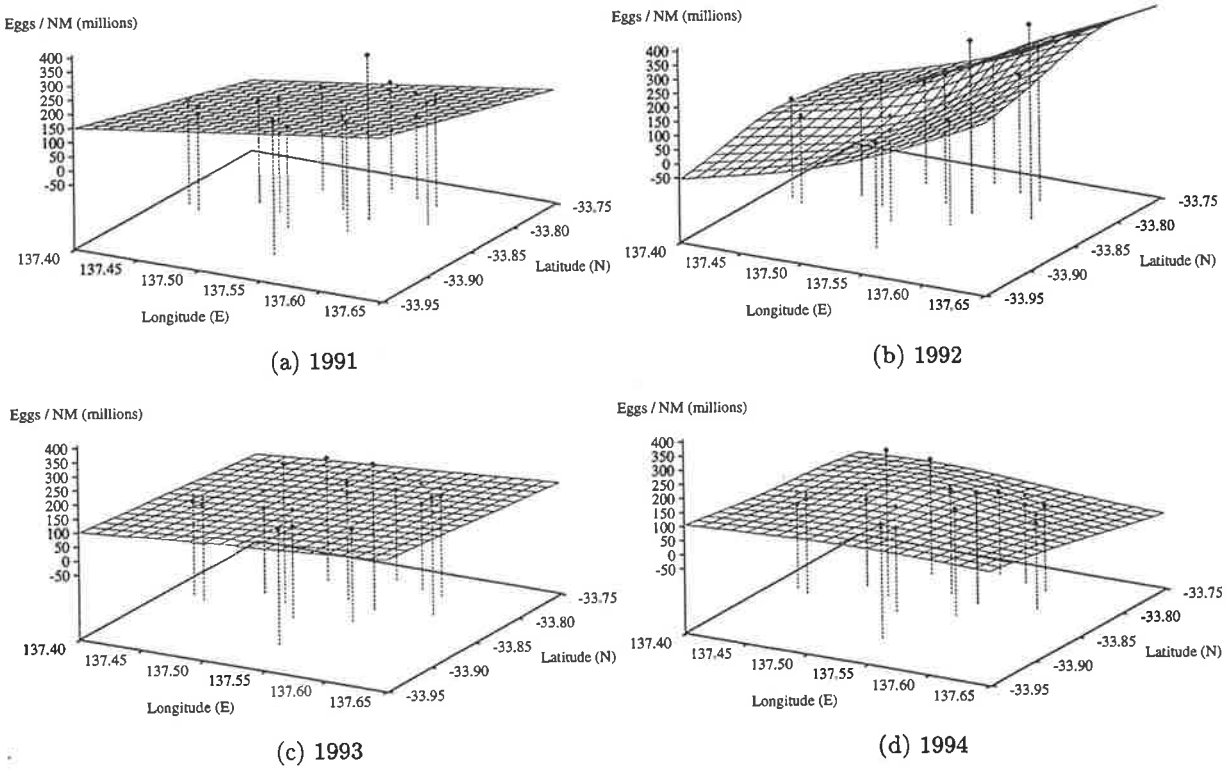

(a) 1991

(b) 1992

(c) 1993

(d) 1994

Figure 2.3: Measured (diamonds) and smoothed (pluses) egg production (millions) per nautical mile for the Wallaroo spawning ground (Region 8). The interpolated surfaces are shown with x and y axis grid–spacings of 0.0125° longitude (E) and 0.0125° latitude (N), respectively.

Wallaroo (Region 8) spawning ground, this procedure can thus result in large differences between measured and smoothed values. This may result in surfaces which undershoot/overshoot the data, as in Figure 2.3(b); those which represent a gentle peak, as in Figure 2.3(d); and those in which the compromise is so great that they are essentially planar, as in Figures 2.3(a) and 2.3(c).

As can be seen from Figure 2.4, calculated using 1988 and 1992–1994 egg production data

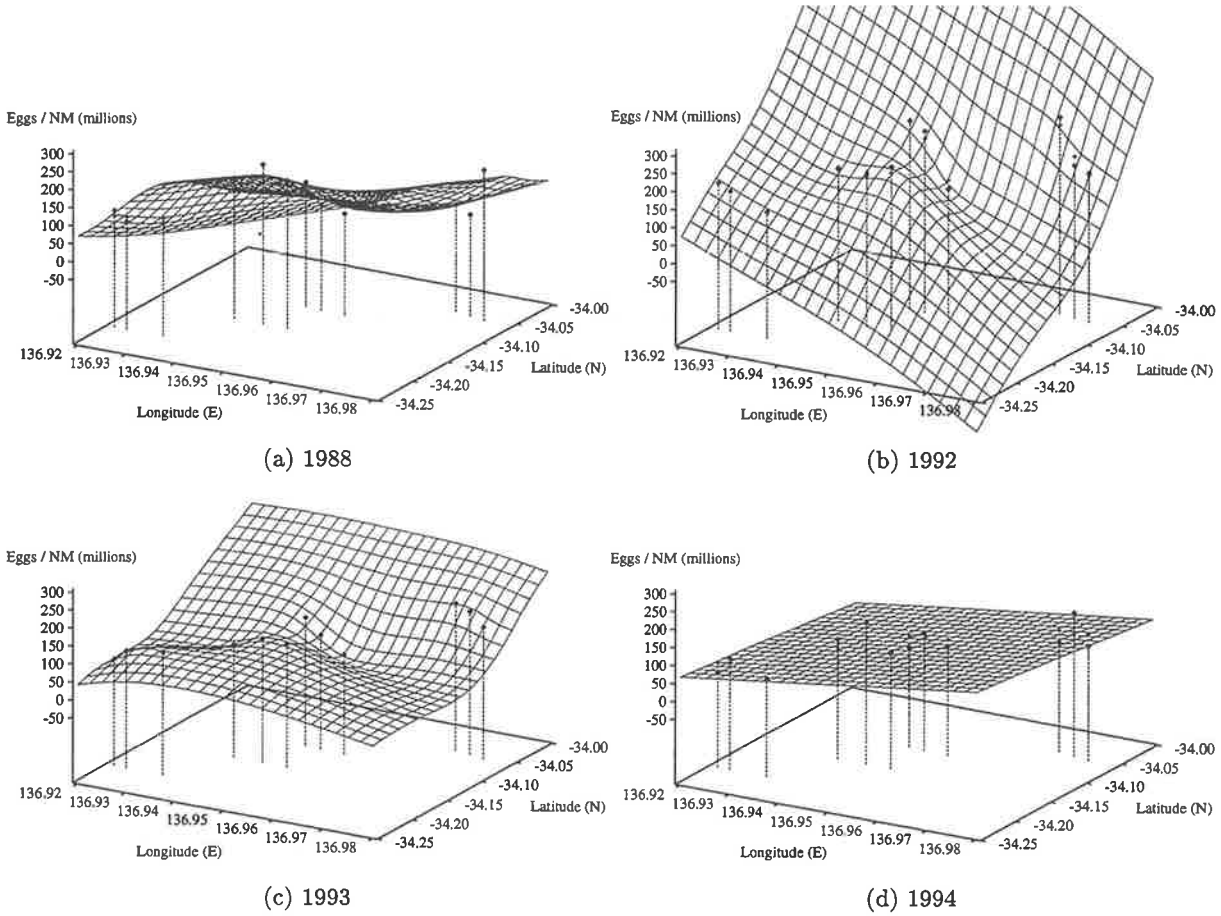

(a) 1988 (b) 1992

(c) 1993 (d) 1994

Figure 2.4: Measured (diamonds) and smoothed (pluses) egg production (millions) per nautical mile for the Gutter spawning ground (Region 13). The interpolated surfaces are shown with x and y axis grid–spacings of 0.0025° longitude (E) and 0.0125° latitude (N), respectively.

from the Gutter (Region 13) spawning ground, this procedure can also result in smaller differences between measured and smoothed values. This may, however, still result in surfaces which undershoot and/or overshoot the data, as in Figures 2.4(b) and 2.4(c); those which are gently curved, as in Figure 2.4(a); and those in which the compromise is still so great that they are essentially planar, as in Figure 2.4(d).

It should be noted that the number and position of measured data points for each of the years depicted within these figures are identical, and hence that the difference in the character of the smoothing surfaces is not an artifact of "missing" or "relocated" data. Between year differences are, therefore, a function only of the data themselves and the GCV procedure used for smoothing and interpolation.

Derived Data

Since most of the data for nearly all of the trawl regions suffer from the deficiencies described above for two representative regions, data were re-interpolated using trawl regions which are more defined spatially. Control points consisting of zero values at all fine resolution Spencer Gulf grid locations immediately surrounding the region boundaries depicted in Figures 2.1–2.2 were added, and the smoothing and interpolating process using the GCV procedure repeated.

For the Wallaroo (Region 8) spawning ground, the inclusion of additional control points avoided the planar nature and undershoot/overshoot of the surfaces fitted only to the data as

originally supplied. This can be seen on comparison of the surfaces in Figure 2.5 with those

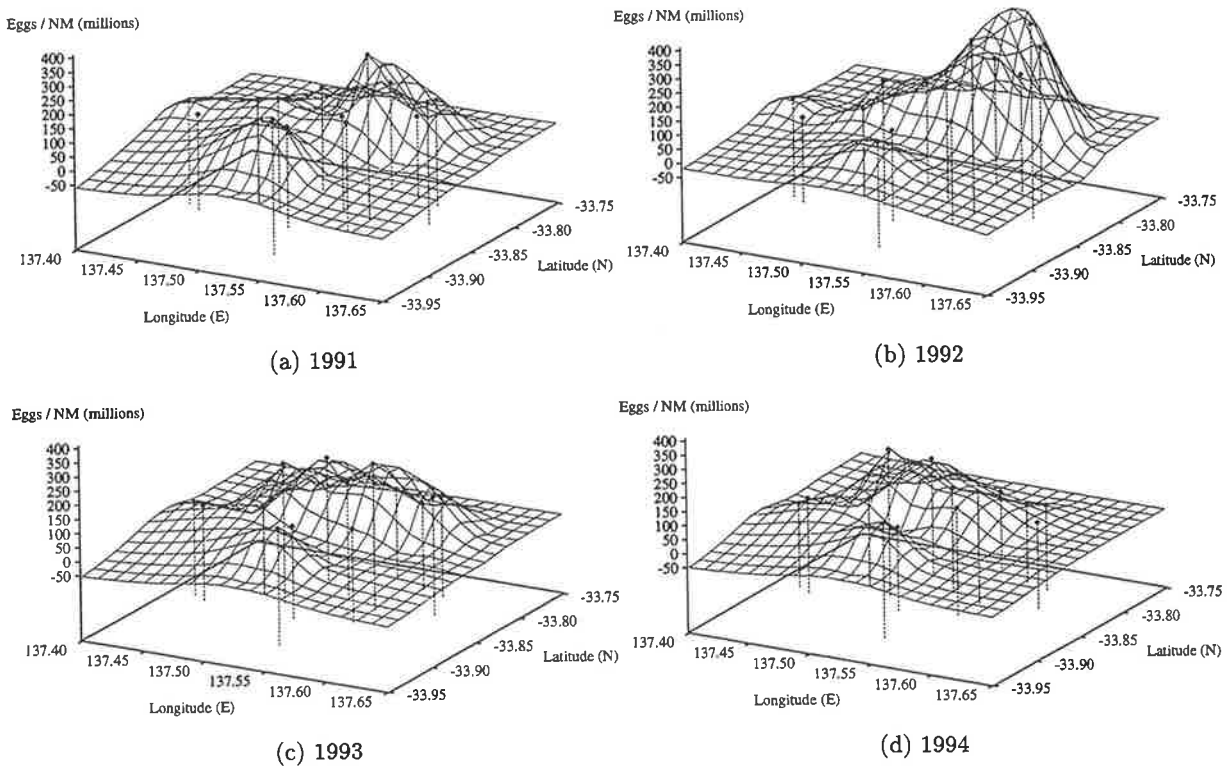

Figure 2.5: Measured (diamonds) and derived (pluses) egg production (millions) per nautical mile for the Wallaroo spawning ground (Region 8). The interpolated surfaces are shown with x and y axis grid–spacings of 0.0125° longitude (E) and 0.0125° latitude (N), respectively.

in Figure 2.3. Compared to the smoothed data, the derived data are such that the differences between measured and interpolated values are significantly smaller. The interpolated surfaces also better represent egg production peaks, since these peaks are more localised to the region of interest.

For the Gutter (Region 13) spawning ground, a similar improvement is obtained, as can be seen on comparison of the surfaces of Figure 2.6 with those of Figure 2.4. Compared to the smoothed data, however, the derived data are such that the differences between measured and interpolated values are unfortunately larger, but the surfaces once again better represent localised egg production peaks.

The inclusion of additional control points also made thin-plate spline construction possible in regions for which this was not originally possible, using only the data supplied, due to insufficient control points for the surface fitting algorithm. Measured and smoothed data for Region 1 (1988) and Region 3 (1991, 1992, and 1993) are shown in Figure 2.7. These indicate that, with few non-zero control points, surface fitting can result in small differences between measured and derived values. It is interesting to note the qualitative difference between Region 3 egg production during 1991, in Figure 2.7(b), and during 1992 and 1993, in Figures 2.7(c) and 2.7(d), respectively. Also of interest is the qualitative similarity of, but quantitative difference in, Region 3 egg production during 1992 and 1993, in Figures 2.7(c) and 2.7(d), respectively.

Combined Data

The inclusion of additional zero-valued control points immediately surrounding *all* spawning trawl regions would result in data inconsistencies in the fine resolution Spencer Gulf grid, as can be appreciated from Figures 2.1–2.2 and the region boundaries indicated therein. The measured

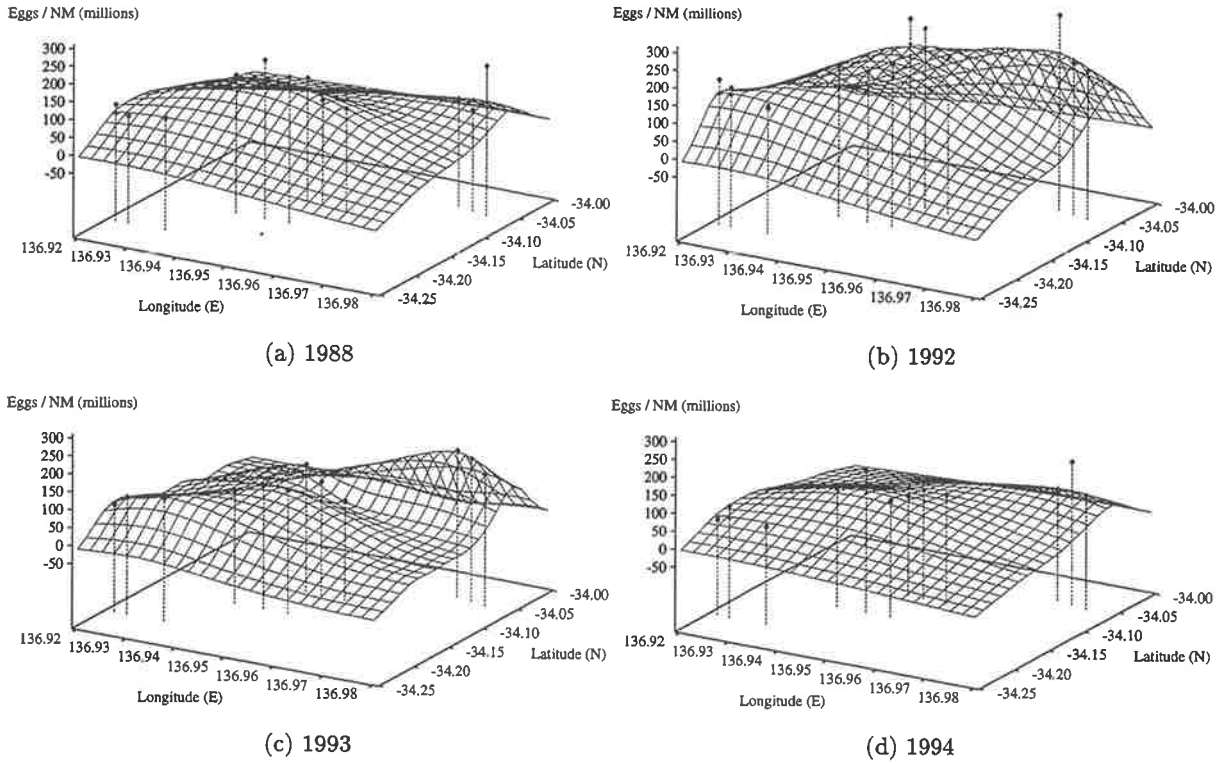

Figure 2.6: Measured (diamonds) and derived (pluses) egg production (millions) per nautical mile for the Gutter spawning ground (Region 13). The interpolated surfaces are shown with x and y axis grid–spacings of 0.0025° longitude (E) and 0.0125° latitude (N), respectively.

data were thus grouped into more physically distinct *combined* trawl regions before the additional control points were defined immediately surrounding the combined regions. Measured data points and interpolated thin-plate surfaces derived in the combined region of interest for northern Spencer Gulf spawning (i.e. trawl Regions 2–7) during 1994 are shown in Figure 2.8 and in Figure 2.9. In both figures, values of the raw and interpolated data are indicated (at top left) in subfigures (a) with diamonds ($\diamond$) and pluses (+), respectively, at the measurement locations, which are themselves indicated with vertical lines. This serves to depict the difference between measured ($\diamond$) and interpolated (+) values. In subfigures (b) (at top right), the interpolated surface is shown. This serves to depict the overall shape of the interpolated data. The interpolated surface with all interpolation-produced negative values set to zero is plotted (at bottom left) in subfigures (c), at the same scale as subfigures (b), so as to show an overview, and to facilitate comparison between the two subfigures. This same truncated interpolated surface is plotted (at bottom right) in subfigures (d), at the same scale as subfigures (a), so as to show more detail, and to facilitate comparison between the two subfigures.

In Figure 2.8 smoothing was carried out using control points from only the data provided. In Figure 2.9 derivation was carried out using control points from both the data provided and zero values immediately outside the combined region of interest. As can be seen on comparison of Figure 2.8(b) with Figure 2.8(c) and Figure 2.9(b) with Figure 2.9(c), data truncation results in a more defined egg production "peak" in the region of interest. This is more evident in the latter case, where more severe undershoot—a result of the additional control points—is negated. This greater definition through data truncation results in no significant increase in differences between measured and interpolated values, as can be seen on comparison of Figure 2.8(a) with Figure 2.8(d), and Figure 2.9(a) with Figure 2.9(d). Data truncation also results in non-negative initial conditions for prawn larvae concentrations, derived from spawning trawl egg production

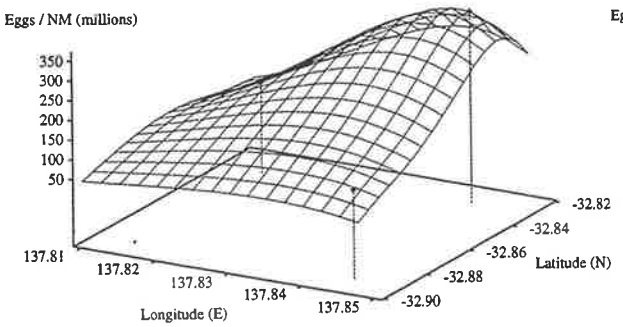

(a) Northern Region 1, 1988, with grid–spacings of 0.0025° longitude (E) and 0.005° latitude (N)

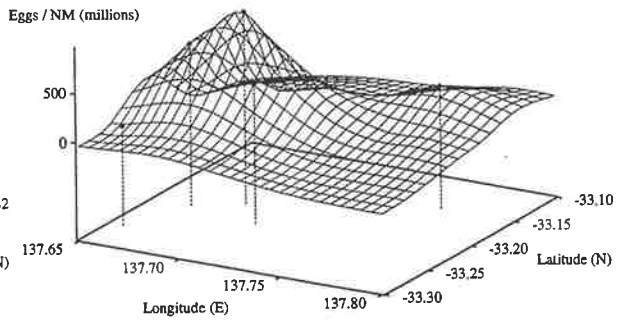

(b) Northern Region 3, 1991, with grid–spacings of 0.005° longitude (E) and 0.0125° latitude (N)

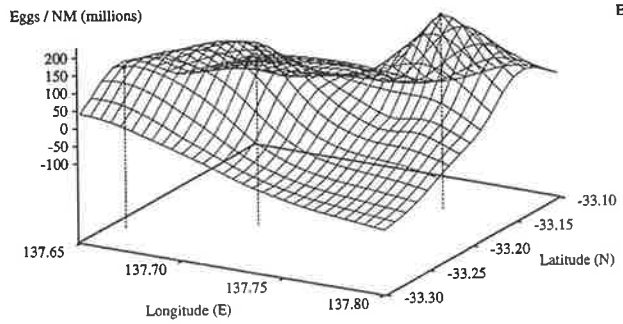

(c) Northern Region 3, 1992, with grid–spacings of 0.005° longitude (E) and 0.0125° latitude (N)

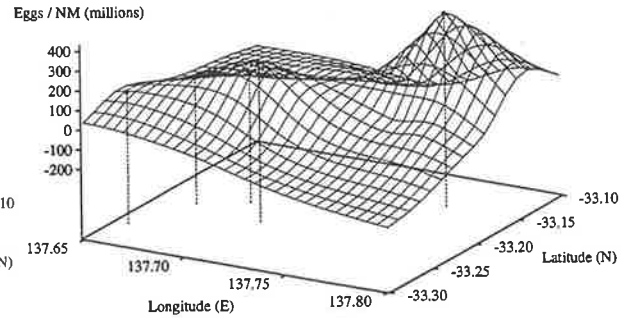

(d) Northern Region 3, 1993, with grid–spacings of 0.005° longitude (E) and 0.0125° latitude (N)

Figure 2.7: Measured (diamonds) and derived (pluses) egg production (millions) per nautical mile for trawl location regions with initially insufficient data for thin-plate surface fitting.

data which are, by definition, non-negative. This is of course a highly desirable characteristic for any concentration initial condition.

2.1.5 Spawning Initial Conditions

In the following then, data are combined—in the manner discussed above—from spawning trawl Regions 1–7 to form a combined northern spawning ground, Regions 10–12 to form a combined Cowell spawning ground, and Regions 9 and 13 to form a combined Gutter spawning ground, with Region 8 forming the Wallaroo spawning ground.

Initial Condition Assumptions

The egg production values supplied by SARDI were calculated from data obtained by trawling between known trawl location endpoints and determining the number of pregnant adult female prawns in the trawl. Account was taken for the average number of eggs per prawn, itself calculated using certain statistical assumptions (Carrick 1994, personal communications). There are a number of other assumptions which must be made when deriving initial conditions for prawn larvae concentrations from the spawning trawl egg production data provided.

Since no exact dates for spawning trawls were available, it may be assumed that the trawls at each location for each year took place over exactly the same time period and that this was of infinitesimal duration, resulting in a purely instantaneous spawning event. Failing that, it may be assumed that the trawls took place over essentially the same time period and that this was of sufficiently small duration that the spawning rates at all locations can be considered constant over that period, resulting in a time-averaged instantaneous spawning event. Given

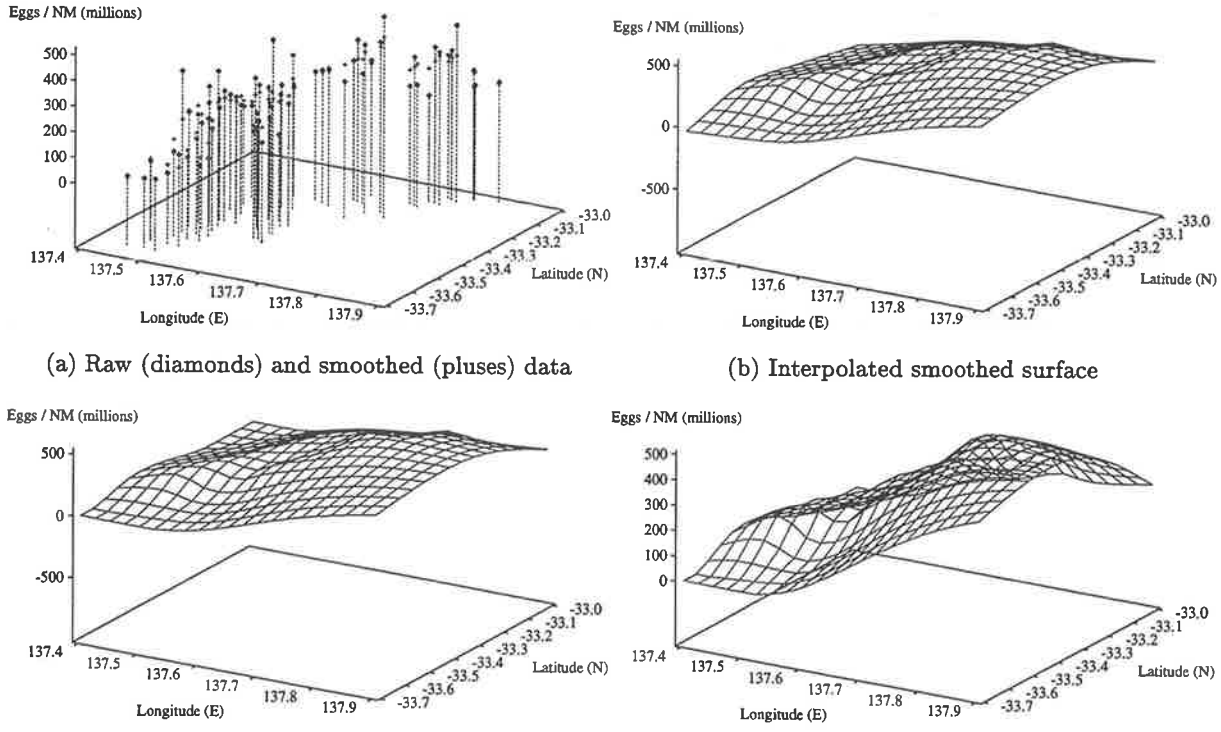

(a) Raw (diamonds) and smoothed (pluses) data

(b) Interpolated smoothed surface

(c) Interpolated and truncated surface overview

(d) Interpolated and truncated surface detail

Figure 2.8: Measured and smoothed egg production (millions) per nautical mile for the northern Spencer Gulf trawl locations in the combined trawl Regions 2–7 during the 1994 spawning season, without further derivation. The interpolated surfaces are shown with grid–spacings of 0.025° longitude (E) and 0.05° latitude (N) along the x and y axes, respectively.

exact dates for spawning trawls it would be possible to determine suitable time series functional forms, such as Gaussian in time, resulting in a continuous spawning event representation. These dates, however, were not available.

If the physical length of the trawl were calculated and then multiplied by the egg production value provided, to give a total per-trawl value, it must also be assumed that spawning was constant over the time taken for any individual trawl. To derive an absolute value the dimensions of the trawl net, also not available, must be known. All spawning initial conditions in this thesis are thus derived using the provided egg production value (in "millions/nautical mile" units), located at the midpoint of the trawl endpoints, and are not converted to absolute egg numbers.

It must also be assumed that the initial prawn larvae population is directly proportional to pregnant adult female egg production. This in turn assumes that fertilisation is either absolutely successful or that the fertilisation success rate is not perfect but is nevertheless constant in space and time. Clearly neither of these assumptions could possibly be valid in the real world but, due to insufficient data to quantify the contrary, direct proportionality is assumed.

As can be appreciated from these discussions, due to the paucity of information needed to qualify, let alone quantify, many of the processes affecting the relationship between the egg production data provided and the larvae concentrations desired as initial conditions for model simulations, some very broad assumptions are required to be made to derive the latter from the former. The initial conditions derived are thus representative of the *relative* rather than the *absolute* larvae concentrations and, as a consequence, the results from the model must be interpreted in the same light. It is for this reason, as well as for reasons concerning clarity of result interpretation, that all results are presented in the manner discussed below.

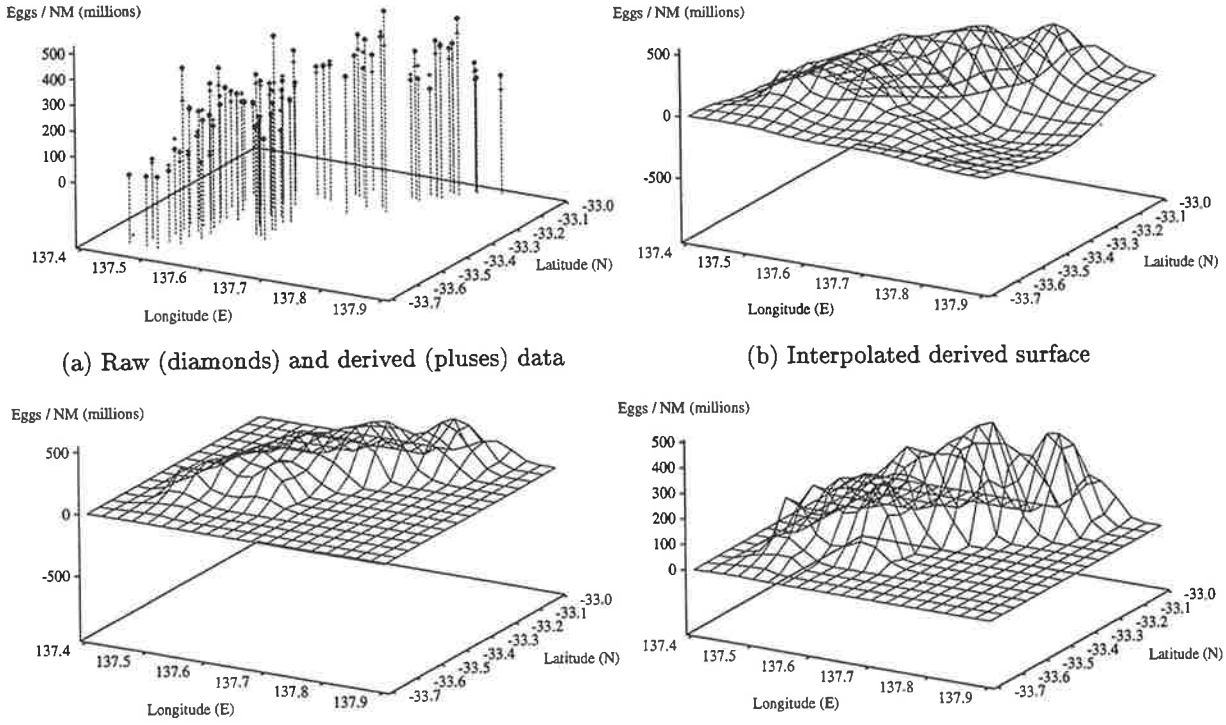

(a) Raw (diamonds) and derived (pluses) data

(b) Interpolated derived surface

(c) Interpolated and truncated surface overview

(d) Interpolated and truncated surface detail

Figure 2.9: Measured and smoothed egg production (millions) per nautical mile for the northern Spencer Gulf trawl locations in the combined trawl Regions 2–7 during the 1994 spawning season, with further derivation. The interpolated surfaces are shown with grid–spacings of 0.025° longitude (E) and 0.05° latitude (N) along the x and y axes, respectively.

Initial Condition Concentrations

In all prawn larvae dispersion simulations discussed in this thesis initial conditions are input, and hence larval concentrations are calculated internally, in the units of the supplied egg production data (millions/nautical mile). In this section, larval concentrations are discussed in terms of these units for convenience. Taking all of the assumptions outlined above into account, the units of the egg production initial conditions input to the proposed prawn larvae dispersion model—"millions per nautical mile" ($10^6\,\mathrm{NM}^{-1}$), and those of the desired postlarvae concentrations output by that model—"millions per square metre" ($10^6\,\mathrm{m}^{-2}$) are, to all intents and purposes, to be considered equivalent. These units are sometimes interchanged in the text, and in figures and tables, as well as their captions, in the remainder of this thesis.

Figures 2.10–2.15 are graphical representations of all prawn larvae dispersion initial conditions used in this thesis. Level curves of initial larval concentration are marked by solid curves. The Spencer Gulf coastline is marked by a finely dashed curve, as are islands in the Gulf. The fine resolution Spencer Gulf model open boundary (see Section 6.4 below) is marked by a coarsely dashed curve constructed of straight line segments. Grid orientation with respect to latitude and longitude is represented by the compass at bottom right. An *x-transect*—at bottom left—is taken along the line $y = \textit{constant}$ through the grid–point of maximum concentration, with the top and bottom axes corresponding to distance (m) from the left hand coastline and the left and right axes corresponding to larval concentration ($10^6\,\mathrm{NM}^{-1}$). A *y-transect*—at top right—is taken along the line $x = \textit{constant}$ through the same grid–point, with the left and right axes corresponding to distance (m) from the top edge coastline and the top and bottom axes corresponding to larval concentration ($10^6\,\mathrm{NM}^{-1}$). The Spencer Gulf tidal observation stations,

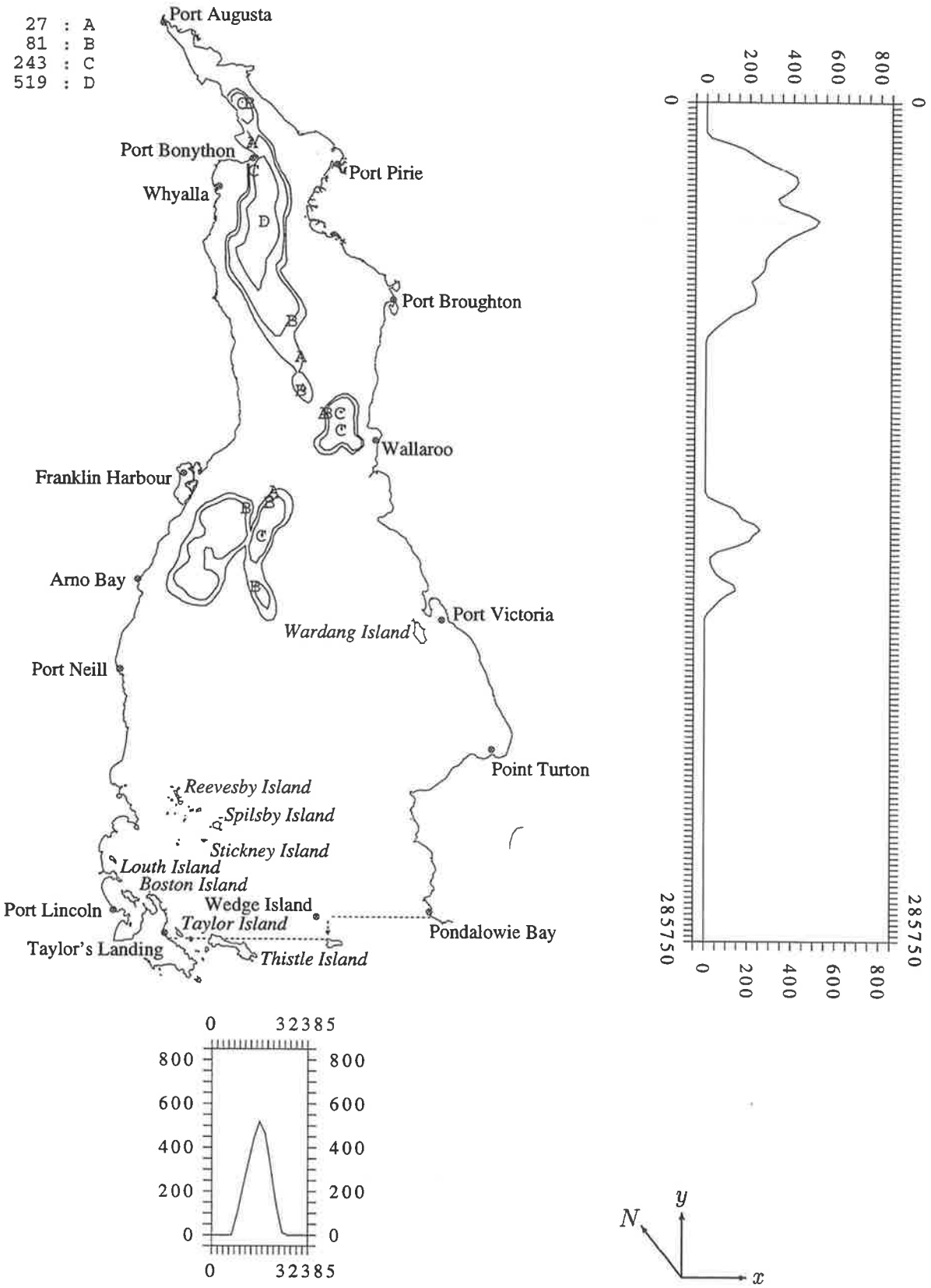

Figure 2.10: The 1988 initial concentration (10^6 NM^{-1}) level curves (top left), and y- (top right) and x- (bottom left) transects through D (south of Whyalla). Tidal stations (roman) and islands (italics) are named.

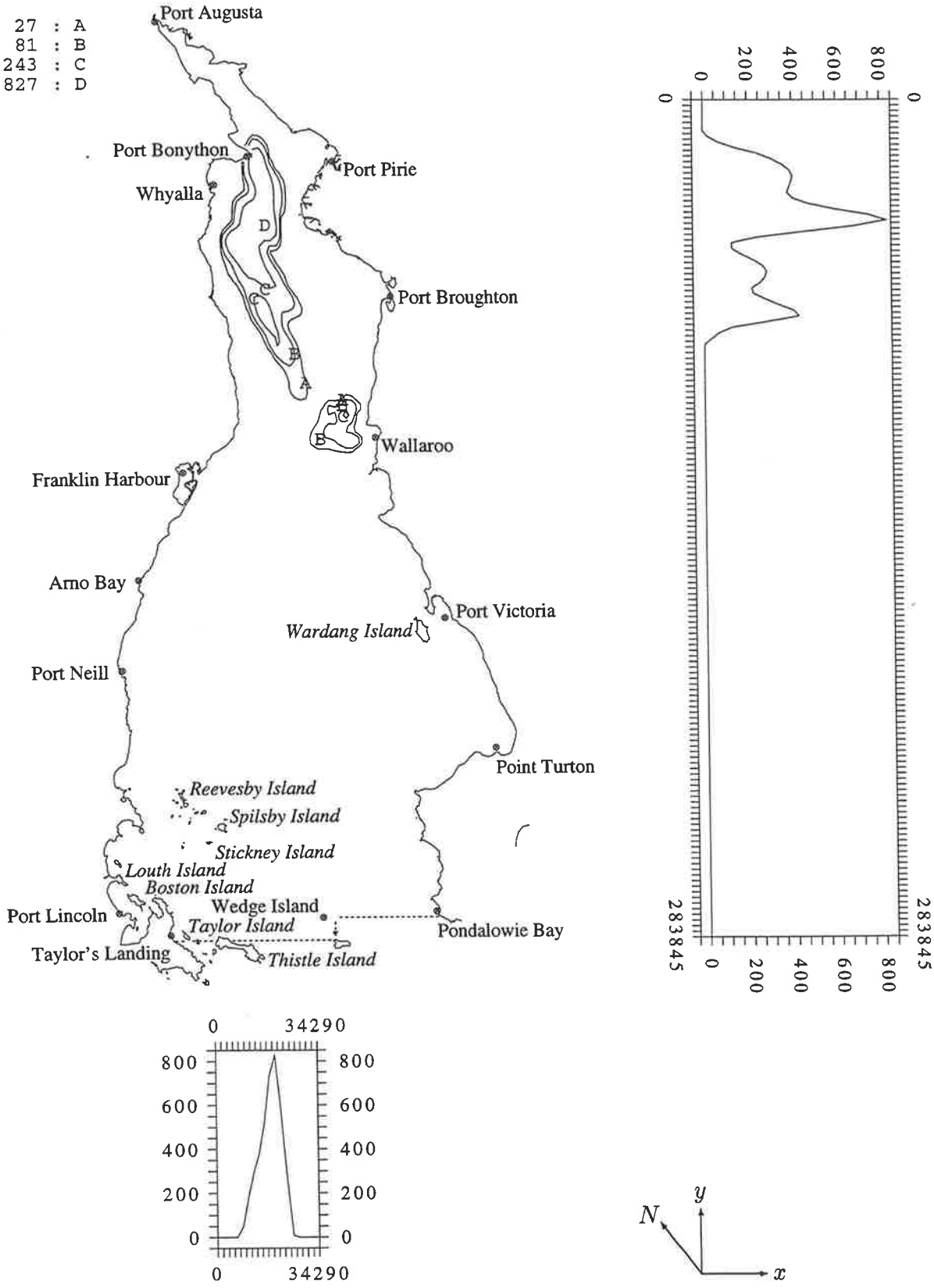

Figure 2.11: The 1991 initial concentration (10^6 NM^{-1}) level curves (top left), and y- (top right) and x- (bottom left) transects through D (south of Whyalla). Tidal stations (roman) and islands (italics) are named.

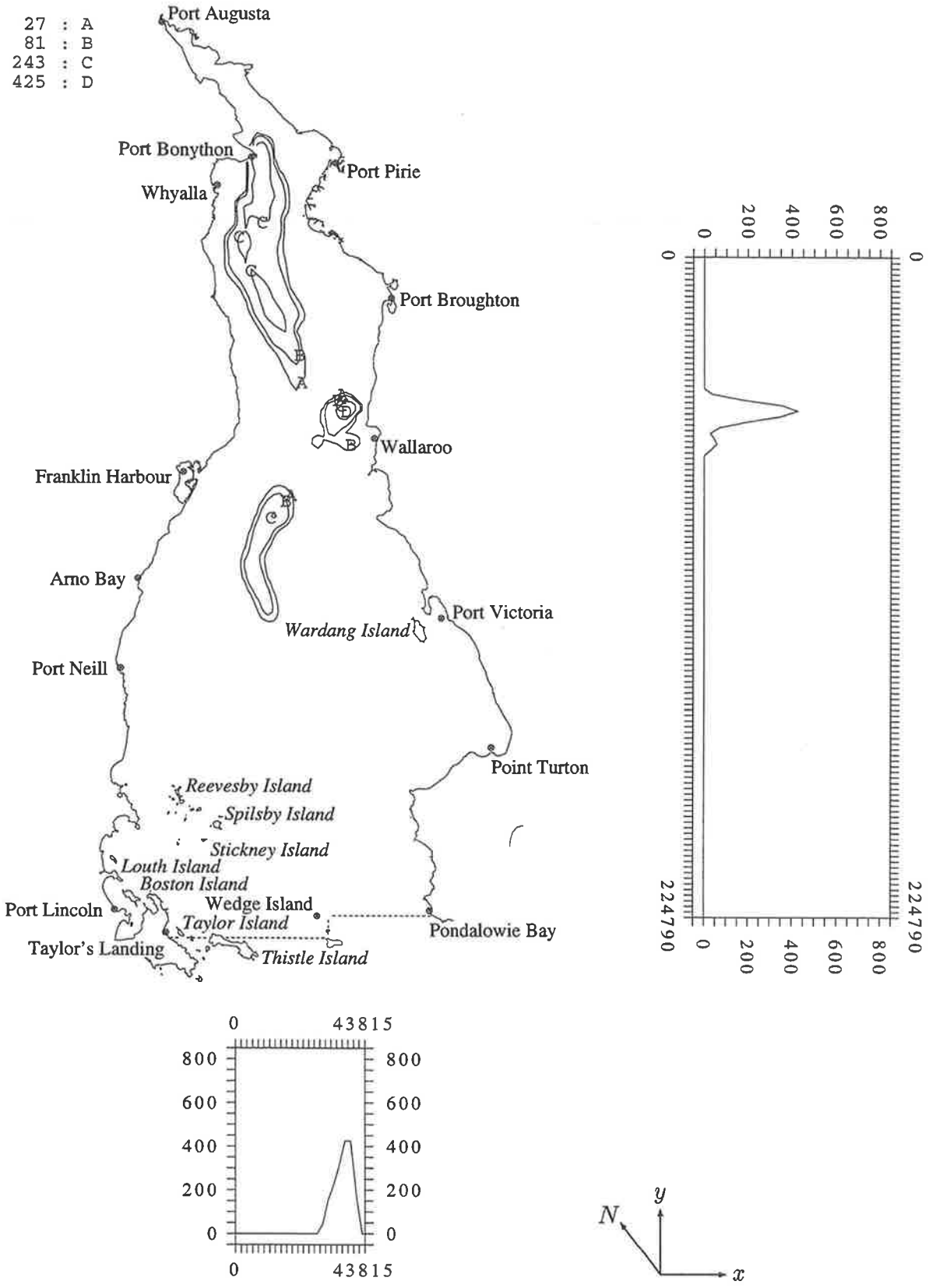

Figure 2.12: The 1992 initial concentration (10^6 NM^{-1}) level curves (top left), and y- (top right) and x- (bottom left) transects through D (north of Wallaroo). Tidal stations (roman) and islands (italics) are named.

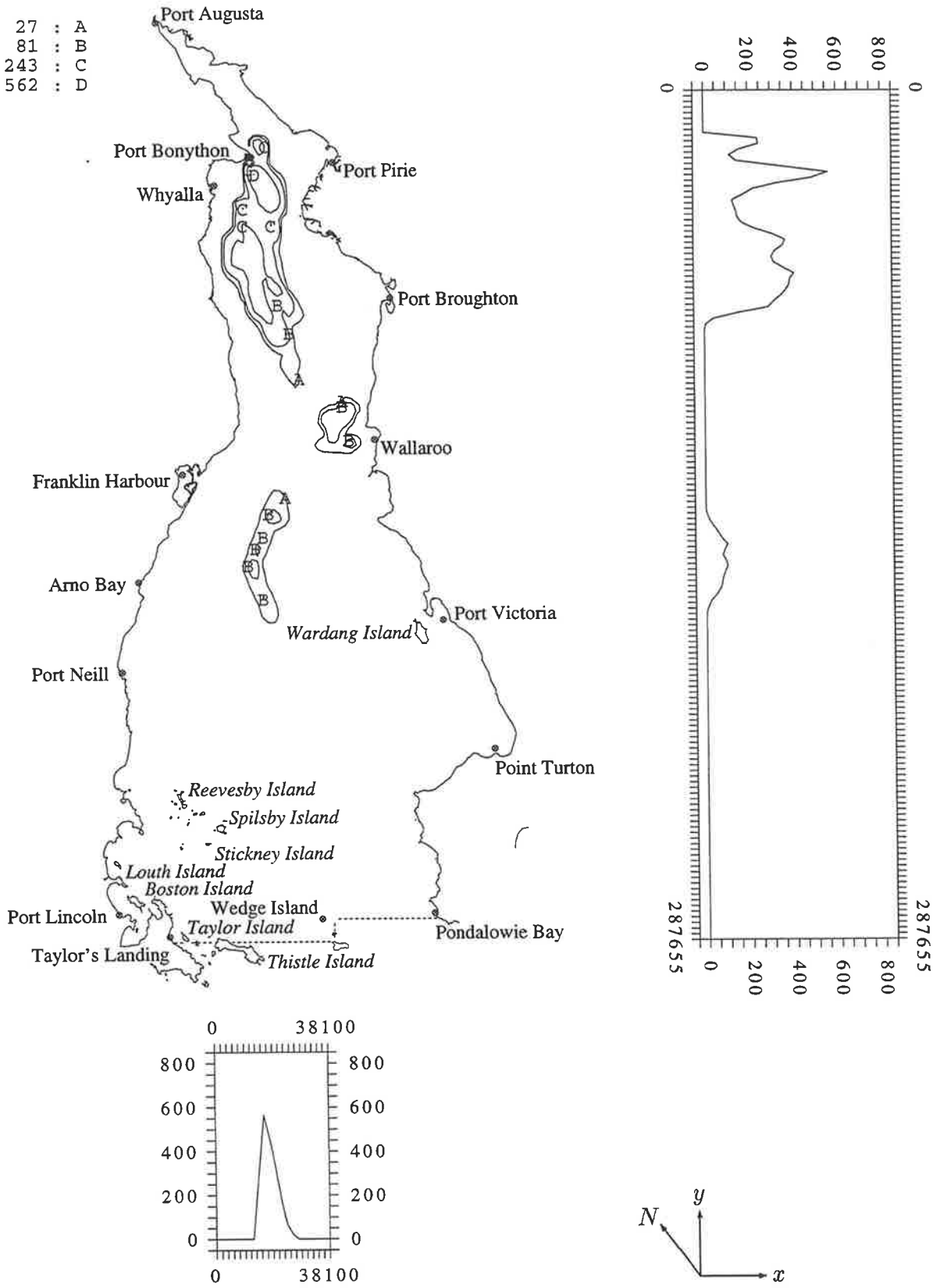

Figure 2.13: The 1993 initial concentration (10^6 NM^{-1}) level curves (top left), and y- (top right) and x- (bottom left) transects through D (south of Port Bonython). Tidal stations (roman) and islands (italics) are named.

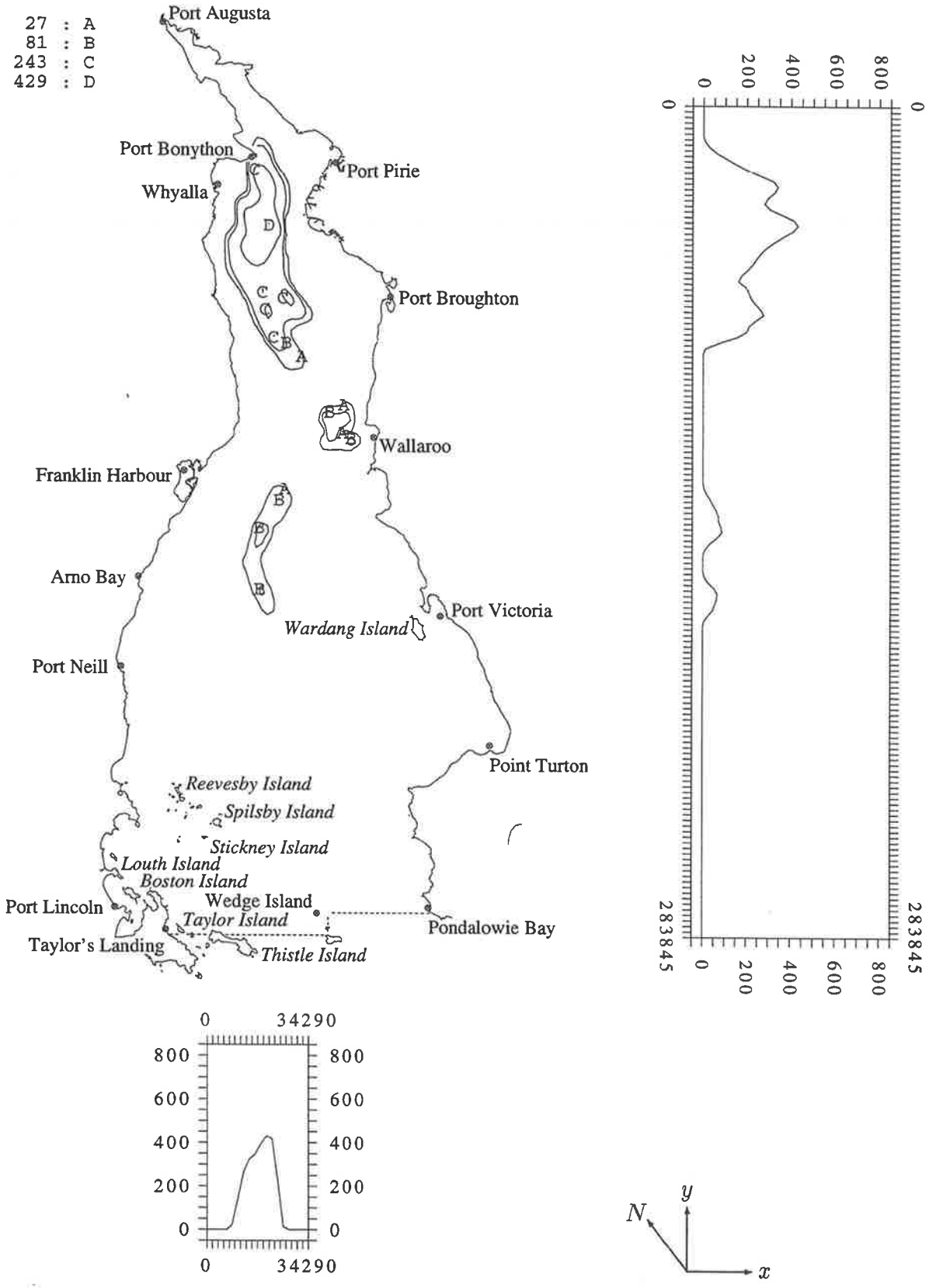

Figure 2.14: The 1994 initial concentration (10^6 NM^{-1}) level curves (top left), and y- (top right) and x- (bottom left) transects through D (south of Whyalla), Tidal stations (roman) and islands (italics) are named.

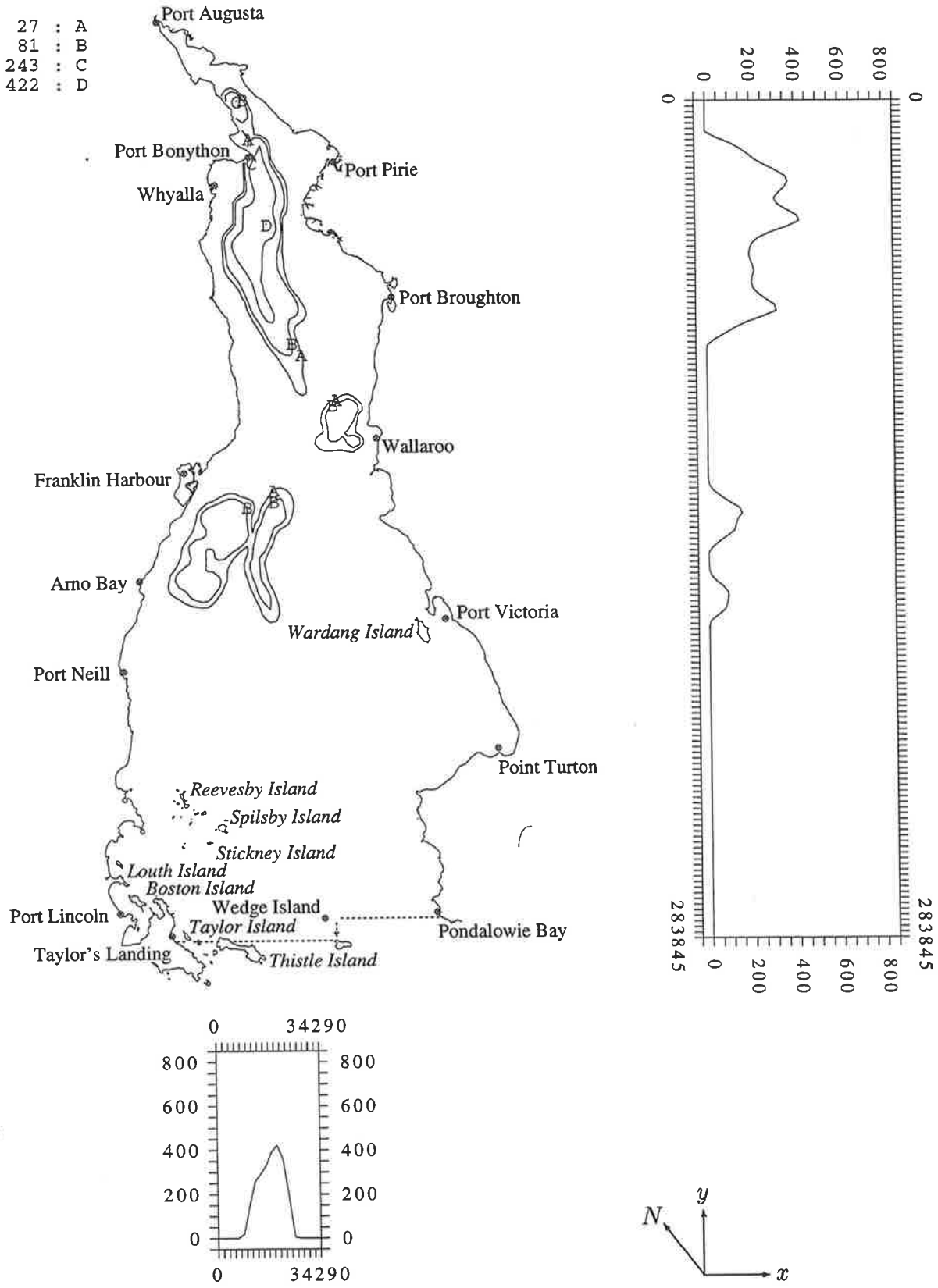

Figure 2.15: The "average" initial concentration (10^6 NM^{-1}) level curves (top left), and y- (top right) and x- (bottom left) transects through D (south of Whyalla), Tidal stations (roman) and islands (italics) are named.

of Section 6.1 below, are indicated for positional reference.

The "average" initial condition illustrated in Figure 2.15 was derived using a region by region average of the 1988 and 1991–1994 initial conditions of Figures 2.10 and 2.11–2.14. In that respect it represents a "typical" spawning season, as far as can be determined from the data available.

2.1.6 Discussion

As a direct consequence of the manner of their derivation, all egg production peaks corresponding to combined spawning regions possess steep concentration gradients at the edges of their extent. This is illustrated by the close proximity of the first three contours, labelled A, B, and C. These increase as a geometric sequence, with first term $A = 27$ and common ratio $r = 3$, for all initial conditions shown. It should be noted that the final "contour" level, labelled D, is set to the maximum egg production value derived for each spawning year. In that regard it appears as a point indicating the location of the concentration maximum over the entire Gulf.

The two broad regions constituting the northern and southern spawning grounds, defined by Carrick (1982) and depicted in Figures 2.1 and 2.2, are evident in Figures 2.10–2.15. The SARDI data used to derive the initial conditions thus suggest the existence of particular well defined spawning areas, contrary to the findings of King (1980).

From Figure 2.15 it is evident that the spawning grounds in the vicinity of Yarraville Shoals (see Figure 1.2) produce, on average, more eggs compared to others, as suggested by Carrick (1990, personal communications) in Noye et al. (1992). It can also be seen that the northern areas in the vicinity of Whyalla and Port Pirie are, on average, important spawning areas for the survey periods during which the data were collected, as suggested by Carrick in Anonymous (1994).

It is also evident that reproductive output varies geographically from year to year, supporting the findings of Rothlisberg et al. (1983). For the years 1988, 1991, and 1994 the spawning maxima are found south of Whyalla in the northern Yarraville Shoals ground, through D in Figures 2.10, 2.11, and 2.14, respectively. These maxima are associated with peaks increasing in intensity from the 1994 to the 1988 to the 1991 spawning seasons, with the latter being the most localised, as evident in the transect as well as the contour plots. In the 1992 initial condition of Figure 2.12, a highly localised peak is found in the mid-Gulf Wallaroo spawning ground, with a local maximum at D, north of Wallaroo. The corresponding peak for 1993 is of much the same magnitude, whereas the maximum is found further north, south of Port Bonython, at D in Figure 2.13.

In the y-transects of the 1988, 1993, and 1994 initial conditions a smaller concentration peak representing the Gutter spawning ground is found, with year-strength intensity decreasing approximately in that year-order. This secondary peak does not occur in the 1991 initial condition of Figure 2.11, because no data for this ground were available, nor in the 1992 y-transect of Figure 2.12, but only because this transect does not intersect the appropriate region.

The initial conditions for all yearly spawning seasons show significant peaks corresponding to the Wallaroo spawning ground. These are of differing shape and intensity but look to be of the general form of that for the 1992 initial condition of Figure 2.12, albeit with measurably smaller local maxima than the maximum in that figure.

In Figure 2.15, the "average" initial condition shows a major peak in the north of Spencer Gulf, as might be expected from inspection of the figures illustrating the initial conditions from which the average was obtained. It has a local maximum south of Whyalla, at D. Secondary peaks corresponding to the Gutter (shown in the y-transect) and Wallaroo (not shown in the y-transect) spawning grounds are evident. These arise out of contributions from the 1988, 1992–1994, and 1998, 1991–1994 data, respectively. Extreme north-Gulf (Region 1 of Figure 2.1) and lower mid-Gulf (Regions 10–12 of Figure 2.2) spawnings, present only in the 1988 data, are also represented.

2.2 The Larval Phase

The timing and duration of the passive dispersion period associated with *Penaeus latisulcatus* larvae in Spencer Gulf is dependent on the timing and duration of both larval spawning and postlarval settlement for the species in the region.

In this section, information from the biological literature on prawn and other marine species plankton is discussed. Observations relating to the duration of the larval phase and to behaviour while in this phase are reported.

2.2.1 Larval Dispersion

Planktonic or, more properly, *planktic* larvae spend a significant portion of their development time swimming freely in surface waters (Jablonski and Lutz 1983, p. 23). Pelagic larvae which feed (*planktotrophic*) might in theory survive indefinitely, though they usually reach the stage at which settlement is possible within two to three weeks, which is barely sufficient time to cross barriers of 50–100 km (Crisp 1978). Planktotrophic planktic larvae depend on smaller planktic organisms (and possibly organic detritus) for nutrition (Jablonski and Lutz 1983, p. 23). The planktic stage of planktotrophic species can be divided into two phases: (1) growth and development (the *precompetent period* of Jackson and Strathmann 1981), followed by (2) a "delay period" (the *competent period* of Jackson and Strathmann 1981) in which development is essentially completed, but larval adaptations for a planktic existence are retained until a substratum suitable for settlement is found. It is the delay period which gives to many species the greatest flexibility in the length of their larval life, since this stage may last from a few minutes to over three months, depending on the species (Jablonski and Lutz 1983, p. 24).

Jackson and Strathmann (1981) predicted that there will be an increased competent period with increased precompetent period among species, and that the competent period will be greater than or equal to the precompetent period (Jackson and Strathmann 1981, p. 22). Thus, when a larva has developed sufficiently to be able to settle, it may have to drift, waiting in the competent phase, until it finds suitable substratum, until it is eaten, or until degeneration ends the competent period. The problem of not being in the proper place at the end of the precompetent period can be acute for planktonic larvae whose adult forms inhabit the coastal environment, because only a thin strip in a large ocean is suitable for them. Larval success in settling will depend on the lengths of the precompetent and competent periods as well as predation rates (Jackson and Strathmann 1981, p. 16), with relatively long competency periods being less important for larvae with large precompetent mortality than for larvae with small precompetent mortality (Jackson and Strathmann 1981, p. 20).

For the most part, available data coincide with the Jackson and Strathmann (1981) models, supporting the hypothesis that, since transport of larvae during a lengthy precompetent period may move them away from suitable substrata, a long delay period is required to enable the larvae to encounter suitable settlement sites once they are capable of metamorphosis (Jablonski and Lutz 1983, p. 24). In temperate-water species, this planktic stage generally lasts from 2 to 6 wk, during which period an ocean current of only $0.5\,\mathrm{km\,h^{-1}}$ could carry a larva 150–550 km (Jablonski and Lutz 1983, p. 24). Hence, in a mathematical model of larval dispersion, good estimates of both the precompetent and competent durations are important for predicting where postlarval settlement may take place. However, there are few data from plankton sampling which permit calculation of the precompetent period, mortality rates from predation, or the maximum competent period (Jackson and Strathmann 1981, p. 21).

In a study of the species in Shark Bay (see Figure 1.1) the time taken for development of *Penaeus latisulcatus* larvae through the postlarval settling state was found to be approximately 21 d at 20°C in laboratory culture, which is in general agreement with published development times for *Penaeus* species (Penn 1975, p. 95). Penn also noted that, as the development time is related to temperature, the length of larval life (precompetent and competent periods) of *P. latisulcatus* is likely to range from 2–4 wk.

2.2.2 Postlarval Settlement

In a study of *P. latisulcatus* postlarval settlement and juvenile density in Spencer Gulf, it was determined that two peaks in settlement occurred over 1991/92—the highest peak occurred in February followed by a minor peak in April (Carrick 1992b, p. 2). The main settlement peak (February) is termed *direct recruitment* as residence in nurseries occurs for a short period (4–5 mo) before recruitment to the prawn grounds in May/June. The April settlement peak is referred to as *over-wintered recruitment* since juvenile prawns stay in nurseries longer (8–10 mo) and recruit as adults to the fishery in January/February in the following year. This process is schematically illustrated in Figure 2.16, where *P. latisulcatus* spawned very early in the

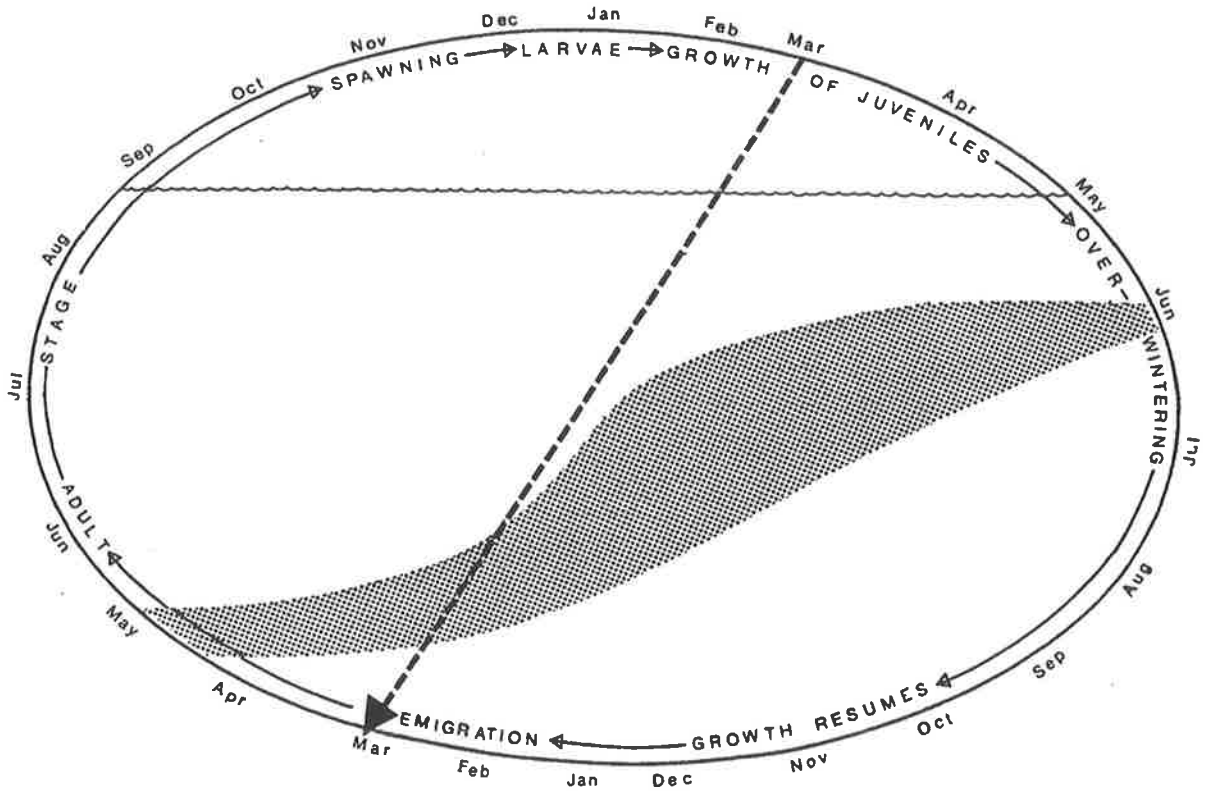

Figure 2.16: The *Penaeus latisulcatus* life cycle. Western king prawns which are spawned early in the season (November) and grow rapidly can emigrate (May) without over-wintering (dashed arrow), thus completing the cycle (solid arrows) in 1 y rather than 2 y (from Zed 1980, Figure 2). Vertical migration of the larvae (shading) within the water column, resulting in their horizontal displacement by ocean currents, is schematically represented.

season emigrating at the end of that summer are represented by the broken arrow. During the following spring and summer rapid growth resumes, and the "adolescents" emigrate offshore where they may live till the next spawning season. The life cycle is thus completed in two years although some individuals may complete it in one year, and some may survive into a third year (Zed 1980, p. 19). Despite resulting from a smaller settlement (at least for the 1991/92 study), the over-wintered group is the mainstay of the fishery (Carrick 1992b, p. 3), as it is likely that most juvenile *P. latisulcatus* overwinter in the nursery areas and emigrate offshore the following summer (Zed 1980, p. 15). This leads to the conclusion that both spawning events corresponding to the two settlement events are of equal modelling interest.

The two peaks in spawning discussed in Section 2.1.2 may explain why there are two distinctive annual (adult) recruitment peaks to the fishery, i.e. one in February—over-wintered recruits from late spawnings in late January/February, and one in May/June—which are likely

to be derived from mid-December spawnings of the previous year (Carrick 1991, p. 4). This adult recruitment, or the ingress of small prawns into the fishing grounds, peaks in February in the northern areas of Spencer Gulf, where the movement of prawns from January to June is in a southward direction and occurs in discrete detectable pulses from February to April (Carrick 1988, p. 4).

2.2.3 Conclusions

The consensus seems to be that *Penaeus latisulcatus* in Spencer Gulf have a larval phase of approximately 1 mo. Observations of two peak spawning and two peak settlement periods, however, indicate that this phase may exist in a "window of opportunity" of approximately 6 mo. It will be shown in the following chapters that these two conclusions have profound effects on the approach required of a realistic numerical prawn larvae dispersion model.

2.3 Juvenile Settlement

At 1980 levels of fishing, there appeared to be no relationship between size of spawning stock in one year and adult recruitment in subsequent years (King 1980, p. 2). King concluded that the recruitment or catch potential of a particular year was therefore likely to be related to the effect of environmental factors on the survival of the previous year's juveniles in the inshore nursery areas. In this thesis it is assumed that the major factor affecting juvenile survival is the successful settlement of postlarval prawns into the nursery areas immediately following the end of the larval period.

In the following sections, detailed information obtained from the literature on larval biology relevant to postlarval settlement, particularly of the species *Penaeus latisulcatus* in Spencer Gulf, is presented.

2.3.1 Temperature, Salinity, and *Penaeus* Species Abundance

In a study of the hydrographic environment of penaeids in the Gulf of Carpentaria, Rothlisberg and Jackson (1987) found that the abundance of larvae of *P. merguiensis*, *P. esculentus*, *P. semisulcatus*, and *P. latisulcatus* showed both spatial and temporal heterogeneity. Most of the larvae of all four species were found where the water was less than 50 m deep, with temperatures and salinities greater than 26°C and 31 (units were not given, but density relative to pure water in units of parts per thousand is assumed), respectively. However, the mean temperatures of the waters in which the larvae were found varied significantly between some species. The mean temperature and salinity of the waters for *P. latisulcatus* were 27.3°C and 33.0. While the range of temperatures in which all four species were found was between 21.5 and 30.6°C, the ranges of salinities were more varied and may have reflected the biogeographic distributions of the species. The three widespread species were found over large salinity ranges: *P. merguiensis* and *P. semisulcatus*, 27.8–34.9; and *P. latisulcatus*, 28.6–34.9 (Rothlisberg and Jackson 1987, p. 19).

These temperatures and salinities are only a subset of the range that these species encounter over their entire geographic distribution and through all stages of their life history. Nevertheless, the measured ranges of temperature (19.8–31.2°C) and salinity (26.2–35.6) encompassed most coastal environments where these species were known to spawn (Rothlisberg and Jackson 1987, p. 25).

2.3.2 Juvenile *Penaeus latisulcatus* Habitats

Many authors have noted that juvenile penaeid prawns appear to be more abundant in low rather than higher salinity waters (Zed 1980, p. 29). The distribution of juvenile *P. latisulcatus*

in relation to salinity is, however, markedly different from that of other penaeid prawns (Zed 1980, p. 35).

Rothlisberg and Jackson (1987) stated that *P. latisulcatus* is known to inhabit hypersaline environments in southern Australia at certain stages of its life history. Spawning females, however, had only been found in water of oceanic salinities. They also suggested that the temperatures and salinities in which the larvae were caught during their study provide a realistic indication of conditions suitable for larval growth and survival and, further, that the means of these parameters may indicate optima, and the ranges may coincide with tolerances. They emphasised, however, that these assumptions need substantiation with laboratory experiments (Rothlisberg and Jackson 1987, p. 25).

In a major study of the species in South Australia, Zed (1980) stated that laboratory studies *have* shown that the survival of juvenile *P. latisulcatus* in high salinities was better than that of other penaeid species, but that in low salinities the survival of *P. latisulcatus* was not as good as that of other species. These laboratory study results were, according to Zed (1980), in keeping with the well-known hypersaline nature of the habitat of juvenile *P. latisulcatus*.

The negative correlation between juvenile recruitment and effective rainfall reported by Zed (1980) supports the hypothesis that *P. latisulcatus* is adapted to the hypersaline conditions occurring in its nursery areas and that reduced salinities are detrimental to the survival of the species (Zed 1980, p. 124). In this study it was shown that the nursery areas inhabited by juvenile *P. latisulcatus* were similar in many respects to those occupied by other penaeid prawns, with the major exception that waters in the *P. latisulcatus* nursery areas are usually hypersaline (Zed 1980, p. 2). This further suggests that the distribution of the penaeid prawn in general may be determined by the salinity of the inshore nursery areas (Zed 1980, p. 2).

In King's (1980) study of the western king prawn in the waters of South Australia and Western Australia, juvenile *P. latisulcatus* were found in sheltered areas of the coastline such as shallow bays, coves, and tidal creeks (King 1980, p. 10). In contrast to other species, juvenile *P. latisulcatus* were found in waters which were hypersaline (King 1980, p. 10). In all nursery areas examined, the salinity of the water was higher than that of adjacent offshore areas where adult animals were found (King 1980, p. 10).

2.3.3 Juvenile *Penaeus latisulcatus* in South Australia

King (1976) found the nursery areas of *P. latisulcatus* in South Australian gulf waters to be usually associated with the mangrove *Avicennia marina*, although there were some areas where large numbers of juveniles occurred but mangroves were not present (King 1980, p. 10). These areas were invariably associated with seagrass communities (*Posidonia australia*, *Zostera mucronata*, *Heterozostera tasmanica*, and sometimes *Amphibolus antarctica* and *halophila*). These findings were consistent with the results of trawling undertaken by Zed (1980).

The nursery areas for juvenile *P. latisulcatus* were usually bounded on the landward side by stands of the mangrove *Avicennia marina* and on the seaward side by seagrass beds (Zed 1980, p. 26). It was also noted that it was on the shallower flats, before the seagrasses develop into dense extensive meadows, that most juvenile *P. latisulcatus* seemed to occur (Zed 1980, p. 27). Penaeid prawns are opportunistic detritivores, and it is likely that the seagrasses and mangroves constitute an important primary food resource for juvenile *P. latisulcatus* (Zed 1980, p. 122). However, the importance of these flora as determinants of the distribution of juvenile *P. latisulcatus* is difficult to assess (Zed 1980, p. 26).

It can be seen from Figure 2.17 that the nursery areas for *P. latisulcatus* in South Australia most lie within regions where the 10 m bathymetric contour is from 5 to 10 km offshore (Zed 1980, p. 23). This contour, as determined by the fine resolution Spencer Gulf model of Chapter 6, is indicated in Figure 2.18, as is a distance scale by which to determine these regions.

A necessary prerequisite for successful juvenile recruitment is the availability of suitable settlement substrates and ultimately an abundant food resource (Black and Moran 1991, p. 64). The nursery areas of *P. latisulcatus* in Spencer Gulf have been found to correspond closely with

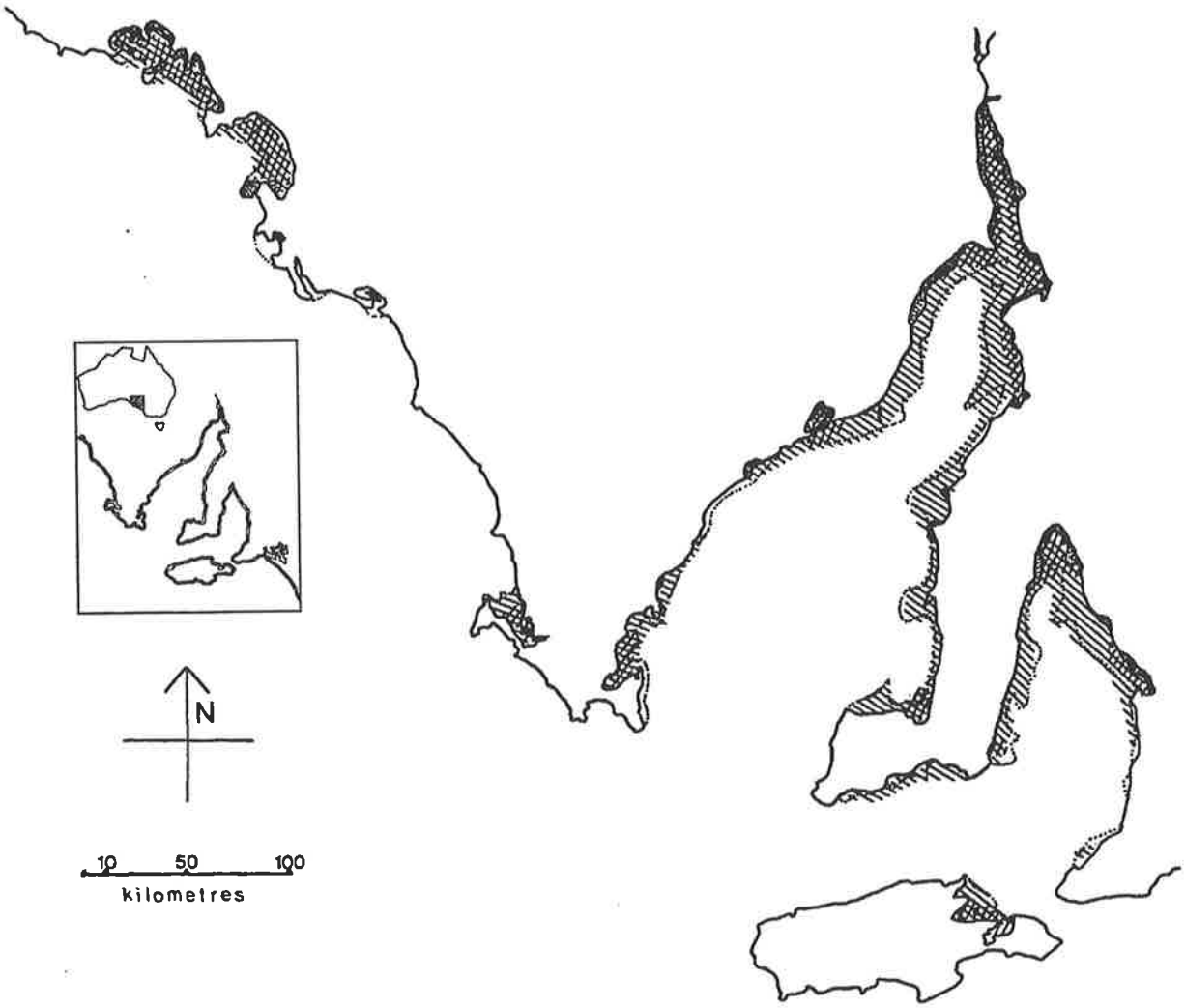

Figure 2.17: The nursery areas of juvenile *Penaeus latisulcatus* in South Australian waters (from Zed 1980, Figure 5). Indicated are the: nursery areas (positive gradient hatching, from King 1976, Figures 2-1–2-4 and 3-2); 10 m bathymetric contour (dotted line); distribution of mangroves (dotted shading, from Butler et al. 1975); and distribution of seagrasses (negative gradient hatching, from Shepherd and Sprigg 1976, Figure 3).

"coastlines of slight wave action with sandy or muddy flats or beaches" (Zed 1980, p. 23). Typically the shore topography comprises "very gently shelving flats above and below low tide level, descending gradually into deeper water or abruptly into channels 4 m deep" (Zed 1980, p. 23). The substrate in the nursery areas sampled by King (1980) varied from silty to clean sand with some shell grit. Substrates of soft mud or large quantities of shell grit appeared not to be preferred by juvenile *P. latisulcatus* (King 1980, p. 10). Most juvenile *P. latisulcatus*, however, have been trawled from the more barren region between the mangroves and the seagrass beds (Zed 1980, p. 27). These sand and mud flats offer little protection from predators. Trawls have also shown that nursery areas for *P. latisulcatus* do exist in sheltered areas on the west coast of South Australia (Zed 1980, p. 22).

2.3.4 Juvenile *Penaeus latisulcatus* in Spencer Gulf

In South Australian waters the major nursery areas of juvenile *P. latisulcatus* occur at the heads of Gulf St. Vincent and Spencer Gulf (Zed 1980, p. 33). High salinities at the heads

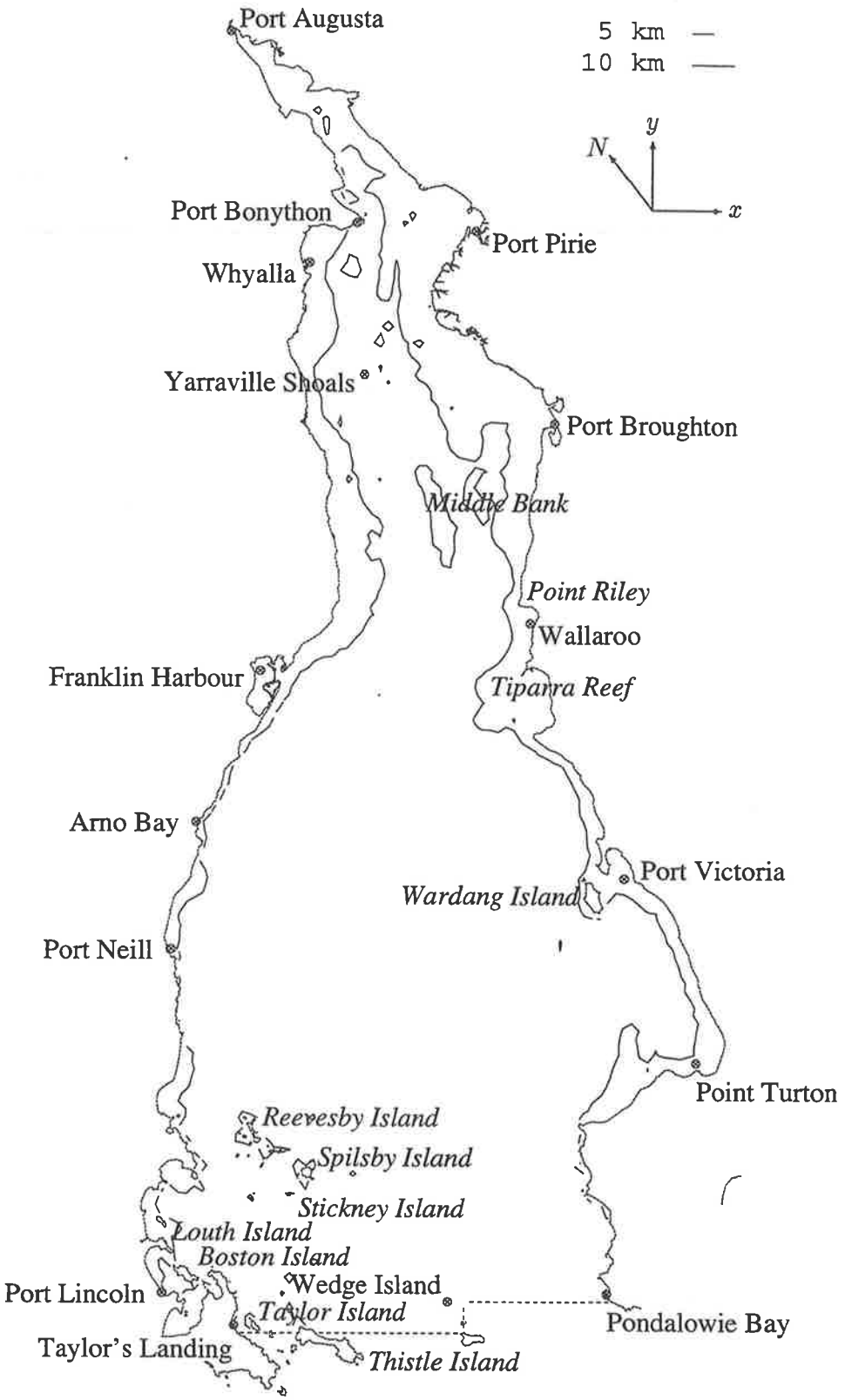

Figure 2.18: The 10 m (mean sea level) depth contour (solid curves) for the fine grid Spencer Gulf model. Tidal stations (roman), places of interest (italics), and coastal (finely dashed curve) and mouth (coarsely dashed line) boundaries are also shown.

of Gulf St. Vincent have been reported by Bye (1976). Similar findings in Spencer Gulf have been reported by Bullock (1975), Bye (1981), Nunes and Lennon (1986), and Lennon et al. (1987). These and other authors have termed Spencer Gulf an *inverse estuary* to emphasise the fact that moving "inland" (i.e. towards the head of the Gulf) sees salinities increase—the opposite of what is usually expected for estuaries. There are no permanent rivers emptying in Spencer Gulf, although freshwater runoff into tidal creeks may be considerable during winter rains (King 1980, p. 10). The fact that the Gulf head is placed well inland within a semi-arid region, suggests that summertime evaporation combined with extremely low freshwater input is the mechanism behind the high evaporation rates reported by Zed (1980).

In general, sheltered areas to the north in Spencer Gulf are more favoured than the more exposed southerly locations; however, large concentrations of juveniles are sometimes found in some isolated areas, e.g. Spalding Cove (King 1980, p. 12), south-east of Boston Island (see Figure 1.2) near Port Lincoln (see Figure 1.3). Port Broughton is also considered an important prawn nursery area in Spencer Gulf (Zed 1980, p. 34). In an annual report for 1994 on the research and management of the Spencer Gulf prawn fishery, Carrick noted that the northern regions in the vicinity of Whyalla and Port Pirie (see Figure 1.3) have been identified as major habitats for larval and juvenile prawns (Anonymous 1994, p. 12). False Bay—between Stony Point (see Figure 1.2) and Whyalla (see Figure 1.3)—is, however, recognised as the most important prawn nursery ground in Spencer Gulf (Anonymous 1994, p. 12) and has been identified as such (Carrick 1992b, p. 5 and Figure 7). This region north of Whyalla is a proposed site for large scale industrial development (Carrick 1991, p. 7) and thus there is concern for the effects this may have on the prawn fishery in the Gulf.

In a comparative study of individual nursery locations, it was found that juvenile settlement densities at False Bay were higher than at Shoalwater Point (see Figure 1.2) over most times, and that a consistent pattern in settlement peak occurred between areas (Carrick 1992b, p. 3 and Figure 4). Considering latitudinal and longitudinal aspects, it was expected that for similar habitat types (sandy mud substrates), the settlement densities should have decreased from north to south, and should also have been higher on the western side of the Gulf (Carrick 1992b, p. 4). The evidence for a consistent linear increase in settlement with latitude on both sides of the Gulf was not, however, supported by results (Carrick 1991, 1992b), although numbers did increase with latitude on the eastern side of the Gulf. Analysis of these preliminary sample data has also indicated that there were significantly higher densities on the western side of the Gulf compared to the eastern side (Carrick 1991, 1992b).

2.3.5 Conclusions

It is evident that juvenile *Penaeus latisulcatus* in Spencer Gulf prefer hypersaline nursery areas, in contrast to other *Penaeus* species. Regions at the head of the Gulf and/or in the shallow waters, where temperatures and evaporation rates are comparatively high, are thus preferred. Sheltered environments, bordered on the seaward side by moderate density seagrass beds—of a range of species—and on the landward side by mangrove strands—of a particular species—may also be preferred. The upper-northern Spencer Gulf shallows of False Bay and Germein Bay, north of Whyalla and Port Pirie, respectively, have been identified as major nursery areas. The mid-northern regions near Shoalwater Point and Port Broughton, on the west and east coasts, respectively, are also significant nursery areas. Less well defined nursery areas are located still further south. There is evidence to suggest that postlarval settlement densities are highest along the western coast. These are consistently higher at False Bay than at Shoalwater Point, but this is not a linear decline with latitude southwards. Densities do, however, decrease linearly with latitude southwards along the northern east coast.

2.4 Vertical Migration

One of the main and yet unsolved problems of planktonology is the mechanism of the rhythmical vertical migration of pelagic animals (Richter 1973, p. 126). There is a need to distinguish between two types of vertical migration. It is well known that various plankton communities, living for example in water at greater depths, move to the surface waters in summer and vice-versa. This type of *annual* migration means a relatively slow movement of entire communities, generally in correlation with the seasonal fluctuations in environmental conditions. The same communities may also take part in *diurnal* vertical migration, a relatively rapid movement of pelagic animals, mainly—but not always—from greater depths to the sea–surface and back in a 24 h-cycle. This thesis is concerned with the latter example only.

Vertical migration is widespread among marine and freshwater Crustacea. Almost as diverse as the organisms involved, are the probable environmental cues that elicit the response and adaptive advantages attributed to this behaviour. Undoubtedly animals have adopted vertical migratory behaviour for a variety of immediate and long-term biological advantages (Rothlisberg 1982, p. 541). Dispersal, during the pelagic larval phase, is the most likely mechanism that brings postlarval and juvenile penaeid shrimp into shallow-water coastal and estuarine nursery areas from their offshore spawning grounds (Kirkegaard 1975). Evidence of vertical migration of penaeid larvae, which might enhance this onshore movement is, however, mixed and inconclusive (Rothlisberg 1982, p. 541). While it is widely thought that changes in light intensity are the primary environmental cues that initiate and control the diel vertical migrations in aquatic animals, there have been cases in which the timing of the migration was not strictly in phase with changes in sub-surface light and/or the feeding history and strategy of the animals (Rothlisberg 1982, p. 548).

In shallow-water coastal environments, factors affecting light penetration and therefore vertical distribution of animals are numerous and subject to rapid change. Turbulence with concomitant turbidity caused by both wind and tidally induced currents, river and coastal runoff, and rapid phytoplankton growth would be the more significant causes of light reduction. It is these short-term changes in submarine irradiance that are probably responsible for some of the conflicting reports about whether or not penaeid larvae migrate vertically (Rothlisberg 1982, p. 548).

Alternatively, the migration rhythm of pelagic larvae may be quite independent of external factors. The rhythmic vertical movement may be a consequence of the facts that larvae generally move upwards while swimming and have to swim while feeding (Richter 1973, p. 133). Downward migration of a cycle may begin when swimming and feeding activity gradually decrease due to exhaustion and/or satiation (Richter 1973, p. 134).

In Section 2.4.1 overviews are given of works presenting results of field studies which show evidence of vertical migration by penaeid prawn and other larvae. In Section 2.4.2 overviews are presented of works presenting results of mathematical and/or numerical models which show the effects on horizontal displacement of various forms of vertical migration by these larvae.

2.4.1 Observational Evidence

It has been stated that, apart from involuntary transport by water currents, the only significant locomotive activity which has been documented for *Penaeus* larvae is their vertical diurnal migration within the water column (Penn 1975, p. 95). Field studies of these and other species have determined that various regimes of vertical migrations by larvae exist in nature, and many hypotheses as to the mechanisms behind these have been proposed. Some are presented here.

Hannan

In Hannan (1984) the hypothesis that infaunal polychaete larvae (*Mediomastus ambiseta*) sink through the water like passive particles in turbulent near-bottom flows was tested in the field. Because the passive sinking hypothesis could not be falsified in these field experiments, it

was concluded that considerations of hydrodynamical phenomena must be included in studies of larval settlement. The results presented emphasised the necessity of routinely including considerations of small-scale hydrodynamical processes in studies of the ecology of soft-bottom marine systems (Hannan 1984, p. 1115).

The specific hypothesis proposed by Hannan (1984) was that larvae initially reach the sea–floor at sites where particulates with similar fall velocities initially settle. This hypothesis did not, however, require that the deposited organisms remain at these sites. Once larvae are passively deposited over relatively large areas of the sea–floor, they may actively reject the location by swimming into the water or by remaining at the sediment surface to be resuspended and transported away, they may be passively resuspended and transported only during storms, they may redistribute themselves at smaller spatial scales by actively selecting a micro-habitat within that locale, or they may be passively redistributed at smaller spatial scales (Hannan 1984, p. 1109).

Fortier and Leggett

Fortier and Leggett (1982) studied the regulation of ichthyoplankton dispersion in the two-layer circulation of the St. Lawrence upper estuary, Québec, by determining larval abundance and vertical distribution during high frequency sampling at three stations. In particular, they attempted to determine whether, and for how long, the dispersal of the early larval stages of Capelin (*Mallotus villosus*) and Atlantic herring (*Clupea harengus harengus*) species was purely passive, and when and how active swimming began to influence their ultimate large-scale longitudinal dispersion. In Fortier and Leggett (1983) the effect of diel or semidiurnal vertical migrations on the horizontal dispersal of the latter species in the same estuary, and the external stimuli triggering these migrations, were investigated.

Given their size, larvae are subject to turbulent diffusion. Active swimming is a supplementary mechanism by which larvae could diffuse, although the major source of variation in abundance, at a given station, was found by Fortier and Leggett (1982) to be the tidal advection of horizontal gradients. Vertical displacement of herring larvae thus resulted from a combination of active diel migrations and tidal mixing. It was noted, however, that day–night differences in catchability could mask real fluctuations in the vertical distribution of the larvae, thereby making the interpretation of field measurements potentially difficult.

Short-term vertical movements of capelin larvae were found to be passive and controlled by tidal processes. The absence of active migrations across the *pycnocline* prevented the larvae from diffusing faster than freshwater in the horizontal plane. Thus, on the scale of a few tidal cycles, the terms of *the Fickian equation* of transport representing diffusion in partially mixed estuaries were thought to be sufficient to describe the fluctuations in capelin abundance, with the dispersal of larvae smaller than 7 mm being entirely passive. The amplitude of the vertical migrations, and thereby the horizontal diffusivity, of herring larvae larger than 10 mm increased with body size until extensive migrations across the pycnocline produced a complicated pattern of horizontal distribution. Thus divergence between the dispersion of herring larvae and the dispersion of salt increased with body length for larvae larger than 10 mm and hence could not be considered as passive dispersion.

In the Fortier and Leggett (1983) study, semidiurnal fluctuations in the vertical position of herring larvae were precisely in phase with current speed. It was concluded, however, that semidiurnal migrations of feeding herring larvae did not constitute an active response to changes in the nature of tidal flow nor a passive response to vertical mixing, but rather a behavioural response to fluctuations in the vertical distribution of their *prey*. Conversely, Gliwicz (1986) examined non-migratory and migratory populations of a copepod, *Cyclops abyssorum*, in alpine clear-water lakes in the Tatra Mountains of Poland and found evidence to support the view that migratory behaviour in zooplankton was selected for as a means of evading fish *predators*. Similar conclusions were drawn by Miller et al. (1984) in a study of five fin-fish species, over 10% of the species encountered, which contributed over 85% of the annual commercial catch off North

Carolina, USA.

The Fortier and Leggett (1983) results indicated that the amplitude and timing of larval vertical displacements were adapted to minimise interference with the general transport strategy of each (predator and prey) species. The effect of the large-scale circulation remained, however, the central determinant of the horizontal dispersion of the larvae.

Rothlisberg

Based on an idealised larval behaviour and limited knowledge of current regimes, Penn (1975) hypothesised that larvae of *Penaeus latisulcatus*, off Western Australia, were capable of moving onshore against prevailing currents during certain times of the year (see Section 9.1 for details of Penn's hypothesis). Rothlisberg (1982) attempted to test Penn's (1975) hypothesis by intensively sampling the changes in vertical distribution of penaeid larvae in the Gulf of Carpentaria, while simultaneously monitoring currents and other environmental parameters in the water column.

Penaid shrimp larvae sampled over discrete depths and time intervals showed a day-night pattern of vertical distribution. The magnitude of the migrations increased with larval development. The patterns of vertical distribution were variable and depended strongly on light penetration. The abundances of larvae in the surface stratum showed the most consistent relationship with time of day, with the larvae rarely at the surface by day and increasing in abundance at the surface by night. It was also determined that: local currents, runoff, rainfall, etc. affected turbidity, and hence light penetration through the water column; vertical migration generally enhanced horizontal advection; horizontal advection distances and directions were dependent on the current regime and the vertical distribution pattern; and differential advection on a seasonal scale may have been responsible for the temporal and spatial recruitment patterns of postlarvae.

2.4.2 Modelling Simulations

The models associated with some of works cited in the following are discussed in detail in Section 7.2 and Chapter 9. This section is concerned chiefly with the assumptions made in order to derive these models, and the interpretation of the results generated by them.

Rothlisberg, Church, and Forbes

Because the Rothlisberg (1982) study (see Section 2.4.1 for details) was localised and short-term, it was determined to be not very useful in explaining the large-scale temporal and spatial patterns of recruitment (Rothlisberg et al. 1983, p. 512). With proximity to nearshore and estuarine nursery grounds, *Penaeus* postlarvae in the Gulf of Carpentaria were reported to shift from a diurnal modulated behaviour pattern to a vertical migration keyed to the tides. This latter pattern was also determined by Kimmerer and McKinnon (1987) to enable zooplankton populations to maintain their horizontal distributions by the interaction of vertical movement with unidirectional tidal current shear in the poorly stratified Westernport Bay, Australia, although the orientating mechanism for such migration was seen to be difficult to identify. As the late *Penaeus* postlarvae were *epibenthic*, Rothlisberg et al. (1983) thought their behaviour could be influenced by a number of additional factors including current speed, pressure, salinity, or environmental cues in the Gulf of Carpentaria region.

This was emphasised in the results of the Rothlisberg et al. (1983) model (see Section 9.6 for details), in which the precise time at dusk and dawn that the larvae left and arrived at their daytime depth was found to be an important parameter. Though variable—thought to be because of changes in light penetration—it seemed that the daily timing of migration, in relation to tidal periodicity (both seasonal and short-term), was just as important as the geographic proximity of the spawning ground to the nursery area in determining whether or not larvae were successfully advected toward the coast.

Hill (1991c) saw the reasons for vertical migration as including predation avoidance and bioenergetic advantages. A further possibility, however, was that, in the presence of vertical current shear, vertical migration may have been used to regulate horizontal position. For planktonic organisms which would otherwise have only very limited capacity for horizontal movement, it was thought that position control by vertical migration potentially provided a means to affect transport to specific locations (nursery sites for example). Even if vertical migration was not principally adapted for position control, it was stated that the latter may nevertheless have been an incidental effect of vertical movements in sheared flows.

It was thought to be obvious that periodic vertical migration against the background of a steady, sheared current could bring about unidirectional transport of larvae. For example, if a current was sheared in the vertical with positive flow at the sea–surface and weaker negative flow at the sea–bed, vertical migration (no matter what its period) would bring about a net larval drift in the positive direction.

On many parts of the continental shelf, however, currents are dominated not by steady flow but by oscillatory motion of the tides. Furthermore, tidal currents are generally sheared in the vertical with flow weaker close to the sea–bed because of the effect of bottom friction. Vertical migration in a (sheared, oscillatory) tidal current can also bring about long-term transport of larvae and is known as *selective tidal stream transport*. This happens when, for example, organisms rise to near the surface on the flood tide but descend to near the bottom (where currents are weaker) on the ebb, resulting in net transport in the flood direction. Hill (1991c) noted that selective tidal stream transport depends upon the fact that the vertical migration period exactly matches the tidal period.

If the vertical migration period and the tidal period are not equal then, over a sufficiently long time, migration induces no net larval transport. This is because the tidal velocity cycle and the migration cycle are not "phase-locked". Many, largely descriptive, field studies (including Angel 1984; Domanski 1984; Pugh 1984; Roe 1984a, 1984b; Roe and Badcock 1984; Roe, James, and Thurston 1984; Roe et al. 1984; Angel 1989; Hays et al. 1994 for example) have identified vertical migration in particular species. Whilst some of these have concluded that migration may influence position control, Hill (1991c) considered few as having attempted to quantify these effects.

The most common form of vertical migration in the ocean is diel, i.e., migration at a 24 h period which is usually locked to the day-night cycle, with organisms near the surface at night and deeper in the water column during the day (Forward Jr. 1988). It is widely accepted that this pattern of migration is principally adapted either for predation avoidance (Forward Jr. 1988) or to optimise metabolic energy gains. Although not primarily adapted for position control, Hill (1991b) stated that diel migration would nevertheless have an incidental influence upon the horizontal motion of the organisms which execute it. In particular, diel migration in diurnal tidal currents with periods of either the K_1 (23.93 h) or P_1 (24.07 h) constituents could induce large horizontal displacements, as the migration period is almost exactly equal to the tidal period. There is, according to Hill (1991b), a potentially more important and apparently overlooked migration-tide interaction which could induce significant horizontal motion in vertically migrating organisms. The principal solar, semi-diurnal, tidal constituent (S_2) has a period of exactly 12 h. Diel (24 h) migration is thus an exact multiple of the S_2 period and unidirectional transport could be induced by migration-tide interaction.

It was concluded that the actual horizontal motion of a vertically-migrating organism depended not only upon migration-tide interaction but also on other components of flow such as tidal and non-tidal (e.g. wind-driven) residual currents. Migration-induced motion may thus interact with other flow components, enabling, for example, an organism to maintain position in a given location against prevailing mean flows.

Richards, Possingham, and Noye

Richards et al. (1996) saw understanding the mechanisms involved in vertical migration as being particularly important when attempting to model dispersion during the pelagic larval phase of a marine organism's life cycle. It was stated that experiments in both the field and laboratory have shown that the onset and rate of vertical movement by zooplankton can be influenced by both *endogenous* and *exogenous* factors. Possible endogenous factors included sex, age, size, and internal rhythms. Plausible exogenous factors included light conditions, predator and prey abundance, currents, and the distribution of temperature, salinity, and oxygen. Although it was thought to be a combination of factors which influenced and regulated vertical movement, some factors were considered to be more important than others. Light was generally agreed to be the most important cue for the timing of diel vertical movement in many species (Ringelberg 1995) although the exact way in which individuals react to it were, according to Richards et al. (1996), yet to be completely determined (see Section 7.2.3 for details).

In a review of the literature, some general conclusions were drawn by Richards et al. (1996) concerning vertical migration of species with larval life cycle stages. The speed at which zooplankton could propel themselves through water was variable between species, and with age within species. Upward swimming speeds were often quite different from downward speeds. In some species swimming was only possible in the up direction and downward movement was achieved by passive sinking.

More specific conclusions were also drawn by Richards et al. (1996). Movement rates given in the literature often neglected the direction of swimming measured, whether it was horizontal or if vertical, up or down. The duration of swimming was also often not mentioned and rates given were probably the maximum speeds observed. These were likely to be achieved only in short bursts and hence may have overestimated the speed which an individual could maintain, on average, over any reasonable period of time. Other studies of vertical migration over a range of species were reported to have also shown that sharp transitions between day and night distributions could occur at sunset and sunrise (Ringelberg 1995), as predicted by both of the two migration mechanisms considered in the Richards et al. (1996) model, as described in Section 7.2.3 in some detail.

2.4.3 Conclusions

Unless vertical distribution and its temporal variations are known, sampling cannot be planned properly, horizontal distributions cannot be fully interpreted, the relations between larval concentrations and variables ranging from temperature to food availability cannot be determined, and movement of larvae by currents cannot be understood or predicted (Leis 1991, p. 157). The consensus of opinion supports the general movement of larvae up into the water column during the night. *Penaeus latisulcatus* is therefore assumed to follow this general pattern of being most abundant in the upper water column at night, and sinking to the depths during the day (Penn 1975, p. 95). It is assumed that all individuals behave more or less alike, but they may not, and there are few data with which to test the assumption (Leis 1991, p. 165). King and Miracle (1995), however, concluded that intrapopulational genetic variation for vertical migration patterns might explain a significant portion of the variability in the depth distributions of zooplankton populations.

In this thesis a simple diel vertical migration wherein larvae exist near the sea–floor during the day and near the sea–surface during the night, with rapid rising and falling at the approximate times of sunset and sunrise, respectively, will be assumed. This simplification is seen to be justified given the discussions in Section 2.4.1 of observations in the field, and in Section 2.4.2 of the results of analytical models. This simplified regime is also implemented in the proposed dispersion model for reasons of computational expediency, as discussed in Section 6.2. The exact manner of this implementation is discussed in Section 7.3. Representations of vertical migration in existing analytical and numerical larval dispersion models are discussed in Section 7.2 and

Chapter 9, respectively.

Chapter 3

The Tidal Model

Over the past decade at The University of Adelaide, a general three-dimensional eddy viscosity model (`ted`) has been developed to predict tidal motions in shallow seas. It has been thoroughly tested (Bills and Noye 1984; Bills 1991) and has been successfully applied to Spencer Gulf (Bills and Noye 1986) and other Australian coastal seas. The model has been applied to a study of tide and wind induced circulation in the Gulf of Carpentaria (Mitchell et al. 1984) and an investigation of the three-dimensional structure of tide and wind induced currents in Bass Strait (Arnold and Noye 1986). These applications demonstrate the generality and flexibility of the numerical algorithm and grid element coding procedure developed by Bills (1991).

The computer model can be interpreted to act as a means of large scale spatial and temporal interpolation taking into account the approximate bathymetry and coastline of the physical region of interest. To calibrate the model and verify its predictions, some quantitative observations of tidal phenomena are required for this region. Simulations of 32 d are conducted to obtain predicted data sets of 29 d duration. These are subjected to *harmonic analysis* procedures (as described in Easton (1977) and based on least-squares and Fourier decomposition methods) to compare predictions with observations at tidal observation stations situated in Spencer Gulf. Details concerning the methods used to calibrate and validate the numerical model are discussed in Section 3.3.

The tidal model is to be used to determine advective velocities applicable to prawn larvae in the Spencer Gulf region. The proposed application is to be carried out at such fine spatial and temporal resolution that computational requirements of the existing tidal model using the conventional computational hardware on which it was originally developed are impractical. Modifications to enable computations on vector supercomputers are thus deemed necessary. Full appreciation of the required modifications, discussed in Chapter 5, is contingent on a detailed understanding of the basic algorithms of the existing model, discussed in Sections 3.1 and 3.2.

In this chapter, the equations describing tidal motion are presented. Pertinent aspects of the mathematical model are discussed, and the computational model is outlined. The means by which the model is calibrated is discussed, and demonstrated for the case of a coarse grid model of Spencer Gulf, South Australia.

3.1 The Mathematical Model

In this section, the three-dimensional equations describing barotropic tidal motion are presented, along with appropriate boundary and initial conditions. Closure is obtained by prescribing a functional form for the vertical eddy viscosity coefficient, two examples of which are also given. For details concerning the mathematical model beyond the present discussion, see Bills (1991) and Noye and Bills (1992). This section briefly summarises the relevant portions of those works.

3.1.1 The Three-Dimensional Equations

The three-dimensional equations describing tidal motion are well known. They are the Reynolds-averaged Navier–Stokes equations for long waves, written for *barotropic* conditions where stratification in the horizontal and vertical due to temperature and density differences is neglected over tidal time scales. For a derivation based on forces which act on a fluid element, see Nihoul (1975).

Although Spencer Gulf can be classified as an *inverse estuary*, indicating that salinity decreases noticeably from the northern end along the major axis of the Gulf, as described by Noye (1984b), Bye (1981), Bowers and Lennon (1987), and Lennon et al. (1987), saline concentration and consequent spatial variation of water density are not significant driving mechanisms of Gulf circulation on tidal time–scales. Similarly, although water temperature varies noticeably from the mouth of the Gulf to its tip (Provis and Lennon 1983), this variation takes place mostly over a short distance at the northern end and is therefore a minor influence in the present context.

Since Spencer Gulf is less than 350 km long and approximately half that in width, spherical coordinates introducing the effect of the Earth's curvature are not required. A Cartesian horizontal grid—which assumes the Earth is locally flat—is therefore used to model the Gulf. The error incurred by not employing a spherical shell model has been estimated as being less than 0.5% in the north-south direction (Bills 1991).

In the orthogonal Cartesian (x, y, z, t) coordinate system, the equations consist of the mass conservation equation for incompressible flow (the continuity equation)

$$\frac{\partial u}{\partial x} + \frac{\partial v}{\partial y} + \frac{\partial w}{\partial z} = 0, \tag{3.1.1}$$

and the three components of the momentum conservation equation (the momentum equations)

$$\begin{aligned} \frac{\partial u}{\partial t} + u\frac{\partial u}{\partial x} + v\frac{\partial u}{\partial y} + w\frac{\partial u}{\partial z} - fv = &-\frac{1}{\rho}\frac{\partial p}{\partial x} \\ &+ \frac{\partial}{\partial x}\left(N_x\frac{\partial u}{\partial x}\right) + \frac{\partial}{\partial y}\left(N_y\frac{\partial u}{\partial y}\right) + \frac{\partial}{\partial z}\left(N_z\frac{\partial u}{\partial z}\right), \end{aligned} \tag{3.1.2}$$

$$\begin{aligned} \frac{\partial v}{\partial t} + u\frac{\partial v}{\partial x} + v\frac{\partial v}{\partial y} + w\frac{\partial v}{\partial z} + fu = &-\frac{1}{\rho}\frac{\partial p}{\partial y} \\ &+ \frac{\partial}{\partial x}\left(N_x\frac{\partial v}{\partial x}\right) + \frac{\partial}{\partial y}\left(N_y\frac{\partial v}{\partial y}\right) + \frac{\partial}{\partial z}\left(N_z\frac{\partial v}{\partial z}\right), \end{aligned} \tag{3.1.3}$$

and

$$\begin{aligned} \frac{\partial w}{\partial t} + u\frac{\partial w}{\partial x} + v\frac{\partial w}{\partial y} + w\frac{\partial w}{\partial z} - F_z = &-\frac{1}{\rho}\frac{\partial p}{\partial z} \\ &+ \frac{\partial}{\partial x}\left(N_x\frac{\partial w}{\partial x}\right) + \frac{\partial}{\partial y}\left(N_y\frac{\partial w}{\partial y}\right) + \frac{\partial}{\partial z}\left(N_z\frac{\partial w}{\partial z}\right). \end{aligned} \tag{3.1.4}$$

These equations are solved in conjunction with the free surface condition

$$w|_{z=\zeta} = \frac{D\zeta}{Dt}, \qquad \text{i.e.} \quad w|_{z=\zeta} = \frac{\partial \zeta}{\partial t} + (u|_{z=\zeta})\frac{\partial \zeta}{\partial x} + (v|_{z=\zeta})\frac{\partial \zeta}{\partial y}, \tag{3.1.5}$$

and the bottom condition

$$w|_{z=-h} = \frac{D(-h)}{Dt} = 0, \quad \text{i.e.} \quad w|_{z=-h} = -(u|_{z=-h})\frac{\partial h}{\partial x} - (v|_{z=-h})\frac{\partial h}{\partial y} = 0. \tag{3.1.6}$$

The symbols used in the above equations have the following meaning:

t: the time (s), measured relative to the commencement of simulation;

x, y, z: the rectangular Cartesian coordinates (m) with $z = 0$ in the mean sea level (MSL) plane and z-axis directed vertically upwards;

u, v, w: the Cartesian velocity component ($\mathrm{m\,s^{-1}}$) in the x, y, z direction, respectively;

p: the pressure ($\mathrm{N\,m^{-2}}$) resulting from the head of the fluid and atmospheric pressure;

p_a: the atmospheric pressure ($\mathrm{N\,m^{-2}}$);

f: the Coriolis parameter $f = 2\Omega \sin\Phi$ ($\mathrm{s^{-1}}$);

Ω: the Earth's angular velocity of rotation $\Omega \approx 2\pi/(3600 \times 23.9333)\,\mathrm{s^{-1}}$;

$\Phi(x, y)$: the northern latitude (°) ($\Phi < 0$ in the southern hemisphere);

ρ: the density of sea water, assumed constant at $\rho \approx 1027\,\mathrm{kg\,m^{-3}}$;

F_z: the z component of the external body forces ($\mathrm{m\,s^{-2}}$), attributed to gravitational acceleration, i.e. $F_z = -g$;

g: the acceleration due to gravity $g \approx 9.81\,\mathrm{m\,s^{-2}}$;

N_x, N_y: the x, y component of horizontal momentum diffusion ($\mathrm{m^2\,s^{-1}}$)—in general these coefficients have both space and time dependence;

N_z: the z component of the vertical eddy viscosity coefficient ($\mathrm{m^2\,s^{-1}}$)—in general this coefficient has both space and time dependence;

ζ: the free surface elevation (m), measured relative to MSL in the positive z direction;

h: the distance (m) of the sea–bed below MSL;

$q|_{z=z^\star}$: a notation indicating that quantity q is evaluated at $z = z^\star$.

In (3.1.2)–(3.1.4), the Boussinesq form of the Reynolds stresses is used. Because vertical fluid acceleration in tidal motions is negligible compared with acceleration due to gravity, (3.1.4) is approximated by the *hydrostatic* equation

$$\frac{\partial p}{\partial z} = -\rho g. \tag{3.1.7}$$

Integration over depth from some level z to the surface ζ gives the z-dependence of p, viz.

$$p = p_a + \rho g\,(\zeta - z)\,. \tag{3.1.8}$$

Equation (3.1.8) is used to eliminate p from (3.1.2)–(3.1.3) by making the substitutions

$$\frac{\partial p}{\partial x} = \frac{\partial p_a}{\partial x} + \rho g \frac{\partial \zeta}{\partial x}, \tag{3.1.9}$$

and

$$\frac{\partial p}{\partial y} = \frac{\partial p_a}{\partial y} + \rho g \frac{\partial \zeta}{\partial y}. \tag{3.1.10}$$

To solve the equations more easily using finite-difference techniques, a transformation of the depth coordinate is introduced which maps the sea–surface $z = \zeta(x, y, t)$ and the sea–bed $z = -h(x, y)$ to the flat surfaces $\eta = 0$ and $\eta = 1$, respectively (see Figure 3.1). This *σ-transform* has the additional advantage of providing greater resolution per unit depth in shallow

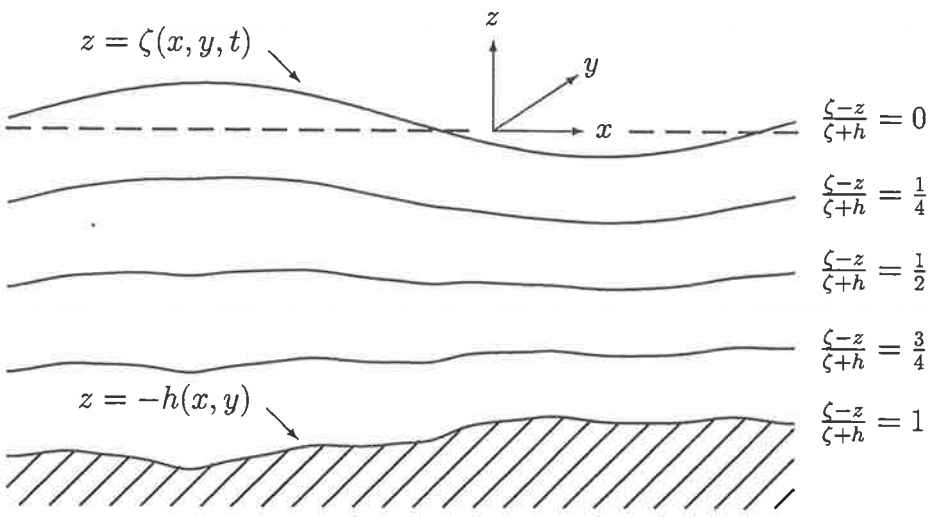

(a) Equally spaced curved surfaces given by $(\zeta - z)/(\zeta + h) = constant$.

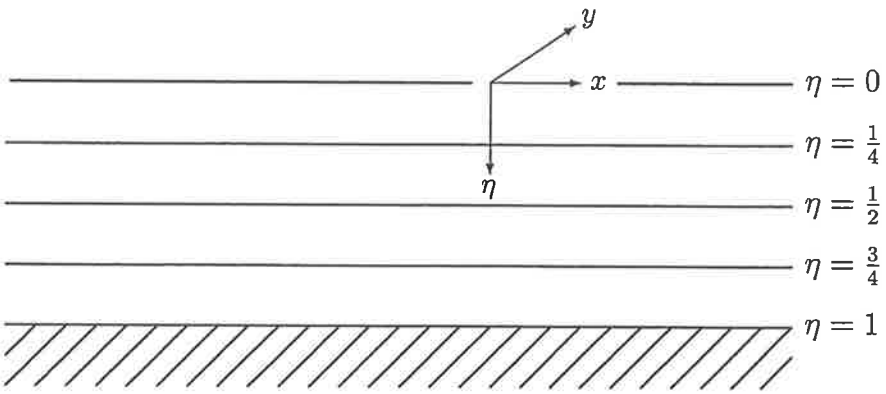

(b) The transformed curved surfaces are level surfaces given by $\eta = constant$.

Figure 3.1: Cartesian (z-x) and transformed (η-x) coordinate system cross–sections.

water. The coordinate transformation from the (x, y, z, t) system to the (x, y, η, t) system is defined by

$$\eta = \frac{\zeta - z}{H}, \tag{3.1.11}$$

where

$$H = \zeta + h \tag{3.1.12}$$

is the total depth. Under the transformation (3.1.11)–(3.1.12), the horizontal velocity components u and v are not changed. However, the vertical velocity component w is transformed and is computed indirectly from a velocity component ω, defined to be normal to the planes $\eta = constant$, as

$$\omega = \frac{D\eta}{Dt}. \tag{3.1.13}$$

Using (3.1.11)–(3.1.12), (3.1.13) can be written as

$$\omega = \frac{1}{H}\left(-w + (1-\eta)\left\{\frac{\partial \zeta}{\partial t} + u\frac{\partial \zeta}{\partial x} + v\frac{\partial \zeta}{\partial y}\right\} - \eta\left\{u\frac{\partial h}{\partial x} + v\frac{\partial h}{\partial y}\right\}\right). \tag{3.1.14}$$

Transformed versions of (3.1.1)–(3.1.4) can also be obtained using (3.1.11)–(3.1.12). For the continuity equation, a depth-averaged form is obtained:

$$\frac{\partial \zeta}{\partial t} = -\frac{\partial (HU)}{\partial x} - \frac{\partial (HV)}{\partial y}, \tag{3.1.15}$$

where U and V are the depth-averaged horizontal velocities

$$U = \int_0^1 u \, d\eta \quad \text{and} \quad V = \int_0^1 v \, d\eta. \tag{3.1.16}$$

The respective forms of the transformed x and y momentum equations used are

$$\begin{aligned} \frac{\partial u}{\partial t} + u\frac{\partial u}{\partial x} + v\frac{\partial u}{\partial y} + \omega\frac{\partial u}{\partial \eta} - fv = -g\frac{\partial \zeta}{\partial x} - \frac{1}{\rho}\frac{\partial p_a}{\partial x} \\ + N_x\frac{\partial^2 u}{\partial x^2} + N_y\frac{\partial^2 u}{\partial y^2} + \frac{1}{H^2}\frac{\partial}{\partial \eta}\left(N_\eta \frac{\partial u}{\partial \eta}\right) \end{aligned} \tag{3.1.17}$$

and

$$\begin{aligned} \frac{\partial v}{\partial t} + u\frac{\partial v}{\partial x} + v\frac{\partial v}{\partial y} + \omega\frac{\partial v}{\partial \eta} + fu = -g\frac{\partial \zeta}{\partial y} - \frac{1}{\rho}\frac{\partial p_a}{\partial y} \\ + N_x\frac{\partial^2 v}{\partial x^2} + N_y\frac{\partial^2 v}{\partial y^2} + \frac{1}{H^2}\frac{\partial}{\partial \eta}\left(N_\eta \frac{\partial v}{\partial \eta}\right). \end{aligned} \tag{3.1.18}$$

Only the leading term in the transformation of the horizontal momentum diffusion terms has been retained in (3.1.17)–(3.1.18). Furthermore, N_x and N_y are here treated as constants.

The equation for the transformed vertical velocity component ω is

$$\omega = -\frac{1}{H}\frac{\partial}{\partial x}\left\{H\left(U^\star(\eta) - \eta U\right)\right\} - \frac{1}{H}\frac{\partial}{\partial y}\left\{H\left(V^\star(\eta) - \eta V\right)\right\}, \tag{3.1.19}$$

and the equation for the Cartesian vertical velocity component w is obtained from (3.1.14) as

$$w = -H\omega + (1-\eta)\left\{\frac{\partial \zeta}{\partial t} + u\frac{\partial \zeta}{\partial x} + v\frac{\partial \zeta}{\partial y}\right\} - \eta\left\{u\frac{\partial h}{\partial x} + v\frac{\partial h}{\partial y}\right\}. \tag{3.1.20}$$

The terms $U^\star(\eta)$ and $V^\star(\eta)$ of (3.1.19) are depth-averaged horizontal velocities over a layer of vertical thickness η extending downwards from the surface $\eta = 0$, i.e.

$$U^\star(\eta) = \int_0^\eta u \, d\eta^\star \quad \text{and} \quad V^\star(\eta) = \int_0^\eta v \, d\eta^\star. \tag{3.1.21}$$

Equations (3.1.16) are equivalent to equations (3.1.21) evaluated with $\eta = 1$, i.e.

$$U = U^\star(1) \quad \text{and} \quad V = V^\star(1). \tag{3.1.22}$$

The form used for the transformed vertical eddy viscosity coefficient N_η is

$$N_\eta(x, y, \eta, t) = \alpha + \beta F(\eta) H \sqrt{U^2 + V^2}, \tag{3.1.23}$$

where the symbols used in this equation have the following meaning:

- α: a minimum absolute (background) N_η value. For tide induced flows $\alpha \geq 0.000014\,\mathrm{m^2\,s^{-1}}$ (corresponding to molecular eddy viscosity). For combined tide and wind induced flows it is typically larger;
- β: a dimensionless constant, determined numerically as the value required to minimise errors between observed and predicted results. The form chosen for $F(\eta)$ and the value chosen for α both influence the optimal value selected for β;

$F(\eta)$: a prescribed function of the transformed depth coordinate η.

The vertical eddy viscosity coefficient used in the simulations presented in this thesis takes the form (3.1.23) with, unless otherwise indicated,

$$F(\eta) = \gamma_1 + 4\eta(1-\eta)(N_{\max} - \gamma_1), \quad \eta \in [0,1] \tag{3.1.24}$$

for purely tide induced flows (following Bills 1991) and

$$F(\eta) = (\frac{1}{2} + \eta)(1-\eta), \quad \eta \in [0,1] \tag{3.1.25}$$

for tide and wind induced flows (following Noye et al. 1981 and 1982). These functions are illustrated in Figure 3.2. In (3.1.24), $F(\eta)$ has a maximum value of $N_{\max}$ at mid-depth and

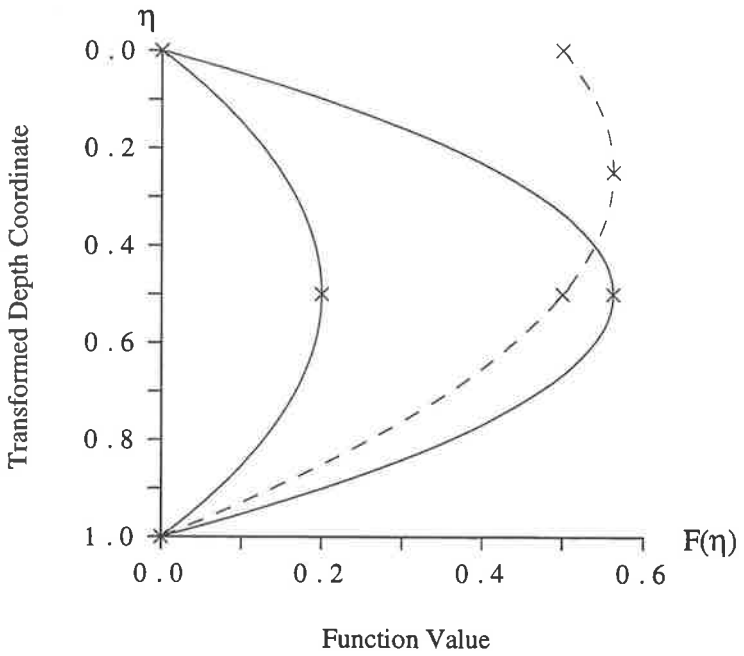

Figure 3.2: Functional forms $F(\eta)$ for vertical variation of vertical eddy viscosity coefficient N_η with tide-only forcing ($\gamma_1 = 0$, $N_{\max} = 0.2$ left solid curve; $\gamma_1 = 0$, $N_{\max} = 9/16$ right solid curve) determined by (3.1.24) and with tide and wind forcing (dashed curve) determined by (3.1.25). Local turning points and other points discussed in the text are indicated (crosses).

has a minimum value of γ_1 at both the sea–bed and the sea–surface. In (3.1.25), $F(\eta)$ has a maximum value of $9/16$ at quarter-depth, a value of $1/2$ at both mid-depth and the sea–surface, with a minimum value of 0 at the sea–bed.

Equations (3.1.15)–(3.1.19) are the basic equations used to solve for the barotropic flow variables ζ, u, v, ω, U, and V. Equation (3.1.23) provides an expression for N_η and closes the system. Equations (3.1.16) and (3.1.21) define the required depth-averaged velocity quantities. Equation (3.1.20) is not necessary to the overall computation, but may be used to calculate the Cartesian vertical velocity w, if required.

3.1.2 The Boundary and Initial Conditions

Appropriate boundary and initial conditions are required to apply the mathematical model to a particular physical region. In the finite-difference approach, the actual boundary of the plan of the region of interest is approximated by horizontal orthogonal line segments parallel to the x and y-axes and it is assumed that the sides of this region can be approximated by rectangular

vertical faces. The latter approximation is required by the nature of the vertical coordinate transformation and follows from the way the interior sea region is modelled by a connected set of flat-bottomed rectangular boxes.

The boundary conditions used are as follows:

1. Assuming the model "coastline" is "solid", a condition of impermeability is

$$(u, v) \cdot \boldsymbol{n} = 0 \quad \text{on the coastline,} \tag{3.1.26}$$

where $\boldsymbol{n}$ is a vector normal to the coastline. If it is assumed that the coastline is constructed of straight line segments passing only through u or v grid–points on a rectangular staggered grid (see Figure 3.3) then (3.1.26) leads to the numerical conditions that, where the coastline runs parallel to the

x-axis, one must have $v = 0$ at v grid–points on the coast,

y-axis, one must have $u = 0$ at u grid–points on the coast.

2. A condition of no-slip is used at the sea–bed so that

$$u = v = \omega = w = 0 \quad \text{at} \quad \eta = 1. \tag{3.1.27}$$

3. Application of the free surface condition (3.1.5) in (3.1.20) with $\eta = 0$ gives

$$\omega = 0 \quad \text{at} \quad \eta = 0 \quad \text{for all time } t. \tag{3.1.28}$$

4. If tide-only forcing is considered, the surface η-gradients of the horizontal velocity components at the sea–surface are zero, i.e.

$$\left.\frac{\partial u}{\partial \eta}\right|_{\eta=0} = 0 \quad \text{and} \quad \left.\frac{\partial v}{\partial \eta}\right|_{\eta=0} = 0. \tag{3.1.29}$$

If there is tide and wind forcing, it is assumed that the surface wind–stress vector (S_x, S_y) is related to the η-gradient of the surface current using the Boussinesq vertical eddy viscosity formulation in the following way

$$S_x = -\frac{\rho}{H}\left(N_\eta \frac{\partial u}{\partial \eta}\right)\Big|_{\eta=0}, \quad S_y = -\frac{\rho}{H}\left(N_\eta \frac{\partial v}{\partial \eta}\right)\Big|_{\eta=0}. \tag{3.1.30}$$

The values of S_x and S_y are determined from the wind velocity using the quadratic laws

$$S_x = \rho_a c_{10} u_{10} \sqrt{(u_{10})^2 + (v_{10})^2}, \quad S_y = \rho_a c_{10} v_{10} \sqrt{(u_{10})^2 + (v_{10})^2}, \tag{3.1.31}$$

with the vertical gradients in horizontal surface velocity components u and v then calculated using (3.1.30). The symbols used in these equations have the following meaning:

ρ_a: the density of air, assumed constant at $\rho_a \approx 1.225\,\mathrm{kg\,m^{-3}}$;

c_{10}: a dimensionless drag coefficient, which depends on wind speed according to some empirical formula. Perhaps the simplest and most widely applicable is that proposed by Wu (1982) for light to hurricane force winds

$$c_{10} = \left(0.8 + 0.065\sqrt{(u_{10})^2 + (v_{10})^2}\right) \times 10^{-3}; \tag{3.1.32}$$

u_{10}, v_{10}: the x and y wind velocity ($\mathrm{m\,s^{-1}}$) components recorded 10 m above MSL.

The wind field may be specified from meteorological data, or may take some idealised time and space dependent form, or may be specified as steady and homogeneous for the entire simulation. Bills (1991) specified zero wind in his simulations, but tide *and* wind forcing is crucial to the present work, as is determined in Sections 4.2 and 10.1.

5. The atmospheric pressure p_a may be specified from meteorological data, or may take an idealised form, or may be assumed to be constant.

6. The open boundaries of the model pass through elevation grid–points and velocity grid–points at which the calculated horizontal velocity component is tangential to these boundaries. Data are not available to provide information about the horizontal velocity component normal to the open boundary. In the case of tide-only forcing, tidal elevation ζ_b at grid element b on the open boundary is specified for all time as the sum of the contributions of the dominant, or major, tidal constituents, i.e.

$$\zeta_b = \sum_{m=1}^{M} f_m a_{m,b} \cos(\omega_m t + V_{0,m} + \mu_m - \gamma_{m,b}), \tag{3.1.33}$$

where the symbols used in this equation have the following meaning:

ζ_b: the tidal elevation (m) specified at the elevation grid–point of open boundary grid element b;

M: the number of dominant tidal constituents m specified at the open boundary;

f_m: the amplitude correction factor for constituent m, taking into account the longer period changes in the celestial positions of the moon and sun;

μ_m: the phase correction (°) for constituent m, taking into account the longer period changes in the celestial positions of the moon and sun;

$a_{m,b}$: the amplitude (m) constant for constituent m at open boundary grid element b;

$\gamma_{m,b}$: the phase (°) constant for constituent m at open boundary grid element b;

ω_m: the angular frequency ($^\circ\,\mathrm{s}^{-1}$) of constituent m, corresponding to idealised motions of the sun and/or moon with period less than one year;

$V_{0,m}$: the phase (°) of constituent m at the start of the epoch: 00:00 hrs on 01/01/1900, Greenwich Meant Time (GMT), at Greenwich, England.

Condition (3.1.33) is applied at each elevation grid–point ζ_b of every grid element b defining the open boundaries, and the specifications of $a_{m,b}$ and $\gamma_{m,b}$ vary with position from element to element. This type of condition is commonly referred to as a *height specified* open boundary condition. The direct effect of the tide-generating forces on the waters of Spencer Gulf is not considered because of the relatively small size of the Gulf.

With tide and meteorological forcing it is not appropriate to constrain the movement of the surface at the open boundaries, as the surface at these grid elements must be able to both accommodate tidal forcing and be free to move in response to the interior solution. The boundary condition used should allow the outward passage of waves (transients produced when modelling commences, meteorologically generated waves, and tidally induced outgoing waves) as well as the inward passage of waves (meteorologically or tidally induced). An appropriately discretised *Sommerfeld condition*

$$\frac{\partial \zeta_b}{\partial t} + c\frac{\partial \zeta_b}{\partial n} = 0, \tag{3.1.34}$$

is used where phase speed c is calculated in the Orlanski (1976) manner (see Bills and Noye 1987), n is measured in the outward normal direction $\boldsymbol{n}$, and meteorological and tidal forcing is specified through the discretisation used for ζ_b.

The initial conditions used are

$$\zeta = u = v = \omega = w = U = V = 0 \quad \text{at time} \quad t = 0. \tag{3.1.35}$$

Consequently, the total depth H is initially set as the MSL depth h. Along the open boundaries, elevation ζ_b at time $t = 0$ is given by (3.1.33) for models forced by both tide and tide and meteorological inputs. The total depth at the open boundaries is therefore given by

$$H_b = h_b + \zeta_b \quad \text{at time} \quad t = 0, \tag{3.1.36}$$

at each open boundary elevation grid–point b.

For numerical solution, the elevation equation (3.1.15) requires one initial condition for every ζ, U, and V grid–point of the model—this is provided by expressions (3.1.33) and (3.1.35). Coastal boundary conditions are also required for the depth-averaged horizontal velocity U and V fields—these are provided by a depth-averaged form of the impermeability condition (3.1.26) applied at coastal velocity grid–points.

The momentum equations (3.1.17) and (3.1.18) require one initial condition for every ζ, u, v, and ω grid–point of the model—this is provided by expression (3.1.35). They require coastal boundary conditions for the depth-dependent horizontal velocity u and v fields—these are provided by the impermeability condition (3.1.26); they also require conditions on flow at the bed and at the free surface—these are provided by the no-slip condition (3.1.27), the free surface condition (3.1.28), and the appropriate horizontal surface conditions (3.1.29)–(3.1.32).

The initial conditions for the vertical velocity equations (3.1.19) and (3.1.20) are given by (3.1.35); the horizontal boundary conditions are those given by the impermeability expression (3.1.26); and the vertical boundary conditions used are the conditions of no-slip (3.1.27) and the free surface condition (3.1.28).

3.2 The Computational Model

In this section, the overall computational process used to solve the equations presented in Section 3.1 is discussed.

A standard uniform Cartesian grid is applied in the horizontal direction to generate cells, or grid elements, of fixed size. A non-uniform grid is applied in the vertical direction η to generate layers, or depth–intervals, of variable size and placement in η-space.

Finite-difference techniques are used to discretise the transformed tidal equations. The equations are differenced on the rectangular "Arakawa C" (Arakawa and Lamb 1977) grid staggered in time and space to maximise the accuracy of the approximations, which are generally second-order convergent, while limiting the number of grid elements involved to nine in the x-y plane—the central grid element and its eight immediate neighbours.

Since the differencing of each equation involves at most a subset of the nine local grid elements, a method of applying the finite-difference equations to a central grid element with any configuration of neighbouring grid elements has been developed by Bills (1991). The method of solution is generally applicable to any bay or coastal sea for which the governing equations are an adequate description of the tidal flow.

For details concerning the computational model beyond what is discussed here, see Bills (1991), or Noye and Bills (1992). This section is essentially a brief summary of the relevant portions of those works.

3.2.1 The Horizontal Grid

In the x-y plane, each grid element contains three grid–points, one each for u and v, and the third for ζ, ω, w, and all other quantities, as shown in Figure 3.3. Because the wind velocity components u_{10} and v_{10} are prescribed values, or are derived from prescribed values, they are also defined at the ζ grid–point, but the depth-averaged horizontal velocity components U and V are defined at the respective u and v grid–points.

The grid used is staggered in space. The spacing between similar grid–points of neighbouring grid elements in the x direction is $2\Delta x$, and in the y direction $2\Delta y$. The horizontal size of a grid element is therefore $2\Delta x \times 2\Delta y$.

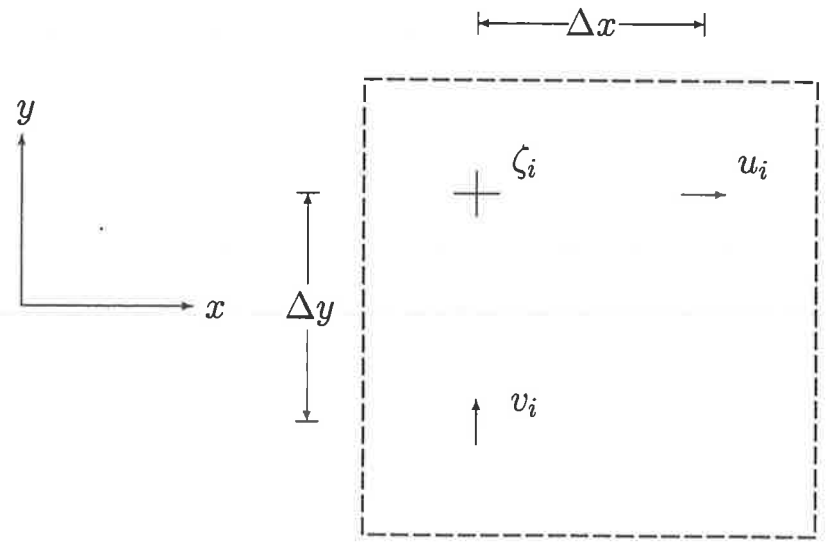

Figure 3.3: A plan view of the ith grid element, indicating the ζ_i, u_i, and v_i grid–points and the horizontal grid–spacings used. The overall element has dimensions $2\Delta x \times 2\Delta y$ m.

3.2.2 The Vertical Grid

Near the sea–bed, vertical gradients in the horizontal velocity components can be large as a result of the no-slip condition (3.1.27) specified there. A grid that is fine near the sea–bed and coarse above it would more accurately model the high shear layer and transmit information to the upper depth–intervals than a uniform grid using the same number of depth–intervals. Near the sea–surface vertical gradients in the horizontal velocity components can again be large, this time as a result of surface wind–stress. In such circumstances, a fine grid near the surface would more accurately convey information to the mid-depth–intervals, and furthermore, would lead to more accurate extrapolations in the horizontal surface velocity discretisation used (Bills 1991), even in the absence of an applied wind–stress. It is therefore best to have a fine grid near the sea–bed, graded to coarse at the middle depth–intervals and back to fine near the sea–surface. Therefore, in the η-direction, a smoothly non-uniform grid–spacing defined by the *Kappa (κ) method* (Sundqvist and Veronis 1970; Noye 1984a; Noye and Bills 1992) is used, with the finest grid near both the transformed sea–bed and sea–surface and a more coarse grid at mid-depths.

The vertical grid–spacings satisfy the second-order convergent relation

$$\Delta\eta_k = \Delta\eta_{k-1}(1 + \kappa\Delta\eta_{k-1}), \quad k = 0, 1, \ldots, \mathbf{nk}, \tag{3.2.1}$$

for a given parameter κ. The terms $\Delta\eta_k$ and $\Delta\eta_{k-1}$ are defined in Figure 3.4; for example, $\Delta\eta_k$ is the distance between the η_k and η_{k+1} depth–levels. Uniform vertical grid–spacings correspond to the value $\kappa = 0$. For $\kappa \neq 0$, the structure of the vertical grid–spacings is chosen to vary symmetrically from fine near the sea–bed, to coarse at mid-levels and back to fine near the sea–surface. In order to generate a symmetrical fine-coarse-fine structure of vertical grid–spacings, equation (3.2.1) is solved iteratively over the interval $\eta \in [0, 0.5]$ and the solution for $\eta \in (0.5, 1]$ is obtained by reflection about $\eta = 0.5$. The values of η required at each depth–level are determined from the spacings $\Delta\eta$.

Numerical tests carried out by Bills (1991) illustrate the necessity to test for the optimum κ for a given application of the three-dimensional numerical model and functional form $F(\eta)$ of the vertical eddy viscosity coefficient N_η chosen. This point is further discussed in Sections 3.3.5 and 3.3.6.

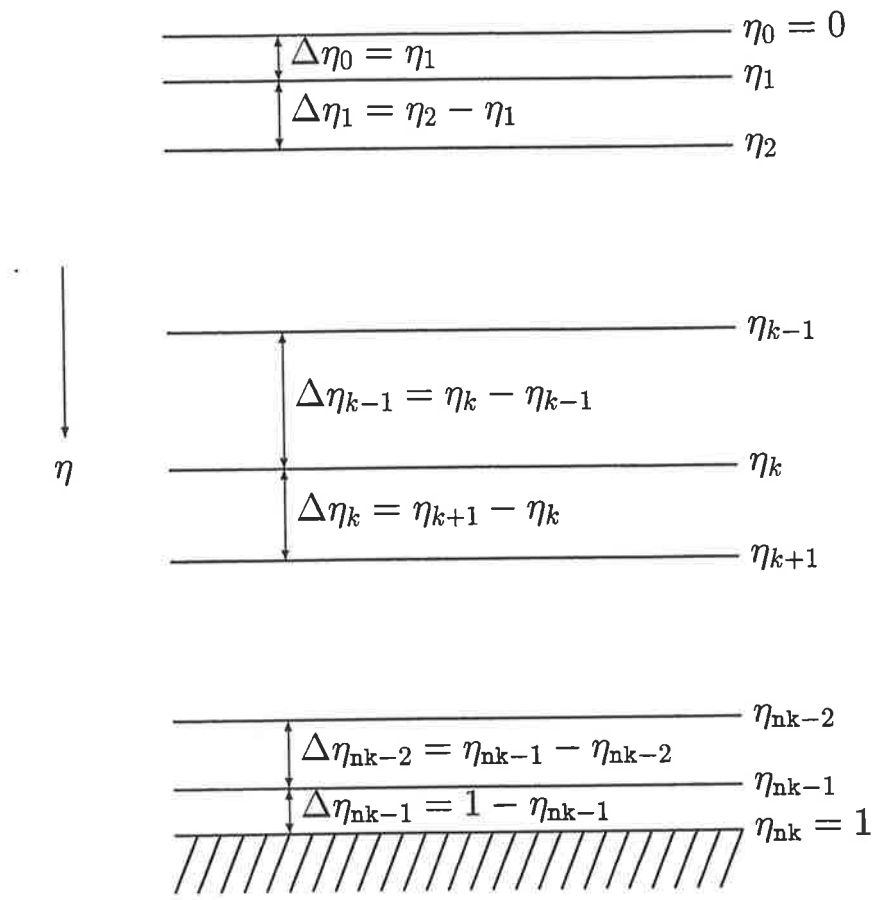

Figure 3.4: An η cross–section of the transformed vertical grid, indicating non-uniformally placed depth–levels η_k and non-uniform depth–intervals $\Delta\eta_k$.

3.2.3 The Finite-Difference Scheme

All difference expressions in the horizontal directions are space-centred and are therefore second-order convergent in space. The difference expressions in the vertical direction are second-order convergent because of the use of the Kappa condition (3.2.1) to specify the vertical grid, as discussed in Section 3.2.2. For details of the differencing used, see Noye and Bills (1992). The difference expressions corresponding to elevation calculations are second-order convergent in time and those corresponding to momentum calculations are approximately second-order convergent in time. The difference expressions for the vertical velocity components ω and w introduce no time discretisation error.

The horizontal momentum diffusion coefficients N_x and N_y depend on the water depth, the horizontal coordinates x and y, and the horizontal grid–spacing, and are computed in the manner adopted by Greenberg (1983), which in turn is based on an approach used by Schwiderski (1980), viz.

$$N_x = (a/2)(2\Delta x)(H_i + H_{i+1})/2 \quad \text{at} \quad U_i, \tag{3.2.2}$$

$$N_x = (a/2)(2\Delta x)(H_i + H_{i_2})/2 \quad \text{at} \quad V_i, \tag{3.2.3}$$

and

$$N_y = (a/2)(2\Delta y)(H_i + H_{i+1})/2 \quad \text{at} \quad U_i, \tag{3.2.4}$$

$$N_y = (a/2)(2\Delta y)(H_i + H_{i_2})/2 \quad \text{at} \quad V_i, \tag{3.2.5}$$

where the reduced eddy coefficient a (s^{-1}) is a specified parameter, subscripts refer to grid elements in the neighbourhood of the central grid element i (as indicated in Figure 3.5) and

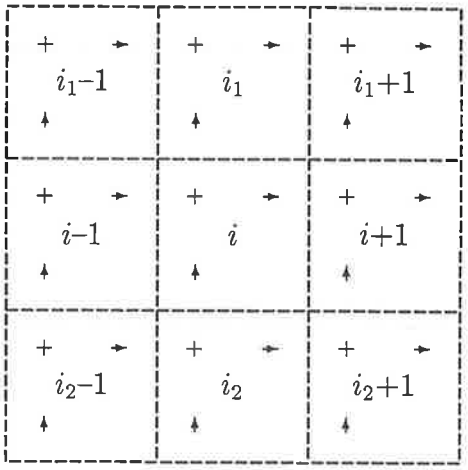

Figure 3.5: A plan view of the ith grid element indicating the relative indexing scheme used for its eight immediate neighbours. The dashed lines represent grid element boundaries. Each quantity defined at the grid–points of a given grid element is indexed according to the index of the central grid element.

$2\Delta x$ and $2\Delta y$ are the horizontal grid element sizes (as indicated in Figure 3.3).

The overall finite-difference scheme is three-level in time. That is, each time–step involves three time–levels: the entry level, the half time–step level, and the full time–step level. For each set of calculations of u and v over one time–step, there are two calculations of ζ, as indicated schematically in Figure 3.6. These are interleaved so that while the first provides

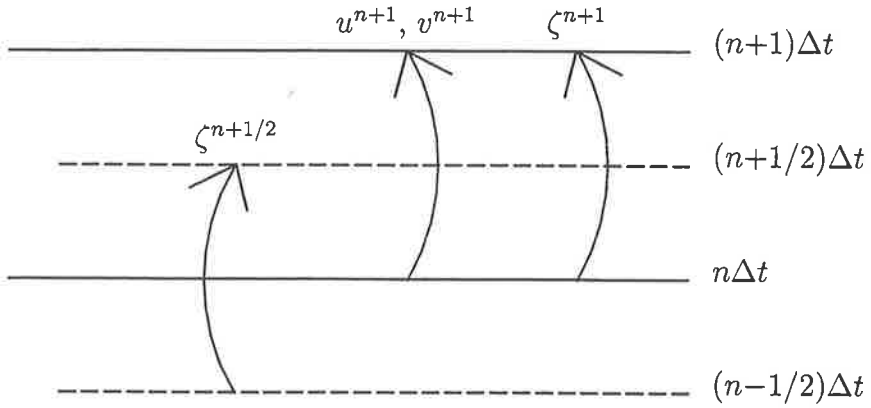

Figure 3.6: The dominant momentum calculations (centre) fed by half time–level calculations of elevation $\zeta^{n+1/2}$ (left) and contributing to full time–level calculations of elevation ζ^{n+1} (right). Superscripts refer to time–levels.

direct calculation of a time-centred value of ζ at the half time–step $(n+1/2)$ for the momentum equations, the second advances this calculation to the full time–step $(n+1)$. The finite-difference scheme is thus dominated by the momentum calculations. There is no need for a forward-time initiation of the scheme since it is commenced by the first ζ calculation which is half a time–step out of phase with the remaining u, v, and ζ calculations—in this way it differs from the usual "*leap-frog*" schemes which do require initiation.

During the $(n+1)$th time–step, ζ is calculated using a time and space-centred explicit scheme at the mid-point of the time–step, $t = (n+1/2)\Delta t$. Space-centred differencing at the $(n+1/2)$ time–level is then used to calculate u and v implicitly in the vertical at each grid element at

the $(n+1)$ time–level—the differencing in time is approximately time-centred. Using accurate discretisations for the surface velocities (Bills 1991; Noye and Bills 1992) the systems of linear equations for u and v are converted to tridiagonal forms which are solved using the Thomas (1949) algorithm. Using the solutions for u and v, the values of U and V are calculated using the third-order convergent composite Simpson's rule for non-uniformly spaced intervals. Then, using these values of U and V, ζ is calculated explicitly at the $(n+1)$ time–level. Finally, ω (and hence w, if required) is calculated explicitly at the $(n+1)$ time–level.

With superscripts to indicate time–levels, the steps of the computational procedure are:

1. Set the model time to time–level $n = 0$
   - Time is $t = n\Delta t = 0$
   - Input the model data and set the initial values
2. Update the model time to time–level $(n+1/2)$
   - Time is $t = (n+1/2)\Delta t$
   - Update the open boundary elevations ζ_b to time–level $(n+1/2)$
   - Calculate the elevations $\zeta^{n+1/2}$ and total depths $H^{n+1/2}$
3. Update the model time to time–level $(n+1)$
   - Time is $t = (n+1)\Delta t$
   - Update the pressure field p_a and hence the pressure p to time–level $(n+1)$
   - Update the wind field (u_{10}, v_{10}) and hence the surface wind–stresses (S_x, S_y) to time–level $(n+1)$
   - Calculate the horizontal depth-dependent velocities u^{n+1} and v^{n+1}
     - Calculate the horizontal depth-averaged velocities U^{n+1} and V^{n+1}
   - Calculate the elevations ζ^{n+1} and the total depths H^{n+1}
   - Update the open boundary elevations ζ_b to time-level $(n+1)$
   - Calculate the transformed vertical velocities ω^{n+1}
     - Calculate the Cartesian vertical velocities w^{n+1}, if required
4. Return to Step 2
   - Repeat this process until the simulation is complete

In the velocity calculations of Step 3, first u^{n+1} and then v^{n+1} are calculated at a given grid element before proceeding to the next. Since computations proceed row by row, the values u^n and v^n calculated in the previous grid row can be used to achieve time-centring for the Coriolis and other terms of the momentum equations in the present row.

3.2.4 The Grid Element Classification Scheme

Grid elements are classified into three types defined according to the nature of their ζ grid–point without regard to neighbourhood configuration:

Type 0: where the ζ grid–point coincides with land;

Type 1: where the ζ grid–point coincides with water inside the model boundaries;

Type 2: where the ζ grid–point coincides with water on a model open boundary;

Type 4: where the ζ grid–point coincides with water outside the model boundaries.

The last classification is used primarily as an aid in visualising the region of interest. Computations are attempted at the ζ, u, and v grid–points of all Type 1 grid elements but are only attempted at u or v grid–points of Type 2 grid elements if they lie inside, and not on, the model open boundary(s). Such elements are called computational elements, as computations are performed *only* on these.

For all depth-independent quantities (such as ζ, U, and V), values are assigned to two one-dimensional vectors in the FORTRAN code, one for each computational element Type (viz. Types 1 and 2). Similarly, for all depth-dependent quantities (such as u and v), two two-dimensional arrays are declared. The positions of the computational elements within the original two-dimensional grid are obtained by means of cross reference lists established at the commencement of modelling. Thus nearly all calculations are carried out using one-dimensional vectors rather than two-dimensional arrays. This approach is computationally efficient since FORTRAN representation of two-dimensional arrays is in essence one-dimensional: a two-dimensional "matrix" is internally stored as a one-dimensional vector constructed by concatenating each successive matrix "column" to the bottom of the previous column. It transpired that this approach also lead to efficient vectorisation of the FORTRAN code. These points are further discussed in Section 5.8.

During each step of the computational process, calculations are carried out in sequential order on the lists of computational elements. This corresponds to passing from one grid element to the next across each grid row from left to right, and down the columns from top to bottom, while suspending all calculations at grid elements of Type 0 and some calculations at grid elements of Type 2. In a computational sweep across a grid row, only computational elements of that row and the rows both immediately preceding and succeeding it are used, due to the computational stencils of the finite-difference representations. Therefore, a computational "*window*" of just three grid rows is required and it is not necessary to retain in memory complete lists for the velocity fields at both time–levels n and $(n+1)$. The advantages of such a system, in terms of memory requirements, are obvious and substantial.

3.2.5 The Finite-Difference Approximations

The advective and diffusive gradients of the x and y momentum equations (3.1.17) and (3.1.18) are differenced across a two-element span and, in that sense, are the most difficult finite-difference approximations of the numerical scheme to implement—all other gradients in these equations are differenced across the span of a single grid element. It is therefore not surprising that for optimal performance these difference approximations should be used in optimal conditions, free from any need to use subordinate approximations or assumptions in providing the values required by their finite-difference expression. If optimal conditions are not present it is better to omit the terms, as necessary, in order to prevent contamination of the solution field by (non-zero) approximations which may result in reduced accuracy when compared to the (zero) "approximation" of omitting them altogether.

Each neighbouring grid element can be considered to contribute information to the calculation of some (finite-difference) quantity at the central computational element. The contribution is included if the neighbourhood of the target computational element is such that all required values are known, approximated if the neighbourhood is such that an appropriate approximation is possible and suitably accurate, and excluded if neither of the above holds. Thus, rather than constructing numerous forms of the discretised equations corresponding to all possible neighbourhood configurations of a computational element, each equation is discretised only once and is written as a set of expressions which constitute the information contributed to the target computational element by a subset of the eight neighbouring grid elements. The contribution of each neighbouring grid element is locally modified according to its Type—the information is either available or, if it is not, an appropriate approximation is constructed if this can be done to a suitable accuracy, or the entire term is omitted if a sufficiently accurate approximation cannot be constructed. Hence each discretised equation is programmed in a general form, and the appropriate differencing of derivatives at any computational element is automated on the

basis of the Type of the grid elements involved.

The Types of the grid elements in the neighbourhood of the target computational element which are involved in the differencing are used in "*integer arithmetic switches*" which perform the same function as logical branches but achieve their aim with fewer FORTRAN statements and better performance (Bills 1991). Minimal use is made of IF...ENDIF constructs.

3.2.6 The Neighbourhood Configuration Scheme

During computations, a *neighbourhood configuration number* (NCN) is used to direct the flow of program control to one of three sections of program code embedded in each subroutine operating on the lists of Type 1 computational elements, each section written for one of the following neighbourhood configurations:

1's: "*open sea neighbourhoods*" where all required grid elements from the neighbourhood of the target computational element i are of Type 1;

0-1's: "*coastal neighbourhoods*" where all required grid elements from the neighbourhood of the target computational element i are a mixture of Types 0 and 1;

0-1-2's: "*open boundary neighbourhoods*" where all required grid elements from the neighbourhood of the target computational element i are of Types 0, 1, or 2.

For each subroutine corresponding to each finite-difference equation, the three sections of FORTRAN code use these three broad classifications of neighbourhood configuration in order to execute correspondingly simplified instructions pertinent to the immediate neighbourhood of the target computational element.

In each case, the first section is the least complicated, involves the fewest computations and is executed most often; the second is more complicated, involves more computations and is executed less often; and the third is the most complicated, is completely general and is executed least often. This is because the fact that there are no open boundary grid elements involved in a "coastal neighbourhood" allows a certain degree of simplification of the general FORTRAN code, which results in modestly improved performance. The fact that there are no coastal grid elements *or* open boundary grid elements involved in an "open sea neighbourhood" allow an even greater degree of simplification of the general FORTRAN code, which results in significantly improved performance. Thus the use of the NCN concept can be thought of as a performance optimisation at the FORTRAN code level. In fact Bills (1991) found that forcing execution through the "open boundary neighbourhood" sections exclusively—thereby employing no simplifications whatsoever based on neighbourhood configuration—results in increases in CPU time on a VAX 11/785 of approximately 98% compared with using the NCN to determine flow of control to the appropriate optimised section. The advantages of this kind of three-way source-code-level acceleration technique, in terms of CPU time requirements, are obvious and substantial. It is shown in Chapter 5 that, while this may be the case for scalar minicomputers such as the VAX 11/785, it may not be for vector supercomputers such as the CRAY Y-MP, depending on the exact implementation of the flow of control.

3.3 Calibration

Once the physical region to be numerically modelled has been determined, the modeller must decide on the values to be assigned to the many parameters which must be input to the program to complete a successful simulation of the tidal motions in the region. Some of these input parameters are to a certain extent bounded by the resources available—in terms of computational power and storage, and the existence and accuracy of measurements of physical constants and field data observations. Some may also be bounded by physical considerations pertinent to the particular application at hand. Many, however, are not subject to any such *a priori*

bounds. The process by which the values of these latter parameters are chosen, with the intent of producing the most physically realistic predictions, is what is meant by the term *calibration*.

There are in fact several parameters by which the model is calibrated. Some of these have greater influence on predictions than others and all are interdependent—that is, changing the value of one parameter influences the effect of the rest, to varying degrees. The suitability of one input parameter set over another is determined by comparison of the predictions of the respective simulations with each other and by establishing error measures to compare the model predictions with field observations recorded in the region of interest—possibly, but not necessarily, during the time interval of interest.

In this section, the observational data pertinent to numerical tidal models of Spencer Gulf are given, and the correspondence between the physical Gulf and the numerical Gulf is outlined. The error measures used to enable comparisons to be made between predictions of different simulations and the field observations are then presented, and their use described. The remaining input parameters to be specified by the modeller are then discussed, and factors influencing their determination are addressed. The points that must be considered when deciding what values are to be input to the program, and possible strategies for their determination, are then discussed.

For further details concerning the calibration process beyond what is discussed here, see Bills (1991).

3.3.1 Spencer Gulf Field Observations

Figure 1.2 indicates important features, towns, and places in Spencer Gulf, South Australia, and Figure 1.3 indicates the position of tidal observation sites within the Gulf. These figures should be consulted to determine the position of any place or station mentioned in the text.

The open boundary of the horizontal grid for both the coarse and fine grid Spencer Gulf models of Section 3.4 and Section 6.4, respectively, is specified so as to span the mouth of the Gulf close to four observation sites where tide–height data are available. The positions of these four tidal observation stations, Taylor's Landing, Thistle Island, Wedge Island, and Pondalowie Bay are indicated in Figure 1.3 and the tide–height constants for the four major astronomical constituents used in the height specified open boundary condition (3.1.33) with $M = 4$ are listed in Table 3.1. Two of the major tidal constituents are diurnal (O_1 and K_1) and two are semi-diurnal (M_2 and S_2). There are 24 other locations at which tidal data have been collected within the Gulf. These are also indicated in Figure 3.9 for the coarse grid Spencer Gulf model and in Figure 6.1 for the fine grid Spencer Gulf model. At nine of the tidal stations, Mike, Lima, Red, Yellow, Green, White, North, Cancer, and Capricorn, observations of tidal current only are available. At two tidal stations, Yarraville Shoals and Blue, observations of both tidal current and tide–height are available. Of the known 28 tidal observation stations, the remaining 17 sites, Port Augusta, Beacon #5, Port Pirie, Port Bonython, Whyalla, Port Broughton, Wallaroo, Franklin Harbour, Arno Bay, Port Victoria, Port Neill, Point Turton, Port Lincoln, Taylor's Landing, Thistle Island, Wedge Island, and Pondalowie Bay provide observations of tide–height only. The four major tidal constituent tide–height constants for all 19 of the interior, coastal, and near open boundary tidal observation stations are listed in Table 3.1.

In Table 3.2 the map coordinates of each of the tidal observation stations are listed along with the model location errors, expressed as a fraction of grid element width $2\Delta x = 2\Delta y$ incurred by approximating the physical location of the station by the location of the nearest elevation grid–point of both the coarse and fine grid Spencer Gulf models of Section 3.4 and Section 6.4, respectively.

Observed Spencer Gulf Major Tidal Constituents								
Tidal Observation Station	Tidal Constituent							
	O_1		K_1		M_2		S_2	
	amp.	phase	amp.	phase	amp.	phase	amp.	phase
Interior and Coastal Tide–Height Observation Stations								
Port Augusta	28.3	52.8	44.0	82.7	64.0	212.2	68.6	272.3
Beacon #5	25.0	48.1	47.0	73.4	57.9	196.0	62.0	255.2
Port Pirie	27.6	49.2	42.5	77.4	48.9	197.2	52.9	258.3
Port Bonython	27.0	42.7	41.6	70.6	45.1	185.3	48.6	245.6
Whyalla	25.7	45.2	40.1	72.8	42.1	184.5	45.4	245.2
Port Broughton	17.4	100.9	27.8	110.4	15.8	214.8	15.2	275.4
Wallaroo	21.8	33.3	32.7	61.9	17.1	132.3	16.8	187.1
Franklin Harbour	20.0	34.0	30.0	61.0	22.0	114.0	23.0	173.0
Arno Bay	19.9	8.4	29.5	37.4	25.6	66.6	26.8	120.1
Port Victoria	16.9	20.7	24.5	51.5	18.9	61.9	20.3	116.4
Port Neill	20.8	5.3	30.8	36.2	28.6	56.1	31.2	112.1
Point Turton	16.0	22.9	23.4	51.7	18.4	60.6	19.5	115.1
Port Lincoln	16.7	0.9	24.0	27.4	24.1	32.4	26.2	85.5
Open Boundary Tide–Height Observation Stations								
Taylor's Landing	15.3	359.1	21.2	26.7	19.9	17.1	21.0	68.1
Thistle Island	15.7	1.1	22.2	30.2	19.1	21.2	19.7	71.4
Wedge Island	15.1	6.6	21.0	36.3	16.6	24.1	17.1	74.4
Pondalowie Bay	13.1	12.9	16.6	44.3	13.9	26.3	13.8	78.0
Interior Tidal Current and Tide–Height Observation Stations								
Yarraville Shoals	24.4	39.2	37.2	69.8	32.2	175.5	33.9	236.9
Blue	18.9	19.2	29.7	48.2	20.7	79.4	21.0	130.6

Table 3.1: Amplitude (cm) and phase (°, local time) tide–height constants of the four major tidal constituents for the 19 tidal observation stations sited in the interior, along the coast, and near the open boundary of Spencer Gulf. These tide–height constants are supplied by the National Tidal Facility at Science Park, The Flinders University of South Australia.

3.3.2 Error Measures for Simulation Comparisons

For the comparison of observed and predicted elevations, two simple error measures are the absolute difference between observed (^{o}) and predicted (^{p}) amplitude (μ) or phase (ϕ) for a particular tidal constituent (c), averaged over the number of *calibration stations* in the model. A calibration station is a tidal observation station within the model region, either in its interior or along its coastline, for which good observation data are available. The error measures are

$$\mu_c = \frac{1}{S}\sum_{s=1}^{S} |\mu^o_{c,s} - \mu^p_{c,s}|, \tag{3.3.1}$$

$$\phi_c = \frac{1}{S}\sum_{s=1}^{S} |\phi^o_{c,s} - \phi^p_{c,s}|, \tag{3.3.2}$$

where the symbols used in these equations have the following meaning:

μ_c: the absolute difference between observed and predicted values of harmonic amplitude (cm) for tidal constituent c, averaged over all S calibration stations s;

ϕ_c: the absolute difference (mod $\{360°\}$) between observed and predicted values of harmonic phase (°) for tidal constituent c, averaged over all S calibration stations s;

Spencer Gulf Tidal Observation Station Locations				
Tidal Observation Station	Map Coordinates		Model Location Error ($\times 2\Delta x$)	
	Latitude (°S)	Longitude (°E)	Coarse Grid ($2\Delta x = 5715$ m)	Fine Grid ($2\Delta x = 1905$ m)
Interior and Coastal Tide–Height Observation Stations				
Port Augusta	32°30′	137°46′	**1.76**	0.90
Beacon #5	32°43.8′	137°49′	0.13	0.55
Port Pirie	33°10′	138°01′	**1.16**	0.59
Port Bonython	33°00′	137°45.8′	0.71	0.39
Whyalla	33°01′	137°36′	0.21	0.63
Port Broughton	33°36.1′	137°55.4′	**0.51**	**0.55**
Wallaroo	33°56′	137°37′	0.74	0.59
Franklin Harbour	33°42′	136°57′	**1.09**	**0.43**
Arno Bay	33°54.5′	136°35′	0.54	0.55
Port Victoria	34°30′	137°27′	0.34	0.28
Port Neill	34°07′	136°21′	0.51	0.63
Point Turton	34°56′	137°21′	0.33	0.55
Port Lincoln	34°43′	135°52′	0.33	0.43
Open Boundary Tide–Height Observation Stations				
Taylor's Landing	34°51.5′	135°57.4′	**0.74**	0.71
Thistle Island	35°00.4′	136°11.0′	**0.34**	**0.79**
Wedge Island	35°04.3′	136°28.2′	0.46	0.28
Pondalowie Bay	35°14.2′	136°49.9′	**0.21**	0.16
Interior Tidal Current and Tide–Height Observation Stations				
Yarraville Shoals	33°17.0′	137°35.6′	0.16	0.35
Blue	34°12.4′	137°17.1′	**0.38**	0.24
Interior Tidal Current Observation Stations				
Mike	33°23.7′	137°30.8′	**0.50**	**0.51**
Lima	33°45.4′	137°22.0′	**0.13**	**0.63**
Red	33°51.4′	136°47.8′	**0.20**	**0.51**
Yellow	34°01.2′	137°00.4′	**0.24**	**0.28**
Green	34°05.7′	137°09.2′	-	**0.55**
White	34°16.6′	137°22.8′	**0.21**	**0.51**
North	34°35′	136°42′	-	**0.32**
Cancer	34°49′	136°33′	-	**0.47**
Capricorn	34°57′	136°32′	-	**0.63**

Table 3.2: Latitude (°S) and Longitude (°E) and model location errors ($\times 2\Delta x$), for the 28 tidal observation stations of both the coarse and fine grid Spencer Gulf models. Map coordinates are provided by the National Tidal Facility at Science Park, The Flinders University of South Australia. Location errors are estimated as the direct distance from the physical location of the tidal station (i.e. the map coordinate) to the model location (i.e. the nearest elevation grid–point) expressed as a multiple of the horizontal element dimension (i.e. $2\Delta x$). Stations Mike, Lima, Red, Yellow, Green, White, North, Cancer, and Capricorn were not considered for the coarse and fine grid Spencer Gulf models presented in this work. The data for these four stations were provided by Dr. Rick Nunes Vaz of the Australian Defence Force Academy, Canberra. Sites **not** used as tidal calibration stations in the models have their respective location error listed in bold face type.

s: the calibration station index;

S: the number of calibration stations s whose model location error is less than $2\Delta x$, the horizontal grid element dimension;

$\mu^o_{c,s}$: the observed amplitude (cm) of constituent c at station s;

$\phi^o_{c,s}$: the observed phase (°) of constituent c at station s;

$\mu^p_{c,s}$: the predicted amplitude (cm) of constituent c at station s;

$\phi^p_{c,s}$: the predicted phase(°) of constituent c at station s.

The overall average absolute amplitude error μ (cm) and phase error ϕ (°), respectively, for a group of constituents are

$$\mu = \frac{1}{C}\sum_{c=1}^{C}\mu_c, \tag{3.3.3}$$

$$\phi = \frac{1}{C}\sum_{c=1}^{C}\phi_c, \tag{3.3.4}$$

where the symbols used in these equations have the following meaning:

C: the number of harmonically analysed tidal constituents c at calibration stations s;

c: the tidal constituent index.

Consider the overall average absolute complex difference between observed and predicted results given by

$$\varepsilon = \frac{1}{CS}\sum_{c=1}^{C}\sum_{s=1}^{S}\left|[\mu e^{\imath\phi}]^o_{c,s} - [\mu e^{\imath\phi}]^p_{c,s}\right|, \tag{3.3.5}$$

where the symbols used in this equation have the following meaning:

ε: the average absolute complex difference (cm) between observed and predicted results over all S calibration stations s and all C harmonically analysed constituents of interest c;

e: the base of natural logarithms;

$\imath$: $\sqrt{-1}$.

The error measure ε effectively takes the lengths of the differences between the complex vectors given by the observed and predicted results and averages them over all calibration stations and the constituents of interest. It may be alternatively expressed as

$$\varepsilon = \frac{1}{CS}\sum_{c=1}^{C}\sum_{s=1}^{S}\sqrt{\left(\mu^o_{c,s}\right)^2 - 2\mu^o_{c,s}\mu^p_{c,s}\cos(\phi^o_{c,s} - \phi^p_{c,s}) + \left(\mu^p_{c,s}\right)^2}, \tag{3.3.6}$$

where the argument of the square root has the form of the cosine rule for determining the length of the unknown side of the triangle formed by the observed and predicted vectors. It should be noted that, although different sets of observed and predicted results may give rise to the same value for the error measure ε, overall it proves to be a useful error measure (Bills 1991).

3.3.3 Specifying the Horizontal Grid

It is generally the case that reducing the grid element size leads to greater accuracy in numerical predictions. However, limits are imposed on horizontal grid element size by the memory capacity of the computer available as well as the central processor unit (CPU) and wall-clock time allocated for running the required simulations. Thus the optimal values for Δx and Δy are usually determined by a compromise between the potential accuracy of using small values and the efficiency of using large values, numerical stability notwithstanding.

3.3.4 Specifying the Horizontal Eddy Viscosity

The values of the coefficients of horizontal eddy viscosity N_x and N_y are calculated using the Schwiderski formulation (3.2.3)–(3.2.5) with the reduced eddy coefficient set at

$$a = 0.0055\,\mathrm{s}^{-1} \tag{3.3.7}$$

for all simulations reported in this thesis. No calibration of this coefficient is attempted here since, based on the calibration for the depth-averaged model of Bills (1991), variation of a is unlikely to have significant effect, as the depth-averaged model was found to be virtually insensitive to this parameter.

3.3.5 Specifying the Vertical Grid

For a uniform arrangement of depth–intervals in the vertical, the accuracy of solution is found to increase as the number of depth–intervals is increased (Bills 1991). However beyond a certain number of intervals, improvement is almost negligible while the costs in terms of increased requirements for computer memory and computational time continue to rise significantly. Each extra depth–interval used must be taken into account when performing depth-averaging and also requires computer memory for another three components of velocity per computational element.

Since Spencer Gulf is not deep and its sea–bed topography is relatively smooth on the scale chosen for the horizontal grid–spacings (see Sections 3.4 and 6.3), the number of depth–intervals required to determine the vertical current structure accurately does not need to be very large. Tidal currents were required to be simulated over a total period of 6 mo, as specified by SARDI research officers and in turn determined by the life cycle of *Penaeus latisulcatus* in Spencer Gulf (see Section 2.2.2). Simulations corresponding to eight different 6 mo periods were requested by SARDI research officers, at high spatial resolution. This, in addition to the computational effort required to calibrate the new high resolution tidal model, necessitated the use of a supercomputer to compute the required tidal velocity predictions. Specification of each additional depth–level would result in a significant increase in computational load, but on the other hand, a suitable spacing of the available depth–levels can improve the accuracy of predictions (Bills 1991).

When all these factors are taken into account, ten depth–intervals spaced in the optimal fashion suffice to provide greatest accuracy, use least computer memory, and give accurate representation of vertical profiles of velocity for a reasonable amount of processing time.

The actual variation of the grid–spacing used in all simulations reported in this thesis is smooth, and is based on the second-order convergent relationship (3.2.1) between consecutive vertical grid–spacings governed by the parameter κ as discussed in Section 3.2.2. For a vertical grid of ten depth–intervals, the influence of κ on the relative depths η_k and the depth–intervals $\Delta\eta_k$ is illustrated qualitatively in Figure 3.7 and quantitatively, for the two values of κ used throughout this thesis, in Table 3.3.

3.3.6 Specifying the Vertical Eddy Viscosity

Tide-Only Forcing

In Bills (1991) it was seen that, for tide-only forcing, symmetric parabolic profiles for the vertical eddy viscosity coefficient which prescribe small values (γ_1 in (3.1.24)) at the sea–surface and sea–bed generated physically reasonable horizontal velocity profiles. In addition, the closer the background values (α in (3.1.23)) approached molecular viscosity, the more accurate were the model predictions of tide–height at calibration stations in Spencer Gulf. As the γ_1 and α values were reduced, it was found that the resolution of depth–intervals in the near boundary regions should be correspondingly refined. It was shown that specifying molecular viscosity for α and zero for γ_1, together with a correspondingly increased vertical resolution of the bottom shear

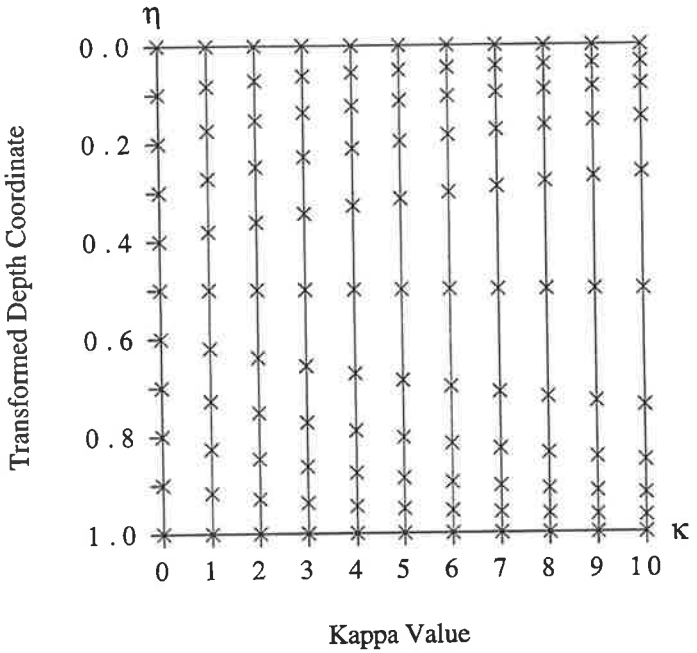

Figure 3.7: The vertical grids generated by using (3.2.1) for different values of κ with 11 depth–levels. The relative positions of depth–levels are indicated by crosses. The structure of the vertical grid is "fine-coarse-fine" symmetrically about mid-depth.

Vertical Grid–Spacing Variation				
Depth Level (k)	Vertical Grid			
	$\kappa = 5.0$		$\kappa = 8.0$	
	η_k	$\Delta\eta_k$	η_k	$\Delta\eta_k$
0	0.000000	0.050378	0.000000	0.039227
1	0.050378	0.063070	0.039227	0.051538
2	0.113448	0.082953	0.090765	0.072786
3	0.196401	0.117364	0.163551	0.115169
4	0.313765	0.186235	0.278720	0.221280
5	0.500000	0.186235	0.500000	0.221280
6	0.686235	0.117364	0.721280	0.115169
7	0.803599	0.082953	0.836499	0.072786
8	0.886554	0.063070	0.909235	0.051538
9	0.949622	0.050378	0.960773	0.039227
10	1.000000	-	1.000000	-

Table 3.3: Relative depths η_k and vertical grid–spacings $\Delta\eta_k$ as determined by (3.2.1) for $\kappa = 5.0$ and 8.0, with 11 depth–levels. The structure of the vertical grid is "fine-coarse-fine" symmetrically about mid-depth. The depth–levels k are numbered from the surface downwards in the direction of increasing η.

layer, gave rise to optimal results for a three-dimensional Spencer Gulf tidal model. It is for this reason that, for all simulations with tide-only forcing reported in this thesis,

$$\alpha = 0.000014\,\mathrm{m^2\,s^{-1}} \tag{3.3.8}$$

in (3.1.23) and

$$\gamma_1 = 0 \tag{3.3.9}$$

in (3.1.24). For the sake of standardisation, $N_{\max}$ is set at

$$N_{\max} = 0.2\,\mathrm{m^2\,s^{-1}}, \tag{3.3.10}$$

as indicated by the left solid curve of Figure 3.2. Whatever the value of $N_{\max}$ chosen, the optimal value of β in (3.1.23) is chosen accordingly. This concept is further discussed in Section 6.6.

Tide and Wind Forcing

For simulations of tide and wind induced flows, the asymmetric vertical viscosity coefficient profile as specified by (3.1.23) and (3.1.25), and indicated by the dashed curve of Figure 3.2, is used. The value of the background viscosity parameter α used is given by (3.3.8) unless otherwise specified, while the value of the parameter β is determined by the calibration process. This concept is further discussed in Section 6.6.

3.3.7 Determining Mean Sea Level from Indian Spring Low Water

Since chart datum is clearly defined as Indian Spring Low Water (ISLW) it is possible to generate mean sea level (MSL) by an iterative process, to the accuracy of the datum depth field used. Rather than manually estimating MSL by judiciously choosing corrections to add to ISLW from the observed tidal amplitude data for the major tidal constituents at each elevation grid–point, the model itself is used to carry out the required correction. The ISLW depth field is used as a zeroth estimate for MSL everywhere interior to the model and along the open boundary. A simulation is then conducted to obtain 29 d of predicted tide–heights for each Type 1 elevation grid–point in the model. The predictions are harmonically analysed (Easton 1977) and a first estimate for the MSL depth field is obtained as

$$\mathrm{MSL}^{(1)} = \mathrm{ISLW} + (\mathrm{O_1} + \mathrm{K_1} + \mathrm{M_2} + \mathrm{S_2})^{(1)}, \tag{3.3.11}$$

where amplitudes are inferred for the bracketed quantities and the superscript "$^{(1)}$" refers to quantities obtained after the first iteration. Along the open boundary, the added amplitudes are taken from the forcing data specified by (3.1.33) with $M = 4$ ($\mathrm{O_1}$, $\mathrm{K_1}$, $\mathrm{M_2}$, and $\mathrm{S_2}$ are used), so no further adjustments there are required. The tidal model is then run using $\mathrm{MSL}^{(1)}$ as the (new) estimate for MSL and, from a harmonic analysis of a new set of predicted tide–heights, a second update, $\mathrm{MSL}^{(2)}$, is obtained for the interior computational elements by adding the new set of predicted amplitudes to ISLW, and so on. The process by which MSL is generated from ISLW can thus be summarised as

$$\mathrm{MSL} = \lim_{i\to\infty}\left\{\mathrm{MSL}^{(i)}\right\} = \mathrm{ISLW} + \lim_{i\to\infty}\left\{(\mathrm{O_1} + \mathrm{K_1} + \mathrm{M_2} + \mathrm{S_2})^{(i)}\right\}, \tag{3.3.12}$$

where

$$\mathrm{MSL}^{(0)} = \mathrm{ISLW}, \tag{3.3.13}$$

and

$$(\mathrm{O_1} + \mathrm{K_1} + \mathrm{M_2} + \mathrm{S_2})^{(0)} = 0, \tag{3.3.14}$$

and the pseudo-equations (3.3.11)–(3.3.14) apply at each elevation grid–point. The iteration process idealised in expressions (3.3.12)–(3.3.14) generates a MSL depth field to an accuracy at least as good as the ISLW depth field used. Three iterations are generally sufficient.

The MSL depth field obtained using this technique depends on the open boundary data used, but these are assumed fixed for both the coarse and fine grid Spencer Gulf models. They are defined in Tables 3.4 and 6.1, respectively. It also depends on the other parameters discussed above, but these also are held constant throughout the iteration process.

3.3.8 Determining the Optimal Time–Step

The time–step used in the numerical scheme is, as usual, determined by computational resource (machine speed and accuracy, and CPU and wall–clock time allocations, etc.), field observations (extent and completeness of surface wind input data, resolution and accuracy of bathymetry data, and hence horizontal grid element dimensions Δx and Δy), and numerical stability constraints. Stability is qualitatively determined by test simulations and can be quantitatively measured by the Courant number

$$c_{\max} = \frac{\sqrt{gh_{\max}}\Delta t}{\min\{2\Delta x, 2\Delta y\}}, \tag{3.3.15}$$

following Flather and Heaps (1975), where

$$h_{\max} = \max\{\mathrm{MSL}_n^{(I)}\}, \tag{3.3.16}$$

and symbols used in these equations have the following meaning:

$\min\{p, q\}$: The minimum of quantities p and q;

$\max\{q_n\}$: The maximum of quantity q over all computational elements n;

$\mathrm{MSL}_n^{(I)}$: the MSL depth (m) of the (final) Ith $\mathrm{MSL}^{(i)}$ iterate at the computational element n.

The standard Courant–Friedrichs–Lewy (CFL) condition

$$c_{\max} \leq 1 \tag{3.3.17}$$

can be used in conjunction with (3.3.15) to derive the relation

$$\Delta t_{\max} \leq \frac{\min\{2\Delta x, 2\Delta y\}}{\sqrt{gh_{\max}}} \tag{3.3.18}$$

for the theoretical maximum stable time–step for a model application. Values for $h_{\max}$, $\Delta t_{\max}$, and $c_{\max}$ calculated for the coarse and fine grid Spencer Gulf models are given in Sections 3.4 and 6.3, respectively.

3.4 The Coarse Grid Spencer Gulf Model

While reading this section, the reader may wish to consult Figures 1.2 and 1.3, or Figures 3.9 and 4.1, for the location of tidal observation stations and other features of Spencer Gulf. In the following, it should be noted that the true orientation of the grid is 33.33° T (or approximately NNE). This orientation is adopted in order to align the grid with the predominantly axial flow in the Gulf. All plots showing model results will be aligned with model axes parallel to the edges of the page, as indicated by the compasses in the relevant figures.

Taking the factors discussed in Section 3.3.3 into account, the grid elements of the coarse Spencer Gulf model were chosen to have horizontal dimensions $2\Delta x = 2\Delta y = 5715\,\mathrm{m}$.

The coarse grid model is defined by the grid element Type input matrix shown in Figure 3.8. In Figure 3.9 Reevesby Island, of the Sir Joseph Banks Group, and Boston Island, in Port Lincoln

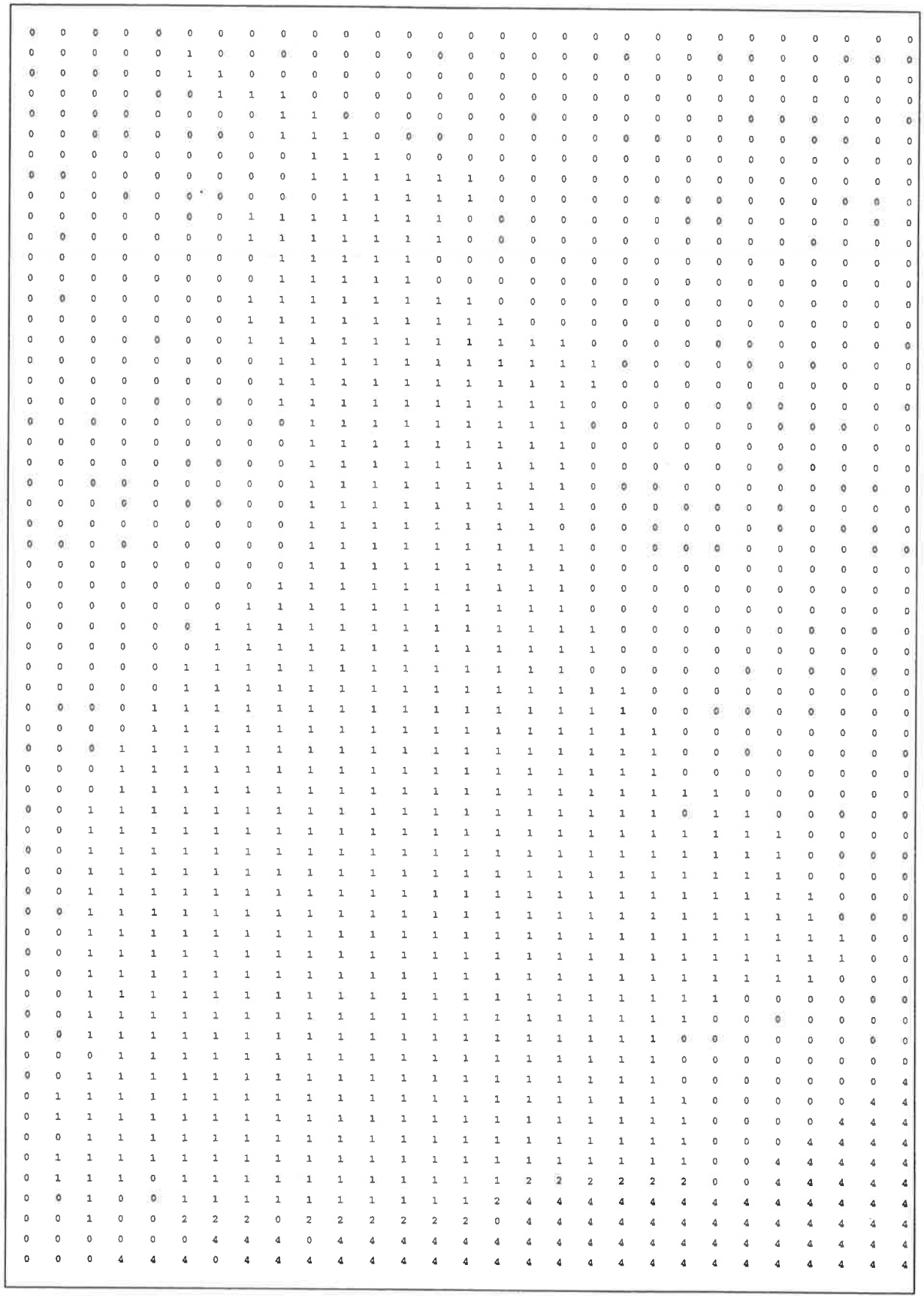

Figure 3.8: The grid element Type input matrix for the coarse grid Spencer Gulf model. Land grid elements are represented by 0, open boundary grid elements by 2, interior (water) computational elements by 1, and exterior (water) grid elements by 4. The latter Type is used for illustrative purposes only.

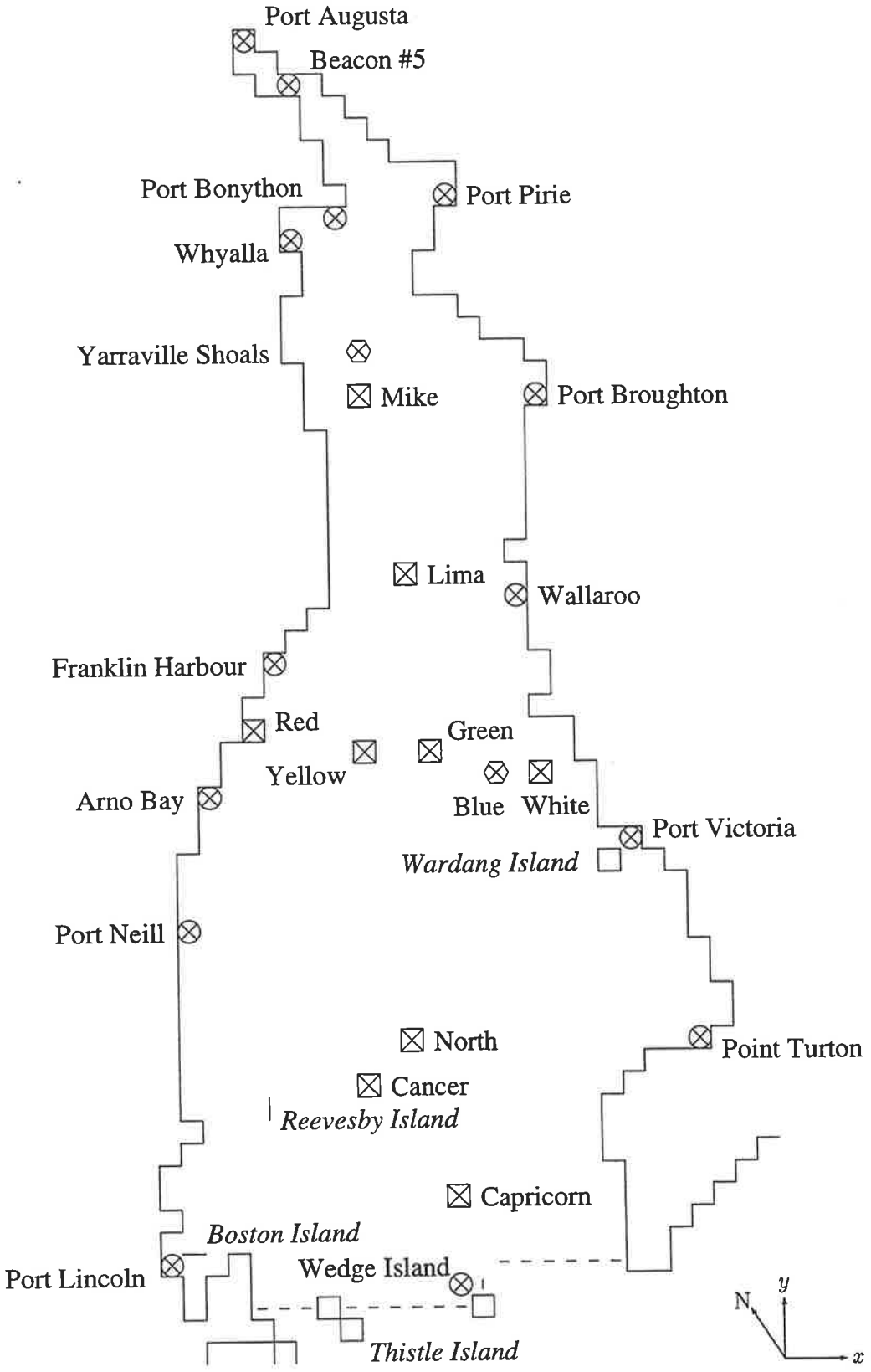

Figure 3.9: The coarse grid Spencer Gulf model, indicating the model location of the coastal boundary (solid line), the open boundary (dashed line), and the tidal observation stations for tide–heights only (crossed circles), tidal currents only (crossed squares), and both (crossed hexagons). Stations (roman) and islands (italics) are named.

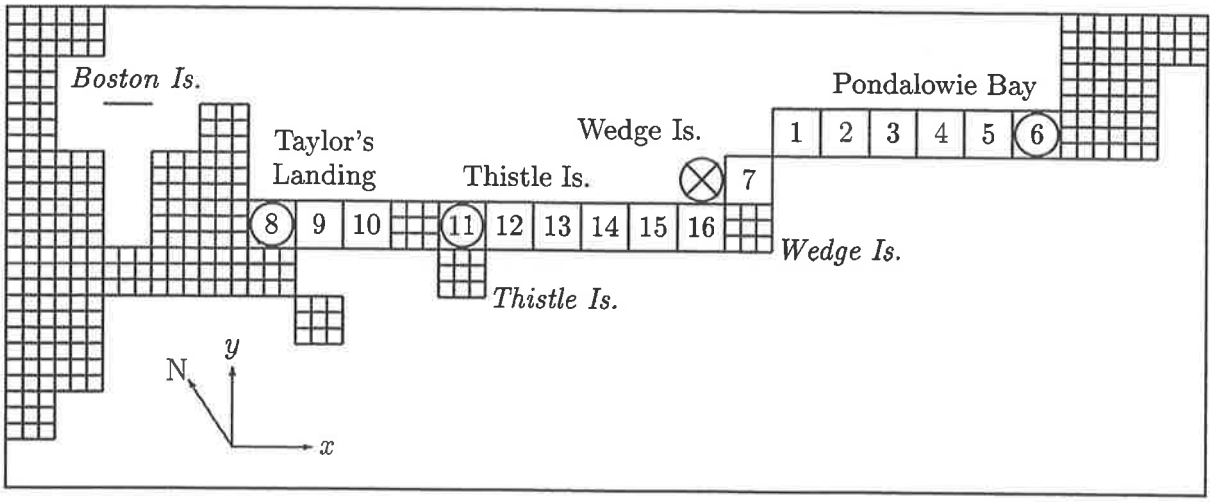

Figure 3.10: The open boundary region of the coarse grid Spencer Gulf model, indicating the numbering scheme for the 16 open boundary Type 2 grid elements. Grid elements corresponding to land are shown hatched. The non-hatched region above the open boundary consists entirely of Type 1 computational elements. Note the barrier to flow in the y direction at upper left, corresponding to Boston Island in Port Lincoln harbour. This island is too small to be represented by a grid element, but is of sufficient size and appropriate orientation to have $v = 0$ assigned there. Tidal observation stations for tide–height constants used to derive forcing at the open boundary are shown (circles).

harbour—barriers to flow in the x and y directions, respectively—are represented by solid line segments.

The numbering scheme for the Type 2 open boundary grid elements b is as shown in Figure 3.10, and the tidal elevations ζ_b at each of these elements is determined by (3.1.33).

The height specified input data for the 16 elevation grid–points of the open boundary of Figure 3.10 are presented in Table 3.4 and were obtained from the tide–height constants for the four major tidal constituents O_1, K_1, M_2, and S_2 at the four tidal observation stations near the entrance to the Gulf given in Table 3.1, in the following manner:

> The data from these four sites [were] first linearly extrapolated to the nearest elevation point of the open boundary line, and then data for the remaining points of the line [were] linearly interpolated from these values in a way consistent with the co-amplitude and co-phase charts drawn for the mouth of Spencer Gulf by Steinberg (1983) (Bills 1991, p. 155).

The grid element to the immediate left of the open boundary grid element $b = 1$ of Figure 3.10 is treated as an interior Type 1 computational element due to the use of an open boundary condition which allows radiation of waves in a uni-directional sense across the boundary, since:

> This ... avoids a complication that arises if the open boundary conditions are applied to a corner element, when one outward normal direction coincides with one part of the boundary line and another coincides with the remaining part. The ... interior element has a neighbourhood configuration of elements unlike that of the other interior elements since there is no Type 2 element in the (i_2+1)th (i.e. the south-eastern) position; consequently special program code is written for it (Bills 1991, pp. 207–208).

The ISLW datum depth at the elevation grid–point of each Type 1 and Type 2 grid element

Coarse Grid Spencer Gulf Model Open Boundary Tidal Constituents								
Element Number (b)	Tidal Constituent							
	O_1		K_1		M_2		S_2	
	amp.	phase	amp.	phase	amp.	phase	amp.	phase
1	14.7	235.8	20.1	253.1	15.9	109.6	16.4	150.5
2	14.4	236.7	19.4	254.7	15.5	109.9	15.9	151.0
3	14.1	237.6	18.7	256.3	15.1	110.1	15.4	151.4
4	13.8	238.5	18.1	257.9	14.7	110.4	14.9	151.9
5	13.4	239.4	17.4	259.5	14.3	110.6	14.4	152.4
6	13.1	240.3	16.7	261.1	13.9	110.9	13.9	152.9
7	14.8	234.4	20.2	253.7	15.8	108.4	16.3	149.6
8	15.3	226.2	21.2	242.5	20.0	103.0	20.9	143.4
9	15.4	226.8	21.4	243.6	19.8	103.6	20.6	144.1
10	15.5	227.4	21.7	244.7	19.6	104.3	20.4	144.8
11	15.6	228.5	22.1	247.0	19.2	105.6	19.8	146.2
12	15.5	229.4	21.8	248.4	18.5	106.0	19.1	146.7
13	15.3	230.3	21.4	249.9	17.8	106.3	18.4	147.2
14	15.2	231.1	21.1	251.4	17.1	106.6	17.6	147.7
15	15.1	232.0	20.7	252.9	16.3	106.9	16.9	148.3
16	14.9	232.9	20.4	254.4	15.6	107.2	16.2	148.8

Table 3.4: Amplitude (cm) and phase (°, GMT) of the four major tidal constituents at the 16 open boundary grid elements indicated in Figure 3.10 for the coarse grid Spencer Gulf model.

was obtained by Bills (1991) by visually interpolating the data on hydrographic maps **Aus 776–778** (Royal Australian Survey Corps 1982a, 1989, 1990a). It is reproduced in Figure 3.11.

Where grid elements are known to be periodically covered and uncovered during the tidal cycle, it must be decided whether or not to include them as computational elements. Normally these grid elements *will* be included as computational elements but care must be taken when specifying ISLW for them, as there is a danger of the total depth H obtaining an undesirably small positive or even a negative value. The former presents a local stability problem (further discussed in Section 6.5.1), while the latter is clearly physically unrealistic.

A starting value for the depth which will allow the numerical model to execute without becoming unstable at such elements must be chosen. A standard value of 2 m was used for such grid elements; thus all ISLW depths in Figure 3.11 are at least 2 m. This choice is somewhat arbitrary and may be unnecessarily large at some of these elements. It is usually sufficient that the value of ISLW depth specified at such grid element be greater than the sum of the major tidal constituent amplitudes; these may be obtained by performing a simulation and harmonic analysis with the proposed depth field. This concept is further discussed in Section 6.5.1.

Three iterations were sufficient to obtain a "converged" MSL depth field; one which was everywhere different from the previous estimate by less than 1 cm. Figure 3.12 gives the MSL depth field used for the coarse grid Spencer Gulf model and Figure 3.13 reproduces this field as a contour plot. Figures 3.11 and 3.12 show that while the MSL depths near the open boundary are 0.6–0.8 m greater than the corresponding ISLW depths, the increase at the head of the Gulf is as high as 2.1 m. The contours of Figure 3.14, which represent the correction from ISLW to MSL over the entire coarse grid Spencer Gulf model, indicate that the procedure for this resulted in a correction which is highly non-uniform.

Using the MSL depth field of Figure 3.12, the model maximum depth is determined as

$$h_{\max} = 54.75\,\mathrm{m}, \tag{3.4.1}$$

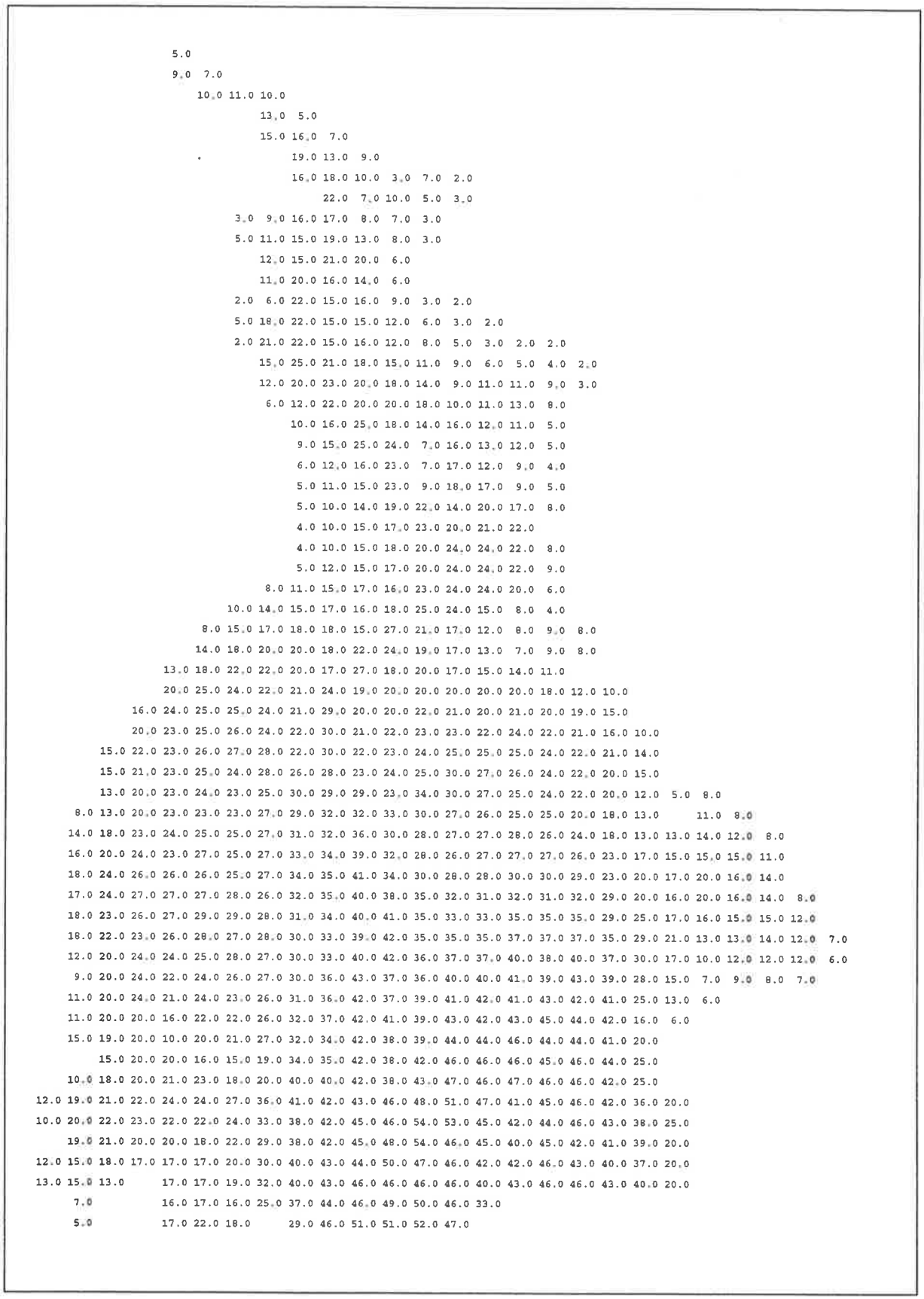

Figure 3.11: The grid element ISLW depths (m) for the coarse grid Spencer Gulf model.

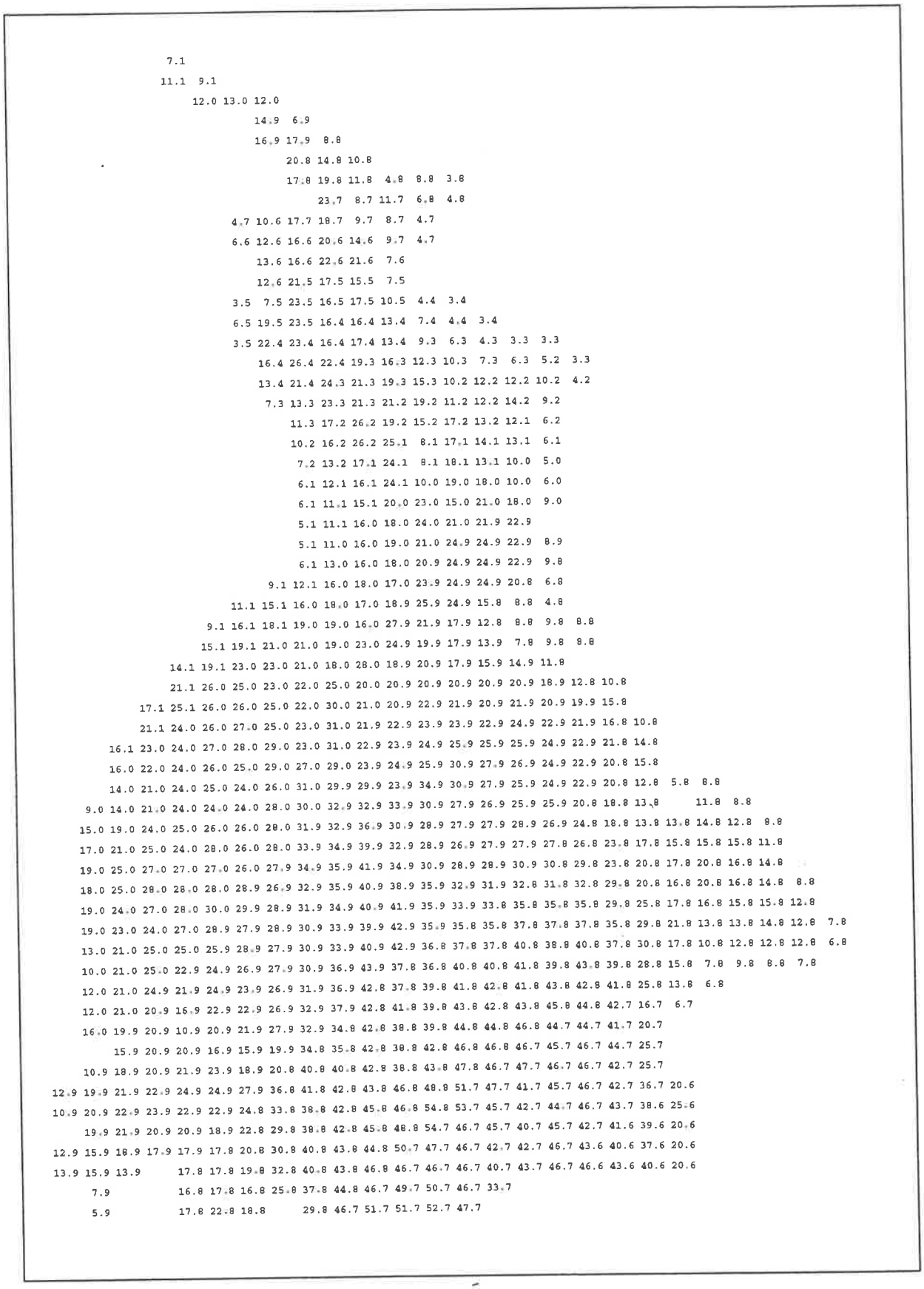

Figure 3.12: The grid element MSL depths (m) for the coarse grid Spencer Gulf model.

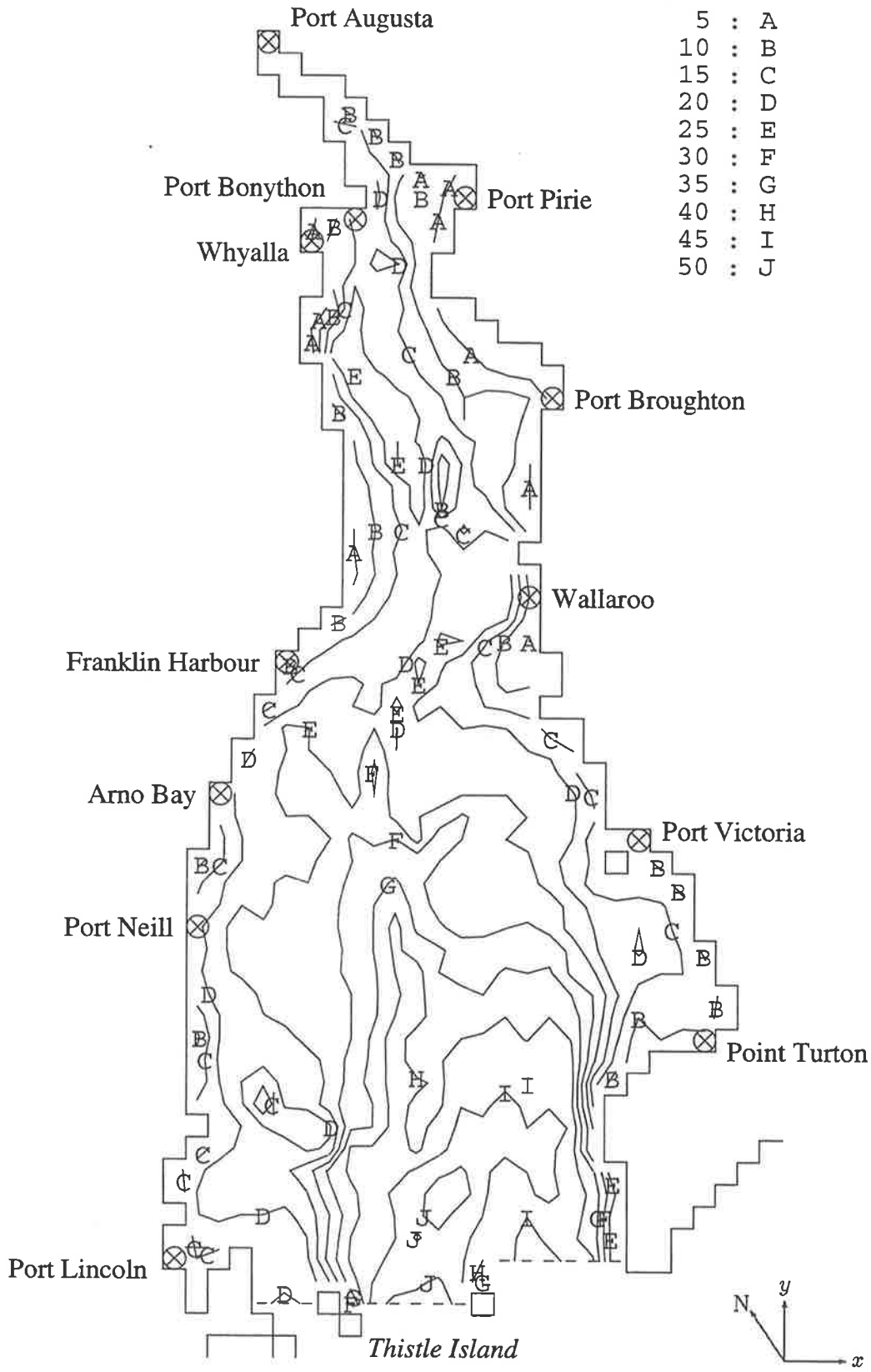

Figure 3.13: The MSL depth contours (m) for the coarse grid Spencer Gulf model. Some stations (roman) and islands (italics) are named.

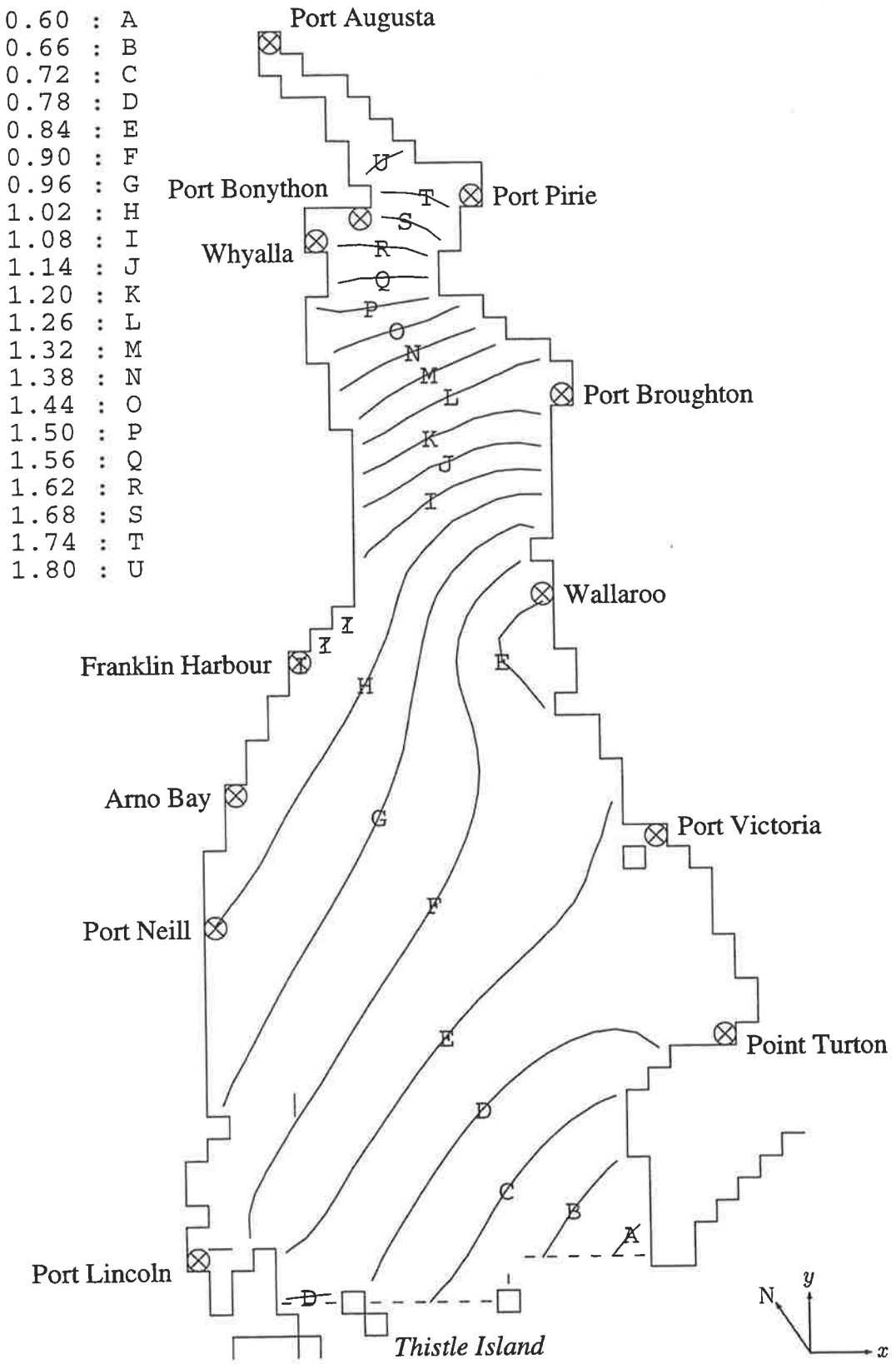

Figure 3.14: The ISLW to MSL depth correction contours (m) for the coarse grid Spencer Gulf model. Some stations (roman) and islands (italics) are named.

giving a model maximum time–step of

$$\Delta t_{\max} = 174.4\,\mathrm{s}, \tag{3.4.2}$$

as determined by (3.3.18). A time–step of $\Delta t = 150\,\mathrm{s}$ was chosen by Bills (1991) to both ensure stability and result in an integer number of time–steps to solution. Experimentally it was found that a time–step of

$$\Delta t = 180\,\mathrm{s}, \tag{3.4.3}$$

resulted in a stable solution having lower CPU time requirements. Using (3.3.15) this time–step results in a Courant number of

$$c_{\max} = 1.03, \tag{3.4.4}$$

which indicates that the theoretical CFL condition (3.3.17) is almost satisfied by the operational parameters of the coarse grid Spencer Gulf model.

3.5 Summary

In this chapter, the mathematical equations that describe tidal flow in shallow seas were stated. A standard transformation of the depth coordinate, used to map the sea–surface and sea–bed onto flat planes, was defined. The boundary and initial conditions used were also presented.

A three-way mechanism for accelerated calculations on computational elements of the most numerous kinds was discussed. A method of automatically generating program code to take account of all plausible coastal and open sea boundary configurations, and dealing with the necessary approximations or omissions, was briefly described.

The method by which the numerical model is calibrated using physical measurements, and a summary of field data for Spencer Gulf were both presented.

Input and calibration data for a coarse grid model of Spencer Gulf were also presented.

The reason for presenting this detailed review of the coarse grid Spencer Gulf model is to contrast the performance of the mathematical and computational algorithms as originally developed for scalar minicomputers by Bills (1991), as discussed in Sections 3.1–3.2, with that of the modified algorithms developed for vector supercomputers by Nixon (1992), as discussed in Chapter 5. The performance gains achieved will enable the fine grid Spencer Gulf model developed in Chapter 6 to then be used to approximate tidal currents in the region at a greater resolution and in a smaller period of time than has ever before been possible. This will in turn enable simulations of prawn larvae dispersion in Spencer Gulf to be carried out at a correspondingly high spatial resolution, as discussed in Chapter 10.

Chapter 4

The Wind Model

Wind has been shown to be the major factor determining net larval transport (Miller et al. 1984; McShane et al. 1988; Johnson and Hess 1990). There exists a nonlinear relationship between the wind-driven circulation and the tidal currents in the Spencer Gulf region, with the direction of the current at a specific location not directly related to the local wind direction (Provis and Lennon 1983). Accurate specification of wind in numerical models of the hydrodynamics and transport in the region is thus of great importance.

In this chapter, the data and methods used to generate the wind field used to determine the surface wind–stress required by the tidal model are described. The format of the original data, the procedure used to derive a suitable wind field from them, and the validity of this procedure are also discussed. Correlations between the wind data obtained, the wind field derived from these data, and summaries of the known historical record are also made.

Following Forbes and Church (1983), throughout this thesis the meteorological convention for winds (i.e. the direction given is that from which the winds come) and the oceanographic convention for currents and wind–stress (i.e. the direction given is that towards which the current or stress points) are used.

4.1 Available Wind Data

Meteorological data were requested from the National Climate Centre (NCC) at the Bureau of Meteorology (BoM) in Melbourne, Australia, for the period from October 1 to March 31, inclusive, of the years 1972/73–1975/76 and 1984/85–1987/88 at meteorological stations in the Spencer Gulf area. These periods correspond to those for which prawn larvae dispersion simulations, and hence tidal current predictions, were requested by SARDI fisheries research officers.

A list of stations from which data were supplied is given in Table 4.1 and the physical location of these stations is shown in Figure 4.1. All data requested were supplied with the exceptions noted in Sections 4.1.1 and 4.1.2. In the following, *surface wind* refers to a station at which only winds at 10 m above the station elevation were recorded (using wind–vane), and *upper wind* refers to one at which both these winds and those at higher elevations were recorded (using radiosonde).

4.1.1 Surface Wind Stations

Surface wind data for stations at Port Augusta, Whyalla, Port Pirie, Port Lincoln, Warooka, Neptune Island, and Althorpe Island were supplied for all days in the periods of interest, with the following exceptions. For Warooka, data for the month January 1986 were not available. For Neptune Island, data for the years 1987 and 1988 and the months December 1985 and January, February, October, November, and December 1986 were not available. For Althorpe Island, data for the years 1984–1988 were not available.

Spencer Gulf Region Meteorological Observation Stations			
Meteorological Observation Station	Map Coordinates		Elevation above MSL (m)
	Latitude (°S)	Longitude (°E)	
Surface Wind Meteorological Observation Stations			
Port Augusta	32°32′	137°46′	4
Whyalla	33°02′	137°32′	13
Port Pirie	33°11′	138°01′	4
Port Lincoln	34°44′	135°52′	4
Warooka	35°00′	137°24′	53
Neptune Island	35°20′	136°07′	37
Althorpe Island	35°22′	136°52′	80
Upper Wind Meteorological Observation Stations			
Woomera	31°09′	136°49′	165
Ceduna	32°08′	133°43′	15
Adelaide Airport	34°57′	138°32′	6

Table 4.1: Latitude (°S) and Longitude (°E), and Elevation (m) above mean sea level (MSL) for the 10 meteorological observation stations of the Spencer Gulf region. Sites used in the qualitative meteorological data verification Figures 4.2–4.10 have their name listed in **bold**.

Wind speed was given in knots, to the nearest 1 kn. Wind direction was given as an integer in the range zero to sixteen inclusive, with zero corresponding to calm, one to a NNE wind, two to a NE wind, ... , fifteen to a NNW wind and sixteen to a north wind. On advice from the BoM, four measurements (for Port Augusta on 30/10/85 at 08:00, Port Lincoln on 04/11/85 at 14:00, Port Pirie on 14/2/86 at 14:00, and Port Augusta on 14/12/87 at 11:00) with zero direction (corresponding to a variable or calm wind) and non-zero magnitude (estimates of 10, 2, 1, and 10 for wind speed, respectively) were set to zero. The maximum wind speed over all surface wind data was 55 kn.

There were some days missing during many months in many years for many stations. For all of the data, the only hours at which readings were supplied were 02:00, 03:00, 05:00, 06:00, 07:00, 08:00, 09:00, 11:00, 12:00, 14:00, 15:00, 17:00, 18:00, 20:00, and 21:00. There was not a single hour at which readings were supplied for all stations for all years, months, and days at which data were recorded, and data for non-daylight hours was particularly sparse.

A representation of the surface wind data at the Port Augusta, Whyalla, Port Pirie, and Port Lincoln stations for the months December 1987–February 1988 as wind vector time–series is shown in Figures 4.2–4.4. A dominant southerly component to surface winds during the summer of 87/88 is evident at all stations shown, in particular at Port Augusta and Whyalla. Significant oscillations in east-west components to surface winds during these times are also evident, particularly at Port Lincoln, with a period of 2–4 d. The paucity of data collected at Port Pirie is obvious from these figures.

4.1.2 Upper Wind Stations

Upper wind data for stations at Woomera, Ceduna, and Adelaide Airport were supplied for all days in the periods of interest.

Wind speed was given in metres per second, to the nearest $1\,\mathrm{m\,s^{-1}}$. Wind direction was given in degrees clockwise from north, to the nearest 10°. On advice from the BoM, measurements with either direction 0 or 360 were interpreted to be northerly winds. The maximum wind speed over all upper wind data was $20\,\mathrm{m\,s^{-1}}$.

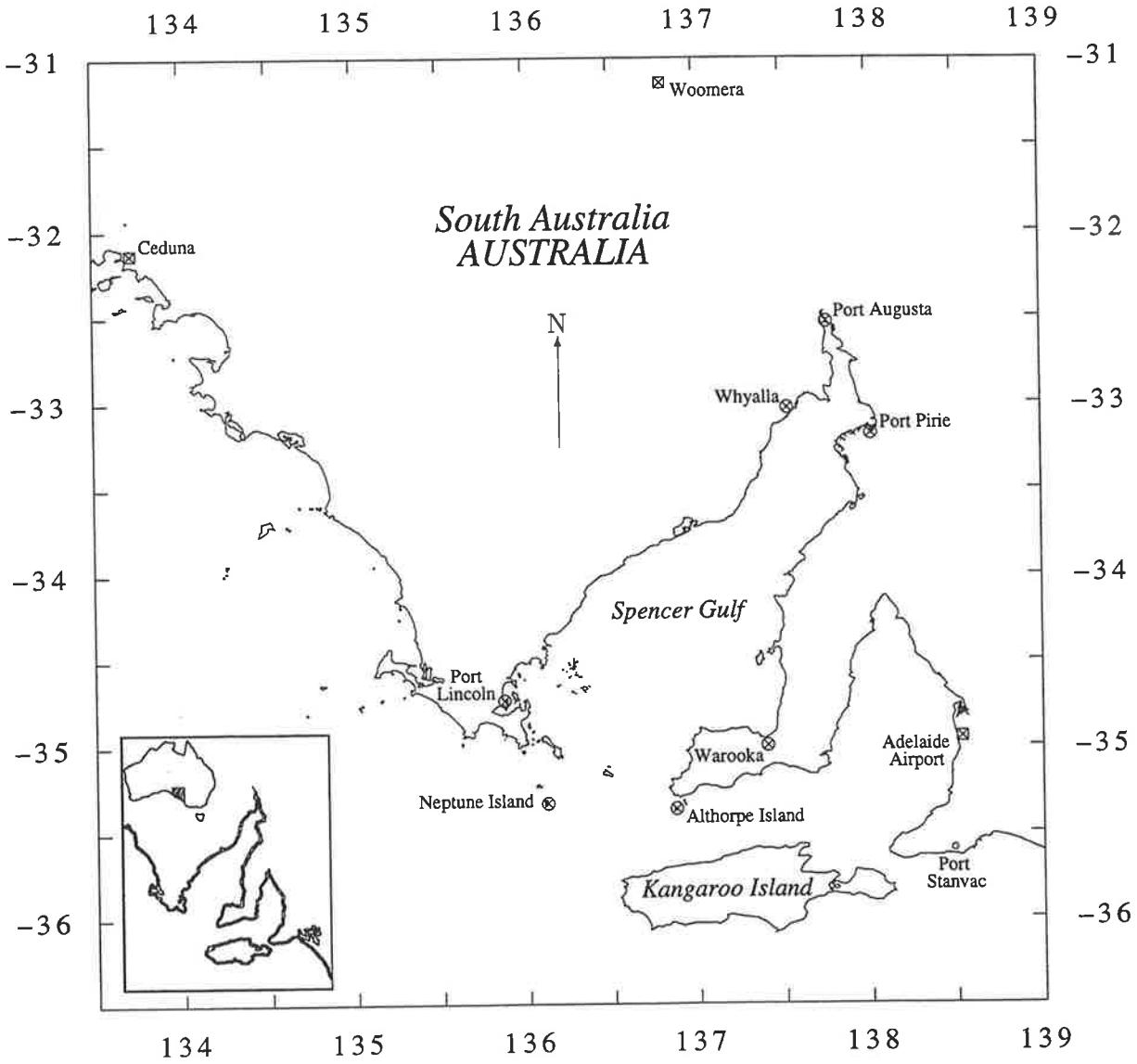

Figure 4.1: Meteorological observation stations for surface wind (crossed circles) and upper wind (crossed squares) in the Spencer Gulf region. Important geographical features (italics) and places of interest (roman) are also shown. The x and y axes indicate longitude (°E) and latitude (°N), respectively.

For all of the data, the hours at which readings were supplied were 00:00, 01:00, 03:00, 04:00, 05:00, 06:00, 07:00, 08:00, 09:00, 10:00, 11:00, 12:00, 16:00, 17:00, 18:00, 20:00, 21:00, 22:00, and 23:00. There was not a single hour at which readings were supplied for all stations for all years, months, and days at which data were recorded, but data for non-daylight hours was not as sparse as that for the surface wind stations.

A representation of the upper wind data at all stations for the months December 1987–February 1988 as wind vector time–series is shown in Figures 4.5–4.7. A dominant southerly component to upper winds during the summer of 87/88 is evident at all stations. Oscillations in east-west components to upper winds during this time are evident at all stations, with periods of 2–4 d.

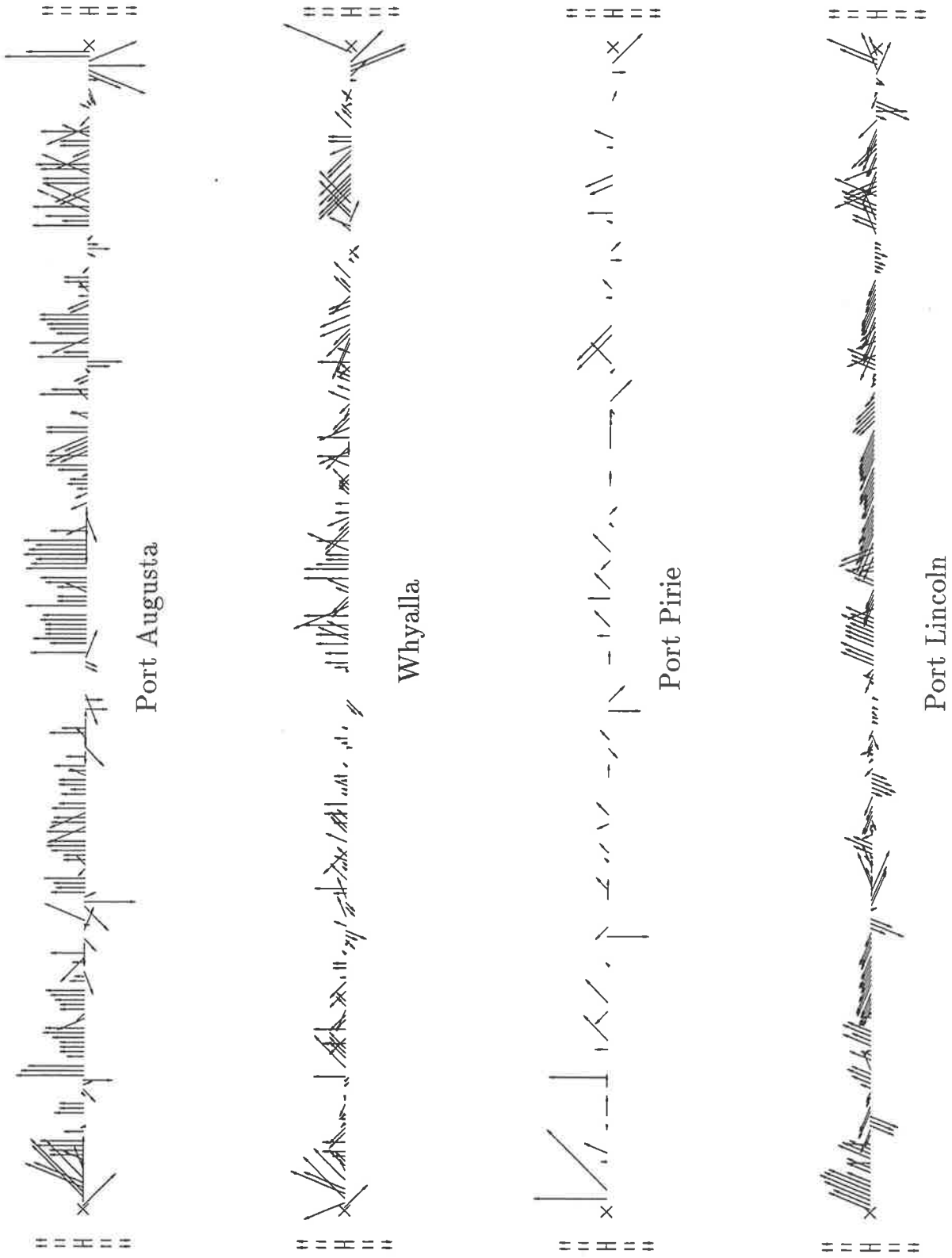

Figure 4.2: Vector time–series of winds measured by the Bureau of Meteorology at surface wind stations Port Augusta, Whyalla, Port Pirie, and Port Lincoln during December 1987. The scale vectors at left and right represent wind speeds of $10\,\mathrm{m\,s^{-1}}$ at a time interval of 4 h directed towards the north (up) and the south (down). The crosses at left and right represent 00:00 hrs on the first of the month and 00:00 hrs 31 d later, respectively. Winds of zero amplitude do not have directional arrows and thus appear as dots.

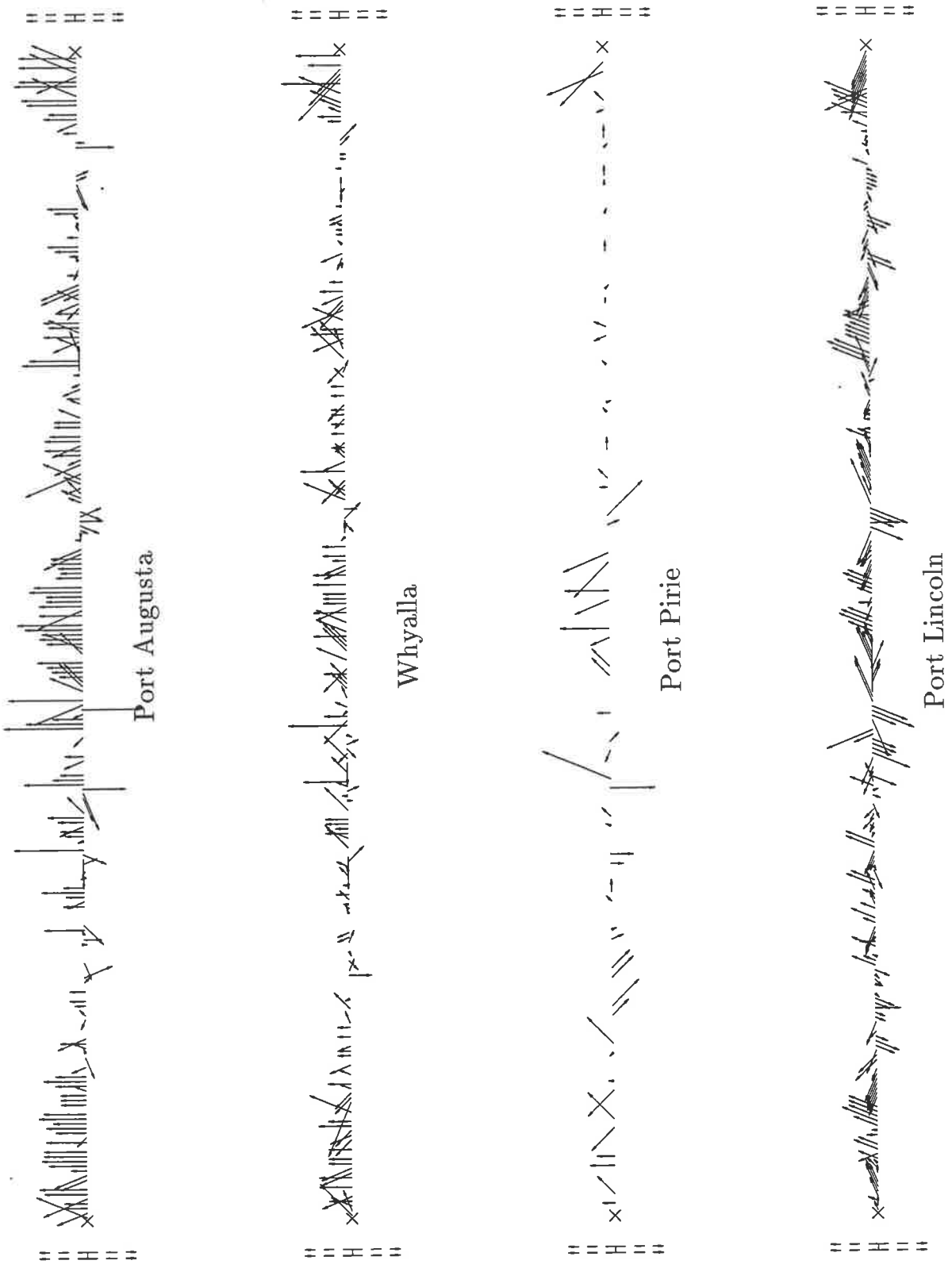

Figure 4.3: Vector time–series of winds measured by the Bureau of Meteorology at surface wind stations Port Augusta, Whyalla, Port Pirie, and Port Lincoln during January 1988. The scale vectors at left and right represent wind speeds of $10\,\mathrm{m\,s^{-1}}$ at a time interval of 4 h directed towards the north (up) and the south (down). The crosses at left and right represent 00:00 hrs on the first of the month and 00:00 hrs 31 d later, respectively. Winds of zero amplitude do not have directional arrows and thus appear as dots.

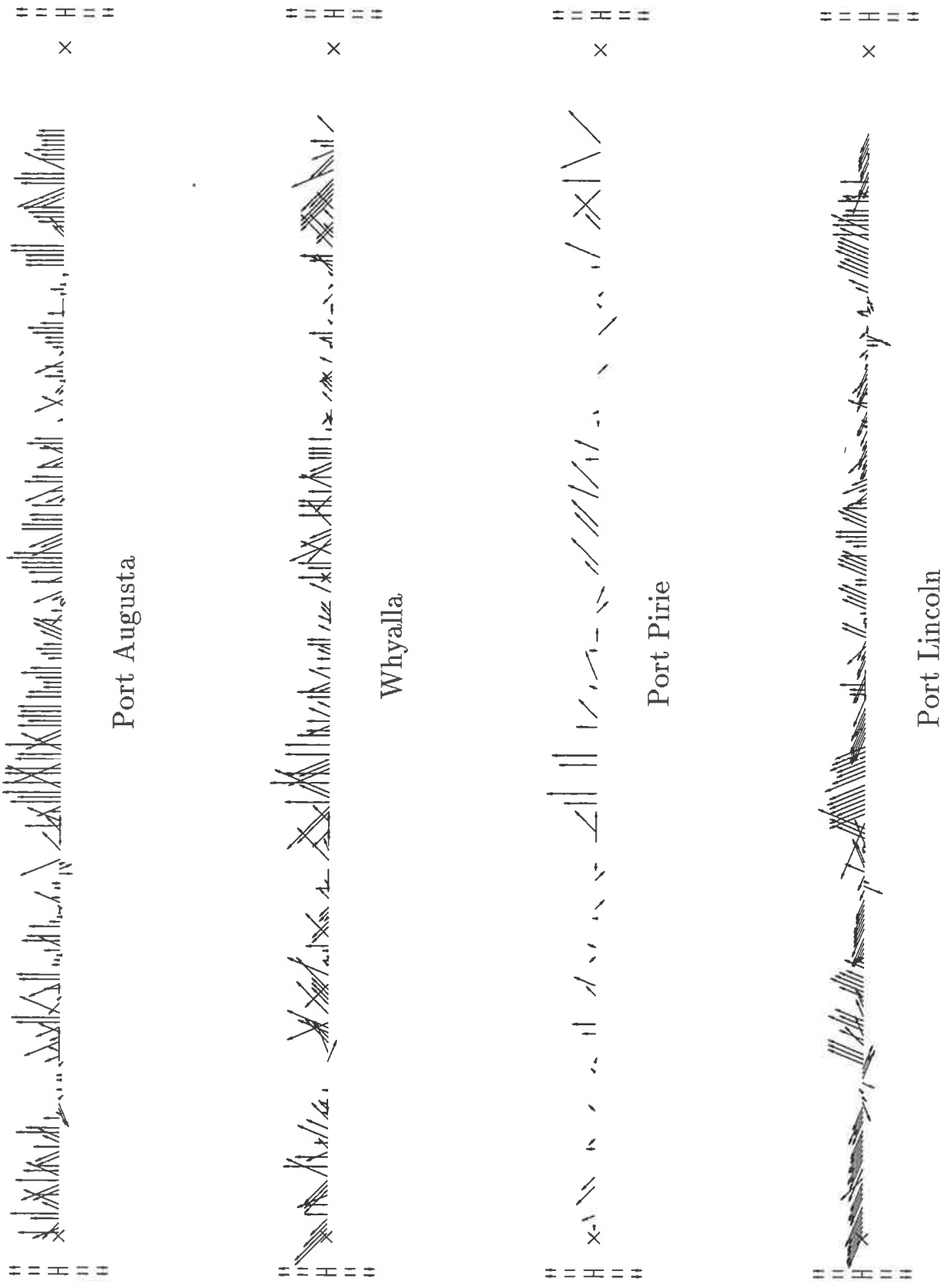

Figure 4.4: Vector time–series of winds measured by the Bureau of Meteorology at surface wind stations Port Augusta, Whyalla, Port Pirie, and Port Lincoln during February 1988. The scale vectors at left and right represent wind speeds of $10\,\mathrm{m\,s^{-1}}$ at a time interval of 4 h directed towards the north (up) and the south (down). The crosses at left and right represent 00:00 hrs on the first of the month and 00:00 hrs 31 d later, respectively. Winds of zero amplitude do not have directional arrows and thus appear as dots.

Figure 4.5: Vector time–series of winds measured by the Bureau of Meteorology at upper wind stations Woomera, Ceduna, and Adelaide Airport during December 1987. The scale vectors at left and right represent wind speeds of $10\,\mathrm{m\,s^{-1}}$ at a time interval of 4 h directed towards the north (up) and the south (down). The crosses at left and right represent 00:00 hrs on the first of the month and 00:00 hrs 31 d later, respectively. Winds of zero amplitude do not have directional arrows and thus appear as dots.

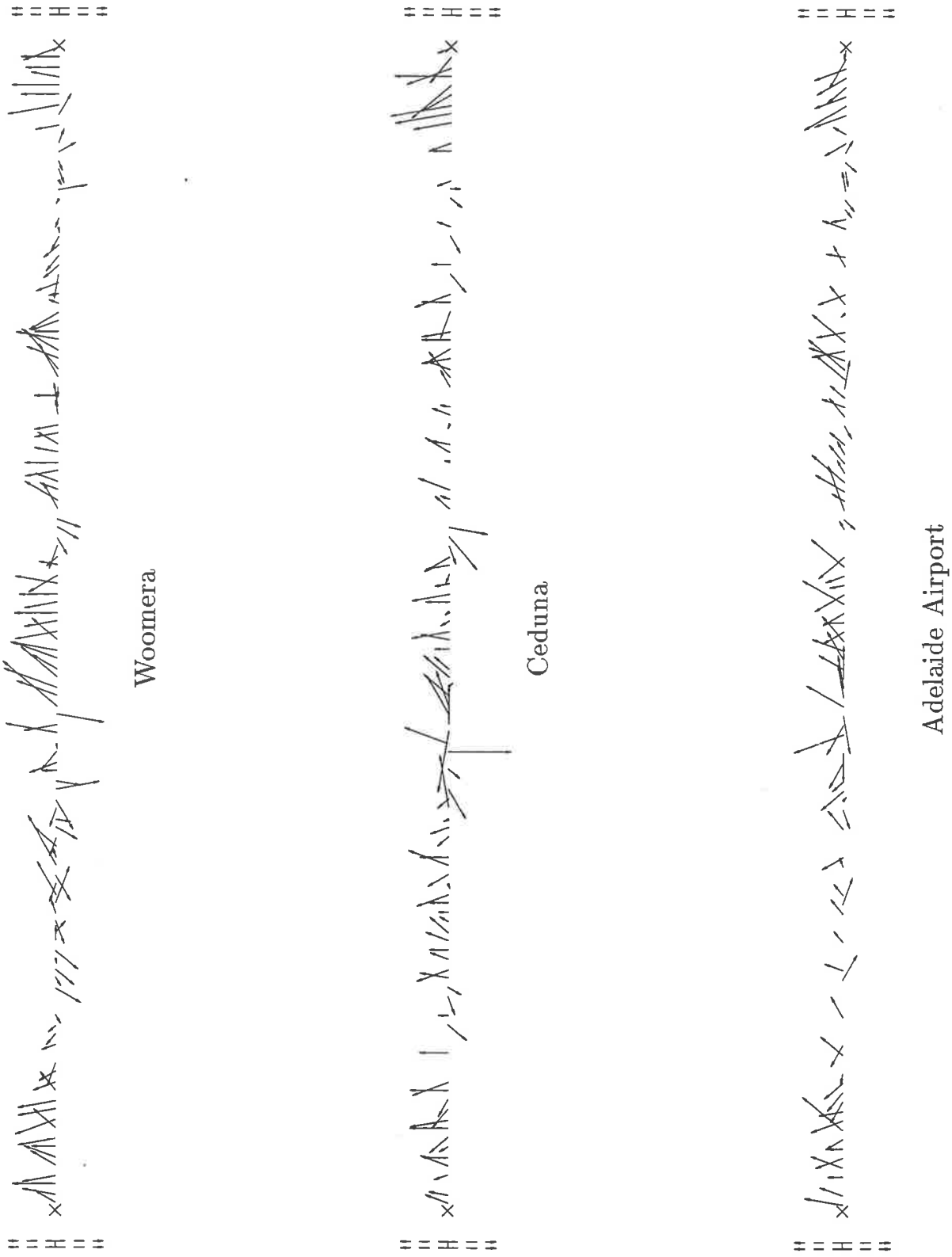

Figure 4.6: Vector time–series of winds measured by the Bureau of Meteorology at upper wind stations Woomera, Ceduna, and Adelaide Airport during January 1988. The scale vectors at left and right represent wind speeds of $10\,\mathrm{m\,s^{-1}}$ at a time interval of 4 h directed towards the north (up) and the south (down). The crosses at left and right represent 00:00 hrs on the first of the month and 00:00 hrs 31 d later, respectively. Winds of zero amplitude do not have directional arrows and thus appear as dots.

Figure 4.7: Vector time–series of winds measured by the Bureau of Meteorology at upper wind stations Woomera, Ceduna, and Adelaide Airport during February 1988. The scale vectors at left and right represent wind speeds of $10\,\mathrm{m\,s^{-1}}$ at a time interval of 4 h directed towards the north (up) and the south (down). The crosses at left and right represent 00:00 hrs on the first of the month and 00:00 hrs 31 d later, respectively. Winds of zero amplitude do not have directional arrows and thus appear as dots.

4.2 Specifying the Wind Field in Spencer Gulf

Preliminary studies (Noye et al. 1992) have shown that sea–surface wind–stress has a significant effect on tidal circulation and hence prawn larvae dispersion. Thus changes in wind direction and magnitude at the times at which prawn larvae are closest to the sea–surface, and hence most susceptible to the influence of sea–surface wind–stress, are required to be well represented. The wind field to be input to the tidal model is therefore derived from upper wind data rather than surface wind data, due to the paucity of measurements recorded during non daylight hours in the latter with respect to the former. However, the surface wind data are used to verify the method of determining surface wind–stress from the upper wind data, as described in Section 4.3.

A data entry error (for Woomera on February 29 of the non-leap year 1985) was deleted from the upper wind database, and values linearly interpolated in time to provide wind vectors at all upper wind stations for each hour of the six-month time periods of interest. All data were converted from direction and speed to vector components directed along the tidal model coordinate axes.

Due to the distance of the upper wind stations from the Gulf waters, as seen in Figure 4.1, an interpolation scheme was devised to generate appropriate wind components at each computational element in the tidal model. At each time–step in the tidal model computations, further linear interpolation in time was applied to determine the components of wind vectors at the three upper wind stations using the hourly data mentioned above as input. For each component, a (plane) surface was fit to the data and, knowing the latitude and longitude of the (three) upper wind stations at which component values are known, values at all computational elements (for which the latitude and longitude are also known) were determined linearly as, in essence, a weighted average. Elevations of the meteorological stations were not taken into account, as it was assumed that the affect of approximations made in the interpolation of sea–surface winds (at a height ideally 10 m above MSL) using land based wind measurements from inland stations (at a height 10 m above the station elevation) would be more significant than that of disregarding elevation effects.

In a study of the circulation in the Gulf of Carpentaria resulting from tide, wind, and other affects, Forbes and Church (1983) derived a model wind field from measurements made at 10 observational stations in the region using a simple weighting approach. If the wind observations at stations on the mainland were initially given equal weight with those on the islands, the spatial wind field variation was found to be pronounced. Island winds, which were generally stronger, and probably more representative of the wind in the interior of the Gulf than the mainland stations, were then weighted accordingly to give a smoother distribution. At each grid point, the wind–stress was thus determined by the vector sum of the stress at all 10 stations, each weighted as the inverse square of its distance from any island station and as the inverse fourth power of its distance from any mainland station. This was thought to give a reasonable representation of the wind–stress over the Gulf of Carpentaria region, although no validity analysis was reported. The validity of the interpolation scheme used in this thesis is, however, assessed in Section 4.3.

At each computational grid–point, wind–stress is calculated by the tidal model from wind velocity components u_{10} and v_{10}, approximated in the manner discussed above, via (3.1.31). A new wind field is calculated at each time–step (rather than using the input at each hour for the whole hour) in order to minimise unwanted instabilities resulting from a non-continuous surface wind–stress forcing.

4.3 Wind Field Specification Validity

The validity of the interpolation of sea–surface winds over the tidal model grid using land based wind measurements from meteorological stations well inland was determined qualitatively by graphical means.

All wind data were converted from a direction and speed to N-S/E-W directed vector components in $m\,s^{-1}$. The upper wind data already linearly interpolated in time to provide hourly values at the upper wind stations were linearly interpolated in space, in the manner described in Section 4.2, to provide values at the spatial positions of the surface wind stations at days and hours at which surface wind data were supplied. Comparison of wind vector time–series for the surface wind station data observed by the BoM and the surface wind station data derived in this manner provides a qualitative check on the validity of the interpolation approach taken.

A representation of the derived surface wind data as wind vector time–series for the months December 1987–February 1988 is shown in Figures 4.8–4.10 for the stations Whyalla, Port Pirie, Port Augusta, and Port Lincoln. These stations were chosen to be representative of all stations at which surface wind data were available, because they are situated on the west and east coast of the Gulf and at the head and mouth of the Gulf, respectively. The example stations are thus well spread spatially, to establish the effect of sea breeze and of extrapolations outside the plane defined by the triangle formed by the upper wind stations as vertices, respectively. These months were chosen to be representative of all times at which surface wind data were available at these chosen surface wind stations as well as at all upper wind stations, because they are months during which prawn larvae are most subject to meteorological effects.

There is a similarity in the derived surface winds for all stations shown which is clearly a result of their derivation as a positionally weighted average from the observed upper winds. The greater southerly component to derived surface winds at Port Augusta and Whyalla during the summer of 87/88 compared to Port Pirie and Port Lincoln, as evident in the measured surface winds, is still evident, however. Oscillations in the east-west components to derived surface winds at *all* stations are now evident, which is a result of the derivation process itself and the fact that these periodic oscillations are evident in the measured upper wind data used in that derivation.

4.4 Historical Wind Data

In this section, findings published in previous studies of the historical wind data for the Spencer Gulf region are discussed. Relationships between the findings presented in these studies and those presented in Sections 4.1–4.3 are made.

4.4.1 "The Stony Point Summer Investigations"

The dearth of statistical wind data available for the Spencer Gulf region is highlighted in Natural Systems Research Pty. Ltd. (1981), where it was stated that

> It was originally envisaged that the winds used for the model would be based on Monte–Carlo estimation from long term climatological wind data. However, it was discovered that suitable data [do] not exist for Spencer Gulf, and hence the time series of Woelfle anemometer data collected at Whyalla from December 1973 to March 1974 [were] used ... , as well as 1979 Redcliff Woelfle data (Natural Systems Research Pty. Ltd. 1981, p. 12).

and that

> There are no wind recording stations or historical data sources which adequately describe the climatological base for northern Spencer Gulf and which possess acceptable resolution for use in the model (Natural Systems Research Pty. Ltd. 1981, p. 18).

with reference to a planned oil trajectory simulation model. This still seems to be the case today, especially with respect to the availability of wind data at the spatial and temporal resolution required of the proposed prawn larvae dispersion model.

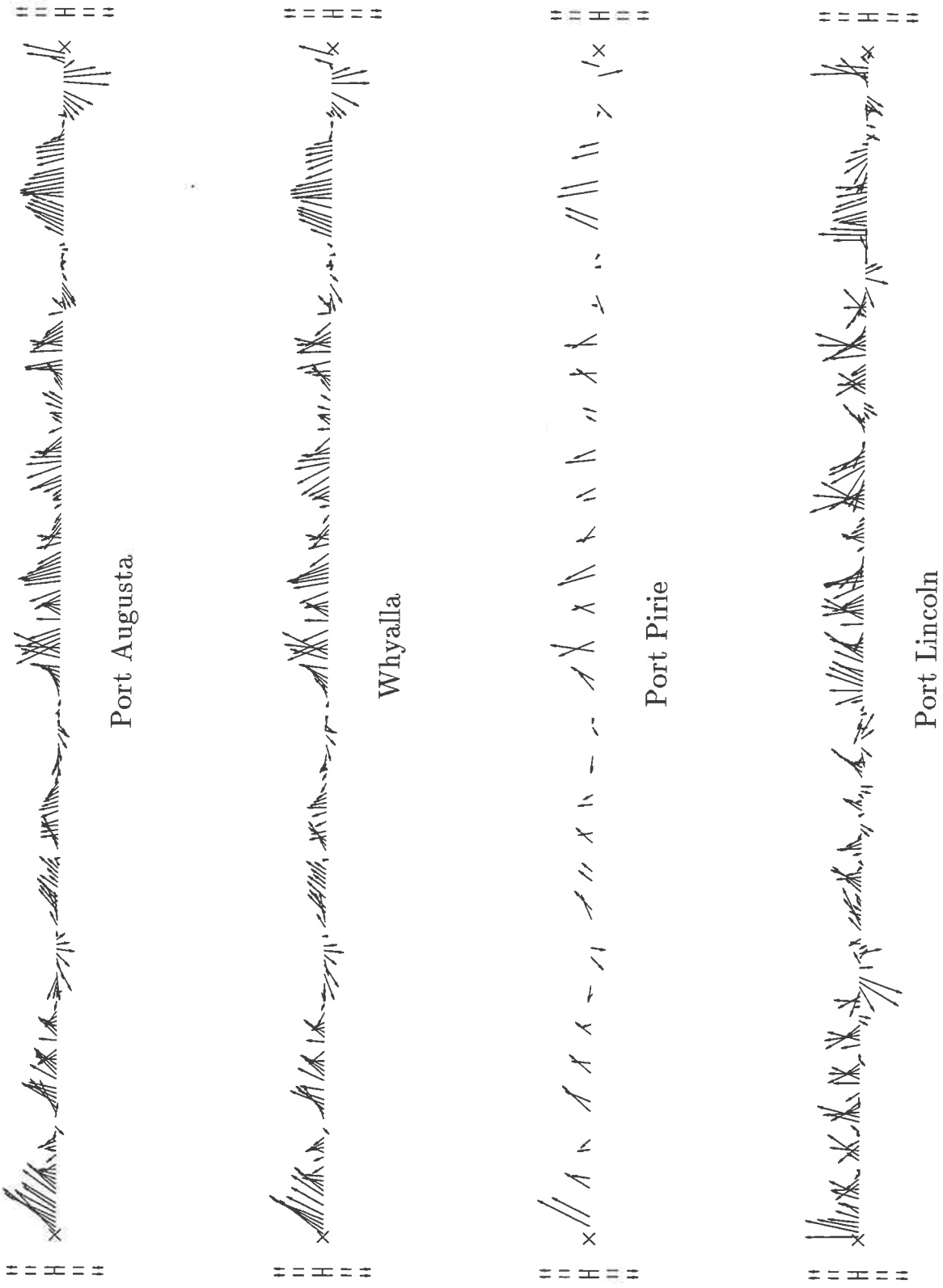

Figure 4.8: Vector time–series of winds derived from upper wind station measurements at surface wind stations Port Augusta, Whyalla, Port Pirie, and Port Lincoln for December 1987. The scale vectors at left and right represent wind speeds of $10\,\mathrm{m\,s^{-1}}$ at a time interval of 4 h directed towards the north (up) and the south (down). The crosses at left and right represent 00:00 hrs on the first of the month and 00:00 hrs 31 d later, respectively. Winds of zero amplitude do not have directional arrows and thus appear as dots.

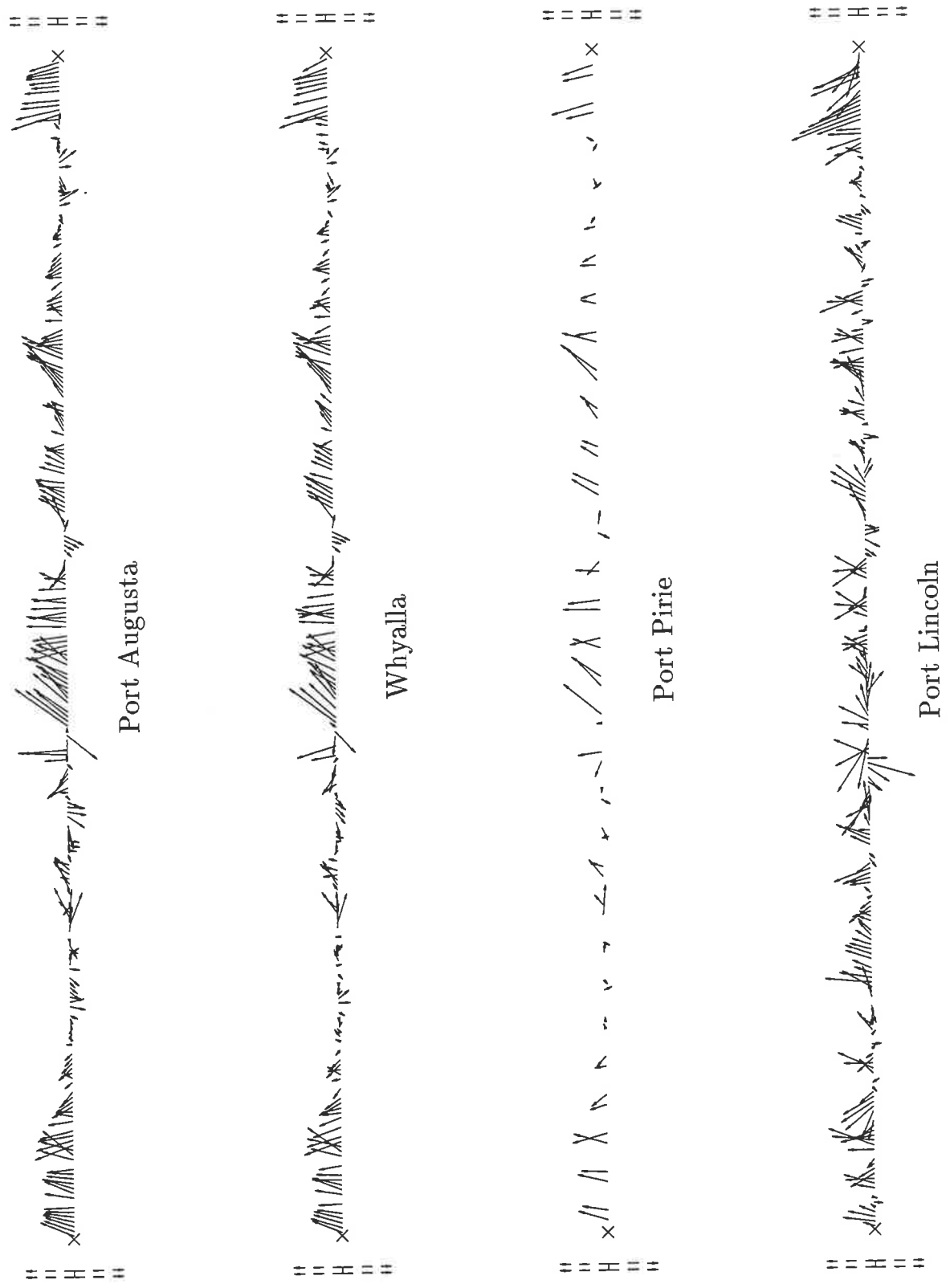

Figure 4.9: Vector time–series of winds derived from upper wind station measurements at surface wind stations Port Augusta, Whyalla, Port Pirie, and Port Lincoln for January 1988. The scale vectors at left and right represent wind speeds of $10\,\mathrm{m\,s^{-1}}$ at a time interval of 4 h directed towards the north (up) and the south (down). The crosses at left and right represent 00:00 hrs on the first of the month and 00:00 hrs 31 d later, respectively. Winds of zero amplitude do not have directional arrows and thus appear as dots.

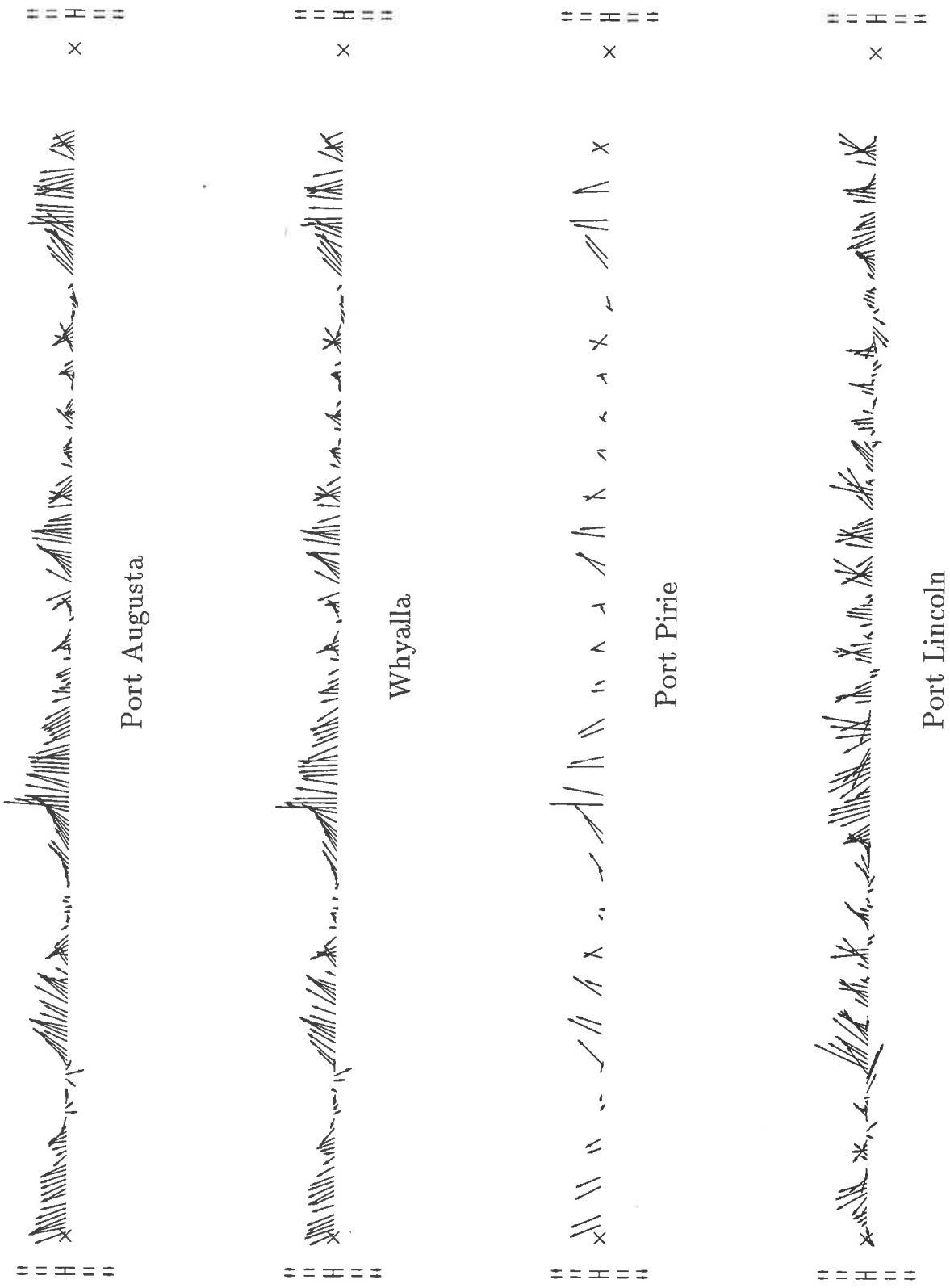

Figure 4.10: Vector time–series of winds derived from upper wind station measurements at surface wind stations Port Augusta, Whyalla, Port Pirie, and Port Lincoln for February 1988. The scale vectors at left and right represent wind speeds of $10\,\mathrm{m\,s^{-1}}$ at a time interval of 4 h directed towards the north (up) and the south (down). The crosses at left and right represent 00:00 hrs on the first of the month and 00:00 hrs 31 d later, respectively. Winds of zero amplitude do not have directional arrows and thus appear as dots.

Some composite wind roses for stations in Spencer Gulf were presented and it was suggested that

> At Port Augusta ... the prevailing wind is from the south. From September to May, southerlies are recorded more than half the time, with an increase in frequency and strength in the afternoon and in the warmest months (when speeds frequently exceed 12 kn).

(where $12\,\text{kn} \approx 6\,\text{m}\,\text{s}^{-1}$) and, furthermore, that

> The high incidence of winds blowing along the north/south axis at Port Augusta results largely from the topographic channelling of flow between the Flinders (900 m [above MSL] on the east) and Middleback Ranges (400 m [above MSL] on the west) which are aligned roughly north/south and converge towards the upper reaches of Spencer Gulf (Natural Systems Research Pty. Ltd. 1981, p. 19).

in which MSL represents mean sea level. These facts are evident in the Port Augusta vector time–series plots of Figures 4.2–4.4 for the months December 1987–February 1988.

The report of Natural Systems Research Pty. Ltd. (1981) further concluded that

> At Port Pirie ... there is a greater proportion of southerly components between October and March .... Easterly winds rarely occur, probably being largely blocked by the lower Flinders Ranges which rise above 900 m to the east of Port Pirie (Natural Systems Research Pty. Ltd. 1981, p. 20).

which is evident in the Port Pirie vector time–series plots of Figures 4.2–4.4 for the months December 1987–February 1988.

In Natural Systems Research Pty. Ltd. (1981), it was also stated (on p. 20) that

> The wind regimes at Whyalla and Redcliff ... are intermediate between those at Port Pirie and Port Augusta. The predominant wind is southerly from November to April ...

and that

> At Port Pirie, Whyalla and Redcliff, the more open exposure to the south and west results in less channelling and more variability in wind directions that at Port Augusta.

as is evident in the Whyalla vector time–series plots of Figures 4.2–4.4 for the months December 1987–February 1988.

In Appendix C of Natural Systems Research Pty. Ltd. (1981) a correlation analysis of 1979 Redcliff, Port Augusta, and Port Pirie wind data was presented. The N-S and E-W components were analysed using auto-correlation within, and cross-correlation between, the time–series. The periods of summertime synchronous data:

1. Redcliff-Port Pirie (1 hourly data)
   11:00 hrs 18 January 1979–15:00 hrs 10 March 1979

2. Port Pirie-Port Augusta (3 hourly data)
   12:00 hrs 16 February 1979–09:00 hrs 28 August 1979

were selected for comparison.

It was found that the N-S component of all station pairs was highly correlated between 0–3 h, indicating that within a time period of 3 h the three stations experienced similar winds along the N-S axis of the Gulf. Plateaus or peaks in the correlation coefficient were evident at 1, 2, and 3 d in the Port Pirie-Port Augusta comparison, reflecting daily sea–breeze effects, and the passage of fronts at longer time scales. Since Port Pirie and Redcliff are on opposite

sides of the Gulf, daily peaks for the E-W component were not found in the cross-correlations (but peaks for the S-W component were found in the cross and auto-correlations). Cross-correlations between the E-W components of all stations were much weaker than those of the N-S components, reflecting the relative weakness of the east-west wind components compared with the north-south components, and the local topographic differences among the sites. High zero lag correlations of the N-S-components implied that the stations compared within Spencer Gulf were fairly similar to each other.

4.4.2 Measured/Derived Surface Wind Correlations

Auto-correlation analyses of December 1987–February 1988 Port Augusta, Whyalla, and Port Lincoln wind data are presented in Figures 4.11, 4.12, and 4.13, respectively. Port Pirie correl-

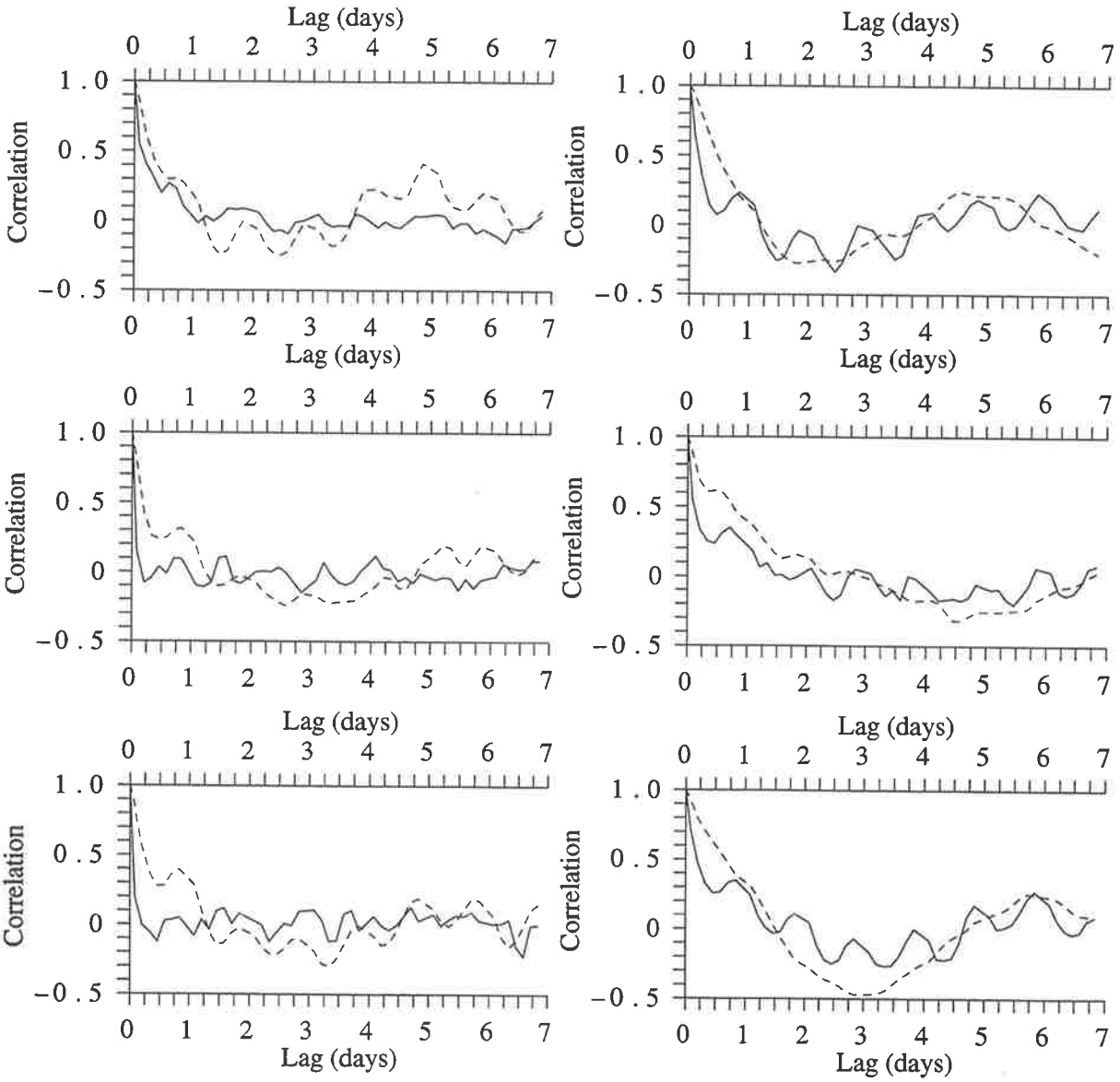

Figure 4.11: Lagged auto-correlations of the E-W (left) and N-S (right) wind velocity components at Port Augusta as determined by the surface wind station data (solid curves) and as derived from the upper wind stations data (dashed curves) for the months December 1987 (top), January 1988 (middle), and February 1988 (bottom).

ations are not included due to the paucity of data available there. Correlation coefficients are

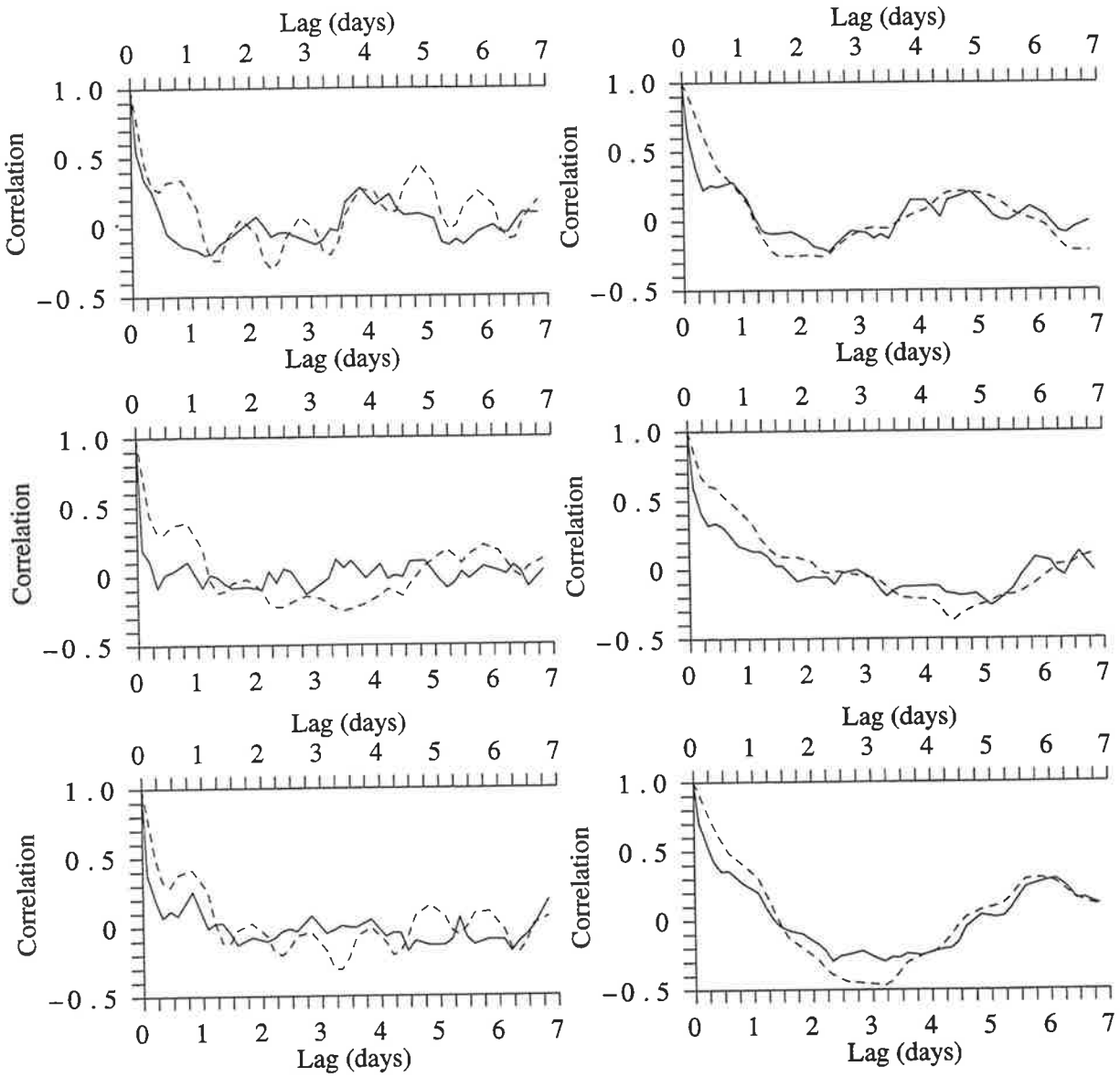

Figure 4.12: Lagged auto-correlations of the E-W (left) and N-S (right) wind velocity components at Whyalla as determined by the surface wind station data (solid curves) and as derived from the upper wind stations data (dashed curves) for the months December 1987 (top), January 1988 (middle), and February 1988 (bottom).

calculated using all available data at the appropriate station for the appropriate month with lags taking all possible values from a zero lag up to but not including a seven day lag, with linear interpolation between the discrete points to give the curves shown. Auto-correlation coefficients are calculated for each surface wind station from the measured and derived wind data. The bulk characteristics of the correlations for measured and derived data agree well for all months with lags of up to a week. Plateaus and peaks in the correlation coefficient are evident at integer days in most plots, reflecting daily sea–breeze effects and the passage of fronts at longer time scales.

The Port Augusta E-W component correlations show that the derived data has slightly enhanced daily sea–breeze related peaks compared to the measured data, whereas for the N-S component this situation is reversed.

This trend is also evident in the Whyalla data, although to a lesser extent.

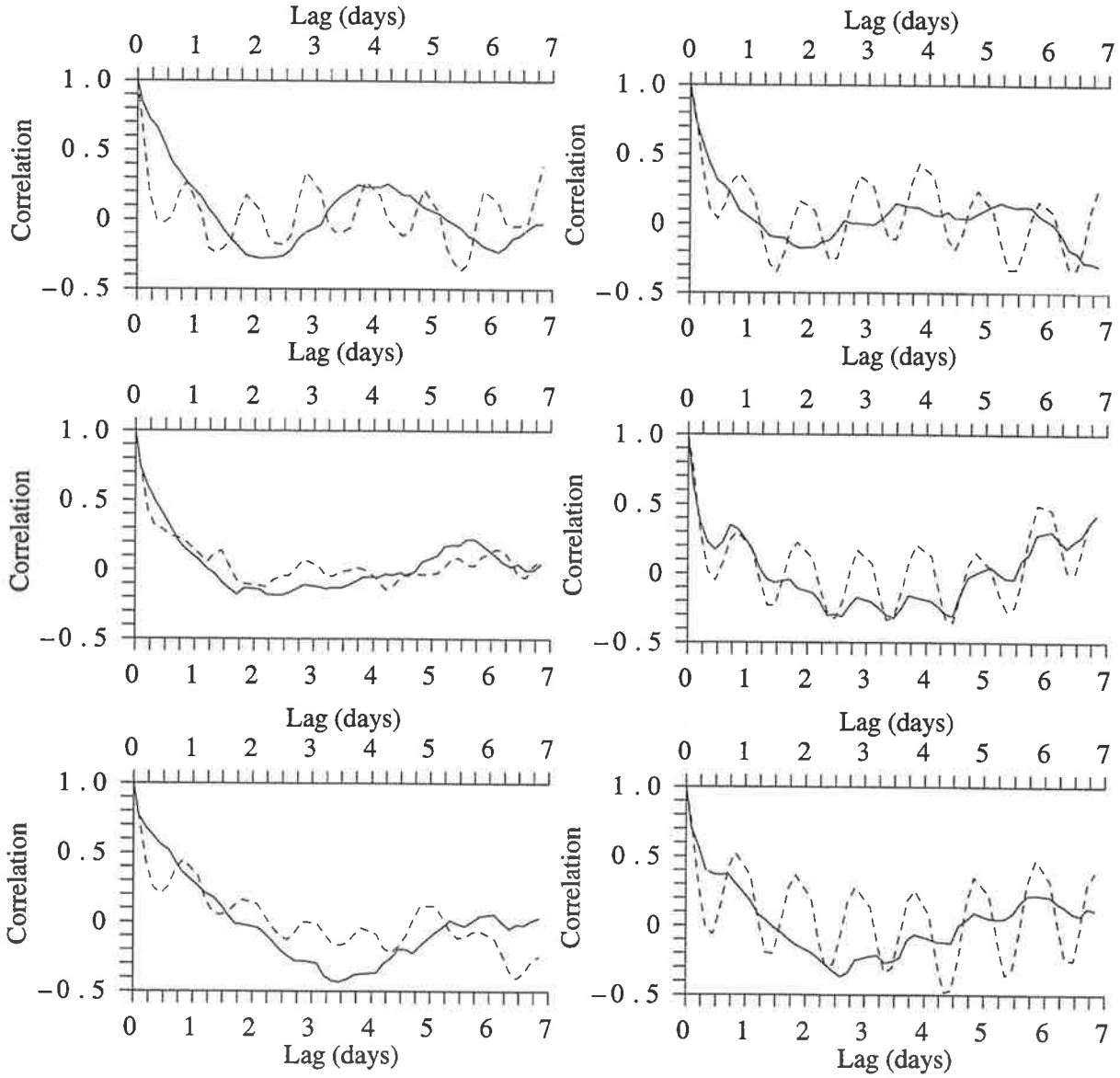

Figure 4.13: Lagged auto-correlations of the E-W (left) and N-S (right) wind velocity components at Port Lincoln as determined by the surface wind station data (solid curves) and as derived from the upper wind stations data (dashed curves) for the months December 1987 (top), January 1988 (middle), and February 1988 (bottom).

The effect of daily sea–breeze is less prevalent for the measured data than the derived data at Port Lincoln, particularly for the N-S component, where correlation peaks for the former are amplified in the latter. For the E-W component correlations of a 24 h period are evident in the derived data that are not in the measured data, particularly in December 1987 and February 1988.

These observations suggest that the process of interpolating surface winds from upper winds, while not reproducing quantitatively the auto-correlations of roughly daily period, does adequately reproduce the qualitative nature of these features. It is felt that the information gained concerning wind during non-daylight hours, by using the upper wind measurements to derive the wind field instead of using the surface wind measurements to specify it, more than offset any loss incurred through the process of interpolative approximation itself. The fact that prawn larvae are near the surface and thus most affected by sea–surface wind–stresses at night,

when upper winds were and surface winds were not available, only emphasises this gain.

4.4.3 Measured Upper Wind Correlations

Auto-correlation analyses of December 1987–February 1988 Adelaide Airport, Ceduna, and Woomera upper wind data are presented in Figures 4.14, 4.15, and 4.16, respectively. Correla-

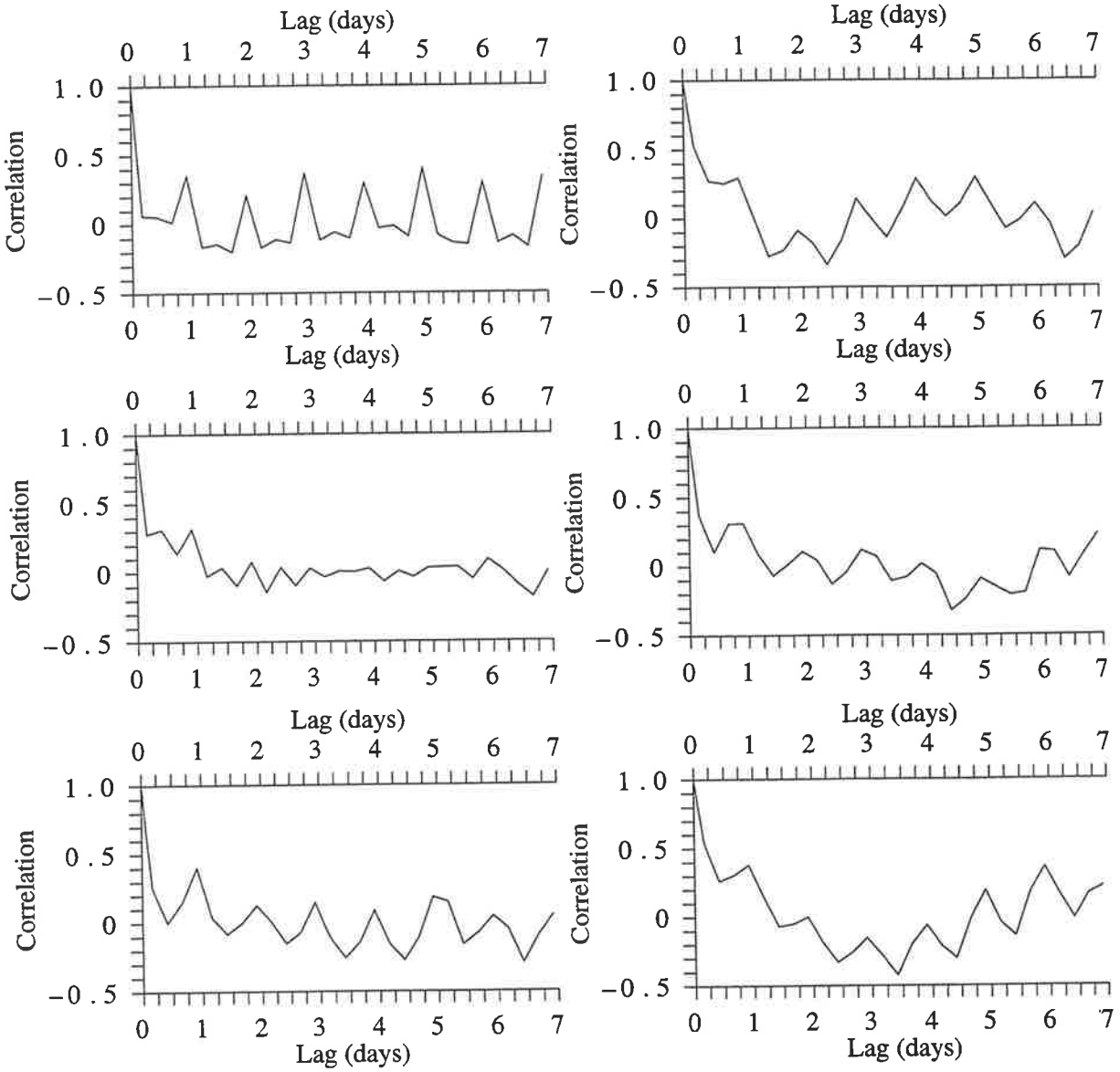

Figure 4.14: Lagged auto-correlations of the E-W (left) and N-S (right) wind velocity components at Adelaide Airport as determined by the upper wind station data for the months December 1987 (top), January 1988 (middle), and February 1988 (bottom).

tion coefficients are again calculated using all available data at the appropriate station for the appropriate month with lags taking all possible values from a zero lag up to but not including a seven day lag, with linear interpolation between the discrete points to give the curves shown.

Plateaus and peaks in the correlation coefficient are evident at integer days in most plots, particularly those for Adelaide Airport, which reflect the strength and regularity of daily sea-breeze effects there. It is evident from Figures 4.13 and 4.14 that the derived Port Lincoln surface wind is highly dependent on the measured Adelaide Airport upper wind. This is due to the

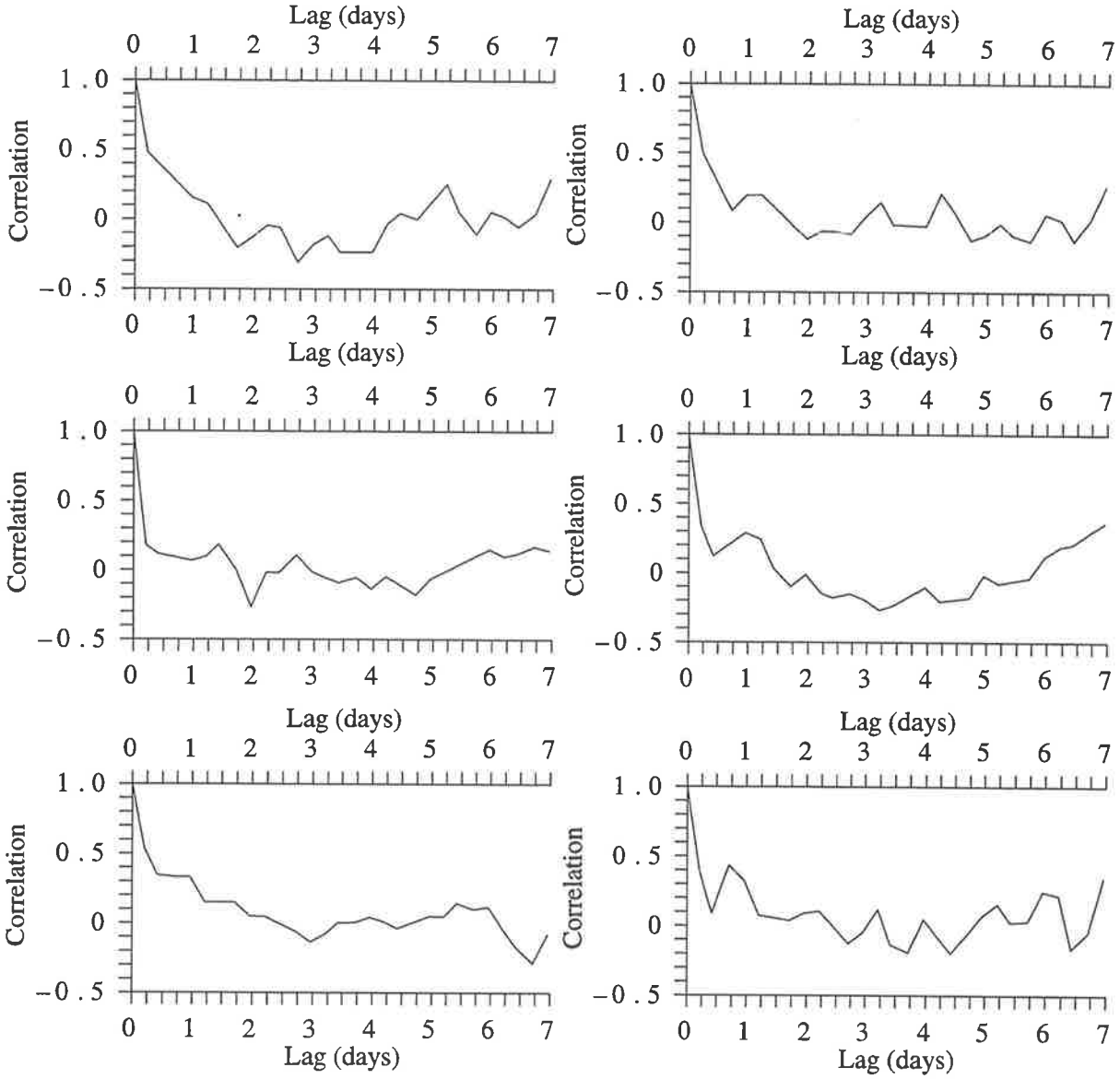

Figure 4.15: Lagged auto-correlations of the E-W (left) and N-S (right) wind velocity components at Ceduna as determined by the upper wind station data for the months December 1987 (top), January 1988 (middle), and February 1988 (bottom).

location of Port Lincoln with respect to Adelaide Airport and to the Adelaide Airport–Ceduna–Woomera triangle on which the interpolation is based. This also illustrates dramatically the limitations in the interpolation scheme, itself devised to overcome limitations in the available data in the first instance.

4.4.4 "Stony Point—South Australia"

In an environmental impact statement (EIS) prepared to assess the ramifications of proposed port and terminal facilities at Stony Point, in northern Spencer Gulf, it was stated that

> The dominant weather patterns ... are derived from the synoptic weather systems moving eastward over the Australian continent and cyclical seasonal fluctuations. Superimposed on the general climatic regime are the often very significant micro-climatic features attributable to the geographical location of the site ... (SANTOS

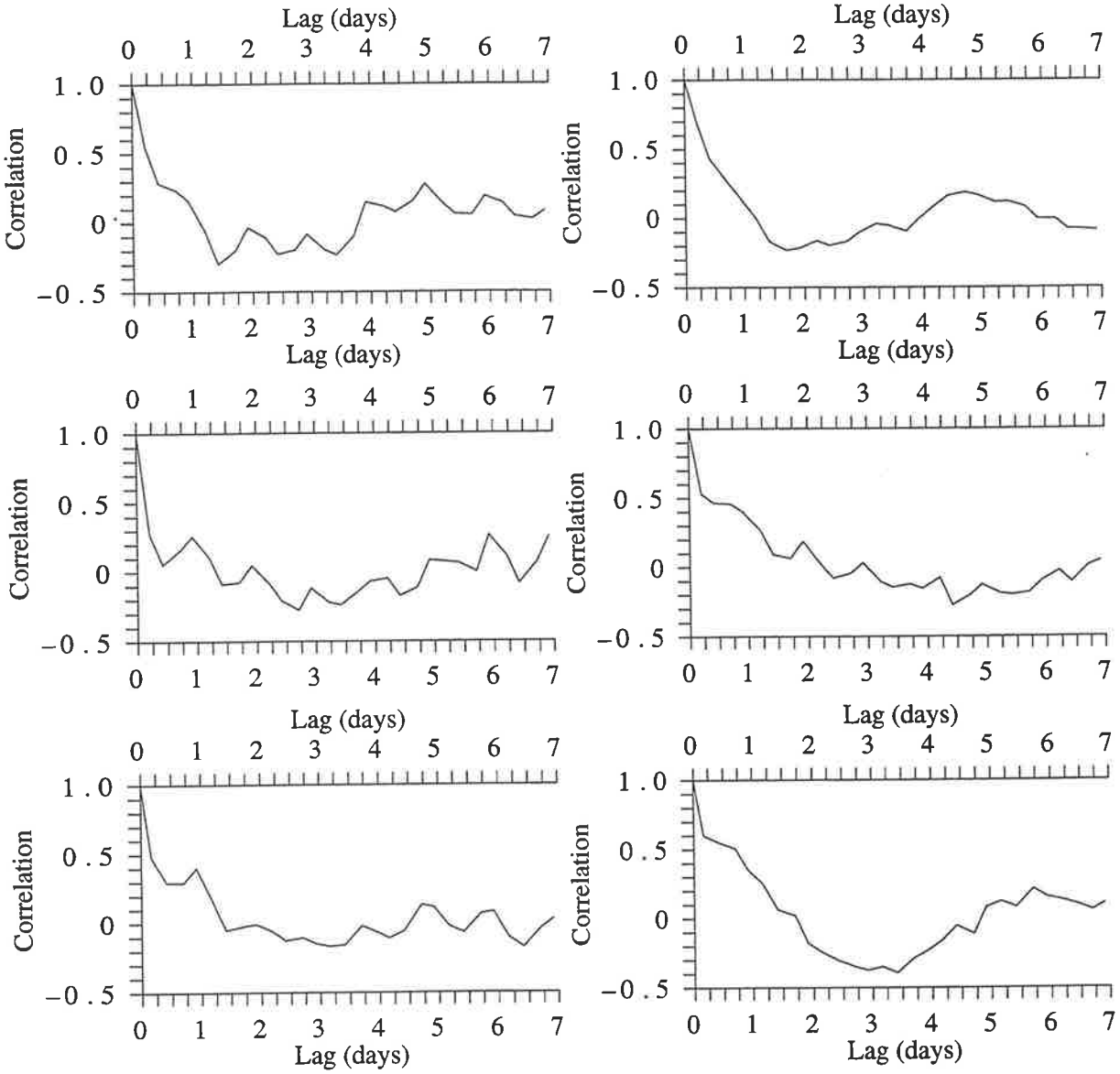

Figure 4.16: Lagged auto-correlations of the E-W (left) and N-S (right) wind velocity components at Woomera as determined by the upper wind station data for the months December 1987 (top), January 1988 (middle), and February 1988 (bottom).

> Limited 1981, p. 23)

and that

> There is a characteristic dominating southerly component from the beginning of November to the end of April, which increases in frequency and strength in the afternoon and in the warmest months (SANTOS Limited 1981, p. 24).

which both emphasise aspects of the meteorology of the local region as discussed previously.

This EIS also reported that

> Strong winds can occur throughout the area. Most violent wind gusts are associated with thunderstorms, but may also be caused by frontal squalls accompanying a southerly change or gales created by strong pressure gradients (SANTOS Limited 1981, p. 144).

and, furthermore, that

> Wind-driven surface currents are a significant feature of the oceanography of the Gulf ... (SANTOS Limited 1981, p. 144)

implying that, for a realistic determination of surface wind–stress in the tidal model, accurate air pressure and/or wind vector data are required.

This report also stated that

> The sea wave climate ... depends on wind strength and direction, and the fetch lengths of sea over which the wind blows. The longest equivalent fetches occur from the south to south-west. This is also the direction of the most persistent and strongest winds (SANTOS Limited 1981, p. 153).

where "surface wind–stress" can be substituted for "sea wave climate" in the context of the Spencer Gulf tidal model. This can be appreciated if one considers the effect of wind strength and direction, and fetch length on the surface currents and hence the return bed currents in a closed steady state circulatory system.

The EIS also reported that

> ... currents ... are dominated by tidal flows and are essentially rectilinear. This produces strong north-south diurnal flows (longshore currents). These are reinforced by wind-generated surface currents produced by the prevailing southerly winds (SANTOS Limited 1981, p. 154).

indicating once again that Spencer Gulf hydrodynamics is, to a certain extent, characterised by effects along the major axis of the Gulf. This was discussed, with reference to the preferred grid orientation of a numerical model of the Gulf, in Section 3.4, and is demonstrated, with reference to the tidal constituent ellipses as predicted by such a model, in Sections 7.4.3 and 10.4.1.

4.4.5 "Stony Point and Port Stanvac"

In a study of the Port facilities at Stony Point, Spencer Gulf and Port Stanvac, Gulf St. Vincent it was reported that

> Since there are no wind recording stations within the main body of Spencer Gulf, wind used to generate the wave climate was taken at an average of the long term records (10 y or longer) from four meteorological stations around Spencer Gulf—Whyalla, Cleve, Neptune Island, and Kadina. The stations at Whyalla, Cleve, and Kadina are at least 5 km inland and hence in order to obtain over-water wind velocities, the observed values were factored up by a value of 1.43 (Connell Eddie & Associates 1981, p. 6).

with reference to the derivation of meaningful wind velocities local to the areas under consideration.

The average wind statistics derived from the Bureau of Meteorology data by Connell Eddie & Associates (1981) using this factoring are reproduced in Table 4.2, with two totals listed for the SE and S winds, and all wind directions and speeds. Wind fetch lengths were tabled in the study, wherein

> The fetch length for each quadrant was computed taking into account the presence of adjacent shorelines and varying bathymetry. The longest equivalent fetches occur from the south to south west where the fetch is about 130 km. This is also the direction of the most persistent and strongest winds (Connell Eddie & Associates 1981, p. 7).

which is in general agreement with the findings of the other studies discussed above.

Summary of Wind Statistics over Spencer Gulf (%)								
Direction (compass bearing)	Speed ($km\,h^{-1}$)							
	0–8	9–16	17–29	30–43	44–58	59–71	over 71	Total
N	2.2	2.8	3.1	1.9	0.9	0.3	0.1	11.3
NE	1.7	1.9	1.9	0.7	0.2	0.1	$\star$	6.5
E	1.5	1.8	2.5	0.5	0.1	$\star$	$\star$	6.4
SE	3.2	5.3	4.8	1.9	0.3	$\star$	$\star$	15.5
"SE + S"	6.2	9.7	9.4	4.5	1.2	0.2	0.1	31.3
S	3.0	4.4	4.6	2.6	0.9	0.2	0.1	15.8
SW	2.2	3.4	3.8	2.5	1.5	0.4	0.1	13.9
W	1.7	2.4	2.7	1.8	1.0	0.4	0.1	10.1
NW	2.0	2.7	2.9	1.6	0.8	0.3	0.1	10.4
Total	17.5	24.7	26.3	13.5	5.7	1.7	0.5	89.9

Table 4.2: Summary of wind statistics (%) over the main body of Spencer Gulf, from Connell Eddie & Associates (1981). Entries marked $\star$ indicate an observed frequency much less than 0.1%, and calm winds totalled 10.1%. The "SE + S" row is a total of the SE and S percentages.

4.4.6 Conclusions

From Table 4.2, it is evident that SE and S winds account for the majority of all winds, with the modal wind speed in the range 9–29 $km\,h^{-1}$. The typical summer wind of $7.5\,m\,s^{-1} \equiv 27.0\,km\,h^{-1} \approx 14.6\,kn$ from the SSE used in simulations with constant wind, as presented in Section 10.1.1, was arrived at taking into account this point and other points made in this section.

With reference to the availability of good wind data near the Stony Point location in northern Spencer Gulf, Connell Eddie & Associates (1981) reported that

> The wind observations that were used were all measured at 9:00 AM and 3:00 PM. While these recordings can reasonably be taken as representative of conditions for an hour or so on either side of the reading they do not provide sufficient information on storms of longer duration (Connell Eddie & Associates 1981, p. 11).

which highlights the lack of temporal resolution in the surface wind data record of the Spencer Gulf region. Observations such as this were, in fact, the original impetus for the derivation of surface wind vectors from upper wind data, as described in Section 4.2.

4.5 Summary

Previous studies of the Spencer Gulf region indicate that historical wind data are incomplete and not of sufficient spatial and temporal resolution as desired to accurately determine wind-stress forced tidal currents required by a realistic prawn larvae dispersion model. The bulk characteristics of summertime wind in Spencer Gulf are such that a SSE wind of moderate speed over the Gulf suffices as a first approximation. More detailed wind specification using existing surface wind station data is inadequate on the grounds that non-daylight hours are not represented. A detailed wind specification derived from existing upper wind station data was compared with existing surface wind station data at selected surface wind stations. This was done directly, using wind vector time–series, and indirectly, using correlation analyses.

The derived wind field reproduces the bulk characteristics of the measured wind field, but the approach taken is far from perfect. There is a general increase in variability of directions associated with the derived vectors, which can be in any orientation—as a result of the derivation process described in Section 4.2, compared to those associated with the recorded vectors, which can be only be in certain orientations—as a result of the measurement process described in Section 4.1.1. The same can be said for vector magnitudes. These two facts account for the apparent smoothness of the derived vector series compared to the measured vector series. Conversely, the apparent variability of the measured vector series compared to the derived vector series can be interpreted as resulting from local effects such as sea–breezes—which would be in approximately opposing directions, for instance, in the evenings at Port Pirie and Whyalla—generating temporally and spatially variable local "noise" in the comparatively generally less "noisy" overall Spencer Gulf wind regime.

LIBRARY

Chapter 5

The Supercomputer Model

With eleven depth–levels in the three-dimensional coarse grid model of Spencer Gulf, a one-month simulation took 3 h 51 min on a Sun SPARC workstation and only 4 min on a CRAY Y-MP supercomputer. In the latter case, the numerical scheme was modified to obtain significantly vectorised program code. These computing times represent costs which are inexpensive relative to the much greater outlays that would be required to establish sufficient observation stations in the region to obtain equivalent information. To obtain observational tidal velocity data, one would need to deploy current gauges at various depth–levels for the period of interest at any particular site—it is simply not practical to obtain the amount of information at the "sites" routinely "monitored" by the computer model.

This chapter documents the experiences of the author in the application of vector supercomputer programming techniques to the tidal model `ted`—originally developed on a scalar minicomputer—described in Sections 3.1–3.2. The computer program was ported from a Digital Equipment Corporation (DEC) VAX 11/785 minicomputer first to a Sun Microsystems SPARCstation 1+ workstation and partially rewritten to comply with the FORTRAN 77 language standard. Then the program was ported to a CRAY Y-MP supercomputer and optimised for this machine with the aim of improving performance by several orders of magnitude. The test problem input data set used as a benchmark represents a real-world application of the program and provides a simulation of the three-dimensional tide and wind induced circulation in Spencer Gulf, South Australia, partly described in Nixon (1992).

5.1 The Test Problem

The original test run was made on a DEC VAX 11/785 minicomputer, under the VMS operating system. The model grid is defined by the grid element Type input matrix of Figure 3.8, the ISLW depths for this grid are indicated in Figure 3.11, and the MSL depths are as shown in Figures 3.12–3.13. The phase and amplitude values for the four major tidal constituents O_1, K_1, M_2, and S_2 used in the height specified boundary condition (3.1.33) are as shown in Table 3.4 and were calculated from those in Table 3.1 as described in Section 3.4.

Other features of the coarse grid Spencer Gulf model test problem include:

- Angle of grid declination = 33.33° T
- Horizontal grid–spacings of $2\Delta x = 2\Delta y = 5715\,\mathrm{m}$
- Time–step of $\Delta t = 180\,\mathrm{s}$
- Number of Type 1 computational elements $N_1 = 762$
- Number of Type 2 grid elements $N_2 = 16$
- Horizontal grid dimensions of 61 rows × 29 columns = 1769 grid elements

- Vertical grid of nk = 10 depth–intervals
- Constant atmospheric pressure of $p_a = 101325\,\mathrm{N\,m^{-2}}$
- Constant wind velocity of $(u_{10}, v_{10}) = (-6.0, 4.5)\,\mathrm{m\,s^{-1}}$ (i.e. $7.5\,\mathrm{m\,s^{-1}}$ from the SSE)
- Constant surface wind–stress of $(S_x, S_y) = (-0.071, 0.053)\,\mathrm{kg\,m^{-1}\,s^{-2}}$ (i.e. $0.089\,\mathrm{kg\,m^{-1}\,s^{-2}}$ from the SSE)
- Constant sea water density of $\rho = 1027\,\mathrm{kg\,m^{-3}}$
- Final time–level $N = 15360$
- Simulation endpoints at 00:00 hrs on 10/12/88 and 00:00 hrs on 11/01/89
- Simulation period of $T = 32\,\mathrm{d}$
- Schwiderski (1980) reduced eddy coefficient of $a = 0.0055\,\mathrm{s^{-1}}$
- Vertical eddy viscosity coefficient profile determined by (3.1.23) with $\alpha = 0.0001\,\mathrm{m^2\,s^{-1}}$ and $\beta = 0.0067$ and $F(\eta)$ determined by (3.1.25) as indicated by the dashed curve in Figure 3.2
- Vertical grid–spacings determined by (3.2.1) with $\kappa = 5.0$ as specified in Table 3.3

The mathematical model is that outlined in Section 3.1, the computational scheme is that outlined in Section 3.2 and there was no calibration of the model attempted, beyond that discussed in Section 3.3 and in Bills (1991), since the results are to be analysed from a comparative and performance point of view only.

An initial test run was performed in order to generate predictions which could be used as a baseline output data set in comparisons of later test runs throughout the optimisation process.

5.2 Porting to a SPARC Workstation

The model was ported to a Sun Microsystems SPARCstation 1+ workstation, under the UNIX operating system. All FORTRAN 66 and VAX/VMS dependent code was removed and in the process replaced with the preferred FORTRAN 77 equivalent (Cray Research, Inc. 1990a). On many computer systems, there exist tools which enable some of these alterations to be applied automatically. Performance enhancements introduced included:

- Replacing floating point divisions with equivalent multiplications, where possible, since such divisions are generally slower than the equivalent multiplications, on all three machines. This is especially true of the CRAY Y-MP, as scalar division requires 23 clock cycles (c.f. 8 for scalar multiplication) and vector division requires 3 vector operations (c.f. 1 for vector multiplication). Division on the CRAY Y-MP is actually achieved by Newton's Method, with 8 bit accurate table lookup to obtain the initial iterate, guaranteed to converge after a single iteration (Micklethwaite 1991, personal communications).
- Replacing arithmetic IF statements with logical IF...ENDIF constructs, since the former are undesirable in vector codes (Cray Research, Inc. 1990c).
- Reducing the overall number of IF...ENDIF constructs, since these are undesirable in vector codes (Cray Research, Inc. 1990c), as they may inhibit vectorisation, or cause "smart" vectorising compilers to generate inefficient code which, with a little source code modification, could be avoided altogether.
- Replacing some other more obviously inefficient and/or outdated FORTRAN code such as computed GOTO, assigned GOTO, and other GOTO statements.

Other, more "cosmetic" improvements were also implemented, including the introduction of improved comments and documentation and a more consistent FORTRAN coding style. The intention of these somewhat less essential alterations was to make further extension, modification, and alteration of the `ted` program suite a less displeasurable experience.

A test run was carried out, and the results compared to the baseline predictions to ensure no coding errors were introduced.

5.3 Porting to a CRAY Supercomputer

The model was ported to a CRAY Y-MP 2D 2-16 supercomputer, under the UNICOS operating system. The program was forced to run in scalar mode using UNIX style switches, or options, in the compilation command line(s) and in the `makefile`.

This scalar mode run was carried out for the purpose of comparison with predictions obtained on scalar machines in previous stages of the optimisation process, and with predictions obtained on this machine in vector mode in subsequent stages of the optimisation process.

5.4 Use of Automatic Vectorisation

Compiler options exist on CRAY systems which, in many cases, will enable a significant level of vectorisation to be achieved automatically. Invoking these dramatically improves the performance of most algorithms amenable to vectorisation with no change in source code required whatsoever. Such compiler options were invoked, a test run executed, and the results compared with previous simulations.

5.5 Use of Compiler Directives

Compiler directives exist on CRAY systems which further facilitate vectorisation and are considered to be comments by all other compilers. It was necessary to use only two of the many available (Cray Research, Inc. 1990a, 1990b) in order to achieve significant levels of vectorisation of the numerical model. These were the SHORTLOOP and UNROLL compiler directives.

Vector pipeline overheads for short vectorisable loops were minimised using the SHORTLOOP compiler directive as indicated in the idealised FORTRAN code snippet of Figure 5.1. In this figure,

```
CDIR$ SHORTLOOP
      DO 00010 k = 1, nk
!       <k loop body>
00010 CONTINUE
```

Figure 5.1: An idealised FORTRAN code snippet illustrating the use of the SHORTLOOP compiler directive to maximise performance for loops of small trip count. Note that $1 \leq \mathtt{nk} \leq V$, where V is the length of vector registers in hardware and that all statements in the `k` loop body must be vectorisable.

$1 \leq \mathtt{nk} \leq 64$ (i.e. this directive is desirable only when attempting to maximise performance for loops of small trip count), 64 is the vector register length on the CRAY Y-MP, and all statements in the `k` loop body are vectorisable.

Vectorisation over long vectorisable outer loops of many nested loop structures was achieved by unrolling short nested inner loops using the UNROLL compiler directive as indicated in the idealised FORTRAN code snippet of Figure 5.2. In this figure, $\mathtt{ni} \gg \mathtt{nk}$ (i.e. this directive is desirable when attempting to achieve vectorisation in, and therefore maximise performance for,

```
      DO 00020 i = 1, ni
!       <i loop body, part I>
CFPP$ UNROLL (nk)
        DO 00010 k = 1, nk
!         <k loop body>
00010   CONTINUE
!       <i loop body, part II>
00020 CONTINUE
```

Figure 5.2: An idealised FORTRAN code snippet illustrating the use of the UNROLL compiler directive to achieve vectorisation and therefore maximise performance for outer loops of much larger trip count than inner loops, in nested loop structures. Note that `ni` $\gg$ `nk` and that all statements in both the body of the inner loop on `k` and in that of the outer loop on `i` must be vectorisable. If this is not the case, unrolling the short inner loop will not have the desired effect.

outer loops of much larger trip count than inner loops) and all statements in both the body of the inner loop on `k` and the body of the outer loop on `i` are vectorisable. Note that if this is not the case, unrolling the short inner loop will not have the desired effect of vectorising the long outer loop and the nested loop structure will require modification in order to achieve vectorisation (see Section 5.7).

Profiling tools (Cray Research, Inc. 1989) determined that `ted` was spending approximately 80% of its time in calculating the horizontal velocity components u and v. The source code listings showed that the subroutines to set up the tridiagonal matrices to be later inverted contained long loops on the computational element number i which could not be vectorised by the `cf77` CRAY compilation system due to the number and complexity of statements contained in these loops—despite efforts to rectify this (see Section 5.2). These matrix determination subroutines, `ucalcn` and `vcalcn`, accounted for approximately 56.2% of the CPU time required for a run of the benchmark problem at this stage in the optimisation process. The general consensus is that simple, "tight" loops of large trip counts are desired in high-performance algorithms for vector architectures (Levesque and Williamson 1988; Cray Research, Inc. 1990b, 1990c).

The subroutine performing the inversion of these matrices at each computational element contained short loops on the depth-interval k, which could not be vectorised due to the data dependent, or recursive, nature of the Thomas (1949) algorithm. This matrix inversion subroutine, `thomas`, accounted for approximately 23.3% of CPU time at this stage.

Discussions of why recursion inhibits vectorisation, which types of recursion do so, and how this can be avoided can be found in Levesque and Williamson (1988) and Cray Research, Inc. (1990b, 1990c).

The subroutine `omega_calcn` for calculating the transformed vertical velocity ω, accounted for approximately 5.4% of CPU time at this stage.

5.6 Removal of Time–Centring

As a first step in what became a complete alteration of the computational procedure, time–centring in the calculation of u and v (see Section 3.2.3) and windowing (see Section 3.2.4) were removed. Without removing time–centring and windowing it was clear that vectorisation in the most computationally intensive subroutines (`ucalcn`/`vcalcn`, `thomas`, and `omega_calcn`) would not be possible. The other modifications to the overall computational scheme required to do this are described in Section 5.7.

In order to minimise the accumulative effects of the overall discretisation error associated

with the differencing of the original equations, for odd time levels n first u^n and then v^n matrices were determined and solved, while for even time levels n first v^n and then u^n was computed. The time step was not reduced.

The `u/vcalcn`, `thomas`, and `omega_calcn` subroutines accounted for approximately 59.8%, 26.7%, and 6.1% of CPU time at this stage, respectively.

5.7 Modification of FORTRAN Code

With time–centring and windowing removed, further alteration of the overall computational scheme towards significant vectorisation followed naturally. The original procedure for computing u and v at time–level n, viz.:

1. Set the computational element number i (in the main program `ted`)

2. Determine the matrix entries for implicitly computing $u^n_{i,k}$ at all depth–intervals $k = 1, 2, \ldots, \mathtt{nk}$, at this i (in the `ucalcn` subroutine)

   - Solve the tridiagonal system for all $u^n_{i,k}$, $k = 1, 2, \ldots, \mathtt{nk}$ at this i (in the `thomas` subroutine)

3. Determine the matrix entries for implicitly computing $v^n_{i,k}$ at all depth–intervals $k = 1, 2, \ldots, \mathtt{nk}$, at this i (in the `vcalcn` subroutine)

   - Solve the tridiagonal system for all $v^n_{i,k}$, $k = 1, 2, \ldots, \mathtt{nk}$ at this i (in the `thomas` subroutine)

4. Return to Step 1

   - Repeat this process until all computational elements i have been processed

was modified to:

1. Determine the matrix entries for implicitly computing $u^n_{i,k}$, for all $i = 1, 2, \ldots, \mathtt{ni}$, $k = 1, 2, \ldots, \mathtt{nk}$ (in the `ucalcn` subroutine)

2. Solve the tridiagonal system for $u^n_{i,k}$, for all $i = 1, 2, \ldots, \mathtt{ni}$, $k = 1, 2, \ldots, \mathtt{nk}$ (in the `thomas` subroutine)

3. Determine the matrix entries for implicitly computing $v^n_{i,k}$, for all $i = 1, 2, \ldots, \mathtt{ni}$, $k = 1, 2, \ldots, \mathtt{nk}$ (in the `vcalcn` subroutine)

4. Solve the tridiagonal system for $v^n_{i,k}$, for all $i = 1, 2, \ldots, \mathtt{ni}$, $k = 1, 2, \ldots, \mathtt{nk}$ (in the `thomas` subroutine)

in order to achieve vectorisation in subroutine `thomas`, and to provide the possibility of vectorisation in subroutines `ucalcn` and `vcalcn`. Note that in the original scheme for velocity calculation, vectorisation of subroutines `ucalcn` and `vcalcn` is contingent on vectorisation of the subroutine `thomas` even if subroutine `thomas` were to be brought "in line"—either manually or via the use of a compiler directive or a command line or `makefile` option (see Cray Research, Inc. 1990a). In the modified scheme, subroutine `thomas` is called by the `ted` main program, so that vectorisation of subroutines `u/vcalcn` is *not* contingent on vectorisation of subroutine `thomas`. The finer details of the code modifications required for vectorisation follow.

5.7.1 Vectorising the thomas Subroutine

The tridiagonal matrix system to be solved by subroutine **thomas** is of the form

$$\boldsymbol{T}\boldsymbol{q} = \boldsymbol{d}, \tag{5.7.1}$$

where

$$\boldsymbol{T} = \begin{pmatrix} b_1 & c_1 & 0 & \cdots & & & & \cdots & 0 \\ a_2 & b_2 & c_2 & 0 & \cdots & & & \cdots & 0 \\ 0 & a_3 & b_3 & c_3 & 0 & \cdots & & \cdots & 0 \\ \vdots & & \ddots & \ddots & \ddots & & & & \vdots \\ 0 & \cdots & 0 & a_k & b_k & c_k & 0 & \cdots & 0 \\ \vdots & & & & \ddots & \ddots & \ddots & & \vdots \\ 0 & \cdots & & \cdots & 0 & a_{\mathrm{nk}-2} & b_{\mathrm{nk}-2} & c_{\mathrm{nk}-2} & 0 \\ 0 & \cdots & & & \cdots & 0 & a_{\mathrm{nk}-1} & b_{\mathrm{nk}-1} & c_{\mathrm{nk}-1} \\ 0 & \cdots & & & & \cdots & 0 & a_{\mathrm{nk}} & b_{\mathrm{nk}} \end{pmatrix}, \tag{5.7.2}$$

$$\boldsymbol{q} = \begin{pmatrix} q_1 \\ q_2 \\ q_3 \\ \vdots \\ q_k \\ \vdots \\ q_{\mathrm{nk}-2} \\ q_{\mathrm{nk}-1} \\ q_{\mathrm{nk}} \end{pmatrix}, \quad \text{and} \quad \boldsymbol{d} = \begin{pmatrix} d_1 \\ d_2 \\ d_3 \\ \vdots \\ d_k \\ \vdots \\ d_{\mathrm{nk}-2} \\ d_{\mathrm{nk}-1} \\ d_{\mathrm{nk}} \end{pmatrix}, \tag{5.7.3}$$

in which **ni** is the number of computational elements i and **nk** is the number of depth–intervals k and, after incorporating surface and bottom boundary approximations and conditions, all a's, b's, c's, and d's are known. The unknown horizontal velocities u and v are returned by the subroutine **thomas** in the vector $\boldsymbol{q}$. The logical structure of the original computational scheme for subroutine **thomas** is represented by the idealised FORTRAN code snippet of Figure 5.3.

The logical structure of the modified computational scheme for subroutine **thomas** is represented by the idealised FORTRAN code snippet of Figure 5.4. The data dependency in the inner loop (which is the target for vectorisation) has, however, been effectively eliminated. This modified scheme allows one step in the matrix inversion to be applied to the matrices for all computational elements in the model before proceeding to the next inversion step, thus introducing long loops on the computational element number i (which vectorise well due to their length **ni** and the simplicity of the statements in the loop body) nested inside existing short loops on the depth–interval k (which do not vectorise at all due to the recursion on k in all statements in the loop body).

Modification of the FORTRAN code in order to achieve these changes in **thomas** required the *promotion* of some one-dimensional vectors to two-dimensional arrays, as can be seen by comparison of Figure 5.3 with Figure 5.4. The tridiagonal system to be solved by subroutine **thomas** as represented in Figure 5.4 is similar to that depicted in (5.7.1)–(5.7.3) but with an "extra" dimension to all matrices, most easily visualised as extending into the page for **ni** "slices". In the modified subroutine **thomas** each step in the solution process is applied to all such slices before the next step is executed.

Summary

Variable promotion (of **a**, **b**, **c**, and **d**) and the transfer of a loop (on i) with large trip count (of **ni**) from one subroutine (**u/vcalcn**) to a previously subordinate subroutine (**thomas**) eliminated recursion (on k) and paved the way for vectorisation of subroutine **thomas**.

```
      DO 00010 i = 1, ni ! This loop is in subroutines u/vcalcn.

!       <Assign the matrices a, b, c, and d in subroutines u/vcalcn.>

        DO 00020 k = 2, nk - 1 ! This loop is in subroutine thomas.
          x = a(k) / b(k - 1)
          b(k) = b(k) - x * c(k - 1)
          d(k) = d(k) - x * d(k - 1)
00020     CONTINUE                ! This loop is in subroutine thomas.

00010 CONTINUE            ! This loop is in subroutines u/vcalcn.
```

Figure 5.3: An idealised FORTRAN code snippet illustrating the logical structure of the original (poorly vectorised) recursive subroutine thomas. Indentation is used to represent both the logical nesting of subroutines and the nesting of loop structures. Thus, loop 00010 occurs within subroutines u/vcalcn, while loop 00020 occurs within subroutine thomas, which is called by both subroutines ucalcn and vcalcn.

```
!     <Assign the matrices a, b, c, and d in subroutines u/vcalcn.>

      DO 00020 k = 2, nk - 1 ! This loop is in subroutine thomas.
        DO 00010 i = 1, ni   ! This loop is in subroutine thomas.
          x = a(i,k) / b(i,k - 1)
          b(i,k) = b(i,k) - x * c(i,k - 1)
          d(i,k) = d(i,k) - x * d(i,k - 1)
00010   CONTINUE             ! This loop is in subroutine thomas.
00020 CONTINUE               ! This loop is in subroutine thomas.
```

Figure 5.4: An idealised FORTRAN code snippet illustrating the logical structure of the modified well vectorised (non-recursive) subroutine thomas. Indentation is used to represent both the logical nesting of subroutines and the nesting of loop structures. Thus, loops 00010 and 00020 both occur within subroutine thomas which is called by both subroutines ucalcn and vcalcn.

5.7.2 Vectorising the ucalcn and vcalcn Subroutines

In order to achieve vectorisation in subroutines ucalcn and vcalcn, it was necessary to abandon the NCN concept—discussed in Section 3.2.6—by removing the 1's and 0-1's neighbourhood code sections altogether, and forcing all calculations through the more general, and computationally intensive, 0-1-2's code sections. The significant reduction in the overall number of loop body statements as a result of this modification and the removal of one IF...ENDIF construct which brought about this forcing was not, however, sufficient to enable vectorisation of the long loops on the computational element number i within these subroutines.

Program code containing conditional blocks associated with boundary conditions (zero flow normal to the coast, see Section 3.1.2), barriers (zero flow across islands too small to be represented by Type 0 grid elements, see Figure 3.9), and the inclusion, exclusion, or approximation of terms (validity and form of contributions from near-boundary computational elements being determined by physical and accuracy considerations, see Section 3.2.5) was altered entirely. This involved the calculation of *all* matrix entries as though the corresponding computational

elements were in the interior of the computational domain and thus required no special treatment, and then later modifying entries corresponding to computational elements associated with boundary conditions and barriers (by reassigning the corresponding augmented matrix equation "slice" to the identity with zero right hand side, in both cases) and the inclusion, exclusion, or approximation of terms (by reassigning individual appropriate matrix slice entries). The matrix solver `thomas` could then be called to invert matrices for all computational elements in one "pass", so to speak, as described above.

Modification of the FORTRAN code in order to achieve these changes in subroutines `ucalcn` and `vcalcn` also required the promotion of some scalar variables to vectors and some one-dimensional vectors to two-dimensional arrays so that one could first calculate all k-independent quantities, then calculate all i and k-dependent matrix slice entries, and finally modify the entries for those elements which required special treatment, before returning to the main program and calling the matrix solver.

The logical structure of the original poorly vectorised subroutines `u/vcalcn` is illustrated in the idealised pseudo-FORTRAN code snippet of Figure 5.5. What was originally one loop: a non-vectorisable loop over i (with an inner vector loop over k) became three loops: one vector loop over i, a second non-vector loop over k (with an inner vector loop over i), and a third vector loop over i (with inner vectorisable loops unrolled over k).

The logical structure of the modified highly-vectorised subroutines `u/vcalcn` is illustrated in the idealised FORTRAN code snippet of Figure 5.6. Note that unrolling the short inner loops on k (depicted by loops 10, 20, and 30 in Figure 5.5) did not allow vectorisation of the long outer loop on i (depicted by loop 40 in Figure 5.5), for two reasons. First, the call to subroutine `thomas` within the outer loop hindered vectorisation, and bringing this "in line" would not have achieved vectorisation since the complete `thomas` subroutine itself could not be vectorised. This fact—determined by the inherent recursive nature of the algorithm itself, as discussed earlier in this section—was an incentive to major code alteration. Second, the complexity of the actual FORTRAN code in subroutines `u/vcalcn` (as distinct from the idealised pseudo-code of Figure 5.5) was such that vectorisation of the outer loop on i was not possible despite the successful unrolling of the inner loops on k. This fact—determined by compiling the matrix setup subroutines with the call to the matrix solver subroutine commented out—was the other incentive to major code alteration.

Modification of the FORTRAN code in order to achieve these changes in `u/vcalcn` also required the promotion of some scalar variables to vectors and some one-dimensional vectors to two-dimensional arrays, as can be seen by comparing Figure 5.5 with Figure 5.6.

Summary

By precalculating all depth-independent quantities in one pass over all computational elements (depicted by loop 10 in Figure 5.6) and splitting up the depth-dependent calculations into two passes (depicted by loops 20 and 60 in Figure 5.6), it was possible to achieve vectorisation in each of the three passes over all computational elements. The aim of this vectorisation technique, known as *loop splitting* is to divide a non-vectorised loop into sub-loops, some of which may vectorise and some of which may not. Ideally the programmer can alter the algorithm or sequence of operations in such a way that, despite possible increases in the total number of arithmetic and indirect addressing operations and the amount of memory required, as many of these sub-loops as possible will be able to be vectorised and overall improvements in performance will be achieved.

5.7.3 Discussion

It is somewhat of a truism of vector supercomputing that such changes in methodology as described here, considerable as they are in both a qualitative sense (involving major modification of mathematical model and/or computational model) as well as in a quantitative sense

```
   s  DO 40 i = 1, ni ! This loop is a long scalar loop (the _only_ pass).
   s    IF ( i .EQ. island ) THEN ! We _are_ at a barrier representing an island.
   s v    DO 10 k = 1, nk ! This loop is a short vector loop.
   s v      q(k,i) = 0.0 ! Set this velocity component to zero.
10 s v    CONTINUE        ! This loop is a short vector loop.
   s    ELSE                      ! We are _not_ at a barrier representing an island.
   s
!  s     . <Do some k-independent calculations, such as determining land.>
   s
   s      IF ( i .EQ. land ) THEN ! We _are_ at a coastal boundary.
   s v      DO 20 k = 1, nk ! This loop is a short vector loop.
   s v        q(k,i) = 0.0 ! Set this velocity component to zero.
20 s v      CONTINUE        ! This loop is a short vector loop.
   s      ELSE                      ! We _are not_ at a coastal boundary.
   s
!  s        <Do some k-independent calculations, such as determining y.>
   s
   s v      DO 30 k = 1, nk ! This loop is a short vector loop.
   s v
!  s v        <Do some k-dependent calculations, such as determining x.>
   s v
   s v        IF ( i .NE. modify ) THEN ! We _do not_ need to modify the differencing.
   s v          z = <?> ! Calculate this only if modification _is not_ required.
   s v        ELSE                      ! We _do_ need to modify the differencing.
   s v          z = 0.0 ! Calculate this only if modification _is_ required.
   s v        ENDIF                     ! We _may_ need to modify the differencing.
   s v
!  s v        <Do some k-dependent calculations, such as:>
   s v
   s v        a(k) = x + y + z ! Calculate the matrix as it _will_ be used.
30 s v      CONTINUE        ! This loop is a short vector loop.
   s      ENDIF                     ! We _may_ be at a coastal boundary.
!  s      We call the matrix solver from _within_ the matrix assignment subroutine...
   s      CALL thomas () ! Solve for q(k,i), using a(k), b(k), c(k), and d(k).
!  s      ... so, subroutine thomas is actually called from subroutines u/vcalcn.
   s    ENDIF                       ! We _may_ be at a barrier representing an island.
40 s  CONTINUE        ! This loop is a long scalar loop (the _only_ pass).
```

Figure 5.5: An idealised pseudo-FORTRAN code snippet illustrating the logical structure of the original poorly vectorised subroutines `u/vcalcn`. Indentation is used to represent nesting of loop structures. Vertical lines of s's and v's in columns 4 and 6, respectively, are used to represent and highlight the scope of scalar and vector loops.

(involving an increase in the number of arithmetic operations and/or the calculation of some quantities more than once) are often required to achieve high levels of vectorisation (Levesque and Williamson 1988; Cray Research, Inc. 1990c).

A test run of the benchmark problem determined that subroutines `u/vcalcn`, `thomas`, and `omega_calcn` now accounted for approximately 74.6%, 5.1%, and 12.1% of CPU time, respectively. The shift in relative effort expended in the modified subroutines, compared to that in the original subroutines, is immediately apparent.

```
   v  DO 10 i = 1, ni ! This loop is a long vector loop (the 1st pass).
   v
!  v    <Do some k-independent calculations, such as determining y(i).>
!  v    <Do some k-independent calculations, such as determining land(i).>
!  v    <Do some k-independent calculations, such as determining modify(i).>
   v
10 v  CONTINUE       ! This loop is a long vector loop (the 1st pass).
*
   s  DO 30 k = 1, nk ! This loop is a short scalar loop.
   s
!  s    <Do some i-independent calculations, such as determining x.>
   s
   s v  DO 20 i = 1, ni ! This loop is a long vector loop (the 2nd pass).
   s v    z(i,k) = <?> ! Calculate this as if modification _is not_ required.
   s v
!  s v    <Do some k-dependent calculations, such as:>
   s v
   s v    a(i,k) = x + y(i) ! Calculate the matrix as it _may_ be used.
20 s v  CONTINUE        ! This loop is a long vector loop (the 2nd pass).
30 s  CONTINUE        ! This loop is a short scalar loop.
*
   v  DO 60 i = 1, ni ! This loop is a long vector loop (the 3rd pass).
   v    IF ( i .EQ. land(i) ) THEN ! We _are_ at a coastal boundary.
   v s    DO 40 k = 1, nk ! This loop is a short unrolled loop.
   v s
   v s      <Set up an identity matrix, with a zero right hand side, such that ...>
   v s      <... q(k,i) := 0.0, i.e. to give this velocity component as zero.>
   v s
40 v s    CONTINUE        ! This loop is a short unrolled loop.
   v    ELSE                        ! We _are not_ at a coastal boundary.
   v      IF ( i .NE. modify(i) ) THEN ! We _do not_ need to modify the differencing.
   v s      DO 50 k = 1, nk ! This loop is a short unrolled loop.
   v s        a(i,k) = a(i,k) + z(i,k) ! Recalculate the matrix as it _will_ be used.
50 v s      CONTINUE        ! This loop is a short unrolled loop.
   v      ENDIF                       ! We _do not_ need to modify the differencing.
   v    ENDIF                       ! We _may_ be at a coastal boundary.
60 v  CONTINUE        ! This loop is a long vector loop (the 3rd pass).
*
! We _may_ have a barrier representing an island.
   v  DO 70 k = 1, nk ! This loop is a short vector loop.
   v
!  v    <Set up an identity matrix, with a zero right hand side, such that ...>
!  v    <... q(k,island) := 0.0, i.e. to give this velocity component as zero.>
   v
70 v  CONTINUE        ! This loop is a short vector loop.
*
! We call the matrix solver from _outside_ the matrix assignment subroutine...
      CALL thomas () ! Solve for q(k,i), using a(i,k), b(i,k), c(i,k), and d(i,k).
! ... so, subroutine thomas is actually called from the main program ted.
```

Figure 5.6: An idealised pseudo-FORTRAN code snippet illustrating the logical structure of the modified well vectorised subroutines u/vcalcn. Indentation is used to represent nesting of loop structures. Vertical lines of s's and v's in columns 4 and 6, respectively, are used to represent and highlight the scope of scalar and vector loops.

5.8 Removal of Memory Bank Conflicts

The computational speed of the vector processor unit far exceeds the capacity of a conventional memory system to deliver the operands of a vector instruction to the vector registers at the required rate. To ensure that an adequate memory transfer rate can be sustained, memory is divided into a number of *banks*. The first memory element is in the first memory bank, and the second in the second bank, and so on. Provided successive memory accesses are made to different banks, the maximum possible memory access rate can be achieved. This is referred to as the *memory bandwidth* of the machine. If an access is made to a memory bank before it is ready, a *bank conflict* occurs and the processor idles until the bank is able to deliver the data. Bank conflicts can substantially reduce program performance, and they can be hard to detect (Levesque and Williamson 1988; Cray Research, Inc. 1990c).

Since the order of most of the nested loops which performed the bulk of `ted`'s work had now been reversed as a result of the modifications described in Section 5.7, all subscripts of two-dimensional array variables present in the original model were interchanged, thus reducing the probability of memory bank conflicts retarding the flow of information between store and registers.

Consider the two-dimensional matrix

$$Q = [\texttt{q(i,k)}] = \begin{pmatrix} \texttt{q(1,1)} & \texttt{q(1,2)} & \cdots & \texttt{q(1,nk)} \\ \texttt{q(2,1)} & \texttt{q(2,2)} & \cdots & \texttt{q(2,nk)} \\ \vdots & \vdots & \ddots & \vdots \\ \texttt{q(ni,1)} & \texttt{q(ni,1)} & \cdots & \texttt{q(ni,nk)} \end{pmatrix} \tag{5.8.1}$$

representing, for example, either of the horizontal velocity components in the `ted` numerical model. Here, the `i` subscript represents the computational element number, and the `k` subscript represents the vertical depth–interval. Consider how this array is stored in memory, i.e. *column-wise* according to the FORTRAN language standard, as shown in Figure 5.7 and as previously

Access Sequence	Memory Location	Matrix Element	Memory Bank
1	1	q(1,1)	1
2	2	q(2,1)	2
⋮	⋮	⋮	⋮
ni	ni	q(ni,1)	ni
ni + 1	ni + 1	q(1,2)	1
ni + 2	ni + 2	q(2,2)	2
⋮	⋮	⋮	⋮
2(ni)	2(ni)	q(ni,2)	ni
⋮	⋮	⋮	⋮
(nk − 1)(ni) + 1	(nk − 1)(ni) + 1	q(1,nk)	1
(nk − 1)(ni) + 2	(nk − 1)(ni) + 2	q(2,nk)	2
⋮	⋮	⋮	⋮
(nk)(ni)	(nk)(ni)	q(ni,nk)	ni

Figure 5.7: Memory access sequence for well optimised FORTRAN array operations. It is assumed that the matrix `q` is stored starting at memory location 1 and that memory is configured into `ni` banks. The memory access order depicted here is contiguous and parallel with the structure of physical memory and is therefore *not* prone to severe memory bank conflicts.

mentioned in Section 3.2.4. A naive straightforward translation of a mathematical matrix operator into the corresponding FORTRAN code could take the form of the idealised FORTRAN code

```
      DO 00020 i = 1, ni
        DO 00010 k = 1, nk
          q(i,k) = x + y(i) + z(i,k)
00010   CONTINUE
00020 CONTINUE
```

Figure 5.8: An idealised FORTRAN code snippet illustrating a poorly optimised nested loop structure. The expression on the right of the assignment statement represents an abstraction of a mathematical operation involving scalar, vector (depth-independent), and matrix (depth-dependent) quantities. Indentation is used to represent the nesting of loop structures. The code depicted here *is* prone to severe memory bank conflicts.

snippet as depicted in Figure 5.8. Consider how this array is accessed in execution, i.e. *row-wise* according to the naive FORTRAN code, with the first subscript changing the least, as shown in Figure 5.9. This figure assumes that the machine has memory configured into ni banks—the

ACCESS SEQUENCE	MEMORY LOCATION	MATRIX ELEMENT	MEMORY BANK
1	1	q(1,1)	1
2	ni + 1	q(1,2)	1
⋮	⋮	⋮	⋮
ni	(nk − 1)(ni) + 1	q(1,nk)	1
ni + 1	2	q(2,1)	2
ni + 2	ni + 2	q(2,2)	2
⋮	⋮	⋮	⋮
2(ni)	(nk − 1)(ni) + 2	q(2,nk)	2
⋮	⋮	⋮	⋮
(nk − 1)(ni) + 1	ni	q(ni,1)	ni
(nk − 1)(ni) + 2	2(ni)	q(ni,2)	ni
⋮	⋮	⋮	⋮
(nk)(ni)	(nk)(ni)	q(ni,nk)	ni

Figure 5.9: Memory access sequence for poorly optimised FORTRAN array operations. It is assumed that the matrix q is stored starting at memory location 1 and that memory is configured into ni banks. The memory access order depicted here is discontiguous and orthogonal with the structure of physical memory and *is* therefore prone to severe memory bank conflicts.

worst possible scenario for such a nested loop structure.

Contrast this with a more considered translation of a mathematical matrix operator into the corresponding FORTRAN code taking the form of the idealised FORTRAN code snippet as depicted in Figure 5.10. According to the considered FORTRAN code *and* FORTRAN standards this array is accessed column-wise, i.e. with the first subscript changing the most, as shown in Figure 5.7. This figure also assumes that the machine has memory configured into ni banks.

One can see from the above that there are definite advantages in the use of lists to represent quantities at all computational grid–points as mentioned in Section 3.2.4. Operations involving exclusively depth-independent quantities translate into single long loops on computational element number i, while operations involving depth-dependent quantities translate into double nested loops on computational element number i and vertical depth–interval k. The choice of loop nesting order, where a choice exists, is contingent upon the relative size of the trip counts

```
      DO 00020 k = 1, nk
        DO 00010 i = 1, ni
          q(i,k) = x + y(i) + z(i,k)
00010   CONTINUE
00020 CONTINUE
```

Figure 5.10: An idealised FORTRAN code snippet illustrating a well optimised nested loop structure. The expression on the right of the assignment statement represents an abstraction of a mathematical operation involving scalar, vector (depth-independent), and matrix (depth-dependent) quantities. Indentation is used to represent the nesting of loop structures. The code depicted here is *not* prone to severe memory bank conflicts.

of the loops involved (here `ni` and `nk`, respectively). The choice of subscript order, itself dependent on the choice made regarding the loop nesting order, is contingent upon the structure of physical memory into logical segments, or banks.

As can be seen in Figure 5.8, when traversing "across the rows" of a two-dimensional array memory, access is orthogonally to the memory structure and there is the possibility of severe performance degradation due to bank conflicts. As can be seen in Figure 5.10, traversing "down the columns" of a two-dimensional array accesses memory contiguously and there are no bank conflicts.

Summary

For optimal vectorisation and minimal memory bank conflict in FORTRAN code involving nested loops, it is generally desirable to have the loop of largest trip count as the innermost loop (ensuring vectorisation on the long inner loop), and the subscripts ordered from left to right in the same order as the nested loops from innermost to outermost (ensuring minimisation of idle processor cycles).

A test run of the benchmark problem determined that subroutines `u/vcalcn`, `thomas`, and `omega_calcn` accounted for approximately 72.7%, 5.5%, and 12.9% of CPU time at this stage in the optimisation process, respectively, indicating that these changes reduced the amount of time setting up the matrices relative to the time spent solving them, albeit only slightly.

5.9 Removal of Obvious Bottlenecks

Profiling tools determined that subroutines `ucalcn` and `vcalcn` were each spending approximately 70% of their CPU time executing a *single* assignment statement. These statements were by far the most complex in these subroutines, in terms of computation (due to the large number of arithmetic operations introduced as a result of abandoning the NCN concept and hence using the completely general `0-1-2`'s code sections) and memory access (due to the indirect addressing introduced as a side-effect of loop splitting and variable promotion). Since the corresponding statements for the by far more frequently encountered `0-1`'s and `1`'s neighbourhood configurations were found to be significantly less complex, the NCN concept was reinstated *for this single statement only* by reinserting a conditional block to test for neighbourhood type in each of these subroutines at the appropriate point. By doing so, the program was required to execute these complicated assignment statements only when absolutely necessary, i.e. for computational elements in "open boundary" neighbourhoods, and equivalent considerably less complex statements for those in "coastal" or "open sea" neighbourhoods.

A test run of the benchmark problem determined that subroutines `u/vcalcn`, `thomas`, and `omega_calcn` accounted for approximately 70.8%, 6.9%, and 11.3% of CPU time at this stage

in the optimisation process, respectively, indicating that once again these changes reduced the amount of time setting up the matrices relative to the time spent solving them.

5.10 Discussion

Some CPU times obtained for the stages in optimisation of the model described in the corresponding subsections above are listed in Table 5.1. Machine type is listed, whether scalar or

Coarse Grid Spencer Gulf Tidal Model CPU Times							
Section No.	Machine Type	Scalar/ Vector	Time-Centred	Optimisation Notes	Error (cm)	CPU (s)	% CPU Reduction
"5.1"	VAX	s	✓	original VAX model	3.85	56366.5	-
"5.2"	SPARC	s	✓	successful SPARC port	3.85	13838.7	75.4
"5.3"	CRAY	s	✓	successful CRAY port	3.91	1762.0	87.3
"5.4"	CRAY	v	✓	auto-vectorisation on	3.91	869.8	50.6
5.5	CRAY	v	✓	compiler directives used	3.91	762.5	12.3
5.6	CRAY	v	×	no time-centring code	3.82	680.3	10.8
5.7	CRAY	v	×	code modified greatly	3.91	341.4	49.8
5.8	CRAY	v	×	subscripts interchanged	3.91	296.5	13.2
5.9	CRAY	v	×	two NCN checks reinserted	3.91	246.4	16.9
-	CRAY	v	×	no profiling overheads	3.91	239.8	2.7
-	SPARC	s	×	no time-centring code	3.76	13875.2	-

Table 5.1: Some CPU times obtained for the coarse grid Spencer Gulf model test problem at various stages in the optimisation process.

vector mode was invoked, and whether time–centring of u and v was implemented. Percentage reduction in CPU time for the scheme described in each subsection relative to that in the previous subsection is also listed. Compiler optimisation was fully enabled for all compilations, for all three machines, except as otherwise indicated. Only one processor was employed on the CRAY. The source code compiled to produce the results listed in Table 5.1 was *identical* for the first five rows, hence the quotation marks in the first column. Thus the CPU times listed in Table 5.1 are *not* those that were required by the test simulations as the optimisation process was in progress, but are times obtained after the fact, so to speak. These test re-runs were so conducted to provide more meaningful comparisons between machine architectures (in the initial stages), and between computational schemes (in the final stages). It was thought that adopting this approach was required to ensure a "fair" test.

The error measure ε calculated from the absolute difference between predicted and observed tide–height constants of the four major tidal constituents at a number of grid elements corresponding to tidal stations in Spencer Gulf (using Equation (3.3.5) of Section 3.3.2) is also listed in Table 5.1. It measures the sensitivity of the model to: roundoff error; machine precision; order in which arithmetic operations are performed; and changes made in computational procedure in the various stages of the optimisation process. During the optimisation process itself, this error measure was useful in determining whether source code alterations had introduced any coding errors, since large deviations from the baseline value of 3.85 cm were an indication that a FORTRAN coding error had been made.

Information derived from profiling outputs generated during these test runs is summarised in Figures 5.11 and 5.12, wherein the horizontal axis values represent the section numbers (x) of this chapter (5) corresponding to the optimisation stage for which the CPU time was determined.

It can be seen from the first three rows of Table 5.1 that the greatest percentage increases in performance were the result of the ports from machines with slower clock cycles to those with faster clock cycles. The difference in the error measures for the initial SPARC and CRAY runs can

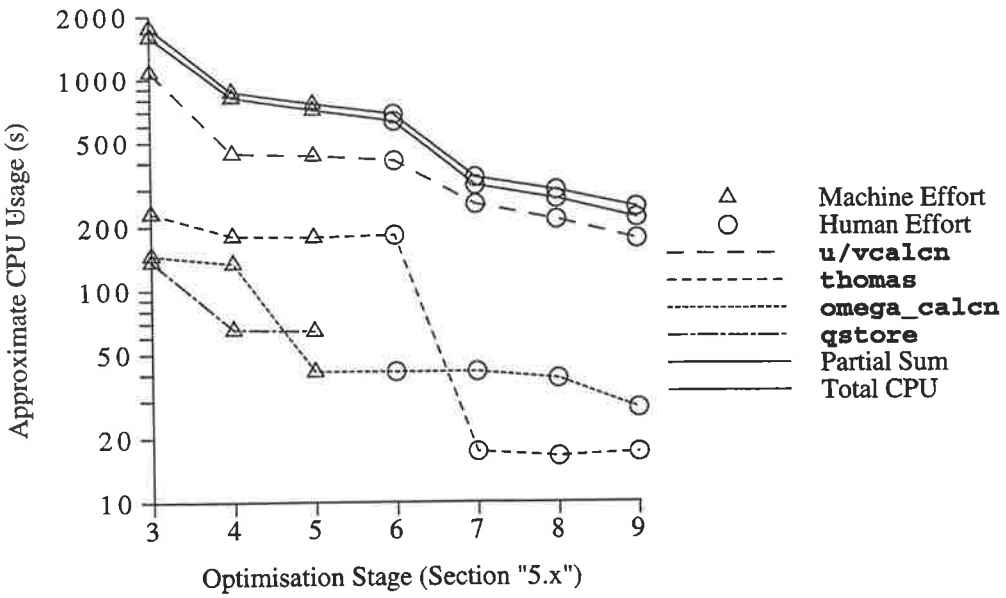

Figure 5.11: Approximate CPU usage (s) graphed against optimisation stage (Section "5.x") for the major `ted` subroutines, with x values representing section numbers. Points attributed to machine effort (i.e. hardware and compiler technology) and human effort (i.e. mathematical model modification and FORTRAN code modification) are plotted using triangles and circles, respectively. The partial sum is determined as the sum of the times for the subroutines with names listed.

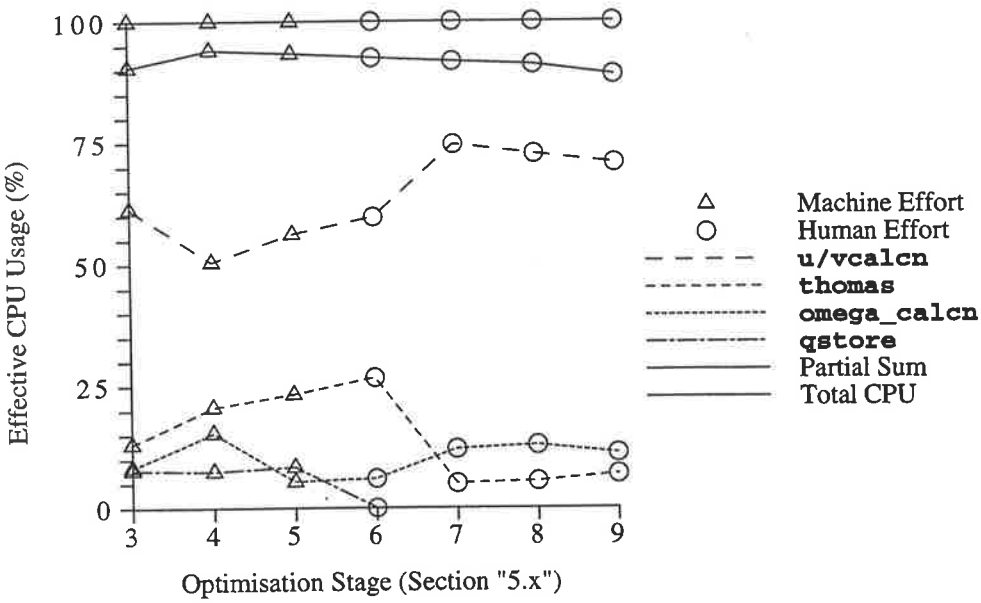

Figure 5.12: Approximate CPU usage (%) graphed against optimisation stage (Section "5.x") for the major `ted` subroutines, with x values representing section numbers. Points attributed to machine effort (i.e. hardware and compiler technology) and human effort (i.e. mathematical model modification and FORTRAN code modification) are plotted using triangles and circles, respectively. The partial sum is determined as the sum of the percentages for the subroutines with names listed.

be attributed to roundoff errors, as the CRAY has essentially twice the accuracy of the SPARC: declaring a REAL variable on the CRAY ensures 64 bit precision compared to the 32 bit precision ensured by the same declaration on the SPARC. Intermediate results of all arithmetic operations are, of course, carried to a corresponding precision, as are the results of calls to run-time library subroutines.

Vectorisation achieved automatically by the CRAY compilation system reduced CPU time by approximately one half, while the use of compiler directives provided further significant improvement in performance for minimal coding effort. Thus, the use of one and two-dimensional vectors to logically represent computational points physically located in two and three-dimensional space, respectively, led to efficient vectorisation. In fact CPU time was reduced by a factor of 2.31 over the first three stages in optimisation on the CRAY (i.e. "5.3"–5.5), an achievement that can be attributed to hardware and compiler technology.

The partial sum curve of Figure 5.12 shows that, once vectorisation was achieved, relatively less CPU time was being spent in the major subroutines compared with the minor subroutines, run-time routines, and main program as optimisation progressed. Note that the scalar run forced all input/output (I/O), etc. to be executed in scalar mode, thus magnifying the influence of the minor routines. Figures 5.11 and 5.12 both show that significant performance gains were achieved with little human intervention.

On the basis of infinite domain wave propagation analyses of the linearised equations (similar to that discussed in Section 8.1.3 below), Bills (1994, personal communications) concluded that a time–centred scheme would produce more accurate results than one with time–centring removed, all else being equal. However, it can be seen that, as a result of removing time–centring, the error measure decreased on both the CRAY (Table 5.1, Sections 5.5 and 5.6) and the SPARC (Table 5.1, Section "5.2" and bottom). Thus, if the error measure listed is to be used as the *only* guide to accuracy, one must conclude that this expectation may not be valid in the presence of finite boundaries to nonlinear equations. Figure 5.11 shows that removing windowing and time–centring had little effect on the CPU time spent in any major subroutine, except for `qstore`. This subroutine was responsible for the windowing described in Section 3.2.4 and was thus no longer required. Overall CPU time spent in the major subroutines decreased moderately.

A performance improvement proportional to the amount of coding effort was achieved as a result of major model/code modifications, which involved loop splitting, variable promotion, and term precalculation. The small increase in the error measure listed in Table 5.1 for Section 5.7 compared to that for Section 5.6 could be attributed to the effects of arithmetic operation "shuffling" brought about by the modifications themselves and compiler optimisation. The precision lost can be regained through recalibration of the model to determine the (new) optimal values of the free parameters, as described in Section 3.3. Figures 5.11 and 5.12 show that this code modification resulted in a modest decrease and a dramatic increase, respectively, in the actual and the relative CPU time spent, respectively, in determining the matrices to be solved for the horizontal velocity components. The time decrease is a result of the vectorisation that was achieved in subroutines `ucalcn` and `vcalcn` and is only modest due to the fact that the abandoning of the NCN concept introduced more work (see Section 5.7). The percentage increase is a result of the vectorisation that was achieved in subroutine `thomas` and is dramatic due to the equally dramatic reductions in the actual and relative CPU time spent in solving the matrices in this subroutine.

Significant improvements in performance were achieved through the reduction of memory bank conflicts by simply interchanging two-dimensional array subscripts (implemented easily with any programmable text editor) and also through the overall reduction of arithmetic and indirect addressing operations by reinstating the NCN concept for a single complex assignment statement (an almost trivial exercise). This can be seen in the table and both figures. In fact CPU time was reduced by a factor of 3.10 over the final five stages in optimisation on the CRAY (i.e. 5.5–5.9), an achievement that can be attributed to programmer effort.

5.10.1 "See ted Run a Four-Minute Mile"

An interesting analogy can be made using the values listed in Table 5.1. The performance of the model at optimisation stage "5.1" can be thought of as `ted` running on the VAX in a time associated with an athlete running an ultra-marathon (15 h 39 min 26.5 s) while that at stage "5.2" can be thought of as `ted` running on the SPARC in a time associated with a marathon (03 h 50 min 38.7 s), and the final performance of the model can be thought of as `ted` running on the CRAY in a time associated with a mile race (00 h 03 min 59.8 s). On the CRAY, over the optimisation stages "5.3"–5.9, performance improvement is given by a 86.0% CPU reduction, corresponding to an increase in computational efficiency of a factor of 7.15. Over all optimisation stages listed in Table 5.1, performance improvement is given by a 99.6% CPU reduction corresponding to an increase in computational efficiency of a factor of 234.97.

5.10.2 Further Optimisation

It was at this point that optimisation efforts were ceased, for a number of reasons. As can be seen from the graphs of Figures 5.11 and 5.12 and the percentages given in Section 5.9, it is apparent that more effort should be expended in further optimisation of the matrix determination subroutines. This would, however, require a major rewrite of these subroutines and, most likely, a major re-evaluation of the data structures which should be declared to achieve greater efficiency through a better arithmetic operation to memory access ratio (which was the essence of the bottleneck discussed in Section 5.9). The programmers' practice of trading memory for CPU time and utilising greater levels of precalculation could be employed to this aim, with only the *possibility* of significant performance improvements. This is because memory usage for the scheme of Section 5.9 was low by supercomputing standards—approximately 2 Megabytes (MB) out of a system maximum of 64 MB—and the rate of arithmetic operations was fairly impressive by CRAY Y-MP standards—approximately 120 millions of floating point operations per second (MFLOPS) out of a theoretical machine peak of 350 MFLOPS.

5.11 Summary

In this chapter, the procedure by which the FORTRAN code for the numerical tidal model—originally developed on a scalar minicomputer—was optimised for performance on a vector supercomputer was explained in detail. Some discussion of vectorisation issues and performance results was also made.

The net result of optimisation stages on the CRAY (i.e. "5.3"–5.9 in Table 5.1) reduced CPU usage by approximately 86.0% (or, equivalently, by a factor of 7.15). The dramatic effect on performance brought about through vectorisation is therefore immediately apparent. Without overheads associated with profiling, the CPU time required by the scheme of Section 5.9 was reduced to 00 h 3 min 59.8 s—a reduction in CPU usage of approximately 99.6% (or, equivalently, by a factor of 234.97) when compared to the CPU time of 15 h 40 min 26.5 s required by the scheme of Section "5.1". Further performance improvements, though theoretically possible, are considered practically not feasible. The enormous effort required to modify the fundamental algorithms "from the ground up" would not be justified by performance improvements of comparable significance within a reasonable time allocated for source code revision. The successful vectorisation of the program allows solution of large problems on the CRAY in times comparable to those required of small problems on the SPARC.

Chapter 6

The Fine Grid Spencer Gulf Model

In this chapter, a fine grid Spencer Gulf model is presented, as required for adequate modelling of prawn larvae dispersion in this region. The method by which a new application of the tidal model is calibrated is illustrated and interesting aspects of this process are discussed. The tidal model discussed in this chapter forms a basis of, and provides input to, the dispersion model discussed in Chapters 10.

The true orientation of the fine resolution model grid is 37.64° T (or approximately NNE). The reason for this approximate orientation is outlined in Sections 3.4 and 6.1. All plots showing model results will be aligned with model axes parallel to the edges of the page.

While reading this chapter, the reader may wish to consult Figures 1.2 and 1.3, or Figure 4.1 for locations of tidal observation stations and other features in the Spencer Gulf region.

6.1 Specifying the Horizontal Grid

Taking the factors discussed in Sections 2.2.2 and 3.3.3 into account, the grid elements of the fine resolution Spencer Gulf model were selected to have horizontal dimensions $2\Delta x = 2\Delta y =$ 1905 m. These dimensions were also chosen in the hope that, with the exception of some coastal elements, there may be a one to one correspondence between a subset of values obtained from coarse grid simulations and a subset of values obtained from fine grid simulations. Unfortunately it was not possible to obtain a fine grid which was aligned in exactly the same way as the coarse grid model, because the alignment was determined by the bathymetry data supplied by the Department of Environment and Planning (DEP).

Other features of the fine grid Spencer Gulf model include:

- Number of Type 1 computational elements $N_1 = 5982$;
- Number of Type 2 grid elements $N_2 = 46$;
- Horizontal grid dimensions of 167 rows × 76 columns = 12692 grid elements.

In Figure 6.1 Stickney Island—a barrier to horizontal current flow in the y direction—is represented by a solid line segment. The model coastline, represented by straight line segments approximating the Spencer Gulf coastline, represented by a dashed curve, can be seen to be a more realistic representation in the fine grid model illustrated in Figure 6.1 than in the coarse grid model of Figure 3.9. The dashed curve in this figure, and all other figures in this thesis indicating the Spencer Gulf coastline, was obtained from hydrographic maps **Aus 341–343**, **776–778**, **780–781**, **1008**, and **2389** (Royal Australian Survey Corps 1981, 1982a, 1982b, 1984, 1989, 1990a, 1990b, 1990c, 1991, 1992) by "hand digitisation".

Reducing horizontal grid–spacing dimensions is one method of obtaining greater spatial resolution, in model results in general and those adjacent to coastlines in particular, for models constructed using finite-difference methods on orthogonal grids. Other methods involve oblique piecewise linear coastal boundary representation (I'Anson et al. 1994; Matthews and

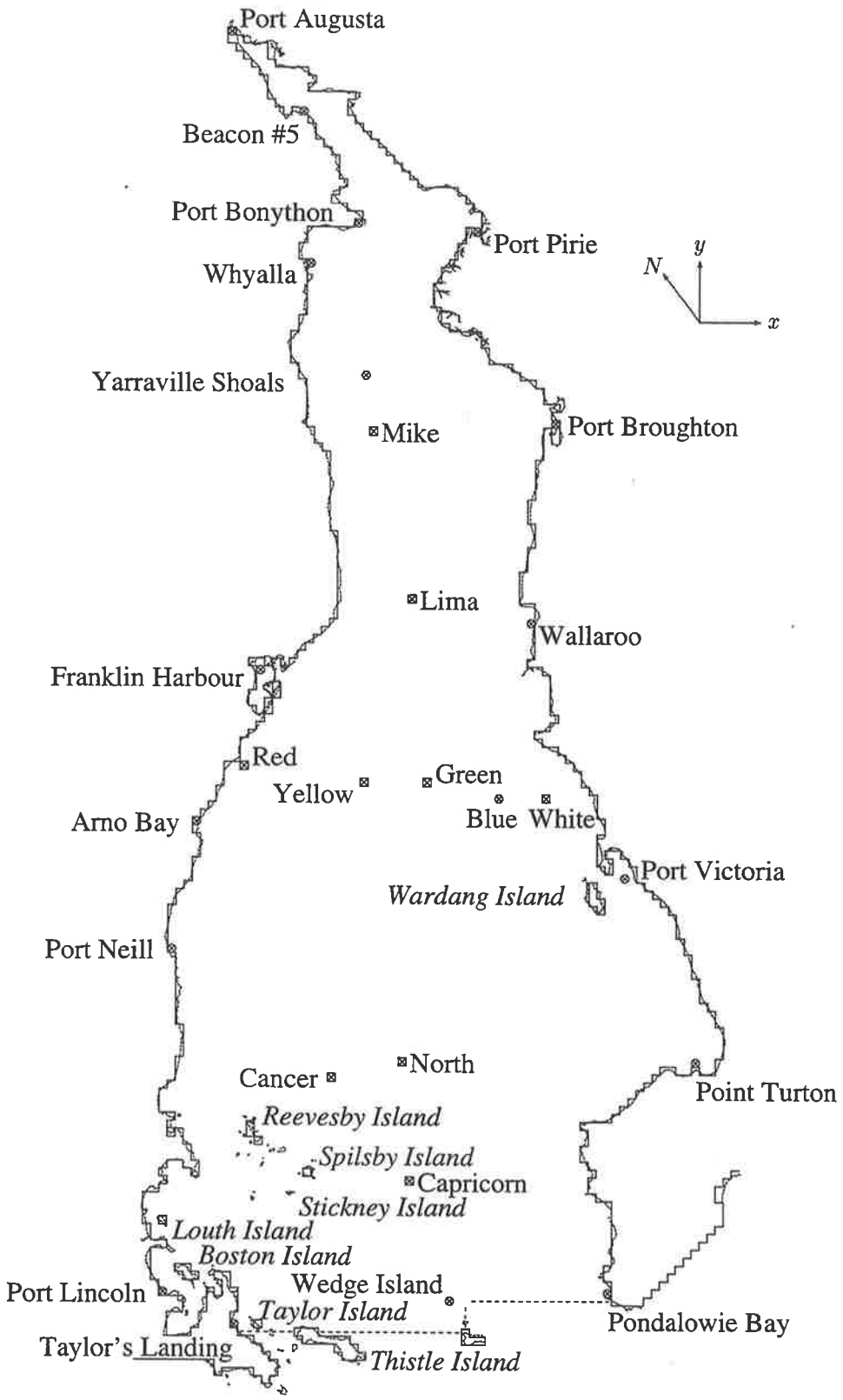

Figure 6.1: The fine grid Spencer Gulf model, indicating the location of the model coastal boundary (solid line) approximating the physical coastal boundary (dashed curve), the model open boundary (dashed line), and the model location of the tidal observation stations for tide–heights only (crossed circles), tidal currents only (crossed squares), and both (crossed hexagons). Stations (roman) and islands (italics) are named.

Noye 1996a, 1996b; Matthews et al. 1995, 1996) or adaptive mesh refinement (Richards and Noye 1994; Richards 1996). These are not considered here.

6.2 Specifying the Vertical Grid

It was decided to use the same number of vertical grid–spacings, or depth–intervals, for the fine resolution model as was used for the coarse resolution model of Section 3.4. The vertical coordinate transformation (3.1.11)–(3.1.12) used and the shallow nature of the waters being modelled, as well as computational resource limitations, influenced this decision. For the fine grid model, however, the value of the vertical grid–spacing parameter κ in (3.2.1) is increased from $\kappa = 5.0$—as used in the coarse grid model—to $\kappa = 8.0$, with the intent of enhancing resolution near the sea–surface and sea–bed. The effect of increasing κ from 5.0 to 8.0 on the vertical grid can be seen in Figure 3.7 and Table 3.3. The prawn larvae dispersion model requires the currents predicted by the tidal model, as discussed in Section 2.4, at only two depth–intervals, i.e. near the surface and near the bed. Increased resolution in these areas, at the expense of possibly reduced accuracy at the mid-depths, is thus desirable. The number of depth–intervals at which predictions are output is limited to two out of the possible ten for two reasons. First, there are insufficient data relating to the mechanisms involved in the vertical movement of prawn larvae in the water column beyond the fact that they spend the majority of their time at the surface or bed, with little time spent in the mid-depths (see Section 2.4). Second, disk space and archival methods determined that a larger number of intervals output would be technically difficult. In fact, with the output regime as specified in this section and Section 6.3, the total amount of data output per six-month simulation approached 700 MB. This would increase to about 2 GB if all depth–levels were required by the prawn larvae dispersion model.

6.3 Determining the Optimal Time–Step

From the MSL depth field of Figure 6.4, the model maximum depth is determined as

$$h_{\max} = 55.59\,\mathrm{m}, \tag{6.3.1}$$

giving a model maximum time–step of

$$\Delta t_{\max} = 57.7\,\mathrm{s}, \tag{6.3.2}$$

as determined by (3.3.18). Initial simulations using the fine grid model were attempted with a time–step of $\Delta t = 80\,\mathrm{s}$. The model was, however, found to be unstable at this value, as well as at values of 75 and 72 s. Operational stability was achieved with

$$\Delta t = 60\,\mathrm{s} \tag{6.3.3}$$

as the time–step for the fine grid Spencer Gulf model. Using (6.3.1) and this time–step, (3.3.15) results in a Courant number of

$$c_{\max} = 1.04, \tag{6.3.4}$$

indicating that the increased model maximum MSL depth of the fine grid model resulted in a slightly larger Courant number compared to that for the coarse grid model.

Due to disk space and archive method limitations, output of tidal currents (and sea–surface elevations) predicted by the tidal model were not attempted at every time–step (i.e. every minute) but at every 60 time–steps (i.e. every hour). Temporal resolution coarser that this would result in inadequate tidal analysis of velocities (see Section 7.4) and of sea–surface elevations required to determine tidal model accuracy (see Section 3.3.2), while resolution finer than this was operationally impossible for reasons discussed in Section 6.2.

Points raised in Section 3.3.5 dictate that many simulations of durations of approximately six months are required. Related features of the fine grid Spencer Gulf model thus include:

- Simulation endpoints at 00:00 hrs on $01/10/(Y-1)$ and 00:00 hrs on $01/04/Y$, where the years $(Y-1)$ to Y encompass the summer spawning period of interest;
- Final time–level $N = 262080$ (or $N = 263520$ if Y is a leap year);
- Simulation period of $T = 182\,\mathrm{d}$ (or $T = 183\,\mathrm{d}$ if Y is a leap year),

indicating that the desired simulations require significant computational resources. This deemed it necessary for the tidal model programs, as described in Chapter 3, to be ported to, and optimised for, a supercomputer, as described in Chapter 5.

6.4 Spencer Gulf Field Observations

The numbering scheme for the Type 2 open boundary grid elements b is as shown in Figure 6.2, where the location of open boundary with respect to the model interior is indicated by the dashed straight line segments of Figure 6.1. The tidal elevations ζ_b at each of these elements is determined by (3.1.33) with $M = 4$ and all other terms specified by the National Tidal Facility at The Flinders University of South Australia.

The height specified input data for the 46 elevation grid–points of the open boundary of Figure 6.1 are presented in Table 6.1. These data were obtained from the tide–height constants for the four major tidal constituents O_1, K_1, M_2, and S_2 at the four tidal observation stations at the entrance to the Gulf, given in Table 3.1, in the following manner.

Referring to Figure 6.2, consider two triangles defined by the vertices of the map locations of the tide–height stations at Taylor's Landing, Thistle Island, and Wedge Island (triangle A) and Thistle Island, Wedge Island, and Pondalowie Bay (triangle B). Phases and amplitudes listed in Table 6.1 were found via linear interpolation/extrapolation (depending) of values from those stations defining triangle A for all open boundary elevation grid–points lying inside this triangle or to the left of the map position of the Thistle Island station, and of values from those stations defining triangle B otherwise. This procedure gave a more physically realistic "smooth" input data set than any other scheme devised, using any combination of stations and linear and/or quadratic interpolation/extrapolation. Figure 6.3—wherein amplitude and phase of the fine grid model open boundary elements, as well as of the tide–height stations used to derive these, are plotted—illustrates this. Note that the four separate line segments, approximately left to right, in each of the Figures 6.3(a)–6.3(d) correspond to the four open boundary element segments consisting of elements numbered b = 22–28, 29–46, 19–21, and 1–18, respectively. From these figures it is apparent that the abrupt change in amplitude along the segment b = 29–46 is an artifact of the observations rather than a side–effect of the derivation. No further calibration, for instance such as that described in Teubner et al. (1996), of the height specified forcing was carried out.

6.5 Determining Mean Sea Level

As discussed in Section 3.4, specification of mean sea level (MSL) is a two part process, consisting of determining bathymetry from a chart datum, typically Indian Spring Low Water (ISLW), and adjusting the latter to the former.

6.5.1 Determining Indian Spring Low Water from Chart Datum

The ISLW datum depth at the elevation point of each Type 1 and Type 2 element is obtained from the recent digitising of the available Spencer Gulf depth information by the Information Services Division (ISD) of the South Australian Department of Environment and Planning (DEP).

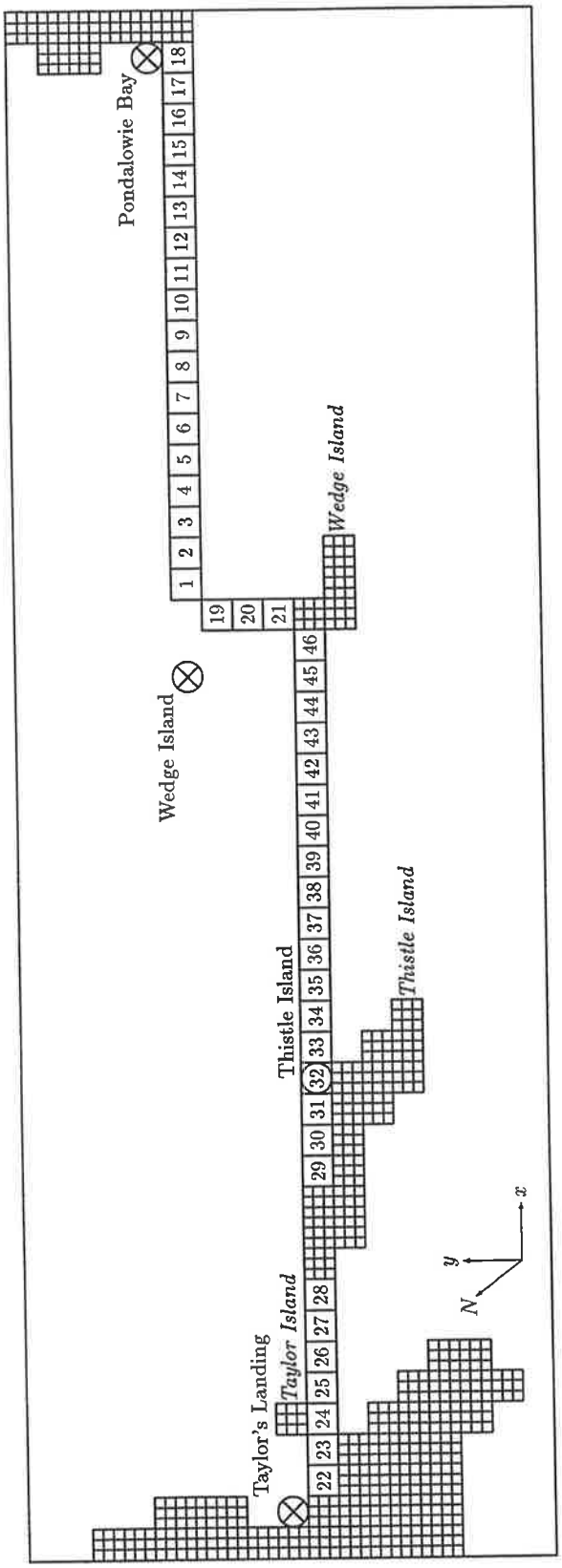

Figure 6.2: The open boundary region of the fine grid Spencer Gulf model, indicating the numbering scheme for the 46 open boundary Type 2 grid elements. Grid elements corresponding to land are shown hatched. The non-hatched region above the open boundary consists entirely of Type 1 computational elements. Tidal observation stations for tide–height constants used to derive forcing at the open boundary are shown (circles).

Fine Grid Spencer Gulf Model Open Boundary Tidal Constituents								
Element Number (b)	Tidal Constituent							
	O_1		K_1		M_2		S_2	
	amp.	phase	amp.	phase	amp.	phase	amp.	phase
1	14.79	235.03	20.40	254.54	16.20	109.08	16.58	149.88
2	14.68	235.33	20.15	254.93	16.07	109.17	16.42	150.05
3	14.57	235.62	19.91	255.33	15.94	109.26	16.26	150.22
4	14.45	235.92	19.66	255.72	15.82	109.34	16.11	150.40
5	14.34	236.22	19.42	256.11	15.69	109.43	15.95	150.57
6	14.23	236.52	19.17	256.50	15.56	109.52	15.79	150.74
7	14.11	236.82	18.93	256.90	15.44	109.60	15.63	150.92
8	14.00	237.12	18.68	257.29	15.31	109.69	15.47	151.09
9	13.89	237.42	18.44	257.68	15.18	109.78	15.31	151.26
10	13.78	237.72	18.19	258.07	15.06	109.87	15.15	151.44
11	13.66	238.01	17.95	258.47	14.93	109.95	14.99	151.61
12	13.55	238.31	17.70	258.86	14.80	110.04	14.84	151.78
13	13.44	238.61	17.46	259.25	14.68	110.13	14.68	151.96
14	13.33	238.91	17.21	259.64	14.55	110.21	14.52	152.13
15	13.21	239.21	16.97	260.04	14.42	110.30	14.36	152.30
16	13.10	239.51	16.72	260.43	14.30	110.39	14.20	152.48
17	12.99	239.81	16.48	260.82	14.17	110.47	14.04	152.65
18	12.87	240.11	16.23	261.21	14.04	110.56	13.88	152.82
19	14.58	234.70	19.93	254.36	16.39	108.69	16.70	149.74
20	14.37	234.37	19.46	254.18	16.58	108.30	16.82	149.61
21	14.17	234.04	18.99	254.00	16.76	107.91	16.93	149.47
22	15.36	226.51	21.37	243.82	19.98	102.04	20.99	143.31
23	15.37	226.71	21.41	244.12	19.90	102.33	20.87	143.55
24	15.39	226.91	21.46	244.42	19.82	102.61	20.76	143.79
25	15.40	227.11	21.50	244.72	19.73	102.90	20.65	144.03
26	15.41	227.31	21.54	245.02	19.65	103.19	20.53	144.27
27	15.43	227.51	21.58	245.31	19.57	103.48	20.42	144.51
28	15.44	227.71	21.63	245.61	19.48	103.76	20.31	144.76
29	15.50	228.51	21.80	246.81	19.15	104.91	19.85	145.72
30	15.51	228.71	21.84	247.11	19.07	105.20	19.74	145.96
31	15.52	228.91	21.88	247.40	18.99	105.49	19.62	146.20
32	15.54	229.11	21.93	247.70	18.90	105.78	19.51	146.44
33	15.55	229.31	21.97	248.00	18.82	106.06	19.40	146.69
34	15.54	229.53	21.94	248.32	18.73	106.30	19.27	146.91
35	15.42	229.83	21.70	248.71	18.60	106.39	19.11	147.09
36	15.31	230.13	21.45	249.11	18.47	106.49	18.96	147.26
37	15.20	230.43	21.21	249.50	18.35	106.57	18.80	147.43
38	15.09	230.73	20.96	249.89	18.22	106.65	18.64	147.61
39	14.97	231.03	20.72	250.28	18.09	106.74	18.48	147.78
40	14.86	231.33	20.47	250.68	17.97	106.83	18.32	147.95
41	14.75	231.63	20.23	251.07	17.84	106.91	18.16	148.13
42	14.63	231.92	19.98	251.46	17.71	107.00	18.00	148.30
43	14.52	232.22	19.74	251.85	17.59	107.09	17.85	148.47
44	14.41	232.52	19.49	252.25	17.46	107.17	17.69	148.65
45	14.30	232.82	19.25	252.64	17.33	107.26	17.53	148.82
46	14.18	232.12	19.00	253.03	17.21	107.35	17.37	148.99

Table 6.1: Amplitude (cm) and phase (°, GMT) of the four major tidal constituents at the 46 open boundary grid elements indicated in Figure 6.2 for the fine grid Spencer Gulf model.

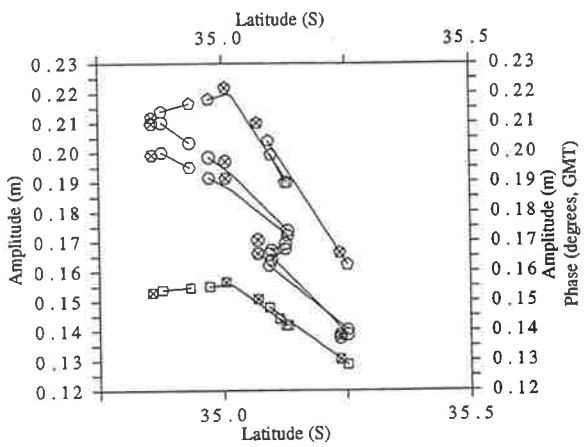

(a) Amplitude (m) with Latitude (°S)

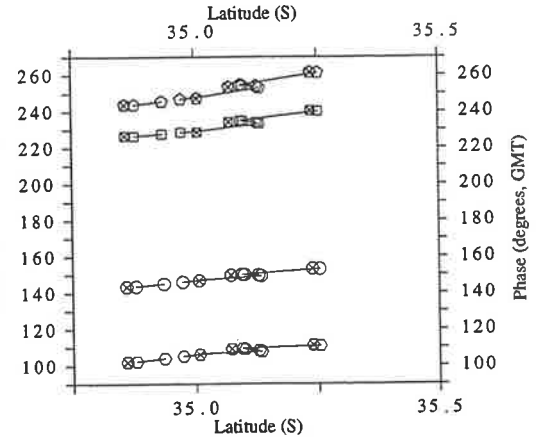

(b) Phase (°GMT) with Latitude (°S)

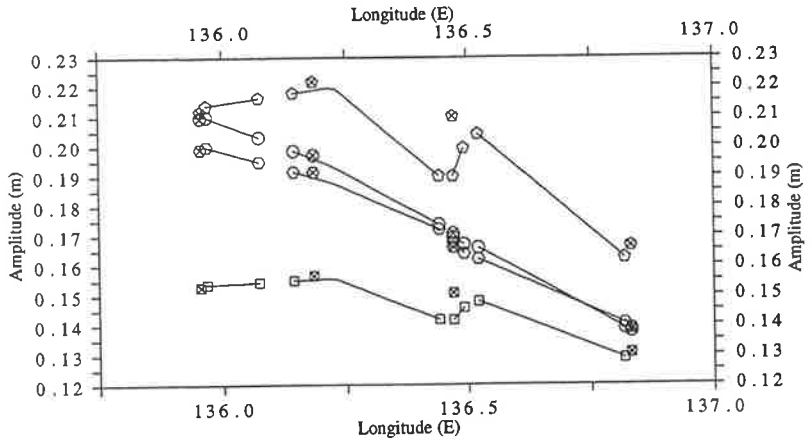

(c) Amplitude (m) with Longitude (°E)

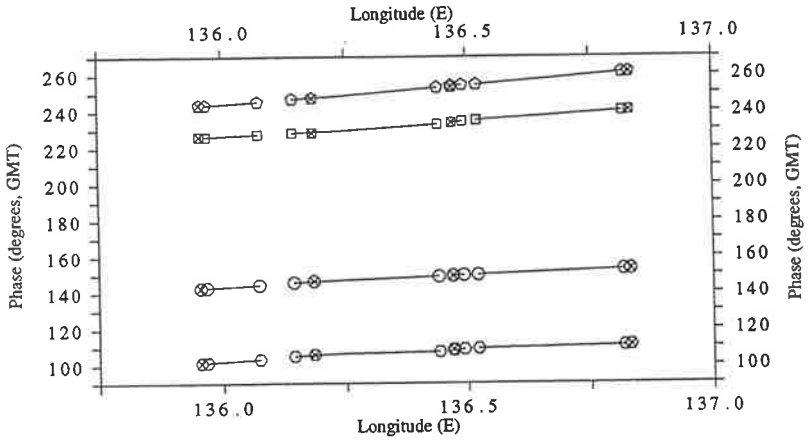

(d) Phase (°GMT) with Longitude (°E)

Figure 6.3: Amplitude (m) and phase (°GMT) of the tidal constituents O_1 (squares), K_1 (pentagons), M_2 (hexagons), and S_2 (circles) at the open boundary grid elements of the fine grid Spencer Gulf model. Constituent values for open boundary elements listed in Table 6.1 at the end points of the open boundary subregions defined in Figure 6.2 are indicated with the appropriate (open) regular polygon/circle. Values for elements between the end points are joined with linear interpolation. Constituent values for open boundary stations listed in Table 3.1 are indicated with an appropriate (crossed) regular polygon/circle. Stations are, left to right, Taylor's Landing, Thistle Island, Wedge Island, and Pondalowie Bay, in all sub-figures.

The original data contained over 300 values which were required to be corrected by hand. This was either due to the fact that a negative depth value was provided (indicating a digitisation or interpolation error produced a value corresponding to a spurious "island" element), or that the value provided resulted in a local instability (indicating a digitisation or interpolation error resulted in a value corresponding to a non-physical bathymetric discontinuity). In either case a resulting local instability was observed when, during a 29 d simulation, a total depth $H < 1.0\,\mathrm{m}$ was automatically adjusted to $H = 1.0\,\mathrm{m}$ and was reported by the `ted` program. It was the set of elements so reported that was hand-adjusted, with this adjustment being made in multiples of 0.5 m increments. This procedure was continued in the first instance until the simulation proceeded for the full 29 d term without numerical overflow (indicating that no local instabilities eventually resulted in global instability), and in the second instance until no automatic total depth adjustment was reported by the program (indicating that no local instabilities resulted in any "dry" computational elements).

Convergence to an entirely stable ISLW specification was accelerated in the following manner. For no automatic total depth adjustments at a particular computational element, it is necessary that the value of ISLW depth specified at that element be greater than the sum of the major tidal constituent amplitudes throughout the entire simulation; these may be obtained by performing a complete 29 d simulation with the proposed depth field, followed by a harmonic analysis. If this condition is satisfied at all elements, even a hypothetical "tide" in which all major tidal constituents are simultaneously at an ebb at every grid element would not leave any element uncovered at any stage in the time period of the analysis. It should be noted, however, that this physically impossible "tide" scenario ignores nonlinear interactions and minor constituent generation by the numerical model. This concept was exploited in order to determine the amount by which manual depth adjustment was required at elements of potentially significant local instabilities. Three iterations of this accelerated procedure were required, in which the values

$$\alpha = 0.00001\,\mathrm{m^2 s^{-1}} \quad \text{and} \quad \beta = 0.007 \tag{6.5.1}$$

were used, along with (3.1.23) and (3.1.25), to parameterise vertical eddy viscosity. Zero wind–stress was applied so as not to bias the results for any particular wind regime, but the asymmetric vertical eddy viscosity parametrisation—normally recommended for simulations without wind–stress—was chosen since the simulations planned for determining the current regime for larval dispersion do in fact have non-zero wind–stress applied.

6.5.2 Determining Mean Sea Level from Indian Spring Low Water

A meaningful harmonic analysis (Easton 1977) is only obtained if sufficient data are available to resolve the chosen analysed constituents. Longer periods of data are required to separate constituents of similar frequency (known as *related constituents*). This means that, in general, the longer period of data to be included in the analysis, the greater the number of constituents which may be determined.

The minimum length of data necessary to separate a pair of constituents is known as their *synodic period*. Required constituents are only those which are separated by at least a complete period from their neighbouring constituent over the time period of data available. So, consulting Table 6.2, to determine M_2 and S_2 requires

$$\frac{360}{30.0 - 28.98}\,\mathrm{h} \approx 14.77\,\mathrm{d} \tag{6.5.2}$$

of tidal signal. Similarly, separation of S_2 and K_2 requires 182.6 d, a much larger synodic period, showing that six months of data is required to resolve these constituents. However, Pugh (1987) suggested that this could be an unnecessarily restrictive criterion where signal noise is low. It can be seen that for 29 d of data

$$\Delta\sigma = 360^\circ/(29 \times 24)\,\mathrm{h} = 0.52^\circ\,\mathrm{h^{-1}} \tag{6.5.3}$$

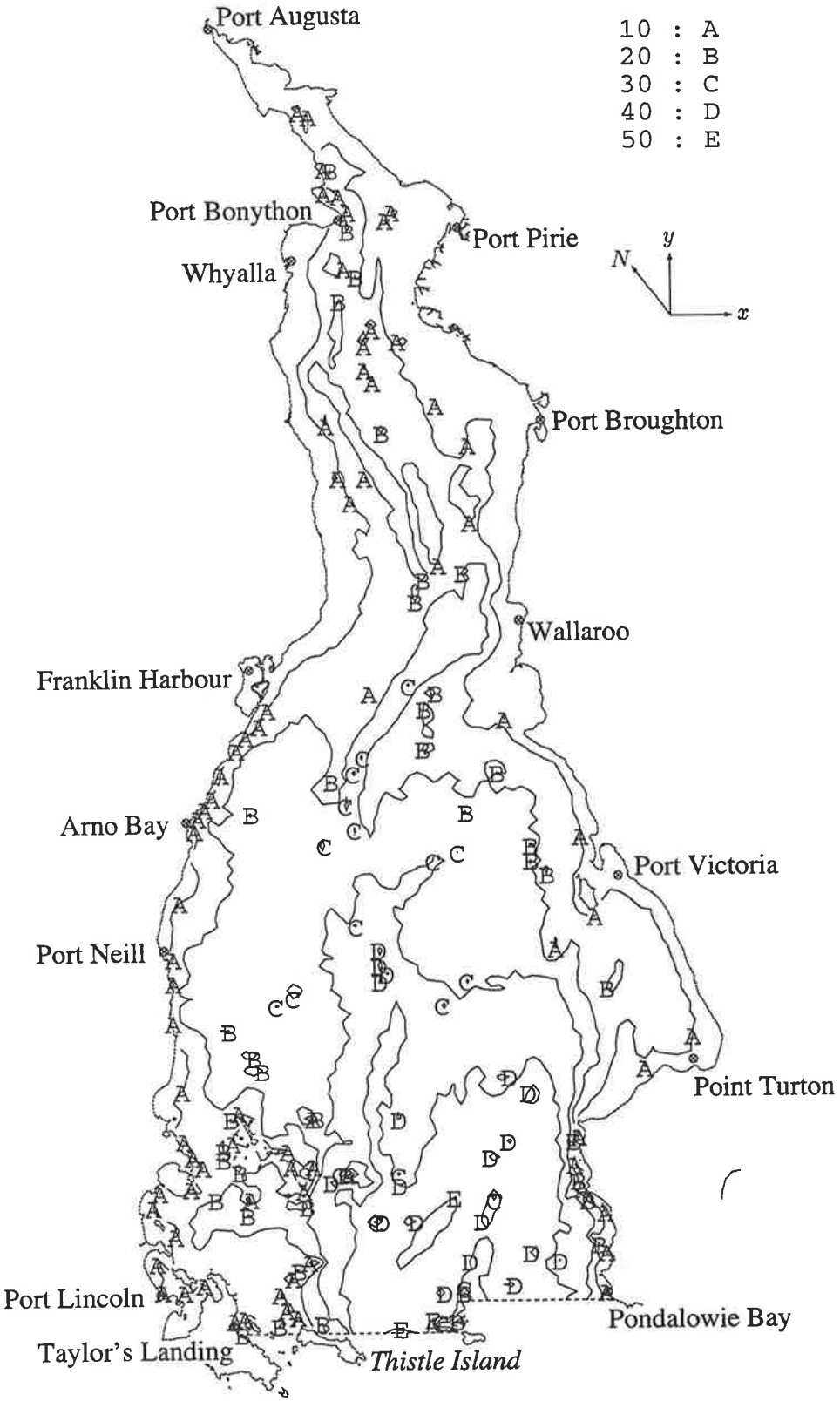

Figure 6.4: The MSL depth contours (m) for the fine grid Spencer Gulf model. Some stations (roman) and islands (italics) are named.

Spencer Gulf Major Tidal Constituents		
Constituent (symbol)	Frequency ($^\circ\,h^{-1}$)	Phase Correction ($^\circ$)
O_1	13.9430355980	356.138
K_1	15.0410686393	10.190
M_2	28.9841042373	6.328
S_2	30.0	0.0

Table 6.2: The major tidal constituents in Spencer Gulf. Listed for each is its Frequency ($^\circ\,h^{-1}$), and Phase Correction (a lag/lead relative to 00:00 hrs on 01/01/1900, GMT).

defines the smallest resolvable speed difference. Noting that M_2 and S_2 provide the smallest speed difference ($\Delta\sigma = 1.16^\circ\,h^{-1}$) between any two of the four major constituents listed in Table 6.2, one can see by (6.5.2) that all chosen constituents will be separated by at least two complete periods from their neighbouring constituent over the 29.53 d time period of data recommended by Pugh (1987) for an analysis of those constituents.

However, by choosing to average over 29.00 d, the current residuals (see Section 7.4.2) derived in this thesis are only slightly contaminated by the major constituents. In 29 d there are exactly 58 cycles of the S_2 constituent and nearly integer multiples of the O_1 (26.96 cycles), K_1 (29.08), and M_2 (56.04) periods. Over 29.53 d the corresponding numbers of cycles are approximately 59.06, 27.54, 29.61, and 57.06 which are no longer near integer.

Simulations producing full 29 d tidal signals were thus made in order to carry out the ISLW to MSL adjustments described in Section 3.3.7. Four iterations of the process idealised in expressions (3.3.12)–(3.3.14) were sufficient to obtain a "converged" MSL depth field, one which was everywhere different from the previous estimate by less than 1 mm. Figure 6.4 illustrates the resulting MSL depth field for the fine grid Spencer Gulf model. All input parameters used are as described in Section 6.1–6.5.1. Similar to those for the coarse grid Spencer Gulf model described in Section 3.4, the MSL depths near the open boundary of the fine grid Spencer Gulf model are 0.5–0.8 m greater than the corresponding ISLW depths. In comparison, the increase at the head of the Gulf is slightly greater, with corrections as high as 2.3 m to the extreme north. The contours of Figure 6.5, representing the correction from ISLW to MSL over the entire fine grid Spencer Gulf model, indicate that the procedure for this resulted in a correction which is, however, qualitatively similar to that of the coarse grid model, shown in Figure 3.14.

6.6 Specifying the Vertical Eddy Viscosity

Numerical experiments determined that simulations with non-zero wind–stress as described in Section 4.2, parameters as described in Sections 6.1–6.5.1, and MSL as described in Section 6.5.2 resulted in small numbers of elements becoming "dry" for small numbers of time–steps during the spring periods of the tidal cycle. Experiments also showed that increasing slightly the background eddy viscosity value α, effectively smoothed the solution and resulted in a reduction in number and frequency of these "drying" events. With all other input parameters constant, altering background eddy viscosity to a value of

$$\alpha = 0.0001\,m^2 s^{-1} \tag{6.6.1}$$

eliminated these events altogether. With all other input parameters chosen, it remained to determine the value of β used in (3.1.23) and (3.1.25) to parameterise vertical eddy viscosity. A small set of simulations were carried out, from which it was determined that a value of

$$\beta = 0.068 \tag{6.6.2}$$

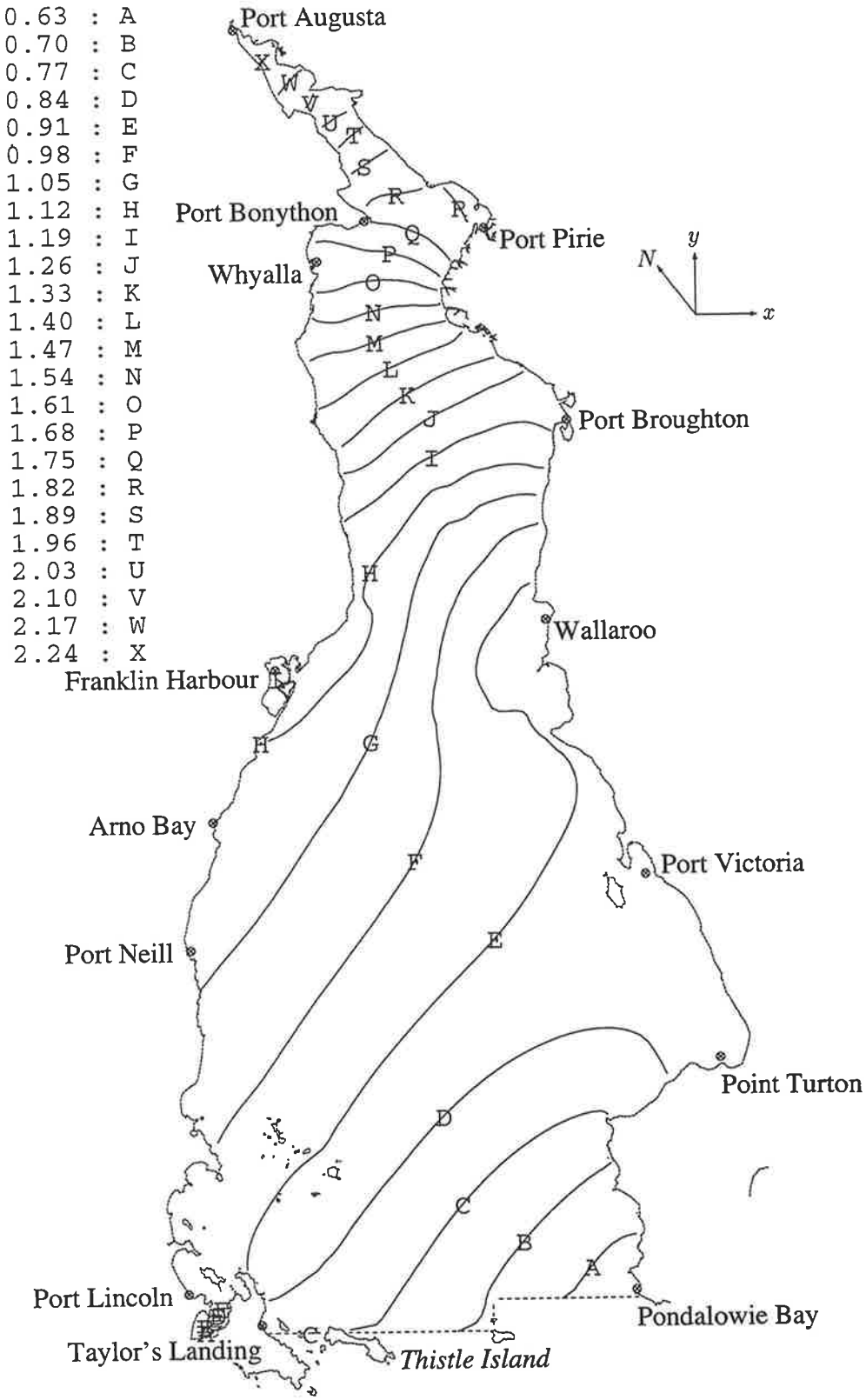

Figure 6.5: The ISLW to MSL depth correction contours (m) for the fine grid Spencer Gulf model. Some stations (roman) and islands (italics) are named.

minimised the error measures of Section 3.3.2, resulting in an overall average absolute complex difference between observed and predicted phase and amplitudes of $\varepsilon = 4.26\,\text{cm}$. The fine grid Spencer Gulf model was at this point considered adequately calibrated.

6.7 Tidal Model Prediction Validity

The error listed in Section 6.6 was calculated using the error measures derived in Section 3.3.2 from predictions determined by the fine grid Spencer Gulf model presented in this chapter, using constant wind–stress and the parameters specified in Sections 6.1–6.6, with the field data presented in Section 3.3.1.

The reader is referred to Bills (1991) for a detailed validation of the coarse grid Spencer Gulf model presented in Section 3.4, with zero wind–stress and the parameters specified in Sections 3.3.4–3.3.6, using the field data presented in Section 3.3.1. This was carried out for both tidal elevation and tidal current, using the error measures derived in Section 3.3.2 and other means.

6.7.1 Sea–Surface Elevation Prediction Validity

The amplitude and phase of the four major tidal constituents of sea–surface elevation predicted by the three-dimensional tidal model were found to be in close agreement with those using the depth-averaged model (Bills 1991, pp. 247–250). These were, in turn, found to be in general agreement with the published observations and numerical results of other authors (Easton 1970; Noye and Tronson 1978; Noye et al. 1981, 1982; Steinberg 1983), yet supplied more detail (Bills 1991, pp. 172–177). Tidal elevations predicted by the original coarse grid three-dimensional model of the Spencer Gulf region with zero wind–stress were shown to agree with those observed in the field with an error of $\varepsilon = 4.02\,\text{cm}$ (Bills 1991, p. 247). Those predicted by the modified coarse grid model with constant wind–stress have been shown to agree with an error of $\varepsilon = 3.76$–$3.91\,\text{cm}$ (Section 5.10, Table 5.1). The error of $\varepsilon = 4.26\,\text{cm}$ for the optimised fine grid model with constant wind–stress, as discussed in Section 6.6, is thus consistent with those calculated from elevations approximated using similar models of the Spencer Gulf region.

Hence, it is concluded that predictions using the present model will be no less accurate than those using previous models. The former will, however, have greater resolution in the temporal and horizontal coordinates compared to the latter. This conclusion is strictly applicable only to predicted tidal elevations. It is reasonable, however, to assume that a similar conclusion can be reached with respect to predicted tidal currents.

6.7.2 Horizontal Current Prediction Validity

Depth-averaged tidal currents derived from the depth-dependent currents predicted by the three-dimensional coarse grid tidal model of Spencer Gulf with zero wind–stress were shown to be in strong agreement with those calculated using the depth-averaged model (Bills 1991, pp. 247 and 251–252). These were, in turn, found to be in general agreement with results and observations of other authors (Lennon 1981; Noye 1984b; Steinberg 1983) yet, as for elevations, supplied more detail (Bills 1991, pp. 178–187). This agreement was determined by Bills (1991) chiefly through comparison of tidal ellipses (see Section 7.4.1) generated using the predictions and the observations. It will be shown in Sections 7.4.3 and 10.4.1 that depth-dependent currents predicted by the three-dimensional fine grid tidal model of Spencer Gulf with variable wind–stress are in general agreement with those reported for the coarse grid model with zero wind-stress (Bills, pp. 259–265).

Analyses were also made of tidal current residuals (see Section 7.4.2) generated using the depth-averaged currents derived from the depth-dependent currents predicted by the three-dimensional coarse grid model of Spencer Gulf with zero wind–stress. The three-dimensional model was found to reproduce the depth-averaged characteristics of the Gulf faithfully (Bills,

pp. 247 and 253) These were, in turn, found to be strongly associated with physical features of the Gulf coastline and/or bathymetry (Bills, pp. 195–196 and 198–199) In Sections 7.4.4 and 10.4.1 depth-dependent currents predicted by the three-dimensional fine grid model of Spencer Gulf with variable wind–stress are discussed. In Section 10.1.1 currents predicted using the coarse grid model with both zero and constant wind–stress, and in Section 10.1.2 those using the fine grid model with both zero and variable wind–stress are discussed. Residuals calculated for the depth-dependent predictions of the three-dimensional coarse grid model with zero wind–stress (Bills, pp. 266 and 271–272) are in general agreement with those presented in this thesis for zero wind–stress. The effect of wind–stress itself on current residuals is discussed in Section 10.1.

6.7.3 Discussion

In Bills (1991) further details concerning depth-dependent currents predicted by the three-dimensional coarse grid Spencer Gulf model were also discussed.

Horizontal velocity vector snapshot sequences for the central Gulf region over neap and spring events were presented and discussed (Bills, pp. 259 and 266–270). Although, for reasons of brevity, they are not presented in this thesis, similar sequences have also been produced for the fine grid model, using animated computer graphics (Doty 1992).

Depth-dependent ellipse characteristics for the four major constituents were also presented for the seven stations at which current data were available (see Table 3.2). These were discussed in great detail, and comparisons with both observations and predictions by the depth-averaged model were made (see Bills, pp. 266 and 273–287). Vertical profile sequences of all three velocity components at two of these stations, during the same neap and spring periods of the vector sequences, were also presented and discussed in some detail (Bills, pp. 287–290).

In this thesis, such detailed analyses of current predictions are not carried out. However, it is anticipated that increased spatial resolution, such as that of the fine grid model over the coarse grid model, will result in greater agreement between predicted and observed depth-dependent ellipse characteristics at tidal current stations in the Spencer Gulf region. This was, in fact, discussed by Bills (1991). The predictions of the tidal models presented in this thesis are considered to be at least as valid as those presented in Bills (1991), as a result of the points made in this section, and the qualitative comparisons discussed in the sections alluded to above.

6.8 Summary

In this chapter, a fine grid tidal model of the Spencer Gulf region was developed and calibrated. Input to this model, in terms of physically measured data as well as experimentally determined parameters, was defined. The tidal model discussed in this chapter forms a basis of, and provides input to the dispersion model discussed in the following chapters.

Chapter 7

The Larval Dispersion Model

Dispersal still ranks among the most poorly documented and imperfectly understood ecological processes in the marine environment (Oliver et al. 1992, p. 873). Direct tracking has generally not been feasible, and biologists have resorted to repeated sampling at discrete locations in the hope of building up a synoptic view of larval concentrations through time. These sampling exercises are a logistic nightmare, and may still result in coarse and inadequate spatial or temporal resolution (Oliver et al. 1992, p. 873).

According to John (1984), for accurate assessment of the drift of marine larvae, as many of the following requirements as possible should be satisfied or be investigated: 1) the spawning area(s) and season(s) of the species considered are known; 2) all planktonic stages are identifiable with certainty to the necessary taxonomic level; 3) the duration of the planktonic phase is known; 4) regional abundance, limits of occurrence and regional length composition of each planktonic stage are known; 5) the short-scale vertical distributions of all stages and in all regions and seasons involved are known; 6*a*) current velocity is measured *in situ* over the entire period, depth range, and area involved; or 6*b*) it is known that the stability of the hydrographic system allows the applicability of data other than *in situ* current measurements. Of course satisfaction of the conditions in this list demands cooperation between physical and biological oceanographers as well as high efforts by gear, ship, and manpower employed (John 1984, p. 54).

The alternative to *in situ* current measurements is accurate numerical modelling of regional hydrodynamics. There has, however, been little attempt within the physical oceanographic literature to place in perspective the relative importance of the distinct processes to understand the impact that the dynamics of water motion will have on larval dispersal and other biological processes (Dight et al. 1990a, p. 116).

In this chapter, these distinct processes are discussed in detail, and the basic framework required of a numerical model of larval dispersion is developed. This development considers formulations of existing analytical and semi-analytical dispersion models. It also considers aspects of prawn larvae biology in general, and *Penaeus latisulcatus* in Spencer Gulf in particular, as discussed in Chapter 2. Considered too are specifics concerning the physical hydrodynamics of the Gulf region and the diffusion, advection, and mortality of *P. latisulcatus* therein. Results presented in Section 7.4.4 have appeared in Nixon and Noye (1996b).

7.1 Larval Dispersion Modelling

The advection–diffusion–mortality (ADM) equation, generally used to model the depth-averaged transport of a passive particle in a turbulent fluid (Holly and Usseglio-Polatera 1984; Power 1984; Wroblewski and Hofmann 1989; Carreras and Menéndez 1990) is given by

$$\frac{\partial}{\partial t}(HC) + \frac{\partial}{\partial x}(HUC) + \frac{\partial}{\partial y}(HVC) - \frac{\partial}{\partial x}\left(K_{xx}\frac{\partial}{\partial x}(HC)\right) - \frac{\partial}{\partial x}\left(K_{xy}\frac{\partial}{\partial y}(HC)\right) - \frac{\partial}{\partial y}\left(K_{yx}\frac{\partial}{\partial x}(HC)\right) - \frac{\partial}{\partial y}\left(K_{yy}\frac{\partial}{\partial y}(HC)\right) + MHC = 0 \quad (7.1.1)$$

in which $H(x,y,t)$ is total water depth, determined by (3.1.12); $U(x,y,t)$ and $V(x,y,t)$ are depth-averaged water velocities in the x and y directions, respectively; $C(x,y,t)$ is depth-averaged concentration of larvae per unit volume; $K_{xx}(x,y,t)$, $K_{xy}(x,y,t)$, $K_{yx}(x,y,t)$, and $K_{yy}(x,y,t)$ are depth-averaged components of the diffusion tensor $\boldsymbol{K}$; $M(x,y,t)$ is a parameter specifying depth-averaged larval loss through mortality, per unit time; and all other variables have previously been defined.

The first term in (7.1.1) represents rate of change of depth-averaged larval flux. The second and third terms represent larval advection in depth-averaged currents. The eighth term represents depth-averaged larval mortality. The remaining terms represent larval diffusion in depth-averaged turbulent fluid motions.

Assumptions made to simplify this equation, in order to obtain a mathematically, numerically, and computationally tractable solution with reasonable accuracy and within a reasonable time, are discussed in the following sections. The definition of what is "reasonable" in the context of attaining this solution will itself become apparent from these discussions.

According to Hill (1991a), the numerical simulations of the sort discussed in Chapter 9 are the best way to tackle the prediction of larval dispersal in particular instances (when resources are available) because they can account for realistic coastal geometry and bottom topography, as well as temporal and spatial variations in the advection and turbulence fields. The analytical models described in Section 7.2, in contrast, are intended for application to cases where such an approach may not be practicable. In such circumstances idealisation of the real situation is necessary for application of the solutions to obtain first order answers. Furthermore, by stripping the dispersal problem down to the bare minimum, the simple analytical solutions can be used to investigate the underlying principles of how dispersal influences population dynamics.

7.2 Analytical Dispersion Models

In this section, overviews of existing analytical and semi-analytical models of larvae dispersion and sub-processes thereof, are given. These are centred around ADM models. The respective models investigated the solution of the one-dimensional (1D) and two-dimensional (2D) partial differential equations (PDEs) governing these processes, using a variety of initial condition (IC), boundary condition (BC), and current regime formulations.

7.2.1 Jackson and Strathmann

In Jackson and Strathmann (1981) a model of larval dispersion of coastal benthic invertebrates was proposed, whereby: eddy mixing spread larvae in the onshore-offshore direction during the period before competence to settle and continued to take larvae both onshore and offshore after they were competent to settle; and predators killed larvae during both precompetent and competent periods.

A 1D constant coefficient diffusion–mortality equation was solved over a semi-infinite spatial domain with spatial BCs corresponding to zero value at the infinite boundary (representing no larvae far down stream) and zero gradient at the zero boundary (representing no larvae diffusing up stream). Larval mortality from offshore mixing was investigated as a link between precompetent and competent periods of settlement. The limitations in this model are that it is 1D with no second horizontal or vertical component, the diffusion coefficient must incorporate advective processes, and the down stream BC is difficult to implement in real-world models.

Distribution of larval stages of several species, as determined by field measurements, were found to be consistent with the model. The model correctly predicted (1) increased competent period with increased precompetent period in comparisons among species, and (2) a competent period greater than or equal to the precompetent period. The model also predicted a decrease in the ratio of competent to precompetent period as the precompetent period increases, which was not apparent in the available data. Some observed competent periods were also longer than those predicted by the model.

7.2.2 Hill

In the first half of the 1990s a series of papers appeared concerning ADM models approximating pelagic larval dispersal. From models encapsulating initially simple forms of the processes involved, considerable complexity was gradually introduced, numerical experiments were carried out, and conclusions were drawn.

Hill (1990)

In Hill (1990) a simple ADM model was used to examine the likely losses of larvae from a *Nephrops norvegicus* system due to pelagic dispersal. The model featured 1D constant advection, 2D isotropic diffusion, and constant mortality. An ADM PDE was solved in a bounded 2D physical domain of characteristic length dimensions, with a IC consisting of an instantaneous point source for spawned larvae. The IC was represented by the Dirac-delta function, and a solution consisting of Gaussian exponentials and integral error functions was derived.

The model was 2D in space and thus contained no information about vertical variations, hence the concentrations were regarded as depth-averaged. Neither did the model include vertical structure of the current and turbulence fields, which were also regarded as depth-mean values. The model assumed that larvae had no capacity for sustained independent horizontal movement (and were thus truly planktonic). If swimming events were directionally random (in response to food particles, say) this motion would have effectively contributed to the horizontal diffusion term. If, on the other hand, large swimming speeds were both sustained in time and constant in direction, treatment of larvae as passive tracers would not have been valid. The model was, however, concerned with dispersal on time scales much longer than a tidal cycle (i.e. 12 h). The main long-term effect of the tide was through its contribution to horizontal diffusion, which was thus subsumed into the value given to the horizontal eddy diffusion coefficient. Similarly, long-term residual transport associated with tidally rectified flow was considered to be incorporated into the value given to the horizontal advective velocity. Only the gross effect of horizontal dispersal was of interest and the precise mechanisms that brought this about, such as those discussed above, were not explicitly considered.

Systematic alteration of the model parameters investigated the relative importance of same to the number of larvae over the considered domain, relative to those in the initial release. Horizontal diffusion was found to increase retention by allowing some material to spread back towards the bounded domain against the prevailing current.

Hill (1991a)

In Hill (1991a) solutions of the 2D ADM PDE were presented which enabled larval losses between well defined release and recruitment sites to be quantified. The model of Hill (1990) was generalised to include 2D constant advection and 2D constant diffusion, and three types of ICs representing instantaneous larval release, namely: (1) point source (Dirac-delta function) in an unbounded region; (2) rectangular source (Gaussian function) in an unbounded region; and (3) coastally parallel source (Gaussian function) in a bounded region, and analytic solutions of a similar form were obtained.

The basic model components were a spatially defined site from which larvae were released and a second well-defined site at which larvae must be located at the end of the planktonic period of given duration. Between these sites, advection–diffusion processes were parameterised in the simplest possible (2D) form, thus permitting relatively simple and general analytical solutions of the governing equation. Aside from the increased range of idealised dispersal phenomena able to be represented as a result of the model generalisations made, the models of Hill (1991a) suffer from essentially the same limitations as those of Hill (1990). These limitations deny a detailed examination of larval concentration fields in response to particular spatially varying circulation structures such as closed gyres and eddies or spatially varying mean flow fields. Solutions obtained by the extended models confirmed, however, that dispersal can make a

significant contribution to pelagic losses and that survival is highly sensitive to the level of mean advection.

Hill (1991c)

In Hill (1991c) the principles which govern horizontal motion induced by vertical migration in oscillatory, sheared (tidal) currents were discussed.

First, in order to gain an appreciation of the kind of horizontal motion induced by migration in sheared flows, the simplest possible model incorporating both shear and migration was presented. This model employed the simplest possible velocity shear (linear) and sinusoidal migration, and had the advantage of being easy to understand both mathematically and physically. The solution for the horizontal displacement of an organism had a number of important properties. Vertically migrating larvae were displaced from their initial position by a mean (time-independent) distance. Superimposed upon this was an oscillating (time-dependent) displacement with amplitude relative to the mean displacement, provided that the vertical migration and tidal frequencies were not exactly equal. Thus it was shown that an organism executing vertical migration in an oscillatory shear flow could not move indefinitely away from its starting point when the migration frequency was different from the tidal frequency. Instead, the horizontal position of a migrating organism was constrained within strict limits. Equal migration and tidal frequencies no longer constrained a vertically migrating organism to a limited range of horizontal motion but, given a large enough duration, the organism's displacement from its initial position was potentially unlimited. The implications of the simple vertical migration model were clear. For linear shear, only vertical migrations with periods that exactly match the tidal period are strictly effective in inducing long-term transport of organisms in a purely oscillatory (tidal) flow. When migration and tidal periods differ widely the maximum displacement of an organism from its initial position will be severely constrained (to no more than a few kilometres). When migration and tidal periods are close, however, larval excursions may be constrained within rather wider limits (up to a hundred kilometres or so).

Migrations in nature, it was argued, are probably more like "square waves" with rapid ascent and descent of zooplankton occurring after long intervening periods at relatively fixed levels. There was little reason, however, to expect that this migration be symmetric. Indeed, if diel migration is basically controlled by light cues then it is reasonable to expect, in latitudes where day and night have unequal length, that time spent by organisms at depth and near the surface will also be unequal.

Thus a second case, one of asymmetric vertical migration, was considered. With such complicated migration patterns simple analytical solutions were not obtainable, and so solutions were calculated by numerical integration. Experimental results clearly indicated that the precise shape of the migration curve was immaterial to the ultimately bounded nature of the horizontal displacement.

Considered third was a simple modification in which the linear tidal velocity profile was represented by a power law. The semi-analytic solution required integration which produced an infinite series of terms. Unlike the linear shear case, infinite displacements (or resonant interactions between tide and migration) could occur at migration periods which were exact multiples of the tidal period. Because virtually any shape of current profile could be approximated by a polynomial curve, the power law velocity structure provided the basic physical insight which could be applied to all nonlinear profiles, namely that displacements are bounded except for migration at periods which are multiples of the tidal period.

All tidal currents so far investigated had been rectilinear. Commonly, however, continental shelf tides are rotary because of the influence of the Earth's rotation upon water motion. A physical model was sought, therefore, which included this effect, compromising between a model reproducing rotation and vertical current structure in reasonable agreement with observations and one of sufficient simplicity to be easily implemented. A suitable candidate was the tidal current structure model of Prandle (1982) which solved the linearised equations of motion,

included a Coriolis parameter and (constant) vertical eddy viscosity, and incorporated boundary conditions of zero (wind) stress at the sea–surface and a linearised form of (quadratic) friction at the sea–bed. In the applications of the model presented, a logarithmic boundary layer was coupled to the Prandle (1982) model in the bottom metre, in order to represent a no slip boundary condition at the sea–bed. This approach was justified on the grounds that, for typical roughness length scales, most of the velocity change in a logarithmic profile actually takes place within a metre or so of the bed. It was noted that the need to splice a sharp velocity gradient onto the model near the bed could have been avoided, but only at the expense of using a more sophisticated model from the outset. The path of an individual larva was found to be fairly complicated, but once again remained bounded (within about 200 km) of the release position.

Hill (1991b)

In Hill (1991b) a mechanism was proposed by which net horizontal transport could be induced in an organism migrating vertically in a purely oscillatory, vertically sheared tidal current. The only important criteria concerning the velocity profile were that velocity should decrease with depth (sheared profile) and that the shear (rate of change of velocity with depth) should also change with depth. If vertical migration was not purely sinusoidal but of a "square wave" form, for example, then even the latter criterion could be relaxed. These conditions are usually met in tidal currents where shear is relatively weak over much of the water column, but there is a region of increased shear near the bed. The key point was that the strongest shear was in the bottom layer, so that the difference between amplitudes of mid-water currents and near-bottom currents was greater than that between those of mid-water currents and surface currents. Thus, over a 24 h vertical migration cycle, the sum of near-surface and near-bottom positive currents was insufficient to overcome the combined mid-water negative current experienced over one cycle. Organisms thus experienced net negative displacement over one migration period.

The principal solar, semi-diurnal, tidal constituent (S_2) has a period of exactly 12 h. Diel (24 h) vertical migration is thus an exact multiple of the S_2 period and, it was argued, uni-directional transport could be induced by migration-tide interaction. Because S_2 is a major tidal constituent and diel vertical migration very common, it was anticipated that the predicted interaction is a widespread phenomenon. The direction of horizontal transport induced by S_2-migration resonance was shown to be strictly controlled by the phase of the S_2 constituent. The hypothesis was proposed, therefore, that geographical variation in the phase of S_2 tidal currents is a key physical parameter controlling the location of sites (such as spawning grounds) which favour a particular transport vector (including retention) for marine planktonic organisms that undergo diel vertical migration.

Hill (1995)

In Hill (1995) it was emphasised that diel vertical migration could, theoretically, interact with the sun-generated part of the semi-diurnal tide to produce net horizontal transport, the direction of which would be controlled by the phase of the S_2 tidal currents. It was further argued that the spatial distribution of phase implies that regions of horizontal convergence and divergence would result from diel migration, and that diel migration in diurnal-period tides would cause the preferred direction of transport to reverse at six-monthly intervals.

In the experiments presented, vertical migration took the form of a step function or a "square wave", and the interaction of this with the four major tidal constituents (O_1, K_1, M_2, and S_2) was, as in previous papers, considered. The effective velocity of migration-induced horizontal transport in an S_2 tidal current regime was shown to be proportional to $\cos\{\phi\}$, where ϕ is the phase of the S_2 current with respect to the peak of the migration cycle. When ϕ is between 90° and 270° migration-induced transport was shown to take place in one direction, whilst for all other values of tidal phase the transport is in the opposite direction. Phase contours of $\phi = 90°$ or $\phi = 270°$ were thus argued to be regions either of horizontal transport convergence or

divergence. It was noted that, for a given location in such a current regime, ϕ does not change with time and thus that the spatial pattern of S_2 phase could provide the key to how diel migratory organisms in a predominantly S_2 tide move. It was concluded that the total transport-producing effect could be obtained by superposition of the migration-induced transport for each constituent, thus providing a powerful and straightforward conceptual approach to this problem, and that this would be far less confusing than attempting to imagine the transport resulting from interaction with the complete tidal signal.

7.2.3 Richards, Possingham, and Noye

Recently, models have been constructed by Richards et al. in order to extend the range of processes represented in the models of Hill, with particular attention to larval release regimes in tidal currents, and vertical migration responses to ambient light variations.

Richards, Possingham, and Noye (1995)

Richards et al. (1995) presented a mathematical model of the dispersal of larvae into a region consisting of a straight coastline and a current dominated by tidal effects. Spawning was near the coast from a well-defined site and the larvae had a relatively short pelagic lifetime. Using a semi-analytic solution to a model based on the 2D ADM equation, the effects of various processes on dispersal were examined. In particular the relative importance of currents, turbulence, pelagic lifetime, and the duration and rate of spawning were assessed. The solutions were termed *semi-analytic* as they were expressed in the form of an integral equation which itself could not be solved analytically, but could be accurately approximated using numerical integration techniques.

The solutions to the model, the spatially varying distribution and abundance of larvae within the larval cloud, were seen to encapsulate the sort of information that field experiments have currently been unable to provide. Considered was a specific current regime—typical of those found in shallow gulfs and large estuaries—in which it was assumed that the tides created a current that oscillated in a direction parallel to the coast over a 12 h period. Also considered was the case of a steady along-shore drift acting in conjunction with the tidal oscillation. Even with these simple currents, surprisingly complex patterns of larval dispersal arose, and this was seen to have important implications for the analysis of field data on larval abundance. The size and shape of the larval cloud was found to be influenced by eddies, in that the larger and stronger the eddies were, the greater the mixing action within the cloud and subsequently the larger the cloud became. The density of larvae within the cloud was also dependent on the current strength at the time of release, in that larvae released into a fast-moving current stream were spread more quickly over a greater area than if the larvae were released into slack water. The timing of larval release with the phase of the tide was important in determining the length of the cloud, especially when the duration of release was of the order of less than a tidal period. For example, release over a short period of time into a fast moving current (i.e. a "racing" tide) produced larval clouds which were larger than if release was during slack water (i.e. a "turning" tide).

The model showed that what may at first glance appear to be chaotic fluctuations in larvae numbers is not necessarily the result of complex currents or complicated larval behaviour.

Richards, Possingham, and Noye (1996)

Richards et al. (1996) developed models representing the way in which light is most likely to be used by zooplankton as a cue for vertical movement. Two behavioural mechanisms, preferred light intensity (PLI) and relative rate of change (RRC), were considered. Animals were assumed to either move towards a PLI or alternatively invoke a swimming reaction in response to the RRC in light intensity. A mathematical model was presented which included these two types of behaviour and produced vertical distributions of zooplankton that varied in space and

time. The model showed that for both mechanisms vertical movement of the population was likely to occur quickly around sunrise and sunset.

For the PLI mechanism it was predicted that the mean midday depth for larvae was largely dependent on the strength of the surface light and clarity of the water column, in that the clearer the water, the deeper the midday depth of zooplankton. With the RRC mechanism a peak in zooplankton density was predicted at the sea–surface shortly after sunset, and the mean daytime depth was dependent on the swimming speeds invoked by the strength of the light stimulus. The two types of distribution generated by the model were shown to compare with field measurements presented in the literature, indicating that both mechanisms alone or in combination may occur in nature.

The underlying zooplankton distribution model was based on a 1D advection–diffusion PDE governing dispersion in the water column of constant depth, ignoring changes in biomass which would result from processes such as mortality, ingestion, excretion, and moulting. The underlying light variation model was based on a representation of the change in light intensity with respect to both the vertical and temporal coordinates. The light intensity variation throughout the water column for two ("clear" and "murky") water cases were depicted by contours of constant light intensity, referred to as *isolumes*.

Assuming the PLI mechanism, the maximum vertical migration speed was found to occur over a short period during sunset and sunrise. Once the preferred isolume was found by a larva, a position on it was maintained for a few hours before sunset. After this time zooplankton were not observed on the isolume as it then moved too quickly to follow, and also as sunset approached light intensity dropped along with the motivation to swim. This resulted in many individuals not reaching the surface during the night. There was found to be little motivation for movement during the night time hours regardless of where animals were located in the water column. If vertical eddy diffusion effects are large, the night time spread of zooplankton would thus be much greater than the daylight distribution, when individuals are battling to maintain themselves within a much smaller region which they consider to be near optimal.

Assuming the RRC mechanism it was found that, as determined by experimental studies (Forward Jr. 1988; Ringelberg 1995), the functional representations showed distinct peaks at sunrise and sunset. The most striking feature of the calculated vertical distribution was the peak in biomass at the sea–surface shortly after sunset. A peak in biomass of lower density was also present at the sea–floor shortly after sunrise. These peaks result from larvae swimming towards and accumulating at the impenetrable boundaries of the water column. The surface peak in biomass was more concentrated as zooplankton were represented so as to swim faster up than down, thus reducing the effect of the diffusion modelled near that boundary.

7.2.4 Summary

It is evident that any detailed model of larval dispersion must accurately represent both biological and physical aspects of the advection–diffusion–mortality process. The interaction of these can lead to significant complexity in results predicted by models of comparative simplicity. Individual advection, diffusion, mortality, and other biological and physical processes must, therefore, each be represented as accurately as possible, using appropriate sub-model formulations. These are detailed in the following sections.

7.3 Vertical Migration

The choice of vertical migration model can have a considerable effect on the simulated advection of larvae (Bartsch et al. 1989, p. 635). One of the most difficult parameters to define or provide a functional form for is the rate of vertical diffusivity. Vertical diffusion of a population through the water column is due to vertical eddy turbulence and variability in individual behaviour. This second process is often ignored in many advection–diffusion type models of vertical migration. It is unlikely that all individuals will respond in exactly the same way to stimuli and have the

same swimming abilities. However, in the absence of detailed data to support the contrary, as discussed in Section 2.4, this will be assumed by the model developed in this thesis.

Points raised in Sections 2.4 and 7.2.3 help to define an appropriate formulation for larval vertical migration. The model developed in this thesis incorporates larval movement in the water column by using tidal model currents determined near the sea–surface (5% of total depth below it) at night (19:30–5:00) and near the sea–bed (5% of total depth above it) during the day (5:00–19:30). These time periods are loosely termed *night* and *day* and the corresponding depth–levels are loosely termed *sea–surface* and *sea–bed* in this thesis. The larvae are assumed to rapidly migrate between these levels, at these times.

Currents of a certain strength in a certain direction at the sea–bed and stronger currents in an opposite direction at the sea–surface can result in a net movement of larvae in the direction of the surface currents, even though the larvae themselves may have almost no direct means of horizontal migration. Because surface currents are generally much larger than bottom currents, most of the transport of the larvae occurs at night. If the phase of the tide is such that the oscillating tidal current is directed toward the shore at night, larvae are more likely to reach coastal nurseries.

Preliminary larval dispersion studies have determined that a purely depth-averaged approach is unsatisfactory (I'Anson 1989; Wong 1990). The three-dimensional current structure provided by a 3D tidal model is clearly required, because the larvae are located at different levels at different times and may be subjected to different lateral forces at these levels. The vertical current velocities at these levels, however, are not required because of the relative magnitude of these compared to that of the vertically migrating larval cloud itself. In fact, horizontal advection in Spencer Gulf is orders of magnitude greater than that in the vertical (Bills 1991, p. 288) and horizontal eddy diffusion is approximately 30 times that in the vertical (Noye 1984b, p. 211). The so called "*layered two-dimensional*" formulation defined above is thus considered to suffice.

7.4 Larval Advection

Advection of *Penaeus latisulcatus* larvae in Spencer Gulf is determined in this thesis by the currents computed using the coarse and fine resolution tidal models of Section 3.4 and Chapter 6, respectively. It is because of the prohibitively long processing time required for the tidal computations that the use of a supercomputer was sought. Any meaningful larval dispersion study will involve simulations spanning the dual spawning seasons of the prawns (mid-December and late-January/early-February each season) observed in Spencer Gulf, as discussed in Section 2.1.2. The uncertainties concerning the observed period in the larval phase imply a baseline simulation of 6–7 mo duration, as discussed in Section 2.2.2. The fine resolution tidal model was used to simulate, on a CRAY supercomputer, currents quantifying advection processes for the period from October 1 to March 31, inclusive, of the years 1972/73–1975/76 and 1984/85–1987/88, by request of SARDI research officers. The corresponding dispersion model will be used to simulate larval advection and diffusion, on a SPARC workstation, for sub-periods—of duration equivalent to the larval phase—within the overall tidal simulation period.

The two horizontal velocity components predicted by the tidal model within each computational grid element are calculated at u and v grid–points which are staggered in the x and y directions, as depicted by the symbols "$\rightarrow$" and "$\uparrow$", respectively, in Figures 3.3. The model constructs an average for each component, using the values from elements to the left and right of (for the x velocity component), and from above and below (for the y velocity component), the ζ grid–point of each element. For example, consider tidal model output of predictions for computational grid element i of Figure 3.5. The value of sea–surface elevation above MSL within this element, calculated at the ζ grid–point depicted by the "+" symbol in Figures 3.3 and 3.5, is output without modification. Velocity in the x direction at this ζ grid–point is determined by an average of the two values calculated at u grid–points of elements to the left (i–1) and to

the right (i). Similarly, velocity in the y direction is determined by an average of the two values calculated at v grid–points of the elements above (i_1) and below (i). The model also accounts for instances in which such averages are not possible, due to the presence of nearby closed or open boundaries, by means of the grid element classification scheme discussed in Section 3.2.4.

It is these average component values which are output by the tidal model, in order to define a velocity vector at each element. This is in turn able to be used as input to a dispersion model, in order to determine the effects of advection within each element. The velocity components input to, and the larval concentrations calculated by, the dispersion model represent values within each computational element at a centrally located grid–point. The tidal model has three grid–points per element staggered in a grid with spacings defined as being $2\Delta x$ and $2\Delta y$ in the x and y directions, respectively. The dispersion model, in contrast, has one grid–point per element in a grid with spacings defined as being Δx and Δy apart. For example, the fine grid Spencer Gulf tidal model has a horizontal grid–spacing of $2\Delta x = 1905\,\mathrm{m}$ separating each elevation grid–point while, possibly somewhat paradoxically, the corresponding fine grid Spencer Gulf dispersion model has a horizontal grid–spacing of $\Delta x = 1905\,\mathrm{m}$ separating each concentration grid–point. These facts should be kept in mind in the context of the discussions of the development of the dispersion model in the following chapters.

In this section, tidal current simulations are computed for the 29 d following an instantaneous spawning event at 21:30 on 1 February 1988, representing the January/February peak spawning of that South Australian summer. Currents are computed by the tidal model described in Chapter 6 with a non-zero wind–stress formulation derived from the BoM wind data available for the Spencer Gulf region over the period of interest, as described in Chapter 4. Results presented in Section 7.4.4 have appeared in Nixon and Noye (1996b).

Tidal oscillations can be resolved and expressed mathematically by harmonic analysis into constituent components corresponding to the principal tide-producing forces of the moon and the sun. The amplitudes and phase lags of each tidal constituent at any location are derived from observations or, as here, from simulations. The uniform rate of change in the tidal phase for each constituent depends upon its period, semi-diurnal constituents having periods of approximately 12 to 12.5 h and the diurnal constituents of 24 to 26 h (Dight et al. 1990a, p. 117).

7.4.1 Tidal Ellipses

Current ellipses provide an effective way of summarising complex time-dependent tidal flows over large spatial scales (Dight et al. 1990a, p. 119). For each constituent, the current vector is resolved conventionally into two perpendicular components, each oscillating at the same frequency. The resultant path traced out by the current vector over a tidal period is an ellipse. The maximum tidal current speed for any given constituent is provided by the magnitude of the semi-major axis; the minimum tidal current is given by the length of the semi-minor axis. Where this is insignificant, the current can be considered as *rectilinear* rather than *rotary*. Tidal currents can be provided either by the analysis of field measurements or as the output of a numerical model.

Each ellipse shows, at the computational element at which it is plotted, the behaviour of the constituent concerned over a complete cycle, the length of which is determined by its frequency, as listed in Table 6.2. At the beginning of the tidal cycle—in this case at 21:30 on 1 February 1988—a vector, without an arrowhead, is drawn indicating the direction and strength of the current after Fourier–decomposition into signals with characteristic frequencies corresponding to those of the major tidal constituents used to force the tidal model. At every increment of $2\pi/20^c$ after the initial vector shaft is drawn, except for the last two such increments, vectors are calculated, with the locus of these endpoints generating an elliptical curve. Because the last two increments are not linked, the direction of rotation for the ellipses can be determined. A small arrowhead at the end of the ellipse is also drawn to aid in this determination. This arrowhead is proportional to the length of the smallest (plotted or not plotted) vector shaft in the set of vectors whose endpoints are the locus of the ellipse itself. It should be noted that, in

the following, ellipses are *not* (usually) plotted for every grid–point, to allow the use of a large vector scale ($\mathrm{m\,s^{-1}}$) without excessive ellipse overlapping.

Tidal ellipses for each of the major tidal constituents O_1, K_1, M_2, and S_2 used to force the tidal model are shown, for both output current depth–levels used by the dispersion model, in Figures 7.1, 7.2, 7.3, and 7.4, respectively.

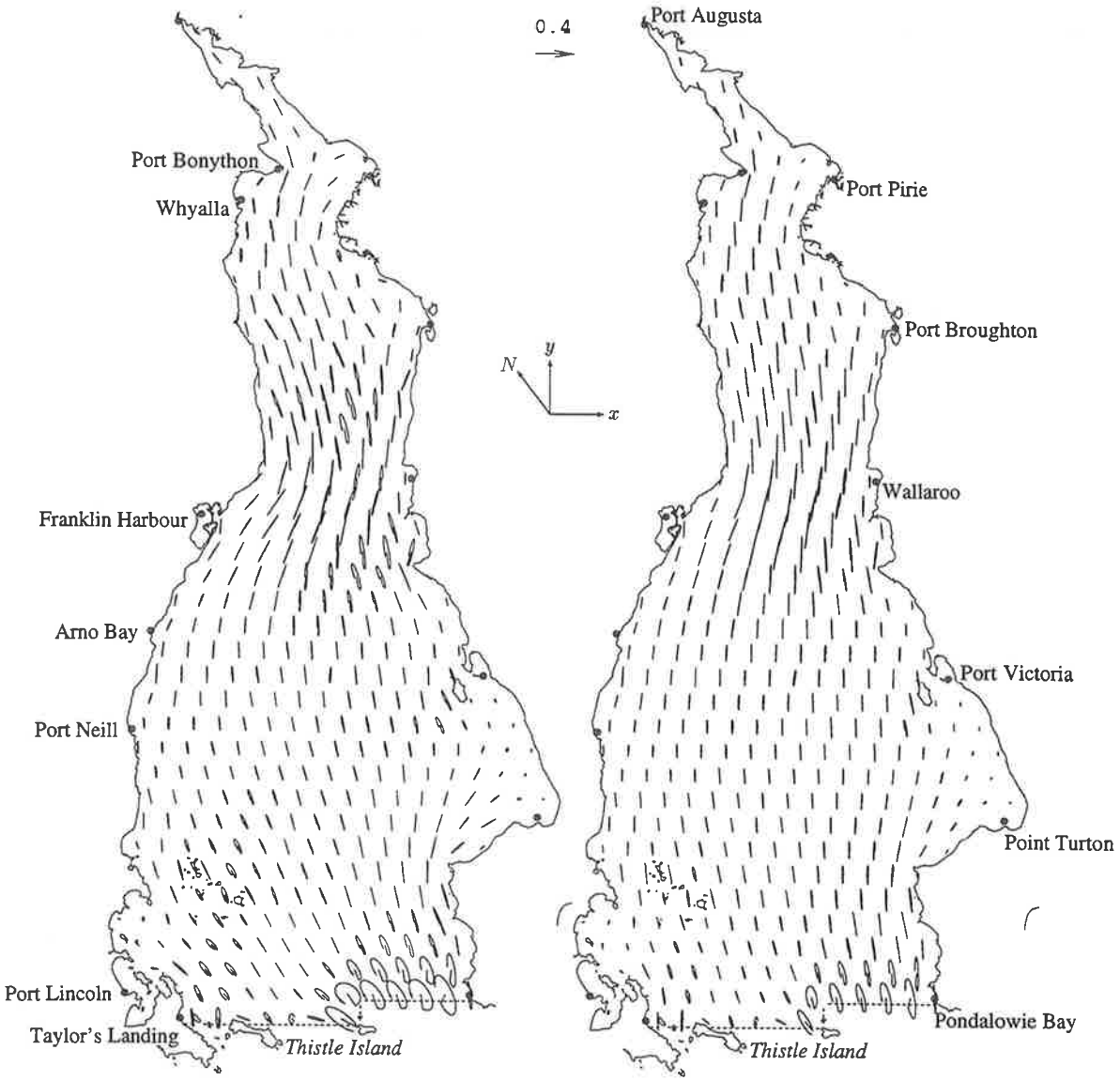

(a) near sea–surface depth–level

(b) near sea–bed depth–level

Figure 7.1: Spencer Gulf depth-dependent tidal ellipses ($\mathrm{m\,s^{-1}}$) for the O_1 tidal constituent for the 29 d period from 21:30 1 February 1988 calculated with wind–stress. Ellipses are plotted for every fourth computational element in both the x and y directions, with small arrowheads indicating vector rotation direction. Tidal stations (roman) and islands (italics) are named.

7.4.2 Residual Currents

Current component time–series are reconstituted from the computed current time–series after Fourier–decomposition into constituent signals with characteristic frequencies corresponding to those of the major tidal constituents used to force the tidal model. Table 6.2 lists these constituents and their characteristic frequencies. Differences between the originally computed components and those reconstituted are averaged over the simulation period and residual cur-

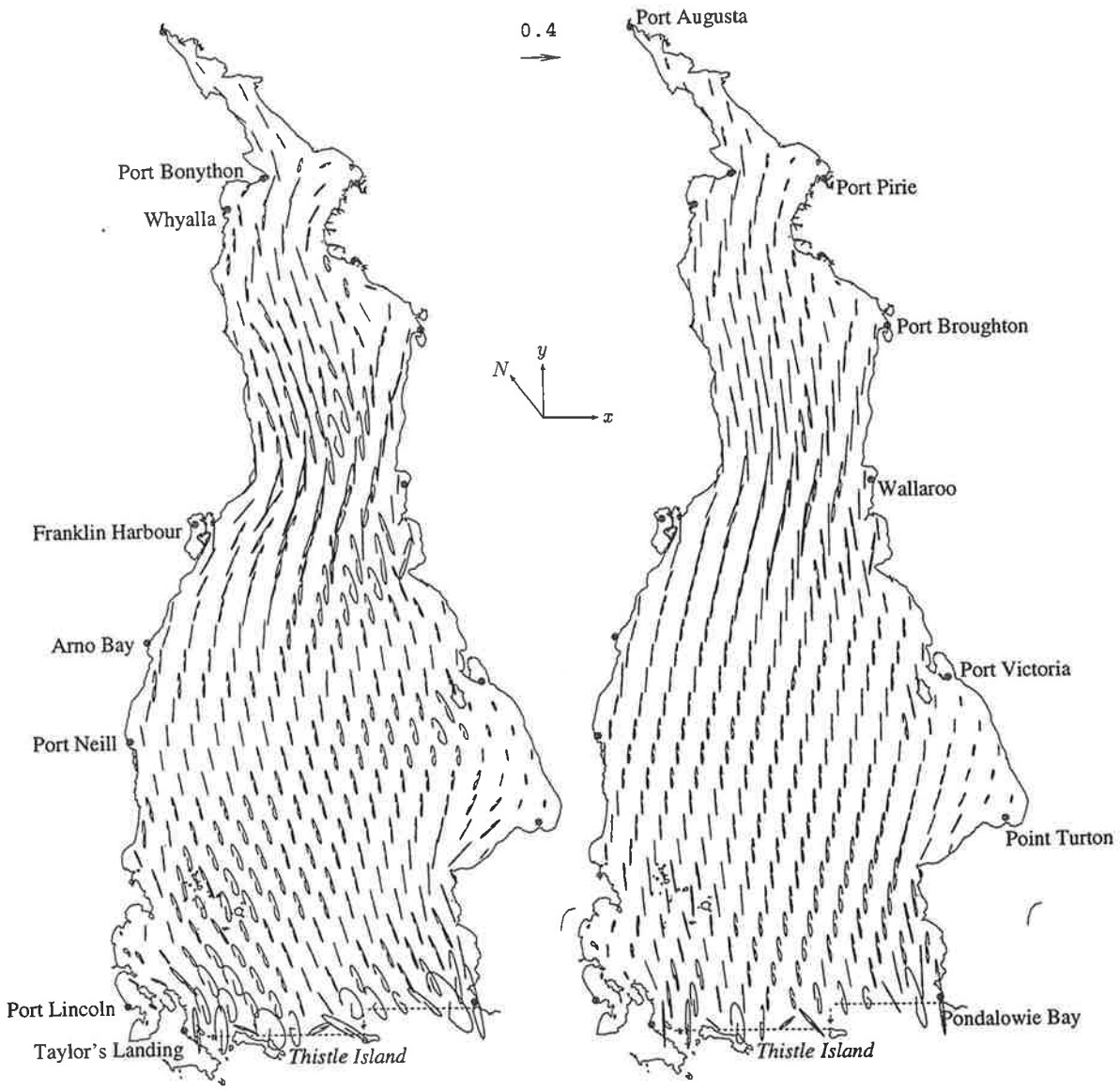

(a) near sea–surface depth–level

(b) near sea–bed depth–level

Figure 7.2: Spencer Gulf depth-dependent tidal ellipses ($\mathrm{m\,s^{-1}}$) for the K_1 tidal constituent for the 29 d period from 21:30 1 February 1988 calculated with wind–stress. Ellipses are plotted for every fourth computational element in both the x and y directions, with small arrowheads indicating vector rotation direction. Tidal stations (roman) and islands (italics) are named.

rents can then be plotted as vector additions of the two components at each computational grid–point. The residual vectors thus represent the nonlinear interactions of the constituents forcing the tidal model, averaged over the period of interest, and hence indicate bulk mean water movements which are non-periodic in relation to the tidal regime.

It should be noted that since other long period constituents are also accounted for in the tidal modelling by means of phase corrections, as listed in Table 6.2, to the specified amplitudes and phases along the open boundary of the modelled region, the residual circulation obtained is dependent on the time period being simulated. This circulation is also dependent on the inclusion or exclusion of wind–stress and, in turn, on the spatial and temporal variation in wind–stress in the latter case.

Residual current vectors for the simulation period are plotted—at every second computational element over the entire Gulf in both the x and y directions—in Figure 7.10. Mid-northern Gulf residuals are also shown in Figure 7.11, where vectors are plotted for every computational

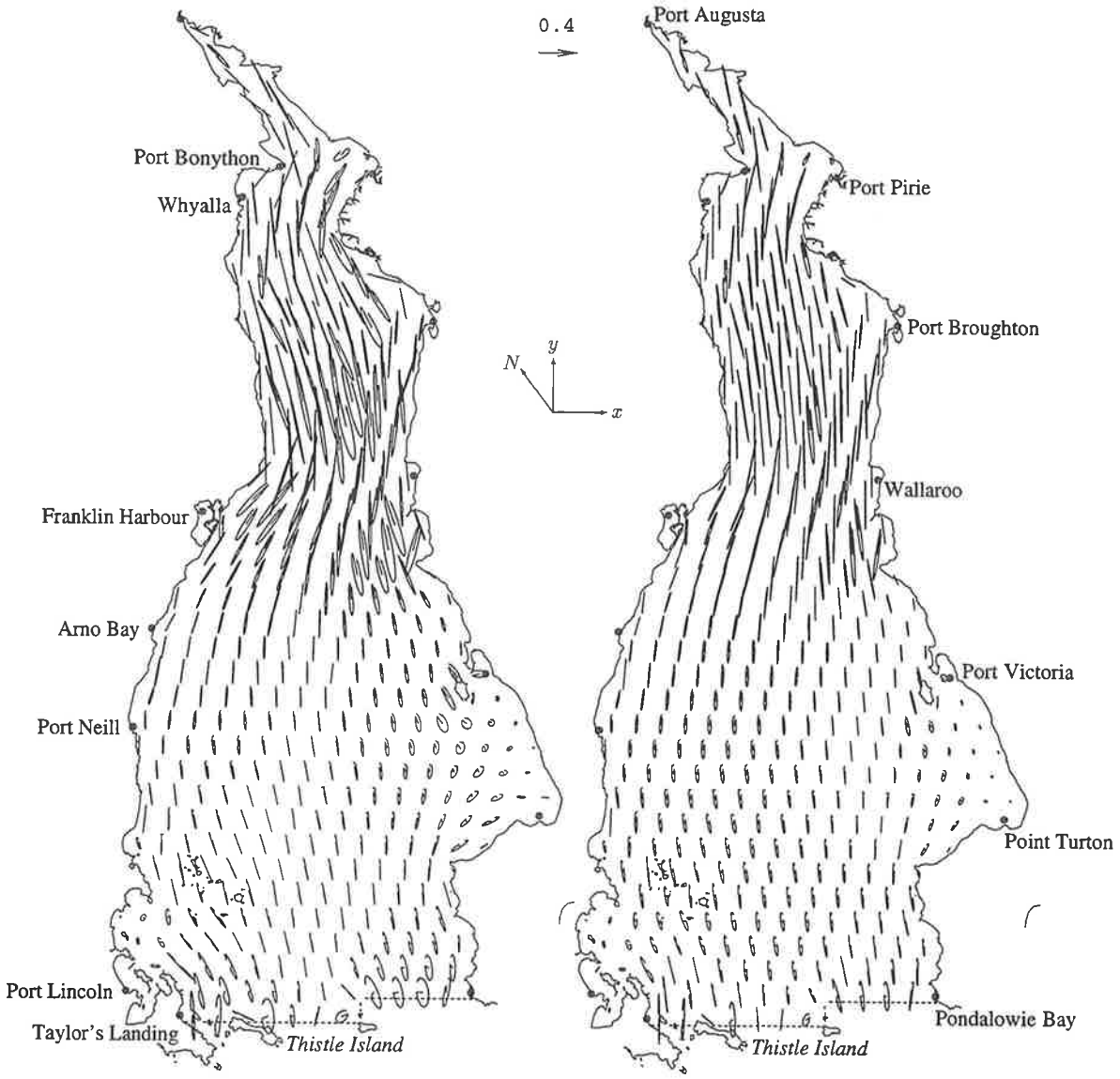

(a) near sea–surface depth–level

(b) near sea–bed depth–level

Figure 7.3: Spencer Gulf depth-dependent tidal ellipses ($m\,s^{-1}$) for the M_2 tidal constituent for the 29 d period from 21:30 1 February 1988 calculated with wind–stress. Ellipses are plotted for every fourth computational element in both the x and y directions, with small arrowheads indicating vector rotation direction. Tidal stations (roman) and islands (italics) are named.

element.

7.4.3 Tidal Ellipses of Spencer Gulf Major Constituents

From Figures 7.1–7.4, the rectilinear nature of the currents in Spencer Gulf is apparent. There are, however, regions where transverse currents result in ellipses which are more rounded, such as in the narrowing part of the Gulf in the region near Wallaroo and again in the lower region near the open boundary. A group of anticlockwise rotating ellipses north of Wallaroo correlates with shallow water (over Middle Bank) while another anticlockwise rotating group to the south-west of Wallaroo correlates with shallow water (over Tiparra Reef). A third group of anticlockwise rotating ellipses due west of Wallaroo correlates with an approximately 25 m deep east-west channel west of Wallaroo, shown in the vicinity of the east-west line of contour points labelled C at the bottom of Figure 7.5, running along the boundary of Tiparra Reef. This ellipse group

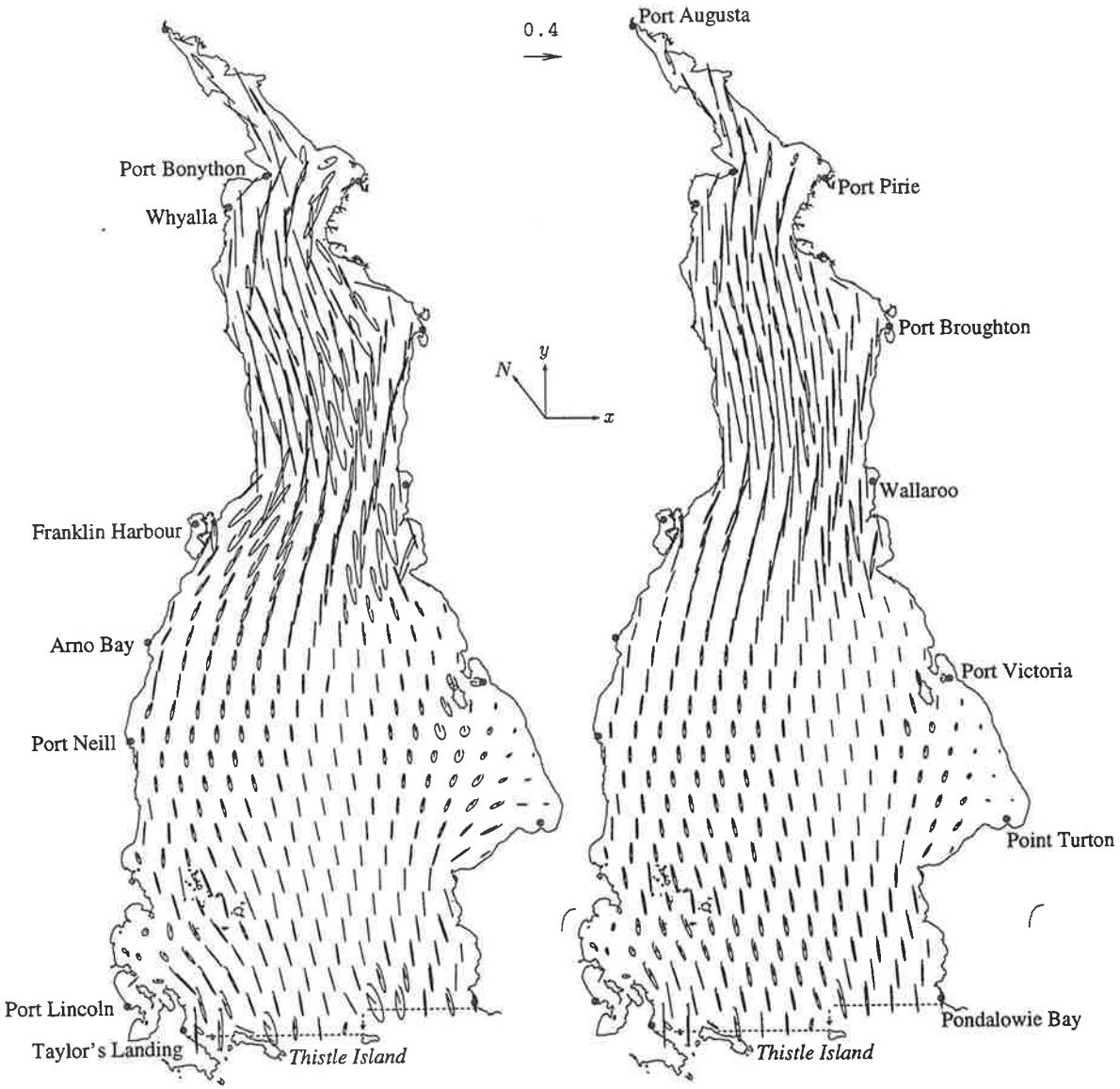

(a) near sea–surface depth–level

(b) near sea–bed depth–level

Figure 7.4: Spencer Gulf depth-dependent tidal ellipses ($m\,s^{-1}$) for the S_2 tidal constituent for the 29 d period from 21:30 1 February 1988 calculated with wind–stress. Ellipses are plotted for every fourth computational element in both the x and y directions, with small arrowheads indicating vector rotation direction. Tidal stations (roman) and islands (italics) are named.

extends diagonally across the Gulf to the western shoreline.

Diurnal Ellipses

Comparing the diurnal ellipses for O_1 (Figure 7.1) and K_1 (Figure 7.2), it is apparent that K_1 current strength is generally about 50% greater than O_1 current strength. Apart from this, both diurnal constituents show similar behaviour everywhere within the Gulf.

The diurnal current is strongest near the open boundary and through the narrowing part of the Gulf near Wallaroo. It is stronger through the middle of the Gulf and weakens close to the coastal boundaries, where the water is shallower, due to frictional dissipation. It is chiefly rectilinear in the large southern Spencer Gulf region and is predominantly rectilinear in the far northern region. Near Wallaroo and the open boundary it shows transverse movement as well as axial movement. These effects are more noticeable in the ellipses associated with the

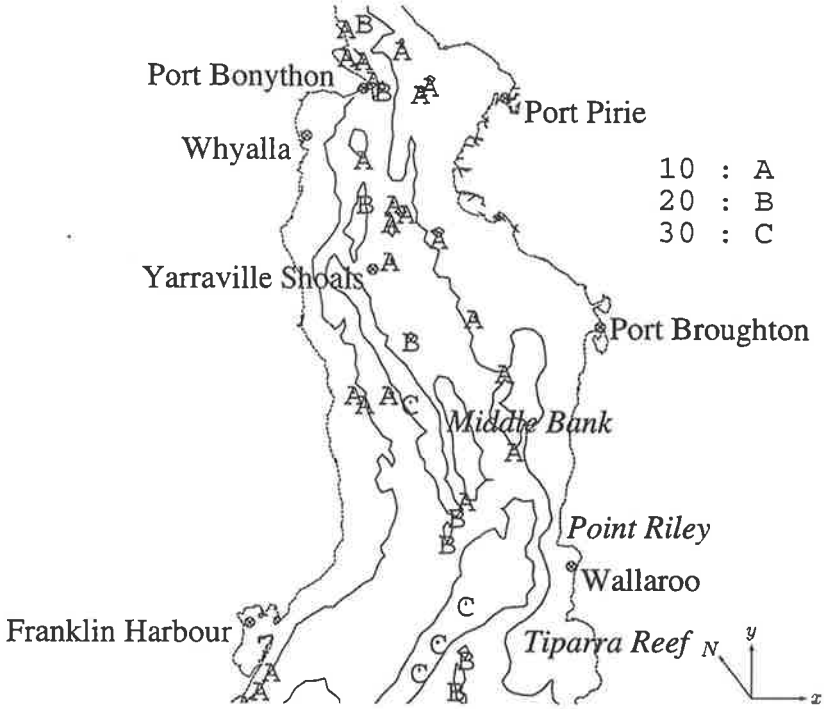

Figure 7.5: Contours of depth (m) below MSL for the narrowing part of mid-northern Spencer Gulf, with tidal stations (roman) and places of interest (italics) named.

near surface current (subfigures (a)) compared to those associated with the near bed current (subfigures (b)).

A noteworthy feature of Figures 7.1–7.2 is a reversal of ellipse rotation near Wallaroo. Approximately south-west of Wallaroo, near Tiparra Reef, the diurnal ellipses are anticlockwise rotating. In fact, over the bulk of the south-eastern lower Spencer Gulf they are anticlockwise or rectilinear, and clockwise in the north-western lower Spencer Gulf. North-west across the Gulf off Wallaroo are clockwise rotating ellipses. These are more noticeable in Figure 7.2 than Figure 7.1, and again in Figure 7.2(a) than Figure 7.2(b), compared to the other figures. This shows that for part of the tidal cycle, the diurnal current flows across the Gulf from the region near Arno Bay toward Wallaroo and vice versa half a cycle later. Off Wallaroo, the ellipses rotate clockwise, while directly opposite Wallaroo the ellipses on the left-hand coast rotate anticlockwise. This effect can be more clearly seen in the enlargements of Figures 7.6–7.7, as can the fact that north of Middle Bank this pattern continues.

It can be deduced that for part of each constituent cycle the diurnal current crosses the Gulf from south-west to north-east (or north-east to south-west) as it passes through the narrowing section near Wallaroo. Accompanying this passage it can be anticipated that an anticlockwise (or clockwise) cell of circulation is set up just north of this flow along the coast opposite Wallaroo, and that a clockwise (or anticlockwise) cell is set up south of it, along the coast adjacent to Wallaroo. Note that these across-Gulf components in the diurnal currents are weak in comparison to the along-Gulf components. This idea will be expanded upon in the discussion of residual tidal eddies in Section 7.4.4.

Figures 7.1–7.4 suggest that K_1 is the strongest of the four major constituents at the open boundary. Not only does it record the largest semi-major axis values, but it also has the largest semi-minor values. These results are in qualitative agreement with observations of along-stream and cross-stream current reported by Steinberg (1983) and those computed by Bills (1991), albeit at lower spatial resolution compared to the results reported here.

In particular, Steinberg notes that across the mouth of Spencer Gulf the

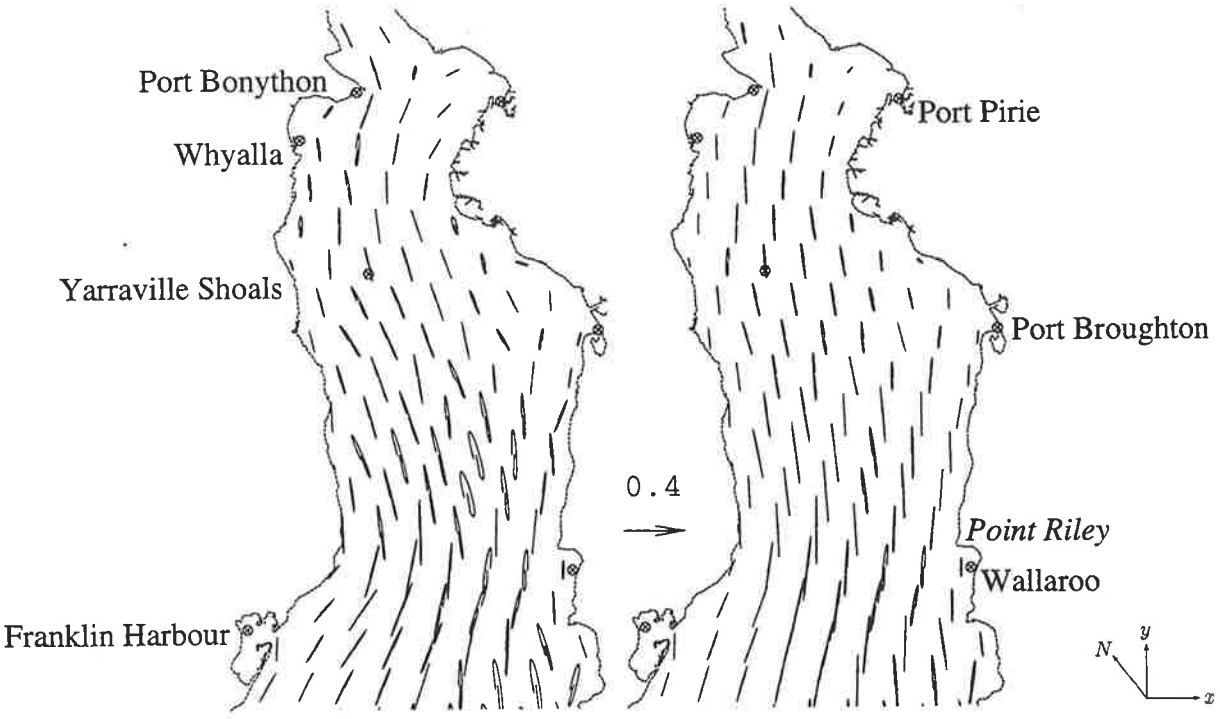

(a) near sea–surface depth–level (b) near sea–bed depth–level

Figure 7.6: Mid-northern Spencer Gulf depth-dependent tidal ellipses ($m\,s^{-1}$) for the O_1 tidal constituent for the 29 d period from 21:30 1 February 1988 calculated with wind–stress. Ellipses are plotted for every fourth computational element in both the x and y directions, with small arrowheads indicating vector rotation direction. Tidal stations (roman) and places of interest (italics) are named.

> major contribution to the cross stream components are from the diurnal constituents (Steinberg 1983, p. 58)

as has been found from both the coarse grid Spencer Gulf model results of Bills (1991) and the fine grid model results presented here.

Semi-Diurnal Ellipses

Comparing Figures 7.3 and 7.4 for the semi-diurnal current constituents, they are of approximately equal strength, though S_2 is slightly stronger over the whole Gulf. They also exhibit similar behaviour everywhere over the Gulf.

The semi-diurnal current is strongest in the northern part of the Gulf, particularly through the narrowing section in the vicinity of Wallaroo. It is noticeably weaker around the shallower coastal edges near Port Lincoln and in the region between Point Turton and Port Victoria.

The semi-diurnal current is generally rectilinear along the axis of southern Spencer Gulf, dividing it into two broad regions of oppositely rotating ellipses. On the western side, the ellipses rotate clockwise. On the eastern side they rotate anticlockwise and some of these, those SW and SSW of Wardang Island (the coastline of which is shown as a closed dashed curve in the figures), near Port Victoria, are nearly circular. There is a repetition in the semi-diurnal ellipses near Wallaroo of the change in rotation noticed in the diurnal ellipses. The clockwise rotating semi-diurnal ellipses along the western Spencer Gulf coastline have a small transverse component at the narrowing part of the Gulf. Figures 7.8–7.9 show that across the Gulf opposite Wallaroo the semi-diurnal current ellipses are either clockwise rotating or rectilinear, and there is almost no transverse component for the ellipses on the central and western side. Above this region, the ellipses are anticlockwise rotating in the central and western regions, and Figure 7.8(a) shows

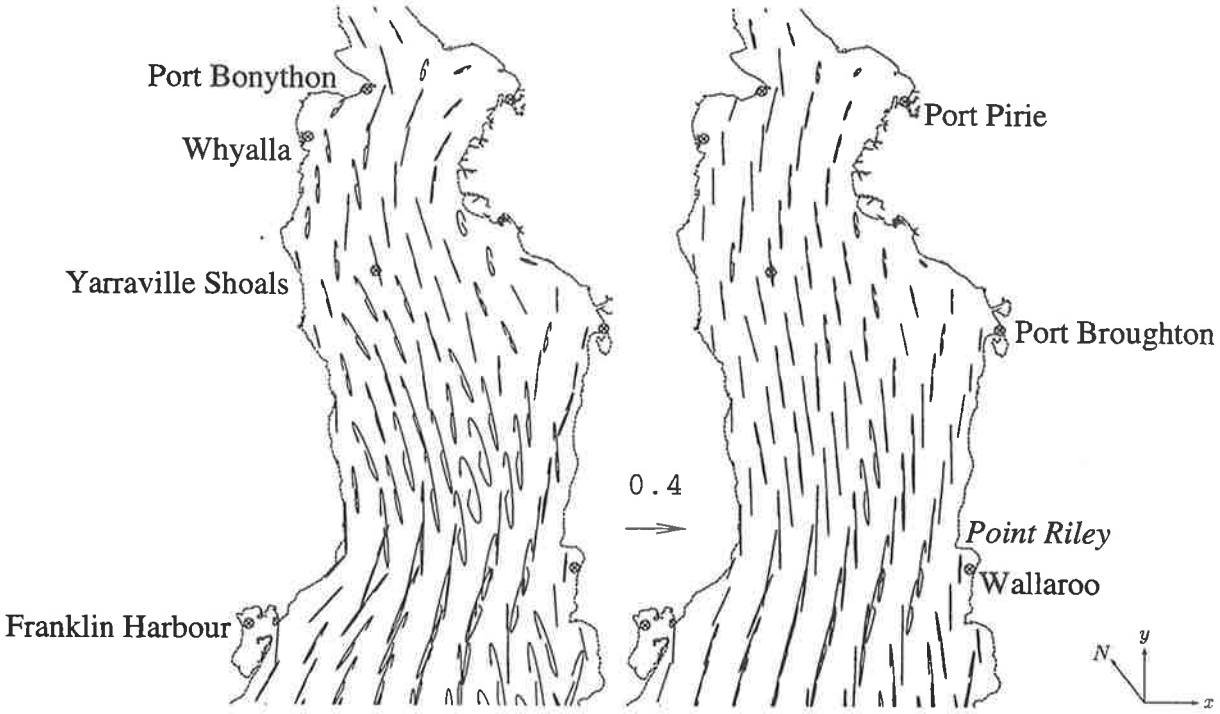

(a) near sea–surface depth–level (b) near sea–bed depth–level

Figure 7.7: Mid-northern Spencer Gulf depth-dependent tidal ellipses ($\mathrm{m\,s^{-1}}$) for the K_1 tidal constituent for the 29 d period from 21:30 1 February 1988 calculated with wind–stress. Ellipses are plotted for every fourth computational element in both the x and y directions, with small arrowheads indicating vector rotation direction. Tidal stations (roman) and places of interest (italics) are named.

this most clearly.

At the open boundary it is clear that the across-stream component due to the semi-diurnal constituents is small. This is also suggested by Steinberg (1983). The along-stream components of M_2 and S_2 are generally stronger than that of O_1, but certainly weaker than that of K_1, again as observed by Steinberg (1983) and reported by Bills (1991).

7.4.4 Residual Currents for Spencer Gulf Major Constituents

Many residual systems can be seen in the overviews of Figure 7.10, as well as the enlargements of Figure 7.11. The relative effects of wind–stress and bottom friction on the residual currents can be clearly seen on comparison of the near sea–surface depth–level vectors in Figure 7.10(a) and the near sea–bed depth–level vectors in Figure 7.10(b), respectively. Current residuals are generally smaller (and can often be in opposing directions) in the latter with respect to the former. The residuals are generally largest where the velocities are largest, i.e. through the narrowing part of the Gulf, particularly west of Wallaroo, and further northwards in the upper Gulf, as well as southwards near the open boundary north of Wedge Island.

Figure 7.10(a) shows a series of near sea–surface residual eddies in the upper- and mid-northern Gulf culminating in a strong easterly residual current across the Gulf width, from below Wallaroo turning clockwise towards Franklin Harbour. Strong residual surface currents flow up the lower Gulf on both sides with another, less intense, right to left stream originating in the vicinity of Wardang Island, off Port Victoria, and culminating in a low intensity eddy system with stagnation point in the lower mid-Gulf, south-east off Arno Bay. An anticlockwise turning residual current can also be seen south-west of Port Victoria.

Figure 7.10(b) shows a near sea–bed residual current stream meandering from off Lowly Point near Port Bonython in the upper northern Gulf, southwards past Whyalla, through Yar-

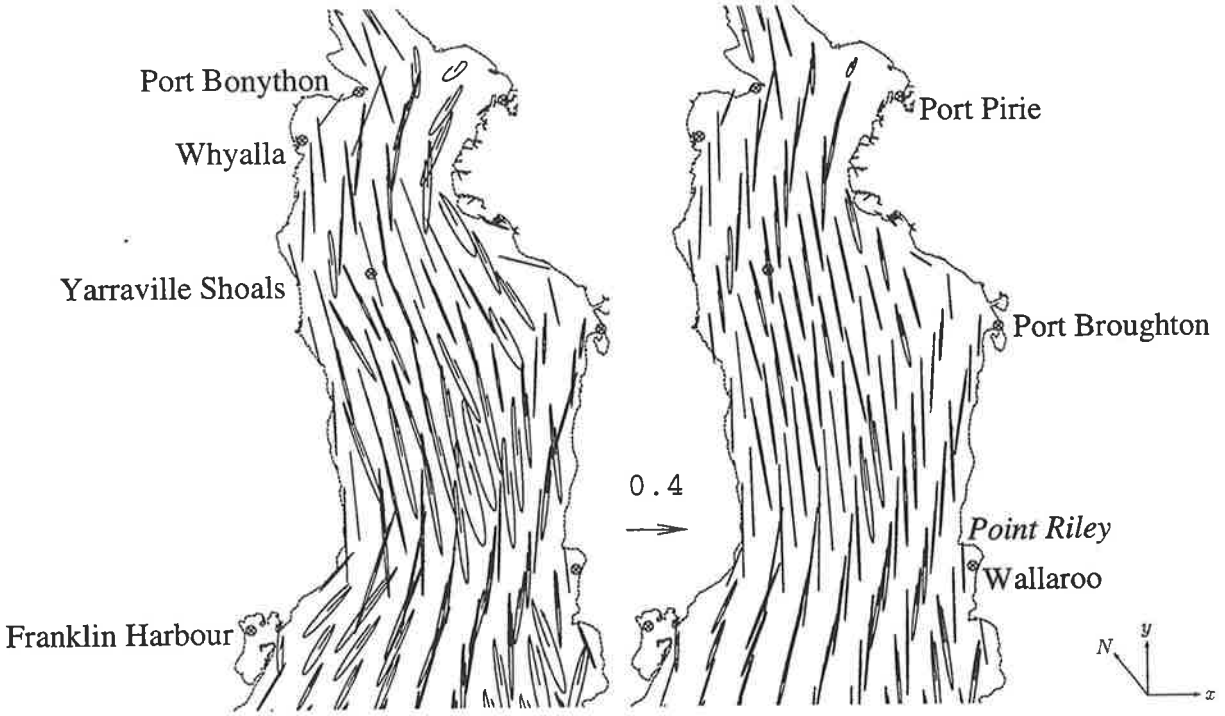

(a) near sea–surface depth–level

(b) near sea–bed depth–level

Figure 7.8: Mid-northern Spencer Gulf depth-dependent tidal ellipses ($\mathrm{m\,s^{-1}}$) for the M_2 tidal constituent for the 29 d period from 21:30 1 February 1988 calculated with wind–stress. Ellipses are plotted for every fourth computational element in both the x and y directions, with small arrowheads indicating vector rotation direction. Tidal stations (roman) and places of interest (italics) are named.

raville Shoals in the mid-northern Gulf, crossing the northern mid-Gulf width towards Wallaroo, then interacting with a clockwise rotating residual eddy centred offshore west of Wallaroo to join up with another residual current stream in the mid-Gulf, south-east off Arno Bay. The mid-north section of this residual bed current stream can also be seen in Figure 7.11(b) threading its way between the eddy systems discussed below, south eastwards from north-east of Yarraville Shoals station to east of Wallaroo station. This next residual bed current stream meanders from a point off Arno Bay down and across the southern Gulf towards Point Turton. A double anticlockwise rotating residual eddy system can also be seen south-west of Port Victoria.

Evident at both depth–levels is the sizable strong clockwise rotating residual stream spanning the Gulf adjacent to Wallaroo. The southern boundary of this eddy is the deep channel mentioned in Section 7.4.3 and indicated by the large valued contours in the vicinity of the east-west line of contour points labelled C at the bottom of Figure 7.5.

Just above this large feature is a smaller system—again at both depth–levels—of one clockwise (at left) and two anticlockwise (at right) rotating eddies positioned at the southern tip of the submerged sandbar known as Middle Bank. This is indicated by the closed contour labelled A at centre right in Figure 7.5.

Just north of this system is another clockwise rotating eddy, adjacent to the coast directly below Yarraville Shoals station, which is also present at both depth–levels. It is associated with steep bathymetric gradients indicated by the contour points labelled A and C outside and inside of, respectively, the large north-south aligned closed contour curve labelled B at centre right in Figure 7.5.

These three eddy systems can be seen in the overviews of Figure 7.10, as well as in the enlargements of Figure 7.11. What can be more readily appreciated from the latter than the former are the associated single anticlockwise rotating eddy to the immediate left for the surface

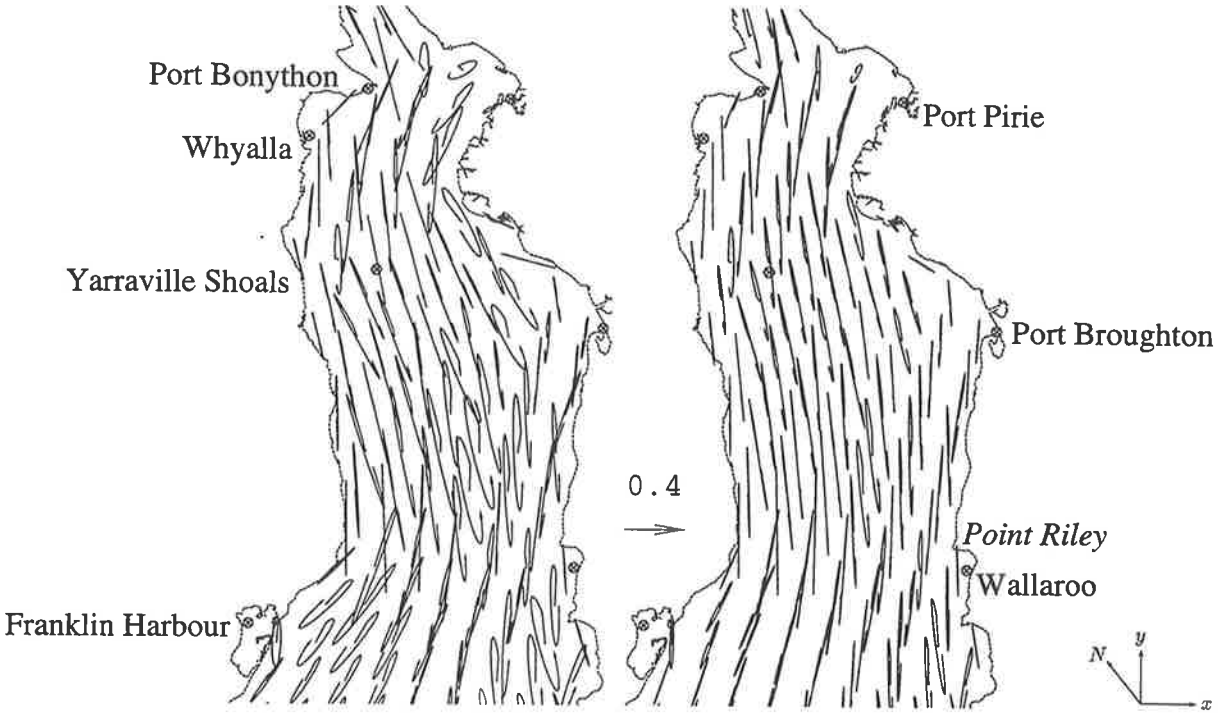

(a) near sea–surface depth–level (b) near sea–bed depth–level

Figure 7.9: Mid-northern Spencer Gulf depth-dependent tidal ellipses $(\mathrm{m}, \mathrm{s}^{-1})$ for the S_2 tidal constituent for the 29 d period from 21:30 1 February 1988 calculated with wind–stress. Ellipses are plotted for every fourth computational element in both the x and y directions, with small arrowheads indicating vector rotation direction. Tidal stations (roman) and places of interest (italics) are named.

residual currents of Figure 7.11(a), and the twin anticlockwise rotating eddies to the right and upper-right for the surface residual currents of Figure 7.11(b).

A clockwise/anticlockwise rotating system, similar to the Middle Bank system, with a similarly postulated generation mechanism, can also be seen in Figures 7.10(a) and 7.11(a) south-west/north-east of Port Bonython, directly below/above Lowly Point.

It should be noted that many of the features mentioned here were evident in the coarse grid results presented by Bills (1991). The anticlockwise eddy associated with the steep bathymetric gradients just below Yarraville Shoals was not discernible in the coarse grid results, possibly due to their lower spatial resolution. Conversely, other small-scale features reported there have, however, not had their existence verified by the results of the fine grid model presented here. The differences may also be attributable to the effects of the inclusion (here) or exclusion (there) of wind–stress, as well as the 29 d simulation period used (from 21:30 1 February 1988 here, and from 00:00 1 January 1900 there) on the residual currents. Aspects of the former effect were discussed in the papers of Nixon and Noye (1996b, 1996c), while aspects of the latter effect are discussed in Section 10.4.1.

7.4.5 Summary

Advection velocities in Spencer Gulf, as determined by a three-dimensional tidal model, have been shown to vary greatly with depth, both in terms of qualitative nature and quantitative magnitude. Analyses of tidal ellipses and residual currents at levels in the water column associated with vertically migrating *Penaeus latisulcatus* dispersing during the larval phase have revealed detailed structure to the advective forces experienced by the larvae. This will be shown in following chapters to have great influence on predictions by the numerical dispersion model of larval abundance following spawning.

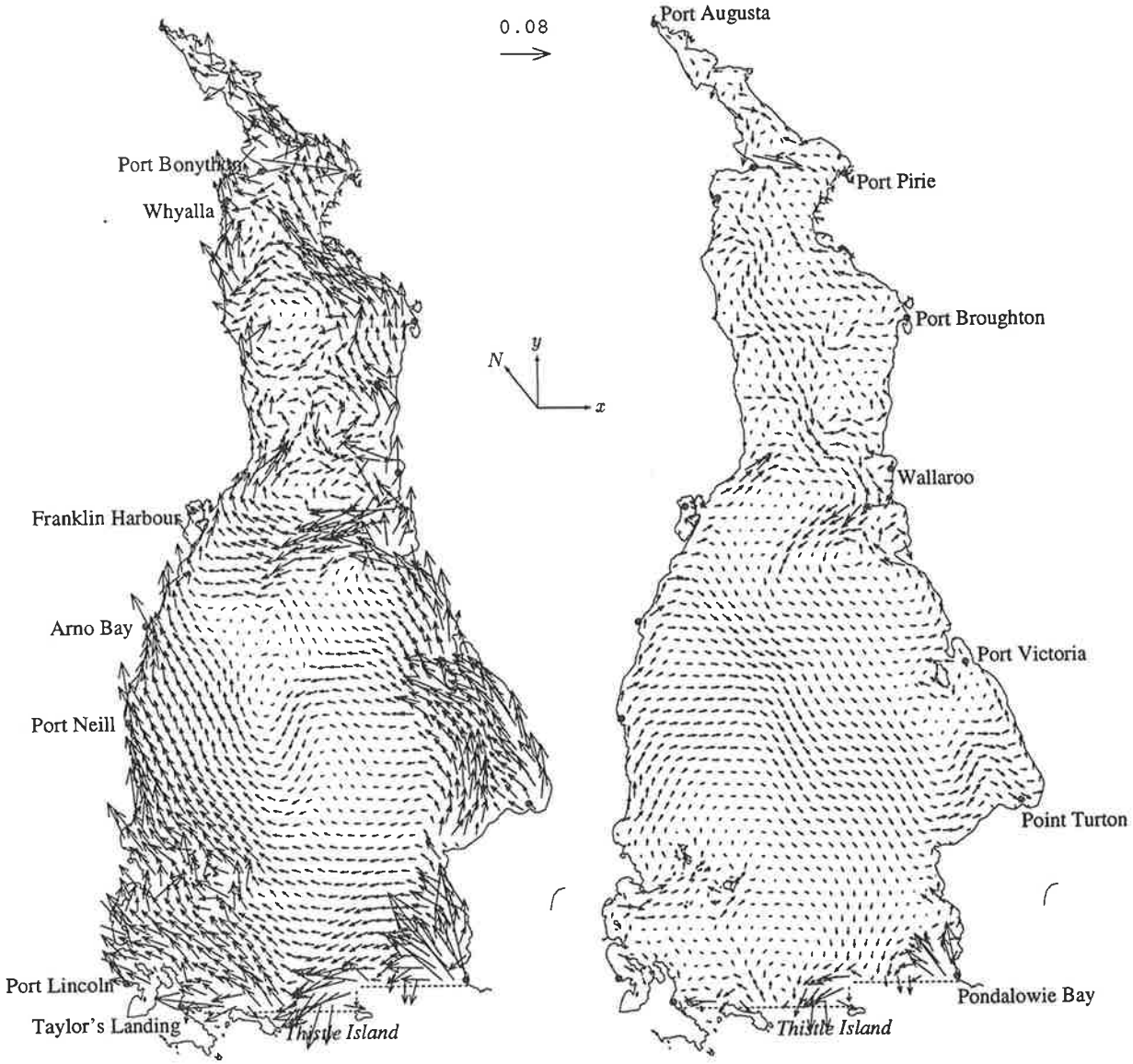

(a) near sea–surface depth–level

(b) near sea–bed depth–level

Figure 7.10: Spencer Gulf tidal current residuals ($\mathrm{m\,s^{-1}}$) for the 29 d period from 21:30 February 1 1988 calculated with wind–stress. Vectors are plotted for every second computational element in both the x and y directions. Tidal stations (roman) and islands (italics) are named.

7.5 Diffusion: Eddy, Molecular, and Shear

Regular distributions of organisms are rare. In most animal species the individuals are unevenly or irregularly distributed and planktonic animals are no exception. Marine plankton shows group-wise distribution, in inshore waters and the open sea, on any scale studied (De Wolf 1973, p. 3). Large variation in the numbers of larvae is thought to be the result of a patch-wise distribution of larvae, characterised by a *dispersion coefficient*. The dispersion coefficient is large during periods of high current velocities, implying that groups of plankton are present, while it becomes smaller later, indicating that the existing groups are gradually broken down until the group-wise occurrence cannot be distinguished from a random distribution. While the gradual breakdown of groups of larvae can be attributed to a random process like eddy diffusion it is not clear how groups can be formed in water with high current velocities (De Wolf 1973).

In Garrett (1983) small-scale mixing across density surfaces (*diapycnal mixing*) and stirring and mixing along density surfaces (*isopycnal mixing*), completely different processes in the

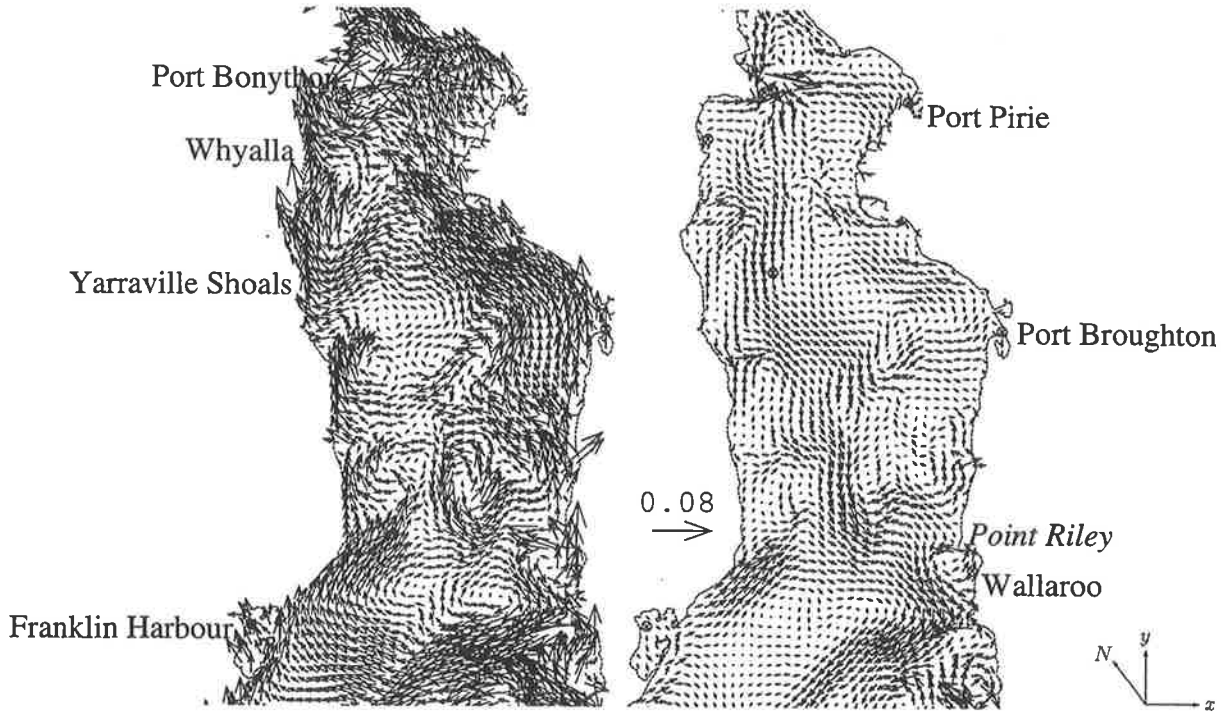

(a) near sea–surface depth–level (b) near sea–bed depth–level

Figure 7.11: Mid-northern Spencer Gulf depth-dependent tidal current residuals ($\mathrm{m\,s^{-1}}$) for the 29 d period from 21:30 February 1 1988 calculated with wind–stress. Vectors are plotted for every computational element in both the x and y directions. Tidal stations (roman) and places of interest (italics) are named.

ocean, were considered in the context of the time-scale of initial streakiness of dispersing tracers. Diapycnal mixing processes (such as breaking internal waves or double diffusive mechanisms) with mixing lengths of no more than a few metres were directly linked to scales small enough for molecular diffusion to act. Thus on vertical scales of more than a few metres the concentration of a dispersing tracer will, it was argued, look smooth. However, along isopycnals the dominant transfer mechanism, neglecting mean currents, is associated with stirring by mesoscale eddies. The problem of streakiness arises in connection with the effect of these eddies, which behave, in many ways, like two-dimensional turbulence (Garrett 1983, p. 266). Streakiness, in the present context representing the evolution of larval "patches" immediately following spawning, will not be explicitly modelled in this thesis since it is found that significant streakiness disappears quite rapidly (Garrett 1983, p. 272). The mixing processes described above will, however, be parameterised by coefficients representing horizontal eddy diffusivity, which have typical oceanic values of the order of $10^3\ \mathrm{m^2\,s^{-1}}$ (Garrett 1983, p. 267). Coefficients of horizontal eddy diffusion applicable to the Spencer Gulf region are derived in Section 7.6.

The effects of horizontal velocity shear are often in the literature seen to be analogous to those of variable horizontal eddy diffusion (McShane et al. 1988, for example). Even with diffusivity which is zero, or time and space independent, a larval cloud will be seen to be "diffused" in a current regime which is space dependent. It is for this reason that such effects would be better described not using the word *diffusion*, but the words *shear diffusion* instead. In a dispersion model, a *shear diffusion* coefficient would thus account for the effects of velocity variability, an *eddy diffusion* coefficient for turbulence on a scale smaller than the grid–scale, and a *molecular diffusion* coefficient for that of Brownian motion. The combined effects of all of these "diffusions" in conjunction with that of advection of the overall larval cloud has, for similar reasons, also been termed *dispersion* in the discussions of the larval transport models discussed in this thesis.

Since the hydrodynamic model used in the present study to specify advective velocities is three-dimensional and the proposed advection–diffusion model is what could be termed *layered two-dimensional*, and the latter uses multiple velocity depth–levels determined by the former, the combined model accounts for vertical velocity shear as well. This is in fact presumed to be the mechanism by which prawn larvae are transported from the interior gulf regions to the coastal regions, viz. by their vertical migration taking advantage of this depth–level velocity differential in the water column. The model, however, accounts for vertical velocity shear only partially and in a way simpler and thus more limited than a fully three-dimensional dispersion model.

7.5.1 Diffusion Coefficients in Mathematical Models

The mechanism by which an inert, neutrally buoyant material is dispersed by turbulent fluctuations in a fluid flow is called *turbulent diffusion*. The process obeys *Fick's law* which incorporates the so-called eddy diffusion coefficient on which the solution to the equation depends. Once the value of this parameter is known, then the spread of a conservative pollutant in a turbulent flow can be predicted (Noye 1984b, p. 210). Dispersion of passive particles in the open ocean due to turbulence depends on the scale of the phenomenon concerned (Okubo 1980). As time passes and the space occupied by the dispersing particles becomes greater, more turbulent currents act to diffuse the particles. Consequently, modelling diffusion using a constant diffusion coefficient is not strictly accurate (Possingham and Roughgarden 1990, p. 977).

7.5.2 Diffusion Coefficients in the Larval Dispersion Model

The spreading of the larval cloud is represented by the terms of (7.1.1) containing the components of the dispersion tensor $\boldsymbol{K}$. These components are used to represent turbulence caused by the existence of eddies which distort and mix the larval cloud. The resulting effect of an eddy on the larval cloud is dependent on scale. If the size of the eddy is much larger than that of the larval cloud, then the cloud will tend to be advected as a whole following the motion of the eddy, whereas if the eddy is smaller than the cloud, it will tend to mix and break up the cloud, resulting in an overall increase in size of the cloud (Bowden 1964; Okubo 1980). Intuitively, the longer a cloud is exposed to eddies, the larger it will become and hence eddies which initially tended to advect the cloud will later aid in the processes of breaking it up. Thus, if there exist eddies at all spatial scales, then the rate at which the larval cloud spreads should increase with time. It will be shown, however, that constant coefficient diffusion is often required to be assumed in the absence of detailed empirical observations. Functional forms for time-independent diffusion coefficients applicable to the Spencer Gulf region are derived in Section 7.6.

7.6 Eddy Diffusion in Spencer Gulf

In this section, experimental data concerning Spencer Gulf horizontal eddy diffusion coefficient estimates are discussed, a form for spatial variation of these coefficients in one dimension is derived, and a value for a constant coefficient suitable for the entire Gulf proposed.

The rate of vertical diffusion is governed by vertical eddy diffusion coefficients. In general, horizontal diffusion is about 30 times faster than in the vertical and, in particular, no measurements of vertical mixing have been made in Spencer Gulf (Noye 1984b, p. 211). These two facts, and the regime chosen to represent vertical migration of prawn larvae in the dispersion model (see Section 7.3), deem the determination of horizontal eddy diffusion coefficients sufficient for the proposed larval dispersion model.

7.6.1 Horizontal Eddy Diffusion in Spencer Gulf

In Holloway (1974), horizontal eddy diffusion coefficients were found for northern Spencer Gulf from the head of the Gulf to Wallaroo Bay—a distance of approximately 180 km. Holloway's

work is summarised, and expanded upon, in the following.

Coefficients were determined by Holloway (1974) using the "4/3 *power law*" (Ozmidov 1958)

$$K_{4/3} = A_{4/3} b^{4/3}, \tag{7.6.1}$$

where symbols used in this equation have the following meaning:

$K_{4/3}$: the horizontal eddy diffusion coefficient ($\mathrm{m^2\,s^{-1}}$);

$A_{4/3}$: the dissipation parameter ($\mathrm{m^{2/3}\,s^{-1}}$);

b: one quarter of the width (m) of the concentration field.

This was done using two independent methods. First, by employing dye tracking techniques and second, by using a knowledge of the salinity distribution in Spencer Gulf. Aerial photographs of the dye tracks and salinity data were collected by members of the Flinders Institute for Atmospheric and Marine Sciences (FIAMS) in the Point Lowly area (see Figure 1.2) during November 1973. Salinity data were also obtained in May 1964 by Bullock (1975), and for the area north of Point Lowly on 24 September 1973 by Holloway (1974).

Fluoroscene dye was continuously released from a fixed source in the Point Lowly area with aerial photographs taken of the dye field to determine values of $4b$ (the width of the dye field) and corresponding values of x (the linear distance from the initial dye source) and the position of drogues (to determine the assumed constant current velocity). From these measurements a mean dissipation parameter value of

$$A_{4/3} = 3.14 \times 10^{-3}\,\mathrm{m^{2/3}\,s^{-1}} \tag{7.6.2}$$

was derived from the solution

$$b(x,z) = \left(\frac{4}{3}\frac{A_{4/3}x}{u} + b_0^{\frac{2}{3}}(z)\right)^{\frac{3}{2}} \tag{7.6.3}$$

to the partial differential equation governing the diffusion of a conservative tracer concentration, with appropriate simplifying assumptions, assuming (7.6.1). Symbols used in the above equation have the following meaning:

x: the distance (m) from the initial Gaussian concentration field;

z: the vertical Cartesian coordinate (m), directed downwards from MSL;

u: the velocity ($\mathrm{m\,s^{-1}}$) in the x direction;

$b(x,z)$: one quarter of the width (m) of the assumed Gaussian concentration field;

$b_0(z)$: one quarter of the width (m) of the initial Gaussian concentration field,

and values taken were

$$u = 0.5475\,\mathrm{m\,s^{-1}} \quad \text{and} \quad b_0(z) = 1/8\,\mathrm{m}. \tag{7.6.4}$$

Spencer Gulf salinity, evaporation, rainfall, and current data were then used to determine horizontal eddy diffusion coefficients using a solution to the water and salt flux balance equations with appropriate simplifying assumptions, such as that eddy diffusion does not change throughout the year.

The coefficients (K_{sg}) determined from the results of the two methods, and those ($K_{4/3}$) determined from (7.6.1)–(7.6.2) and the width of the Gulf ($4b$) at the corresponding southern latitudes ($|\Phi|$), are reproduced from Holloway (1974) in Table 7.1 and are plotted against distance (x) from the head of the Gulf in Figure 7.12 using solid curves.

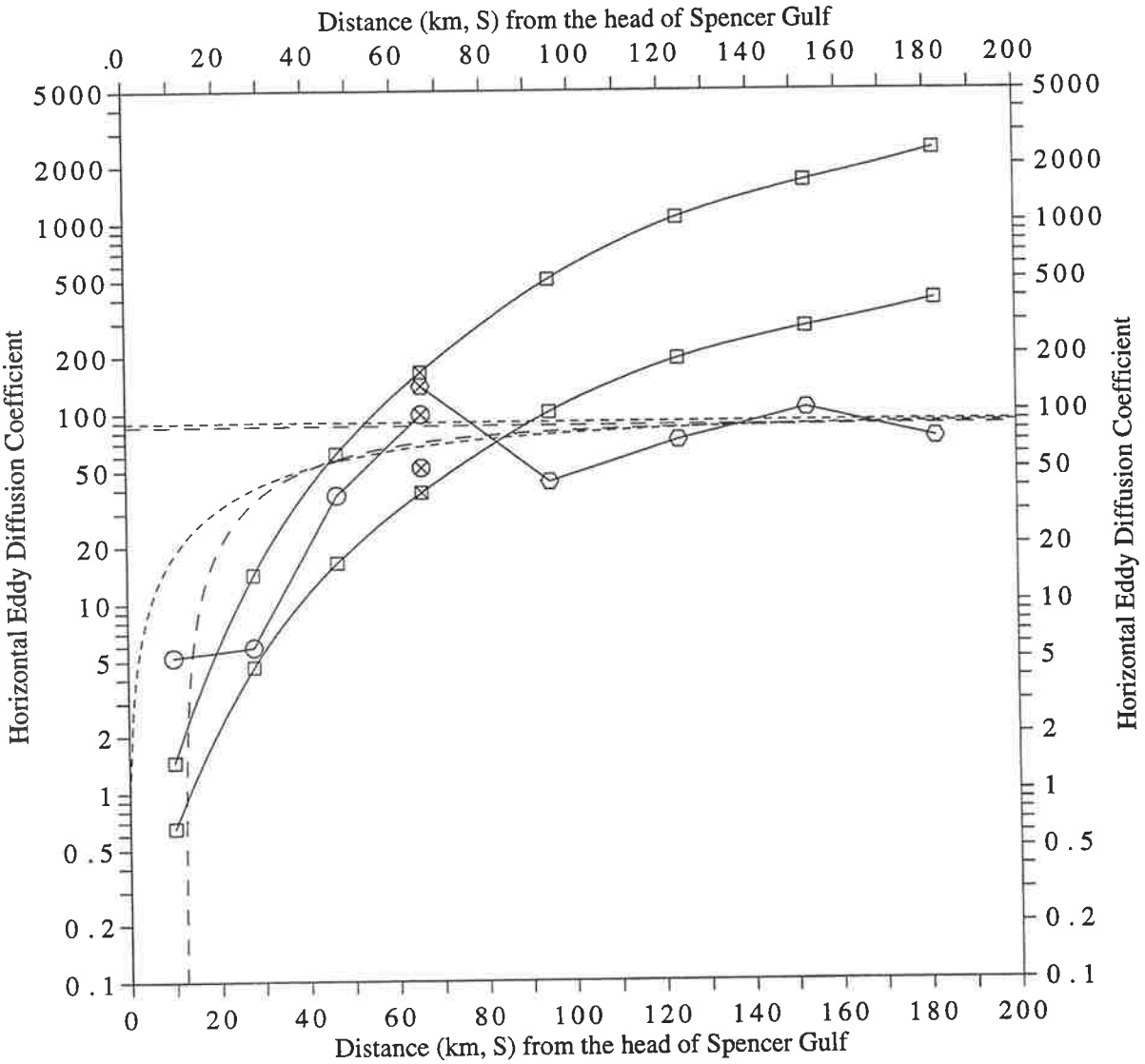

Figure 7.12: Horizontal eddy diffusion coefficients ($m^2\,s^{-1}$) against distance (km, S) from the head of Spencer Gulf. Point values are listed in Table 7.1 reproduced from Holloway (1974) and were determined from salinity distribution estimates made in September 1973 (circles), November 1973 (octagon), and May 1964 (hexagons) and from upper bounds (squares) calculated by (7.6.1)–(7.6.2), the "4/3 power law" (Ozmidov 1958) (upper), and by (7.6.5)–(7.6.6), the "Okubo empirical relation" (Okubo 1971) (lower). Values corresponding to Lowly Point are highlighted (crosses). The solid curves are determined by linear interpolation for the salinity data and by bi-cubic spline interpolation for the upper bound data. The dashed curves are exponential function best fits of the salinity data using (7.6.9)–(7.6.10) (coarse) and (7.6.12)–(7.6.13) (fine), with the coarse and fine dashed horizontal lines as the appropriate asymptotes.

Spencer Gulf Horizontal Eddy Diffusion Coefficients							
Date	Place	Latitude $\lvert\Phi\rvert$ (°S)	Distance x (km)	Width $4b$ (km)	Coefficient		
					$K_{4/3}$ ($m^2\,s^{-1}$)	$K_{23/20}$ ($m^2\,s^{-1}$)	K_{sg} ($m^2\,s^{-1}$)
September 1973	Port Augusta	32°30′	10	0.4	1.5	0.7	5.2
	—	32°40′	28	2.2	14.2	4.6	5.9
	—	32°50′	47	6.6	61.3	16.4	37.0
	Point Lowly	33°00′	66	13.8	163.9	38.2	98.3
November 1973	"	"	"	"	"	"	51.6
May 1964	"	"	"	"	"	"	138.5
	—	33°15′	95	32.0	503.1	100.5	43.3
	—	33°30′	124	56.0	106.1	191.3	71.3
	—	33°45′	153	78.0	1650.3	280.1	104.2
	Wallaroo Bay	34°00′	182	104.0	2421.8	389.9	72.9

Table 7.1: Horizontal eddy diffusion coefficients in Spencer Gulf. Values are determined from salinity distribution estimates (K_{sg}) made in September 1973 (Holloway 1974), November 1973 (Holloway 1974), and May 1964 (Bullock 1975) and from upper bounds ($K_{4/3}$ and $K_{23/20}$) calculated using (7.6.1)–(7.6.2), the "4/3 power law" (Ozmidov 1958), and (7.6.5)–(7.6.6), the "Okubo empirical relation" (Okubo 1971), respectively. The width of Spencer Gulf ($4b$) and the distance (south) from the head of Gulf (x) at the corresponding (southern) latitude ($|\Phi|$) are also listed.

7.6.2 Eddy Diffusion Coefficient Empirical Data

A more restrictive horizontal eddy diffusion coefficient upper bound determined by the "*Okubo empirical relation*" (Okubo 1971, 1976)

$$K_{23/20} = A_{23/20} b^{23/20}, \tag{7.6.5}$$

where symbols used in the above equation have the following meaning:

$K_{23/20}$: the horizontal eddy diffusion coefficient ($m^2\,s^{-1}$);

$A_{23/20}$: the dissipation parameter ($m^{17/20}\,s^{-1}$),

is also listed in Table 7.1. This is plotted against distance (x) from the head of the Gulf in Figure 7.12 using a solid curve. From the Holloway (1974) measurements, a mean dissipation parameter value of

$$A_{23/20} = 3.26 \times 10^{-3}\,m^{17/20}\,s^{-1} \tag{7.6.6}$$

is derived from the solution

$$b(x,z) = \left(\frac{17}{10}\frac{A_{23/20}x}{u} + b_0^{\frac{17}{20}}(z)\right)^{\frac{20}{17}} \tag{7.6.7}$$

to the partial differential equation governing the diffusion of a conservative tracer concentration with appropriate simplifying assumptions, assuming (7.6.5).

7.6.3 Eddy Diffusion Coefficient Upper Bounds

From Figure 7.12 it can be seen that the horizontal eddy diffusion coefficient values roughly follow (7.6.1)–(7.6.2) and (7.6.5)–(7.6.6) from the head of Spencer Gulf to near Point Lowly, further south of which the Gulf rapidly increases in width. The largest eddies between Port Augusta and Point Lowly thus appear to be as wide as the Gulf, in agreement with the "4/3 power

law" and the "Okubo empirical relation". Further south of Point Lowly the upper bounds determined by (7.6.1)–(7.6.2) and (7.6.5)–(7.6.6) predict continually increasing values, whereas those obtained from the salinity distribution are approximately constant. Advection processes with water outside of the Gulf only take place as far as 33°45′S (Bullock 1975) and from this area to Point Lowly, Holloway's (1974) results indicate that the flow consists mainly of large eddies, but of a size smaller than the width of the Gulf.

7.6.4 Spatially Variable Horizontal Eddy Diffusion

The results of Holloway's (1974) calculations indicate that the diffusion coefficients increase from small values ($\approx 5\,\mathrm{m^2\,s^{-1}}$) at Port Augusta to to an approximately constant value ($\approx 80\,\mathrm{m^2\,s^{-1}}$) at Point Lowly. In Bye (1981), the function

$$K_{\mathrm{Bye}} = \begin{cases} 0.01b^{4/3} & b < 3.3\,\mathrm{km} \\ 80\,\mathrm{m^2\,s^{-1}} & b \geq 3.3\,\mathrm{km} \end{cases} \tag{7.6.8}$$

was used to approximate the deduced variation. To determine a more accurate functional variation of Spencer Gulf horizontal eddy diffusion coefficients along the Gulf major axis, the dashed best fit curves of Figure 7.12 are derived from the data of Table 7.1 using the quasi-Newton method (a compromise between the Steepest Descent method and the Newton method) using two exponential functions. Coefficient uncertainties are estimated from the variance-covariance matrix calculated from the Jacobian matrix, and the values presented are the square roots of the diagonal elements. Two fit error measures are also presented, namely the *sum of squares error* (ESS) (with a perfect fit corresponding to ESS = 1—the larger the value of ESS, the poorer the fit) and the *correlation coefficient* (r^2) (with a perfect fit corresponding to $r^2 = 1$—the smaller the value of r^2, the poorer the fit). The function

$$f_3(x) = -a\exp\{-bx\} + c \tag{7.6.9}$$

is fit to the data to give coefficients and uncertainties

$$a = 126.0 \pm 63.0\,\mathrm{m^2\,s^{-1}}, \quad b = 0.032 \pm 0.030\,\mathrm{m^{-1}}, \quad c = 85.8 \pm 22.7\,\mathrm{m^2\,s^{-1}} \tag{7.6.10}$$

and error measures

$$\mathrm{ESS} = 9116.5, \quad r^2 = 0.45, \tag{7.6.11}$$

resulting in the coarsely dashed function curve and horizontal asymptote line of Figure 7.12. The function (7.6.9)–(7.6.10) is not suitable as a measure of horizontal eddy diffusion at the head of Spencer Gulf since constituents are specified in this region with values less than zero. Hence the function

$$f_2(x) = -(c-1)\exp\{-bx\} + c \tag{7.6.12}$$

is fit to the data to give coefficients and uncertainties

$$b = 0.021 \pm 0.018\,\mathrm{m^{-1}}, \quad c = 89.4 \pm 28.6\,\mathrm{m^2\,s^{-1}} \tag{7.6.13}$$

and error measures

$$\mathrm{ESS} = 9841.9, \quad r^2 = 0.41, \tag{7.6.14}$$

resulting in the finely dashed function curve and horizontal asymptote line of Figure 7.12. The function (7.6.12)–(7.6.13) is more suitable as a measure of horizontal eddy diffusion at the head of Spencer Gulf since constituents are specified in this region with a value greater than unity, preventing undesirable possibly singular behaviour of dispersion models at the extreme head of the Gulf.

In order to make use of the experimental data of Holloway (1974) in numerical diffusion models, the reference latitude

$$\Phi_0 = 32°24'46'' \text{ (S)} \tag{7.6.15}$$

is derived from the linear relationship between $|\Phi|$ and x in Table 7.1 and the best fit functions determined as above. The function

$$f_3(|\Phi|) = -a\exp\{-b(|\Phi| - \Phi_0)\} + c \tag{7.6.16}$$

is fit to the data to give coefficients and uncertainties

$$a = 124.8 \pm 61.4\,\mathrm{m^2\,s^{-1}}, \quad b = 3.5 \pm 3.3^{°^{-1}}, \quad c = 86.1 \pm 23.4\,\mathrm{m^2\,s^{-1}} \tag{7.6.17}$$

and error measures

$$\text{ESS} = 9173.6, \quad r^2 = 0.45, \tag{7.6.18}$$

and the function

$$f_2(|\Phi|) = -(c-1)\exp\{-b(|\Phi| - \Phi_0)\} + c \tag{7.6.19}$$

is fit to the data to give coefficients and uncertainties

$$b = 2.3 \pm 2.1^{°^{-1}}, \quad c = 89.9 \pm 29.6\,\mathrm{m^2\,s^{-1}} \tag{7.6.20}$$

and error measures

$$\text{ESS} = 9860.8, \quad r^2 = 0.41, \tag{7.6.21}$$

resulting in the coarsely and finely dashed function curves and asymptote lines, respectively, of Figure 7.13. It can be seen from this figure that the best fit of (7.6.16)–(7.6.17) to the Holloway (1974) data is indeed not suitable for determining horizontal eddy diffusion coefficients at the head of the Gulf in a fine grid Spencer Gulf model, and that the approximate fit of (7.6.19)–(7.6.20) is more suitable. This figure also emphasises the northern bias to the Holloway (1974) data when compared to the entire length of Spencer Gulf, represented by the horizontal distance between the solid circles of the best fit function end points. Further field experiments to determine eddy diffusion coefficients in southern Spencer Gulf may be required in order to determine a more complete representation of the variability with increasing southern latitude. The diffusion coefficients calculated by Holloway (1974) are based on a steady state approximation. More comprehensive salinity data could be collected by a programme of measurements at several locations along the Gulf over a longer period of time. This would enable the inclusion of time dependence in the calculation of horizontal eddy diffusion coefficients.

7.6.5 Constant Eddy Diffusion

While one would expect some seasonal variation in the diffusion coefficients, an average corresponding to the salinity distribution is perhaps that which is required initially in a study of tracer distributions (Bye 1981). The special behaviour of tracers other than vertically mixed conservative and atmospherically exchanged quantities also has not been considered. For example, the behaviour of surface and bottom seeking substances—such as the vertically migrating larval species of this thesis—would be significantly different and require individual treatment (Bye 1981). Since it is probable that the dispersion estimates given here have an accuracy of about 25% (Bye 1981), it seems likely that a constant eddy diffusion coefficient value suffices.

Consulting Table 7.1 and Figures 7.12–7.13 and Equations (7.6.1)–(7.6.2) and (7.6.12)–(7.6.13), and (7.6.5)–(7.6.6) and (7.6.19)–(7.6.20), a horizontal eddy diffusion parameter with value

$$K_\mathrm{h} = 100\,\mathrm{m^2\,s^{-1}} \tag{7.6.22}$$

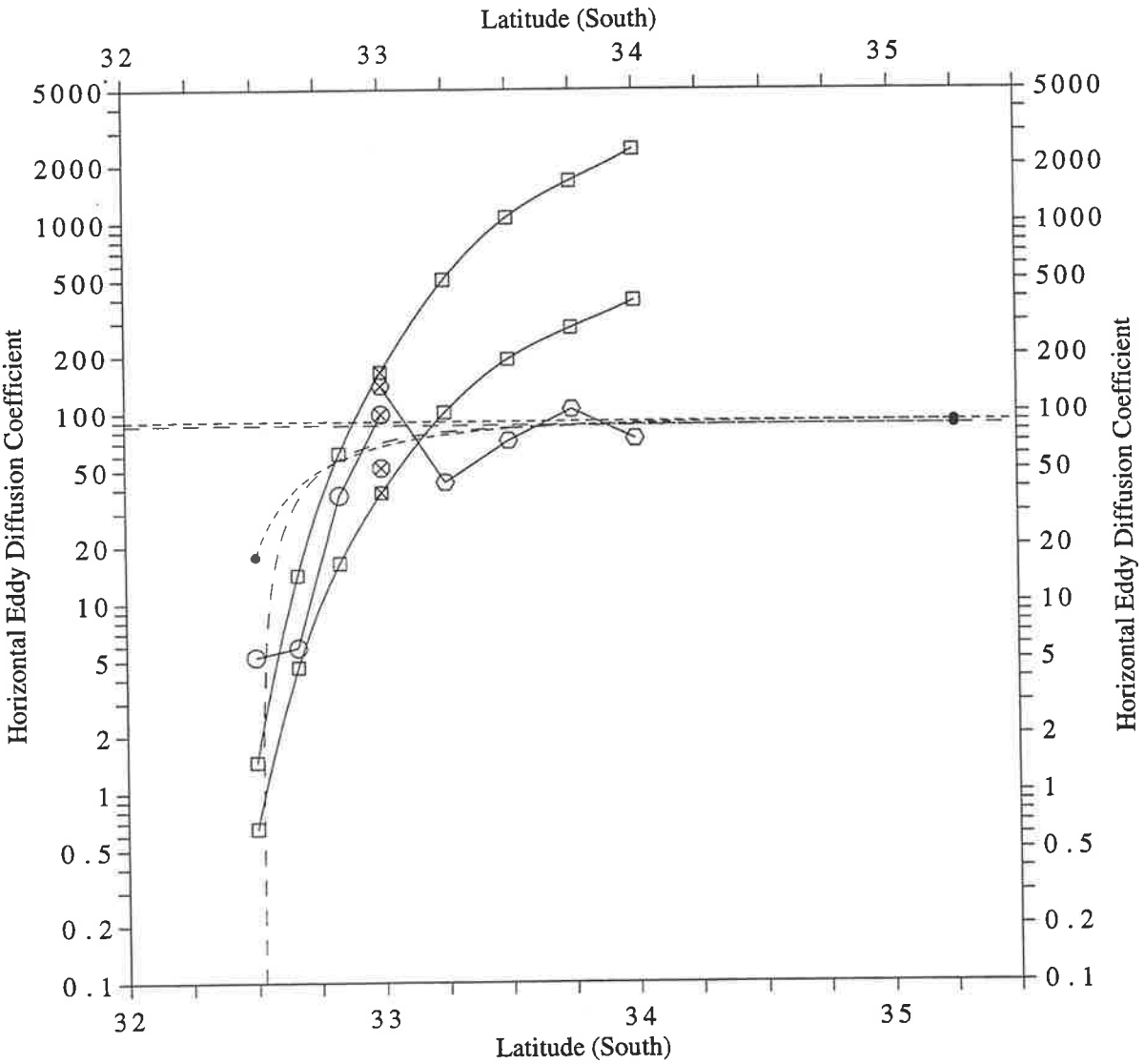

Figure 7.13: Horizontal eddy diffusion coefficients ($m^2\,s^{-1}$) against latitude (°S) in Spencer Gulf. Point values are listed in Table 7.1 reproduced from Holloway (1974) and were determined from salinity distribution estimates of September 1973 (circles), November 1973 (octagon), and May 1964 (hexagons) and from upper bounds (squares) calculated by (7.6.1)–(7.6.2), the "4/3 power law" (Ozmidov 1958) (upper), and by (7.6.5)–(7.6.6), the "Okubo empirical relation" (Okubo 1971) (lower). Values corresponding to Lowly Point are highlighted (crosses). The solid curves are determined by linear interpolation for the salinity data and by bi-cubic spline interpolation for the upper bound data. The dashed curves are exponential function best fits of the salinity data using (7.6.16)–(7.6.17) (coarse) and (7.6.19)–(7.6.20) (fine) at latitudes for all elements in the fine grid Spencer Gulf model, with the coarse and fine dashed lines as the appropriate asymptotes. The best fit function end points are emphasised (solid circles).

is proposed as suitable for simulations requiring a constant value over the entire Spencer Gulf region, by taking into account the experimental data of Holloway (1974), the upper bounds determined by the "4/3 power law" and the "Okubo empirical relation", and the increased width of the Gulf south of Wallaroo.

7.6.6 Discussion

Space and time dependence of eddy diffusion coefficients is related to residual currents on longer time scales than those predicted by the tidal model as input to the proposed prawn larvae dispersion model, and are thus not considered in this thesis. Long time–scale *thermohaline currents* are brought about by horizontal pressure gradients due to density variations in the Gulf, which are caused by temperature and salinity differences, produced in part by outside water entering the Gulf, and in part by variation in the effect of evaporation over the Gulf. The magnitude of these currents is typically about $0.07\,\mathrm{m\,s^{-1}}$ (Bullock 1975). This fact, combined with the vertical homogeneity of the hydrology (Bullock 1975; Bye and Whitehead 1975; Bye 1981) in contrast to the vertical inhomogeneity observed in the tidal currents of Spencer Gulf and that assumed of the prawn larvae concentrations in the water column, suggests that thermohaline currents have little significance to the present study. It is surmised that the cause of the thermohaline circulation persistence in the Gulf is external, i.e. it is due to water from the Southern Ocean moving up under influences that determine the pattern of flow in this region (Bullock 1975) and the prevailing winds. The former is for the most part accounted for by the height-specified boundary condition at the open boundary of the tidal model (see Section 3.1.2), while the latter are accounted for by the surface wind interpolation over the entire Gulf from the upper wind data (see Section 4.2). A fuller understanding of the dispersion process would of course rely on extended programmes of observation. In particular, observations of the actual water balance of Spencer Gulf, including evaporation, rainfall, and run-off are required as time–series extending over several years. These could then be used, together with observed profiles of salinity and other introduced tracers, to specify in greater detail the dispersion process in this region (Bye 1981).

7.6.7 Conclusions

It should be noted that the diffusion tensor $\boldsymbol{K}$ of (7.1.1) represents a statistical average of the effects of diffusion. In reality eddies will distort a larval cloud, resulting in it having complicated boundary and internal structures which cannot be resolved by (7.1.1). The solution obtained from (7.1.1) represents an average (i.e. not typical) concentration cloud which is smoother than that which would be observed in the field (Richards et al. 1995).

Assuming that diffusion is composed of longitudinal and transverse components only, then

$$K_{xy} = K_{yx} = 0 \tag{7.6.23}$$

define the diffusion tensor diagonal components (van Dam 1982; Holly and Usseglio-Polatera 1984) of (7.1.1). Spatial independence of the two remaining diffusion tensor components is assumed despite the fact that, in reality, the presence of a nearby coastline and the depth of the water may influence the rate of diffusion, as discussed above. Assuming also that these components are, at least on the time-scale of *Penaeus latisulcatus* dispersal in Spencer Gulf, constant in time, these are denoted by

$$K_{xx} = \alpha_x \quad \text{and} \quad K_{xx} = \alpha_y \tag{7.6.24}$$

in the following. In all numerical experiments presented in this thesis involving simulations of diffusion in two dimensions

$$\alpha = \alpha_x = \alpha_y \tag{7.6.25}$$

is assumed and, as a result of the points made in Section 7.6.5

$$\alpha = K_h = 100\,\mathrm{m^2\,s^{-1}}, \tag{7.6.26}$$

unless otherwise stated.

7.7 Larval Mortality

Year–class strength of many marine populations is widely believed to be controlled in large part by the survival of their early life history stages. Consequently, the causes of mortality of eggs and larvae form an important area of fisheries research (McGurk 1989, p. 1). Because larvae and juveniles are characterised by high mortality rates, the deductions of migratory patterns from changes in distribution (abundance) must include subtraction of the effects of mortality (Miller et al. 1984, p. 210).

Predation, starvation, and other factors take a tremendous toll of planktotrophic larvae, with estimated mortality exceeding 99% in many species. However, the enormous numbers of planktic larvae produced by planktotrophic species counterbalance this extremely high larval mortality (Jablonski and Lutz 1983, p. 23). In order for a population to be self-sustaining, it is necessary for sufficient larvae to survive to the settling stage in order to replace organisms (juveniles and adult) that have been lost through mortality (Hill 1990, p. 219). This pelagic survival has associated with it a mortality rate, which is in most cases the result of entirely different mechanisms to that associated with older organisms. Little is known about the presumably high mortality present in the early life histories of many marine invertebrates, and it may be that settlement and early post-settlement, rather than planktic larval life, are actually the times of greatest mortality (Jablonski and Lutz 1983, p. 23).

Intuitively, there must be a relationship between the length of the larval state and the mortality rate during that state but, as stated in Section 2.2.1, Jackson and Strathmann (1981) postulated that this relationship is not necessarily straightforward. Mortality from predation may vary with place or stage of development. Lower mortality rates from predation at later larval stages could also result in greater returns from an extension of the competent period (Jackson and Strathmann 1981, p. 24). This has important implications for the manner in which selective (and stochastic) forces shape populations during larval development as well as during recruitment and maturation (Jablonski and Lutz 1983, p. 23). It can thus be seen that pelagic mortality is important in determining life cycle dynamics.

Mortality rates of pelagic larvae are difficult to measure and are bound to be variable (Richards et al. 1995, p. 64). In a study of the population structure of barnacles, Minchinton and Scheibling (1991) reported that in open systems, larvae may be dispersed within and between local populations and the reproductive output among these populations may be variable, obscuring any relationship between reproductive output and larval abundance on a local scale. In these systems, local populations may be best described as a function of: (1) the number of competent larvae that reach a potential settlement location; (2) the probability of successful settlement; and (3) the mortality between successive life history stages. This may be density dependent due to competition for resources such as space, nutrients, and light or density independent due to various biotic (e.g. predation, grazing) or physical (e.g. dessication, dislodgement) factors, indicating that mortality is not necessarily constant (Minchinton and Scheibling 1991, p. 1867). Possibly due to the number and complexity of contributing factors, however, for many species there is little evidence relating to mortality during the juvenile period (Hill 1990, p. 219).

7.7.1 Mortality Variability with Density

If the population is at a level that is close to the carrying capacity of the environment this implies some form of density-dependent mortality operates at the settling or juvenile stage (Hill

1990, p. 224). Mortality rates for settled cyprids (spats) of the barnacle *Balanus cretatus* were, in fact, found to be density dependent (De Wolf 1973). Although these findings relate to mortality at the time of settlement, it is not unreasonable to assume that density dependence and therefore space (and time) variability applies equally to larval mortality.

7.7.2 Mortality Variability with Time

In a study of estuarine-dependent fish larvae and juveniles, Miller et al. (1984) observed that as size increased, specific growth rate declined but mortality rate declined even faster (Miller et al. 1984, p. 210). Starvation mortality was measured for two cohorts of Pacific herring larvae *Clupea harengus pallasi* in Bamfield Inlet, British Columbia by McGurk (1989). Starving larvae were found in the 1–26 d age group of both cohorts and starvation mortality followed the same trajectory in both cohorts: an increase in magnitude from $0\,d^{-1}$ at hatch to a maximum of $1.0\,d^{-1}$ at ages 5–7 d and then a decline to $0\,d^{-1}$ at 20 d (McGurk 1989, p. 1). From these findings, the possible temporal variability of mortality in larval organisms is well apparent.

7.7.3 Estimating Larval Mortality

As suggested by Fortier and Leggett (1982), the mortality of a particular larval species can be determined through direct field measurement, if one assumes that early larval stages simply act as passive contaminants of the environment and are distributed by the same processes that distribute salt or temperature. As salt is a conservative contaminant, the divergence between the evolution of salt concentration and the evolution of larval concentration, within a given volume of water, will be a measure of larval mortality (i.e. disappearance by predation or decay after death) during the time and at the location of the measurements (Fortier and Leggett 1982, p. 1151). Accurate measurement of total mortality, however, depends on how well the method of measurement accounts for potential bias introduced by dispersal of larvae into or out of the sampling area (McGurk 1989, p. 1).

Ideally, it is preferable to estimate advection, diffusion, and mortality parameters simultaneously (McGurk 1989, p. 2). To this aim, in McGurk's paper, the best fit to four available data sets was obtained by searching among the nine parameters of postulated mortality models corresponding to the different advection–diffusion–mortality population models that are possible, assuming non-zero mortality, given the assumed governing equation. This was a two-dimensional constant coefficient advection–diffusion–mortality partial differential equation, such as (7.8.5), with an instantaneous Gaussian peak initial condition, such as (8.9.1), in Cartesian space. In interpreting the results, McGurk thought it possible that the unexplained variance of two of the four cohorts may have been due to violations of the two major assumptions of the population models: that mortality was constant with age, and that x and y eddy diffusion coefficients (see Section 7.5) were constant with x and y, respectively (McGurk 1989, p. 8). McGurk stated that the unexplained variance may also have been due to an interaction between the frequency of sampling in space and time and the spatial patchiness of the fish (McGurk 1989, p. 9).

Advection, diffusion, total mortality, and starvation mortality were all measured by McGurk (1989) in order to determine the roles of offshore dispersal, population density, and starvation in the dynamics of populations. The most striking differences between the two cohorts were in initial density, total mortality, and diffusion. That the average magnitude of starvation mortality did not vary with total mortality (as did initial density and the rates of diffusion) suggested that starvation was only one of several agents of mortality and that density-dependent predation and offshore dispersal were equally important factors (McGurk 1989, p. 1). This conclusion depends crucially on the accuracy with which total mortality and starvation mortality were measured (McGurk 1989, p. 14). The major assumptions that were used to obtain total mortality were a constant total mortality with age and Fickian diffusion, which followed from the constraints of the population model used. McGurk noted the importance of measuring advective and diffusive dispersal as a necessary component of the process of measuring total mortality, and

that some form of population modelling that incorporates advective and diffusive transport is always necessary for the production of reliable estimates of total mortality (McGurk 1989, p. 14). McGurk also stated that a constant total mortality was chosen because it was the simplest kind of mortality rate and therefore the easiest to incorporate in a dispersion model and that, in fact, all studies of the population dynamics of fish eggs and larvae in which both total mortality and eddy diffusion have been measured have assumed constant total mortality (McGurk 1989, p. 14). McGurk also thought it unlikely that the herring larvae were actually transported as if they were passive Brownian particles, as is assumed by Fickian diffusion, and that the estimated diffusion and mortality rates were independent of the initial hatching density (McGurk 1989, p. 14). These rates should have, in the light of the results of McGurk's analysis, been taken into account.

7.7.4 Conclusions

From the discussions above, it is evident that estimating mortality coefficients is a delicate business at best. Many factors influence mortality and many other processes can be interpreted by statistical analyses as, rightly or wrongly, contributing to mortality estimates. The most difficult conclusion to come to terms with, in reference to the choice of mortality coefficients in dispersion models, is that dispersion has a major effect on mortality estimates as determined in the field, while at the same time the mortality coefficients used will have a major effect on dispersion results produced by the numerical simulations.

7.7.5 Mortality Estimates

Jackson and Strathmann (1981) quoted a range of figures from $0.034\,\mathrm{d}^{-1}$ for a crab of the genus Halicarcinus up to $0.65\,\mathrm{d}^{-1}$ for *Calanus* nauplii.

Total mortality was measured for two cohorts of Pacific herring larvae *Clupea harengus pallasi* in Bamfield Inlet, British Columbia by McGurk (1989). Total mortality was 8 times lower in a cohort hatched in 1981, $0.02\,\mathrm{d}^{-1}$, than in a cohort hatched in 1982, $0.16\,\mathrm{d}^{-1}$ (McGurk 1989, p. 1).

For the period of pelagic dispersal of the Norway Lobster *Nephrops norvegicus*, Hill (1990) estimated an instantaneous larval mortality rate of 0.03 to $0.04\,\mathrm{d}^{-1}$.

In a study of shrimp larvae in the Gulf of Carpentaria, Rothlisberg et al. (1983) pointed out that larval mortality can only be approximated in the Gulf from estimates of fecundity and mortalities of other life history stages. Juvenile mortality in the nursery areas was estimated at $15\%\,\mathrm{wk}^{-1}$ (Rothlisberg et al. 1983, p. 529).

In a preliminary study of *Penaeus latisulcatus* dispersion in Spencer Gulf, Noye et al. (1992) provided a mortality estimate in the following manner. Assuming only one successful spawning for each female in a population involving equal numbers of adult males and females, and a balance in population dynamics, only two out of 500,000 eggs need to develop into adults in order to maintain prawn numbers, if one assumes this to be the average fecundity. Following Rothlisberg et al. (1983), they estimated that only 0.1% of the spawned eggs must reach the nursery areas (after 21 d in Noye et al.'s case) to maintain a stable population level (Rothlisberg et al. 1983, p. 529). Thus a mortality rate of approximately $3.8 \times 10^{-6}\,\mathrm{s}^{-1}$ was suggested as being applicable during this period. The small number of prawn larvae that survive and reach the nursery grounds is thus offset by the high fecundity of female adults. It is interesting to note that only two out of the surviving 500 postlarvae are required to develop through the remaining prawn life stages, into adults capable of successful spawning, to achieve the desired population balance. This implies an average postlarval stage to spawning stage mortality of not greater than 0.4% during that period.

For all the results given by the simulations of Richards et al. (1995), the mortality rate was constant at $0.02\,\mathrm{h}^{-1}$ ($0.48\,\mathrm{d}^{-1}$). At this rate approximately 38% of the larvae die per day (Richards et al. 1995, p. 64). This rate, however, may be greater than the "typical" rate

experienced by most species (Richards 1995, personal communications).

Two values for instantaneous *P. latisulcatus* larvae mortality in Spencer Gulf were supplied by SARDI fisheries officers. During the protozoea stage (0 to 15 d inclusive) mortality is approximately $0.299\,\mathrm{d}^{-1}$, while during the mysis stage (15 to 28–30 d inclusive) mortality is approximately $0.058\,\mathrm{d}^{-1}$ (Carrick 1994, personal communications).

7.7.6 Variable Mortality

McGurk's conclusion that predation, controlled or modified by offshore dispersal or population density, may be the dominant agent of mortality for some cohorts, supports aspects of previous work (McGurk 1989, p. 15), in that some of the conclusions reached by previous authors are similar to those reached by McGurk's study. These were that: (1) total mortality is sometimes highly variable between cohorts or between seasons; (2) starvation mortality occurs over a relatively short period of time soon after the exhaustion of yolk reserves; and (3) although starvation may be the major source of mortality in first-feeders, it may not be the dominant agent of mortality over the entire larval period, implying that variation in total mortality may not always be due to variation in starvation mortality (McGurk 1989, p. 16). All of these conclusions, except the first, support the hypothesis that mortality in young larvae is a multi-factor process, with starvation being only one of several factors. The first conclusion is, however, supported by McGurk's finding that the principal cause of death for fish larvae hatched from spawn was their passive transport by inshore water currents to the open sea (McGurk 1989, p. 15). It should be noted that this particular cause of larval mortality is, however, quite the reverse for *P. latisulcatus* larvae in Spencer Gulf, where prawn larvae are spawned in the "open sea" and are (hopefully) transported to suitable nursery areas by the time they mature to the postlarval/juvenile stage. The corresponding principal cause of death, in this instance, is a combination of two factors. First, some larvae may be transported by offshore water currents to a biologically undesirable inshore area, which is the inverse of the principal cause of death of which McGurk speaks. Second, some larvae may indeed be transported by water currents to the open sea (beyond the open boundary of the numerical model at the Gulf mouth), although numerical simulations reported in Sections 10.2, 10.3, and 10.4 indicate that this effect is not significant for *P. latisulcatus* larvae in Spencer Gulf.

The absolute importance of "infant" mortality in marine species is neatly summed up in the following statement.

> In fishes, for example, it is widely believed that usual egg and larval mortality is on the order of 99.99% of eggs spawned and fertilised. Given that larval mortality, from whatever the cause, will be likely to vary, at least slightly, from time to time and place to place, it is clear that recruitment to the juvenile stage must show relatively much more extreme variations. This occurs because survivorship (about 0.01% of eggs spawned) is proportionally so much smaller than is larval mortality yet shares the same absolute variance. In such species, recruitment will vary to a marked degree, even if production of fertilised eggs were completely constant from one breeding occasion to the next (Sale 1990, p. 26).

These points, it could be argued, are likely to be equally valid for juvenile recruitment in prawn species.

7.7.7 Mortality Variability

The time-independent and time-dependent rates for larval mortality quoted in this section are listed in Tables 7.2 and 7.3, respectively. These mortality rates are also plotted in Figures 7.14(a) and 7.14(b), respectively. For the McGurk (1989) starving mortality rates, a linear increase is assumed in the first period to 7 d, followed by a constant rate for 2 d, then a linear decrease to 20 d and finally a constant rate for the remaining period, as plotted by a dashed line in

Time-Independent Larval Mortality Rates				
Reference (bibliographic)	Species (scientific name)	Comment (distinctive)	Value (d^{-1})	Symbol (Figures 7.14(a)/(c))
Hill (1990)	*Nephrops norvegicus*	lower bound	0.03	cross
Hill (1990)	*Nephrops norvegicus*	upper bound	0.04	cross
Jackson and Strathmann (1981)	*Calanus*	-	0.65	triangle
Jackson and Strathmann (1981)	*Halicarcinus*	-	0.034	triangle
McGurk (1989)	*Clupea harengus pallasi*	total 1981	0.02	square
McGurk (1989)	*Clupea harengus pallasi*	total 1982	0.16	square
Noye et al. (1992)	*Penaeus latisulcatus*	-	0.329	pentagon
Richards et al. (1995)	indeterminate species	-	0.48	hexagon
Rothlisberg et al. (1983)	various *Penaeus* species	-	0.022	circle

Table 7.2: Time-independent larval mortality rates.

Time-Dependent Larval Mortality Rates					
Reference (bibliographic)	Species (scientific name)	Comment (distinctive)	Period (days)	Value (d^{-1})	Symbol/Line (Figures 7.14(b)/(d))
Carrick (1994)	*Penaeus latisulcatus*	protozoea	0–15	0.299	cross/solid
Carrick (1994)	*Penaeus latisulcatus*	mysis	15–30	0.058	cross/solid
Carrick (1994)	*Penaeus latisulcatus*	-	7.5	0.299	triangle/dashed
Carrick (1994)	*Penaeus latisulcatus*	-	22.5	0.058	triangle/dashed
McGurk (1989)	*Clupea harengus pallasi*	starving	0	0.0	square/dashed
McGurk (1989)	*Clupea harengus pallasi*	starving	5	1.0	square/dashed
McGurk (1989)	*Clupea harengus pallasi*	starving	7	1.0	square/dashed
McGurk (1989)	*Clupea harengus pallasi*	starving	20	0.0	square/dashed

Table 7.3: Time-dependent larval mortality rates.

Figure 7.14(b). In order to determine the effect of a continuous rate decrease, as well as the discrete rates supplied by Carrick (1994, personal communications), mortality rates were also calculated assuming a linear rate decrease defined by the two rates supplied, specified at the mid-points of the appropriate periods, as also plotted by a dashed line in Figure 7.14(b). On inspection of the figures, it is apparent that the mortality rates reported in the literature vary dramatically, as can be appreciated by the use of logarithmic scales on the vertical axes of Figures 7.14(a)–7.14(b). The effect of the different mortality rates on larval numbers can be determined from the plots of Figures 7.14(c)–7.14(d). In deriving these, it is assumed that larval patches follow exponential decay of the form

$$\frac{\partial C}{\partial t} = -m(t)C, \tag{7.7.1}$$

which can be derived from the two-dimensional advection–diffusion–mortality equation (7.8.5) used in many larval modelling studies, with zero advection and diffusion in both Cartesian directions. Here, larval concentration is denoted by $C(t)$ and has units of individuals, and the time-dependent mortality rate is denoted by the function $m(t)$ and has units of individuals per day. The general solution to (7.7.1) is

$$C(t) = C_0 \exp\left\{-\int_0^t m(\tau)d\tau\right\}, \quad C_0 = C(0), \tag{7.7.2}$$

in which $t = 0$ defines the beginning of the time period for which mortality rates are known and larval concentrations are required. For constant or linear mortality rates of the form

$$m(t) = m_1 t + m_0, \tag{7.7.3}$$

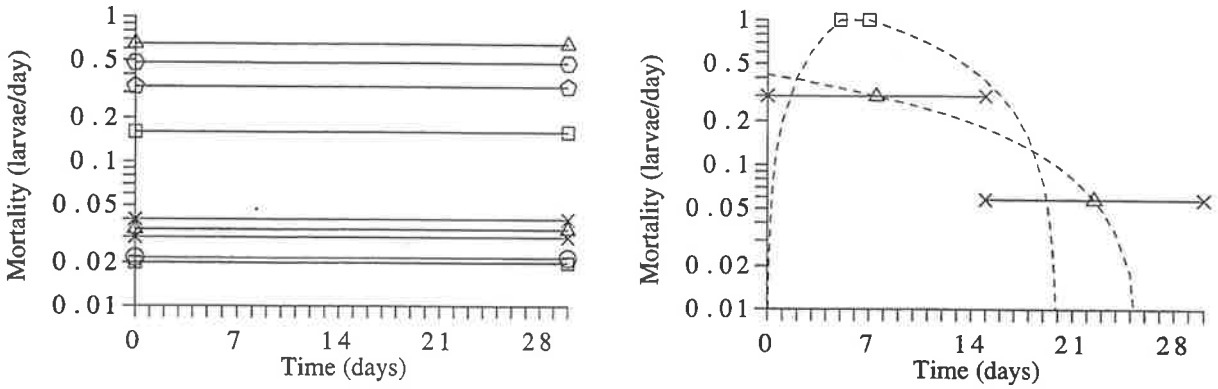

(a) Time-independent mortality rates

(b) Time-dependent mortality rates

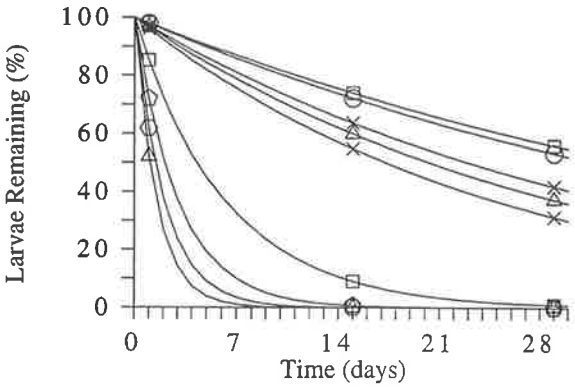

(c) Time-independent mortality abundance

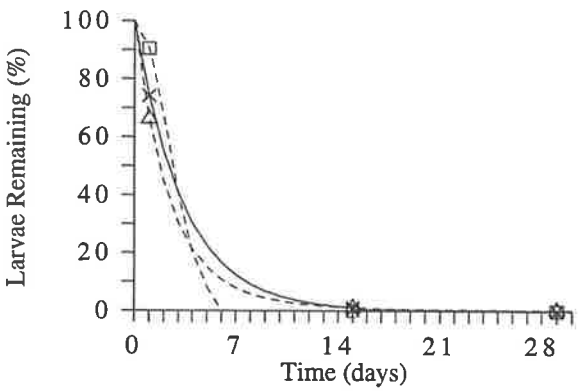

(d) Time-dependent mortality abundance

Figure 7.14: Larval mortality rates and resulting abundances.

with values for the constants m_0 and m_1 to define the mortality rate function,

$$C(t) = C_0 \exp\left\{-\left(0.5m_1t^2 + m_0t\right)\right\}, \quad C_0 = C(0), \tag{7.7.4}$$

is the solution to (7.7.1). In Figures 7.14(c)–7.14(d), appropriate symbols (consult Tables 7.2–7.3) have been used to mark points corresponding to larvae remaining after 1, 15, and 29 d, in order to indicate the effect of each mortality rate during the beginning, middle, and end of the larval period. It is apparent from Figure 7.14(c) that a small difference in constant mortality rate can have a significant effect on the number of larvae remaining, particularly near the mid-point of the dispersion period. From Figure 7.14(d) it is also apparent that there is little qualitative, but significant quantitative difference between the effect of the discrete mortality rates (solid line) of Carrick (1994, personal communications) and the continuous mortality rates (dashed line) derived from these. For both of these mortality regimes larvae numbers are almost negligible after the 29 d postulated as the duration of the larval period, but do not quite fall to the 0.1% of the spawned eggs as suggested by Rothlisberg et al. (1983). The remaining larvae are, in fact, approximately 0.22% and 0.42% in the discrete and continuous cases, respectively. For the starving mortality of McGurk (1989), larvae numbers are negligible, by this criterion, between days 5 (8.22%) and 6 (0.02%).

7.7.8 Summary

According to Okubo (1980), the mortality of eggs or larvae must be taken into account in any discussion of their dispersal patterns; however, the variance of the spatial distribution from

an instantaneous source would not be altered by mortality, provided the process is density-independent. The variance will also be influenced by mortality if it is density-dependent or if the source is continuous (Okubo 1980). Thus, the close interaction between spawning, mortality, and dispersion processes is well apparent.

Some factors influencing larval mortality were presented above with reference to both theoretical discussions in the literature and practical measurements in the field. Prawn larvae mortality rates were obtained from SARDI, and from the literature on prawn biology. Some larval abundances were calculated using both different prawn larvae mortality rates and periods to which these rates apply. It was found that the effect of a small change in mortality rate can be a comparatively large change in the number of larvae remaining after a given time period.

It should be noted that all larval mortality rates presented here were reported as constant in space, and only very few were reported as variable in time. Spatially independent mortality can be affected via an appropriate scaling during post-processing of any larval dispersion modelling results and will not effect the *relative* abundances resulting from dispersion simulations. It is for this reason that it was decided to not include mortality effects in the larval dispersion simulations reported in this thesis. Other larval dispersion studies in which a 100% survival rate was assumed so that the interpretation of results was simplified and/or since adequate biological data were unavailable include those of McShane et al. (1988), Bartsch et al. (1989), Johnson and Hess (1990), and Black and Moran (1991). As a result of this decision, the mortality coefficient of (7.1.1) is defined by

$$\lambda = M(x, y, t) = 0\,\mathrm{s}^{-1} \tag{7.7.5}$$

to represent zero larval loss.

Consequent to the exclusion of mortality effects, all results reported in this thesis are to be interpreted as depicting larval concentrations relative to the initial larval concentration, and thus results are expressed in the same units as the initial conditions derived in Sections 2.1.4–2.1.5 from data supplied by SARDI research officers, i.e. millions per nautical mile.

7.8 The Advection–Diffusion–Mortality Model

Equation (7.1.1) is two-dimensional and treats all variables as depth-averaged values, so solutions to this equation specifically apply if the larvae behave in one of two ways. First, the larvae are neutrally buoyant and well mixed (evenly distributed) throughout the water column from the surface to the bottom. In this case the input parameters to the model, such as the horizontal current velocities and the horizontal dispersion coefficients, are depth-averaged values. Second, larvae maintain themselves within a bounded region in the vertical and they are evenly distributed within this region. Here, depth, current, and diffusion values represent averages over the region where the larvae reside. Taking into account the points discussed in Sections 2.4 and 7.3, it is this second alternative that is assumed.

In making this assumption, the total water depth $H(x, y, t)$ in (7.1.1) represents the thickness of the bounded region. This region is considered to be represented by a depth–level number η_k (see Section 3.2.2) of depth–interval thickness $\Delta\eta_k$ (see (3.2.1)) in the η vertical coordinate (see (3.1.11)), in which k specifies the appropriate depth level and interval. The definition of

$$\hat{\tau}(x, y, t) = \Delta\eta_k(x, y, t)C(x, y, t) \tag{7.8.1}$$

as the depth-integrated larval concentration within the depth–interval at which the larval cloud resides at time t, which by definition is the product of the depth-averaged concentration per unit volume and the depth–interval thickness, thus applies. In the following, then, $\hat{\tau}$ will be considered to have units of m^{-2} to emphasise that larval concentrations are, in this manner, depth-integrated.

At the particular depth–level η_k occupied by the larval cloud at any particular instant t, the depth-averaged velocity components $U(x, y, t)$ and $V(x, y, t)$ in (7.1.1) represent the velocity

within the bounded depth–interval $\Delta\eta_k$. The definitions of

$$U(x,y,t) = u(x,y,\eta_k,t) \quad \text{and} \quad V(x,y,t) = v(x,y,\eta_k,t) \tag{7.8.2}$$

thus apply at a specific depth level and interval k. During the process of determining a solution to the ADM equation it is also assumed, at least in the local vicinity in which this solution is being computed, that

$$u\frac{\partial\hat{\tau}}{\partial x} \gg \hat{\tau}\frac{\partial u}{\partial x} \tag{7.8.3}$$

and

$$v\frac{\partial\hat{\tau}}{\partial y} \gg \hat{\tau}\frac{\partial v}{\partial y} \tag{7.8.4}$$

are applicable.

Taking into account the points discussed in Sections 7.3–7.7, in general, and the variables defined by equations (7.6.23)–(7.6.24), (7.7.5), and (7.8.1)–(7.8.4), in particular, the original partial differential equation (7.1.1) governing ADM processes is able to be simplified considerably. The 2D ADM partial differential equation (PDE)

$$\frac{\partial\hat{\tau}}{\partial t} + u\frac{\partial\hat{\tau}}{\partial x} + v\frac{\partial\hat{\tau}}{\partial y} - \alpha_x\frac{\partial^2\hat{\tau}}{\partial x^2} - \alpha_y\frac{\partial^2\hat{\tau}}{\partial y^2} + \lambda\hat{\tau} = 0 \tag{7.8.5}$$

is thus considered to be applicable at the appropriate depth–interval. In this context: $\hat{\tau}(x,y,t)$ is the number, at position (x,y) and time t, of larvae per unit area of the x-y horizontal transformed coordinate plane; $u(x,y,t)$ and $v(x,y,t)$ are x and y horizontal velocity components, respectively; $\alpha_x(x,y,t)$ and $\alpha_y(x,y,t)$ are x and y horizontal eddy diffusion coefficients, respectively; $\lambda(x,y,t)$ is a parameter specifying larval loss through mortality, per unit area and time; and all other variables have been previously defined.

Given the elongated configuration of Spencer Gulf, tidal currents are fundamentally one-dimensional (1D) and essentially oscillate parallel to the major (y) axis with, typically, little lateral movement for most of the 12 h (semi-diurnal) tidal cycle. However, small space– and time–scale inhomogeneities in the current structure which appear as localised tidal eddies resulting from bathymetric, coastal topographic, and Coriolis effects, and large space– and time–scale residual circulations which result from surface wind–stress during episodic meteorological events are also observed. In the following Spencer Gulf simulations, these currents are accurately determined by the coarse and fine grid tidal models of Section 3.4 and Chapter 6, respectively. In other simulations of idealised "gulfs", currents are specified by analytical means.

In the following Spencer Gulf simulations, horizontal eddy diffusion is considered constant with $\alpha_x = \alpha_y = 100\,\mathrm{m^2 s^{-1}}$, as discussed in Section 7.6. In other simulations of idealised "gulfs", diffusion is also specified as constant in both directions.

In the following, larval mortality is also considered constant, as discussed in Section 7.7. The effect of constant λ is to scale larval concentrations by $\exp\{-\lambda t\}$ after a time t from release. Since this can be accounted for in post-processing, and relative larval concentrations only are considered here, $\lambda = 0\,\mathrm{s^{-1}}$ is assumed without loss of generality.

7.9 Summary

It is becoming increasingly evident that a more complete understanding of dispersal processes and their impact upon recruitment will come only through an integrated approach which recognises that there is a spectrum of physical phenomena which affect the organism at different spatial and temporal scales (Dight et al. 1990a, p. 122). In this chapter, the major phenomena affecting *Penaeus latisulcatus* dispersal in Spencer Gulf were identified and discussed, and then abstracted to formulations readily represented in a mathematical model by the model variables. With advection, diffusion, and mortality coefficients in this model specified, (7.8.5) can now be solved using numerical methods. A selection of these are developed and tested in Chapter 8.

Chapter 8

The Advection–Diffusion Model

In this chapter, finite-difference methods approximating the constant coefficient advection–diffusion partial differential equation (PDE) in one and two dimensions are presented, in Sections 8.1 and 8.5, respectively. Convergence, consistency, stability, and other properties of each finite-difference equation (FDE) corresponding to a finite-difference method (FDM) approximating these PDEs are presented and compared.

In Section 8.2.1 a FDM for approximately solving the one-dimensional (1D) advection–diffusion equation is discussed. In Section 8.7.4 it is used to derive a FDM for approximately solving the two-dimensional (2D) advection–diffusion equation.

In Section 8.3 a FDM approximating the 1D constant coefficient advection equation is also presented, in a similar manner to those solving the advection–diffusion equations.

In the following sections, a FDM is termed a "(k,l,m) method" if the associated FDE involves k, l, and m grid–points at the $(n+1)$, n, and $(n-1)$ time–levels, respectively and is termed a "p-level method" if the FDE involves grid–points at the p time–levels $(n+1), n, \ldots, (n-p+2)$. A FDM is also termed a "q-point method" where q is defined to be the maximum of k, l, and m.

8.1 One-Dimensional Advection–Diffusion

The 1D advection–diffusion equation, used to describe the transport of passive scalars in a moving fluid, may be scaled and written in the form

$$\frac{\partial \hat{\tau}}{\partial t} + u\frac{\partial \hat{\tau}}{\partial x} - \alpha\frac{\partial^2 \hat{\tau}}{\partial x^2} = 0, \tag{8.1.1}$$

where $\hat{\tau}(x,t)$ may represent, for example, a pollutant concentration at position x and time t.

In the following, $\alpha > 0$ and u are considered to be constants quantifying the diffusion and advection processes, respectively. The PDE (8.1.1) has been used to describe transport in studies of: thermal pollution in river systems (Chaudhry et al. 1983); dispersion of dissolved salts in groundwater (Guvanasen and Volker 1983); flow in porous media (Kumar 1983); adsorption of chemicals into beds (Lapidus and Amundson 1952); and dispersion of contaminants in estuaries and coastal seas (Noye 1987a).

The solution domain of the problem is covered by a mesh of grid–lines $t = n\Delta t, n = 0,1,\ldots,N$, and $x = j\Delta t, j = 0,1,\ldots,J$, parallel to the space and time coordinate axes, respectively. Approximations τ_j^n to $\hat{\tau}(j\Delta x, n\Delta t)$ are calculated at the points of intersection of these lines, namely, $(j\Delta x, n\Delta t)$ which is referred to as the (j,n) grid–point. In the following, the approximation to the derivative $\frac{\partial^p \hat{\tau}(j\Delta x, n\Delta t)}{\partial x^p}$ is denoted $\left.\frac{\partial^p \tau}{\partial x^p}\right|_j^n$.

8.1.1 Equivalent and Modified Equivalent Partial Differential Equations

Consider the FDE

$$\mathcal{L}_\Delta\{\tau_j^n\} = 0, \tag{8.1.2}$$

which is consistent with the given PDE (8.1.1), in which $\mathcal{L}_\Delta$ is a 1D finite-difference operator. If

$$\left.\frac{\partial \hat{\tau}}{\partial t}\right|_j^n + u \left.\frac{\partial \hat{\tau}}{\partial x}\right|_j^n - \alpha \left.\frac{\partial^2 \hat{\tau}}{\partial x^2}\right|_j^n = 0, \tag{8.1.3}$$

represents PDE (8.1.1) evaluated at the (j,n) grid–point, each term can be approximated by a finite-difference form. For example, if the first-order convergent forward-time (FT) difference form is used for the temporal derivative, the second-order centred-space (CS) form for the spatial derivative in the advection term, and the second-order centred-space form for the spatial derivative in the diffusion term, (8.1.3) becomes

$$\begin{aligned}\left(\frac{\hat{\tau}_j^{n+1} - \hat{\tau}_j^n}{\Delta t} + \mathrm{O}\left\{\Delta t\right\}\right) + u\left(\frac{\hat{\tau}_{j+1}^n - \hat{\tau}_{j-1}^n}{2\Delta x} + \mathrm{O}\left\{(\Delta x)^2\right\}\right) \\ - \alpha\left(\frac{\hat{\tau}_{j+1}^n - 2\hat{\tau}_j^n + \hat{\tau}_{j-1}^n}{(\Delta x)^2} + \mathrm{O}\left\{(\Delta x)^2\right\}\right) = 0,\end{aligned} \tag{8.1.4}$$

in which Taylor series expansions were used to derive these forms and determine their convergence.

Rearranging (8.1.4) yields an equation of the form (8.1.2), wherein

$$\mathcal{L}_\Delta\{\tau_j^n\} = \frac{1}{2}(2s+c)\tau_{j-1}^n + (1-2s)\tau_j^n + \frac{1}{2}(2s-c)\tau_{j+1}^n - \tau_j^{n+1}, \tag{8.1.5}$$

which is consistent with PDE (8.1.1) with an apparent *discretisation error* of $\mathrm{O}\left\{(\Delta x)^2, \Delta t\right\}$. Rearranging (8.1.2) with (8.1.5) yields

$$\tau_j^{n+1} = \frac{1}{2}(2s+c)\tau_{j-1}^n + (1-2s)\tau_j^n + \frac{1}{2}(2s-c)\tau_{j+1}^n, \tag{8.1.6}$$

which is the explicit forward-time centred-space (FTCS) type finite-difference equation.

The coefficients of the terms in FDE (8.1.2) and (8.1.5)–(8.1.2) are functions of the *Courant* and *diffusion* numbers

$$c = u\Delta t/\Delta x \tag{8.1.7}$$

and

$$s = \alpha\Delta t/(\Delta x)^2 \geq 0, \tag{8.1.8}$$

respectively. Note that, since in the following analyses u, α, Δt, and Δx are all constant, c and s are fixed. In the following FDM analyses and numerical tests, it should also be noted that two values for the 1D diffusion number s of (8.1.8) are used. These are determined by

$$s = 100 \times 3600/(5715)^2 \approx 0.011 \tag{8.1.9}$$

and

$$s = 100 \times 1200/(1905)^2 \approx 0.033, \tag{8.1.10}$$

which are in turn determined by the parameters chosen for the coarse and fine grid Spencer Gulf models of Section 3.4 and Chapter 6, respectively.

Expanding each term of FDE (8.1.2) in Taylor series about the (j,n) grid–point yields the *equivalent partial differential equation* (EPDE)

$$\frac{\partial \tau}{\partial t} + u\frac{\partial \tau}{\partial x} - \alpha\frac{\partial^2 \tau}{\partial x^2} + E = 0, \tag{8.1.11}$$

in which

$$E = \sum_{p=2}^{\infty} \sum_{q=0}^{p} C_{q,p-q} \frac{\partial^p \tau}{\partial x^q \partial t^{p-q}}, \tag{8.1.12}$$

without loss of generality. For example, FDE (8.1.2) with (8.1.5) yields

$$\frac{\partial \tau}{\partial t} + u\frac{\partial \tau}{\partial x} - \alpha\frac{\partial^2 \tau}{\partial x^2} + \frac{1}{2}\Delta t \frac{\partial^2 \tau}{\partial t^2} + \mathrm{O}\left\{(\Delta x)^2, (\Delta t)^2\right\} = 0, \tag{8.1.13}$$

indicating that the FTCS FDE (8.1.6) has an EPDE given by (8.1.11)–(8.1.12) with

$$C_{0,2} = \Delta t/2, \quad C_{1,1} = C_{0,2} = 0, \tag{8.1.14}$$

to leading order.

The leading terms in E given by (8.1.12)—called the *truncation error* of FDE (8.1.2) relative to PDE (8.1.1)—contain derivatives with respect to both space and time, and the magnitude of these terms indicate the order of accuracy and convergence of the resulting FDM. However, errors introduced through spatial discretisation may cancel with errors introduced through temporal discretisation by considering the *modified equivalent partial differential equation* (MEPDE), found by converting all time derivatives in (8.1.12) into derivatives with respect to space (Warming and Hyett 1974). An efficient computational procedure for achieving this is described in Noye and Hayman (1986).

In this way it is found that all FDEs which are consistent with PDE (8.1.1) have MEPDEs of the form (8.1.11) in which the truncation error E may be re-written

$$E = u\sum_{p=2}^{\infty} \frac{(\Delta x)^{p-1}}{p!} \eta_p(c,s) \frac{\partial^p \tau}{\partial x^p}, \tag{8.1.15}$$

without loss of generality. For example, the Warming and Hyett (1974) procedure applied to the EPDE (8.1.13) results in the MEPDE

$$\frac{\partial \tau}{\partial t} + u\frac{\partial \tau}{\partial x} - \alpha\frac{\partial^2 \tau}{\partial x^2} - \frac{uc\Delta x}{2}\frac{\partial^2 \tau}{\partial x^2} + \mathrm{O}\left\{(\Delta x)^2\right\} = 0, \tag{8.1.16}$$

indicating that the FTCS FDE (8.1.6) has a MEPDE given by (8.1.11), (8.1.15) with

$$\eta_2(c,s) = c, \tag{8.1.17}$$

to leading order. The FDE (8.1.6) is thus second-order convergent. This example is in fact an illustration of the cancellation of errors discussed above, since in this case a FDE constructed using first-order differencing in time and second-order differencing in space resulted in a FDM of overall second-order convergence.

8.1.2 Convergence, Consistency, Stability, and Non-Negativity

A FDM which approximates a given PDE is said to be *convergent* if, at each point in the solution domain, the finite-difference solution approaches the exact solution in the limit as $\Delta x, \Delta t \to 0$. By the Lax equivalence theorem (Lax and Richtmyer 1956) a FDE which is consistent, in this limit, with a linear PDE representing a well posed initial boundary value problem is convergent if and only if the FDE remains stable in the same limit. The von Neumann method of analysis (O'Brien et al. 1950) determines stability of a FDE governing transport of a scalar in just such a limit, whereas the frequently used matrix stability analysis (Smith 1985) is based on a fixed temporal grid–spacing with the number of time iterations, N, tending to infinity. In order to use the equivalence theorem to ensure convergence, the former stability analysis is chosen.

The *von Neumann stability analysis* is based on the condition

$$|G(N_\lambda)| \leq 1 + \mathrm{O}\{\Delta t\}, \qquad N_\lambda \geq 2, \tag{8.1.18}$$

where N_λ is the number of grid–spacings, Δx, in the wavelength, λ, of a component wave of $\hat{\tau}(x,0)$. The function G, the so called *von Neumann amplification factor*, is obtained by means of the substitution

$$\tau_j^n = (G)^n \exp\left\{\iota\left(\frac{2\pi j}{N_\lambda}\right)\right\}, \qquad \iota = \sqrt{-1}, \tag{8.1.19}$$

into FDE (8.1.2). The FDM is stable, in the von Neumann sense, if the roots of the resulting polynomial in G are such that $|G(\beta)| \leq 1$ for all $\beta \in [0, 2\pi]$, where $\beta = 2\pi/N_\lambda$. Criteria on the coefficients of the polynomial for this to be true are given in Noye (1990).

It is sometimes important that the numerical solution of a PDE and its associated initial and boundary conditions reflects a particular property of the exact solution of the system represented. For instance, when PDE (8.1.1) is used to predict the spread of pollutants, it is essential for the predicted values to be either positive or zero since negative concentrations have no physical meaning. Clearly, an explicit FDE approximating a PDE with non-negative initial and boundary conditions will produce non-negative values if all the coefficients on the right-hand side of the explicit equation are themselves non-negative (Noye 1988). It should be emphasised that this *non-negativity* criterion is a sufficient but not necessary condition.

All FDMs considered in this section have non-negative and von Neumann stability regions which are symmetrical about $c = 0$. In the following then, the region in the first quadrant of the c-s plane in which FDMs are non-negative, as well as von Neumann stable, will be determined.

8.1.3 Wave Propagation Characteristics

As a means of estimating the accuracy of a FDM, an investigation of the changes to the amplitude and wave speed of an initial infinite travelling wave of unit amplitude which is propagating according to PDE (8.1.1) is made. The *amplitude response* ζ, which is the ratio of the numerical amplitude a_N to the true amplitude a_T, after the wave has travelled one wavelength, together with the *relative wave speed* μ, which is the ratio of the numerical wave speed u_N to the true wave speed u, are parameters which indicate the accuracy of FDE (8.1.2). The coefficients of the truncation error terms of the MEPDE corresponding to a FDE are related to ζ and μ as follows. The reader is directed to Noye (1984a) for a detailed derivation of a_T, a_N, ζ, u_N, and μ from first principles, considering the traversal of the true and numerical waves.

The amplitude response $\zeta = a_N/a_T$, given in terms of G, is

$$\zeta(c, s, N_\lambda) = |G(c, s, N_\lambda)|^{N_\lambda/c} \exp\left\{\frac{4\pi^2 s}{cN_\lambda}\right\}, \tag{8.1.20}$$

whereas in terms of the $\eta_p(c,s)$ functions in MEPDE (8.1.11), (8.1.15), it is given by

$$\zeta(c, s, N_\lambda) = \exp\left\{2\pi \sum_{r=1}^{\infty} \frac{(-1)^{r+1}}{(2r)!}\left(\frac{2\pi}{N_\lambda}\right)^{2r-1} \eta_{2r}(c, s)\right\}, \tag{8.1.21}$$

in which exp is the exponential of the real variable. The relative wave speed $\mu = u_N/u$, given in terms of G, is

$$\mu(c, s, N_\lambda) = -\frac{N_\lambda}{2\pi c} \arg\{G(c, s, N_\lambda)\}, \tag{8.1.22}$$

whereas in terms of the $\eta_p(c,s)$ functions in MEPDE (8.1.11), (8.1.15), it is given by

$$\mu(c, s, N_\lambda) = 1 + \sum_{r=1}^{\infty} \frac{(-1)^r}{(2r+1)!}\left(\frac{2\pi}{N_\lambda}\right)^{2r} \eta_{2r+1}(c, s), \tag{8.1.23}$$

in which arg is the argument of the complex variable. From (8.1.21) and (8.1.23), it is clear that the error in modelling wave amplitude is associated with even-order derivatives in the MEPDE, and that the error in modelling wave speed is associated with odd-order derivatives. Note that (8.1.21) and (8.1.23) only hold for large N_λ—clearly $\zeta \to 1$ and $\mu \to 1$ as $N_\lambda \to \infty$. In particular, ζ and μ approach unity faster for high-order than for low-order convergent FDMs.

In obtaining the wave propagation graphs in the following, values of the amplitude response and relative wave speed for the FDM under discussion were obtained by application of (8.1.20) and (8.1.22), respectively. These are plotted for various Courant numbers within the FDM's von Neumann stability range. The value of N_1—the largest N_λ for which there was an error of at least 1% in the respective wave propagation parameter ζ or μ—was also calculated. Graphs of N_1 against c for values of s within the appropriate stability region are also plotted in the following figures.

8.2 One-Dimensional Advection–Diffusion Methods

In Nixon and Noye (1990) two implicit three-point three-level FDMs approximating PDE (8.1.1) were described. These were developed using differencing on a (3,1,1) computational stencil. One is unconditionally stable with second-order convergence, the other is conditionally stable with third-order convergence. In Nixon and Noye (1991), two explicit three-point three-level FDMs for PDE (8.1.1) were described. These were developed using differencing on a (1,3,1) computational stencil. One is conditionally stable with second-order convergence, the other is conditionally stable with third-order convergence. The four new FDMs were compared, theoretically and in numerical experiments, with the "leapfrog"/Du Fort and Frankel (1953) type (1,2,1) explicit FDM, the only three-level FDM presently employed to solve PDE (8.1.1). The new explicit FDMs were generally found to posess larger and more useful regions of stability than the Du Fort and Frankel (1953) type FDM. All four new FDMs involve no numerical diffusion and were generally found to be more accurate than the Du Fort and Frankel (1953) FDM.

In Section 8.2.1 a well-known, but less accurate, FDE approximating the 1D advection–diffusion equation is discussed. This two-level FDE has properties which, it will be demonstrated, determine it to be of great use in approximating the 2D advection–diffusion equation. This is achieved by what is termed *time-splitting* the solution of the two-dimensional problem into two one-dimensional FDE applications (see Noye and Hayman (1994), for example). Since time-splitting is not possible using three-level FDEs, and solution of the 2D rather than the 1D advection–diffusion equation is a major subject of this thesis, the four new FDMs discussed in the works referred to above will not be considered further here.

8.2.1 The Lax–Wendroff Type (1,3) Method

The Lax and Wendroff (1964) type FDE

$$\tau_j^{n+1} = [\{2s + c + c^2\}\tau_{j-1}^n + 2\{1 - 2s - c^2\}\tau_j^n + \{2s - c + c^2\}\tau_{j+1}^n]/[2] \qquad (8.2.1)$$

can be derived via a weighted MEPDE approach (similar to that outlined in Section 8.7.3), as was presented in Noye and Hayman (1986). It has a MEPDE of the form (8.1.11), (8.1.15), with $\eta_2(c,s) = 0$ and

$$\eta_3(c,s) = 1 - 6s - c^2, \quad \eta_4(c,s) = (12s^2 - 2s - 12sc^2 - 3c^4 + 3c^2)/c, \qquad (8.2.2)$$

indicating that it introduces no numerical diffusion. The FDE (8.2.1) is second-order convergent and, as this is the greatest order possible for a stencil involving only four grid–points, it is termed the *optimal* FDM for the (1,3) *computational stencil* shown in Figure 8.1(a)

A von Neumann stability analysis of FDE (8.2.1) gives

$$G(c,s,N_\lambda) = 1 - 2(2s + c^2)\sin\{\pi/N_\lambda\} - \iota(c\sin\{2\pi/N_\lambda\}) \qquad (8.2.3)$$

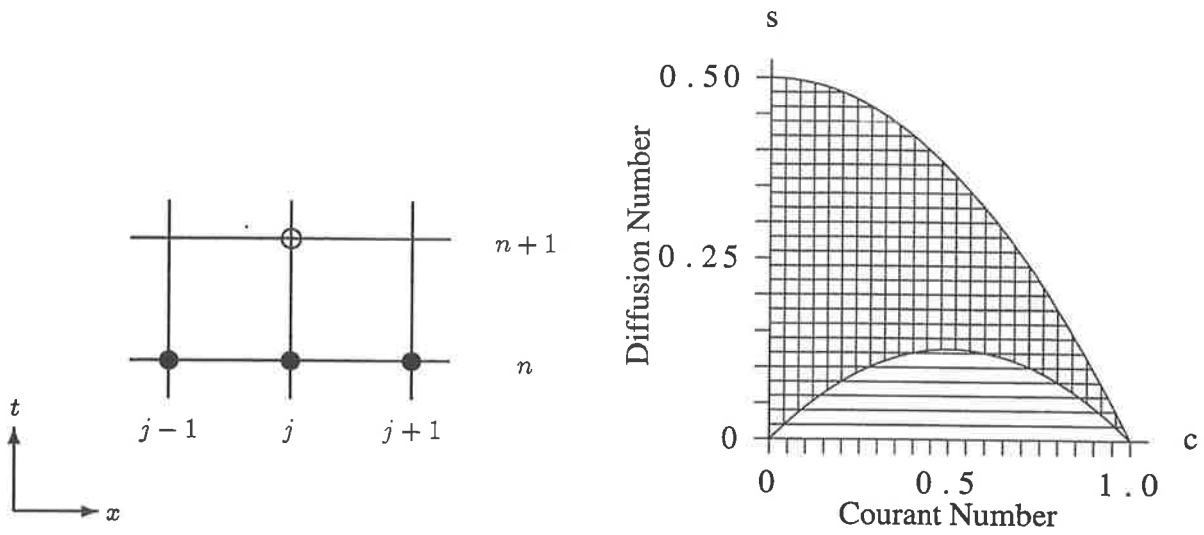

(a) the (1,3) stencil

(b) stability regions

Figure 8.1: The Lax–Wendroff type (1,3) FDE (8.2.1) computational stencil, von Neumann stable (horizontal hatching) region (8.2.4), and non-negative (vertical hatching) region (8.2.5).

as the amplification factor (Noye 1987b), which yields the stability region defined by

$$0 \leq s \leq (1 - c^2)/2, \tag{8.2.4}$$

as shown horizontally hatched in Figure 8.1(b). Within the region

$$|c|(1 - |c|)/2 \leq s \leq (1 - c^2)/2, \tag{8.2.5}$$

shown vertically hatched in Figure 8.1(b), the FDE (8.2.1) guarantees non-negative solutions (Noye 1991a). The relative wave speed associated with FDE (8.2.1) is

$$\mu(c, s, N_\lambda) = 1 - \frac{4\pi^2}{3N_\lambda^2}(1 - 6s - c^2) + \mathrm{O}\left\{(N_\lambda)^{-4}\right\}, \tag{8.2.6}$$

to leading order (Noye 1988). The amplitude response, to leading order, is given by

$$\zeta(c, s, N_\lambda) = 1 + \frac{2\pi^4(12s^2 - 2s - 12sc^2 - 3c^4 + 3c^2)}{3c(N_\lambda)^3} + \mathrm{O}\left\{(N_\lambda)^{-4}\right\}, \tag{8.2.7}$$

on expansion of (8.1.21). Wave propagation characteristics for FDE (8.2.1) with two diffusion numbers defined in (8.1.9) and (8.1.10)—determined by the coarse and fine grid parameters defined in Section 3.4 and Chapter 6, respectively—are plotted in Figure 8.2. Indicated in Figures 8.2(b) and 8.2(d) is the trend

$$\mu(c, s, N_\lambda) \to 1(\pm) \quad \text{for} \quad c^2 \gtrless 1 - 6s \quad \text{as} \quad N_\lambda \to \infty \tag{8.2.8}$$

since, from (8.2.2), (8.2.4), and (8.2.6), it can be seen that the choice of Courant number

$$c = \pm\sqrt{1 - 6s} \tag{8.2.9}$$

results in a FDM which is effectively third-order convergent for large N_λ (i.e. small Δx if λ fixed), is von Neumann stable, and has minimal wave speed error, respectively. For the time–steps, grid–spacings, and diffusion numbers corresponding to the coarse and fine grid models, (8.2.9) corresponds to constant advective velocity of $u \approx \pm 1.53\,\mathrm{m\,s^{-1}}$ ($c \approx \pm 0.97$) and $u \approx \pm 1.42\,\mathrm{m\,s^{-1}}$

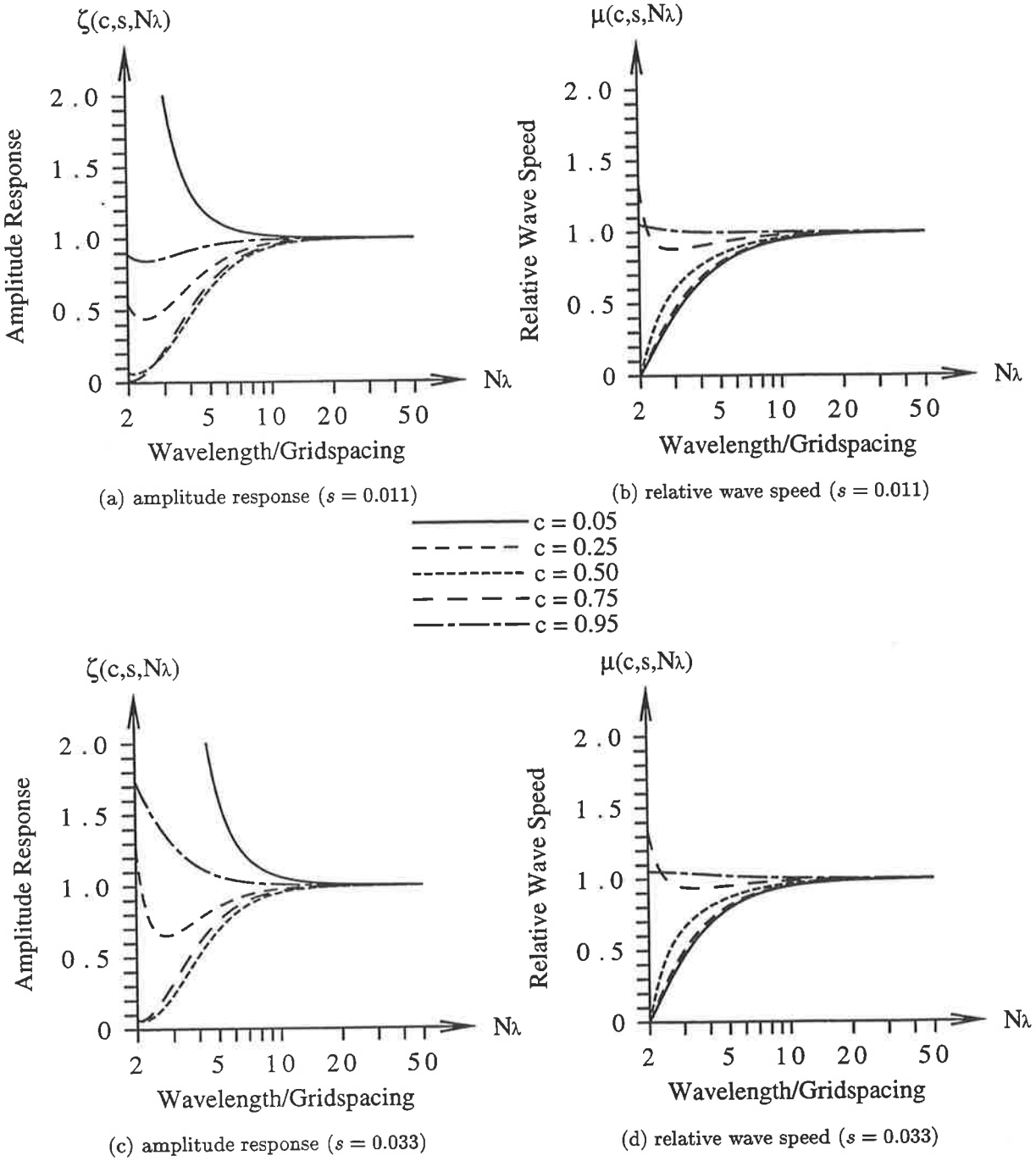

(a) amplitude response ($s = 0.011$)

(b) relative wave speed ($s = 0.011$)

(c) amplitude response ($s = 0.033$)

(d) relative wave speed ($s = 0.033$)

Figure 8.2: The Lax–Wendroff type (1,3) FDE (8.2.1) wave propagation characteristics.

($c \approx \pm 0.90$), respectively. Similarly, from (8.2.2), (8.2.4), and (8.2.7), it can also be shown that the choice of Courant numbers $c \approx \pm 0.085$ and ± 0.974 ($u \approx \pm 0.135$ and $\pm 1.546\,\mathrm{m\,s^{-1}}$) and $c \approx \pm 0.144$ and ± 0.920 ($u \approx \pm 0.229$ and $\pm 1.461\,\mathrm{m\,s^{-1}}$), corresponding to coarse and fine grid model parameters, respectively, results in a FDM which is von Neumann stable and has minimal amplitude error. In Figure 8.3, where the percentage error trends are also plotted, these facts are graphically illustrated for positive Courant numbers.

Note that the rapid N_1 increase for ζ as $c \to 0$ from the minima for small c is a result of the definition of amplitude response itself (see (8.1.20)), as well as characteristics specific to the LW FDE (see (8.2.7)). It should also be noted that during application of FDE (8.2.1) the Courant

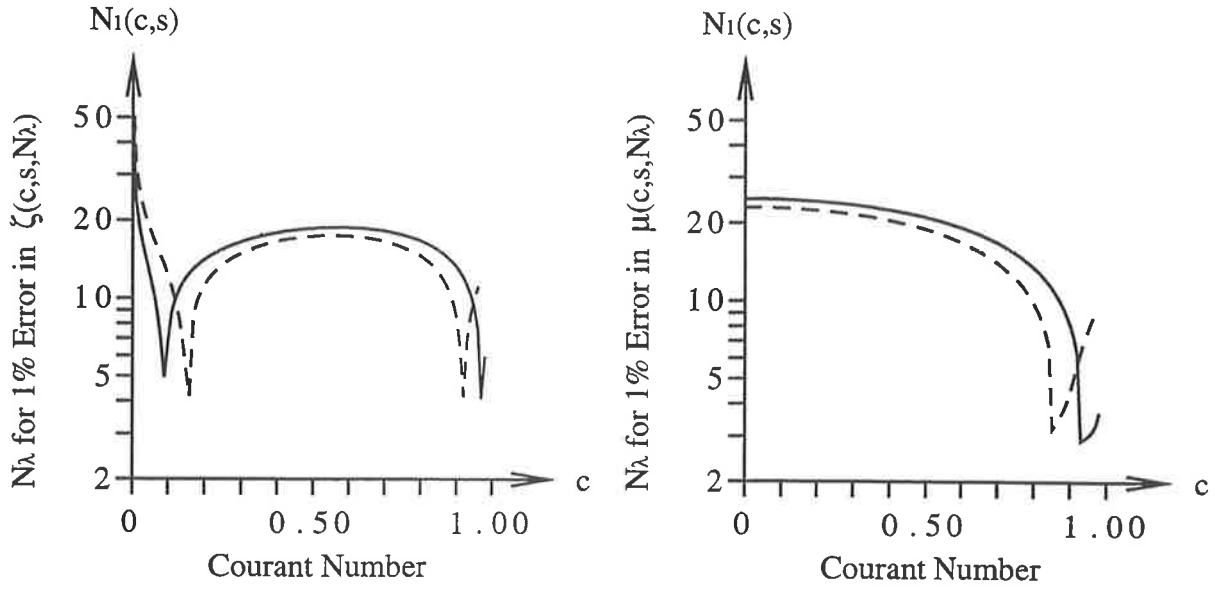

(a) amplitude response

(b) relative wave speed

Figure 8.3: The Lax–Wendroff type (1,3) FDE (8.2.1) percentage error trends for $s = 0.011$ (solid curve) and $s = 0.033$ (dashed curve).

number is

$$c|_j^n = u_j^n \Delta t/\Delta x \quad \text{where} \quad u_j^n = u(j\Delta x, n\Delta t), \tag{8.2.10}$$

since advective velocities are no longer constant.

8.3 One-Dimensional Advection

Consider the 1D advection equation

$$\frac{\partial \hat{\tau}}{\partial t} + u\frac{\partial \hat{\tau}}{\partial x} = 0 \tag{8.3.1}$$

with constant u. Following an argument analogous to that presented in Section 8.1.1, the MEPDE corresponding to a FDE (8.1.2) consistent with PDE (8.3.1) may be written

$$\frac{\partial \tau}{\partial t} + u\frac{\partial \tau}{\partial x} + u\sum_{p=2}^{\infty} \frac{(\Delta x)^{p-1}}{p!}\eta_p(c)\frac{\partial^p \tau}{\partial x^p}, \tag{8.3.2}$$

with the convergence, consistency, stability, and non-negativity of a FDE approximating this PDE also defined in an analogous manner as is discussed in Section 8.1.2.

In Section 8.4, wave propagation characteristics are plotted in a manner analogous to that outlined in Section 8.1.3. The characteristic functions themselves, however, are defined as follows (Noye 1984a). The amplitude response is given by

$$\zeta(c, N_\lambda) = |G(c, N_\lambda)|^{N_\lambda/c}, \tag{8.3.3}$$

in terms of the von Neumann amplification factor G determined by (8.1.19), and also by

$$\zeta(c, N_\lambda) = \exp\left\{2\pi \sum_{p=1}^{\infty}(-1)^{p-1}\left(\frac{2\pi}{N_\lambda}\right)^{2p-1}\frac{\eta_{2p}(c)}{(2p)!}\right\}, \tag{8.3.4}$$

in terms of MEPDE (8.3.2). The relative wave speed is given by

$$\mu(c, N_\lambda) = -\frac{N_\lambda}{2\pi c} \arg\{G(c, N_\lambda)\}, \tag{8.3.5}$$

in terms of G and also by

$$\mu(c, N_\lambda) = 1 + \sum_{p=1}^{\infty} (-1)^{2p-1} \left(\frac{2\pi}{N_\lambda}\right)^{2p} \frac{\eta_{2p+1}(c)}{(2p+1)!}, \tag{8.3.6}$$

in terms of MEPDE (8.3.2).

8.4 One-Dimensional Advection Methods

In Section 8.4.1, a FDM solving the 1D advection equation is presented. In Section 8.7 it is used to derive boundary conditions for use in FDMs solving the 2D advection–diffusion equation.

8.4.1 The "Box" Type (2,2) Method

Consider PDE (8.3.1) discretised at the grid–point $(x_{j-1/2}, t_{n+1/2})$, where $x_{j-1/2} = (j - 1/2)\Delta x$ and $t_{n+1/2} = (n + 1/2)\Delta t$, using the "box" type computational stencil of Figure 8.4. Using a

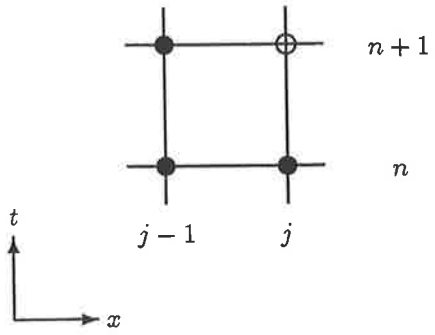

Figure 8.4: The "box" type (2,2) scheme computational stencil.

centred-time (CT) and centred-space (CS) differencing over this stencil, the FDE

$$\{1 - c\}\tau_{j-1}^{n+1} + \{1 + c\}\tau_j^{n+1} = \{1 + c\}\tau_{j-1}^{n} + \{1 - c\}\tau_j^{n} \tag{8.4.1}$$

is obtained. A derivation using this type of differencing is outlined in Section 8.8.1. Two alternative derivations of this FDM, both using a weighted differencing approach similar to that outlined in Section 8.7.3, can be found in Noye (1986) and Noye (1991b). Having a von Neumann amplification factor of

$$G(c, N_\lambda) = \frac{(1 - c)\exp\{\iota\pi/N_\lambda\} + (1 + c)\exp\{-\iota\pi/N_\lambda\}}{(1 + c)\exp\{\iota\pi/N_\lambda\} + (1 - c)\exp\{-\iota\pi/N_\lambda\}} \tag{8.4.2}$$

with a modulus of unity, the FDE (8.4.1) is unconditionally stable. This FDE never, however, guarantees non-negative non-trivial solutions. It has a MEPDE with dominant second-order error term with

$$\eta_3(c) = -(1 - c^2)/2, \quad \eta_5(c) = -(1 - c^2)(2 - c^2)/2, \tag{8.4.3}$$

and all even-indexed η coefficients identically zero. Therefore FDE (8.4.1) is second-order convergent with amplitude response

$$\zeta(c, N_\lambda) \equiv 1 \tag{8.4.4}$$

and relative wave speed

$$\mu(c, N_\lambda) = 1 + \frac{\pi^2(1-c^2)}{3(N_\lambda)^2} + \mathrm{O}\left\{(N_\lambda)^{-4}\right\}, \tag{8.4.5}$$

indicating that

$$\mu(c, N_\lambda) \to 1(\pm) \quad \text{for} \quad c^2 \lessgtr 1 \quad \text{as} \quad N_\lambda \to \infty \tag{8.4.6}$$

and hence that, for large N_λ, the numerical wave is too fast for $c^2 < 1$ and too slow for $c^2 > 1$. This is indicated in Figure 8.5 which shows the relative wave speed for $N_\lambda \geq 2$ obtained by

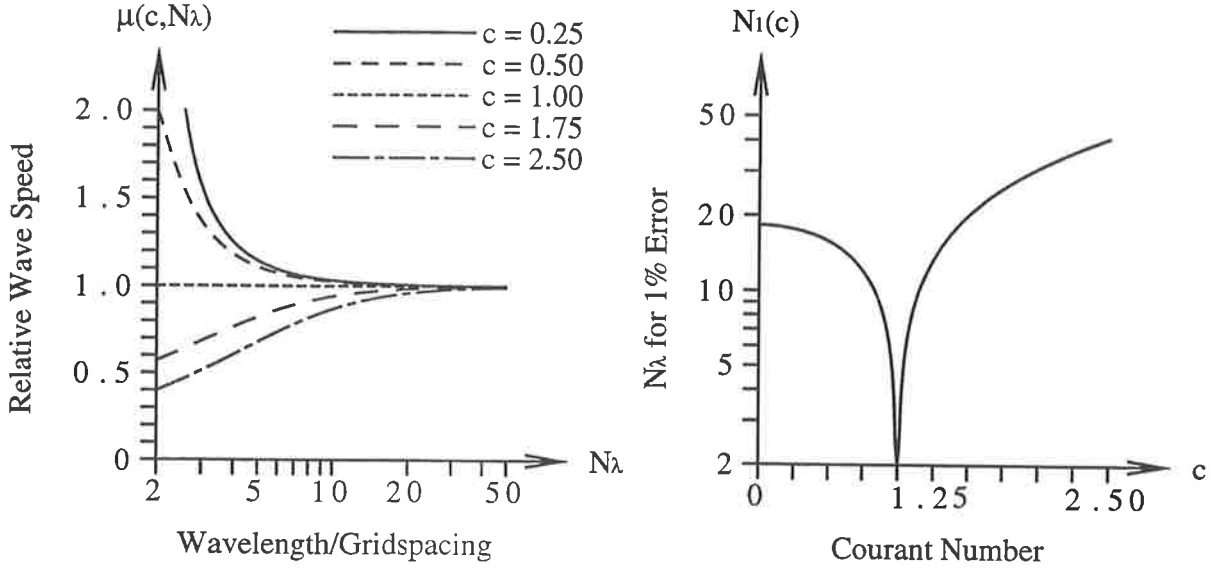

(a) relative wave speed value

(b) relative wave speed error

Figure 8.5: The "box" type (2,2) FDE (8.4.1) relative wave speed characteristic and trend.

substituting (8.4.2) into (8.3.5). In fact, except for values of c near unity, when FDE (8.4.1) is exact (since it becomes the well-known first-order convergent upwind formula), the number of grid–spacings per wave length must only be larger than 40 for the error in the relative wave speed to be less than 1% for all Courant numbers in the range $0 \leq c \leq 2.5$. For a given value of c, as the number of grid–spacings in a wavelength decreases or the lengths of the component waves in the initial condition become shorter, the wave speed error increases. Therefore, components with smaller wavelengths propagate faster than those with larger wavelengths when $c^2 < 1$.

8.5 Two-Dimensional Advection–Diffusion

Consider the 2D advection–diffusion equation

$$\frac{\partial \hat{\tau}}{\partial t} + u\frac{\partial \hat{\tau}}{\partial x} + v\frac{\partial \hat{\tau}}{\partial y} - \alpha_x \frac{\partial^2 \hat{\tau}}{\partial x^2} - \alpha_y \frac{\partial^2 \hat{\tau}}{\partial y^2} = 0, \tag{8.5.1}$$

a generalisation of PDE (8.1.1) as discussed in Section 8.1. Concentrations $\hat{\tau}(j\Delta x, k\Delta y, n\Delta t)$ satisfying PDE (8.5.1) at grid–points (j, k, n) on an appropriate $\Delta x \times \Delta y \times \Delta t$ grid can be approximated by $\tau^n_{j,k}$ using a finite-difference equation

$$\mathcal{L}_\Delta\{\tau^n_{j,k}\} = 0, \tag{8.5.2}$$

where $\mathcal{L}_\Delta$ is a 2D finite-difference operator. In the following, the notation

$$\frac{\partial^{p+q}\hat{\tau}(j\Delta x, k\Delta y, n\Delta t)}{\partial x^p \partial y^q} \approx \left.\frac{\partial^{p+q}\tau}{\partial x^p \partial y^q}\right|_{j,k}^{n}, \quad 1 \le p+q \le 2, \quad 0 \le p,q \le 2, \tag{8.5.3}$$

is used to denote differencing approximations to the derivatives.

Following an argument similar to that in Section 8.1, it can be shown (see Noye and Tan 1989) that if FDE (8.5.2) is consistent with PDE (8.5.1) and $\alpha_x > 0$, $\alpha_y > 0$, u, and v, are constant, then (8.5.2) is equivalent to the MEPDE

$$\frac{\partial\tau}{\partial t} + u\frac{\partial\tau}{\partial x} + v\frac{\partial\tau}{\partial y} - \alpha_x\frac{\partial^2\tau}{\partial x^2} - \alpha_y\frac{\partial^2\tau}{\partial y^2} + \sum_{p=2}^{\infty}\sum_{m=0}^{p} C_{p-m,m}\frac{\partial^p\tau}{\partial x^{p-m}\partial y^m} = 0, \tag{8.5.4}$$

in which

$$C_{p-m,m} = \begin{cases} \frac{u(\Delta x)^{p-m-1}(\Delta y)^m}{(p-m)!m!}\eta_{p-m,m}(c_x, c_y, s_x, s_y) & \text{if } p-m > m, \\ \frac{v(\Delta y)^{p-m-1}(\Delta x)^m}{(p-m)!m!}\eta_{p-m,m}(c_x, c_y, s_x, s_y) & \text{if } p-m \le m, \end{cases} \tag{8.5.5}$$

where

$$c_x = u\Delta t/\Delta x, \qquad c_y = v\Delta t/\Delta y, \tag{8.5.6}$$

and

$$s_x = \alpha_x\Delta t/(\Delta x)^2 \ge 0, \quad s_y = \alpha_y\Delta t/(\Delta y)^2 \ge 0 \tag{8.5.7}$$

are relevant Courant and diffusion numbers, respectively.

A FDE (8.5.2) approximating PDE (8.5.1) is termed "*r^{th}-order convergent*" if $\eta_{p,q} = 0$ for all p, q such that $p+q = 2, 3, \ldots, r$ and $\eta_{P,Q} \neq 0$ for at least one P, Q pair such that $P+Q = r+1$ in the corresponding MEPDE (8.5.4)–(8.5.7). If $\eta_{2,0}$ or $\eta_{0,2}$ are non-zero, the diffusion coefficients are not α_x or α_y, respectively, as required for correct solution of (8.5.1), and the finite-difference method (FDM) is termed first-order convergent. Such a FDM is said to introduce "*numerical diffusion*" into the solution of (8.5.1), in the x and y directions, respectively. Note that the "cross-diffusion" term in (8.5.4)–(8.5.7) with coefficient $v\Delta x\,\eta_{1,1}\partial^2\tau/\partial x\partial y$ also affects the amplitude of component waves in the approximate solution of PDE (8.5.1) by FDE (8.5.2). For u and v non-constant in space and/or time, Courant numbers are defined by

$$\begin{aligned} c_x|_{j,k}^n &= u_{j,k}^n\Delta t/\Delta x \quad \text{where} \quad u_{j,k}^n = u(j\Delta x, k\Delta y, n\Delta t), \\ c_y|_{j,k}^n &= v_{j,k}^n\Delta t/\Delta y \quad \text{where} \quad v_{j,k}^n = v(j\Delta x, k\Delta y, n\Delta t), \end{aligned} \tag{8.5.8}$$

and assessment of FDE (8.5.2) by MEPDE (8.5.4)–(8.5.7) gives only an approximate estimate of the accuracy of the associated FDM, since theoretical accuracy is less rigorously defined.

In the following FDM analyses and numerical tests, it should be noted that two values for the 2D diffusion numbers s_x and s_y of (8.5.7) are frequently used. These are determined by (8.1.9) and (8.1.10) as defined in Section 8.1.1.

8.6 Finite-Difference Method Criteria

Many difference schemes have been reported in the literature for approximating (8.5.1), some having distinct advantages over others. Schemes considered appropriate for the application at hand require the following attributes.

1. A two-level FDE, which is desirable in order to:

(a) avoid the artificiality of an imposed "intermediate" IC, as discussed in Section 8.9.1

(b) minimise the overall memory requirements of the FDM implementation, as is immediately obvious

2. An explicit nature, which is desirable in terms of:

   (a) minimising overall programming effort on any computer

   (b) maximising vectorisation/parallelisation on supercomputers

3. A compact computational stencil, restricted to at most the eight immediate neighbours of the target grid–point, which is desirable in regions:

   (a) at the domain boundaries, where approximations must be devised due to the unavailability of values at outlying grid–points, as is discussed in Section 8.8.1

   (b) in the domain interior, where a small number of locally grouped grid–points facilitates enhanced performance on serial, vector, and parallel architectures by minimising floating point operations, minimising memory accesses, and localising memory accesses, as is discussed in Chapter 5

4. A simple differencing, which is desirable in order to facilitate the:

   (a) individual modification of separate advection and diffusion terms, where necessary, near open and/or closed boundaries

   (b) analyses for order of convergence and regions of stability for the constant coefficient and, where possible, variable coefficient case

5. Stability in the von Neumann sense, where possible, over:

   (a) a wide range of values of u and v corresponding to observations of current velocities, as discussed in Section 7.4

   (b) at least a small range of α_x and α_y appropriate with the approximation of eddy diffusion coefficients discussed in Section 7.6

   (c) at least a choice of "coarse" to "fine" grid–spacings, in accordance with those used in the tidal models of Section 3.4 and Chapter 6, respectively, to generate the current data input

   (d) a choice of time–step appropriate to the frequency of input of current data to the transport model (discussed in Chapter 7), as determined by the frequency of output of current data from the tidal model (discussed in Section 3.4 and Chapter 6)

6. A guarantee that approximations produced are non-negative, given:

   (a) non-negative ICs and BCs, such as those discussed in Section 8.8.1

   (b) a sufficiently large subset of diffusion and Courant numbers within the bounds determined by von Neumann stability analysis

   (c) the obvious physical artificiality of negative larval concentrations

This list of criteria is distilled from discussions presented in sections of previous chapters, where these have been indicated appropriately.

Given this list of criteria, some possible FDM candidates for a larval dispersion model of *Penaeus latisulcatus* in Spencer Gulf using currents computed by the tidal model of Chapter 3 are now presented, commencing with the scheme first used by Noye et al. (1992) in preliminary studies of prawn larvae dispersion in the Gulf.

8.7 Two-Dimensional Advection–Diffusion Methods

Since all stability and non-negativity regions presented in this section are symmetrical about $c_x = 0$ and $c_y = 0$, they are plotted in the first quadrant of the c-s and c_x-c_y planes only. The latter are calculated using diffusion numbers determined by (8.1.9) and (8.1.10), namely those defined in turn by the Spencer Gulf coarse and fine grid model test parameters, respectively.

Portions of this section, in particular of Sections 8.7.1 and 8.7.4, have appeared in Nixon and Noye (1995).

8.7.1 The "Leapfrog"/Du Fort–Frankel Type (1,4,1) Method

The "leapfrog"/Du Fort and Frankel (1953) type (DF) (1,4,1) FDE

$$\tau_{j,k}^{n+1} = [\{2s_x + c_x\}\tau_{j-1,k}^{n} + \{2s_y + c_y\}\tau_{j,k-1}^{n} + \{2s_y - c_y\}\tau_{j,k+1}^{n} + \{2s_x - c_x\}\tau_{j+1,k}^{n} + \{1 - 2s_x - 2s_y\}\tau_{j,k}^{n-1}]/[1 + 2s_x + 2s_y] \tag{8.7.1}$$

is derived from a centred-time (CT), centred-space (CS) differencing of PDE (8.5.1) with $\tau_{j,k}^{n}$ in the CS diffusion term approximations replaced by the average of $\tau_{j,k}^{n-1}$ and $\tau_{j,k}^{n+1}$. It has a four-point three-level (1,4,1) computational stencil as shown in Figure 8.6(a) and a MEPDE of

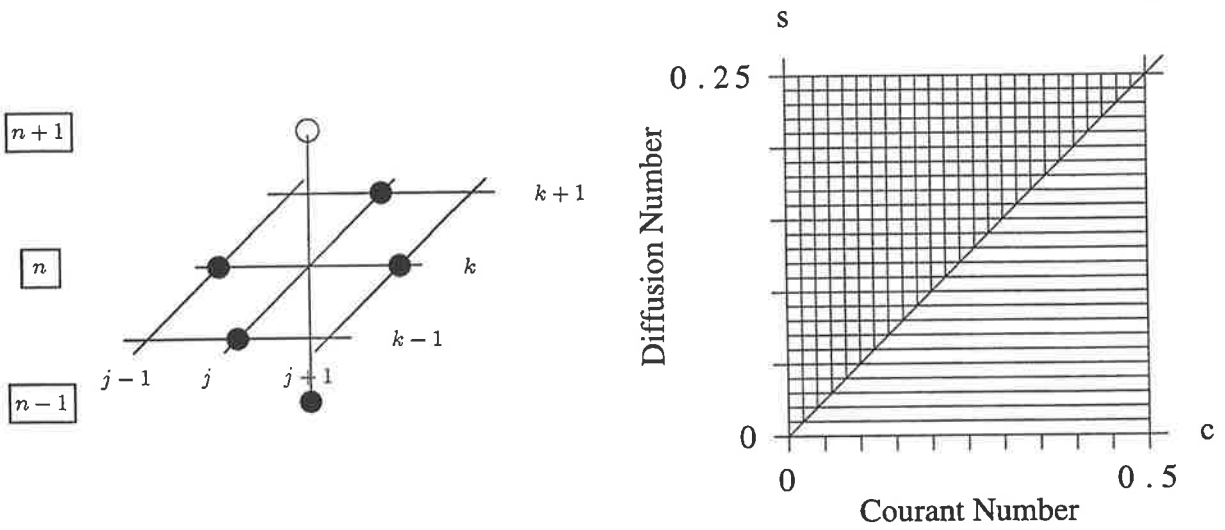

(a) the (1,4,1) stencil

(b) $c = c_x = c_y$ and $s = s_x = s_y$

Figure 8.6: The Du Fort–Frankel type (1,4,1) FDE (8.7.1) computational stencil, von Neumann stable (horizontal hatching) region (8.7.4), and non-negative (vertical hatching) region (8.7.7).

the general form of (8.5.4)–(8.5.7) with

$$\eta_{2,0} = 2c_x(s_x + s_y), \quad \eta_{1,1} = 2c_x(s_x + s_y), \quad \eta_{0,2} = 2c_y(s_x + s_y). \tag{8.7.2}$$

The first-order convergent FDE (8.7.1) is von Neumann stable in the region

$$c_x^2 + c_y^2 \leq 1/2 \tag{8.7.3}$$

or

$$|c| \leq 1/2, \tag{8.7.4}$$

on substitution of

$$c = c_x = c_y \quad \text{and} \quad s = s_x = s_y. \tag{8.7.5}$$

The region (8.7.4) is shown horizontally hatched in Figure 8.6(b). With the stipulations listed above, values produced by (8.7.1) are guaranteed to be non-negative in the region

$$s_x \geq |c_x|/2, \quad s_y \geq |c_y|/2 \quad \text{and} \quad s_x + s_y \leq 1/2 \tag{8.7.6}$$

or

$$s \geq |c|/2 \quad \text{and} \quad s \leq 1/4, \tag{8.7.7}$$

on substitution of (8.7.5). The region defined by (8.7.7) is shown vertically hatched in Figure 8.6(b).

The regions defined by (8.7.3) and (8.7.6) are shown horizontally and vertically hatched, respectively, in Figures 8.7(a) and 8.7(b) for diffusion numbers defined by (8.1.9) and (8.1.10)

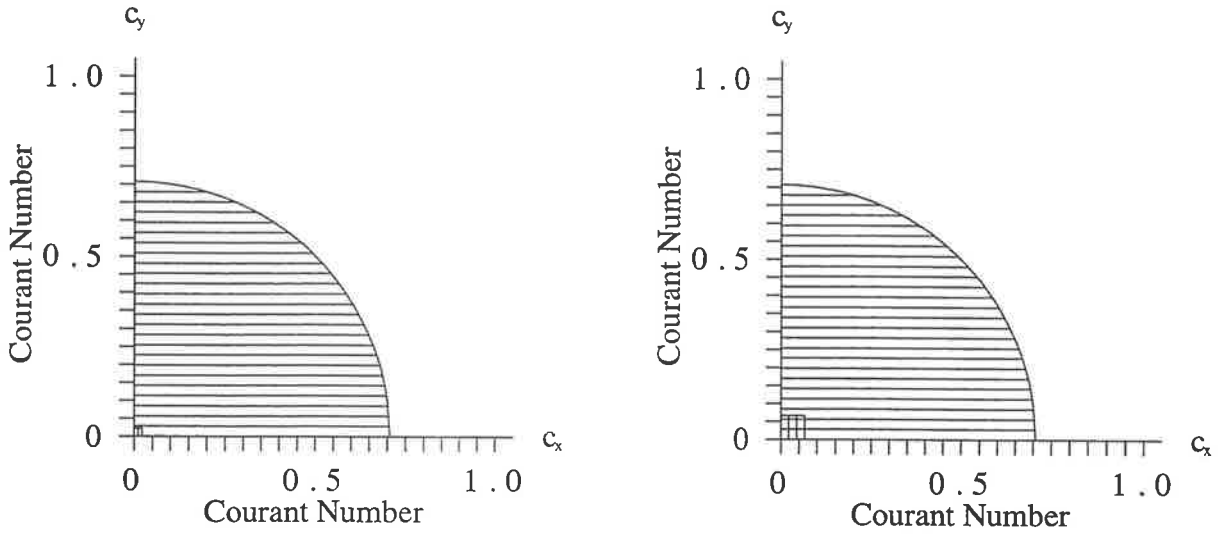

(a) $s_x = s_y = 0.011$ (b) $s_x = s_y = 0.033$

Figure 8.7: The Du Fort–Frankel type (1,4,1) FDE (8.7.1) von Neumann stable (horizontal hatching) region (8.7.3), and non-negative (vertical hatching) region (8.7.6).

appropriate to the coarse and fine grid model parameter sets, respectively.

8.7.2 The Forward-Time Centred-Space (1,5) Method

If the differencing of PDE (8.5.1) is forward-time (FT), and centred-space (CS) for all advection and diffusion terms, the following FDE is obtained (see Noye 1984a)

$$\begin{aligned}\tau_{j,k}^{n+1} = [\{2s_x + c_x\}\tau_{j-1,k}^n + \{2s_y + c_y\}\tau_{j,k-1}^n + 2\{1 - 2(s_x + s_y)\}\tau_{j,k}^n + \\ \{2s_y - c_y\}\tau_{j,k+1}^n + \{2s_x - c_x\}\tau_{j+1,k}^n]/[2]\end{aligned} \tag{8.7.8}$$

which has a five-point two-level (1,5) computational stencil as shown in Figure 8.8(a) and a MEPDE of the general form of (8.5.4)–(8.5.7) with

$$\eta_{2,0} = c_x, \quad \eta_{1,1} = c_x, \quad \eta_{0,2} = c_y. \tag{8.7.9}$$

The first-order convergent FDM is von Neumann stable in the region (Hindmarsh et al. 1984)

$$c_x{}^2/s_x + c_y{}^2/s_y \leq 2, \quad s_x + s_y \leq 1/2, \tag{8.7.10}$$

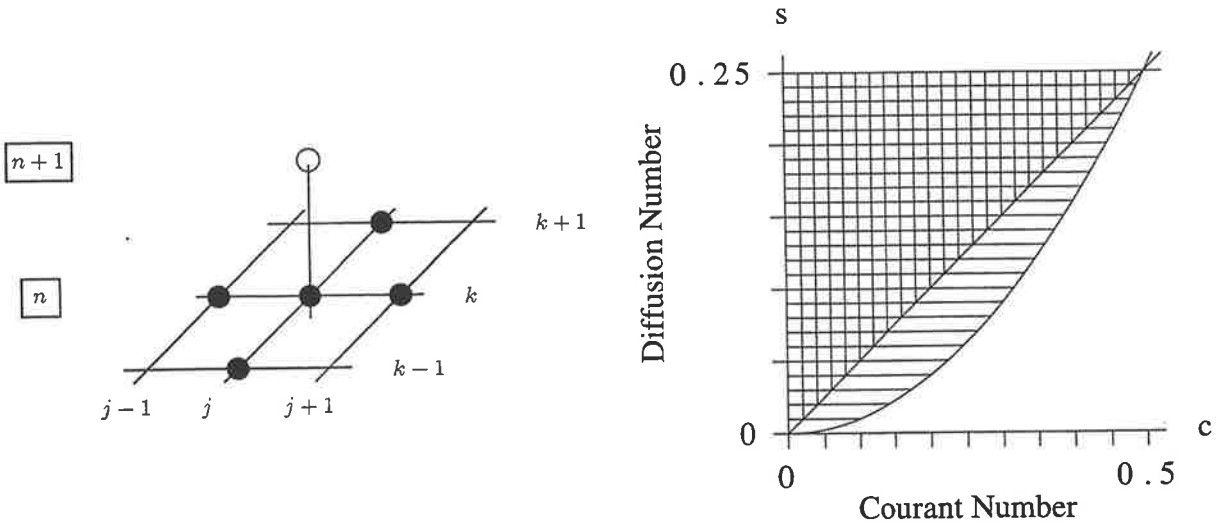

(a) the (1,5) stencil

(b) $c = c_x = c_y$ and $s = s_x = s_y$

Figure 8.8: The FTCS (1,5) FDE (8.7.8) computational stencil, von Neumann stable (horizontal hatching) region (8.7.11), and non-negative (vertical hatching) region (8.7.13).

which is shown, for diffusion numbers defined by (8.1.9) and (8.1.10), horizontally hatched in Figure 8.9. The region defined by (8.7.10) becomes

$$c^2 \leq s, \quad s \leq 1/4 \tag{8.7.11}$$

on substitution of (8.7.5), and is shown horizontally hatched in Figure 8.8(b). The FDE (8.7.8) guarantees non-negative results when

$$s_x \leq |c_x|/2, \quad s_y \leq |c_y|/2 \quad \text{and} \quad s_x + s_y \leq 1/2 \tag{8.7.12}$$

which is shown, for diffusion numbers defined by (8.1.9) and (8.1.10), vertically hatched in Figure 8.9. The region defined by (8.7.12) becomes

$$s \leq |c|/2 \quad \text{and} \quad s \leq 1/4 \tag{8.7.13}$$

on substitution of (8.7.5), and is shown vertically hatched in Figure 8.8(b).

8.7.3 The "Modified" Forward-Time Centred-Space (1,5) Method

A FDM based on the same two-level computational stencil as that of the well known FTCS (1,5) FDM of Section 8.7.2 can be derived using the substitutions

$$\alpha_x = \alpha_x + u^2\Delta t/2, \quad \alpha_y = \alpha_y + v^2\Delta t/2 \tag{8.7.14}$$

in the original FTCS differencing (Hindmarsh et al. 1984) or, equivalently, by a weighted differencing approach (Noye and Tan 1989).

The modified differencing derivation is effected by the substitutions

$$s_x = s_x + {c_x}^2/2, \quad s_y = s_y + {c_y}^2/2 \tag{8.7.15}$$

in (8.7.8), (8.7.10), and (8.7.12).

The weighted differencing derivation is effected as follows. If FT differencing for the time derivative, CS for the second-order spatial derivatives and weighted combinations of CS and

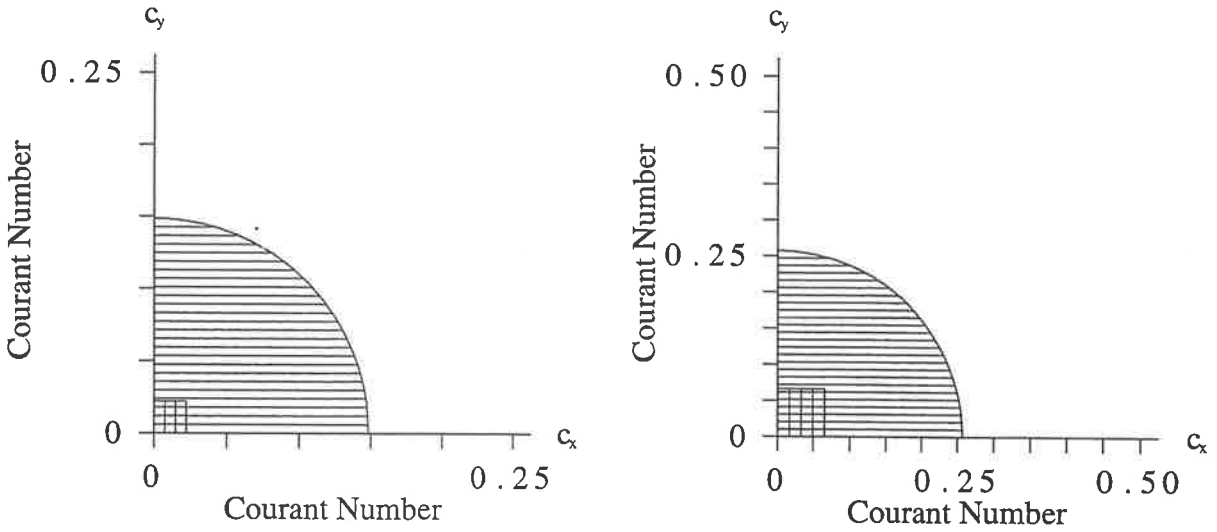

(a) $s_x = s_y = 0.011$ (b) $s_x = s_y = 0.033$

Figure 8.9: The FTCS (1,5) FDE (8.7.8) von Neumann stable (horizontal hatching) region (8.7.10) and non-negative (vertical hatching) region (8.7.12).

backward-space (BS) differencing are used for the first-order spatial derivatives in PDE (8.5.1), such as

$$\begin{aligned} \partial\hat{\tau}/\partial x|^n_{j,k} &\approx \phi \times [\text{BS at } (j,k,n)] + (1-\phi) \times [\text{CS about } (j,k,n)], \\ \partial\hat{\tau}/\partial y|^n_{j,k} &\approx \gamma \times [\text{BS at } (j,k,n)] + (1-\gamma) \times [\text{CS about } (j,k,n)], \end{aligned} \tag{8.7.16}$$

a FDE is obtained which has a MEPDE of the general form of (8.5.4)–(8.5.7) with

$$\eta_{2,0} = c_x - \phi, \quad \eta_{1,1} = c_x, \quad \eta_{0,2} = c_y - \gamma. \tag{8.7.17}$$

Choosing the weights $\phi = c_x$ and $\gamma = c_y$ so as to set $\eta_{2,0} = \eta_{0,2} = 0$ in (8.7.17) results in the optimal FDM for the (1,5) computational stencil shown in Figures 8.8(a) and 8.10(a).

The "modified" FTCS (MFTCS) (1,5) FDM has the FDE

$$\begin{aligned} \tau^{n+1}_{j,k} = [&\{2s_x + c_x + c_x^2\}\tau^n_{j-1,k} + \{2s_y + c_y + c_y^2\}\tau^n_{j,k-1} + \\ &2\{1 - 2(s_x + s_y) - c_x^2 - c_y^2\}\tau^n_{j,k} + \\ &\{2s_y - c_y + c_y^2\}\tau^n_{j,k+1} + \{2s_x - c_x + c_x^2\}\tau^n_{j+1,k}]/[2]. \end{aligned} \tag{8.7.18}$$

The first-order convergent FDE is von Neumann stable in the region (Hindmarsh et al. 1984)

$$c_x^2 c_y^2 \le 4 s_x s_y, \quad 2s_x + c_x^2 + 2s_y + c_y^2 \le 1 \tag{8.7.19}$$

as shown horizontally hatched, for diffusion numbers defined by (8.1.9) and (8.1.10), respectively, in Figures 8.11(a) and 8.11(b), or

$$c^2/2 \le s, \quad s \le (1 - 2c^2)/4, \tag{8.7.20}$$

on substitution of (8.7.5), as shown horizontally hatched in Figure 8.10(b). The FDE (8.7.18) guarantees non-negative results when

$$s_x \ge c_x(1 - c_x)/2, \quad s_y \ge c_y(1 - c_y)/2 \quad \text{and} \quad 2s_x + c_x^2 + 2s_y + c_y^2 \le 1, \tag{8.7.21}$$

as shown, for diffusion numbers defined by (8.1.9) and (8.1.10), vertically hatched in Figures 8.11(a) and 8.11(b), respectively, or

$$s \ge c(1 - c)/2 \quad \text{and} \quad s \le (1 - 2c^2)/4, \tag{8.7.22}$$

on substitution of (8.7.5), as shown vertically hatched in Figure 8.10(b).

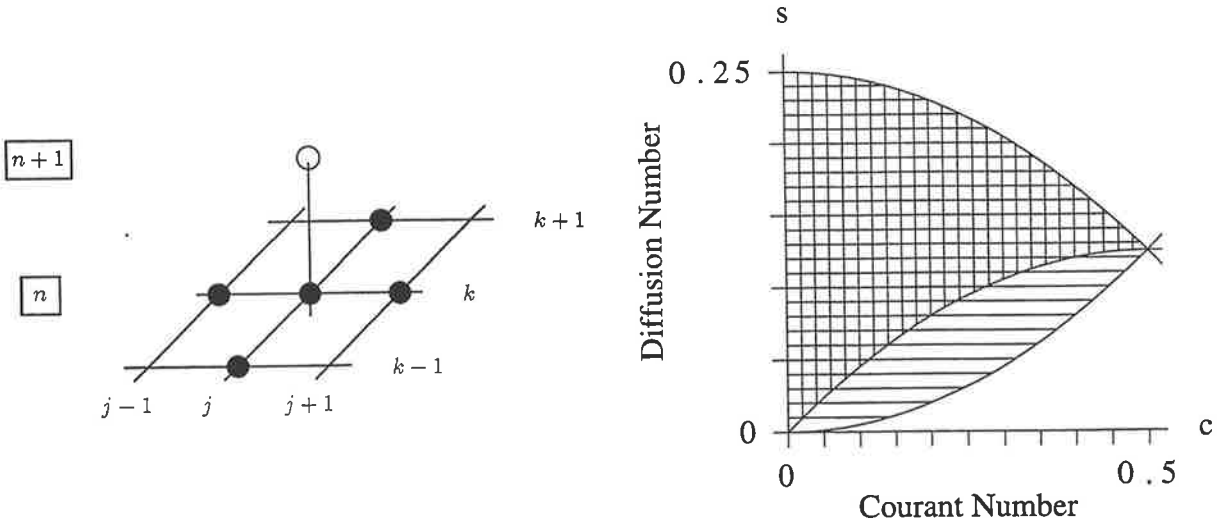

(a) the (1,5) stencil

(b) $c = c_x = c_y$ and $s = s_x = s_y$

Figure 8.10: The MFTCS (1,5) FDE (8.7.18) computational stencil, von Neumann stable (horizontal hatching) region (8.7.20), and non-negative (vertical hatching) region (8.7.22).

8.7.4 The Lax–Wendroff Type 2(1,3) Method

If a 1D second-order convergent FDE of the Lax and Wendroff (1964) type

$$2\tau_{j,k}^{n+1/2} = \{2s_x + c_x + c_x^2\}\tau_{j-1,k}^{n} + 2\{1 - 2s_x - c_x^2\}\tau_{j,k}^{n} + \{2s_x - c_x + c_x^2\}\tau_{j+1,k}^{n} \quad (8.7.23)$$

is used to approximate the 1D analogue (in x) of PDE (8.1.1) with double the diffusion and advection coefficients in the first half time–step and a similar FDE

$$2\tau_{j,k}^{n+1} = \{2s_y + c_y + c_y^2\}\tau_{j,k-1}^{n+1/2} + 2\{1 - 2s_y - c_y^2\}\tau_{j,k}^{n+1/2} + \{2s_y - c_y + c_y^2\}\tau_{j,k+1}^{n+1/2} \quad (8.7.24)$$

is used to approximate a similar 1D PDE (in y) in the second half time–step, the resulting FDE, which approximates PDE (8.5.1) over the full time–step, is obtained by substituting (8.7.23) into (8.7.24). This FDE has a MEPDE of the form (8.5.4)–(8.5.7) with $\eta_{2,0} = \eta_{1,1} = \eta_{0,2} = 0$ and

$$\eta_{3,0} = 1 - c_x^2 - 6s_x, \quad \eta_{2,1} = 0, \quad \eta_{1,2} = 0, \quad \eta_{0,3} = 1 - c_y^2 - 6s_y, \quad (8.7.25)$$

and is thus second-order convergent. The two-level computational stencils for the component (1,3) FDEs (8.7.23) and (8.7.24), as well as that for the combined 2(1,3) FDE (8.7.23)–(8.7.24), are shown in Figure 8.12. The stability of the overall two-dimensional, but locally one-dimensional (LOD) Lax–Wendroff type (LW) 2(1,3) FDE is determined by that of the two constituent (1,3) FDEs. The von Neumann stable region, defined by (8.2.4), is shown horizontally hatched in Figure 8.1(b), and the region of guaranteed non-negative results, defined by (8.2.5), is shown vertically hatched in Figure 8.1(b). In the equations and figure, $c = c_x$ and $s = s_x$ for FDE (8.7.23), or $c = c_y$ and $s = s_y$ for FDE (8.7.23) is assumed. Stability for the coarse and fine grid–spacing parameter sets, defining diffusion numbers given by (8.1.9) and (8.1.10), are similarly shown in Figures 8.13(a) and 8.13(b), respectively.

8.7.5 Discussion

If each candidate FDM is checked against the list of criteria in Section 8.6, the most suitable method can be chosen for the application at hand. It is apparent that the DF (1,4,1) FDM violates criterion 1., satisfies criterion 2., and only partially satisfies all other criteria. The

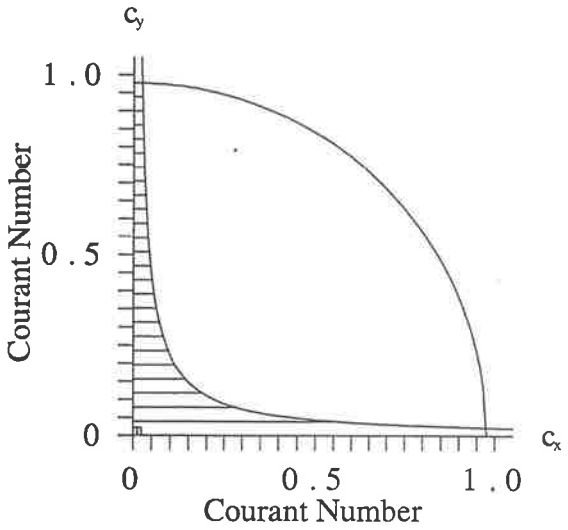

(a) $s_x = s_y = 0.011$

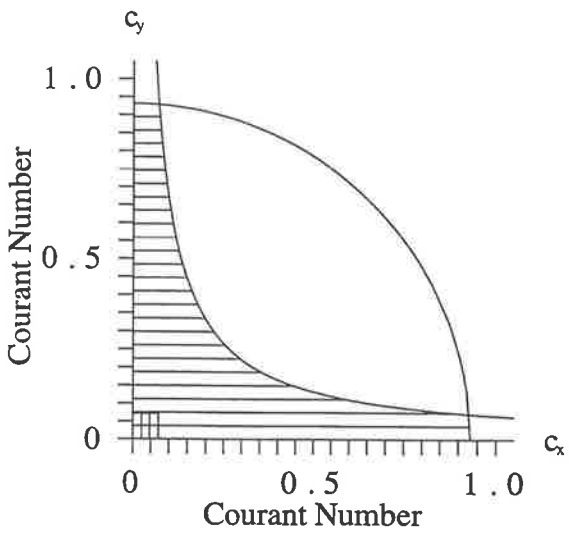

(b) $s_x = s_y = 0.033$

Figure 8.11: The MFTCS (1,5) FDE (8.7.18) von Neumann stable (horizontal hatching) region (8.7.19) and non-negative (vertical hatching) region (8.7.21).

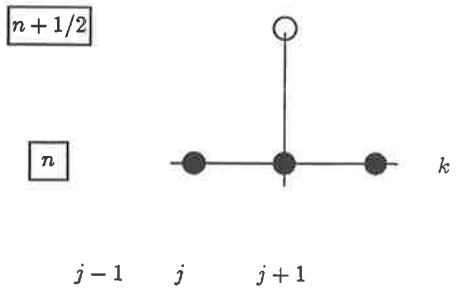

(a) the (8.7.23) stencil

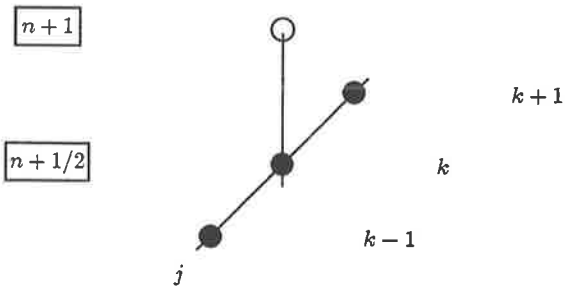

(b) the (8.7.24) stencil

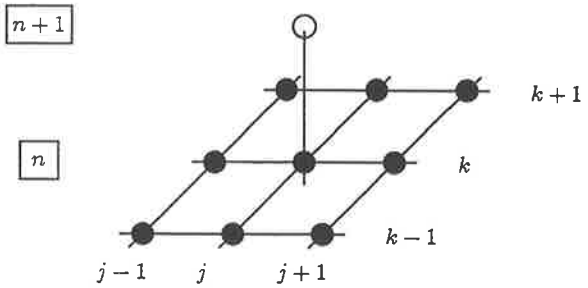

(c) the (8.7.23)–(8.7.24) stencil

Figure 8.12: The Lax–Wendroff type 2(1,3) FDE (8.7.23)–(8.7.24) computational stencils.

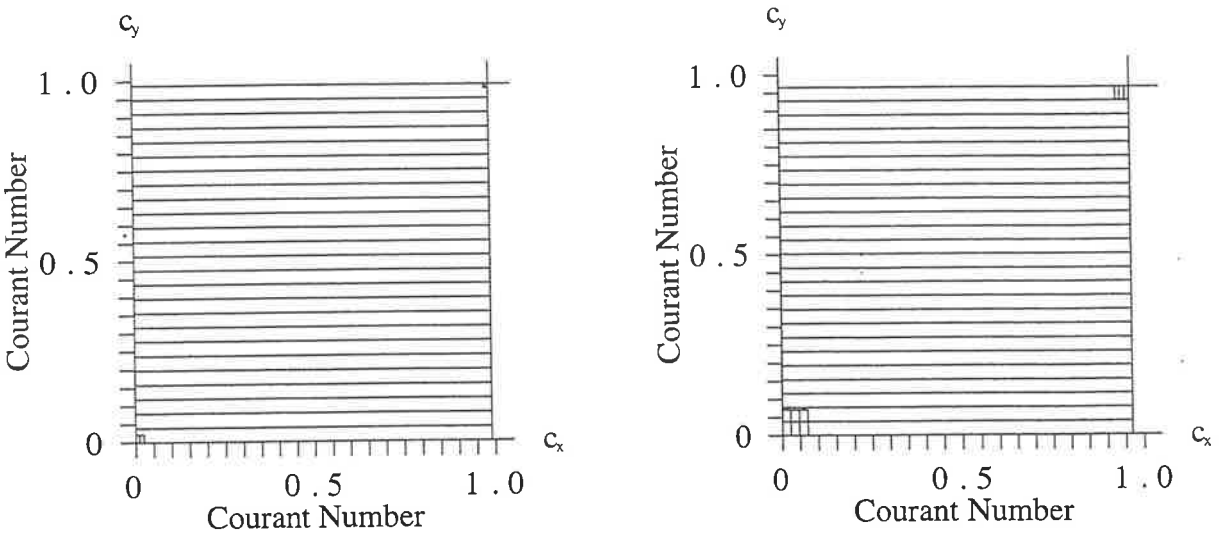

(a) $s_x = s_y = 0.011$ (b) $s_x = s_y = 0.033$

Figure 8.13: The Lax–Wendroff type 2(1,3) FDE (8.7.23)–(8.7.24) von Neumann stable (horizontal hatching) region (8.2.4) and non-negative (vertical hatching) region (8.2.5).

FTCS (1,5) FDM satisfies criteria 1. and 2., and only partially satisfies all other criteria. It posesses smaller regions of stability compared to, and is theoretically less accurate than, the DF (1,4,1) method. The MFTCS (1,5) FDM satisfies criteria 1. and 2., and only partially satisfies all other criteria. It posesses smaller regions of stability compared to either the DF (1,4,1) or FTCS (1,5) methods, but is theoretically as accurate as either method. The LW 2(1,3) FDM satisfies criteria 1. and 2., and more fully satisfies all other criteria than all other methods considered. The two-step process satisfies criterion 3. and the 1D computational stencils of each step satisfy criterion 4. This FDM posesses larger regions of stability (as required by criteria 5. and 6.) compared to, and is theoretically more accurate (as desired in any numerical scheme) than, the lower-order FDMs. This can be appreciated from the stability diagrams, which show that the LW 2(1,3) FDM has by far the most useful von Neumann stability regions, and non-negative regions comparable to the other FDMs, and from the MEPDE analysis, which determines that it is theoretically one order of magnitude more accurate than all other methods discussed.

8.8 The Finite-Difference Scheme

In this section, the overall finite-difference scheme used to approximate (8.5.1) is outlined, including techniques by which initial and boundary conditions are implemented in real-world simulations.

8.8.1 Initial and Boundary Conditions

At the commencement of simulation the numbers of larvae must be specified either exactly by an analytical solution—as is the case in the numerical tests of Sections 8.9.2–8.9.4 and 10.1.1, or approximately with field-measured data—as is the case in the simulation tests of Sections 10.1.2 and 10.2–10.4. All real-world and idealised initial conditions used in the following simulations are thus defined as noted in Sections 2.1.5 and 8.9.1, respectively.

Before settlement occurs in suitable nurseries, zero net larval flux across coastal boundaries, in an outwardly normal direction $\boldsymbol{n}$, is assumed with

$$(\partial \hat{\tau}/\partial \boldsymbol{n})|_{\text{“coast”}} = 0 \tag{8.8.1}$$

being an appropriate reflecting boundary condition (BC), where "coast" refers to the position of the closed boundaries. Settlement is assumed to occur at the instant simulations cease, i.e. postlarvae are assumed to settle at the location in which they are found, regardless of whether this may or may not constitute an ideal juvenile prawn habitat.

At open boundaries the numbers of larvae must be specified, either directly by an analytical solution, as is the case in the numerical tests of Sections 8.9.2–8.9.3, or indirectly by other means, possibly by a BC analogous to (8.8.1), such as

$$(\partial\hat{\tau}/\partial n)|_{\text{"open"}} = constant, \tag{8.8.2}$$

where "open" refers to the position of the open boundaries.

In any real-world application of an approximation to PDE (7.8.5) the conditions (8.8.1) and (8.8.2) themselves must be approximated, as discussed in Section 8.6. The grid element classification scheme described in Section 3.2.4 is used by the tidal model to determine the grid element location relative to the model boundaries. It is also used by the larval dispersion model. The tidal model uses this scheme to determine, by means discussed in Section 3.2.5, appropriate finite-difference approximations to invoke near model boundaries. Similarly, the larval dispersion model uses this same scheme to determine the location of grid–points at which the boundary conditions (8.8.1) and (8.8.2) must be determined.

Closed Boundary Condition Approximations

The BC (8.8.1) is approximated at closed boundaries by what is termed *reflection in a bilinear locally* 1D *sense* in the finite-difference equation (FDE) representation. This is achieved by specifying the unavailable (exterior) concentration as being that of the known (interior) concentration and is thus equivalent to a reflection at the closed boundary. This procedure enforces zero gradient across this boundary and is thus also equivalent to the desired boundary condition.

The coastal boundary condition (8.8.1), illustrated in plan view in Figure 8.14, can be

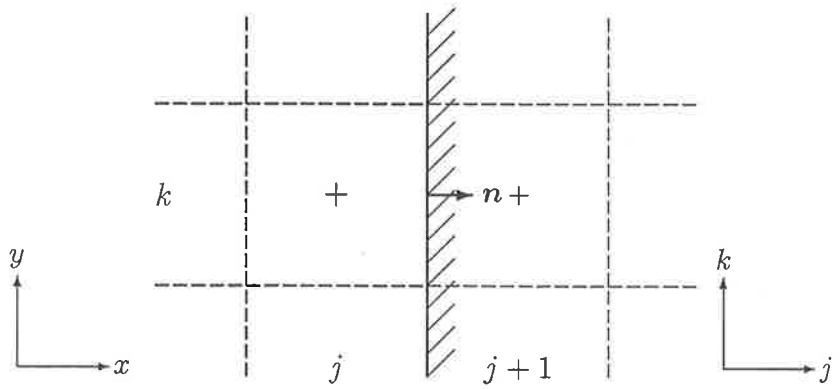

Figure 8.14: A plan view of coastal boundary elements, indicating the reflecting boundary condition. The dashed lines represent grid element boundaries. The model interior and exterior are to the left and right, respectively, of the closed boundary at $j + 1/2$.

written as

$$\left.\frac{\partial\hat{\tau}}{\partial x}\right|_{j+1/2,k}^{n+1} = 0. \tag{8.8.3}$$

This can be approximated by

$$\frac{\hat{\tau}_{j+1,k}^{n+1} - \hat{\tau}_{j,k}^{n+1}}{\Delta x} + \mathrm{O}\left\{(\Delta x)^2\right\} = 0 \tag{8.8.4}$$

using second-order convergent CS differencing. Omitting the discretisation error, this approximation can be written as

$$\tau_{j+1,k}^{n+1} = \tau_{j,k}^{n+1}, \tag{8.8.5}$$

to give the reflective boundary condition which is applied at the coastal boundary in this instance.

Since none of the FDEs of Section 8.7 used to approximate the PDE (8.5.1) are of a type that requires more than one model exterior grid–point when being applied adjacent to a closed boundary, this simple procedure can be used without loss of accuracy. Similarly, since none of these FDEs are of a type that requires more sophisticated (i.e. fully 2D) treatment at the closed boundaries, this simple (i.e. bi-linear locally 1D) treatment can be used without reservation. These two important characteristics can be summed up in the fact that all have a computational stencil which: is of at most five grid–points, *and* has width of no greater than three grid-points, *and* is symmetrical *and* does not include grid–points along the stencil diagonals.

Open Boundary Condition Approximations

The BC (8.8.2) is approximated at open boundaries by what is termed *semi-implicit differencing of the advective terms in a linear locally* 1D *sense* using a finite-difference method (FDM) which is appropriate. The "box" method described in Section 8.4.1 is used to determine the unknown (exterior) concentration at the open boundary element using two known (interior) concentrations and one known (exterior) open boundary concentration. The latter value is known from the previous time–level, and the former values are known from both the previous and the present time–levels.

The open boundary condition (8.8.2), illustrated in plan view in Figure 8.15, can be written

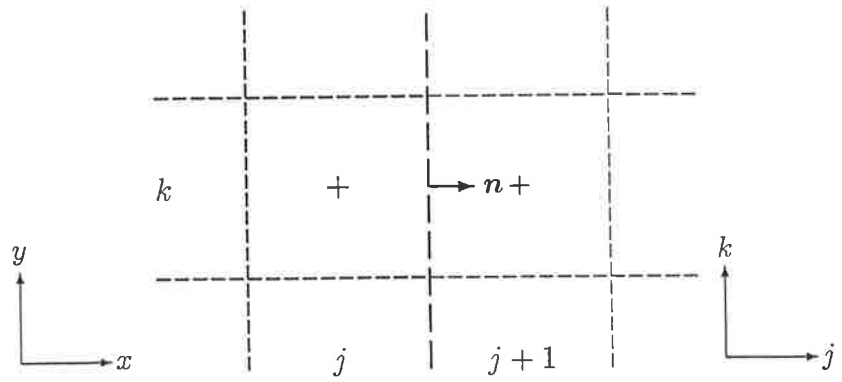

Figure 8.15: A plan view of open boundary elements, indicating the open boundary condition. The dashed lines represent grid element boundaries. The model interior and exterior are to the left and right, respectively, of the open boundary at $j + 1/2$.

as

$$\left.\frac{\partial \hat{\tau}}{\partial x}\right|_{j+1/2,k}^{n+1/2} = -\frac{1}{u_{j+1/2,k}^{n+1/2}} \left.\frac{\partial \hat{\tau}}{\partial t}\right|_{j+1/2,k}^{n+1/2}. \tag{8.8.6}$$

This is a form of the 1D advection equation (8.3.1) discretised at the grid–point indicated. This discretisation can be approximated by

$$\begin{aligned} &\frac{1}{2}\left(\left.\frac{\partial \hat{\tau}}{\partial t}\right|_{j,k}^{n+1/2} + \left.\frac{\partial \hat{\tau}}{\partial t}\right|_{j+1,k}^{n+1/2} + \mathrm{O}\left\{(\Delta x)^2\right\}\right) + \\ &\frac{u_{j+1/2,k}^{n+1/2}}{2}\left(\left.\frac{\partial \hat{\tau}}{\partial x}\right|_{j+1/2,k}^{n} + \left.\frac{\partial \hat{\tau}}{\partial x}\right|_{j+1/2,k}^{n+1} + \mathrm{O}\left\{(\Delta t)^2\right\}\right) = 0, \end{aligned} \tag{8.8.7}$$

to leading order. Approximating the derivatives in (8.8.7) using second-order convergent CT and CS differencing results in the "box" type (2,2) FDE of Section 8.4.1. Omitting $O\{(\Delta x)^2, (\Delta t)^2\}$ discretisation errors, this approximation can be written as

$$\tau_{j+1,k}^{n+1} = [\{1 + c_x\}\tau_{j,k}^{n} + \{1 - c_x\}\tau_{j+1,k}^{n} - \{1 - c_x\}\tau_{j,k}^{n+1}]/[\{1 + c_x\}] \tag{8.8.8}$$

to give the boundary condition which is applied at the open boundary in this instance.

It should be noted that this treatment takes no account of advection in any direction other than orthogonal to the particular open boundary segment at which it is being applied. Nor does it take into account diffusion processes across or along the open boundary.

There is also another error associated with applying (8.8.8), since in this equation

$$c_x = c_x|_{j+1/2,k}^{n+1/2} = u_{j+1/2,k}^{n+1/2}\Delta t/\Delta x \tag{8.8.9}$$

strictly holds. The u velocity at grid–point (j, k, n) (as obtained from the tidal model output) is used to approximate u at the grid–point $(j + 1/2, k, n + 1/2)$ (as required by the "box" method) in order to determine the concentration at grid–point $(j + 1, k, n + 1)$ (as required by the dispersion model). There are interesting parallels between this procedure and that used in the Sommerfeld type radiation boundary condition specification in the tidal model (see Section 3.1.2) to determine the transient wave velocity (equivalent to u here) from the interior sea–surface elevation (equivalent to the interior concentration here), which is in turn used determine the required alteration the open boundary height specified forcing (equivalent to the specification of the open boundary concentration here). The approximations in the case of the tidal model, however, result in errors of translation of greater than one grid–spacing in time and space, whereas in this approximation these are of less than one grid–spacing in both dimensions.

With these reservations, the FDE (8.8.8) type approximation of the BC (8.8.2) was shown in Section 8.4.1 to result in concentrations determined at the model open boundary which are theoretically of the same order of accuracy as those determined in its interior. Simulations in the following sections and chapters will be shown to result in larval concentrations in the vicinity of the open boundary which are both small in magnitude and low in significance with respect to the overall *Penaeus latisulcatus* larvae dispersion patterns prevalent in Spencer Gulf. Taking these points into consideration, a more sophisticated (i.e. fully 2D, including diffusion) and computationally difficult/expensive treatment at the open boundaries than this fairly straightforward (i.e. linear locally 1D, excluding diffusion) and computationally simple/inexpensive treatment is not considered necessary.

8.8.2 Discussion

The overall computational scheme for approximating PDE (8.5.1) is thus as follows.

The initial condition is specified over the entire model region, including at the model open boundary, and represents the larval spawning event at the commencement of simulations.

A 2D FDM approximating PDE (8.5.1) is then applied to determine concentrations in the interior at the present time interval. Since these methods are of a "compact" type as described above, they can be applied to determine concentrations everywhere except possibly at locations along the open and closed boundaries.

The boundary condition at the coastal boundaries is satisfied automatically, in a manner as described in Section 8.8.1, as part of the solution process.

The 1D "box" type FDE approximating, at any single application, the appropriate advective term of PDE (8.5.1) is then applied to determine concentrations at the open boundary from those defined there by the initial condition and those defined in the interior by this condition and by the 2D FDE.

With concentrations now defined at the present time interval (by this process) and at the previous time interval (by the initial condition), the process itself may be repeated until the desired number of time intervals have been simulated.

Again it is stressed that, due to the nature of the assumptions made to derive it, the model provides what is in essence a statistical average of the number of larvae as its output. Hence the shape and internal structure of an observed larval cloud would in reality be more complicated than is suggested by the smooth contour plots resulting from the simulations which will be presented. These results, presented in Section 8.9 and Chapter 10, should thus be interpreted with this in mind.

8.9 The Finite-Difference Method Tests

In Section 7.8 an overview of prawn larvae dispersion modelling was presented, in which physical and mathematical properties of both the problem itself and the region in which it is to be solved were discussed. In Section 8.6 criteria required of an ideal numerical scheme for solution to the mathematical problem of advection–diffusion models were listed. In Section 8.7 four candidate schemes were presented along with their numerical properties and a discussion of the extent to which each met, or failed to meet, the criteria proposed.

The first-order (O{1}) "leapfrog"/Du Fort and Frankel (1953) type (DF) (1,4,1), first-order (O{1}) forward-time centred-space (FTCS) (1,5), first-order (O{1}) "modified" FTCS (MFTCS) (1,5), and second-order (O{2}) locally one-dimensional Lax–Wendroff type (LW) 2(1,3) schemes were the finite-difference methods (FDMs) considered. It was determined that the LW 2(1,3) FDM more fully satisfies all criteria of Section 8.6 than all other methods considered. Numerical testing is still desirable to ensure sufficient accuracy of this method, as efficiency and stability without accuracy have nothing to recommend them.

In this section, these four schemes are numerically tested against known analytical solutions for two "gulfs" with simple geometry and "current" regimes. The schemes are also used to predict prawn larvae dispersion from the Cowell spawning ground in Spencer Gulf, following the spawning period of December 1988, using initial larval concentrations supplied by fisheries officers (Carrick 1994, personal communications) of the South Australian Research and Development Institute (SARDI) and tidal velocities predicted by the three-dimensional (3D) tidal model of Bills (1991).

Portions of this section, in particular of Section 8.9.4, have appeared in Nixon and Noye (1995).

8.9.1 The Numerical Tests

In the open ocean, an initial patch of fertilised eggs or prawn larvae may be approximated by

$$\hat{\tau}(x,y,0) = \exp\left\{-[(x-x_0)^2]/[2\sigma_x^2] - [(y-y_0)^2]/[2\sigma_y^2]\right\} \tag{8.9.1}$$

which is a Gaussian distribution initial condition (IC) with centre (x_0, y_0) and variances σ_x^2 and σ_y^2 in the x and y directions, respectively. In the tests that follow this is the IC used to commence simulations.

For the three-level DF (1,4,1) FDM tests, the required first time–step solution is provided by exact values in the tests with analytical solutions. In the test with no analytical solution, the solution at the first time–level is determined assuming constant diffusion and zero advection of the IC peak. This is exactly the kind of "intermediate" IC that can be avoided on the use of two-level FDMs that satisfy the FDM criteria listed in Section 8.6.

In the figures that follow, graphical depictions of the analytical solution (AS), where appropriate, and the numerical predictions are presented. In the tables that follow, for each numerical scheme (FDM) the maximum positive concentration (Max$\{+\tau\}$), minimum negative concentration ($-$Max$\{-\tau\}$), total of positive concentrations (Tot$\{+\tau\}$), total of negative concentrations ($-$Tot$\{-\tau\}$), maximum absolute error (Max$\{|$Err$|\}$), and average absolute error (Ave$\{|$Err$|\}$) are listed, where each is calculated using values from interior elements only (i.e. excluding those at the open boundary) and the AS (excluding the IC), where appropriate. The Ave$\{|$Err$|\}$ listed

in the tables for the entire simulation has been divided by the number of time–steps in the simulation to produce a measure of the overall average accuracy of each scheme. Also listed, where appropriate, is the *relative peak height* (RPH) calculated as the ratio of the numerical to the true peak height at the element of maximum concentration in each case, and the *central processor unit* (CPU) time taken to complete the simulation. Note that the CPU times listed are to be considered only approximate estimates of the computational requirements of the different schemes, as the UNIX timing mechanism `time` used is not renowned for its great accuracy.

Two sets of results are given for all tests, one in which "*clipping*" was implemented—whereby any negative concentrations (clearly a non-physical occurrence) generated by the numerical schemes are set to zero, but recorded in a total of negative concentrations discarded—and one in which there is *no* "*clipping*". In the latter case the recorded total (the $-\text{Tot}\{-\tau\}$ value) is a measure of the negative concentrations which are generated and consequently carried along with the computations as part of the solution process. In the case of clipping, the $-\text{Max}\{-\tau\}$ value is calculated after clipping, and as such is always of value zero. In the figures, the results using the clipping procedure are generally found on the right and in the tables they are listed with the FDM named in italics.

8.9.2 The "Oscillating Tide" Test

The PDE (8.1.1) is approximated for an oscillatory channel flow in the y direction given by

$$u(x,y,t) = 0, \quad v(x,y,t) = v_a \sin\{2\pi t/v_p\} \tag{8.9.2}$$

in which: v_a is the amplitude and v_p the period of the oscillation; the IC is given by (8.9.1) with $x_0 = x$; the BC (8.8.1) is approximated at coastal boundary grid–points as defined in Section 8.8.1; and values at open boundary grid–points determined by the AS

$$\hat{\tau}(x,y,t) = \frac{\sigma_y}{\sqrt{\sigma_y^2 + 2\alpha_y t}} \exp\left\{ -\frac{(y - y_0 - v_a v_p \sin^2\{\pi t/v_p\}/\pi)^2}{2(\sigma_y^2 + 2\alpha_y t)} \right\} \tag{8.9.3}$$

(Noye 1987a) on a 9×43 uniform mesh representative of the rectilinear nature of the middle and northern regions of the coarse grid Spencer Gulf model discussed in Section 3.4. Other parameters used, representative of the Gulf in general and this model in particular, are: $\Delta t = 3600\,\text{s}$, $\Delta x = \Delta y = 5715\,\text{m}$, $\sigma_y^2 = 32661225\,\text{m}^2$, $\alpha_y = 100\,\text{m}^2\text{s}^{-1}$, $y_0 = 0\,\text{m}$, $v_a = 1\,\text{m}$, $v_p = 43200\,\text{s}^{-1}$, with results obtained at time $t = N\Delta t = 1814400\,\text{s}$. These parameters are chosen in order to represent a diurnal tide with maximum tidal velocity close to that recorded in the Spencer Gulf region, propagating an initial unit concentration pulse up and down the Gulf for 28 d.

As indicated in the stability diagrams of Section 8.7, the FTCS (1,5) scheme is not von Neumann stable for these parameters—which correspond to a constant diffusion number of $s_y = 0.011$ and a variable Courant number in the range $0 \leq c_y \lesssim 0.63$—and so results for this FDM are not presented. It is for this reason that the test in Section 8.9.3—using parameters resulting in diffusion and Courant numbers for which all schemes are fully von Neumann stable—is made.

The IC and AS for this test with an "oscillating tide" are represented graphically in Figure 8.16 and the approximations produced by the schemes discussed above are represented graphically in Figures 8.17–8.19. The level curves (solid curves) in Figure 8.16 have x and y axes aligned horizontally and vertically, respectively, with (x_0, y_0) centred in the region enclosed by the closed boundary (solid lines) and open boundary (dashed lines). The transects in Figures 8.16–8.19 have the y axis aligned horizontally with y_0 marked, and were taken along the $x = x_0 = 0$ line from the bottom of the gulf to the top. These are thus termed y-transects.

The stability diagrams of Section 8.7 indicate that for much of the tidal cycle *all* of the FDMs presented in that section are capable of producing both negative and non-negative values. The results presented in Figures 8.17–8.19 and the statistics presented in Tables 8.1–8.2 indicate that to eliminate the production of leading and trailing oscillations about the zero concentration

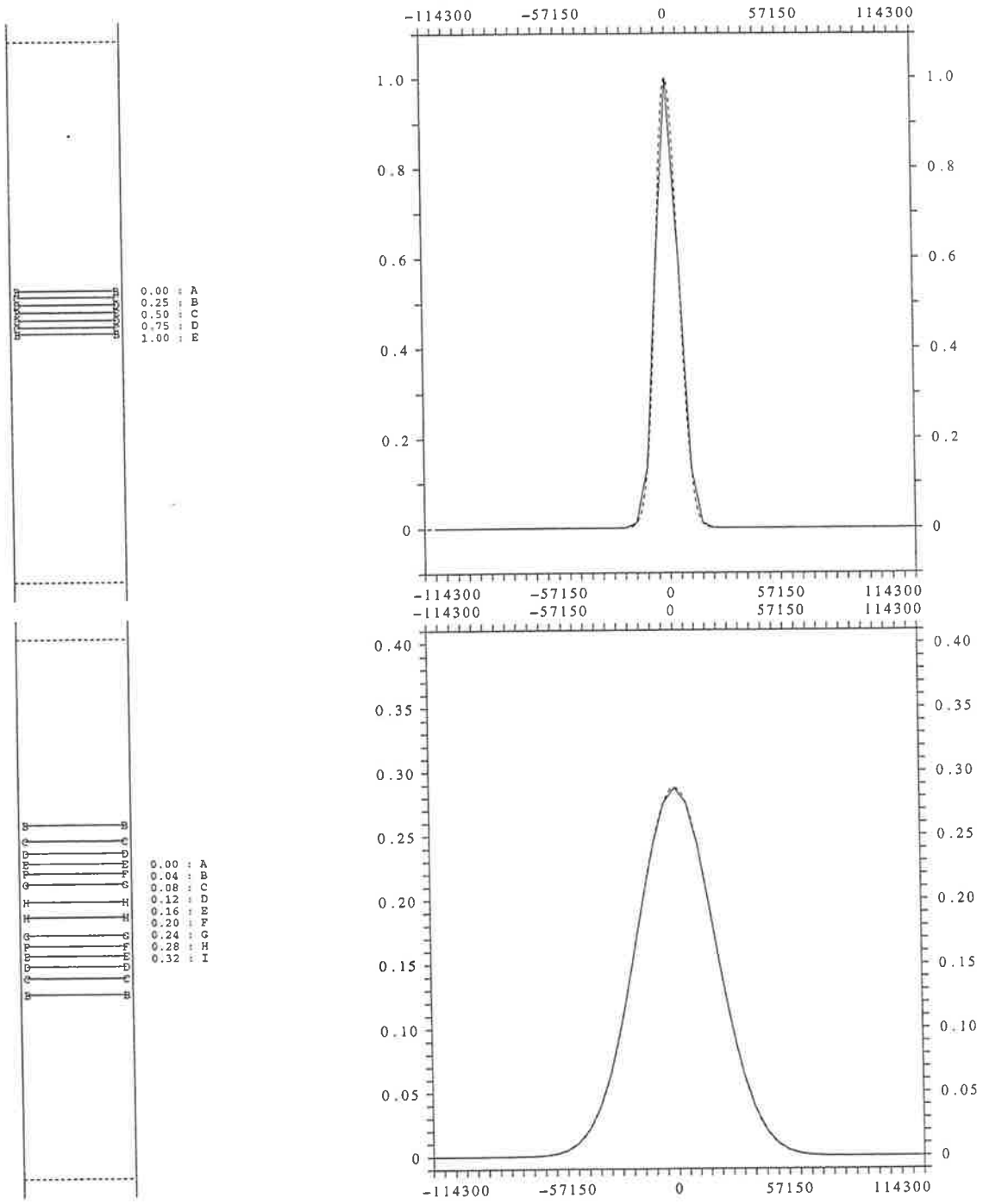

Figure 8.16: Level curves (left) and y-transects (right) for the initial condition (top) and analytical solution (bottom) of the "oscillating tide" test. Level curves are shown at the appropriate grid–scale (solid curves) in the interior domain only, excluding the open boundary (dashed lines), with the closed boundary (solid lines) also shown. Transects are shown at the appropriate grid–scale (solid curve) and at a finer grid–scale (dashed curve) in the entire domain, including the open boundary, with y (m) and τ (m^{-2}) along the top/bottom and left/right axes, respectively.

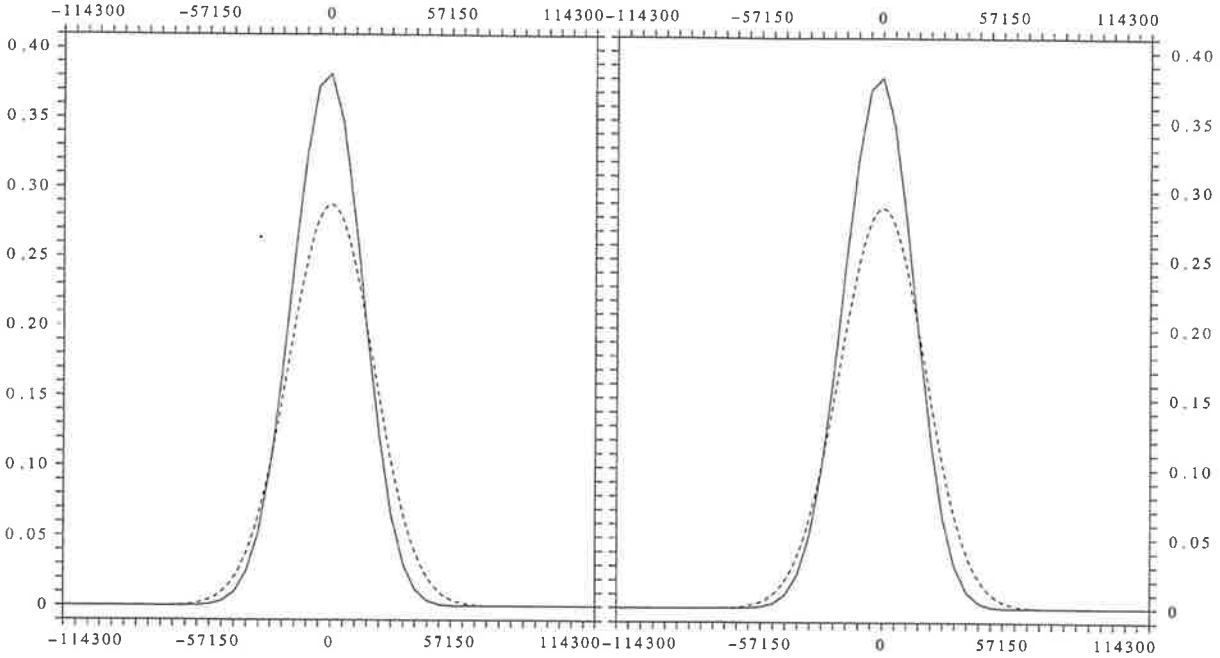

(a) without clipping

(b) with clipping

Figure 8.17: The y-transects for the Du Fort–Frankel type (1,4,1) O{1} approximation to the "oscillating tide" analytical solution. Transects are shown for the numerical solution at the appropriate grid–scale (solid curve) and the analytical solution at a finer grid–scale (dashed curve) for the entire domain, including the open boundary, with y (m) and τ (m^{-2}) along the top/bottom and left/right axes, respectively.

The "Oscillating Tide" Test Statistics for the Final Time–Step							
FDM (name)	Max{$+\tau$} (m^{-2})	$-$Max{$-\tau$} ($-m^{-2}$)	Tot{$+\tau$} (m^{-2})	$-$Tot{$-\tau$} ($-m^{-2}$)	Max{|Err|} (m^{-2})	Ave{|Err|} (m^{-2})	RPH
Analytic	2.87×10^{-1}	0.0	2.26×10^{1}	0.0	0.0	0.0	1.00
DF (1,4,1)	3.63×10^{-1}	2.79×10^{-5}	2.26×10^{1}	4.39×10^{-4}	7.55×10^{-2}	1.37×10^{-2}	1.26
DF *(1,4,1)*	3.82×10^{-1}	0.0	2.46×10^{1}	0.0	9.66×10^{-2}	1.52×10^{-2}	1.33
MFTCS (1,5)	2.60×10^{-1}	3.15×10^{-3}	2.28×10^{1}	1.94×10^{-1}	2.69×10^{-2}	6.07×10^{-3}	0.91
MFTCS *(1,5)*	2.73×10^{-1}	0.0	2.56×10^{1}	0.0	3.34×10^{-2}	8.10×10^{-3}	0.95
LW 2(1,3)	2.72×10^{-1}	1.04×10^{-3}	2.26×10^{1}	5.25×10^{-2}	1.55×10^{-2}	3.30×10^{-3}	0.95
LW *2(1,3)*	2.78×10^{-1}	0.0	2.37×10^{1}	0.0	1.83×10^{-2}	4.20×10^{-3}	0.97

Table 8.1: The "oscillating tide" test statistics for the final time–step.

The "Oscillating Tide" Test Statistics Over All Time–Steps							
FDM (name)	Max{$+\tau$} (m^{-2})	$-$Max{$-\tau$} ($-m^{-2}$)	Tot{$+\tau$} (m^{-2})	$-$Tot{$-\tau$} ($-m^{-2}$)	Max{|Err|} (m^{-2})	Ave{|Err|} (m^{-2})	CPU (s)
Analytic	9.77×10^{-1}	0.0	1.14×10^{4}	0.0	0.0	0.0	-
DF (1,4,1)	1.02×10^{0}	1.98×10^{-1}	1.13×10^{4}	3.47×10^{1}	5.89×10^{-1}	1.62×10^{-2}	22.2
DF *(1,4,1)*	1.02×10^{0}	0.0	1.24×10^{4}	3.88×10^{0}	5.48×10^{-1}	1.76×10^{-2}	23.0
MFTCS (1,5)	9.52×10^{-1}	6.20×10^{-2}	1.16×10^{4}	1.86×10^{2}	2.48×10^{-1}	1.01×10^{-2}	22.8
MFTCS *(1,5)*	9.52×10^{-1}	0.0	1.25×10^{4}	2.42×10^{0}	2.45×10^{-1}	1.15×10^{-2}	23.0
LW 2(1,3)	9.52×10^{-1}	3.06×10^{-2}	1.14×10^{4}	7.53×10^{1}	5.89×10^{-1}	1.39×10^{-2}	25.4
LW *2(1,3)*	9.52×10^{-1}	0.0	1.19×10^{4}	1.14×10^{0}	5.88×10^{-1}	1.43×10^{-2}	27.2

Table 8.2: The "oscillating tide" test statistics over all time–steps.

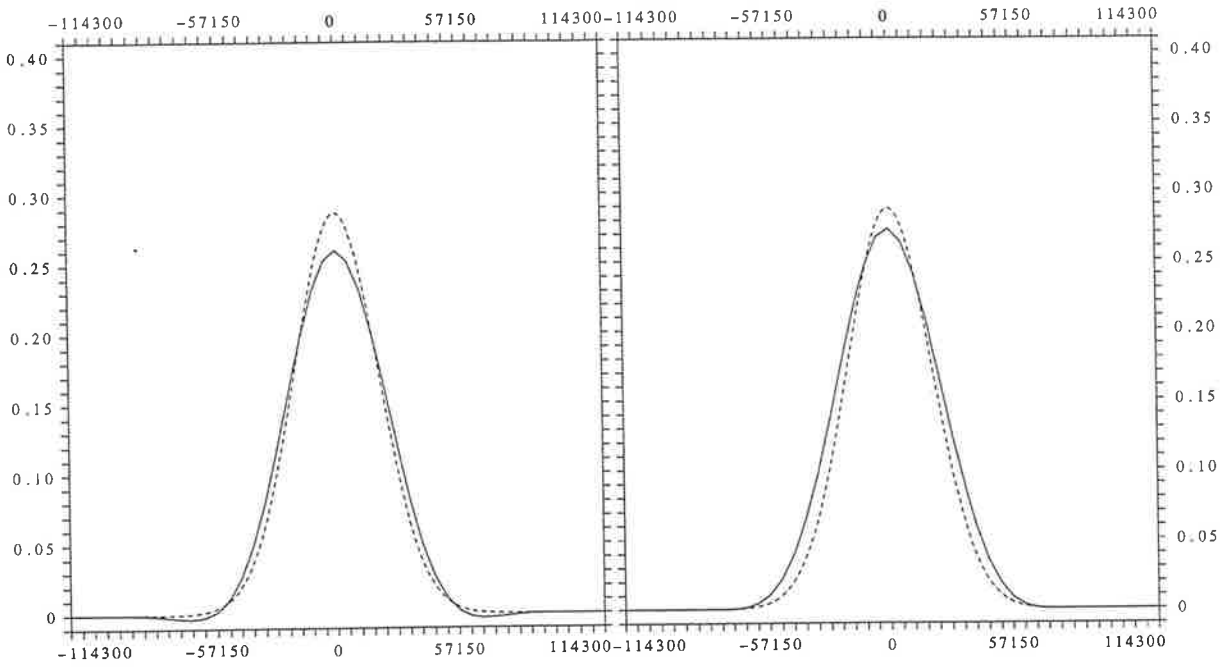

(a) without clipping

(b) with clipping

Figure 8.18: The y-transects for the "modified" FTCS (1,5) O $\{1\}$ approximation to the "oscillating tide" analytical solution. Transects are shown for the numerical solution at the appropriate grid–scale (solid curve) and the analytical solution at a finer grid–scale (dashed curve) for the entire domain, including the open boundary, with y (m) and τ (m^{-2}) along the top/bottom and left/right axes, respectively.

line either side of the main transect peak, clipping is, in fact, desired. This comes at the cost of an artificial production of larval biomass (indicated by Tot$\{+\tau\}$ values greater than that of the AS and transects with greater variance than that of the AS), and an artificially exaggerated pulse height (indicated by Max$\{+\tau\}$ and RPH values greater than those for the AS and transects with exaggerated local maxima compared to that of the AS), especially for FDMs with inherent numerical anti-diffusion (such as the DF (1,4,1) FDM). The benefits of clipping include the elimination of "undershoot" (indicated by $-$Max$\{-\tau\}$ values closer to that of the AS and transects which, like that for the AS, never cross below the zero concentration line) and a beneficially exaggerated pulse height (indicated by Max$\{+\tau\}$ and RPH values closer to those for the AS and transects with enhanced local maxima converging to that of the AS), especially for FDMs with inherent numerical diffusion (such as the MFTCS (1,5) and LW 2(1,3) FDMs).

In all FDM tests, however, clipping resulted in greater Ave$\{|\text{Err}|\}$ when compared to no clipping. The Max$\{|\text{Err}|\}$ followed the same trend as Ave$\{|\text{Err}|\}$ for the final solution, but the converse is true for the corresponding overall statistic. This somewhat perplexing phenomenon can be rationalised when one considers that for all FDMs, on examination of the transects, the clipped solution is a worse fit to the AS than the non clipped solution, but that during tidal oscillations where phase lag or lead comes into effect, this may not always be the case.

Clipping issues aside, the FDMs are listed in the tables in order of increasing attractiveness on the basis of Max$\{|\text{Err}|\}$ and Ave$\{|\text{Err}|\}$ in the final solution. This is not the case if the corresponding overall statistics are considered, however, where the MFTCS (1,5) FDM performs significantly better that the other two, with this trend repeated if one considers RPH.

For best minimisation of negative concentrations, and fair representation of maximum concentrations, the LW 2(1,3) FDM, despite its greater CPU requirements, could be considered the most appropriate of the three FDMs for biomass-conserving prawn larvae dispersion simulations in "oscillating tides" for open gulfs.

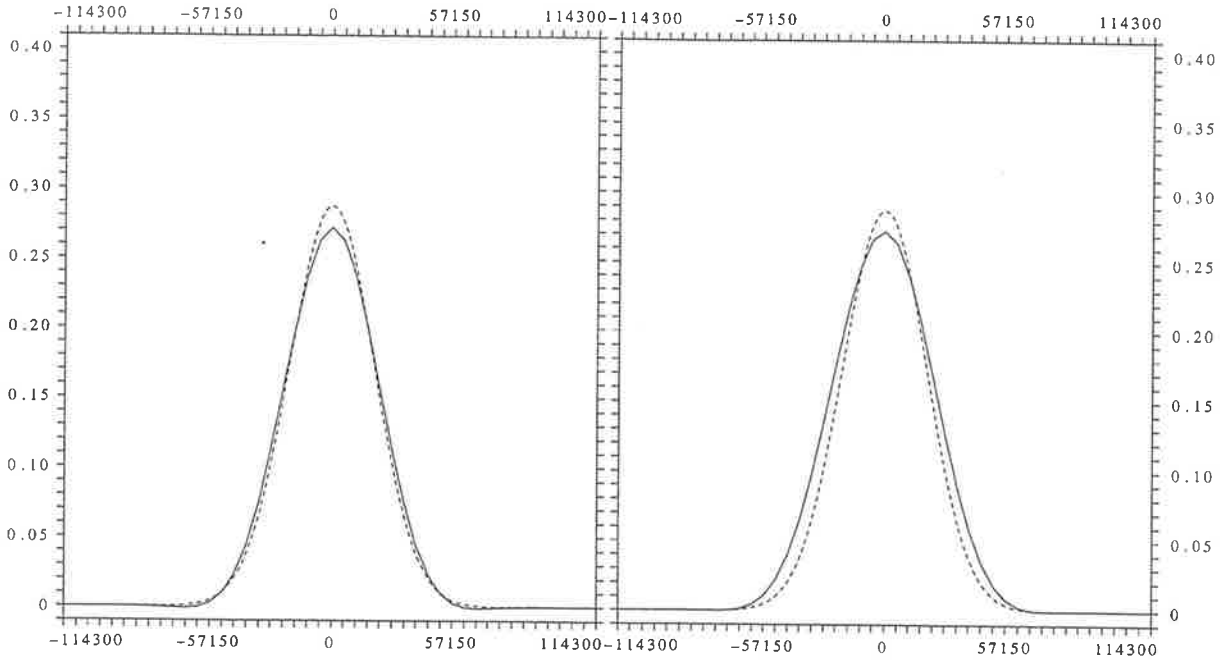

(a) without clipping

(b) with clipping

Figure 8.19: The y-transects for the Lax–Wendroff type 2(1,3) O{2} approximation to the "oscillating tide" analytical solution. Transects are shown for the numerical solution at the appropriate grid–scale (solid curve) and the analytical solution at a finer grid–scale (dashed curve) for the entire domain, including the open boundary, with y (m) and τ (m^{-2}) along the top/bottom and left/right axes, respectively.

8.9.3 The "Constant Current" Test

The PDE (8.1.1) is approximated for a constant flow in the x and y directions given by

$$u(x,y,t) = u_a, \quad v(x,y,t) = v_a, \tag{8.9.4}$$

in which: u_a and v_a are the velocities in the x and y directions, respectively; the IC is given by (8.9.1) with

$$2\sigma_x^2 = \alpha_x, \quad 2\sigma_y^2 = \alpha_y; \tag{8.9.5}$$

the BC (8.8.1) is approximated at coastal boundary grid–points as defined in Section 8.8.1; and values at open boundary grid–points determined by the AS (Noye 1987a)

$$\hat{\tau}(x,y,t) = \frac{\sigma_x\sigma_y}{\sqrt{{\sigma_x}^2 + 2\alpha_x t}\sqrt{{\sigma_y}^2 + 2\alpha_y t}} \exp\left\{\frac{-(x-x_0-ut)^2}{2({\sigma_x}^2 + 2\alpha_x t)} \frac{-(y-y_0-vt)^2}{2({\sigma_y}^2 + 2\alpha_y t)}\right\} \tag{8.9.6}$$

on a 19×19 uniform mesh representative of the symmetrical nature of the southern regions of the coarse grid Spencer Gulf model discussed in Section 3.4. An AS corresponding to a similar current regime, and simulation results produced by a number of FDMs approximating PDE (8.1.1) within such a regime, were presented in Noye and Tan (1989).

Other parameters used, *not* representative of Spencer Gulf, are: $\Delta t = 0.025\,\mathrm{s}$, $\Delta x = \Delta y = 0.05\,\mathrm{m}$, $\alpha_x = \alpha_y = 0.005\,\mathrm{m^2 s^{-1}}$, $x_0 = y_0 = -0.5\,\mathrm{m}$, $u_a = v_a = 0.4\,\mathrm{m\,s^{-1}}$, and results obtained at time $t = N\Delta t = 2.5\,\mathrm{s}$. These parameters were chosen in order to represent a 2D "constant current" propagating a concentration unit pulse with constant diffusion.

The stability diagrams of Section 8.7 indicate that all FDMs are von Neumann stable for these parameters—which correspond to constant diffusion numbers of $s_x = s_y = 0.05$ and constant

Courant numbers of $c_x = c_y = 0.2$—and that all are capable of producing both negative and non-negative values. The parameters used in this test are not, however, consistent with the Spencer Gulf region or the existing coarse grid associated with the tidal model of the Gulf. It is for this reason that the test in Section 8.9.4, using parameters consistent with a coarse grid Spencer Gulf tidal model—for which not all schemes are at all times von Neumann stable—is made.

The IC and AS are represented graphically in Figure 8.20 and the approximations produced by the schemes discussed above are represented graphically in Figures 8.21–8.24. The level curves (solid curves) in Figures 8.20–8.24 have x and y axes aligned horizontally and vertically, respectively, with (x_0, y_0) centred in the region enclosed by the open boundary (dashed lines). The transects in these figures were taken along the lines from the bottom-left to the top-right of the region of interest (referred to as a *longitudinal* transect) and from the top-left to the bottom-right of the region of interest (referred to as a *transverse* transect). The coordinate marked along the top/bottom axes in either case is x as the transect progresses left to right across the physical region of interest.

The results presented in Figures 8.21–8.24 and the statistics presented in Tables 8.3–8.4 are, in contrast to the "oscillating tide" test results, identical to the given precision with or

The "Constant Current" Test Statistics for the Final Time-Step							
FDM (name)	Max$\{+\tau\}$ (m^{-2})	$-$Max$\{-\tau\}$ ($-m^{-2}$)	Tot$\{+\tau\}$ (m^{-2})	$-$Tot$\{-\tau\}$ ($-m^{-2}$)	Max$\{\|Err\|\}$ (m^{-2})	Ave$\{\|Err\|\}$ (m^{-2})	RPH
Analytic	9.09×10^{-2}	0.0	6.26×10^{0}	0.0	0.0	0.0	1.000
DF (1,4,1)	9.06×10^{-2}	0.0	6.23×10^{0}	0.0	8.92×10^{-3}	1.27×10^{-3}	0.997
DF *(1,4,1)*	9.06×10^{-2}	0.0	6.23×10^{0}	0.0	8.92×10^{-3}	1.27×10^{-3}	0.997
FTCS (1,5)	1.06×10^{-1}	2.14×10^{-6}	6.25×10^{0}	2.14×10^{-6}	1.90×10^{-2}	3.13×10^{-3}	1.163
FTCS *(1,5)*	1.06×10^{-1}	0.0	6.25×10^{0}	1.03×10^{-6}	1.90×10^{-2}	3.13×10^{-3}	1.163
MFTCS (1,5)	8.90×10^{-2}	0.0	6.10×10^{0}	0.0	1.18×10^{-2}	1.76×10^{-3}	0.979
MFTCS *(1,5)*	8.90×10^{-2}	0.0	6.10×10^{0}	0.0	1.16×10^{-2}	1.76×10^{-3}	0.979
LW 2(1,3)	8.71×10^{-2}	0.0	6.10×10^{0}	0.0	7.56×10^{-3}	9.13×10^{-4}	0.958
LW *2(1,3)*	8.71×10^{-2}	0.0	6.10×10^{0}	0.0	7.56×10^{-3}	9.13×10^{-4}	0.958

Table 8.3: The "constant current" test statistics for the final time–step.

The "Constant Current" Test Statistics Over All Time-Steps							
FDM (name)	Max$\{+\tau\}$ (m^{-2})	$-$Max$\{-\tau\}$ ($-m^{-2}$)	Tot$\{+\tau\}$ (m^{-2})	$-$Tot$\{-\tau\}$ ($-m^{-2}$)	Max$\{\|Err\|\}$ (m^{-2})	Ave$\{\|Err\|\}$ (m^{-2})	CPU (s)
Analytic	1.55×10^{-1}	0.0	2.82×10^{2}	0.0	0.0	0.0	-
DF (1,4,1)	1.55×10^{-1}	0.0	2.79×10^{2}	0.0	9.30×10^{-3}	3.87×10^{-3}	7.0
DF *(1,4,1)*	1.55×10^{-1}	0.0	2.79×10^{2}	0.0	9.30×10^{-3}	3.87×10^{-3}	7.0
FTCS (1,5)	1.57×10^{-1}	2.13×10^{-6}	2.77×10^{2}	6.00×10^{-6}	1.91×10^{-2}	8.63×10^{-3}	6.0
FTCS *(1,5)*	1.57×10^{-1}	0.0	2.77×10^{2}	2.98×10^{-6}	1.91×10^{-2}	8.63×10^{-3}	6.0
MFTCS (1,5)	1.55×10^{-1}	0.0	2.74×10^{2}	0.0	1.23×10^{-2}	5.22×10^{-3}	6.1
MFTCS *(1,5)*	1.55×10^{-1}	0.0	2.74×10^{2}	0.0	1.23×10^{-2}	5.22×10^{-3}	6.0
LW 2(1,3)	1.53×10^{-1}	0.0	2.75×10^{2}	0.0	8.16×10^{-3}	3.15×10^{-3}	7.9
LW *2(1,3)*	1.53×10^{-1}	0.0	2.75×10^{2}	0.0	8.16×10^{-3}	3.15×10^{-3}	7.7

Table 8.4: The "constant current" test statistics over all time–steps.

without clipping, except for those pertaining to the FTCS (1,5) FDM and production of negative values. In this case the trend for these statistics for all FDMs discussed in the previous section is repeated for this particular FDM as is evident from the tables, the level curves and, to a much less apparent extent, the transects pertaining to this FDM. The FTCS (1,5) FDM over emphasises maximum values and peak height, while the other FDMs, including the MFTCS (1,5) FDM—as

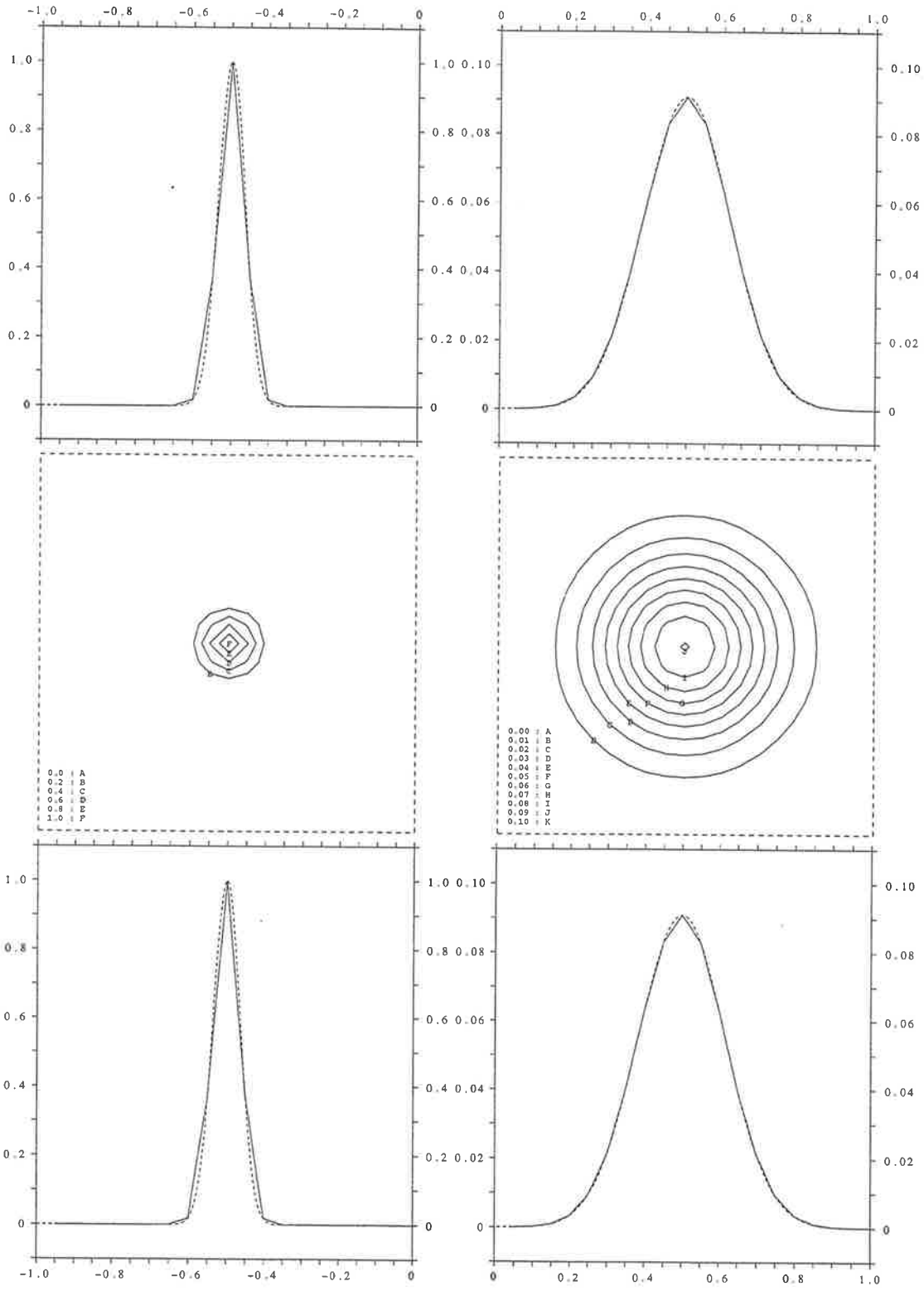

Figure 8.20: Longitudinal transects (top), level curves (middle), and transverse transects (bottom) for the initial condition (left) and analytical solution (right) of the "constant current" numerical test. Level curves are shown at the appropriate grid–scale (solid curves) in the interior domain only, excluding the open boundary (dashed lines). Transects are shown at the appropriate grid–scale (solid curve) and at a finer grid–scale (dashed curve) for the entire domain, including the open boundary, with x (m) and τ (m^{-2}) along the top/bottom and left/right axes, respectively.

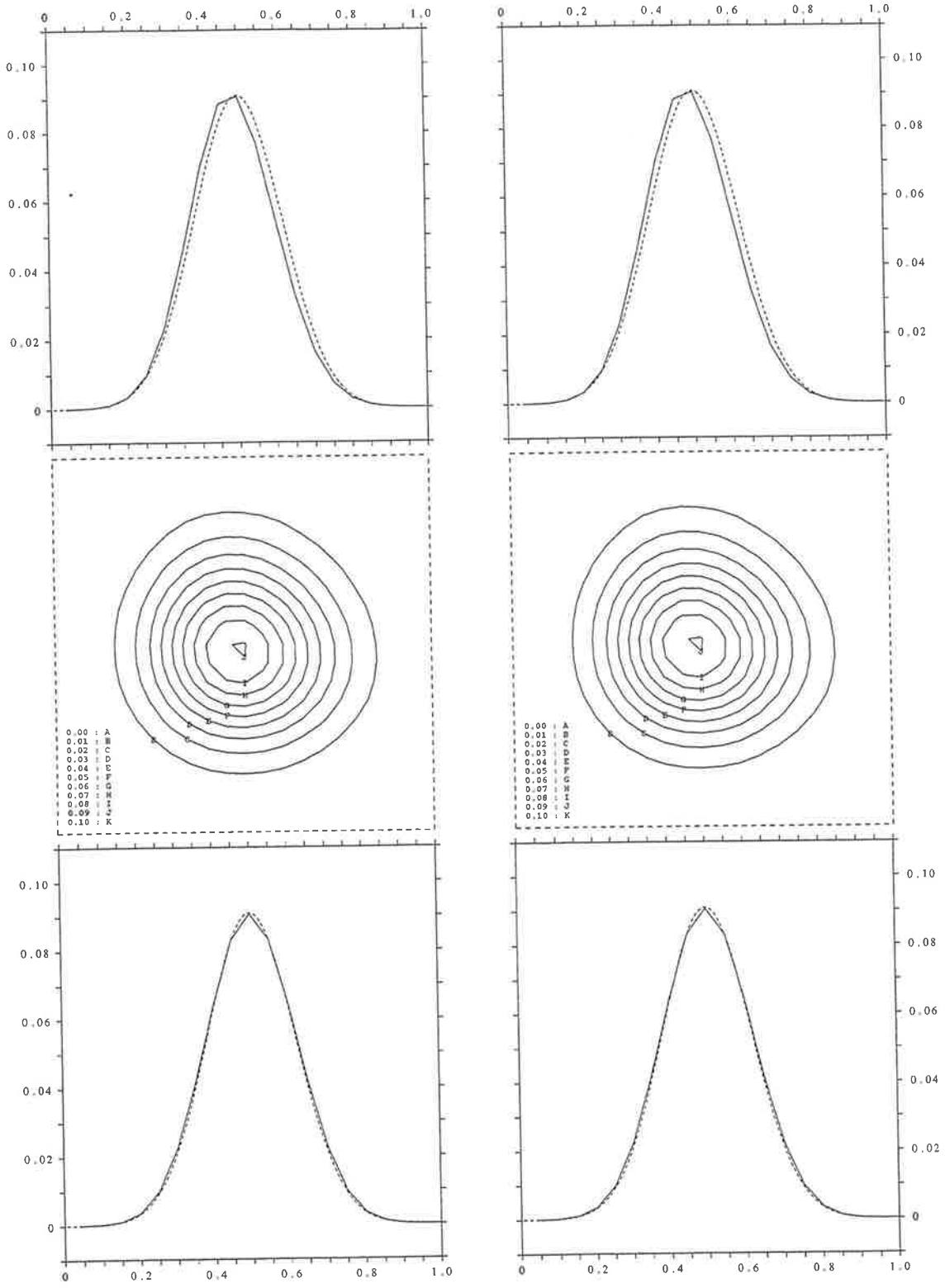

Figure 8.21: Longitudinal transects (top), level curves (middle), and transverse transects (bottom) for the no clipping (left) and clipping (right) Du Fort–Frankel type (1,4,1) O{1} approximation to the "constant current" analytical solution. Level curves are shown at the appropriate grid–scale (solid curves) in the interior domain only, excluding the open boundary (dashed lines). Transects are shown for the numerical solution at the appropriate grid–scale (solid curve) and the analytical solution at a finer grid–scale (dashed curve) for the entire domain, including the open boundary, with x (m) and τ (m^{-2}) along the top/bottom and left/right axes, respectively.

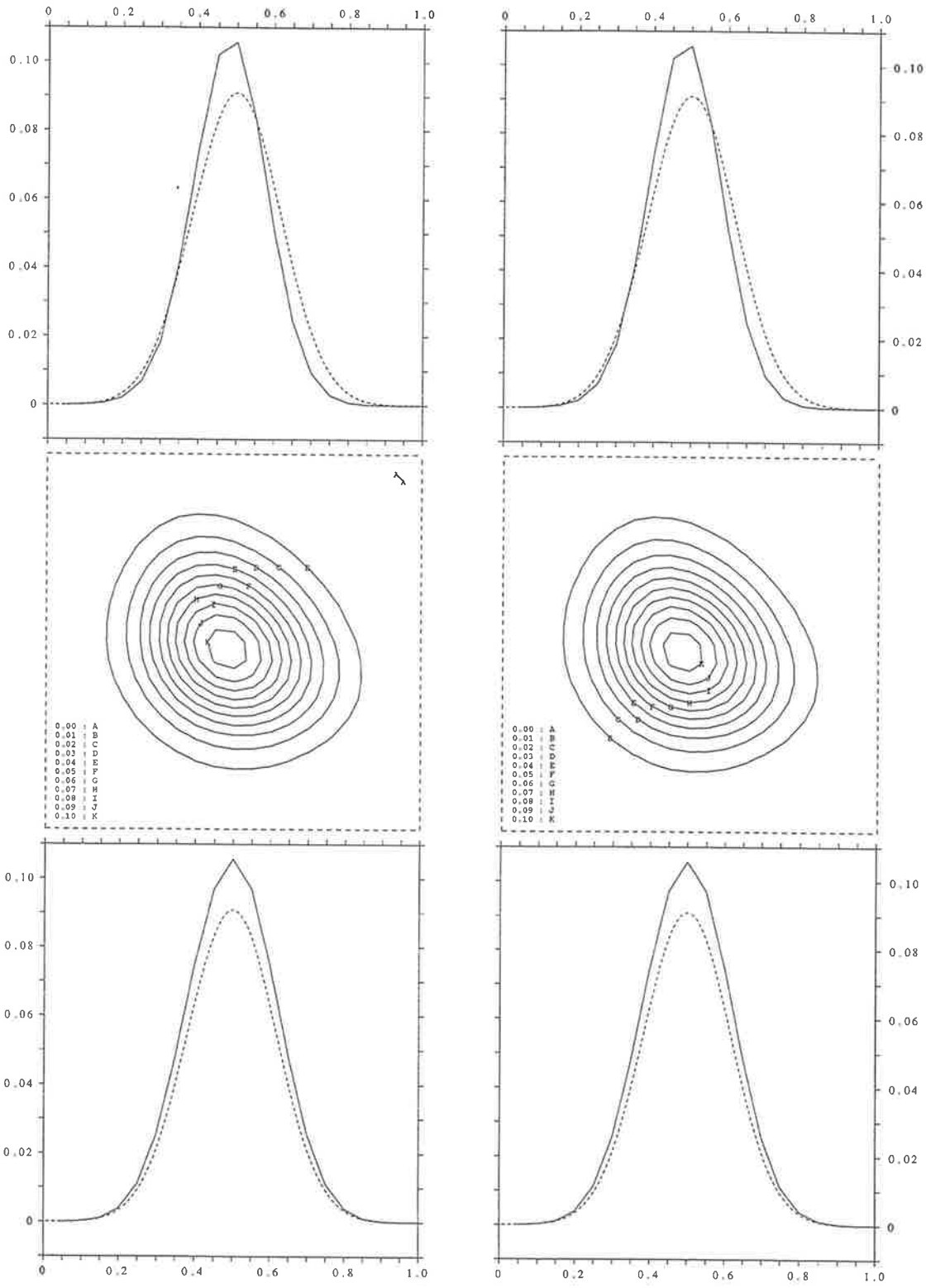

Figure 8.22: Longitudinal transects (top), level curves (middle), and transverse transects (bottom) for the no clipping (left) and clipping (right) FTCS (1,5) O{1} approximation to the "constant current" analytical solution. Level curves are shown at the appropriate grid–scale (solid curves) in the interior domain only, excluding the open boundary (dashed curve). Transects are shown for numerical solution at the appropriate grid–scale (solid curve) and the analytical solution at a finer grid–scale (dashed lines) for the entire domain, including the open boundary, with x (m) and τ (m^{-2}) along the top/bottom and left/right axes, respectively.

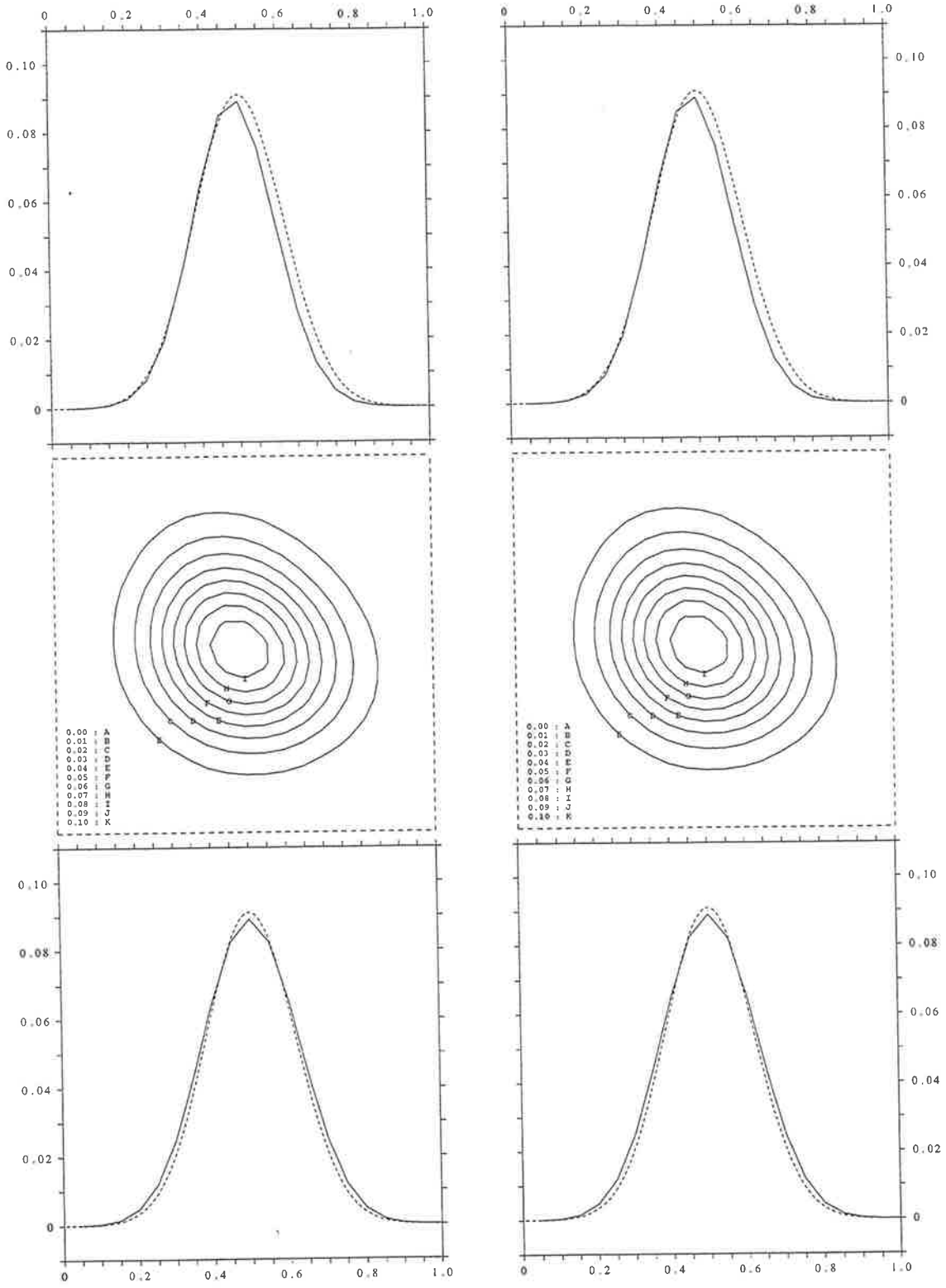

Figure 8.23: Longitudinal transects (top), level curves (middle), and transverse transects (bottom) for the no clipping (left) and clipping (right) MFTCS (1,5) O{1} approximation to the "constant current" analytical solution. Level curves are shown at the appropriate grid–scale (solid curves) in the interior domain only, excluding the open boundary (dashed curve). Transects are shown for numerical solution at the appropriate grid–scale (solid curve) and the analytical solution at a finer grid–scale (dashed lines) for the entire domain, including the open boundary, with x (m) and τ (m^{-2}) along the top/bottom and left/right axes, respectively.

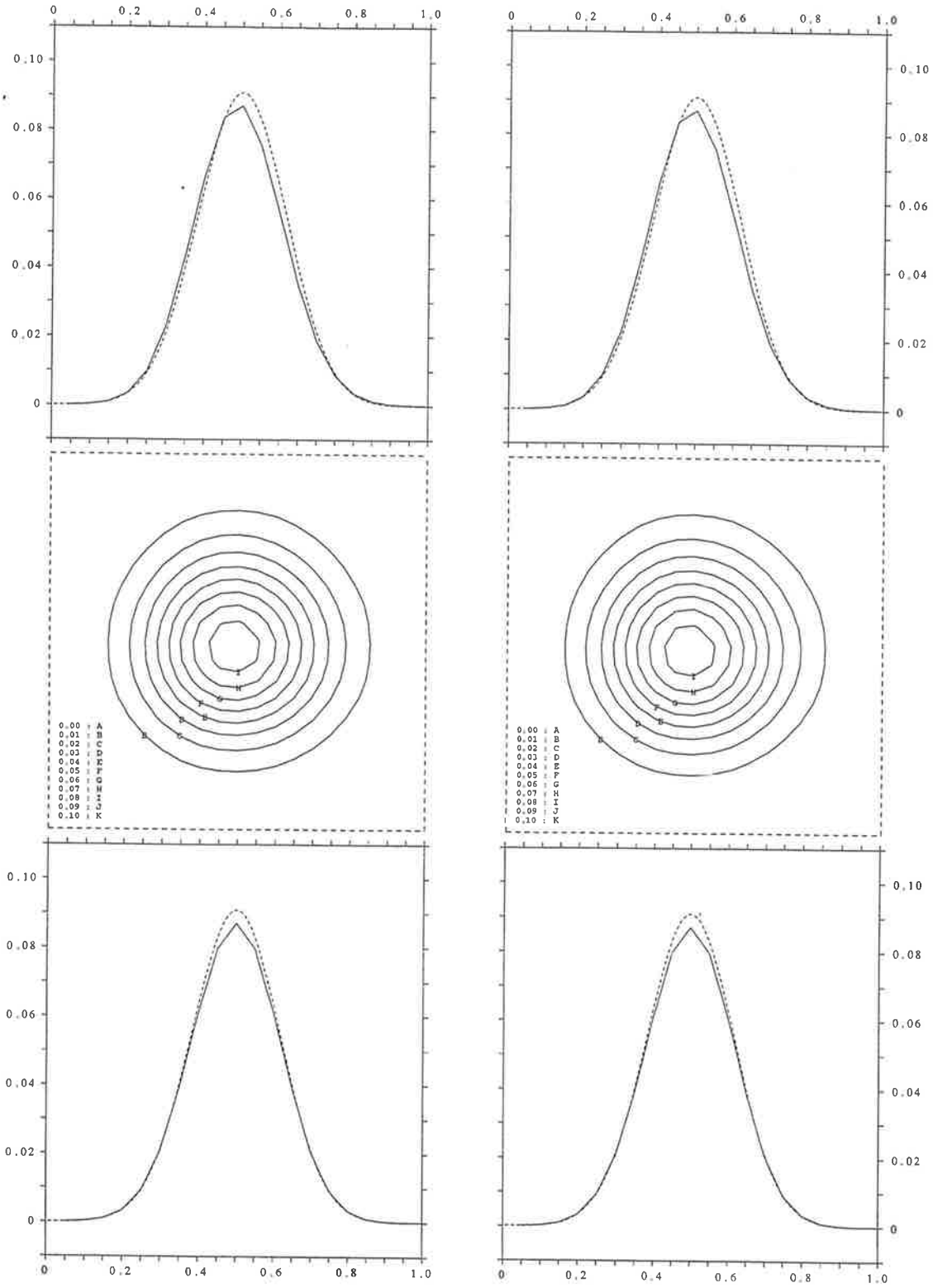

Figure 8.24: Longitudinal transects (top), level curves (middle), and transverse transects (bottom) for the no clipping (left) and clipping (right) Lax–Wendroff type 2(1,3) O{2} approximation to the "constant current" analytical solution. Level curves are shown at the appropriate grid–scale (solid curves) in the interior domain only, excluding the open boundary (dashed lines). Transects are shown for the numerical solution at the appropriate grid–scale (solid curve) and the analytical solution at a finer grid–scale (dashed curve) for the entire domain, including the open boundary, with x (m) and τ (m^{-2}) along the top/bottom and left/right axes, respectively.

was *not* the case in the previous test—do not.

In terms of positive value production, there is no definite trend evident, although it is apparent that the DF (1,4,1) FDM performs favourably even compared to the theoretically more accurate LW 2(1,3) FDM. This fact is emphasised if one considers that the FDMs would be listed in the tables in order of increasing attractiveness—in terms of absolute errors—if the DF (1,4,1) results were translated to just before those of the LW 2(1,3) FDM. Examination of the level curves supports this trend, while the transects indicate that, due mainly to numerical diffusion effects, the DF (1,4,1) FDM could be considered superior to the LW 2(1,3) FDM.

A thorough MEPDE analysis may determine that the test parameters chosen in fact unfairly bias this test in favour of the DF (1,4,1) FDM compared to the LW 2(1,3) FDM. With the parameters chosen, the first non-zero MEPDE coefficients of (8.5.4)–(8.5.5) for the former are

$$\eta_{2,0} = \eta_{1,1} = \eta_{0,2} = 0.04 \tag{8.9.7}$$

and those of the latter are

$$\eta_{3,0} = \eta_{0,3} = 0.66 \tag{8.9.8}$$

indicating that, depending on the magnitude of the spatial derivatives involved, the leading error terms associated with the two FDMs could be an order of magnitude in favour of the DF (1,4,1) over the LW 2(1,3) FDM.

Clearly the choice of the best method of those tested is either the DF (1,4,1) or the LW 2(1,3) FDM, depending on whether peak height or overall peak shape resolution, respectively, is the most desired characteristic. The transects and level curves, respectively, are the most obvious illustrations of this conclusion.

8.9.4 The "Cowell Spawning Ground, Spencer Gulf" Test

As an indication of the performance of the different schemes in determining prawn larvae dispersion resulting from real-world current regimes in real-world physical regions, each is applied to Spencer Gulf. The region of interest is depicted in Figure 1.2, which shows local place names and geographical points of interest. Tidal currents are provided by the coarse grid Spencer Gulf model of Section 3.4, depicted in Figure 3.9—which shows some of these locations in relation to the model approximation, and in Figure 3.13—which shows mean sea level (MSL) as determined by hydrographic maps and the tidal model itself.

The PDE (8.1.1) is approximated for the real-world current regime, with the BC (8.8.1) approximated at coastal boundary grid–points, and the BC (8.8.2) at open boundary grid–points as determined by methods discussed in Section 8.8.1. Other parameters used, representative of Spencer Gulf, are: $\Delta t = 3600\,\mathrm{s}$, $\Delta x = \Delta y = 5715\,\mathrm{m}$, and $\alpha_x = \alpha_y = 100\,\mathrm{m^2 s^{-1}}$, with results obtained at time $t = N\Delta t = 2419200\,\mathrm{s}$. The approximations produced by the schemes discussed above are represented graphically in Figures 8.25–8.32 with these results incorporating the diurnal movement of the prawns in the water column. This is achieved by solving the PDE (8.1.1) with currents determined by the tidal model near the sea–surface (5.0% of total depth below it) at night (19:30 to 5:00) and near the sea–bed (5.0% of total depth above it) during the day (5:00 to 19:30), as discussed in Section 7.3.

The level curves (solid curves) in the figures have x and y axes aligned horizontally and vertically, respectively, in the region bounded by the closed boundary (solid lines) and open boundary (dashed lines) and are shown at the appropriate grid–scale in the interior domain only. An x-transect—at bottom left—is taken along the line $y = \textit{constant}$ through the grid–point of maximum concentration, with the top and bottom axes corresponding to distance (m) from the left hand closed boundary and the left and right axes corresponding to larval concentration ($\mathrm{m^{-2}}$). A y-transect—at top right—is taken along the line $x = \textit{constant}$ through the same grid–point, with the left and right axes corresponding to distance (m) from the top edge closed boundary and the top and bottom axes corresponding to larval concentration ($\mathrm{m^{-2}}$).

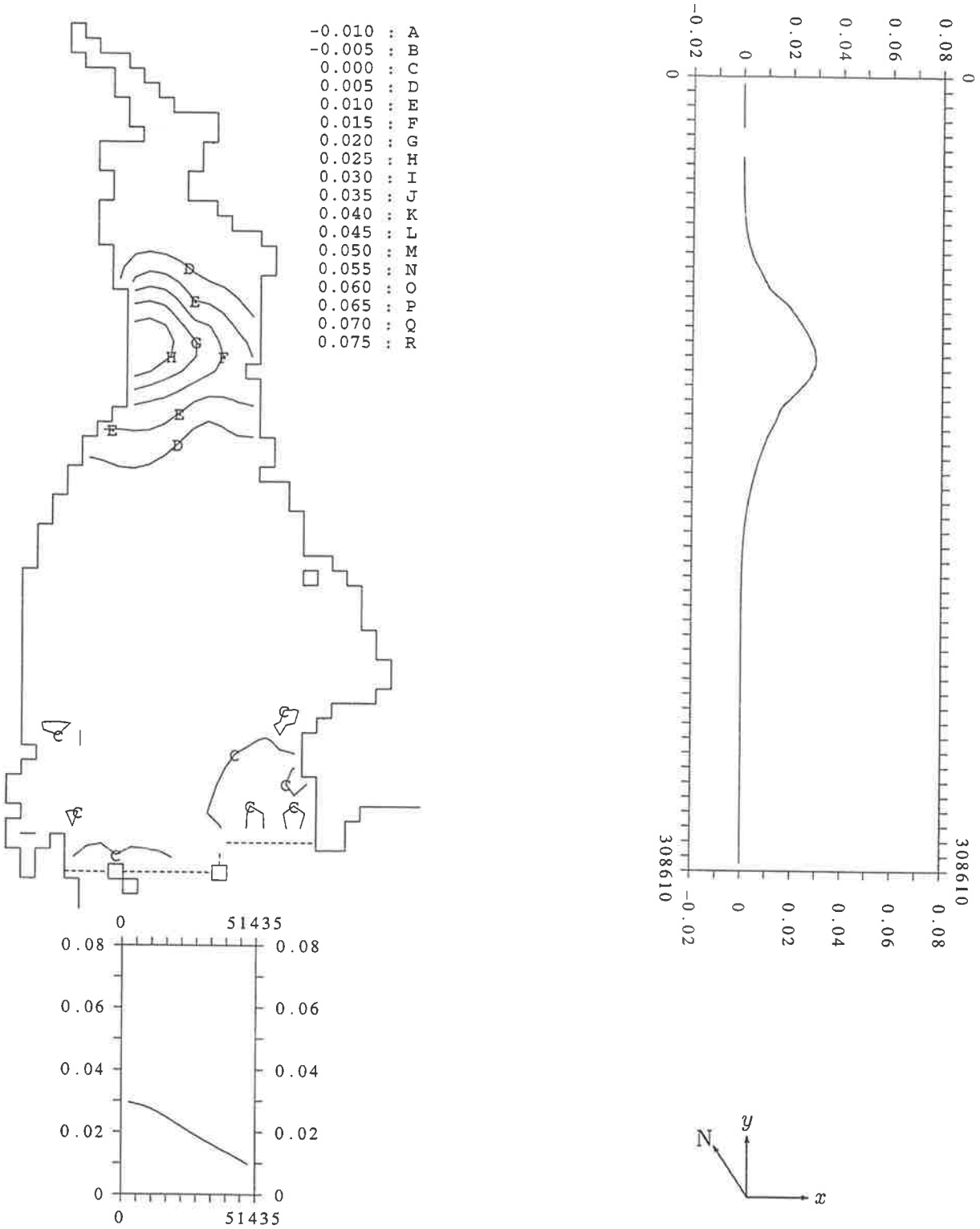

Figure 8.25: Level curves (top left), and y- (top right), and x- (bottom left) transects for the no clipping Du Fort–Frankel type (1,4,1) O{1} approximation to the "Cowell spawning ground, Spencer Gulf" prawn larvae distribution. Level curves are shown at the appropriate grid–scale (solid curves) in the interior domain only, excluding the open boundary (dashed lines). Transects are shown at the appropriate grid–scale (solid curve) and with cubic-spline smoothing (dashed curve). Concentrations (m^{-2}) and distances (m) are indicated.

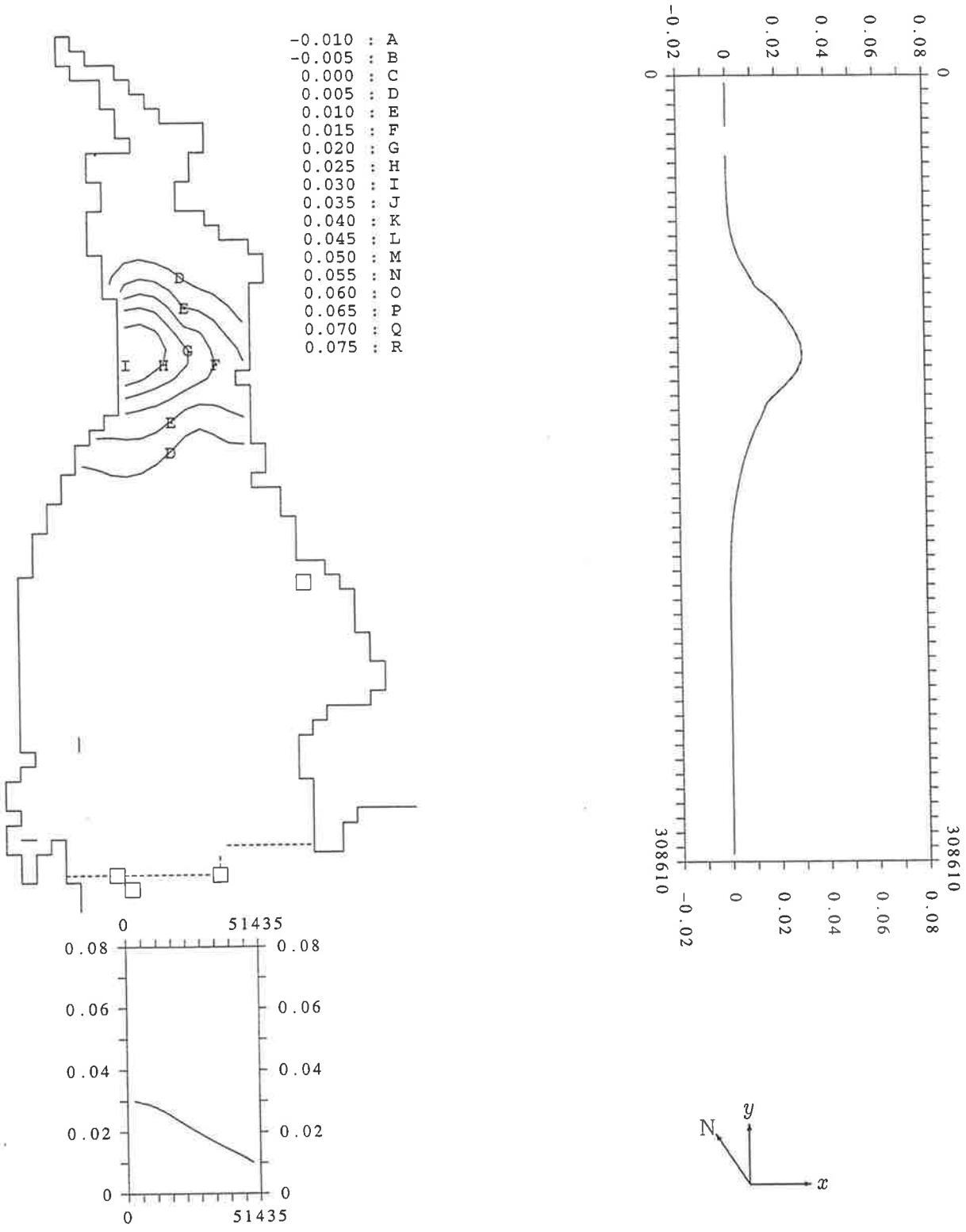

Figure 8.26: Level curves (top left), and y- (top right) and x- (bottom left) transects for the clipping Du Fort–Frankel type (1,4,1) O{1} approximation to the "Cowell spawning ground, Spencer Gulf" prawn larvae distribution. Level curves are shown at the appropriate grid–scale (solid curves) in the interior domain only, excluding the open boundary (dashed lines). Transects are shown at the appropriate grid–scale (solid curve) and with cubic-spline smoothing (dashed curve). Concentrations (m^{-2}) and distances (m) are indicated.

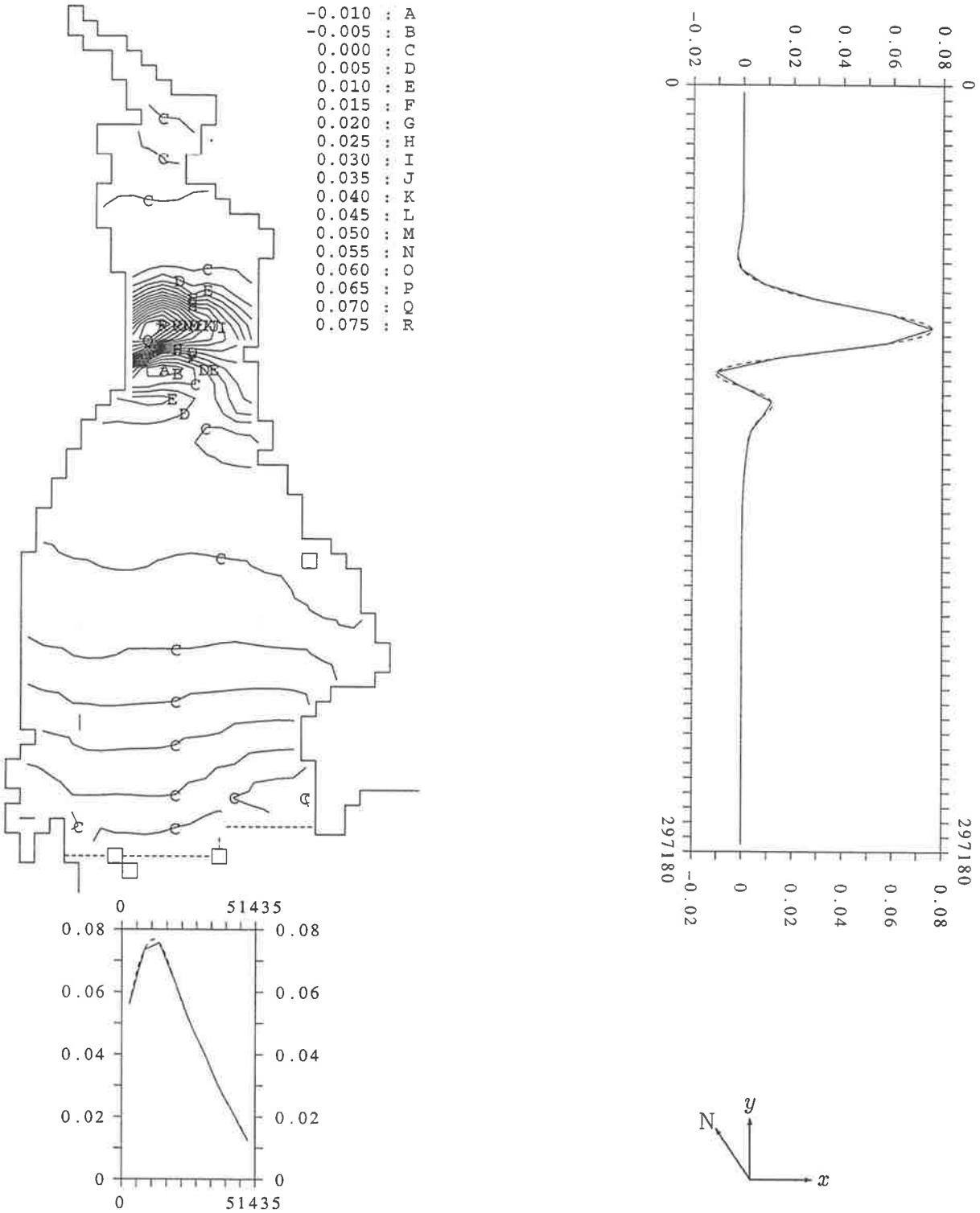

Figure 8.27: Level curves (top left), and y- (top right) and x- (bottom left) transects for the no clipping FTCS (1,5) O{1} approximation to the "Cowell spawning ground, Spencer Gulf" prawn larvae distribution. Level curves are shown at the appropriate grid–scale (solid curves) in the interior domain only, excluding the open boundary (dashed lines). Transects are shown at the appropriate grid–scale (solid curve) and with cubic-spline smoothing (dashed curve). Concentrations (m^{-2}) and distances (m) are indicated.

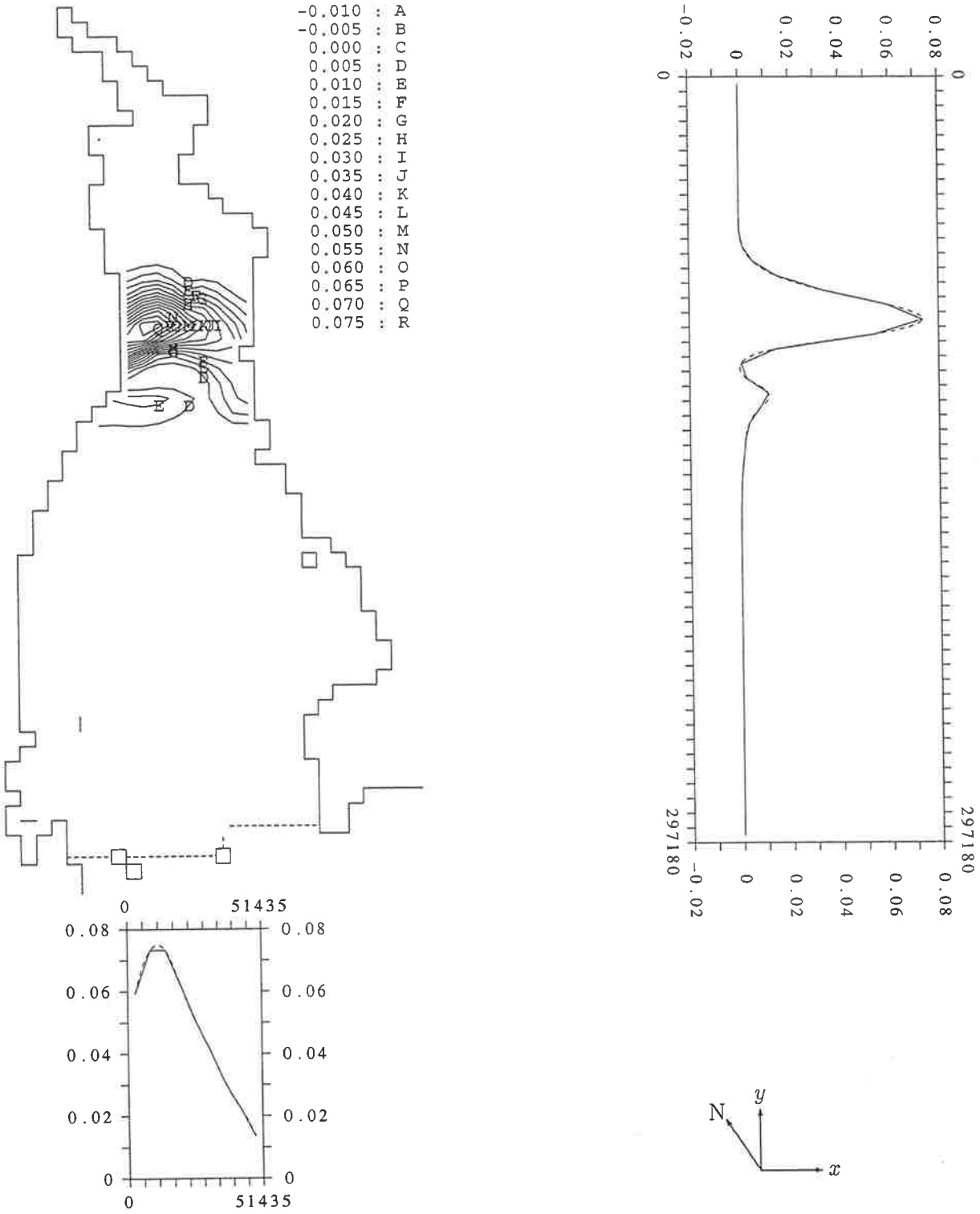

Figure 8.28: Level curves (top left), and y- (top right), and x- (bottom left) transects for the clipping FTCS (1,5) O{1} approximation to the "Cowell spawning ground, Spencer Gulf" prawn larvae distribution. Level curves are shown at the appropriate grid–scale (solid curves) in the interior domain only, excluding the open boundary (dashed lines). Transects are shown at the appropriate grid–scale (solid curve) and with cubic-spline smoothing (dashed curve). Concentrations (m^{-1}) and distances (m) are indicated.

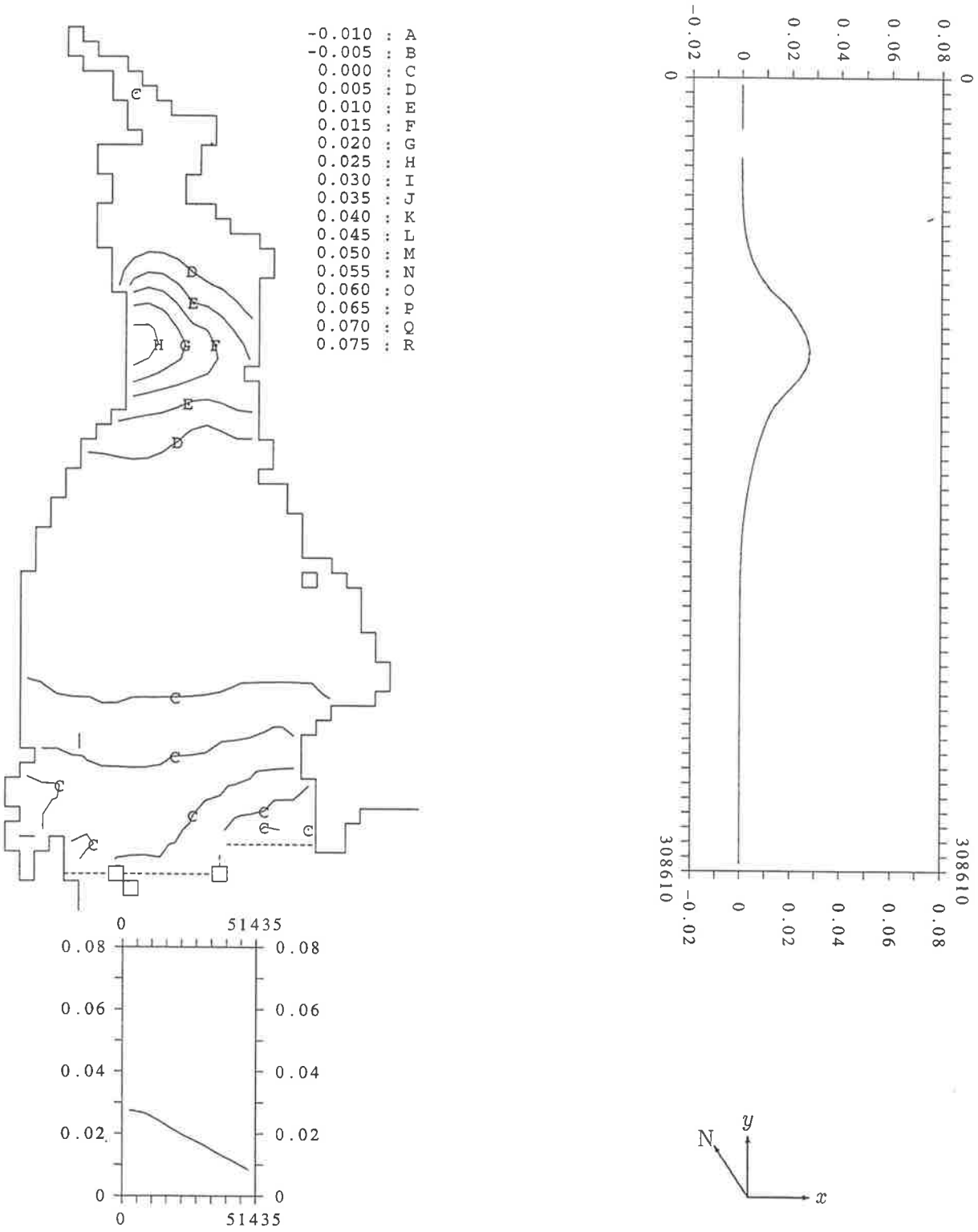

Figure 8.29: Level curves (top left), and y- (top right) and x- (bottom left) transects for the no clipping MFTCS (1,5) O{1} approximation to the "Cowell spawning ground, Spencer Gulf" prawn larvae distribution. Level curves are shown at the appropriate grid–scale (solid curves) in the interior domain only, excluding the open boundary (dashed lines). Transects are shown at the appropriate grid–scale (solid curve) and with cubic-spline smoothing (dashed curve). Concentrations (m^{-2}) and distances (m) are indicated.

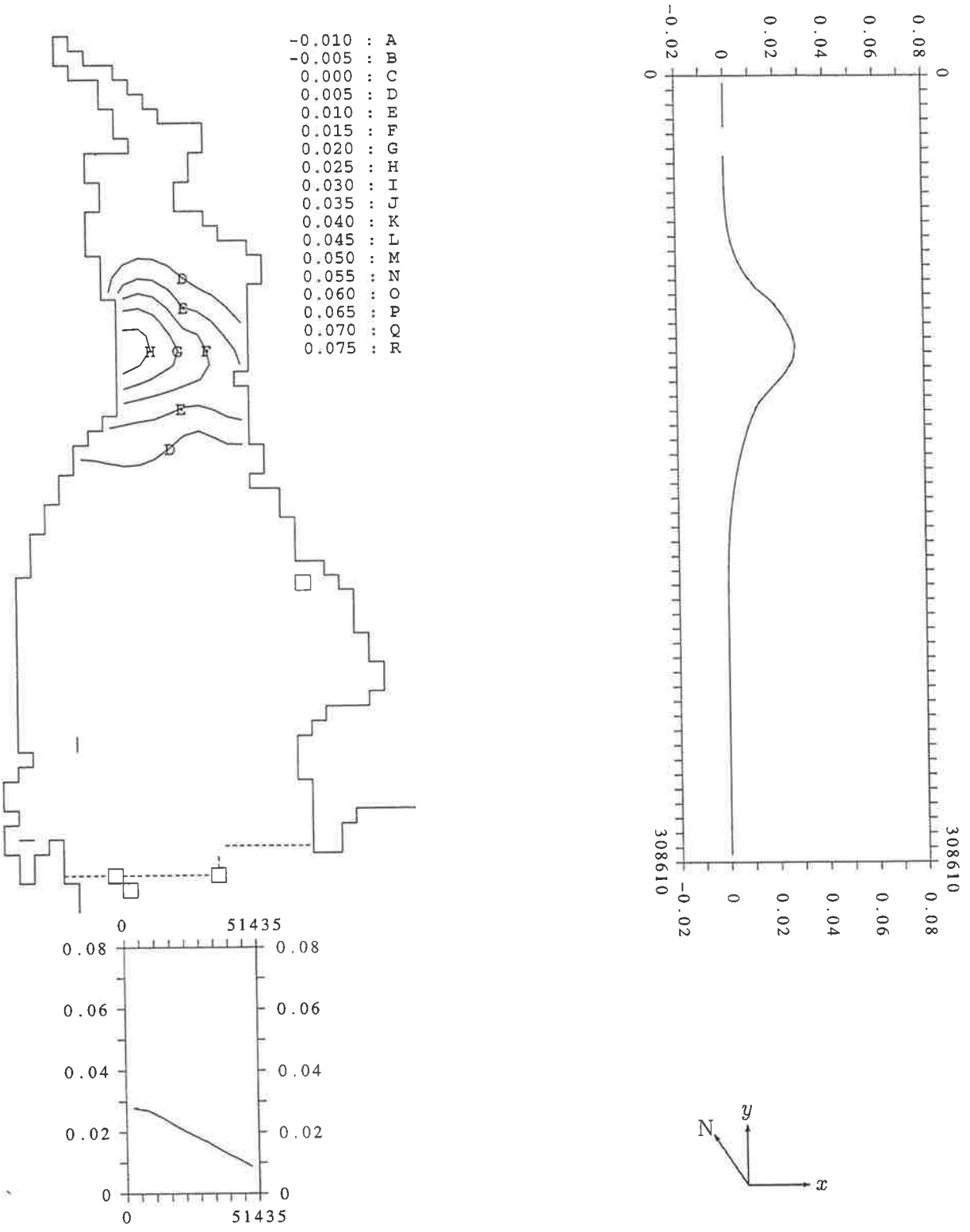

Figure 8.30: Level curves (top left), and y- (top right) and x- (bottom left) transects for the clipping MFTCS (1,5) O{1} approximation to the "Cowell spawning ground, Spencer Gulf" prawn larvae distribution. Level curves are shown at the appropriate grid–scale (solid curves) in the interior domain only, excluding the open boundary (dashed lines). Transects are shown at the appropriate grid–scale (solid curve) and with cubic-spline smoothing (dashed curve). Concentrations (m^{-2}) and distances (m) are indicated.

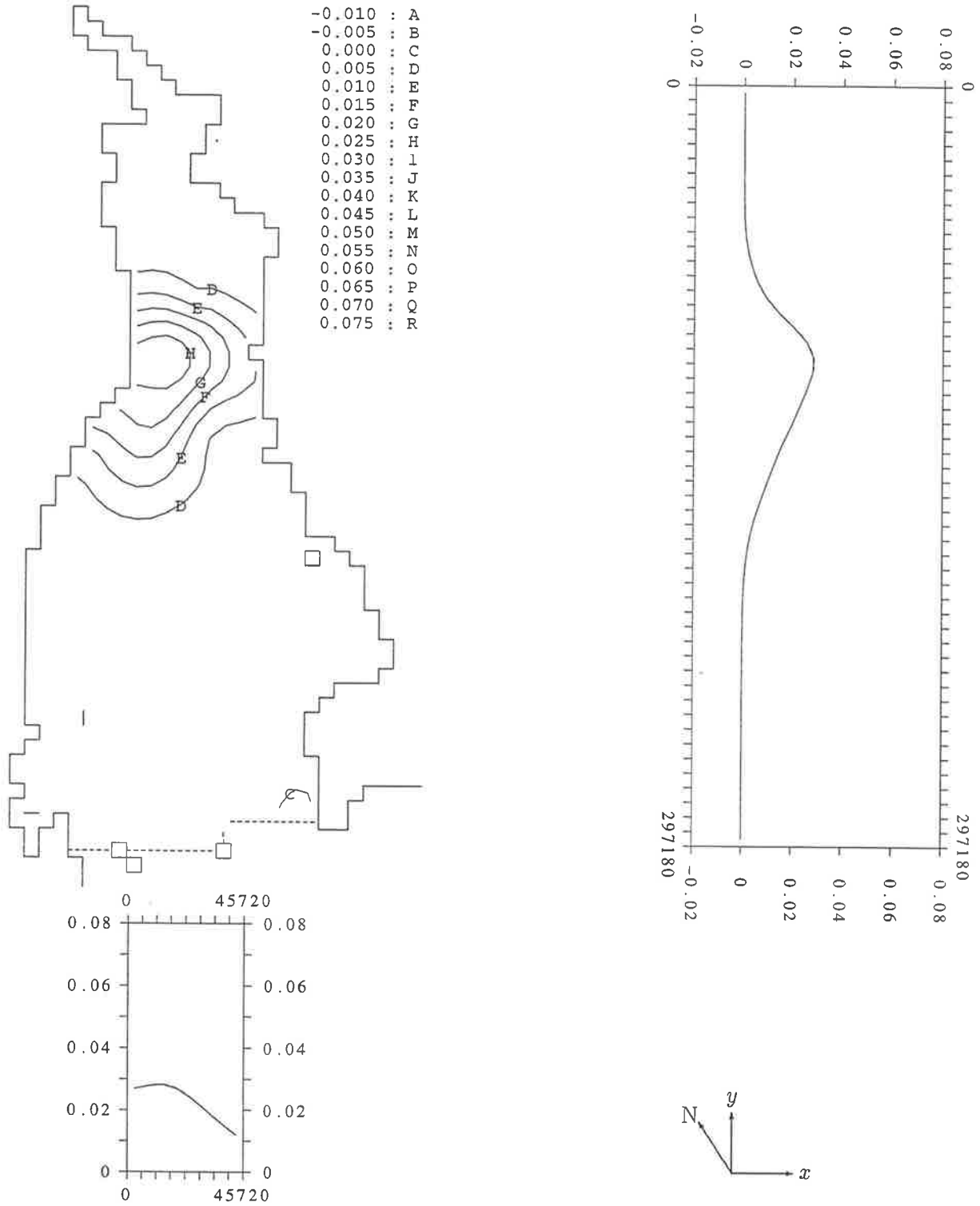

Figure 8.31: Level curves (top left), and y- (top right) and x- (bottom left) transects for the no clipping Lax–Wendroff type 2(1,3) O{2} approximation to the "Cowell spawning ground, Spencer Gulf" prawn larvae distribution. Level curves are shown at the appropriate grid–scale (solid curves) in the interior domain only, excluding the open boundary (dashed lines). Transects are shown at the appropriate grid–scale (solid curve) and with cubic-spline smoothing (dashed curve). Concentrations (m^{-2}) and distances (m) are indicated.

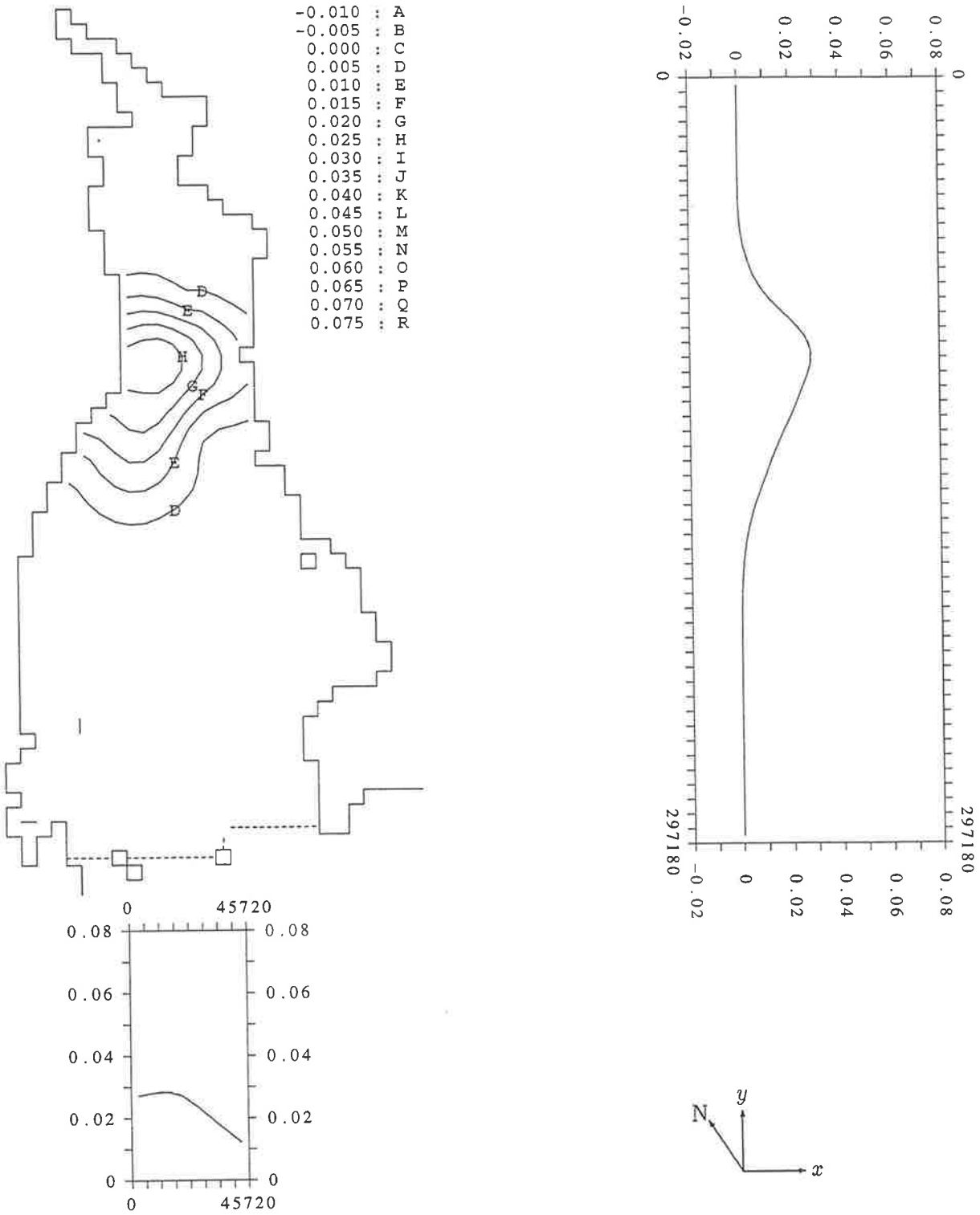

Figure 8.32: Level curves (top left), and y- (top right) and x- (bottom left) transects for the clipping Lax–Wendroff type 2(1,3) O {2} approximation to the "Cowell spawning ground, Spencer Gulf" prawn larvae distribution. Level curves are shown at the appropriate grid–scale (solid curves) in the interior domain only, excluding the open boundary (dashed lines). Transects are shown at the appropriate grid–scale (solid curve) and with cubic-spline smoothing (dashed curve). Concentrations (m^{-2}) and distances (m) are indicated.

There is an overall 26×58 uniform mesh, with 762 interior elements and 16 open boundary elements from a total of 1508 in the entire interior grid. Reevesby Island, of the Sir Joseph Banks Group, and Boston Island, in Port Lincoln harbour—barriers to horizontal flow in the x and y directions, respectively—are represented by solid lines. Grid orientation with respect to latitude and longitude is represented by the compass at bottom right. The IC for scaled prawn larvae concentration derived from Cowell spawning ground data—supplied by fisheries officers of SARDI—is depicted at right in Figure 8.33 as level curves (top left) and as x- and y-transects through the peak centre (bottom left and top right, respectively), with the solid and dashed curve representing the initial concentration at grid–scale and finer resolutions, respectively. Modelling commenced at 21:30 on 12 December 1988 and results are presented after 28 d of simulations.

In Tables 8.5–8.6, the grid coordinates i and j of the maximum concentration—relative to

The "Cowell Spawning Ground" Test Statistics for the Final Time–Step						
FDM (name)	Max$\{+\tau\}$ (m^{-2})	$-$Max$\{-\tau\}$ ($-m^{-2}$)	Tot$\{+\tau\}$ (m^{-2})	$-$Tot$\{-\tau\}$ ($-m^{-2}$)	Row (i)	Column (j)
DF (1,4,1)	2.94×10^{-2}	1.04×10^{-11}	1.71×10^{0}	1.51×10^{-11}	24	10
DF *(1,4,1)*	3.00×10^{-2}	0.0	1.75×10^{0}	3.37×10^{-15}	24	10
FTCS (1,5)	7.57×10^{-2}	1.04×10^{-2}	1.82×10^{0}	6.96×10^{-2}	23	12
FTCS *(1,5)*	7.34×10^{-2}	0.0	1.97×10^{0}	4.37×10^{-6}	23	12
MFTCS (1,5)	2.75×10^{-2}	4.27×10^{-10}	2.20×10^{0}	7.13×10^{-9}	23	10
MFTCS *(1,5)*	2.79×10^{-2}	0.0	6.10×10^{0}	8.98×10^{-18}	23	10
LW 2(1,3)	2.83×10^{-2}	6.19×10^{-12}	2.20×10^{0}	2.48×10^{-11}	25	12
LW *2(1,3)*	2.84×10^{-2}	0.0	2.21×10^{0}	1.21×10^{-11}	25	11

Table 8.5: The "Cowell Spawning Ground" test statistics for the final time–step.

The "Cowell Spawning Ground" Test Statistics Over All Time–Steps					
FDM (name)	Max$\{+\tau\}$ (m^{-2})	$-$Max$\{-\tau\}$ ($-m^{-2}$)	Tot$\{+\tau\}$ (m^{-2})	$-$Tot$\{-\tau\}$ ($-m^{-2}$)	CPU (s)
DF (1,4,1)	4.83×10^{-1}	3.59×10^{-2}	1.64×10^{3}	5.44×10^{-1}	33.1
DF *(1,4,1)*	4.83×10^{-1}	0.0	1.69×10^{3}	1.68×10^{-1}	32.5
FTCS (1,5)	4.91×10^{-1}	3.47×10^{-2}	1.67×10^{3}	2.86×10^{1}	31.5
FTCS *(1,5)*	4.91×10^{-1}	0.0	1.76×10^{3}	3.41×10^{-1}	32.8
MFTCS (1,5)	4.81×10^{-1}	1.84×10^{-2}	1.61×10^{3}	8.99×10^{-1}	37.7
MFTCS *(1,5)*	4.81×10^{-1}	0.0	1.64×10^{3}	7.14×10^{-2}	38.8
LW 2(1,3)	4.81×10^{-1}	6.48×10^{-3}	1.77×10^{3}	2.68×10^{-1}	39.9
LW *2(1,3)*	4.81×10^{-1}	0.0	1.77×10^{3}	2.01×10^{-2}	40.1

Table 8.6: The "Cowell Spawning Ground" test statistics over all time–steps.

the interior domain confined to $(i_{\text{top}}, j_{\text{left}}) = (2, 2)$ and $(i_{\text{bottom}}, j_{\text{right}}) = (59, 27)$—are also listed.

For all FDMs, the level curves indicate that clipping eliminates the spurious oscillations associated with negative larval concentrations particularly in the south of the Gulf near the open boundary. The contours also suggest that the effect of clipping is minimal on the overall form of the final localised concentration peak, with this notion being supported by the transects shown. A notable exception to this trend is the y-transect for the FTCS method, in which clipping suppresses the severe spurious oscillations, particularly the small and large "undershoots" immediately northeast and southwest, respectively, of the local y-transect concentration peak.

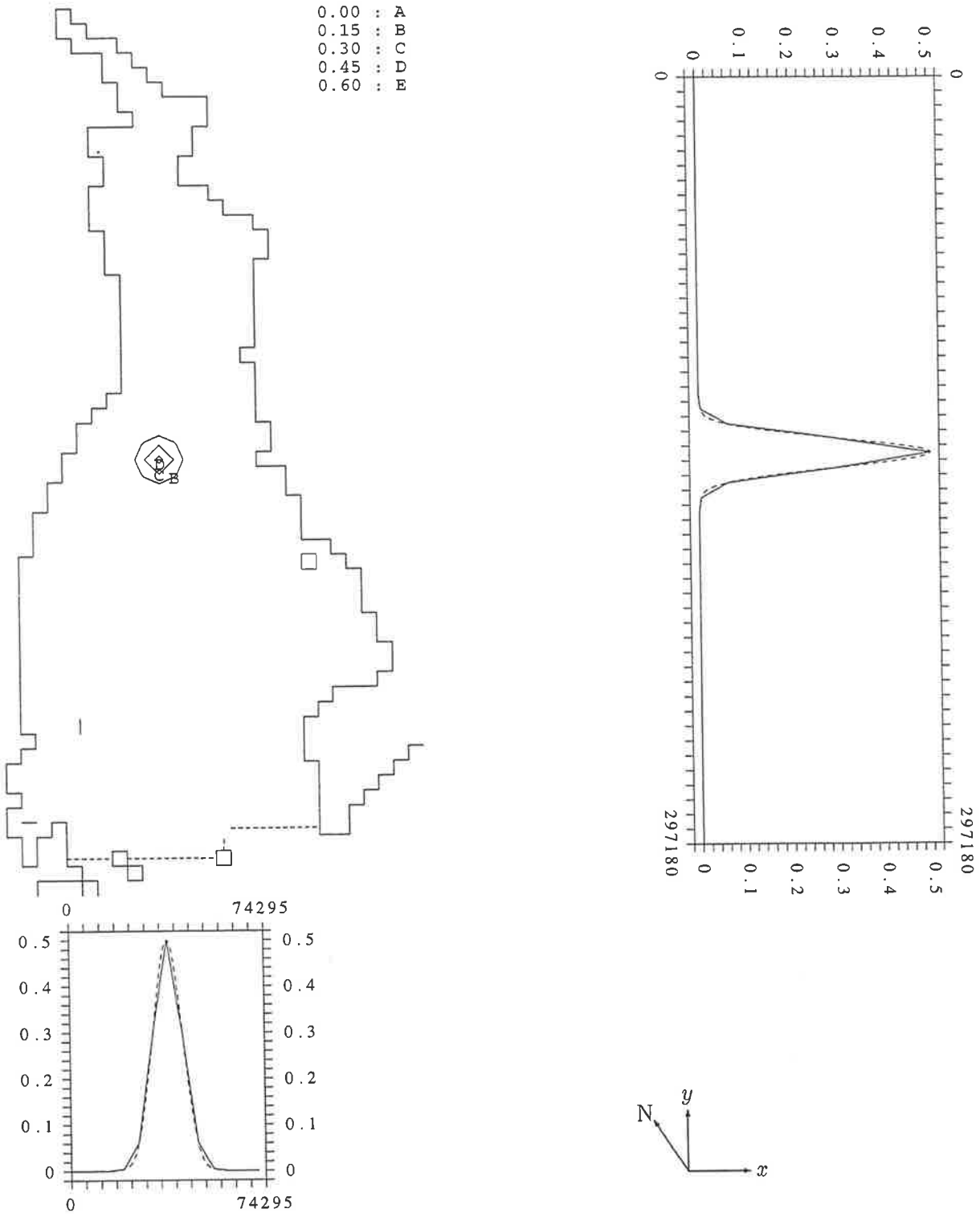

Figure 8.33: Level curves (top left), and y- (top right) and x- (bottom left) transects for the "Cowell spawning ground, Spencer Gulf" larval concentration initial condition (8.9.1). Level curves are shown at the appropriate grid–scale (solid curves) in the interior domain only, excluding the open boundary (dashed lines). Transects are shown at the appropriate grid–scale (solid curve) and at a finer grid–scale (dashed curve). Concentrations (m^{-2}) and distances (m) are indicated.

Tables 8.5–8.6 indicate that for all FDMs clipping had varying effects on $\text{Max}\{+\tau\}$ for the final solution but had no measurable effect on the corresponding overall statistic. Both $\text{Tot}\{+\tau\}$ measures increased with clipping for all FDMs, with this effect least apparent for the LW 2(1,3) FDM compared to all others presented. Without clipping, both $-\text{Max}\{-\tau\}$ measures decrease as one progresses down the tables, with the exception of the final time-step measure for the DF (1,4,1) FDM. Both $-\text{Tot}\{-\tau\}$ measures decreased with clipping for all FDMs, as is expected. For this measure there is no clear trend across FDMs, except that the MFTCS (1,5) and LW 2(1,3) FDMs produce fewer non-physical negative results.

The level curves and transects indicate that the DF (1,4,1) and MFTCS (1,5) FDMs produce solutions with similar bulk characteristics for the main concentration peak. The FTCS (1,5) solution is clearly unrealistic, with an exaggerated peak crest (evident in the level curves and in the transects) in close proximity to a severe concentration trough (most clearly depicted in the y-transects) which is somewhat, but not completely, moderated by the introduction of clipping. This is undoubtedly a spurious numerical artifact resulting from the repeated application of the corresponding FDE with Courant/diffusion numbers outside of the appropriate von Neumann stability region. In fact the stability regions of Section 8.7 indicate that, assuming currents of magnitude not much greater than the $1\,\text{m}\,\text{s}^{-1}$ said to be observed in Spencer Gulf (Noye 1984b), for much of the tidal cycle *only* the LW 2(1,3) FDM is guaranteed to be von Neumann stable. It is the nature of both FDMs themselves and the determination of their von Neumann stability that instability in a small region of space–time may not necessarily result in fully unstable approximations in which predictions soon become unbounded. Such approximations are calculated using the FTCS (1,5) FDE with such small s_x and s_y and large c_x and c_y derived from the coarse grid model parameters chosen. In fact, assuming equal velocity magnitude $W = u = v$ in both horizontal directions, the FTCS (1,5) FDE von Neumann stability criterion (8.7.10) dictates that velocities $W > 1/6 \approx 0.17$ will generate local instabilities.

When compared to the DF (1,4,1) and MFTCS (1,5) FDMs, the LW 2(1,3) FDM produces a peak to the relative lower left of Spencer Gulf, resulting in a local concentration maximum comparatively further offshore and farther south. This concentration "tongue" extending below the LW 2(1,3) FDM peak towards the centre of the Gulf, is a phenomenon which is further investigated, in Chapter 10, using the fine grid Spencer Gulf model of Chapter 6.

8.9.5 Discussion

It has been shown that, of the methods tested, the FTCS (1,5) FDM is clearly inferior and the remainder each have their relative merits. Each method performed adequately with respect to the theoretically more accurate LW 2(1,3) FDM to varying degrees, in particular the DF (1,4,1) FDM. Advantages of the former over the latter include the fact that, on the whole, absolute errors were less significant (for tests with analytical solutions) and stability and non-negative regions are larger and more useful (for coarse grid Spencer Gulf model parameters).

This last point is particularly relevant considering the use to which the chosen FDM is to be put—this being an application to the fine grid Spencer Gulf tidal model of Chapter 6—in which both Δx and Δt are a third of those for the coarse grid model discussed in this section. In the fine grid model, with α unchanged, Courant numbers remain as for the coarse grid model, while diffusion numbers are multiplied by a factor of three. As can be appreciated from the stability diagrams of Section 8.7, for periods of the tidal cycle in which a current velocity component magnitude exceeds $\approx 1.12\,\text{m}\,\text{s}^{-1}$—routinely the case for the y current component during a spring tidal event in Spencer Gulf with the grid orientation as defined—the MFTCS (1,5) and LW 2(1,3) FDMs are the only von Neumann stable methods of those presented. With a very small lateral velocity component in the x-direction, the former is no longer von Neumann stable and the LW 2(1,3) FDM remains the *only* theoretically stable method of those presented.

Compared to all other schemes, the LW 2(1,3) FDM generally produces more physically realistic results with clipping compared to without. Since clipping is desired in order to eliminate negative valued oscillations in the final solution, this fact is particularly pertinent.

Overall accuracy, stability, and physical realism considerations thus determine the LW 2(1,3) FDM superior to all FDMs considered in this section, in particular for the specific application at hand, at a small cost in execution time.

8.9.6 Tidal Model and Dispersion Model Coupling

Often the space and time requirements of physical versus biological models are different. Thus one direction for research is to develop the methods and techniques for interfacing the circulation output from eddy resolving models with models for the distribution of biological or chemical substances (Wroblewski and Hofmann 1989, p. 89). It is also often preferable to compute the three-dimensional current predictions first and then use these afterwards as input to a larval dispersion model, rather than to incorporate both models into one computer program, because the generation of the tidal current fields, over such a vast region at the fine scale desired, is extremely computationally expensive. The former approach allows the researcher to, after approximating the current regime by one simulation using the hydrodynamic model, investigate the dispersion of larvae from different spawning grounds, with other parameters, etc., with ease. For these reasons, the tidal and dispersion models described in this thesis were not coupled. As it transpired, computational resource limitations—discussed elsewhere in this thesis—deemed direct model coupling impossible.

As discussed in Section 6.3, the 60 s time–step of the fine grid Spencer Gulf tidal model calculations of advective velocities was, due to disk-space limitations increased to one of 60 min for output. This time–step corresponds to both that of the coarse grid Spencer Gulf tidal model of 3.4 and that of the corresponding coarse grid Spencer Gulf larval dispersion model of Section 8.9.4 above, and Section 10.1.1 below. Using temporal interpolation of the fine grid Spencer Gulf tidal model output, flow-field variability will be determined, for input to the fine grid Spencer Gulf dispersion model, to a smaller time–step. Quadratic interpolation is used so as to preserve the second-order accuracy of the overall numerical scheme. For fine grid Spencer Gulf model simulations, calculations were thus carried out by using a time–step of 20 min. This effective time–step was not reduced further, in order to ensure approximate equality of local Courant numbers in the coarse grid and fine grid Spencer Gulf models. Separate diffusion numbers for the coarse and fine resolution dispersion models are, however, defined by (8.1.9) and (8.1.10), respectively. This time–step could have been reduced further, but at the cost of increased computational requirements for both the tidal and dispersion models.

8.10 Summary

In this chapter, criteria desired of a finite-difference approximation to the two-dimensional transport equation were presented. A suite of suitable candidate difference schemes were compared both theoretically and experimentally, in terms of stability, accuracy, and convergence properties, and performance measures in tests against two current regimes with analytical solutions and one real-world simulation, respectively. The explicit, three-point, two-level Lax–Wendroff type 2(1,3) locally one-dimensional method was chosen as the most desirable for the larval dispersion application at hand, for reasons of generality of application, accuracy of solution, and physical realism of approximations. In all prawn larvae dispersal simulations discussed in Chapter 10, it is this scheme which is used to approximate advection and diffusion of *Penaeus latisulcatus* larvae in models of the Spencer Gulf region.

A major objective in developing the numerical scheme was to maximise accuracy while involving the minimum number of spatial grid–points in computations. Another objective was to write program code which is general, so that the same subroutines can be applied to any coastal region. Once the user has classified each grid element of the model as one of only three distinct types, the subroutines automatically select the correct form of each finite-difference term, taking into account appropriate boundary conditions along both closed and

open boundaries, for each grid element of the model. It is thus felt that these objectives were achieved.

Chapter 9

Numerical Larval Dispersion Models

In this chapter, overviews of existing numerical models of larval dispersion are given. In Sections 9.1–9.8, where appropriate, comparisons are made between pertinent characteristics of these models and of the model developed for *Penaeus latisulcatus* larvae dispersion in the Spencer Gulf region. In Section 9.9, special attention is given to two works forming a critique of a subset of the existing models discussed here, and the manner in which the model developed in this thesis attempts to overcome many of the criticisms made is highlighted.

A complete study of the role of larval dispersion must include the use of large-scale numerical models that are able to simulate the patterns of water movement over large distances and the resulting transport of larvae (James and Scandol 1992, p. 570). The present study uses the tidal model described in Chapter 3 to do this. In the following sections then, the overviews of models used in previous studies and the comparisons of those with that used in this study discuss relevant features of the underlying hydrodynamic models as well as of the advection–diffusion–mortality models themselves.

9.1 Penn

In Penn (1975) the means by which *P. latisulcatus* larvae in Shark Bay (see Figure 1.1) migrate from the offshore spawning areas to the inshore nursery grounds were studied. The assumption that penaeid larvae move at random and are carried into the nursery areas by ocean currents was found to be impossible in Shark Bay, where the general movement of water in the period of larval migration is against the required direction. Examination of the tidal flow during the hours of darkness revealed a yearly cycle with flood and ebb flow dominating for alternate halves of the year. This nocturnal tidal cycle and the reduced rate of tidal flow with increasing depth was shown to interact with the vertical diurnal movements of the larvae to provide a mechanism by which larvae could be transported a greater distance inshore at night than offshore during the day within the larval migration period. This was seen to provide a means by which larvae could move inshore against the general movement of water.

To determine the differences in flow between surface and bottom, records of tidal velocity near the spawning ground and the nursery areas were examined. Tidal currents were approximated by dominant night time flows calculated from water level differences between dawn and dusk, whereby a rise corresponded to a flood and a fall to an ebb, where only the maxima and minima in the night tides cycle, i.e. four points per lunar month, were considered.

Observed velocity profiles showed that there would be a difference in the rate of movement of larvae with depth, with this difference accentuated in shallower water, i.e. nearer the nursery areas. It might possibly be assumed that, in order to utilise the tides for migration, larvae are able to distinguish between flood and ebb tides and find some means of avoiding offshore displacement by the ebb tide. Such abilities have, however, not been shown for *P. latisulcatus* larvae, and would not appear reasonable for postlarvae in deep water where activity triggering mechanisms, such as differences in salinity or hydrostatic pressure between flood and ebb tides,

are minimal (Penn 1975, p. 100). Although pressure changes could affect juveniles and possibly postlarvae in shallow water, it is unlikely that larvae or postlarvae in the deeper embayments could react to a pressure change generated by the maximum tide height since they move vertically within the water column much greater distances, and hence experience greater pressure changes.

The transport mechanism described by Penn (1975) does not in fact require any special ability of the larvae in terms of sensing minor salinity or depth changes due to tide, but only that larvae follow a simple diurnal migration. Penn suggested that this mechanism may be fairly universal of penaeid species in tidal flows. Penn also discussed the possibility of juveniles using it to aid their movement back out of nurseries under the ebb tide, during the juvenile migration period in the second half of the year.

9.2 Bartsch, Brander, Heath, Munk, Richardson, and Svendsen

Bartsch et al. (1989) investigated larval transport processes for North Sea herring (*Clupea harengus L.*). They modelled the advection of larvae and compared the results with sequential field data on the actual distribution of larvae. A 3D nonlinear numerical model simulated the circulation of the North Sea and adjacent shelf areas. The circulation model was forced by the M_2 tide, climatological mean summer and winter stratification, and three-hourly surface wind–stress and air pressure fields. Daily values of current velocity and variance were calculated by integrating over two tidal cycles.

The daily 3D current velocity and variance field served as the input to an advection model which incorporated horizontal and vertical advection, as well as diffusion which was parameterised using the daily current variance.

Herring larvae were represented in this model by tracer particles which were programmed to undertake diurnal vertical migrations. In the absence of a comprehensive theoretical model of larval migrations, a simplified scheme was used in the advection model: in water deeper than 40 m, the lower level of migration was stipulated to be at 0.6 times the water depth, with the upper level lying 20 m higher. At dusk, the tracers were moved to the lower level over a period of 6 h and remained there until dawn, whereupon they were moved to the upper level, again over 6 h. In water shallower than 40 m, the upper level of migration was fixed at 4 m and the lower level remained the same as for deeper waters. At every time–step, each tracer was displaced by the current vector at the actual depth of the tracer. The vertical migration of *Penaeus latisulcatus* larvae of the Spencer Gulf region is, in the dispersion model of this thesis, similarly presented by a mechanism based on time-dependent depth, proportional to percentage of total water column.

It was found by Bartsch et al. (1989) that the pattern of larval dispersion varied from year to year, depending on the meteorological conditions, although "favourable circulation" in the North Sea was seen a necessary, but not sufficient, prerequisite for good recruitment. The observational data did, however, support the use of the 3D circulation and advection models for studying the advection and dispersion of vertical migrating larvae.

9.3 Johnson and Hess

In Johnson and Hess (1990) wind- and current-induced drifts of blue crab larvae hatching near the mouth of Chesapeake May, Virginia, USA, were simulated using numerical models to examine the relationship between larval recruitment and environmental forcing. The circulation was produced with a 3D model of the bay and adjacent continental shelf. This model included density gradient, wind–stress, and atmospheric pressure gradient forcings. The computed circulation was then used by a drifter advection model to produce Lagrangian drift tracks. Observed winds at a single location, predicted tides from harmonic analysis, and daily river discharges from major tributaries were used as driving forces. By alternately removing forcing by winds, river

flow, and density differences, the relative influence of the three forcings was evaluated. The wind component was found to have the greatest effect on larval recruitment, although this could either increase or decrease recruitment. River flow and gravitational circulation each had a smaller influence.

9.3.1 The Hydrodynamic Model

The Johnson and Hess (1990) hydrodynamic model, similar to that of Blumberg and Mellor (1987), used finite-difference approximations to the momentum, continuity, and salinity conservation equations to simulate water levels, 3D water currents, and salinities at 10 levels in a shallow water domain. A major difference between the Blumberg and Mellor (1987) type model, used by Johnson and Hess, and the Bills (1991) and Nixon (1992) model, used in this thesis, is the ability of the former to approximate circulations driven by water density gradients resulting from salinity and temperature transport.

Although Spencer Gulf can be classified as an *inverse estuary* (Lennon et al. 1987), indicating that salinity decreases noticeably from the head in the north along the axis of the Gulf to the mouth in the south, saline concentration and consequent changes in water density are not significant driving mechanisms of Gulf circulation on tidal scales, particularly during the summer months of *Penaeus latisulcatus* larval dispersion. Likewise, although water temperature increases noticeably from the Gulf mouth to the head (Nunes and Lennon 1986), this variation takes place mostly in the shallow regions nearest the extreme head. In fact, spatial uniformity of temperature in Spencer Gulf is evident, with an estimated representative mean temperature of $\approx 22°C$ and, with the exception of the shallowest regions, departures from the mean are less than 1.1–1.5°C (Nunes and Lennon 1986, p. 43). While large scale *baroclinic* motions in Spencer Gulf have been inferred from hydrological observations (Bullock 1975) it is expected, following Forbes and Church (1982) and Church and Forbes (1983), that with the exceptionally large tidal variation from springs to neaps (Provis and Lennon 1983; Noye 1984b) and the comparative shallowness of the gulf (see Figure 6.4), the *barotropic* tidal and wind-induced currents would be larger than the baroclinic motions. Direct current measurements have revealed tidal currents of over $1.0\,\mathrm{m\,s^{-1}}$ (Easton 1978; Noye 1984b) and thermohaline currents of the order of only $0.1\,\mathrm{m\,s^{-1}}$ (Bullock 1975; Bowers and Lennon 1987), while calculations have estimated that the circulation due to a severe $14\,\mathrm{m\,s^{-1}}$ southeast wind results in flow being accentuated typically by about $0.16\,\mathrm{m\,s^{-1}}$ (Bullock 1975, p. 50). However, Tronson (1975) and Noye and Tronson (1978) showed that density driven currents in the Gulf are at least an order of magnitude less than wind driven currents. This result was confirmed by a simple scale analysis as conducted by Steedman (1982) which throws doubt on Bullock's results. Measurements of the currents in South Australian gulf waters have shown, however, that the non-tidal circulation depends on the strength of the tidal currents and hence on the spring–neap cycle (Provis and Lennon 1983) and, importantly, the local wind (Bye 1976).

Provis and Lennon (1983) also pointed out that temperature and salinity (i.e. baroclinic) effects may be important components of the *residual* current during neaps in the South Australian gulfs. The residual circulation is important because it may contribute to the transport of prawn larvae (Forbes and Church 1983). Detailed discussions concerning the residual currents predicted in Spencer Gulf by the tidal model of Chapters 3 and 6—and their effects on *P. latisulcatus* larvae dispersion—feature in Sections 7.4.2 and 7.4.4 and Chapter 10.

Tidal forcing at the deep-water boundaries was represented in the Johnson and Hess (1990) tidal model by the amplitudes and phases of 20 tidal constituents, as described in Section 3.1.2, adjusted to reproduce the tides at one reference tide gauge. The model used a dimensionless vertical sigma-coordinate, as described in Section 3.1.1, with a differencing which was semi-implicit in both the vertical and horizontal directions.

The wind data consisted of three-hourly observations at a single location and in the model simulations the wind was assumed to be spatially uniform. Winds at times between observations and for missing observations were estimated by quadratic interpolation of each component.

Wind speeds were also multiplied by a factor of 1.5 in an attempt to better represent over-water wind speeds.

9.3.2 The Dispersion Model

A 3D Lagrangian drift model simulated the movements and distribution of planktonic drifters using the 3D velocity field calculated by the Johnson and Hess (1990) hydrodynamic model. New positions for each drifter were calculated by three-dimensionally interpolating the horizontal components of velocity from the hydrodynamic model. Simulations of larval drift lasting 65 d were completed in which, after 35 d, each drifter moved vertically from its near-surface location to a position 1 m above the bottom. These simulations thus tested for possible recruitment of late-stage larvae by bottom currents. Results suggested that this mechanism was not effective for returning significant numbers to Chesapeake Bay. In all subsequent modelling, 45 d simulations of larvae drifting 1 m below the surface were carried out.

Because the horizontal velocity field may vary over the space a drifter moves within a time-step, the Johnson and Hess (1990) dispersion model incorporated an iterative scheme which could accommodate a curved trajectory by averaging the interpolated velocities at the initial and updated drifter positions and recalculating the path. Tests showed that four iterations accurately simulated circular trajectories. The interaction of water-borne drifters with the shoreline was also algorithmically controlled, in that their position was reset to a distance of 10 m from land if they encountered a land boundary. Drift parallel to land boundaries, however, was not restricted.

9.3.3 Simulations and Results

The relative influence of three environmental forcing factors was evaluated by alternately substituting zero for each input value of wind, river flow, and salinity variation. Zero was used in lieu of other values (e.g. long term daily averages) to allow comparisons, not only between years, but also within seasons. Each of the ambient environmental forcings introduced substantial variability in blue crab recruitment to Chesapeake Bay.

Simulations also indicated that the Chesapeake Bay blue crab may use a combination of two modes of recruitment. The dominant mode was the export and subsequent return of surface drifting larvae from the adjacent coastal waters. As a secondary mode of recruitment, a smaller percentage of larvae was retained in Chesapeake Bay throughout larval development.

9.4 Noye, Bills, I'Anson, and Wong

Using the DF (1,2,1) finite-difference scheme (see Section 8.7.1), with reflective boundary conditions (see Section 8.8.1) and linear extrapolation at the closed and open boundaries, respectively, simulations of 15 December 1988 and 15 February 1989 instantaneous spawning events idealised by Gaussian pulses (see Section 8.9.1) centred at the Cowell, Wallaroo, Middle Bank, and Yarraville Shoals spawning grounds of Spencer Gulf (see Section 2.1.1) were reported by Noye et al. (1992).

Three scenarios (similar to those in Section 10.1.1) of zero wind, a $6\,\mathrm{m\,s^{-1}}$ SSE wind, and a $6\,\mathrm{m\,s^{-1}}$ NNE wind, corresponding to mathematically idealised, typical summer, and hypothetical storm surge current regimes, respectively—as determined by the coarse grid Spencer Gulf model of Section 3.4—were used to compute tidal currents for the 21 d of larval dispersion between the spawning events and the corresponding settlement events. Percentages, with respect to total concentrations in all coastal regions, of larvae settling in arbitrarily defined subregions were presented, and conclusions—many of which are expanded upon as a result of the simulations presented in this thesis—were drawn.

9.5 Possingham and Roughgarden

In Possingham and Roughgarden (1990) the growth and spread of a marine organism with a coastal adult phase and a pelagic larval phase was studied with numerical experiments, using baseline age-integrated parameters derived from data on the barnacle *Balanus glandula*.

In nature, the larvae are produced by the adults, disperse in the water column, and may settle where they strike the coastline. In the models, the larvae were considered passive particles in the ocean whose movement was modelled with a transport equation. The water column was represented by a 2D plane and the coast by a straight line. A "larval settlement coefficient" was used to parameterise the rate at which larvae settled along a particular section of coastline. While in the water column, the movement of larvae was considered to be governed by two forces: diffusion and advection.

In a 1D model it was shown that the rate at which larvae diffuse in the water column also affected the population's viability. In a 2D model—solved using alternating-direction, semi-implicit, finite-difference techniques (Noye 1984a, 1987a)—the persistence of the barnacle population also depended on the length of a suitable habitat, the strength and structure of the along-shore flow field, and biological parameters of the species concerned. Considered was one simple pattern of water movement: flow parallel to the coast. It was assumed that either (*i*) there was no flow exactly at the coast and the flow parallel to the coast increased asymptotically to some constant value away from the coast, or (*ii*) flow parallel to the coast was constant everywhere. It was found that initial conditions may have a large influence on the growth and spread of a population, especially in the presence of along-shore flow.

9.6 Church, Forbes, Jackson, Pendrey, and Rothlisberg

In the 1980s a series of papers appeared concerning the water movements in the Gulf of Carpentaria in relation to the distribution of *Penaeus* species therein. In Church and Forbes (1981) a hydrodynamic model of, and its application to, the region was described. In Church and Forbes (1983) observations of the circulations in the region were described, and in Forbes and Church (1983) these observations were compared with the results of simulations computed using the hydrodynamic model. In Rothlisberg et al. (1985, 1987), and Rothlisberg and Jackson (1987) observations of the distribution and abundance of early penaeid larvae in the region were described, and in Forbes and Church (1982), and Rothlisberg et al. (1983) applications of the hydrodynamic model to larval dispersion simulations in the region were presented. In the following, the models and methods used in these studies and the experiments carried out, as well as some of the results obtained, are discussed.

9.6.1 Models and Methods

In Church and Forbes (1981) a nonlinear numerical model was applied to the Gulf of Carpentaria to determine the depth-averaged barotropic tidal circulation associated with the four major tidal constituents (O_1, K_1, M_2, and S_2) of the region. The hydrodynamic equations were solved by an alternating-direction, implicit, finite-difference scheme (Leendertse 1967). In the evaluation of the advective acceleration terms at the open boundaries, some velocities were located outside the computation region. To overcome this difficulty, the advective acceleration terms were set to zero at the model open boundaries. The manner in which this problem is dealt with by the tidal model used in this thesis is discussed in overview in Section 3.2.5 of this thesis, described in brief on page 120 of Bills and Noye (1992), and dealt with in detail in Section 3.6 of Bills (1991).

Since frictional effects at the surface due to wind–stress and at the bottom due to bottom friction lead to significant departures of the current from its depth-averaged value, the results of the 2D model were extended to three dimensions using an approach whereby the currents

were driven by the sea–surface slope (determined by the 2D model), surface wind–stress, and bottom friction. The currents as a function of depth below the surface were then derived.

Rothlisberg et al. (1983) assumed the velocity was driven by the surface pressure gradient, determined by the 2D model of Church and Forbes (1981) and Forbes and Church (1983) and surface wind–stress, and that a logarithmic sub-layer existed. Rather than model this layer explicitly, Rothlisberg et al. (1983) assumed linear friction at the top of this layer and used constant viscosity in the rest of the water column. Neglecting all nonlinear terms and horizontal viscosity, and assuming a constant level of turbulence throughout the tidal cycle, an Ekman model enabled the 3D velocity profile to be approximated from the 2D velocities computed.

Water motion on a daily to monthly time scale may be decomposed into *geostrophic flow*, caused by pressure differences within the ocean combined with the Coriolis force, and *Ekman flow*, caused by wind blowing on the water's surface together with that force (Roughgarden et al. 1988, p. 1462). Ekman transport in the ocean leads to water motion near the water's surface. Ekman transport perpendicular to a coastline produces upwelling near the coast, typically bringing cold nutrient-rich salty water to the surface. Thereafter, this water moves offshore and becomes progressively warmer. The main difficulty with applying this theory is that the depth of the Ekman layer is not well specified and, therefore, neither is the speed of the water flow. A given total volume of transport can be achieved by either a thin layer moving rapidly or a thick layer moving slowly (Roughgarden et al. 1988, p. 1462). Calculations of water movements using Ekman's original transport equations are also probably wrong in relatively shallow shelf waters subject to cross-shelf winds and density currents (Miller et al. 1984, p. 209).

In the Rothlisberg et al. (1983) model, the sea–surface elevation at the few closest grid-points was fitted with a bi-linear ($f(x, y) = a + bx + cy + dxy$) function and the surface slopes evaluated by differentiating this function. Assuming the largest currents to be barotropic tide- and wind-induced currents, the Ekman model determined the vertical current structure as driven by the surface pressure gradient, itself derived from the surface slope and the surface wind–stress. The depth-dependent horizontal velocity components were calculated using a semi-analytic solution based on a truncated infinite series recession formula attributed to Jordan and Baker (1980), of which the Prandle (1982) model used in the Hill (1991c) semi-analytical model (see Section 7.2.2) may be regarded as a special case.

Since assumptions made in deriving this solution assume friction dominated flow in a well mixed fluid with constant turbulence throughout the tidal cycle and neglect all nonlinear terms, it is impossible for this method to reproduce accurately the second-order tide-induced residual currents (Rothlisberg et al. 1983, p. 516).

The surface elevations resulting from the 2D model were combined with the Ekman model and the vertical structure of the horizontal currents was thus determined at the location of the larvae, using a single step time-centred scheme. With the smooth bathymetry, slow spatial change in tidal character, and slow horizontal movement of larvae in the Gulf of Carpentaria region, the difference between computing the 3D current structure on an Eulerian grid and interpolating to the larvae, and computing the current structure in a Lagrangian grid, was considered to be negligible. The Rothlisberg et al. (1983) type of numerical experiments do, however, require caution on the part of the modeller to ensure that the modelled particle trajectories are the result of the physical and biological dynamics rather than numerical noise (Wroblewski and Hofmann 1989, p. 79). Further details of the algorithm used to approximate the advection of larvae were not disclosed, except to say that "all terms were time-centred" (Rothlisberg et al. 1983, p. 534).

9.6.2 Experiments and Results

In Church and Forbes (1983), data from three current–meter moorings in the south-east corner of the Gulf of Carpentaria indicated that barotropic diurnal tidal currents predominated the tidal currents, wind-induced currents, and any baroclinic motions in the region. In the second paper of the series, Forbes and Church (1983), the residual circulation in the Gulf was discussed.

The results of some of the tidal analysis presented in Church and Forbes (1983) were also used by Church and Forbes (1981) to verify the numerical model of the tidal circulation in the Gulf.

Forbes and Church (1982) used the available historical and field data to support mathematical computer models of the various mechanisms which control the movement of banana prawn (*Penaeus merguiensis*) larvae in the Gulf of Carpentaria. The residual circulation (i.e. that part of the current remaining after removal of the tides) was investigated. Since banana prawn larvae move vertically through the water column (Rothlisberg 1982) on a diurnal cycle, it was thought necessary to extend the 2D model of Church and Forbes (1981) to three dimensions, as described in Section 9.6.1, for direct computation of the movement of the larvae.

Various hypothetical schemes of larval migration were coupled with the current models. The simplest scheme assumed that the larvae remained at one level (i.e. near surface, mid-depth, or near bottom) throughout the day/night cycle. A more realistic scheme moved the larvae vertically through the water column close to the surface at night and back to the bottom layers during the day. The larvae were considered to move either through the entire water column or only a small fraction of the water column, and the extent of this vertical migration was taken as dependent on larval age. The simplest scheme used the depth-averaged velocities and assumed that (*a*) the larvae did not migrate vertically or that (*b*) the larvae moved into the water column during the night but during the day they either settled on the bottom or at least remained very close to the bottom.

When there was no vertical migration there was very little net horizontal movement, but when vertical migration was introduced this picture changed dramatically. The use of the 3D model currents and various vertical migration schemes changed the quantitative figures but the general picture remained the same, i.e. little horizontal movement when no vertical advection was considered and movement when vertical migration was included. A similar result was obtained in the studies of *P. latisulcatus* larval dispersion in Spencer Gulf by I'Anson (1989) and Wong (1990) using preliminary versions of the dispersion model discussed in this thesis. Other results obtained using this preliminary model have been published as Noye et al. (1992).

In Rothlisberg et al. (1983) the role of larval advection in determining the complex, large-scale patterns of immigration of penaeid postlarvae in the Gulf of Carpentaria was investigated by modelling the interaction between diurnal vertical migration of larvae with wind-forced and tidal currents. Eight vertical migration schemes were modelled in which both the timing of the migration and the position of the larvae in the water column were varied. These schemes were then coupled with both the 2D and 3D models of the currents of the Gulf, to examine horizontal advection of larvae. When the larvae migrated vertically with a diurnal period, their horizontal advection was enhanced. The largest horizontal advection distances occurred when the larvae moved diurnally from the water column into the bottom boundary layer. The eight vertical migration schemes formulated were based on behaviour patterns observed in the field (Rothlisberg 1982) plus some extreme situations for comparison. The water column, regardless of depth, was divided into tenths, level 0 representing the surface, level 5 mid-depth, level 10 the bottom of the calculated Ekman current profile where there is a finite velocity, and level L the logarithmic layer. If the larvae entered the logarithmic layer it was assumed they were close enough to the bottom so that they would be in a near-zero velocity field.

In addition to using the 3D current structure for computing the advection of the larvae, Rothlisberg et al. (1983) also used directly the currents computed with the 2D model. The velocities of the larvae were obtained by bi-linearly interpolating from velocities at the surrounding four grid–points. In this scheme the larvae were considered to be either in the water column, when they were advected with the ambient current, or close to the bottom and assumed stationary. This simple alternative was included to determine whether approximate results, which could be determined more quickly and more cheaply with the 2D model, would be useful as general indicators of advective trends.

The most significant difference in advection was between the larvae which do not migrate vertically and those which migrate. In the shallow, well-mixed Gulf of Carpentaria the vertical extent of the migration was less important than the proximity to the bottom. The advective

distances and directions of all schemes in which the larvae moved into the water column at night were comparable. From the modelling it also became apparent that an *epibenthic mode* (where larvae settled on the bottom) during the day but rose into the water column at night significantly increased horizontal advective distances. The differences in horizontal distance and direction under various migratory schemes, in the Rothlisberg et al. (1983) study, were found to be considerable, even though the vertical migratory distances were small, the planktonic period short, and the current barotropic.

The close agreement between modelled results and field measurements was considered to be encouraging and there was thought to be tremendous scope for development of advective models for other animals.

9.7 Andrews, Black, Gay, McShane, Moran, and Smith

In McShane et al. (1988), Black et al. (1990), and Black and Moran (1991), studies of various aspects of larval dispersal in marine environments were carried out. Idealised applications of, and specifics related to, the hydrodynamic model used to derive the current fields represented in these studies were described in detail in Black and Gay (1987) and Black (1989).

9.7.1 The Hydrodynamic Model

The hydrodynamic model was depth-integrated and included the nonlinear terms and a horizontal momentum diffusion representation, "which primarily only act in fine-scale simulations" (Black and Gay 1987, p. 9515). Intertidal zones were represented with a model flooding and drying algorithm for shallow-water cases.

Such tidal-flat covering and uncovering algorithms have been developed for the 2D version of the hydrodynamic model discussed in Chapter 3 and are published in Bills and Noye (1992). Tidal-flats are not, however, represented in the hydrodynamic modelling discussed in this thesis.

The open boundary treatment was general, and values were specified as sea–surface levels, or depth-averaged velocities. Alternatively, transmission radiative boundary procedures were invoked.

The Sommerfeld type radiation open boundary condition of the model used in this thesis is discussed in brief in Section 3.1.2 and in detail in Bills and Noye (1987).

A wind–stress term, quadratic bed friction, optional treatments of the nonlinear terms, and a boundary slip parameter, all of which were variable in space, made the model readily applicable to new locations (Black and Gay 1987, p. 9515).

In the 2D analogue of the tidal model used in this thesis, described in Bills and Noye (1986), the wind–stress term is also variable in time (as discussed further in Section 9.9.1) and the special treatment given nonlinear terms must be defined at compile-time (as dealt with in detail in Section 3.6 of Bills (1991), described in brief on p. 120 of Bills and Noye (1992), and discussed in overview in Section 3.2.5), while the grid elements at which this treatment is appropriate are defined at run-time. The coastal boundary slip layer can be treated in a physically and mathematically correct manner by using the oblique boundary representation of I'Anson et al. (1994), Matthews (1995), Matthews and Noye (1996a, 1996b), and Matthews et al. (1995, 1996).

9.7.2 The Dispersion Model

McShane et al. (1988), Black et al. (1990), and Black and Moran (1991) calculated larval dispersal rates using a procedure denoted as "particle tracking with spatially uniform velocities" in a Lagrangian particle dispersion model (McShane et al. 1988, p. 181). The method, which utilised a full 2D Lagrangian tracking algorithm, corrected for flow curvature to second-order with an advection scheme which was second-order accurate, i.e. velocity gradients across the model cells were accounted for (McShane et al. 1988, p. 182). The model was said to eliminate

the numerical dispersion characteristics of Eulerian finite-difference schemes (Black and Moran 1991, p. 56) and so made possible the examination of concentrations at sub-grid scales (McShane et al. 1988, p. 182).

Diffusion was modelled as a *random walk*, the coefficients of which represented a level of diffusion which was in proportion to the local water speed (McShane et al. 1988, p. 183). In fact,

> Lagrangian residuals (i.e. the distance moved by a particle over a known time interval and starting from a known location) were used in preference to Eulerian residuals (i.e. the average current over a time interval at a point in space) as they account for spatial variations in currents and thus are the better indicator of larval transport over a tidal cycle (Black and Moran 1991, p. 56).

according to Black and Moran. The manner in which the dispersion model of this thesis accounts for spatial variations in currents is discussed in Section 7.5. A direct comparison of Lagrangian (stochastic particle) and Eulerian (finite-difference) approaches to oil spill dispersion modelling, with underlying hydrodynamic modelling by the 2D analogue of the hydrodynamic model used in this thesis, was carried out by Lewis et al. (1996).

The Lagrangian approach of McShane et al. (1988), Black et al. (1990), and Black and Moran (1991) approximates larval groups or "patches" as individual "particles" where, since it is computationally infeasible to represent each individual as they number in the billions, what is essentially a statistical sub-sample is considered a "particle" in the dispersion model. In contrast, the Eulerian approach of the present work represents larvae as a continuous "cloud" which, in many respects, can be thought of as a probability density. The distinctions between these two approaches are graphically illustrated in the results presented by Black and Moran (1991), which were not quantitative concentrations but regions of significant qualitative abundance or "hot spots", determined by summation in time and normalisation by the total number of occurrences over the full model run. These provided an indication of the locations which were frequently visited or where particles spent most time (Black and Moran 1991). The results produced by the dispersion model in this thesis are in the form of instantaneous concentration contours (see Figure 2.10 or 10.7, for example) over the model region, transect trends (see Figure 10.21(a) for example) within a model subregion, or time-series (see Figure 10.35, for example) at individual locations.

9.7.3 Black and Gay (1987)

In Black and Gay (1987) the case of a simplified 1D tide in a channel was used to illustrate the production mechanism for a so called *phase eddy*. It was demonstrated that even such a simple system exhibits this behaviour, which was the subject of the rest of the paper. Results were then presented for a more realistic 2D case, in which the Coriolis term was omitted, the bed friction was constant in time and space, and the model was un-calibrated with measurements—at least for one of the three harbours to which the model was applied. In the two better-specified harbours, numerically simulated eddies which had been physically observed were found to appear at specific times in the tidal cycle.

9.7.4 Black (1989)

In Black (1989) eddy circulation in the numerical hydrodynamic model was examined to show how eddies with diameters of the order of 10^2 m could be adequately simulated. By utilising a third-order finite-difference approximation for the nonlinear terms and by judicious selection of the horizontal eddy viscosity coefficient, results were demonstrated numerically—using the schematised bathymetry of flow past a rectangular step and examples of eddy circulation in natural environments—which approximated eddy formation in natural unsteady flows.

9.7.5 McShane, Black, and Smith (1988)

In McShane et al. (1988) regional larval dispersal was examined using measurements of horizontal water velocities near the sea–bed and at the surface of one reef in south-eastern Australia. The measurements showed that *Haliotis rubra* larvae entering the water column would be dispersed if they left the shelter of the local reef topography. This dispersal was confirmed by numerical hydrodynamic and dispersal modelling which simulated, using the hydrodynamic model described in .Section 9.7.1, the temporal and spatial variation of wind-driven currents near the reefs. The 2D model did not include larval vertical migration, as it was found that surface wave action rapidly dissipated temperature gradients, with the rapid and thorough vertical mixing observed indicating the amount of mixing which larvae would be subjected to. Thus it was argued that the wave turbulence, which effectively neutralised the temperature gradients, would be expected to mix the plankton throughout the water column also, thereby preventing many larvae from remaining at a depth conducive to settlement (McShane et al. 1988, p. 189). It was, however, concluded that larval availability is controlled by the hydrodynamics directing larval transport and by production from the parent stock (McShane et al. 1988, p. 197).

9.7.6 Black, Gay, and Andrews (1990)

In Black et al. (1990) coral reef flushing times at an individual reef scale were specified and a general formula to determine these times was developed. The formula was derived by considering simplified reef topologies and making assumptions concerning reef topology (18 simplified cases and 6 observational cases were studied), tidal regime (single tidal constituent and linear sinusoidal tide perpendicular to the reef, with constant residual tidal current), longshore current (constant amplitude, parallel to the reef), etc. Numerical (tidal and dispersal) modelling was carried out to obtain values for a coefficient in this formula, and the two coefficients (from the detailed and computationally expensive numerical model, and the simplified and efficient analytical model) were compared. The formula was also confirmed by comparison with residence times predicted by numerical small-scale reef models, and was proven to be a satisfactory alternative to the numerical modelling (Black et al. 1990, p. 105).

Black et al. discussed the manner in which continuous spawning release complicates greatly the time–series of larval concentrations at an observation site. Constant "magnitude" larval releases at every half hour for the first tidal cycle were considered. The combined effects of time-varying spawning regimes in various tidal regimes are discussed in Section 7.2 of this thesis.

Black et al. carried out simulations in which the spatial distribution of the initial condition for larval distribution was altered from initially uniform concentrations over the entire reef surface to concentrations on the reef faces only, conserving identical overall larval biomass. It was found that after only a little while the two simulations produced similar results, and after simulation's end, were remarkably similar. This was thought to be a result of the horizontal advective mixing, i.e. the combined effects of horizontal velocity shear and horizontal diffusion.

9.7.7 Black and Moran (1991)

In Black and Moran (1991) numerical hydrodynamic and particle dispersion simulations showed that neutrally buoyant larvae were subject to a complex circulation pattern which induced a spatial variability in their relative numbers. Data on the distribution and abundance of *Acanthaster planci* and associated coral mortality were combined with those from numerical model investigations of larval dispersal, with the objective of comparing these data with those from numerical hydrodynamical and particle dispersion simulations. For the grids employed, which had four open boundaries, it was necessary to apply analytical solutions for coastal influences outside the grid and the nonlinear interactions of the current components which occur on the Great Barrier Reef continental shelf (Black and Moran 1991, p. 56). During the modelling no attempt was made to impose a larval mortality rate onto the solution, although

this could have been included if adequate biological data were available (Black and Moran 1991, p. 60). Results suggested that hydrodynamics had a major influence on not only the dispersal of larval *A. planci* but also perhaps the location of their initial recruitment (Black and Moran 1991, p. 55).

The "hydrodynamic modelling was undertaken with a two- and three-dimensional numerical model" (Black and Moran 1991, p. 56). However, "dispersion associated with turbulent current oscillations and vertical shear was modelled as a random walk, with separate lateral and longitudinal horizontal diffusion coefficients" (Black and Moran 1991, p. 57). These statements suggest that vertical current profiles calculated by the 3D hydrodynamic model were not in fact taken into consideration when calculating larval transport. Also, "dispersal modelling was undertaken with a fully Lagrangian two- and three-dimensional particle model" (Black and Moran 1991, p. 56) in which "all particles were treated as being neutrally buoyant" (Black and Moran 1991, p. 57), which supports this view.

Because of the complex flow patterns on a coral reef, advective dispersion caused by horizontal velocity gradients dominated, and the general conclusions presented were found to be unaffected by the choice of the horizontal diffusion coefficients, except in that high diffusion caused gradients in integrated particle retention rates to be spatially smoothed (Black and Moran 1991, p. 57). This phenomenon is a well-known result of increasing diffusion coefficients in numerical dispersion simulations.

A fully 3D hydrodynamic model is used in this thesis to derive the horizontal and vertical current shear regime, wherein this is used to full resolution in the horizontal and partial resolution in the vertical by a "layered 2D" dispersion model. Vertical velocity shear is partially accounted for since simulated currents at two depth–levels are used in applying the dispersion model at predetermined times, thus effectively also specifying, *a priori*, larval vertical migration. Details of this two-layer approach are given in Section 7.3.

9.8 Bode, Dight, James, and Scandol

In Dight et al. (1990b), James and Scandol (1992), and Scandol and James (1992), studies of *Acanthaster planci* larvae dispersal in the Cairns Section of the Great Barrier Reef Marine Park (GBRMP) were carried out. Specifics related to the hydrodynamic model used to derive the current fields discussed in these studies were described in detail in Dight et al. (1990a).

9.8.1 The Hydrodynamic Model

The 2D depth-integrated equations were linearised by omitting the "normally small advective acceleration terms" and were solved by an explicit finite-difference technique on a uniform grid that was staggered both spatially and temporally, with wind–stress and the East Australian Current (EAC) both treated as steady-state (Dight et al. 1990a, p. 117). However, considerable vertical structure in the velocity field was expected for wind driven flows where current velocities were expected to decrease with depth (Dight et al. 1990a, p. 122). Deviations between predicted and observed current speeds were expected to be greatest in the surface layer where, also, the water motion was expected to be more closely aligned to the direction of the wind–stress. It was suggested that the extrapolation of surface current direction and speed from the depth-averaged model results, for predictive purposes, should therefore be conducted with some caution. The transport of larvae with distinct patterns of behaviour, such as those of penaeid shrimp which, such as *Penaeus latisulcatus*, move diurnally from the water column into the benthic boundary layer, or others which may be able to maintain themselves within the surface wind-driven layer, may not be reproduced accurately by the model. It was thought, however, that for larvae with less pronounced patterns of behaviour, the variation in current speed with depth may result simply in differences in the time spent within the water column or the distances over which they will be advected. Such variation was expected to be small relative to the total time and distance over which larvae were transported (Dight et al. 1990a, p. 122). It will be shown, using

results of the simulations discussed in Chapter 10, that for vertically migrating *P. latisulcatus* larvae in Spencer Gulf such variation is, however, quantifiable and significant.

Derived from the hydrodynamic model were outputs representing the astronomical tides, wind-driven flows, and the EAC. These provided the database which characterised the current pattern for all combinations of wind, tide, and EAC by which the advection and diffusion of larvae were simulated by the dispersion model.

9.8.2 The Dispersion Model

In the absence of any knowledge of the behaviour of *Acanthaster* larvae in the field, these were assumed to behave as passive particles. This assumption was justified as a first approximation on the basis of limited knowledge of other *echinoderm* larvae (Dight et al. 1990b, p. 126). Thus the larvae were assumed to be neutrally buoyant and to be passively advected with a velocity equal to that of the water current.

While essentially deterministic, given a set of forcing parameters, the dispersion model was run under time-dependent tidal flow and a randomly varying wind field based upon an historical record. The net water transport at any point within the computational field was found by linear superposition of the three transport components (tide, wind, and EAC) output from the hydrodynamic model. Nonlinear effects which would result from simultaneous application of the forcing mechanisms were therefore excluded. Nonlinearities were acknowledged as being important to the dynamics in regions of shallow water, particularly on and around reefs. However, it was stated that scaling arguments could be used to show that linear dynamics provide an accurate description of the flow in deeper regions where the transport of most larvae occurs (Dight et al. 1990b, p. 126). Furthermore, it was stated that the presented methodology provided the only feasible means—at the time of publication—of representing these multifarious events, in the geometrically complex setting of the Great Barrier Reef (GBR).

The advection of larvae was affected by using a Lagrangian "marker and cell" technique. Particle velocity was calculated by linear interpolation between data points which defined the surrounding velocity field. Investigation of the sensitivity of results to the computational time–step revealed relatively little error in particle displacement up to a time-step of 1 h (Dight et al. 1990b, p. 126). This time-step was therefore chosen, and represented a compromise between adequate resolution of the time-varying tidal currents and limitations imposed by computer speed and storage.

The movement of larvae following a spawning event was simulated for a period of 28 d. The larvae cloud was represented by seven particles, the movements of which were tracked and intersections of reefs recorded. The initial arrangement of the seven particles was in the form of a hexagon (one particle corresponding to each vertex and one for the centroid) with a long axis of 0.5 NM. The hexagon approximated the initial spread of larvae soon after a mass-spawning. Relative dispersion of the seven particles representing the larval cloud was seen to occur as a result of spatial variation in the velocity field (Dight et al. 1990b, p. 126).

9.8.3 Dight, Bode, and James (1990a)

In Dight et al. (1990a) models were presented which provided an overview of the physical processes controlling the advection of larvae on the scale of tens to hundreds of kilometres. Overall, model outputs corresponded well to known understanding of the large-scale features and dynamics of water circulation over the continental shelf within the Cairns Section of the GBRMP (Dight et al. 1990a, p. 115).

It was stated that, at the time of publication, the best estimates of larval advection within the region had been limited to progressive vector plots (Dight et al. 1990a, p. 116). While such estimates may be based on data from a number of moorings, they cannot account for the spatial variation in the current field due to changing bathymetry and reef geometry, nor the long term temporal variability within the system. In such physically complex environments, progressive

vector plots, such as those resulting from the models of Forbes and Church (1982), Rothlisberg (1982), and Rothlisberg et al. (1983), must thus be interpreted with caution. Together with low frequency forcing of water motion, including current modulation and reversals as a result of synoptic scale meteorological forcing, such spatial and temporal variation was seen to be too often neglected when considering models of larval advection (Dight et al. 1990a, p. 116). This leads to an over-simplified view of dispersal processes. It was thus concluded that numerical hydrodynamical models provide the only feasible approach to understanding the dynamics of dispersal processes and their impact upon recruitment at the same spatial and temporal scales as the biological phenomena under investigation (Dight et al. 1990a, p. 116).

Steady-state surface wind shear forcing was applied over a spectrum of 16 directions at 22.5° intervals. The nonlinear relationship between surface wind speed and shear stress necessitated a similar procedure for the range of wind speeds (at 5 kn intervals) that would be experienced during larval dispersal (Dight et al. 1990a, p. 119).

9.8.4 Dight, Bode, and James (1990b)

In Dight et al. (1990b) larval distributions which resulted from passive transportation were simulated and the resulting patterns of dispersal compared with the distribution of adults and the observed pattern of *Acanthaster* population spread. Asymmetries in the long-shelf and cross-shelf transport of larvae indicated that larval dispersal within the Cairns Section of the GBRMP cannot be considered as an *isotropic* random process and that the recruitment of reefs is not from a *homogeneous* larval pool (Dight et al. 1990b, p. 125). The currents which transport larvae were seen to be directed by shelf topography, and resulted in distributions of larvae which were not spatially uniform. In addition, however, source–sink relationships in the level and strength of reef connectivity further emphasised the unsuitability of this concept of larval dispersal as isotropic (Dight et al. 1990b, p. 132). There was, however, strong support for the idea that the propagation of populations is through larval dispersal and juvenile recruitment (Dight et al. 1990b, p. 125).

During the initial two weeks of development, larvae of *A. planci* were assumed to be precompetent and unable to settle. Only intersections with reefs following the two week precompetent period were therefore considered. Once an intersection occurred during the competent period, the remaining track and any further intersections were ignored.

From each of the fifteen reefs studied, forty spawning events were simulated using randomly selected tide and wind histories. Each spawning event and subsequent larval track over a period of 28 d ran under a different current regime. Maximum distances over which larvae were transported during the 28 d simulation period were as great as 150 km, although, such distances were the exception rather than the rule. Recorded net flows within the reef matrix, and current reversals, resulted in generally smaller larval excursions (Dight et al. 1990b, p. 131).

It was emphasised, however, that while the model and results provided a means of predicting the course of outbreaks and the risks associated with individual reefs, they did not adequately describe phenomena operating on a finer scale of resolution. That is, the model as presented could help to define the variable larval pool, but small scale features of flow around individual reefs will ultimately determine the proportion of the available larval pool that is actually able to settle onto a reef and under what conditions (Dight et al. 1990b, p. 133).

9.8.5 James and Scandol (1992)

In James and Scandol (1992) concern was chiefly with the large-scale statistical patterns of *A. planci* larval dispersal in the GBR, the central hypothesis being that passive hydrodynamic dispersal plays an important role in the recruitment process. The dispersal simulations made use of hydrodynamic data generated by the numerical model discussed in Section 9.8.1 on a computational grid with a resolution of 5 NM. The depth-averaged Navier–Stokes equations were, using this model, solved *separately* for different forcings corresponding to the EAC, each

of seven major tidal constituents, and each of a set of spatially uniform wind vectors (James and Scandol 1992, p. 573). The shortcomings of this linear supposition approach are discussed in Section 9.9.1.

9.8.6 Scandol and James (1992)

Scandol and James (1992) presented results of a modelling study of the large-scale population dynamics of *A. planci* in the central GBR in which dispersal patterns generated by the larval transport model were used to drive the simulation. Population patterns generated by the model were found to be consistent with observations of starfish outbreaks (Scandol and James 1992, p. 583).

It was stated that the most difficult stage of the starfish life cycle to study in the field is the larval phase, yet its importance cannot be overestimated (Scandol and James 1992, p. 583). However, it was also stated that the model was not concerned with the dynamics of low-level populations or with actual densities of starfish since the chief objective was to simulate and represent large-scale patterns (Scandol and James 1992, p. 586). Consequently the prime limitation of the model was identified to be the inability to represent the transition between low- and high-density populations (Scandol and James 1992, p. 593).

9.9 Babcock, King, Oliver, Willis, and Wolanski

In Wolanski (1993) existing models of the dispersal of crown of thorns starfish (*A. planci*) in the GBR were critiqued and were found to suffer from problems with numerical algorithms, unrealistic assumptions about open-boundary forcings, and unrealistic parameterisation of dispersion processes in the presence of salient topography. This paper questioned the reliability of the predictions determined by the larval dispersion models of Black et al. (1990), Dight et al. (1990a, 1990b), Black and Moran (1991), Scandol and James (1992), and others. Since none of these models were verified by extensive hydrodynamic data it was suggested that these problems invalidate some of the published model results, and that these models should probably not be used for management of the GBRMP (Wolanski 1993, p. 427).

In Oliver et al. (1992) a comparison was made between observed larval concentrations around a coral reef and predicted concentrations derived from hydrodynamic and dispersion models. There was virtually no correlation between the two data sets (Oliver et al. 1992, p. 873). Despite the fact that their model utilised real-time inputs for the tide, far-field currents, and wind, Oliver et al. could not even obtain a coarse agreement between model predictions and actual larval concentrations (Oliver et al. 1992, p. 884). Although the more general predictions of the Dight et al. (1990a, 1990b) studies were in agreement with other oceanographic and biological data, there was no quantitative test of the accuracy of the more specific predictions (Oliver et al. 1992, p. 887). In the Black et al. (1990) and Black and Moran (1991) studies there was a substantial effort to obtain data from the field and from the existing literature to validate the model predictions. Nevertheless, no detailed tests of the model outputs were carried out which compared observed and expected values in a comprehensive manner over space and time. In the absence of such data, and considering the failure of the attempts of Oliver et al. (1992), doubts inevitably arise concerning the far-reaching conclusions which Black et al. (1990) and Black and Moran (1991) have drawn (Oliver et al. 1992, p. 887).

Many of the criticisms by Oliver et al. (1992) and Wolanski (1993) of these particular models apply equally well to other larvae dispersion models described in Sections 9.1–9.8, and thus the points raised in these two papers are considered in detail here. Specifics related to reef vicinity circulation/dispersion in general and the Great Barrier Reef (GBR) region in particular will not be emphasised, but suggestions will be made as to what measures can be taken to overcome these problems. In what manner some of these measures are implemented in the hydrodynamic tidal and larvae dispersion models of Spencer Gulf (SG) in this thesis will also be discussed.

9.9.1 Bode, Dight, James, and Scandol

There were several reasons for the Dight et al. (1990a)/Scandol and James (1992) results to be of qualitative value only and unlikely to yield quantitative information. There may also have been additional errors arising from questionable assumptions in this advection–diffusion model (Wolanski 1993, p. 427). Wolanski (1993) pointed out that the Dight et al. (1990a)/Scandol and James (1992) advection–diffusion model cannot yield more-reliable results than the underlying hydrodynamic model, which already yields unreliable results. This comment is applicable to many of the other models discussed in Sections 9.1–9.8 but, it will be argued, is less applicable to the model constructed in the present work.

Nonlinear Interactions

The hydrodynamic model used linearised equations of motion. Linear equations of motion are unable to simulate complex flows around obstacles at high Reynolds numbers since such dynamics are in fact highly nonlinear (Batchelor 1967). The hydrodynamic models of Dight et al. (1990a, 1990b), Penn (1975), and Possingham and Roughgarden (1990), used linear approaches and thus suffer from such shortcomings.

The hydrodynamic model of Bills (1991) and Nixon (1992) (described in Chapters 3.1 and 5, respectively), however, does not.

Similarly, allowing either (*a*) linear superposition of contributions due to the individual tidal constituents or (*b*) full nonlinear interaction of these constituents, is found to significantly affect tidal model predictions.

The qualitative difference in predictions of a 2D form of the tidal model used in this thesis as produced by these two approaches was discussed by Lewis et al. (1996) in an application to oil spill trajectory modelling in northern Spencer Gulf. Such superposition, as conducted in the hydrodynamic models of James and Scandol (1992), and Scandol and James (1992), is not carried out in this thesis.

The hydrodynamic motions driven by tides, wind, and the prevailing currents are modelled separately and added linearly for the final predictions. This approach neglects the nonlinear hydrodynamic interaction between these various motions, which cannot be added linearly (Provis and Lennon 1983). The hydrodynamic models of Dight et al. (1990a, 1990b), James and Scandol (1992), and Scandol and James (1992), used this approach, while those of Penn (1975), and Possingham and Roughgarden (1990), ignored wind–stress altogether.

In the present work wind–stress is accounted for, as hydrodynamical modelling progresses, according to (3.1.32). Furthermore wind–stress is prescribed as space *and* time varying, as discussed in Chapter 4. In the models of Forbes and Church (1982), Rothlisberg et al. (1983), Black and Gay (1987), Dight et al. (1990a, 1990b), and Noye et al. (1992) it was constant in time, and in those of James and Scandol (1992), Scandol and James (1992), Johnson and Hess (1990), and Noye et al. (1992) it was constant in space. Prevailing currents are not, as is discussed below, a feature of the SG region and so are not specified as forcing to the hydrodynamic modelling of this thesis.

9.9.2 Andrews, Black, Gay, McShane, Moran, and Smith

The Black et al. (1990) model was a dedicated attempt to model trapping phenomena around obstacles (reefs). Nonlinear equations of motion were used, and the mesh size was small so that a GBR region reef was typically represented by a few to a dozen model meshes. Nevertheless, there are several reasons for caution to be exercised in accepting the model's predictions (Wolanski 1993, p. 428).

The combined tidal/dispersion model of the present work has a mesh size chosen to adequately represent closed boundaries (coastlines) and topography (bathymetry)—as discussed in Chapter 6—since obstacles (islands) are not a major concern in the SG region. Limitations in

the accuracy of predictions made by the model are discussed in the relevant sections throughout this thesis.

Open Boundary Conditions

The Black et al. (1990) "far-field" open boundary conditions, specified as sea–level elevations along open boundaries located "far" from the study reef "field", resulted in smooth horizontal currents with negligible horizontal shear along the individual open boundaries. This assumption is unrealistic because field studies have shown that the horizontal shear is extremely large in the GBR region, and that small errors in predicting open boundary currents can result in large errors in current predictions (Wolanski 1993, p. 428). This may be attributed to "the inability of the model boundary conditions to incorporate the observed large-scale inter-reefal shear (i.e. non-homogeneous boundary conditions) which exists in this topographically-complex region" (Oliver et al. 1992, p. 876).

In the hydrodynamical model of this thesis, sea–surface elevations are specified at the open boundary, as discussed in Section 3.1.2, including variability in the x and y horizontal directions, as discussed in Sections 3.4 and 6.4 for the coarse and fine grid SG models, respectively. Using such a height–specified boundary condition incorporates both time varying non-homogeneous *horizontal* and, since the model is 3D, *vertical* velocity shear in the following manner. Through the momentum equations (3.1.17)–(3.1.18) spatial changes in elevation are converted into temporal changes in velocity. Through the continuity equation (3.1.15) spatial changes in depth-integrated velocity (derived from the depth-dependent velocity field in the 3D model) are then transformed into temporal changes in elevation.

Horizontal velocity shear is evident along the open boundaries of the SG model, with appreciable currents across the whole entrance (Steinberg 1983, p. 68). Diurnal current amplitudes increase significantly and semi-diurnal amplitudes decrease less significantly with distance west across the SG mouth (Steinberg 1983, p. 50). The observed major diurnal constituent phase lag across the gulf mouth is over 6.5 h, which indicates that when there is maximum inflow at the extreme east of the mouth, there is a small outflow at the extreme west, with the semi-diurnal phase lags being much less pronounced (Steinberg 1983, p. 51). This observed horizontal velocity shear is, in addition to vertical velocity shear, adequately represented in the numerical SG model results (Bills 1991), through the mechanism outlined above.

Numerical Diffusion

Another problem is that of numerical diffusion in the Black et al. (1990) particle-tracking algorithm. The advection–diffusion model employed a sophisticated second-order accurate Lagrangian scheme to reduce the tendency for particles to drift off the flow streamlines in a highly variable horizontal velocity gradient. To save computer time, the Black et al. (1990) advection–diffusion calculations were carried out by using a time–step of typically 0.5 or 1 h, during which time the velocity field was assumed to be stationary. This assumption, however, leads to numerical dispersal problems because flow varies within 0.5 h (Wolanski 1993, p. 429).

The Eulerian scheme of this thesis is, for constant coefficient advection–diffusion, second-order convergent with zero numerical diffusion, as discussed in Section 8.7.4. As discussed in Section 8.9.6, the effective time–step of the fine grid SG model simulations is 20 min, during which flow variability is assumed to be small and the "numerical dispersal problems" suggested by Wolanski (1993) negligible.

Free Shear Layers and Vortex Sheets

The influence of sub-grid–scale *free shear layers* was not parameterised by Black et al. (1990). Free shear layers (*vortex sheets*) are a common sight around reefs during periods of strong currents, even in the absence of density stratification (Wolanski 1993, p. 429). Wolanski's observations suggest the presence of intense eddies the width of the free shear layer and that these

interact strongly with the sea–bottom. Barotropic free shear layers in shallow waters inhibit mixing between water masses on either side, as if there was a solid boundary or a baroclinic front. This phenomenon has profound implications for determining the fate of nonbuoyant particles because diffusion is anisotropic in the presence of a free shear layer (Wolanski 1993, p. 433). Using the example of uniform current flow past an island in a sea of uniform depth, it was graphically illustrated in Figure 7 of Wolanski (1993) that there is measurable tracer particle trapping in the absence of a free shear layer, as in the model of Black et al. (1990), but no trapping in the presence of one. In the latter case, trapping was eliminated by allowing no diffusion (presumably by setting to zero the appropriate diffusion coefficient) across the free shear layer (the exact determination of which was not discussed) but elsewhere a uniform horizontal diffusion coefficient with the same value as used in the former case. It should be noted that this example was constructed by Wolanski (1993) with depth-averaged steady state currents.

Since field observations have revealed the existence of sub-grid–scale free shear layers in the GBR region, the neglect of free shear layers in *A. planci* advection–diffusion models may invalidate predictions for near-reef dispersal in the presence of flow separation (Wolanski 1993, p. 434). In the predictions of SG coastal-water dispersal of *P. latisulcatus* larvae by the advection–diffusion model of this thesis, the parametrisation of sub-grid–scale free shear layers in a manner similar to that by Wolanski (1993) is not considered to be a serious oversight for a number of reasons.

First, Noye et al. (1994) showed that a 2D form of the Bills (1991) hydrodynamic model used in this thesis was well able to reproduce the location, strength, and dynamics of an eddy (actually a pair of eddies (Lewis 1993, personal communications) depending on whether the tide is at flood or ebb) formed in the lee of Lowly Point (the point north of Port Bonython in upper SG), as is illustrated in Noye et al. (1994), Figure 3. This eddy is similar to that observed in the lee of Bench Point (a rocky headland in the Whitsundays area of north-western Australia) as used by Wolanski to illustrate the intense eddies in the presence of a free shear layer in Wolanski (1993), Figures 2–4. The basic equations solved by a 2D form of the hydrodynamic model used in this thesis (outlined in Noye et al. 1994) are similar to those used in the Wolanski (1993) example (outlined in Oliver et al. 1992), except for the manner in which Reynolds and wind–stress terms are represented, and the fact that the former model includes horizontal momentum diffusion terms while the latter does not. Both the Bills (1991) and Oliver et al. (1992) models, however, use finite-difference approximations to the governing equations which are second-order convergent, with the former being explicit and the later being implicit in nature. The reader is referred to Chapter 3 for a discussion of how the stress and horizontal momentum terms are represented in the 3D model and is advised that analogous representation is used in the 2D analogue. A detailed discussion—beyond that found in Chapter 3—of the relative merits of various specifications for these terms, including that used in this thesis, can be found in Bills (1991).

Second, it appears that it is the intense 3D motion in a free shear layer in shallow water that generates a strong lateral flow (Wolanski 1993, p. 433). None of the models discussed by Wolanski (1993) are 3D, as is the tidal model used in this thesis. Thus accurate simulation of these motions by these models is highly unlikely since a fully 3D, time-variable approach is important for simulating surface currents (as opposed to layer-averaged currents) and for simulating the rapid changes in currents expected to occur when tides and winds are important (Johnson and Hess 1990, p. 198). In fact, of the models discussed in Sections 9.1–9.8, only those of Bartsch et al. (1989), Johnson and Hess (1990), and Noye et al. (1992) consider fully 3D circulations. Thus, except for these, the crucial difference between *all* hydrodynamic models discussed above and that used to derive the velocity field in this thesis is that the former are essentially depth-averaged while the latter is depth-dependent.

Third, "reefs", either in the form of isolated islands (as in the Wolanski (1993) depth-averaged steady state current example) or in the form of lagoonal reefs (as in the Oliver et al. (1992) Bowden Reef case study), are not abundant in the SG region. Where they do exist, larval

dispersion is insignificant, as will be shown in Chapter 10.

9.9.3 Model Realism

The problem of models unable to reproduce realistic circulation may also be due to mesh size. More reliability might result if the mesh size were made small enough to cope with the complex topography. There are physical limitations, however, because it is unrealistic to use a mesh size smaller than the water depth (Wolanski 1993, p. 434), below which the assumptions used to derive the so-called "shallow water equations" discussed in Section 3.1 are no longer valid.

The vertical migration (by buoyancy or swimming) of larvae remains an unresolved problem (Wolanski 1993, p. 434). Most existing models—such as the McShane et al. (1988), Black et al. (1990), Dight et al. (1990b), Possingham and Roughgarden (1990), Black and Moran (1991), James and Scandol (1992), and Scandol and James (1992) models—predict long-term larval dispersion patterns on the assumption that the larvae are neutrally buoyant and do not swim vertically. However, such predictions are invalid in the presence of small vertical velocities (by buoyancy or swimming) because the 3D circulation can lead, not only to dispersion, but to aggregation (negative dispersion). This aggregation becomes particularly important when dispersion patterns or retention rates need to be modelled over long periods (days to weeks). As discussed above, few of the existing models take into account the 3D flow structure, let alone 3D aspects of larval behaviour. The present model does both, as is discussed in Sections 3.1 and 7.3, respectively.

9.10 Summary

To reliably predict the transport of larvae it is first necessary to model the water circulation reliably. This involves taking into account several key fluid-dynamics processes: the equations must be nonlinear; the forcing by winds, tides and, if they exist, prevailing currents must not be treated separately; the specification of the open boundaries must, if such exists, include horizontal and/or vertical velocity shear; an appropriate mesh size must be chosen to cope with small-scale phenomena, or these must be explicitly parameterised; and the hydrodynamic model must be carefully and extensively verified, especially in relation to the near-shore circulation. Predictions should in any case be validated with quantitative field data collected at the appropriate temporal and spatial scales (Wolanski 1993, p. 435).

The hydrodynamic model used in this thesis has been shown to adequately satisfy these criteria. It will be shown in the following chapter that, limited only by the availability of quality larval dispersion field data, the dispersion model derived in the present work adequately satisfies all but the final criterion. In view of the obvious problems in prediction at fine scales, it is essential that any non-trivial conclusions arising from the application of such models be backed up by detailed concurrent field observations, of both currents *and* larvae, at similar spatial and temporal scales (Oliver et al. 1992, p. 887).

Chapter 10

Larval Dispersion Simulations

> The phenomenon of recruitment variation is best documented in commercially harvested species of fish. Under moderate fishing pressure, the size of a fish population is normally bounded within a range of about one order of magnitude, but the annual recruitment to it fluctuates much more widely, and without obvious relation to adult population size. In many species, recruitment variation has been sufficiently great from year to year, that fisheries are built upon the backs of single highly successful cohorts; the populations are often composed largely of single-aged individuals, all the product of a single highly successful episode of reproduction, which grow and are fished over a succession of years. With luck, a new successful cohort appears in time to sustain the fishery. Without luck, the fishery fades and fishermen find new employment (Sale 1990, p. 26).

The characteristically high and variable rate of loss between the time of reproduction and recruitment of a new cohort may be due to any of several factors during larval life. Marine larvae may fail to find adequate supplies of food, and either starve or succumb early to pelagic predators. Physical processes of the water mass may carry them to places from which they are unable to return to suitable habitat. Conditions in the adult habitat may change and fail to offer the correct cues to induce settlement by passing larvae. Recruitment to the adult phase may be further modified by factors influencing survivorship after settlement (Sale 1990, p. 26).

Models have the potential to produce otherwise unattainable detail on currents and larval densities at virtually any spatial and temporal scale, and for a wide range of geographic, hydrographic, and meteorological situations. However, before such models can be considered as reliable adjuncts or surrogates for *in situ* observation, it is essential that they be tested as rigorously as possible against detailed field data on actual currents and larval densities (Oliver et al. 1992, p. 874).

At the time of the First National Prawn Seminar in November 1973, fisheries were well established in a number of Australian states and territories, including South Australia, and in the ensuing decade this state developed a highly regulated fishery in Gulf St. Vincent and Spencer Gulf, based on research done by the Department of Fisheries—now part of the South Australian Research and Development Institute (Dall 1985, p. 11). In relation to distribution and stock density surveys of adult populations, collection on *Penaeus latisulcatus* in South Australia by the Fisheries department was started in 1968, and is still continuing. The work done has included studies on recruitment, growth, migration, mortality, and yield and has served as the basis for a very closely managed fishery, but so far only preliminary data have been published (Carrick 1982, 1985, 1988). With respect to population dynamics, tagging and log book data on *P. latisulcatus* have been collected in South Australia by M. G. King and N. A. Carrick since 1972 and then used to manage the fishery, but results have not yet been published (Dall 1985, p. 15).

In this chapter, simulations are conducted in which some input parameters are altered from baseline values to provide information on the sensitivity of the larval dispersion model to such

alterations. Since there are no available observational data with which to compare simulation output, quantitative errors measures are not able to be reported.

In all prawn larvae dispersion simulations discussed in this chapter, unless otherwise stated, the initial condition input is that of the "average" spawning concentration discussed in Section 2.1.5 and represented graphically in Figure 2.15. This initial condition is used to represent a "typical" spawning season, at least as far as can be determined from the data available.

The effects of varying input to the tidal and/or dispersion model is assessed chiefly in terms of the approximations as output by the dispersion model. In Sections 10.1.1, 10.1.2, 10.2.1, and 10.4.1, however, some aspects of the effects of varying tidal model input (i.e. the forcing provided) on tidal model output (i.e. the currents predicted) are also discussed. These discussions are concerned primarily with tidal ellipses (see Section 7.4.1) and tidal current residuals (see Section 7.4.2).

10.1 Wind–Stress Sensitivity

In this section, numerical simulations of larval dispersion in Spencer Gulf as determined using tidal currents predicted by the Bills (1991) and Nixon (1992) tidal model, with a range of input wind–stress specifications, are discussed.

In Section 10.1.1, the coarse grid Spencer Gulf model of Section 3.4 is forced with wind which is constant in both space and time. In Section 10.1.2, the fine grid Spencer Gulf model of Chapter 6 is forced with wind which is variable in both space and time. Results presented in Section 10.1.2 have appeared in Nixon and Noye (1996c).

In both simulation sets a control larval dispersion simulation using currents predicted with zero wind–stress is carried out. The effects of varying wind–stress as input to the tidal model is assessed chiefly in terms of the approximations as output by the dispersion model. Some aspects of the effects of varying tidal model input (i.e. the wind–stress forcing provided) on tidal model output (i.e. the residual currents predicted) are also discussed.

In Tables 10.1–10.4, for all wind–stress regime simulations, the maximum positive concentration ($\mathrm{Max}\{+\tau\}$), total of positive concentrations ($\mathrm{Tot}\{+\tau\}$), and a tally of "clipped" negative concentrations ($-\mathrm{Tot}\{-\tau\}$) are listed, where each is calculated excluding open boundary grid–points. Tables 10.1 and 10.3 list statistics for the final simulation time–step. Table 10.2 and 10.4 list statistics over all simulation time–steps, excluding the initial condition. In Table 10.1 and 10.3 the y and x grid coordinates i and j, respectively, corresponding to the position in the coarse and fine grid Spencer Gulf models, respectively, of maximum concentration are also listed.

10.1.1 Space and Time Independent Wind–Stress

In Figures 10.1–10.3 simulated final prawn larvae concentration (m^{-2}) level curves (top left), and y- (top right) and x- (bottom left) transects at the appropriate grid–scale (solid curve) and with cubic-spline smoothing (dashed curve) are depicted, and are as defined in Section 8.9.4. The initial condition imposed is that of the idealised Gaussian peak derived to approximately represent a Cowell ground spawning event at 21:30 on 12 December 1988, as described in Section 8.9.4 and illustrated in Figure 8.33. The 28 d simulations were carried out using the LW 2(1,3) type FDM with other model parameters as defined in Section 8.9.4. Clipping of negative values as they are generated is implemented, following the numerical tests carried out in that section. In Tables 10.1–10.2 simulation statistics as discussed in Section 8.9.4 are listed for the three constant wind scenarios simulated.

A Zero Wind Scenario

Figure 10.1 depicts larval concentrations predicted by the dispersion model using currents predicted by the tidal model with zero wind–stress. A global maximum in larval concentration

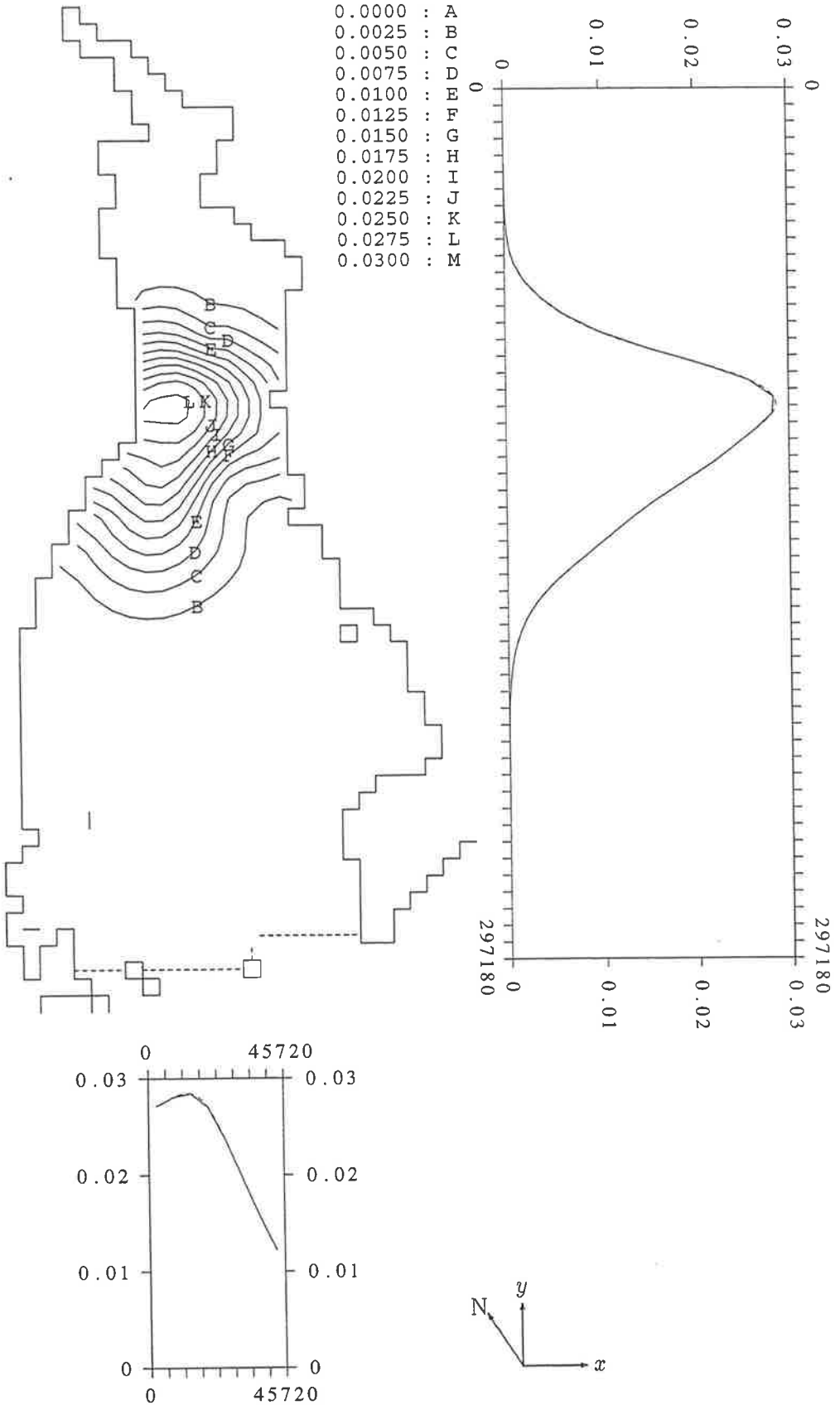

Figure 10.1: Zero wind–stress simulation concentration (m^{-2}) level curves (top left), and y- (top right) and x- (bottom left) transects through the concentration maximum.

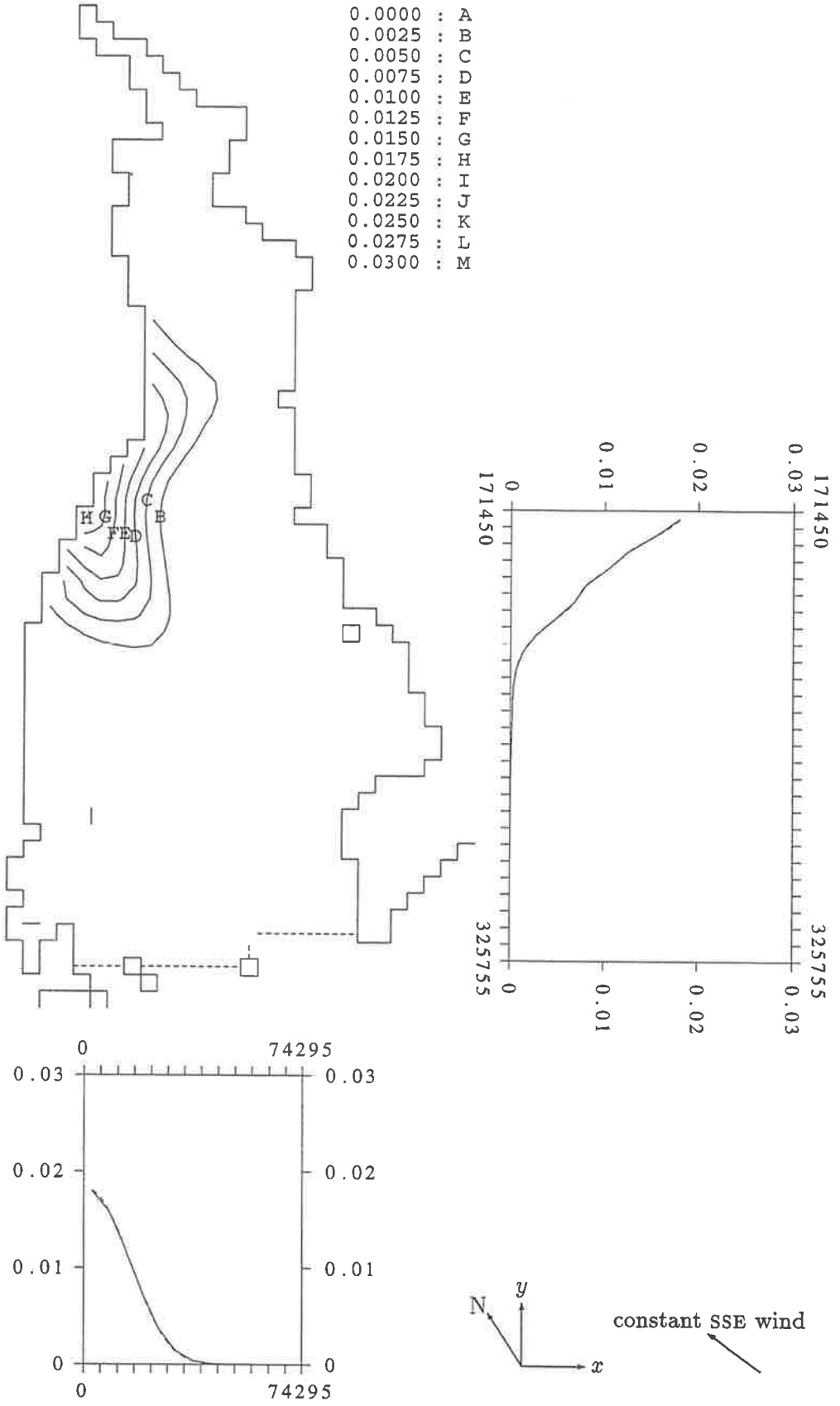

Figure 10.2: Constant SSE wind–stress simulation concentration (m^{-2}) level curves (top left), and y- (top right) and x- (bottom left) transects through the concentration maximum.

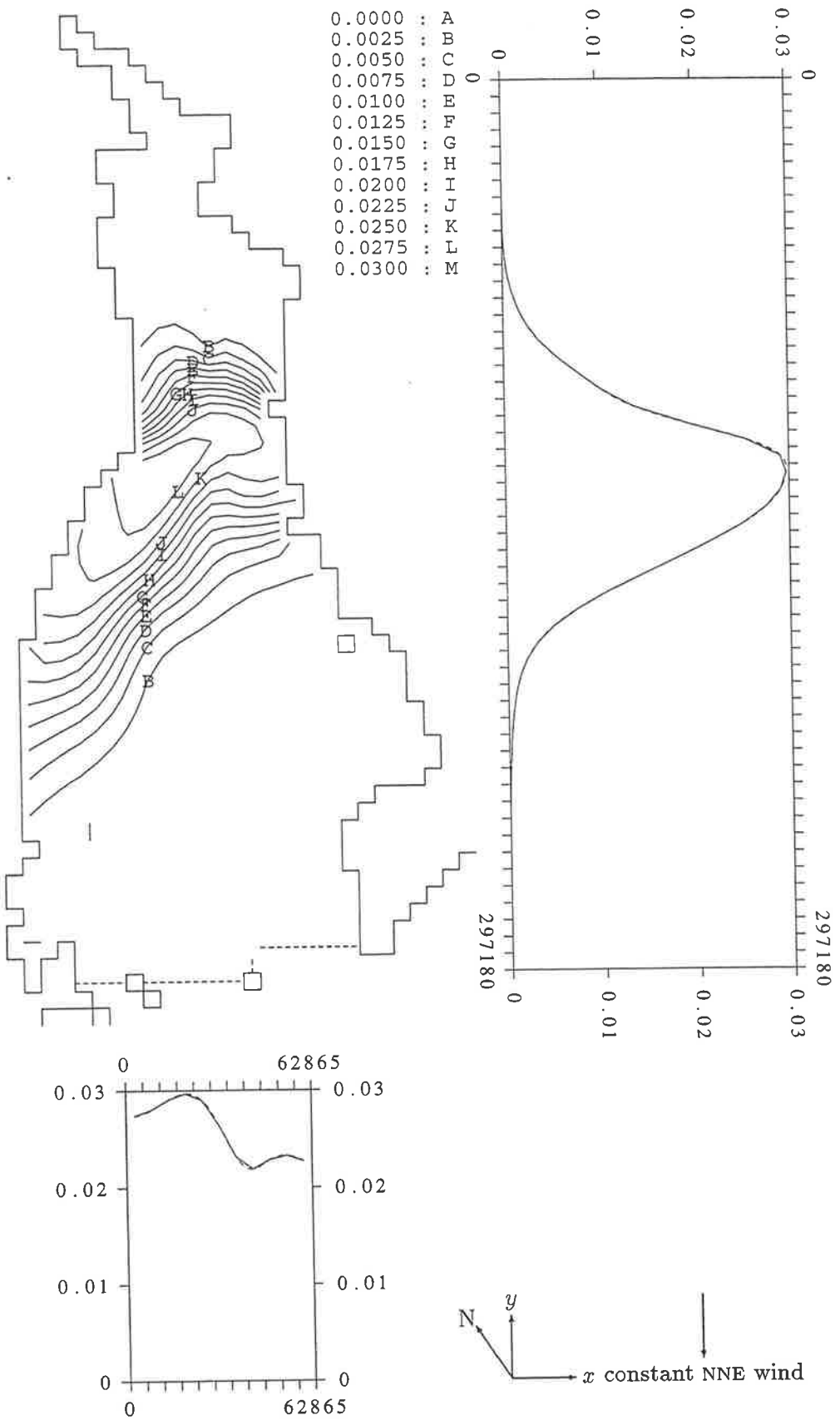

Figure 10.3: Constant NNE wind–stress simulation concentration (m^{-2}) level curves (top left), and y- (top right) and x- (bottom left) transects through the concentration maximum.

Constant Wind–Stress Test Statistics for the Final Time–Step					
Wind Direction (from)	Max$\{+\tau\}$ (m^{-2})	Tot$\{+\tau\}$ (m^{-2})	$-$Tot$\{-\tau\}$ ($-m^{-2}$)	Row (i)	Column (j)
zero	2.84×10^{-2}	2.21×10^{0}	1.21×10^{-11}	25	12
SSE	1.80×10^{-2}	7.61×10^{-1}	1.69×10^{-8}	32	6
NNE	2.97×10^{-2}	4.05×10^{0}	8.53×10^{-8}	29	11

Table 10.1: The constant wind–stress simulation statistics for the final time–step.

Constant Wind–Stress Test Statistics Over All Time–Steps			
Wind Direction (from)	Max$\{+\tau\}$ (m^{-2})	Tot$\{+\tau\}$ (m^{-2})	$-$Tot$\{-\tau\}$ ($-m^{-2}$)
zero	4.81×10^{-1}	1.77×10^{3}	2.01×10^{-2}
SSE	4.80×10^{-1}	1.22×10^{3}	2.61×10^{-2}
NNE	4.81×10^{-1}	2.45×10^{3}	2.29×10^{-2}

Table 10.2: The constant wind–stress simulation statistics over all time–steps.

is seen near L directly above (i.e. NNE of) the spawning site, with a concentration "intrusion" extending from this to the southwest into the middle of the Gulf and towards the mouth. The initial peak has been dispersed across the entire mid-north Gulf width, with insignificant larval concentrations predicted in the upper-north and southern Gulf reaches. The transects show the peak to be offshore from the coast northeast of Franklin Harbour station (see Figure 3.9) and to be skewed about the maximum towards the open boundary.

A Constant SSE Wind Scenario

Figure 10.2 depicts larval concentrations predicted by the dispersion model using currents predicted by the tidal model with constant wind–stress calculated from a SSE wind of $7.5\,m\,s^{-1}$. This was chosen to represent typical summer wind conditions determined from the historical record, as discussed in Section 4.4.6. A global maximum in larval concentration is seen near L directly left (i.e. NW) of the spawning site, with two concentration "intrusions" extending from this to the south into the middle of the Gulf towards the mouth and to the east into the middle of the Gulf towards the head. The initial peak has been dispersed along the western coastline of the mid-north Gulf, with insignificant larval concentrations predicted in the upper-north and southern Gulf reaches. The transects show the peak to be adjacent to the coast southwest of Franklin Harbour station (see Figure 3.9), with a height greatly reduced compared to that of the zero-wind predictions. Note that the peak did *not* shift from the initial position (see Figure 8.33) in the direction of the prevailing wind.

A Constant NNE Wind Scenario

Figure 10.3 depicts larval concentrations predicted by the dispersion model using currents predicted by the tidal model with constant wind–stress calculated from a NNE wind of $7.5\,m\,s^{-1}$. This was chosen to approximate atypical summer wind conditions representing a hypothetical storm surge event during which one might intuitively expect SSW larval transport, possibly out of the Gulf mouth. A global maximum in larval concentrations is seen directly to the north of the spawning site, with two concentration "intrusions" extending from this to the east into the middle of the Gulf towards Wallaroo and to the west along the coast towards Arno Bay (see Figure 3.9). The initial peak has been dispersed across the entire mid-north Gulf width

and along the western coastline of the mid-north and mid-south Gulf, with insignificant larval concentrations predicted in the upper-north and southern Gulf reaches. There is also dispersion in the mid-north Gulf southwards along the eastern coast, which is illustrated by the secondary local maximum in the x-transect shown. The transects show the major peak to be adjacent to the coast southeast of Franklin Harbour (see Figure 3.9) and to be less skewed about the maximum towards the open boundary than, but of a height comparable to that of, the zero wind predictions. Note that, as in the SSE wind simulation, the peak did *not* shift in the direction of the prevailing wind.

Residual Currents

Residual current vectors for the simulation period are plotted—at every computational element over the entire Gulf—in Figures 10.4–10.6, for both the near sea–surface and near sea–bed

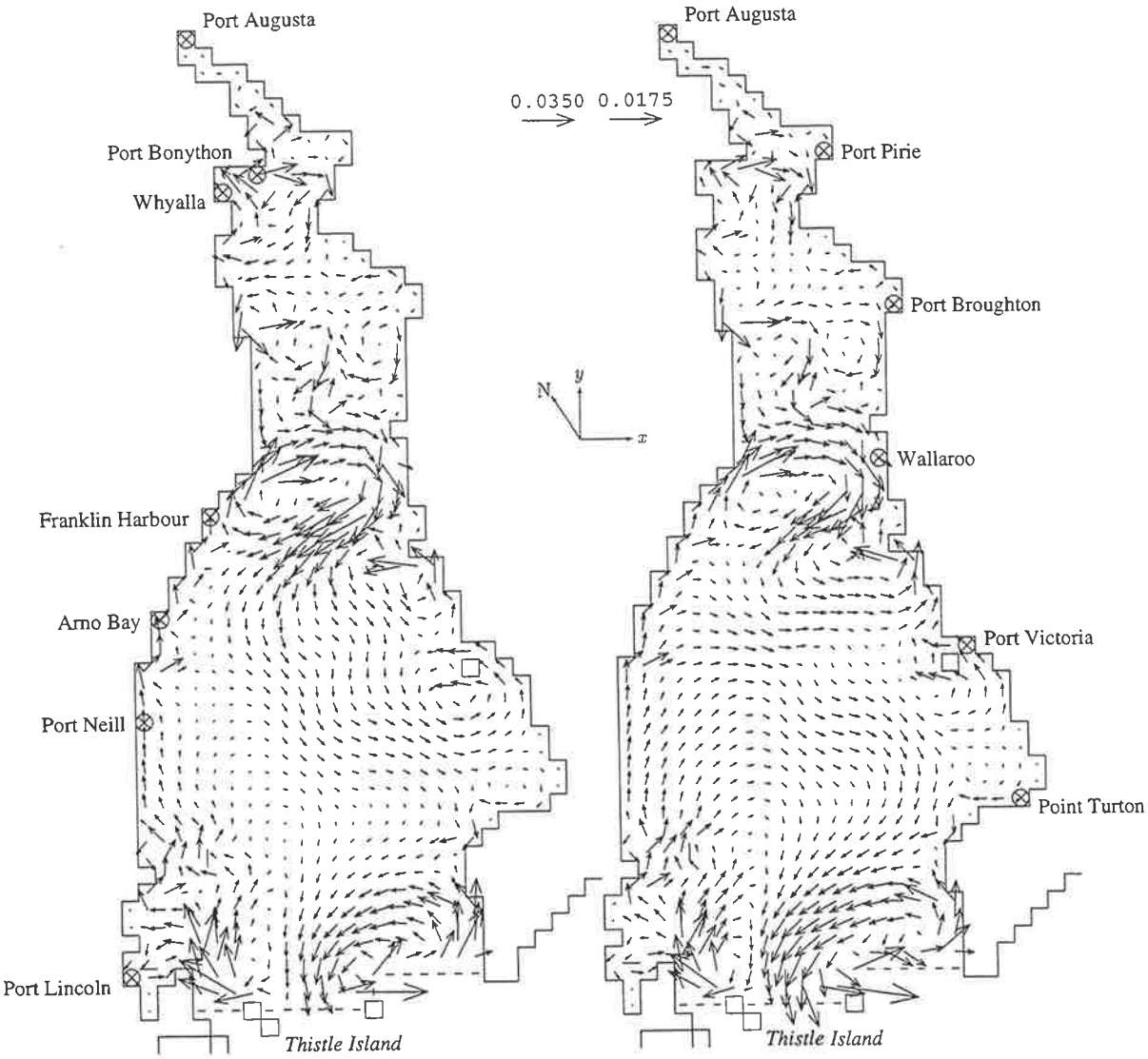

(a) near sea–surface depth–level

(b) near sea–bed depth–level

Figure 10.4: Spencer Gulf tidal current residuals ($\mathrm{m\,s^{-1}}$) for the 29 d period from 09:30 December 12 1988 calculated with (constant) zero wind–stress. Vectors are plotted for every computational element. Tidal stations (roman) and islands (italics) are named.

depth–levels. Currents used to derive the residuals of Figure 10.4 were simulated using zero wind–stress, currents used to derive the residuals of Figure 10.5 were simulated using a constant

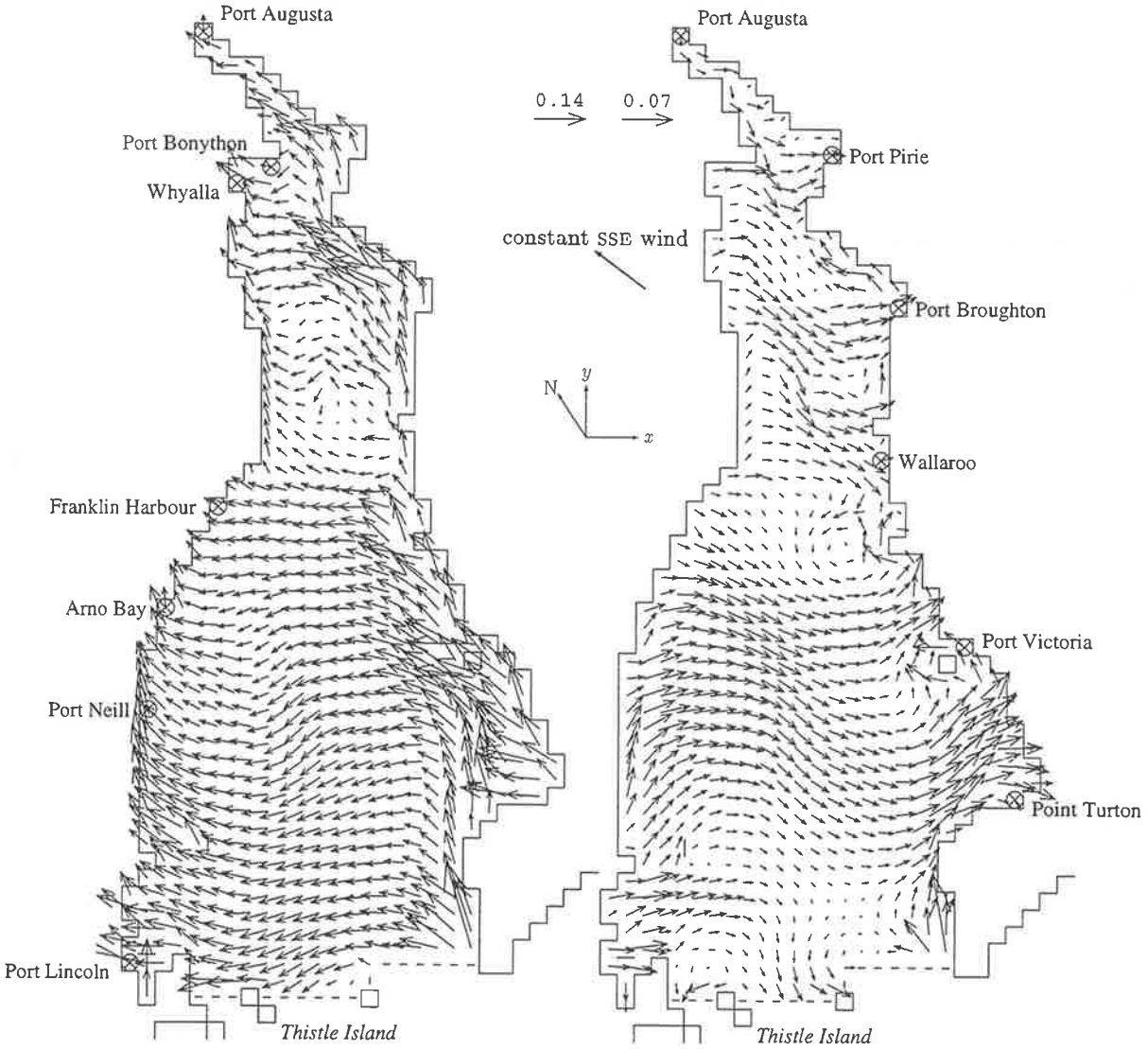

(a) near sea–surface depth–level

(b) near sea–bed depth–level

Figure 10.5: Spencer Gulf tidal current residuals ($m\,s^{-1}$) for the 29 d period from 09:30 December 12 1988 calculated with constant SSE wind–stress. Vectors are plotted for every computational element. Tidal stations (roman) and islands (italics) are named.

SSE wind–stress, and currents used to derive the residuals of Figure 10.6 were simulated using a constant NNE wind–stress.

Comparing Figures 10.4(a), 10.5(a), and 10.6(a), it is apparent that near sea–surface residual currents for the constant wind–stress simulations are markedly affected by the direction of the prevailing wind. Figures 10.4(b), 10.5(b), and 10.6(b) indicate that bottom return currents produced by surface wind–stress result in residual currents near the sea–bed which are also markedly affected by the direction of the prevailing wind. In all three wind scenarios it is evident that near sea–bed residuals are of approximately half the magnitude of sea–surface residuals. The constant SSE and NNE wind–stress simulations result in current residuals of approximately four times the magnitude of those for the zero wind–stress simulation. These facts are highlighted by the chosen vector scales.

Comparing Figure 10.4(a) with Figure 10.4(b) it is apparent that, aside from an approximately 50% reduction in strength due to bottom friction effects, residual currents for the zero wind–stress simulation are remarkably similar near the sea–surface and the sea–bed. It is speculated then, that the dominant features of the residual currents of the zero wind–stress simulation

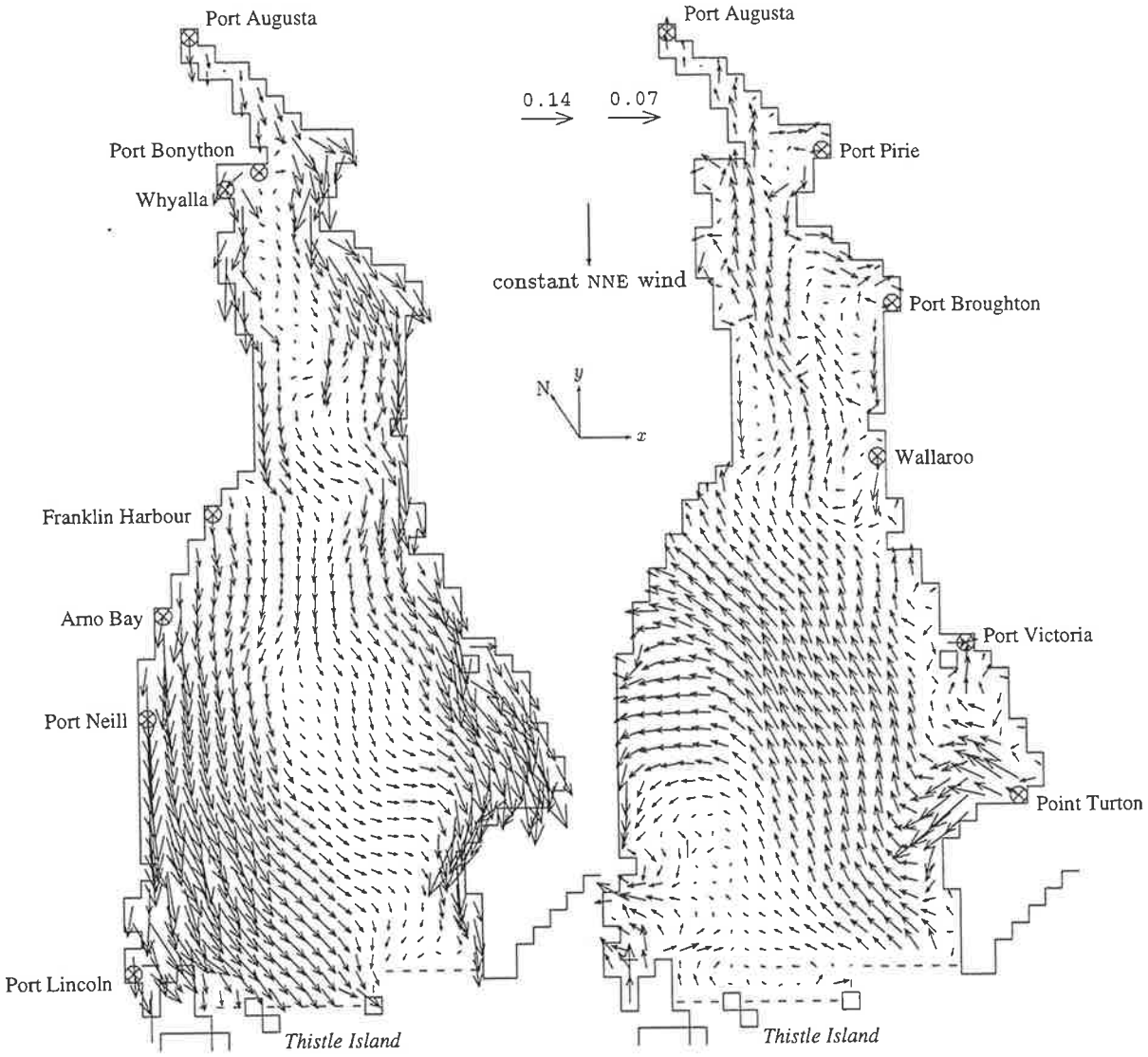

(a) near sea–surface depth–level

(b) near sea–bed depth–level

Figure 10.6: Spencer Gulf tidal current residuals ($m\,s^{-1}$) for the 29 d period from 09:30 December 12 1988 calculated with constant NNE wind–stress. Vectors are plotted for every computational element. Tidal stations (roman) and islands (italics) are named.

result from the interaction of the forcing at the open boundary with the bathymetric and topographic characteristics of Spencer Gulf itself. These features, which include the clockwise rotating residual eddy spanning the Gulf between Franklin Harbour and Wallaroo, are evident in the vectors of both Figures 10.4(a) and 10.4(b).

Discussion

The Max$\{+\tau\}$ measures in both Table 10.1 and Table 10.2 indicate that the SSE wind simulation consistently resulted in significantly lower numbers of predicted larvae than the zero and NNE wind simulations. It is speculated—based on the tidal velocity residuals illustrated—that, due to greater sea–bed return currents produced by the the SSE wind, increased larval loss through the open boundary is the mechanism underlying this phenomenon. The final and overall Tot$\{+\tau\}$ measures in Tables 10.1 show the NNE wind simulation consistently resulted in greater numbers of predicted larvae. The greater height of, and larger area beneath, the transects in Figure 10.3 compared to those in Figures 10.1 and 10.2 illustrate these points.

For the final $-\text{Tot}\{-\tau\}$ measure, the NNE wind simulation produced more non-physical negative results than the other two. This point is less obvious in the figures—with the chosen transect axis scales—as these discarded spurious negative concentrations correspond to at most 2.2×10^{-6} % of the total. It is of interest to note that the initial larval peak west of Wallaroo (see Figures 3.9 and 8.33) is well dispersed after 28 d in all three simulations.

It has been shown that the LW method performs well using tidal velocities computed with zero or constant wind–stress. Advantages of the former over the latter include the fact that, in the simulations reported here, a more localised concentration peak with fewer spurious negative values was produced.

10.1.2 Space and Time Dependent Wind–Stress

In Figures 10.7–10.8 simulated final prawn larvae concentration ($10^6\,\text{m}^{-2}$) level curves (top left), and y- (top right) and x- (bottom left) transects are depicted, and are analogous to those as defined in Section 8.9.4. Note that the y-transect at top right in these figures appears incomplete due to land mass encountered along the transect line. The initial condition imposed is that of the "average" determined from SARDI field data, derived to represent a typical Spencer Gulf spawning event at 21:30 on 1 February 1988, as described in Section 2.1.5 and illustrated in Figure 2.15. The 29 d simulations were carried out using the LW 2(1,3) type FDM with model parameters as defined in Chapter 6 and Section 8.7. Clipping of negative values as they are generated is implemented, following the numerical tests carried out in Section 8.9.4. In Tables 10.3–10.4 simulation statistics as defined in Section 8.9.4 are listed for the two wind–

Variable Wind–Stress Test Statistics for the Final Time–Step					
Wind–Stress (variation)	$\text{Max}\{+\tau\}$ (m^{-2})	$\text{Tot}\{+\tau\}$ (m^{-2})	$-\text{Tot}\{-\tau\}$ ($-\text{m}^{-2}$)	Row (i)	Column (j)
zero	9.34×10^{1}	9.79×10^{4}	2.41×10^{-6}	40	20
non-zero	7.94×10^{1}	7.58×10^{4}	1.47×10^{-5}	40	20

Table 10.3: The variable wind–stress simulation statistics for the final time–step.

Variable Wind–Stress Test Statistics Over All Time–Steps			
Wind–Stress (variation)	$\text{Max}\{+\tau\}$ (m^{-2})	$\text{Tot}\{+\tau\}$ (m^{-2})	$-\text{Tot}\{-\tau\}$ ($-\text{m}^{-2}$)
zero	4.13×10^{2}	2.06×10^{8}	7.00×10^{1}
non-zero	4.19×10^{2}	1.82×10^{8}	5.01×10^{1}

Table 10.4: The variable wind–stress simulation statistics over all time–steps.

stress scenarios simulated.

A Zero (Space and Time) Wind–Stress Variability Scenario

Figure 10.7 depicts larval concentrations predicted by the dispersion model using currents predicted by the tidal model with zero wind–stress. The final postlarval concentration global maximum is located in a bay of the north-western Spencer Gulf coast, directly below Whyalla, at N. This is the bay of Cowleds Landing, indicated in Figure 1.2. The results are characterised by a contour grouping and x-transect which indicate a gradual concentration decline from the model global maximum to the moderate transect local minimum, south-eastwards across the upper Gulf to the opposite coast.

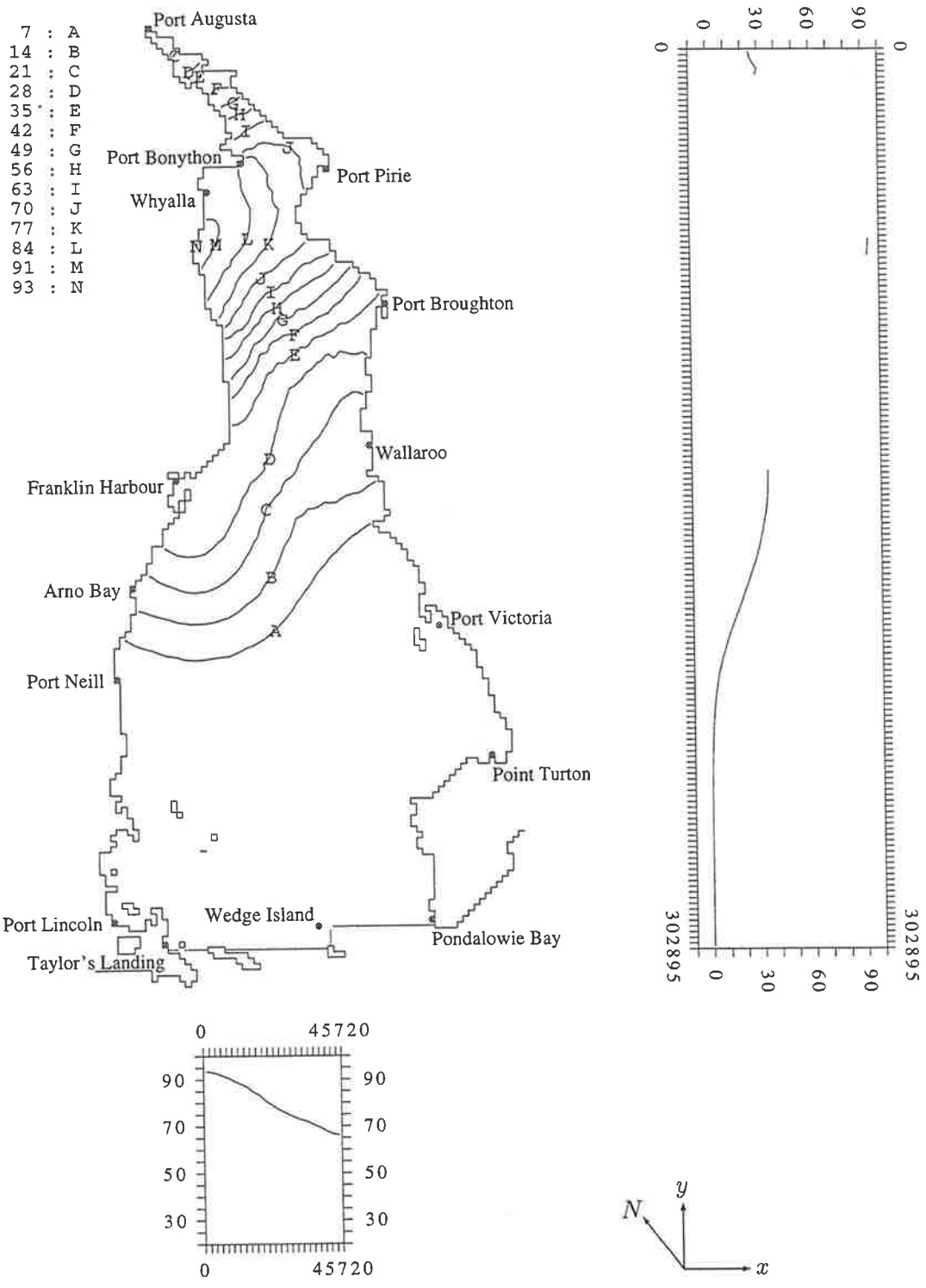

Figure 10.7: Zero wind–stress simulation concentration (10^6 m^{-2}) level curves (top left), and y- (top right) and x- (bottom left) transects through N (southwest of Whyalla). Tidal stations are named.

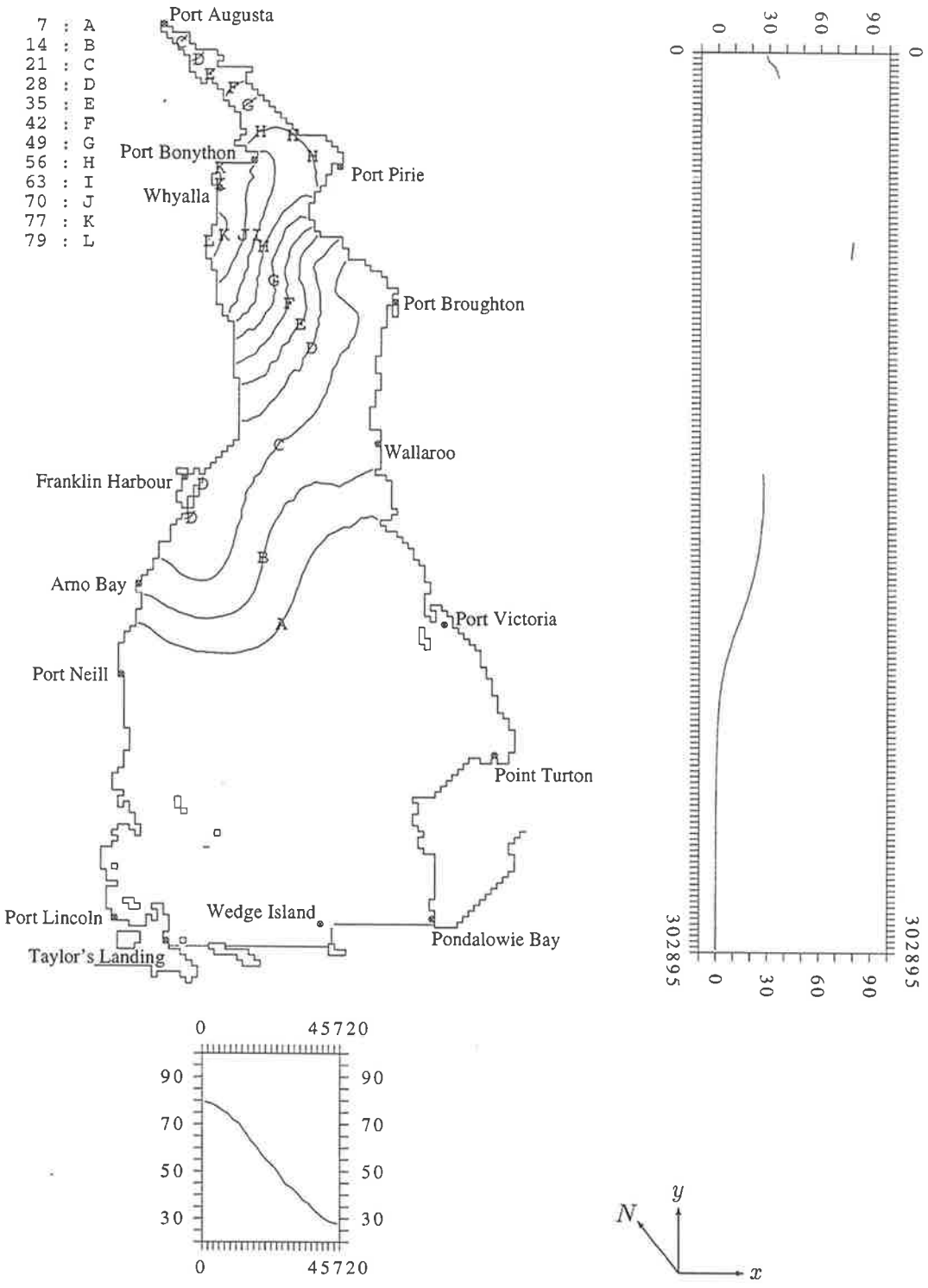

Figure 10.8: Non-zero wind–stress simulation concentration ($10^6\,\mathrm{m}^{-2}$) level curves (top left), and y- (top right) and x- (bottom left) transects through L (southwest of Whyalla). Tidal stations are named.

A Non-Zero Space and Time Wind–Stress Variability Scenario

Figure 10.8 depicts larval concentrations predicted by the dispersion model using currents predicted by the tidal model with wind–stress calculated from a time and space varying wind field determined in the manner discussed in Section 4.2. A global maximum in larval concentration is seen at L, of slightly smaller magnitude compared to, but in exactly the same position (to the nearest computational grid–point) as for, the zero wind–stress simulation. The results are characterised by a contour grouping and x-transect which indicate a sudden concentration decline from the model global maximum to the significant transect local minimum, south-eastwards across the upper Gulf to the opposite coast.

Residual Currents

Residual current vectors for the simulation period are plotted—at every second computational element over the entire Gulf in both the x and y directions—in Figures 10.9 and 10.10, for

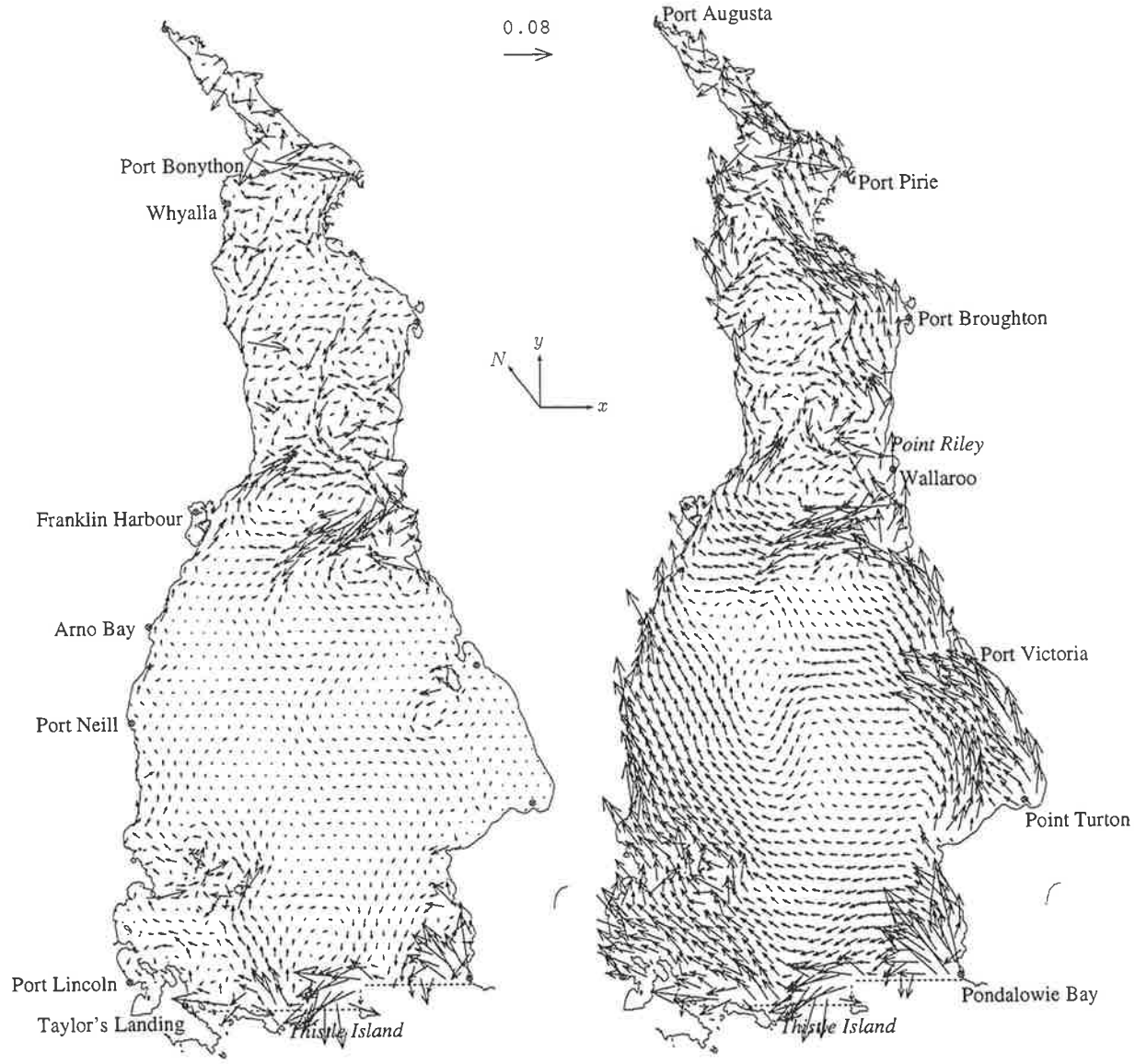

(a) zero wind–stress

(b) non-zero wind–stress

Figure 10.9: Spencer Gulf near sea–surface depth–level tidal current residuals ($\mathrm{m\,s^{-1}}$) for the 29 d period from 21:30 February 1 1988. Vectors are plotted for every second computational element in both the x and y directions. Tidal stations (roman) and places (italics) are named.

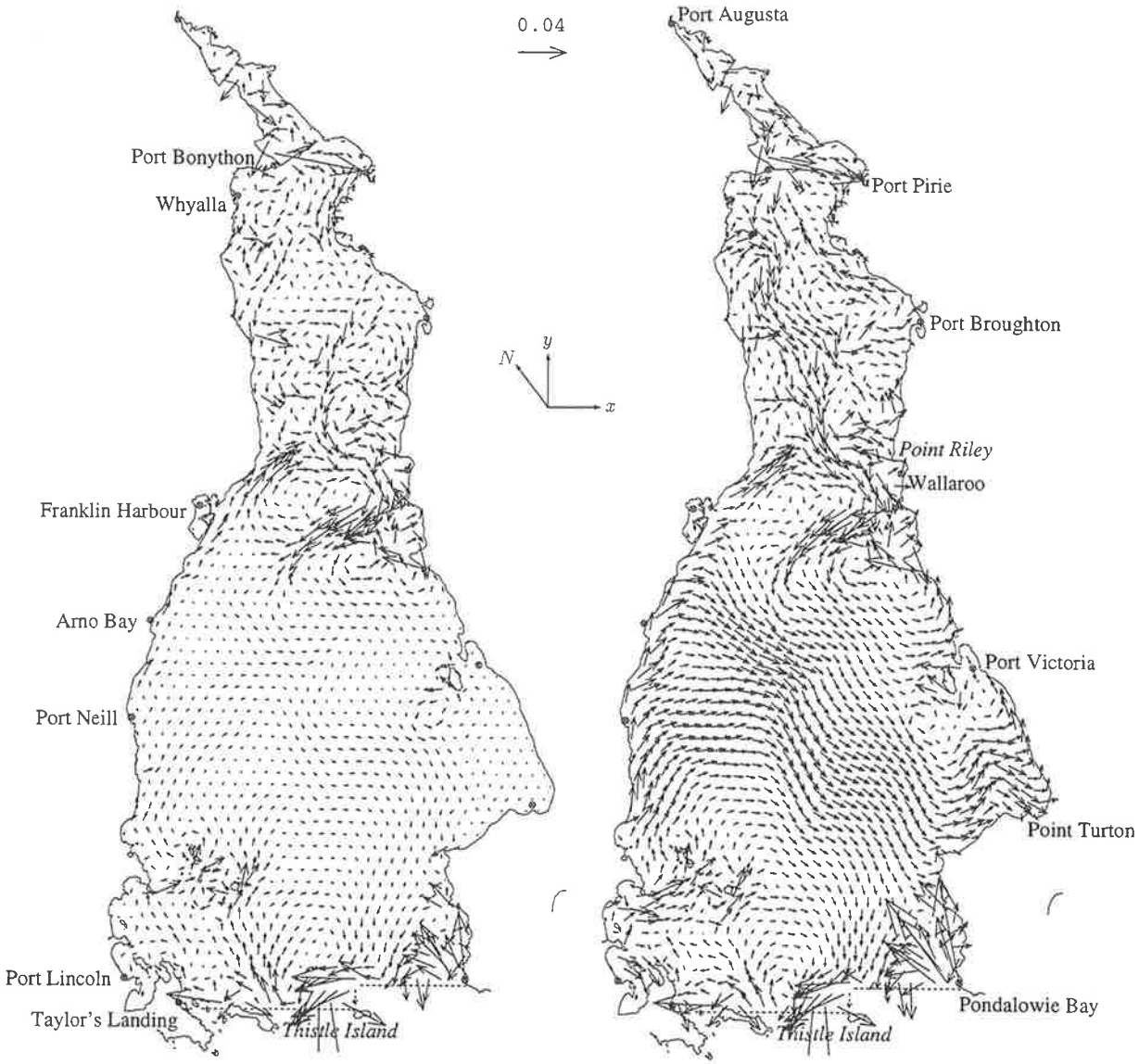

(a) zero wind-stress

(b) non-zero wind-stress

Figure 10.10: Spencer Gulf near sea–bed depth–level tidal current residuals ($\mathrm{m\,s^{-1}}$) for the 29 d period from 21:30 February 1 1988. Vectors are plotted for every second computational element in both the x and y directions. Tidal stations (roman) and places (italics) are named.

the near sea–surface and near sea–bed depth–level currents, respectively. Currents used to derive the residuals of Figures 10.9(a) and 10.10(a) were simulated using zero wind–stress, while currents used to derive the residuals of Figures 10.9(b) and 10.10(b) were simulated using space and time varying wind–stress. Mid-northern Gulf residuals are also shown in Figures 10.11 and 10.12, with Figures 10.11(a) and 10.12(a) derived from the zero wind–stress simulation and Figures 10.11(b) and 10.12(b) from the variable wind–stress simulation.

Comparing Figure 10.9(a) with Figure 10.10(a) and Figure 10.11(a) with Figure 10.12(a) it is apparent that, aside from an approximately 50% reduction in strength due to bottom friction effects, residual currents for the zero wind–stress simulation are remarkably similar near the sea–surface and the sea–bed. It is again speculated that the dominant features of the residual currents of the zero wind–stress simulation result from the interaction of the forcing at the open boundary with the bathymetric and topographic characteristics of Spencer Gulf itself. These features include the clockwise rotating residual eddy spanning the Gulf between Franklin Harbour and Wallaroo, the residual stream flowing south-westwards from the middle of the

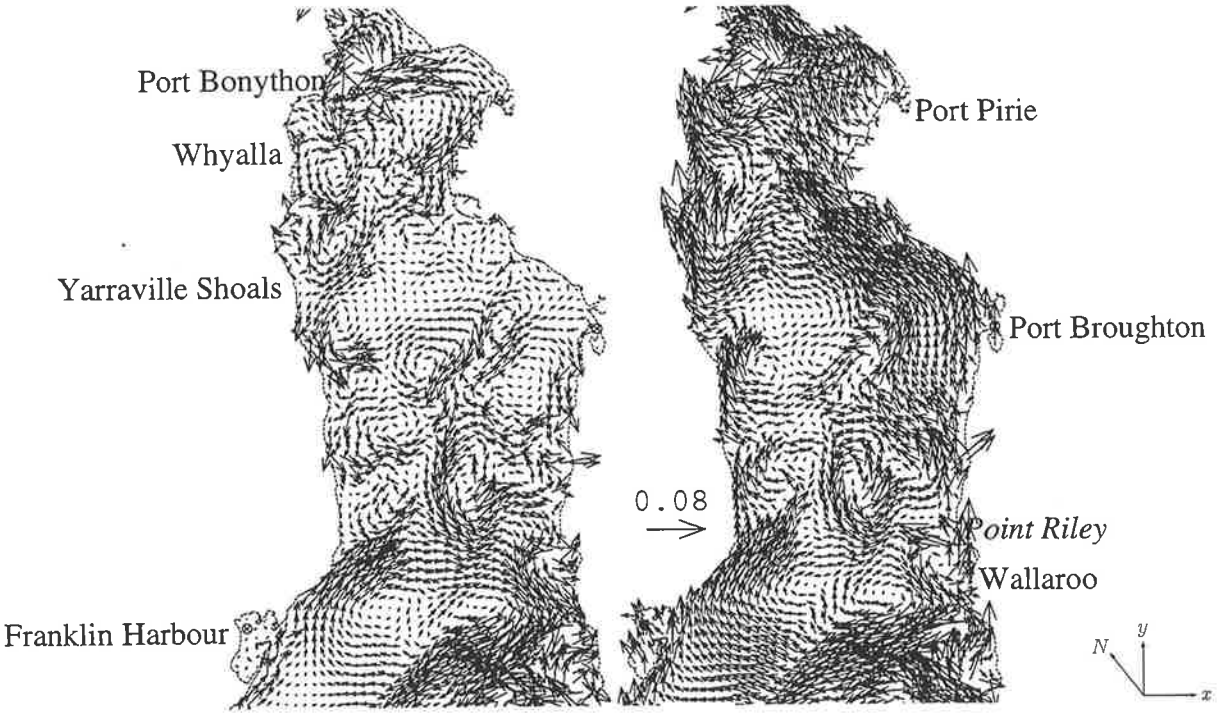

(a) zero wind–stress (c) non-zero wind–stress

Figure 10.11: Mid-northern Spencer Gulf near sea–surface depth–level tidal current residuals ($m\,s^{-1}$) for the 29 d period from 21:30 February 1 1988. Vectors are plotted for every computational element. Tidal stations (roman) and places of interest (italics) are named.

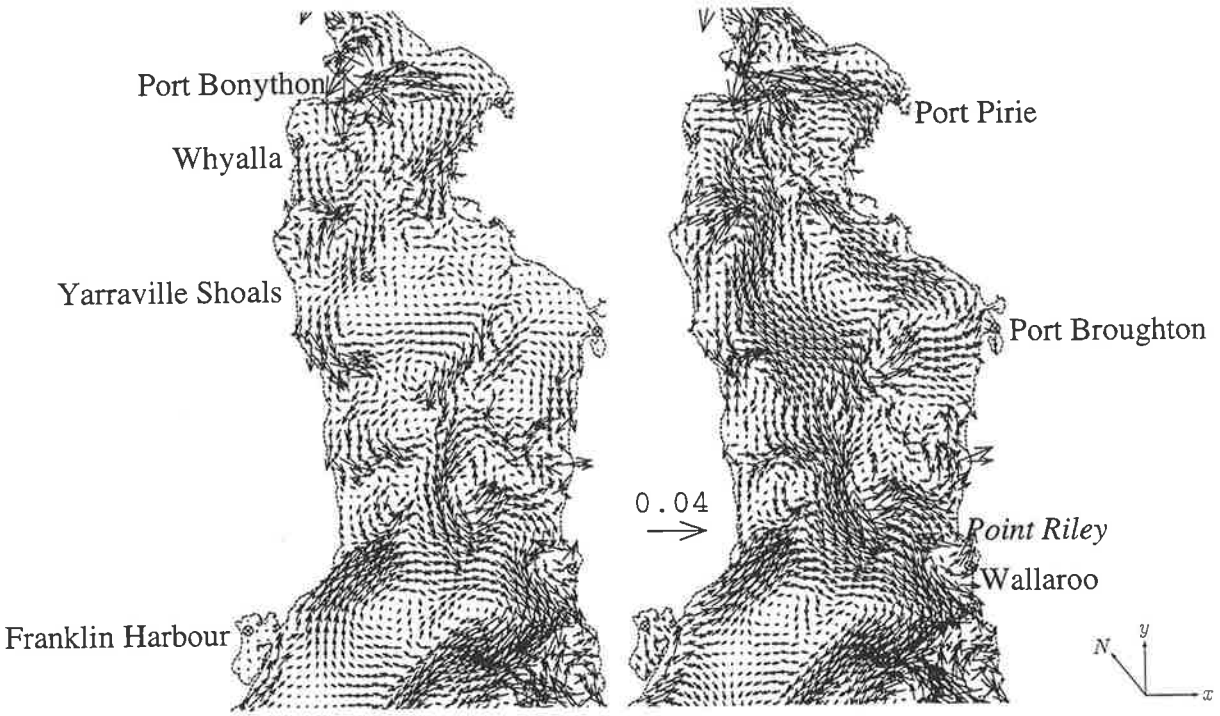

(a) zero wind–stress (c) non-zero wind–stress

Figure 10.12: Mid-northern Spencer Gulf near sea–bed depth–level tidal current residuals ($m\,s^{-1}$) for the 29 d period from 21:30 February 1 1988. Vectors are plotted for every computational element. Tidal stations (roman) and places of interest (italics) are named.

northern part of the Gulf above Point Riley and then southwards to feed this eddy, and the residual stream curving anticlockwise from below Wallaroo joining to, and then separating from, this eddy and then continuing westwards across towards Arno Bay. They are evident in the vectors of all of Figures 10.9(a)–10.10(b) and, where appropriate, Figures 10.11(a)–10.12(b).

Two features, namely the small anticlockwise rotating residual eddy west-south-west of Wallaroo (below the Gulf-spanning residual eddy mentioned above) and an eddy with similar characteristics west of Port Victoria (below Wardang Island shown with coastline dashed), are evident in Figures 10.9(a), 10.10(a), and 10.10(b) but not in Figure 10.9(b). It is speculated that the prevailing winds result in surface wind–stresses which prevent non-tidal currents from persisting in such a way so as to form these features in the manner in which they are seen to form in the absence of wind–stress. Nearer the sea–bed, however, the physical characteristics of the respective areas dominate the non-tidal flow regimes therein, and both residual eddies evolve irrespective of the presence or absence of wind–stress.

Other features, however, are evident in the residual currents corresponding to the variable, but not to the zero, wind–stress simulation. The applied variable wind–stress, the result of winds blowing chiefly from the SSE as reported in Chapter 4, generates residual surface currents correspondingly north-north-eastwards, from the southwestern Gulf regions up along the western coast, from the vicinity of Port Turton up around past Port Victoria, and from the waters off Port Broughton along the section of coastline immediately above this towards the middle of upper Spencer Gulf. In this region of the Gulf, where the water is shallow (see Figure 6.4), this latter feature persists in the residual bed current (see Figure 10.12(b)) although at greatly reduced strength. The former features, however, are not mirrored in the sea–bed residuals. These show evidence of return bed currents affecting water balance to the surface currents, in the residual streams meandering south-eastwards from the waters off Franklin Harbour, Arno Bay, and Port Neil, across the lower Gulf expanse turning both eastwards towards the coastal regions near Point Turton and westwards towards the open boundary near Thistle Island.

Discussion

The Max$\{+\tau\}$ measures in Table 10.3 indicate that, relative to the variable wind–stress simulation, the zero wind–stress simulation produced a comparatively greater maximum concentration. The final and overall Tot$\{+\tau\}$ measures in Tables 10.3 and 10.4 show the zero wind–stress simulation consistently resulted in greater numbers of predicted larvae. The greater height of, and larger area beneath, the transects in Figure 10.7 compared to those in Figure 10.8 illustrate these points. It is speculated—based on the near sea–surface and sea–bed tidal velocity residuals discussed above—that, due to greater bed return currents set up in response to the surface currents produced by the chiefly SSE regional summer winds, increased larval loss through the open boundary is the mechanism underlying this phenomenon.

For both $-$Tot$\{-\tau\}$ measures, the zero wind–stress simulation produced more non-physical negative results. This point is less obvious in the figures—with the chosen transect axis scales—as these discarded spurious negative concentrations correspond to at most 3.4×10^{-5} % of the respective totals. When compared to the simulation with variable wind–stress, the zero wind–stress simulation produced a peak of greater height, at the same grid–point, representing a stronger local concentration maximum at a similar location.

The observed concentration "intrusion" in Figure 10.8, extending beside the maximum concentration peak northwards into the Gulf head, correlates with the surface residual current stream—evident in Figures 10.9(b) and 10.11(b)—and the bed residual current stream—evident in Figures 10.10(b) and 10.12(b)—from the waters off Port Broughton along the section of coastline immediately above this towards the middle of upper Spencer Gulf. In shallow waters such as these, with complex shorelines and irregular bottom topography, such secondary, nonlinear flows can develop, which may produce a significant mean flow in one particular direction. In this region of upper Spencer Gulf, the mean flow at the bottom is in fact indicated by asymmetric mega-ripples on the sea–bed (Noye 1984b, p. 206).

Such "intrusions" and other larval dispersion simulation features are phenomena which can be further investigated on detailed comparison with SARDI postlarval settlement data. Since these data were not available, quantitative error measures are not reported here. The final peak settlement site in both simulations does, however, correspond qualitatively with a recently located nursery (Carrick 1994, personal communications). It is also of interest to note that the initial larval peak south of Whyalla (see Figure 2.15) is well diffused after 29 d in both simulations.

It has been shown that the LW $2(1,3)$ method performs well using tidal velocities computed with zero or space and time varying wind–stress. An advantage of the latter over the former is that, in the simulations reported here, a more localised concentration peak was produced. The chief advantage, however, is that it has been experimentally demonstrated that currents calculated assuming zero and time and space varying wind–stress result in non-tidal currents of significantly different characters, which in turn results in significant differences in larval distributions predicted under these two current regimes. The importance of realistic wind–stress representation in larval dispersion models is in other ways apparent since, for studies of year to year variations in larval transport, there is a need for space and time variable winds to force any model (Rothlisberg et al. 1983, p. 531) and the Spencer Gulf wind driven circulation not only depends on the direction, duration, and strength of the wind, but also on the phase of the tide (Noye 1984b, p. 208).

10.1.3 Conclusions

Based solely on the criterion of theoretical accuracy, the simulation results determined using the fine grid tidal and dispersion models are superior to those determined using the coarse grid models, in particular for the application at hand: the prediction of prawn larvae dispersion in a region of significant coastal topographic and sea–bed bathymetric variation. This point is further discussed in Sections 10.2.1 and 10.4.1.

It has been shown that the LW $2(1,3)$ FDM performs well using tidal velocities computed with or without wind–stress. Based solely on the criterion of physical realism, the simulation results with time and space varying wind–stress are superior to those with zero or constant wind–stress, in particular for the application at hand: the prediction of prawn larvae dispersion in a region of seasonally and spatially variable wind–stress. This point is further discussed in Sections 4.2 and 4.4.

It is thus concluded that an accurate representation of wind is required as input to the tidal model in order to accurately predict the 3D current regime, enabling the dispersion model to accurately predict 2D prawn larvae concentrations.

10.2 Initial Condition Sensitivity

Species that show the greatest recruitment variation tend to be highly fecund, laying thousands to millions of eggs in a clutch, and to suffer very high larval and juvenile mortality. In such species, a period of exceptionally favourable conditions for larval and juvenile survival has the potential to create a pronounced recruitment peak. In less fecund species the range of variation is necessarily more limited (Sale 1990, p. 26).

In order to determine the effects changing fecundity may have on postlarval *Penaeus latisulcatus* distributions in Spencer Gulf, simulations were made in which all model parameters were kept constant, except for the initial condition used.

Simulations were computed of the 29 d following an instantaneous spawning event at 21:30 on 1 February 1988. Currents were computed by the tidal model described in Chapter 6 with a non-zero wind–stress formulation derived from the BOM wind data available for the Spencer Gulf region over the period of interest, as described in Chapter 4. Some results presented in Sections 10.2.1–10.2.2 have appeared in Nixon and Noye (1996b).

10.2.1 Tidal Currents

The tidal ellipses and residual currents associated with this simulation are discussed in Sections 7.4.3 (Figures 7.1–7.4, and 7.6–7.9) and 7.4.4 (Figures 7.10–7.11), respectively.

The surmised effect of the combined residual currents is significant mixing in the upper Gulf with less significant mean transport southwards, past Wallaroo, and then westwards towards the lower mid-Gulf due south of Franklin Harbour—directly right, offshore from Arno Bay. The surface residual current stagnation regions offshore east of Arno Bay, combined with the relatively stronger southerly directed bed residual current stream, suggest mean transport southwards from these regions towards the middle of the Gulf. Little transport is expected from the Spencer Gulf interior through the open boundary to the ocean beyond, due to strong residual surface currents directed away from the open boundary into the interior on both sides of the Gulf, and only very weak residual surface *and* bed currents directed towards it in the middle of the Gulf. Such transport may well be expected from areas due north off Pondalowie Bay and/or directly above Thistle Island, however, as a result of the residual surface and bed current streams flowing out of the open boundary through the passage between Thistle and Wedge Islands.

10.2.2 Larval Dispersion

Contour and transect plots of the simulation results are shown in Figures 10.13–10.18 and are presented in a similar manner to the corresponding initial conditions of Figures 2.10–2.15. The level curves (solid curves) have x and y axes aligned horizontally and vertically, respectively, in the region defined by the closed boundary (solid lines) and open boundary (dashed lines). It should be noted that the final level curve in each figure is set to be the maximum postlarval concentration value computed for each simulation, and in that regard appears as a point indicating the location of the distribution maximum over the entire Spencer Gulf region. Note also that the y-transects at top right in these figures appear incomplete due to land mass encountered along the transect line. A barrier to flow in the y direction—depicted by a solid, horizontal straight line segment—represents Stickney Island. Because non-negativity of the finite-difference solution is not guaranteed at all grid-points, results are presented which implement "clipping". In this procedure any negative value generated is set to zero, since negative concentration is clearly a non-physical occurrence and clipping was shown in Section 8.9 to have little effect on the final solution.

In Tables 10.5–10.6, for all initial condition simulations, the maximum positive concentra-

Initial Condition Test Statistics for the Final Time–Step					
Initial Condition	$\mathrm{Max}\{+\tau\}$ ($10^6\ \mathrm{m}^{-2}$)	$\mathrm{Tot}\{+\tau\}$ ($10^6\ \mathrm{m}^{-2}$)	$-\mathrm{Tot}\{-\tau\}$ ($-10^6\ \mathrm{m}^{-2}$)	Latitude (°S)	Longitude (°E)
1988	7.97×10^{1}	7.76×10^{4}	1.46×10^{-5}	32°58.74′	137°36.84′
1991	9.50×10^{1}	6.52×10^{4}	4.48×10^{-10}	33°07.74′	137°28.56′
1992	6.92×10^{1}	6.36×10^{4}	2.00×10^{-5}	33°07.74′	137°28.56′
1993	7.49×10^{1}	5.76×10^{4}	1.14×10^{-5}	33°07.74′	137°28.56′
1994	7.54×10^{1}	5.52×10^{4}	8.33×10^{-6}	33°07.74′	137°28.56′
"average"	7.94×10^{1}	7.58×10^{4}	1.47×10^{-5}	33°07.74′	137°28.56′

Table 10.5: The initial condition simulation statistics for the final time–step. The tidal currents used in the simulation of the 29 d from 21:30 1 February 1988 were calculated with wind–stress.

tion ($\mathrm{Max}\{+\tau\}$), total of positive concentrations ($\mathrm{Tot}\{+\tau\}$), and a tally of "clipped" negative concentrations ($-\mathrm{Tot}\{-\tau\}$) are listed, where each is calculated excluding open boundary grid-points. Table 10.5 lists statistics for the final simulation time–step. Table 10.6 lists statistics

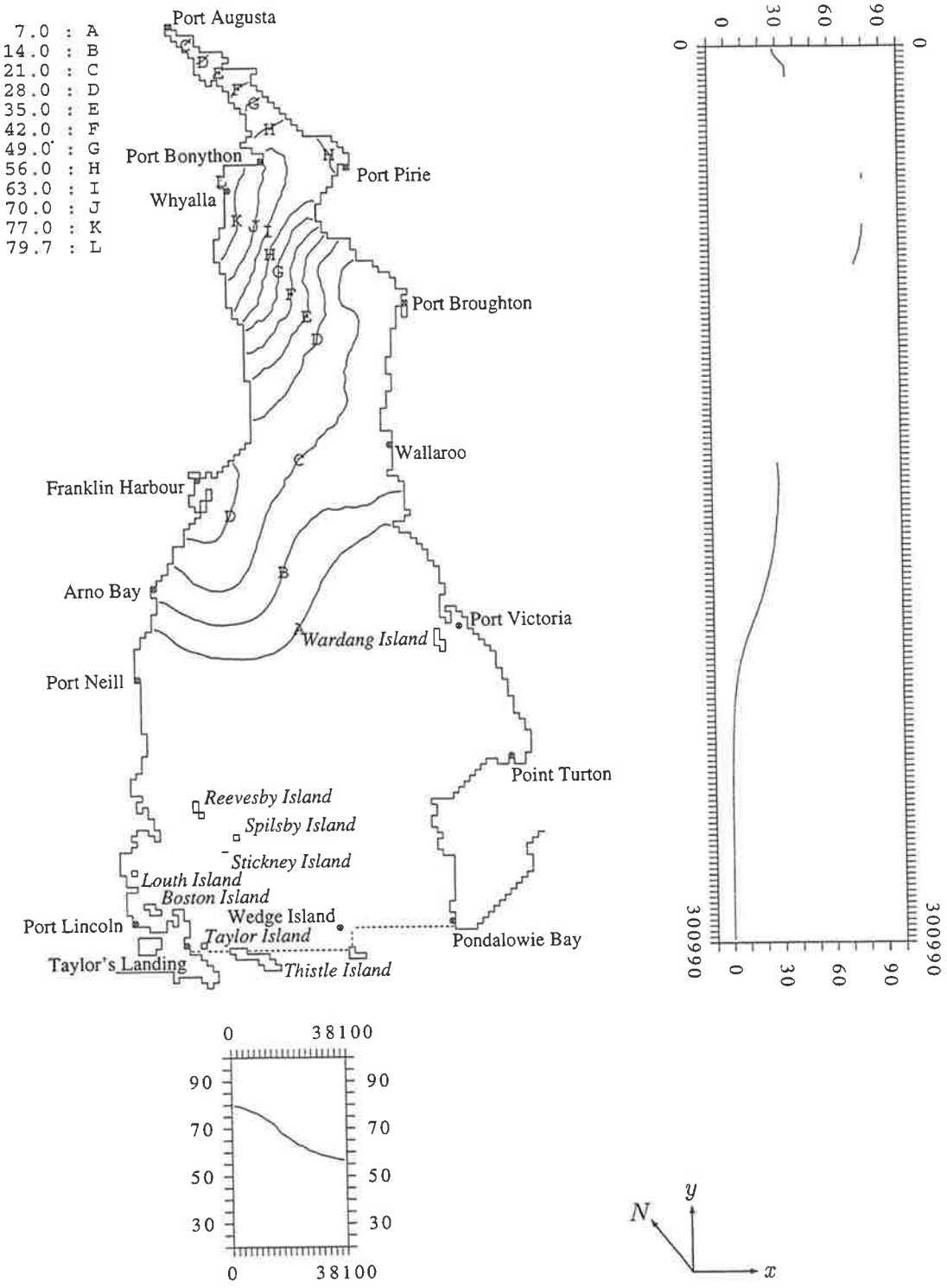

Figure 10.13: The 1988 initial condition simulation larval concentration (10^6 m^{-2}) level curves (top left), and y- (top right) and x- (bottom left) transects through L (north of Whyalla). The tidal currents used in the simulation of the 29 d from 21:30 1 February 1988 were calculated with wind–stress. Tidal stations (crossed circles), islands (italics), and closed (solid lines) and open (dashed lines) boundaries are also shown.

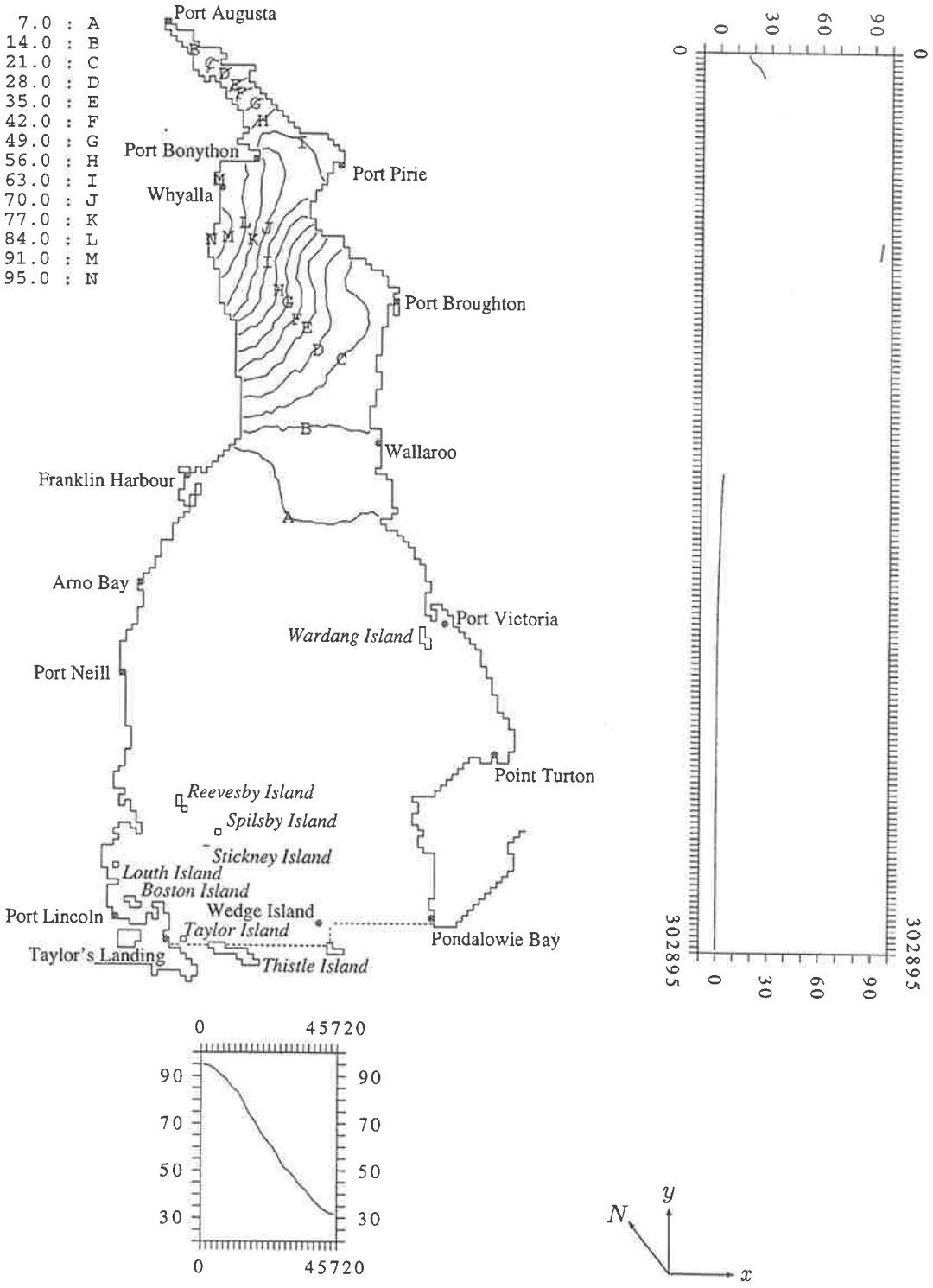

Figure 10.14: The 1991 initial condition simulation larval concentration ($10^6\,\mathrm{m}^{-2}$) level curves (top left), and y- (top right) and x- (bottom left) transects through N (southwest of Whyalla). The tidal currents used in the simulation of the 29 d from 21:30 1 February 1988 were calculated with wind–stress. Tidal stations (crossed circles), islands (italics), and closed (solid lines) and open (dashed lines) boundaries are also shown.

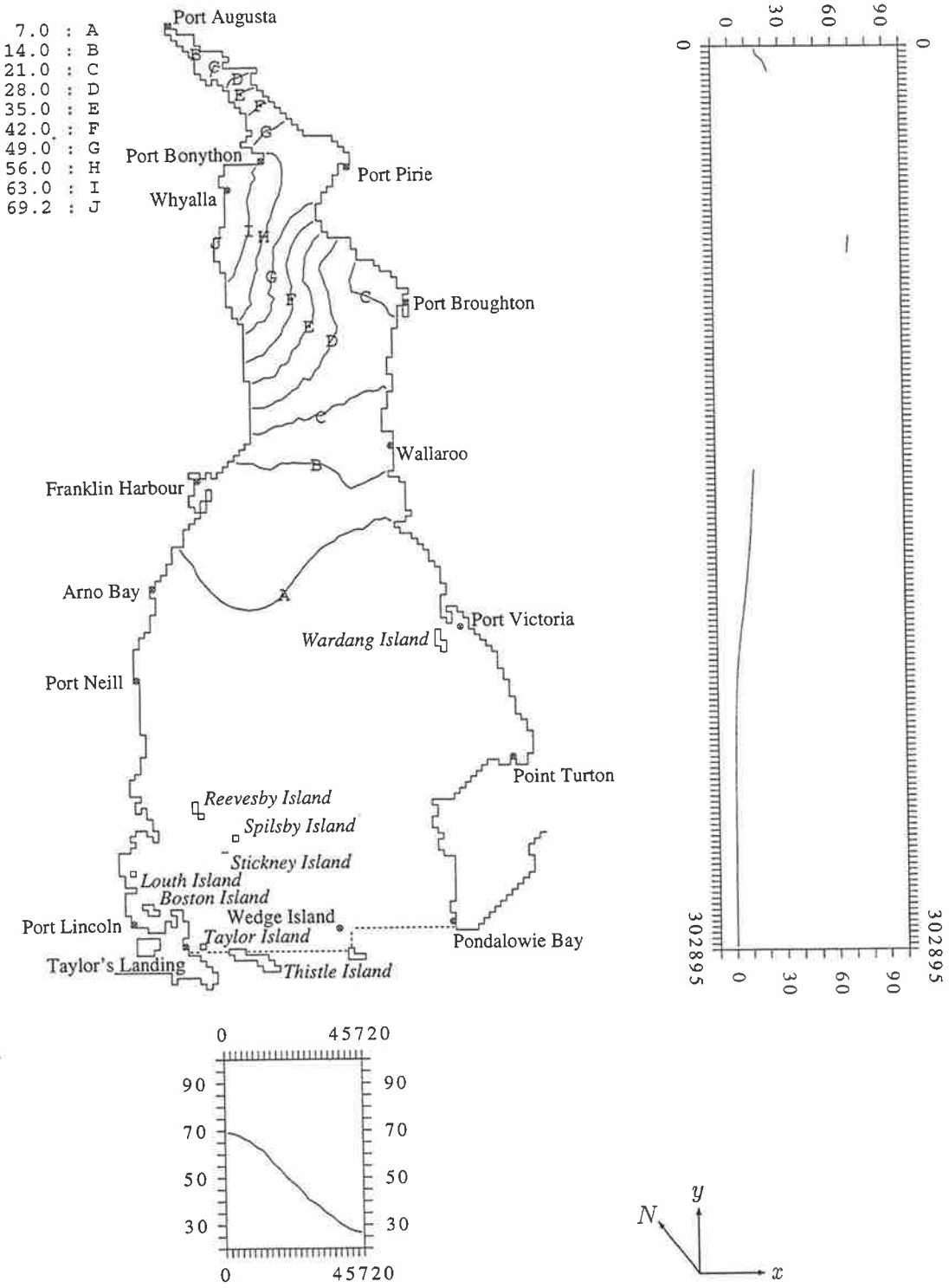

Figure 10.15: The 1992 initial condition simulation larval concentration ($10^6\,\mathrm{m}^{-2}$) level curves (top left), and y- (top right) and x- (bottom left) transects through J (southwest of Whyalla). The tidal currents used in the simulation of the 29 d from 21:30 1 February 1988 were calculated with wind–stress. Tidal stations (crossed circles), islands (italics), and closed (solid lines) and open (dashed lines) boundaries are also shown.

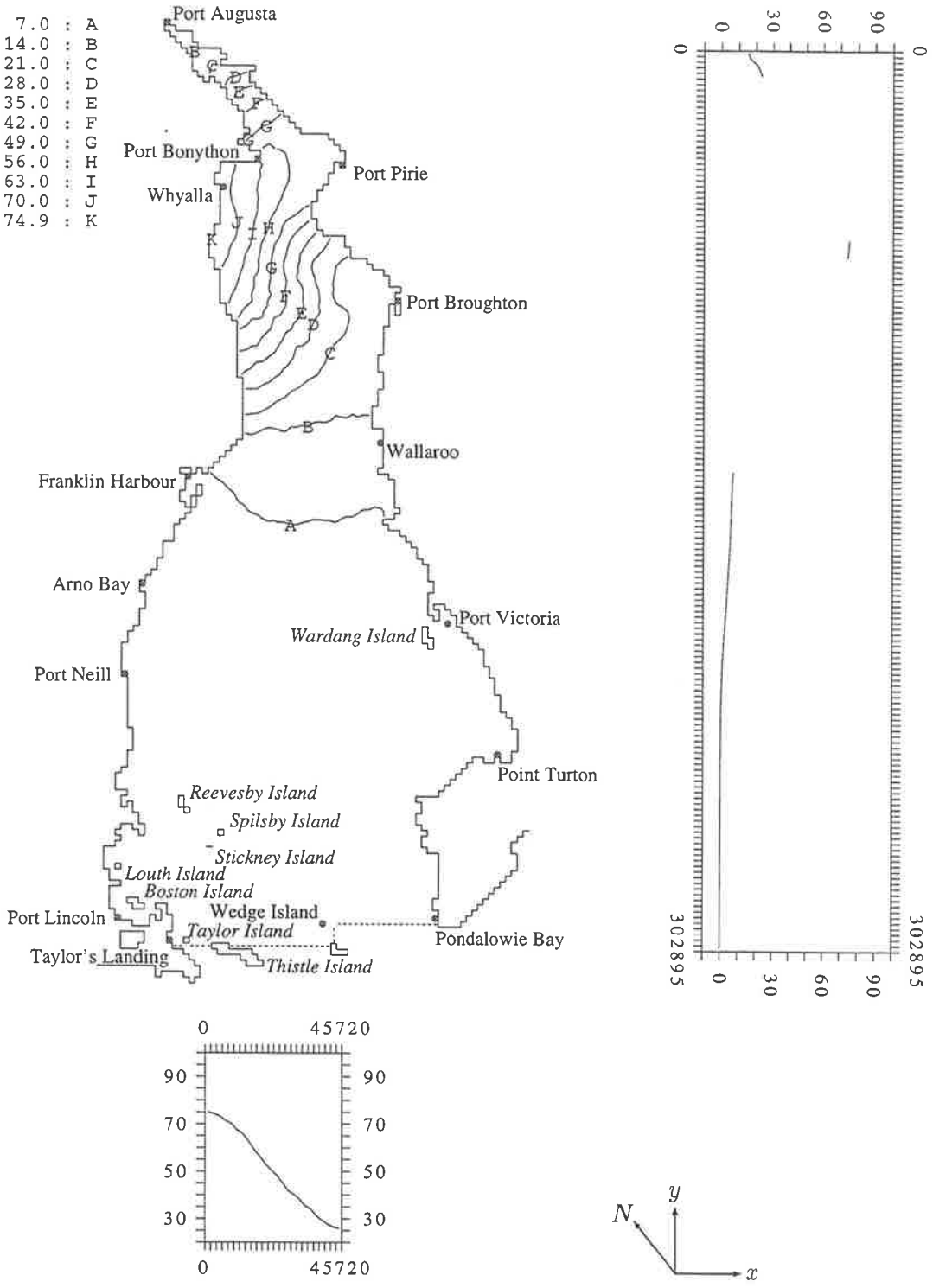

Figure 10.16: The 1993 initial condition simulation larval concentration ($10^6\,\mathrm{m}^{-2}$) level curves (top left), and y- (top right) and x- (bottom left) transects through K (southwest of Whyalla). The tidal currents used in the simulation of the 29 d from 21:30 1 February 1988 were calculated with wind–stress. Tidal stations (crossed circles), islands (italics), and closed (solid lines) and open (dashed lines) boundaries are also shown.

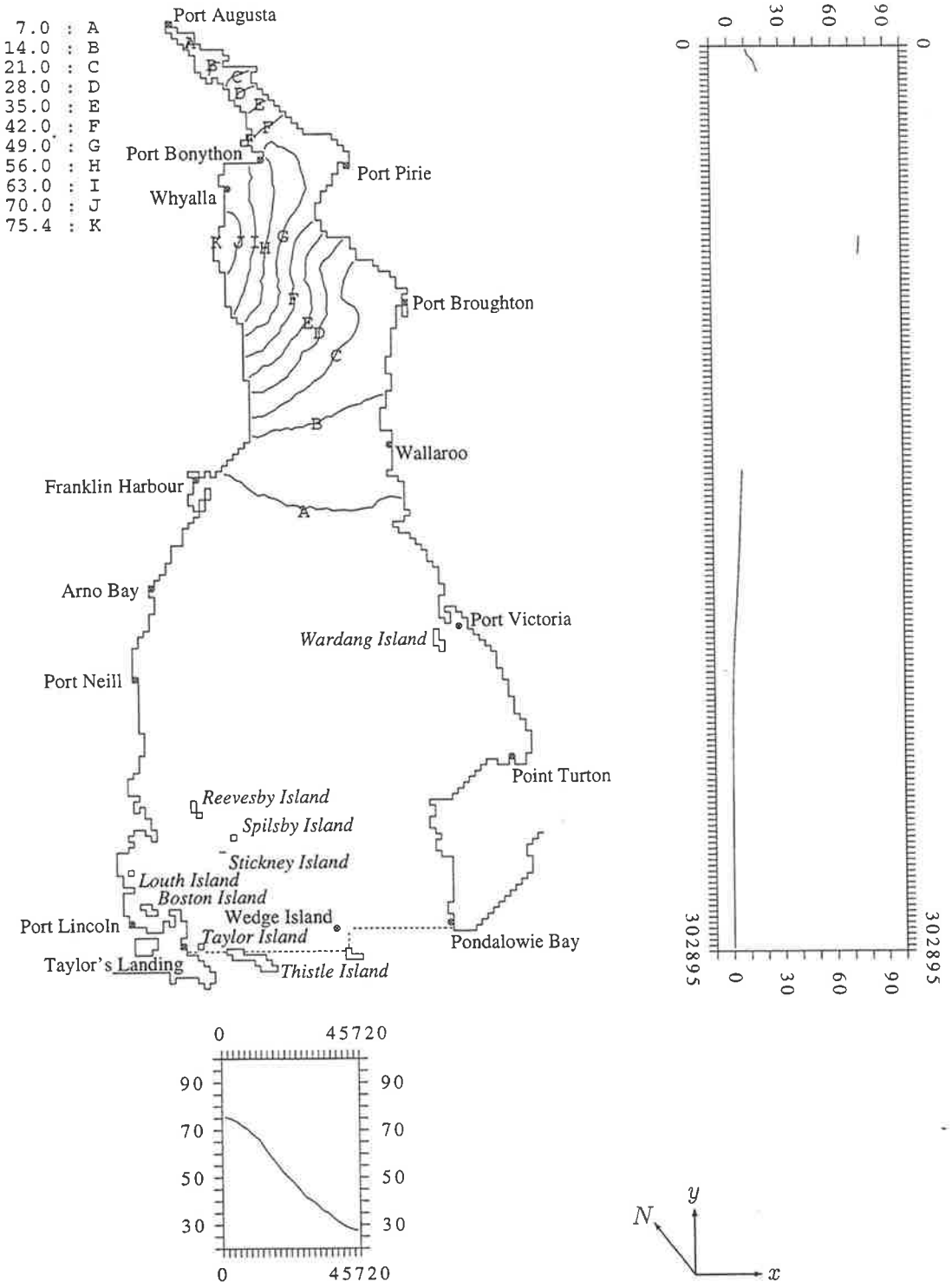

Figure 10.17: The 1994 initial condition simulation larval concentration ($10^6\,\mathrm{m}^{-2}$) level curves (top left), and y- (top right) and x- (bottom left) transects through K (southwest of Whyalla). The tidal currents used in the simulation of the 29 d from 21:30 1 February 1988 were calculated with wind–stress. Tidal stations (crossed circles), islands (italics), and closed (solid lines) and open (dashed lines) boundaries are also shown.

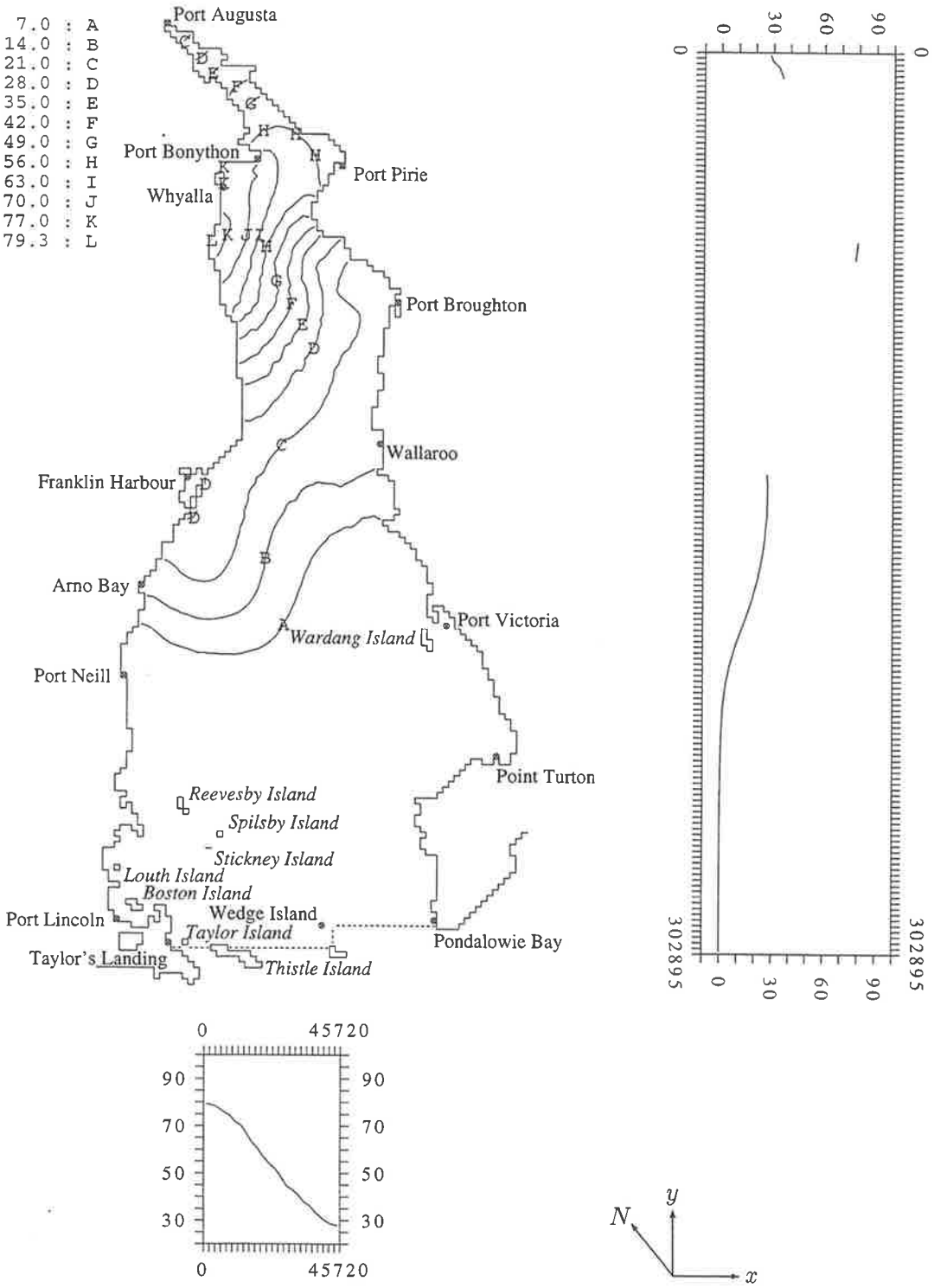

Figure 10.18: The "average" initial condition simulation larval concentration ($10^6\,\mathrm{m}^{-2}$) level curves (top left), and y- (top right) and x- (bottom left) transects through L (southwest of Whyalla). The tidal currents used in the simulation of the 29 d from 21:30 1 February 1988 were calculated with wind–stress. Tidal stations (crossed circles), islands (italics), and closed (solid lines) and open (dashed lines) boundaries are also shown.

Initial Condition Test Statistics Over All Time–Steps			
Initial Condition	$\text{Max}\{+\tau\}$ (10^6 m^{-2})	$\text{Tot}\{+\tau\}$ (10^6 m^{-2})	$-\text{Tot}\{-\tau\}$ (-10^6 m^{-2})
1988	5.14×10^2	1.85×10^8	4.42×10^1
1991	8.10×10^2	1.55×10^8	3.98×10^1
1992	4.16×10^2	1.48×10^8	4.84×10^1
1993	5.53×10^2	1.36×10^8	6.08×10^1
1994	4.27×10^2	1.31×10^8	2.13×10^1
"average"	4.19×10^2	1.82×10^8	5.01×10^1

Table 10.6: The initial condition simulation statistics over all time–steps. The tidal currents used in the simulation of the 29 d from 21:30 1 February 1988 were calculated with wind–stress.

over all simulation time–steps excluding the initial condition. In Table 10.5 the Latitude (°S) and Longitude (°E) of the fine resolution model grid coordinates corresponding to the position of maximum concentration are also listed.

For place name locations in the following discussions, please refer to Figures 1.2 and 6.1. The figures and tables indicate that the 1991–1994 and "average" initial condition simulations resulted in postlarval local maxima located in a bay (Cowleds Landing) of the north-western Spencer Gulf coast, directly below Whyalla. The results are characterised by contour groupings and x-transects which indicate a reasonably sudden concentration decline, from the various local maxima values to the reasonably similar local minima values, south-eastwards across the upper Gulf to the right hand coastline.

The exception to this trend is the 1988 initial condition simulation, for which the maximum is located in another bay (False Bay) of the north-western Spencer Gulf coast, between Whyalla and Port Bonython. This postlarval distribution is characterised by contour groupings and an x-transect which indicate a relatively leisurely concentration decline from the local maximum value to the relatively greater—with respect to all other simulations—local minimum value. This comparatively northern concentration of the 1988 simulation results with respect to all other simulations can be explained in terms of the qualitative differences between the initial conditions concerned. Figure 2.10 indicates that the 1988 initial condition has a similar northern concentration, chiefly due to the inclusion of SARDI data from spawning Region 1 (see Figure 2.1) in the derivation (see Section 2.1.3), but also due to a comparatively greater concentration in the other northern spawning grounds represented by Regions 2–7 (see Figure 2.1). The "average" initial condition, as a result of the averaging process, consists of the same contribution from the former region, but reduced contributions from the latter regions, which may account for the results from the corresponding simulation not having characteristics similar to the 1988 simulation.

The generally northern trend in the final postlarval concentrations from all simulations is a result of the similar trend in the initial larval concentrations, combined with the mixing in the upper Gulf resulting from residual currents, as discussed in Sections 7.4.4 and 10.2.1. The residual current streams across the Gulf from Port Broughton towards Whyalla, near both the sea–surface (Figure 7.10(a)) and the sea–bed (Figure 7.10(b)), tend to transport the larvae from the northern-Gulf spawning grounds into that area. Specific to the 1988 simulation, it is hypothesised that the residual current eddy system bisected by Point Lowly near Port Bonython—as also discussed in Sections 7.4.4 and 10.2.1—would tend to result in persistence of the larval concentration resulting from the spawning of Region 1 (by the upper anticlockwise rotating eddy) and that from the comparatively greater—with respect to all other initial conditions—contributions from the spawnings of Regions 2, 3, and 5 (by the lower clockwise rotating eddy).

The final and overall Max$\{+\tau\}$ measures in both tables indicate that the 1991 initial condition simulation produced a greater maximum concentration compared to all other simulations. The greater height of the transects in Figure 10.14 compared to those in Figures 10.13 and 10.15–10.18 illustrate this point. This result correlates with the fact that this initial condition, as depicted in Figure 2.11, consists of a significantly large peak localised directly within the Port Broughton/Whyalla residual current streams.

The final and overall Tot$\{+\tau\}$ measures in both tables show that the 1988 initial condition simulation consistently resulted in greater numbers of predicted larvae. The greater area beneath the transects in Figure 10.13 compared to those in Figures 10.14–10.18 illustrate this point. As discussed above, since the corresponding initial condition consists of overall greater larval numbers, particularly in the northern regions where it is evident that larvae are concentrated by the residual currents, it stands to reason that the 1988 simulation produces this result.

Other qualitative differences between the results from the simulations using each initial condition can also be related to the qualitative differences between the initial conditions themselves. Generally, the presence or absence of data from individual spawning trawl *regions*, or collections of these as spawning *grounds*, determines the major characteristics of the results obtained. In the results using the 1988 and "average" initial conditions, the presence of Regions 10–12 and 9 and 13 (see Figure 2.2) in the SARDI egg production data representing the Cowell and Gutter spawning grounds, respectively, results in postlarval distributions that feature an associated concentration peak. This is evidenced in Figures 10.13 and 10.18 by the "tongue" features protruding from Franklin Harbour southwards towards the Gulf interior, with a related low intensity local maximum in the corresponding y-transects. No such features are seen in the 1991 results (Figure 10.14)—the initial condition for which neither the Cowell nor the Gutter spawning grounds are represented, nor in those for the 1993 and 1994 results (Figures 10.16 and 10.17)—the initial conditions for which the Cowell spawning ground is not represented. The Cowell and Gutter spawning ground larvae initially located in the vicinity of the residual surface current stagnation point off Arno Bay, with the combination of residual bed currents southwards from that point and residual surface currents back northwards up the western coast, is the surmised mechanism for the persistence of this feature.

The results from the 1992 simulation show a comparatively slight contour "protrusion" and y-transect local maximum, despite the absence of data from the Cowell spawning ground in the initial condition. The comparatively greater—with respect to all other initial conditions—numbers of Wallaroo and Gutter spawning grounds larvae, combined with the residual currents from Wallaroo at the surface and at the bed towards the aforementioned stagnation point—as evident in Figures 7.10(a) and 7.10(b), respectively—allow a similar, but less intense, mechanism to be postulated.

Considerations of this nature are what lead to the realisation that a derivation of an "average" initial condition—determined from the data available, and nominally used to represent a "typical" spawning season—was required to be carried out. From the plots of Figures 2.15 and 10.18 and the entries of Tables 10.5–10.6, as well as the related discussions, it could be argued that the requirement was justified by the results obtained.

For all $-\text{Tot}\{-\tau\}$ measures, the simulations produced few non-physical negative results. This point is not immediately obvious in the figures—with the chosen transect axis scales—as these discarded spurious negative concentrations correspond to at most 4.5×10^{-5} % of the respective totals.

The effect of the concentration "intrusions", extending towards the 1988 peak, and beside the 1991–1994 and "average" peaks, northwards into the head of the Gulf in Figures 10.13 and Figures 10.14–10.17 and 10.18, respectively, is a phenomenon which could be further investigated on detailed comparison with SARDI postlarval settlement data. Since these data were not available, quantitative error measures are not reported here. The two final peak settlement sites in all simulations do, however, correspond qualitatively with known nurseries (Carrick 1994, personal communications) in the Whyalla vicinity. It is also of interest to note that all

initial larval peaks are well diffused after 29 d, in all simulation results.

10.2.3 Conclusions

A complete set of the initial conditions derived in Section 2.1.5 from the spawning data supplied by SARDI, supplemented by the idealised "average" initial condition, forms a sufficient range of initial conditions for use in all prawn larvae dispersion simulations reported in this thesis.

The sensitivity of the larval dispersion model to the initial conditions input to it is well evident. It is felt, however, that the specific characteristics of the initial conditions derived from egg production data for individual-year spawning seasons may not adequately represent the initial *Penaeus latisulcatus* larvae distributions in Spencer Gulf. The fact that in many years some spawning regions, and in some years entire spawning grounds, were not sampled suggests that predicted postlarval distributions may be subject to bias introduced through the initial condition specification.

The results of the simulations discussed in this section suggest that the "average" initial condition may be the most appropriate to use when conducting further simulations of larval dispersion in the Gulf, particularly when the effects of varying spawning—determined by the egg production data to hand—on the model results is surmised to be a product of sampling bias and not of individual-year egg production variation itself.

10.3 Postlarval Settlement

Samples of prawn larvae at five stations along each of four transects across the width of Spencer Gulf have been taken by SARDI researchers. The locations of these sample sites are indicated in Figure 10.19, where each is labelled according to the scheme specified in Table 10.7. The corresponding fine grid Spencer Gulf model coordinates for each site, as listed in Table 10.7, define the locations, shown in Figure 10.20, at which prawn larvae dispersion model predictions will be analysed in detail.

It should be noted that there is a small error associated with simply specifying a computed larval concentration at a larval sampling site to be just that value at the nearest computational element in the simulations. Since no sampling data were available with which to compare simulated concentrations, this error can be overlooked and the approximate larval sampling sites can be used as convenient places at which to compare results of various model simulations carried out. These comparisons are thus a means of qualitatively relating the results of numerical simulations to one another, rather than quantifying the differences between simulation results and field measurements.

10.3.1 Postlarval Transect Trends

Figures 10.21 and 10.22 plot the final postlarval concentrations (crossed points) from the mid-December—21:30 15/12/87 to 21:30 13/01/88 (circles)—and January/February—21:30 01/02/88 to 21:30 01/03/88 (squares)—dispersion simulations and indicate trends (solid lines) in the east-west and north-south direction, respectively.

East-West Postlarval Transect Trends

Figures 10.21(a), 10.21(b), 10.21(c), and 10.21(d) plot trends for the SARDI Transects 1, 2, 3, and 4, respectively, by linearly interpolating concentrations (10^6/nautical mile) at each computational element corresponding to the SARDI Stations 1–5 locations (Longitude, °E). Mean trends over transect groups are plotted in Figures 10.21(e) (Transects 1 and 2, representing the northern-Gulf mean), 10.21(f) (Transects 2 and 3, representing the mid-Gulf mean), 10.21(g) (Transects 3 and 4, representing the southern–Gulf mean), and 10.21(h) (Transects 1–4, representing the overall Gulf mean). The trends for both peak spawning simulations are similar in overall form, with some specific differences.

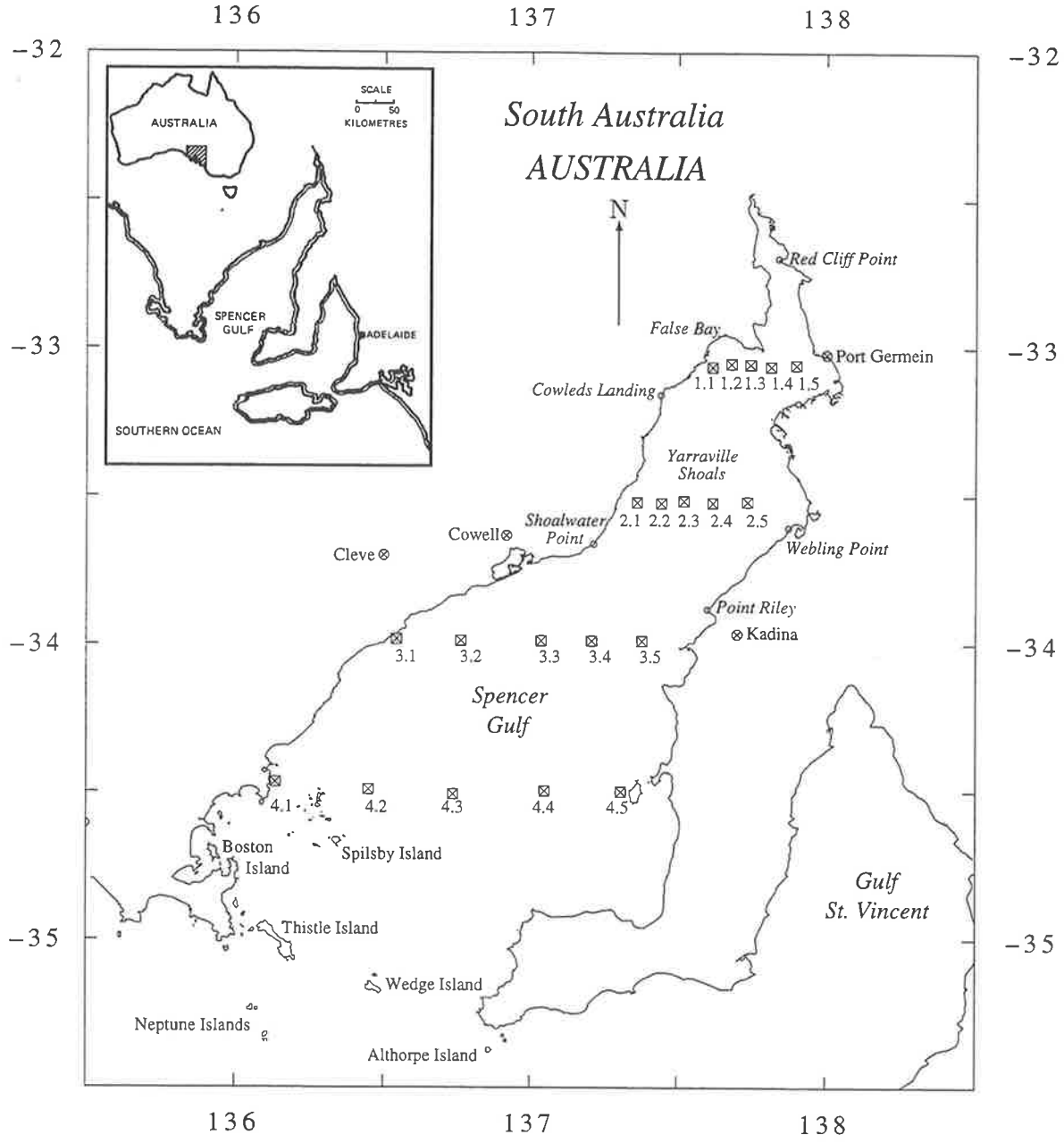

Figure 10.19: Prawn larvae observation stations (crossed squares) in Spencer Gulf. Important geographical features (italics) and places of interest (roman) are also shown. The x and y axes indicate longitude (°E) and latitude (°N), respectively.

The mid-December peak spawning simulation resulted in a final larval maximum which is larger and further north than for the January/February simulation. Inspection of the upper-northern trend of Figure 10.21(a) indicates this point much more effectively than the x-transects of Figures 10.23 and 10.24, respectively, as alluded to in Section 10.4.1.

In northern Spencer Gulf, the initial maximum concentration was, in general, less dispersed towards the south-westerly direction for the mid-December peak spawning simulation than for the January/February simulation. This can be seen from the lower-northern trend of Transect 2 (Figure 10.21(b)) and the mean northern combined trend of Transects 1 and 2 (Figure 10.21(e)).

In the mid-Gulf, it can be seen that the initial larval concentration is dispersed more in the southern direction by the currents of the January/February peak spawning dispersion period

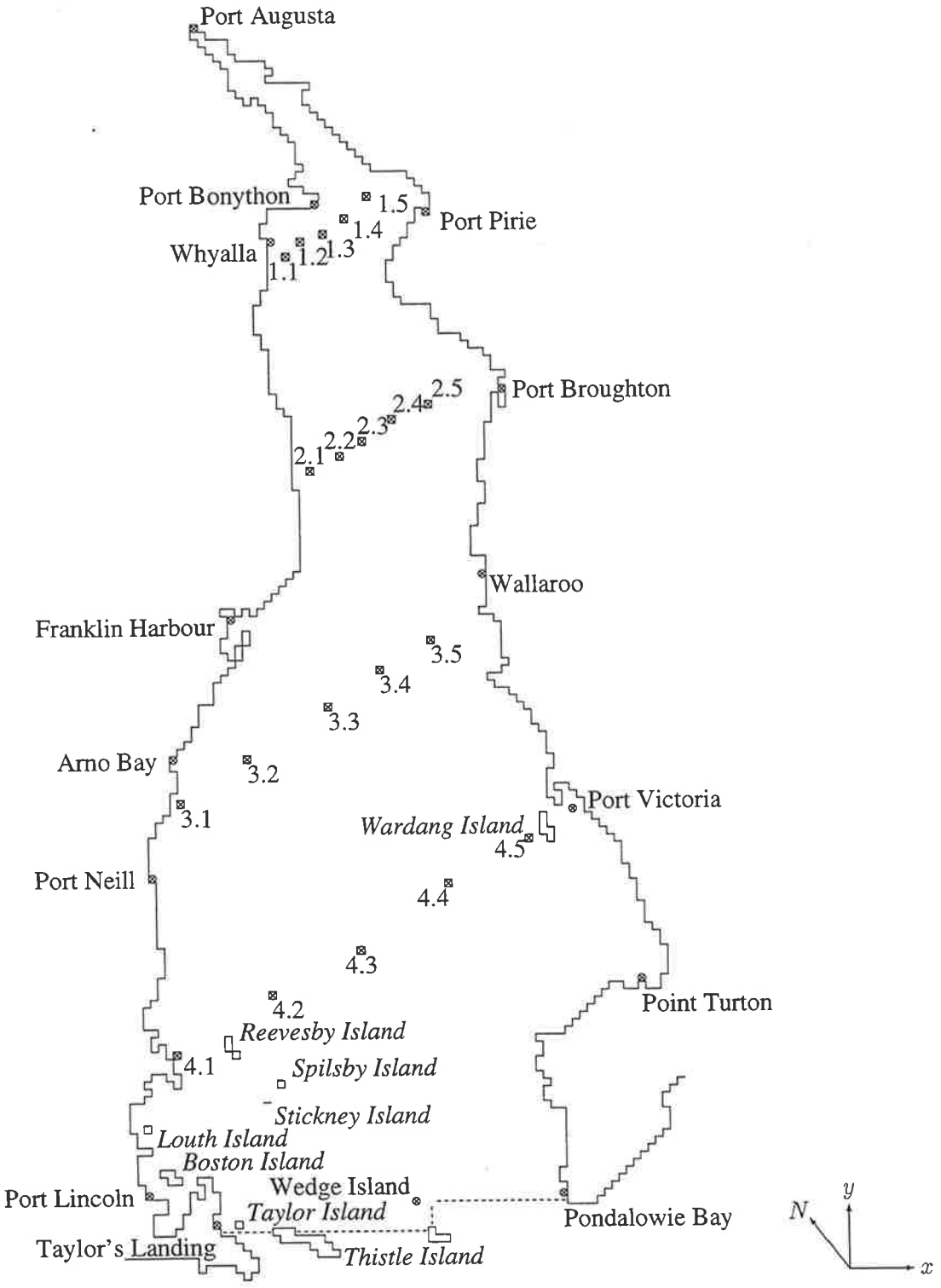

Figure 10.20: The fine grid Spencer Gulf model, indicating the model location of the coastal (solid line) and open boundaries (dashed line), and of the prawn larvae (crossed squares) and tide–height (crossed circles) observation stations. Prawn larvae stations (numbers) are labelled, and tide–height stations (roman) and islands (italics) are named.

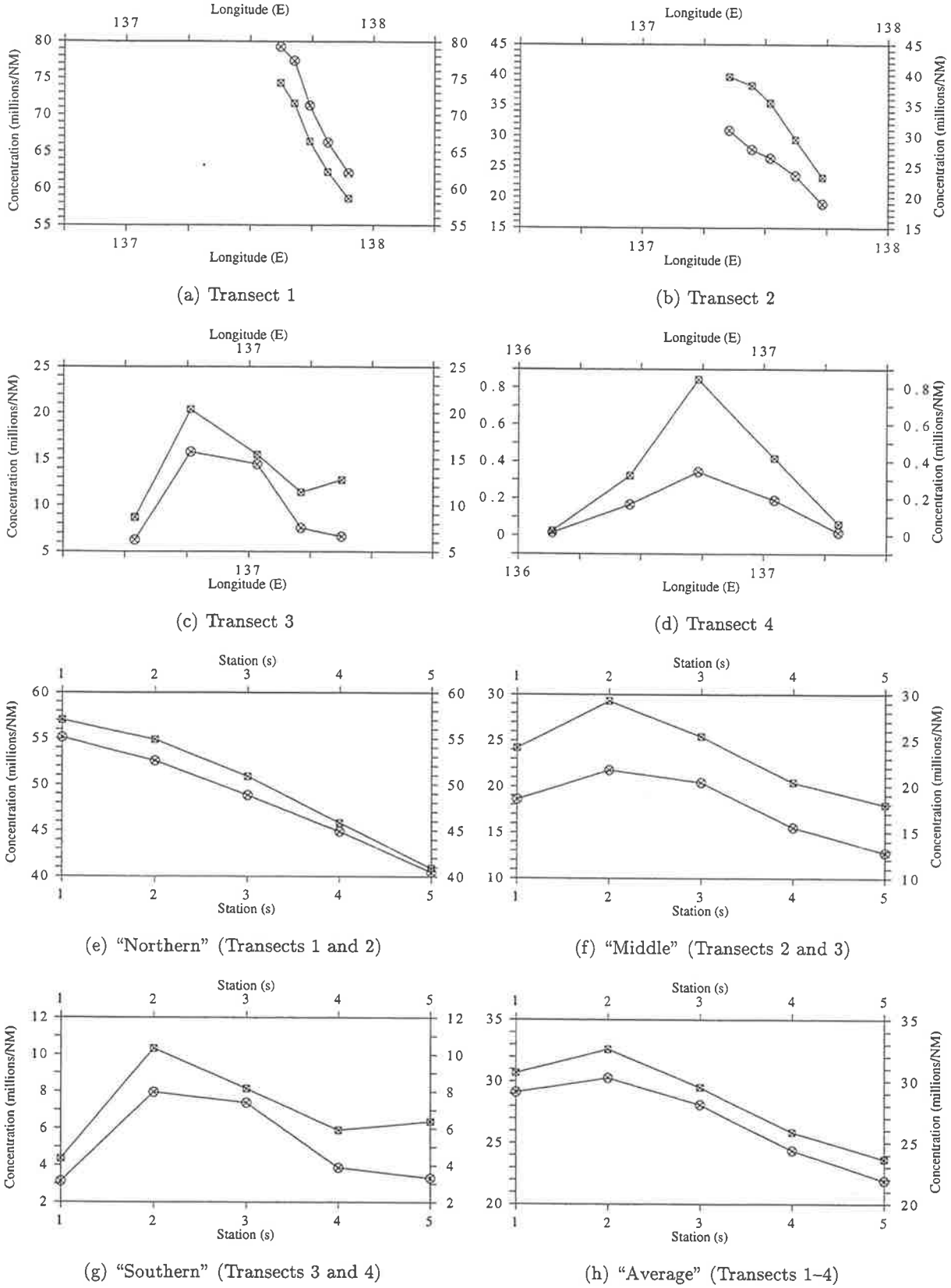

(a) Transect 1

(b) Transect 2

(c) Transect 3

(d) Transect 4

(e) "Northern" (Transects 1 and 2)

(f) "Middle" (Transects 2 and 3)

(g) "Southern" (Transects 3 and 4)

(h) "Average" (Transects 1–4)

Figure 10.21: The east-west trends and trend means for postlarval concentrations (10^6/nautical mile) at SARDI larval sampling locations (Longitude, °E; Station, s) for the mid-December 1987 (circles) and January/February 1988 (squares) larval dispersion periods.

Spencer Gulf Prawn Larvae Sampling Sites						
Larval Sampling Site			Map Coordinates		Model Location	
Transect (t)	Station (s)	Label (t.s)	Latitude (°S)	Longitude (°E)	Row (i)	Column (j)
1	1	1.1	33°03.88′	137°36.99′	33	24
	2	1.2	33°03.28′	137°40.82′	31	26
	3	1.3	33°03.42′	137°44.65′	30	29
	4	1.4	33°03.84′	137°48.72′	28	32
	5	1.5	33°03.53′	137°53.83′	25	35
2	1	2.1	33°31.32′	137°21.63′	62	27
	2	2.2	33°31.46′	137°26.65′	60	31
	3	2.3	33°31.03′	137°31.25′	58	34
	4	2.4	33°31.44′	137°37.12′	55	38
	5	2.5	33°31.22′	137°44.11′	53	43
3	1	3.1	33°58.98′	137°32.59′	107	9
	2	3.2	33°59.28′	137°45.82′	101	18
	3	3.3	33°59.30′	137°02.19′	94	29
	4	3.4	33°59.34′	137°12.50′	89	36
	5	3.5	33°59.37′	137°22.66′	85	43
4	1	4.1	34°28.00′	137°08.02′	141	8
	2	4.2	34°29.45′	137°27.01′	133	21
	3	4.3	34°30.42′	137°44.27′	127	33
	4	4.4	34°29.76′	137°02.92′	118	45
	5	4.5	34°29.94′	137°18.43′	112	56

Table 10.7: Map Coordinates (Latitude, °S and Longitude, °E) and Model Location (i and j), for the 20 prawn larvae sampling sites of the fine grid Spencer Gulf model. Map coordinates are provided by the South Australian Research and Development Institute. Labels are derived from the associated Transect and Station specifications as supplied. Model locations are determined by the grid coordinate of the nearest elevation grid–point.

compared to those of the mid-December period. This can be appreciated from the upper-southern trend of Transect 3 (Figure 10.21(c)) and the mean mid-Gulf combined trend of Transects 2 and 3 (Figure 10.21(f)). In particular, the concentration protrusions—seen in Figures 10.23 and 10.24 and alluded to in Section 10.4.1—southwards from Arno Bay into the interior (represented by Station 2) and also from the interior off Wallaroo southwards parallel to the coast above Port Victoria (represented by Station 5) are relatively weaker, respectively, in the mid-December than January/February the simulation.

In the southern-Gulf this trend continues, as indicated in the mean southern-Gulf trend of Transects 3 and 4 (Figure 10.21(g)). This is, however, primarily associated with the trend of Transect 3 (Figure 10.21(c)) as the lower-southern trend of Transect 4 (Figure 10.21(d)) makes little contribution. This latter figure does, however, indicate that the generally greater southerly dispersion during the January/February period compared to the mid-December period continues towards the southern Gulf expanses, at least in the Gulf interior.

The overall average mean trend of Figure 10.21(h) suggests that comparatively more simulated larvae are dispersed towards, but not immediately adjacent to, the western Spencer Gulf coast throughout the entire Gulf, with this feature being slightly more pronounced during the mid-December than the January/February dispersion period.

North-South Postlarval Transect Trends

Figures 10.22(a), 10.22(b), 10.22(c), 10.22(d), and 10.22(e) plot trends for the SARDI Stations 1, 2, 3, 4, and 5, respectively, by linearly interpolating concentrations (10^6/nautical mile) at each computational element corresponding to the SARDI Transects 1–4 locations (Latitude, °S). Mean trends over station groups are plotted in Figures 10.22(f) (Stations 1–5, representing the overall Gulf mean), 10.22(g) (Stations 1 and 2, representing the western-Gulf mean), and 10.22(h) (Stations 4 and 5, representing the eastern-Gulf mean).

The figures, all with the same vertical axis scales, show that the north-south trends are remarkably similar at all five stations. This is also indicated in the three means calculated. The northern trend in postlarval concentrations is well apparent, with Transect 1 recording the largest concentrations declining to near-zero concentrations along Transect 4.

In all cases, the mid-December simulation resulted in greater postlarval concentrations along Transect 1, lesser concentrations along Transects 2 and 3, and near-equal concentrations along Transect 4, when compared to the January/February simulation. The near-zero concentrations along Transect 4 indicate that recordings at these stations may not represent efficient allocation of SARDI field data collection resources.

10.3.2 Conclusions

All simulations resulted in very low concentrations along Transect 4 compared to those at all other transects. Simulations thus indicate that recordings at Stations along Transect 4 may not represent efficient allocation of SARDI field data collection resources. This fact illustrates the point that numerical simulations carried out before planning field sampling can be very useful in saving time, effort, and money. Approximate parameter values can be input to numerical models. The predictions output can be used to assist in developing sampling strategies which can lead to better input parameter specification.

10.4 Dispersion Period Sensitivity

In this section, two sets of results from numerical experiments are presented and discussed. Both involve analysis of the relative effects of the different current regimes experienced by the larvae released during the mid-December and January/February spawning events. Simulations were computed of the 29 d following an instantaneous spawning event at 21:30 on 15 December 1987 and 1 February 1988, respectively. All other parameters used in the simulations discussed in this section are as described in Section 10.2.

In the first analysis of results, the differences and similarities of only the final results of the simulations for the two peak spawnings are discussed. This discussion will relate the final larval distributions to the prevailing and residual tidal currents associated with the two time periods involved. In the second analysis of results, the differences and similarities of the results are discussed in terms of the temporal aspects of larval distributions from the moment of release to the end of the simulation. This discussion will also take into account the possibility of a variable dispersion period for the larvae.

10.4.1 Fixed Dispersion Periods

Larval concentrations and transects resulting from dispersion simulations of the 29 d following an instantaneous spawning event at 21:30 corresponding to the mid-December (i.e. 15/12/87–13/01/88) and the January/February (i.e. 01/02/88–01/03/88) peak spawnings are shown in Figures 10.23 and 10.24, respectively. Each simulation commenced with the "average" initial condition derived in Section 2.1.4, but had currents specified as those computed by the tidal model for the appropriate time period. Tables 10.8 and 10.9 lists statistics—as defined in Section 10.2.2—for the final simulation time–step and over all simulation time–steps, respectively, excluding the initial condition.

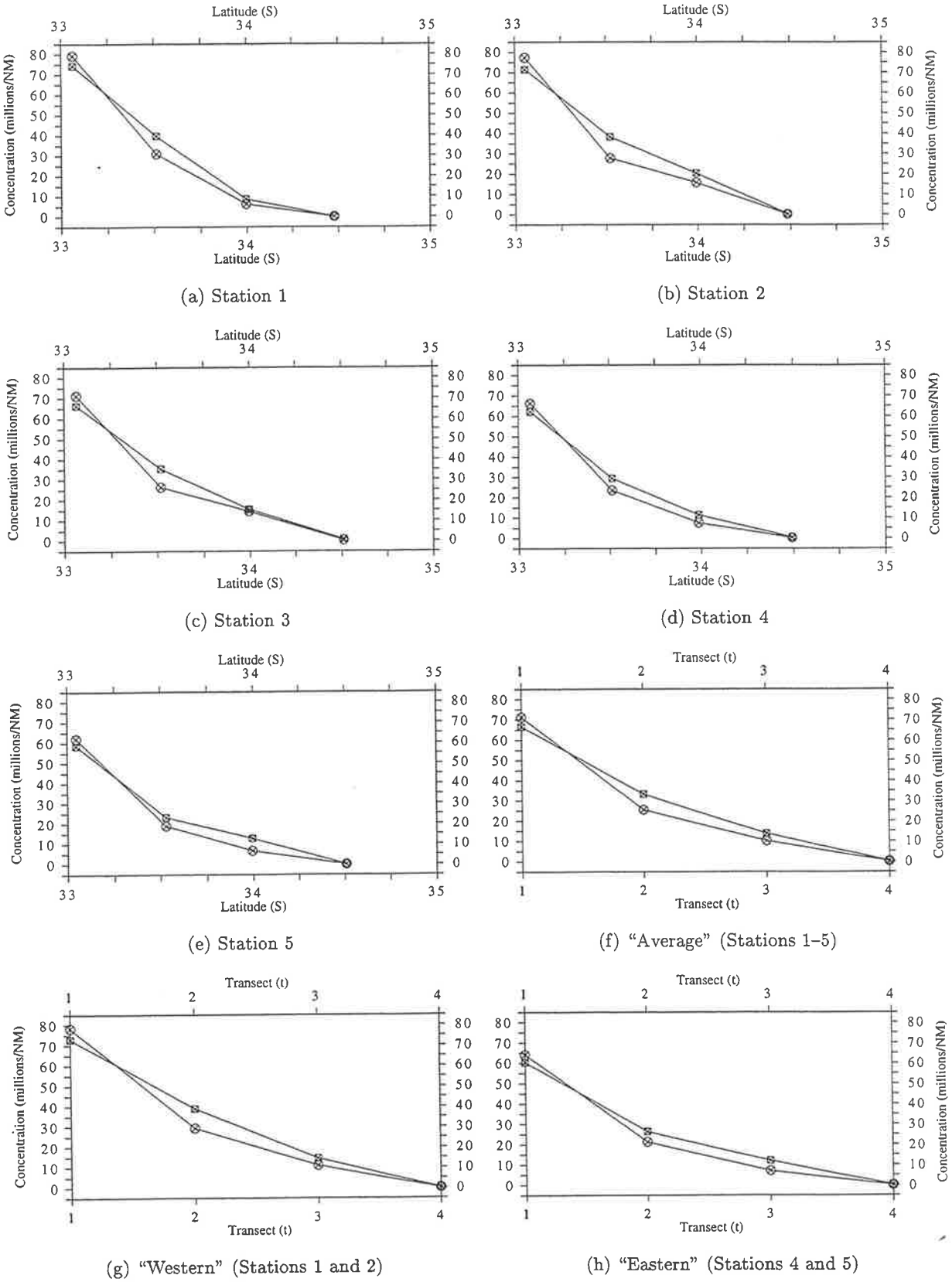

(a) Station 1

(b) Station 2

(c) Station 3

(d) Station 4

(e) Station 5

(f) "Average" (Stations 1–5)

(g) "Western" (Stations 1 and 2)

(h) "Eastern" (Stations 4 and 5)

Figure 10.22: The north-south trends and trend means for postlarval concentrations (10^6/nautical mile) at SARDI larval sampling locations (Latitude, °S; Transect, t) for the mid-December 1987 (circles) and January/February 1988 (squares) larval dispersion periods.

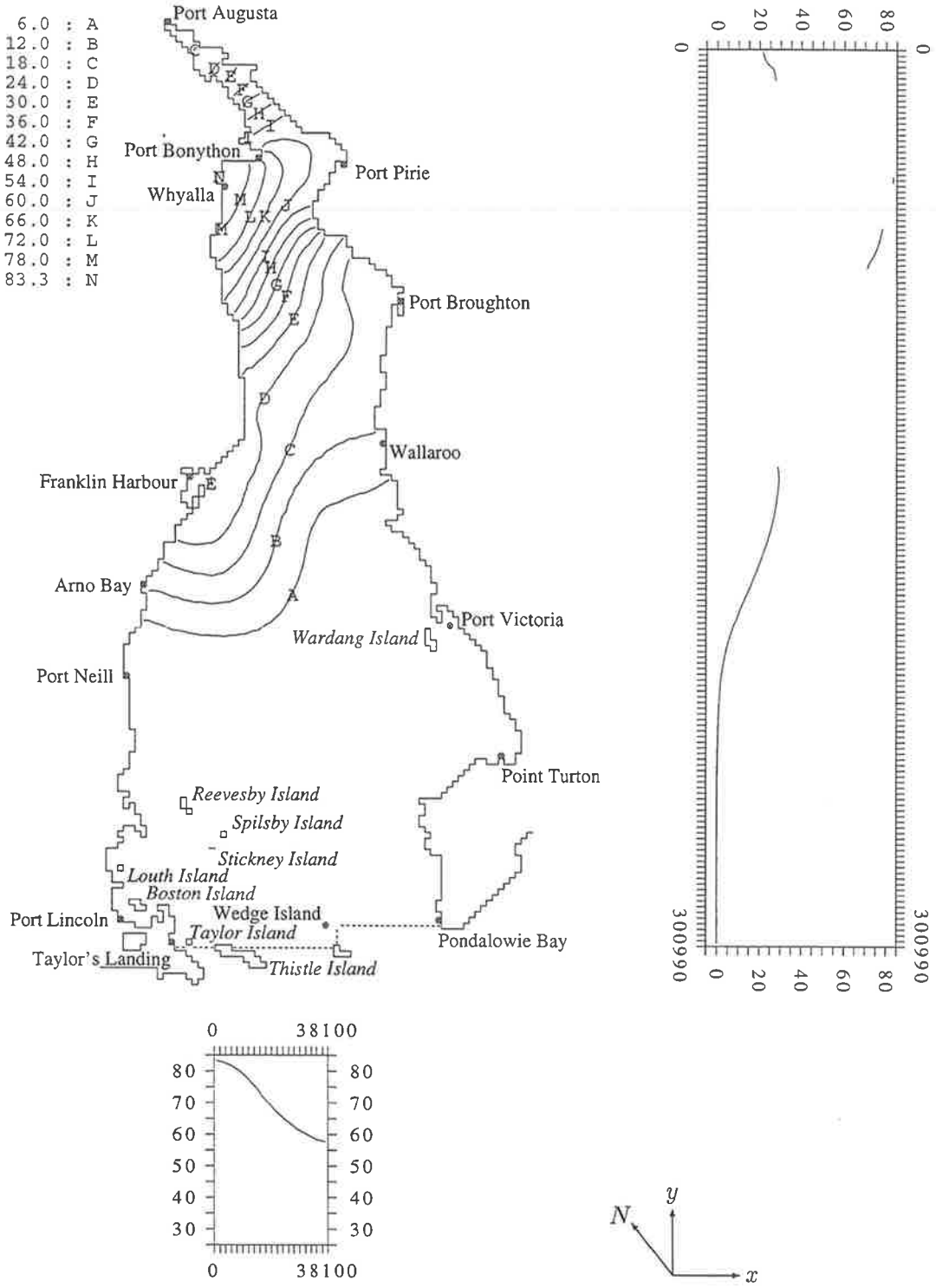

Figure 10.23: The 21:30 15/12/87–21:30 13/01/88 dispersion period simulation larval concentration (10^6 m^{-2}) level curves (top left), and y- (top right) and x- (bottom left) transects through N (north of Whyalla). The "average" initial condition was used. Tidal currents calculated with wind–stress were used. Tidal stations (crossed circles), islands (italics), and closed (solid lines) and open (dashed lines) boundaries are also shown.

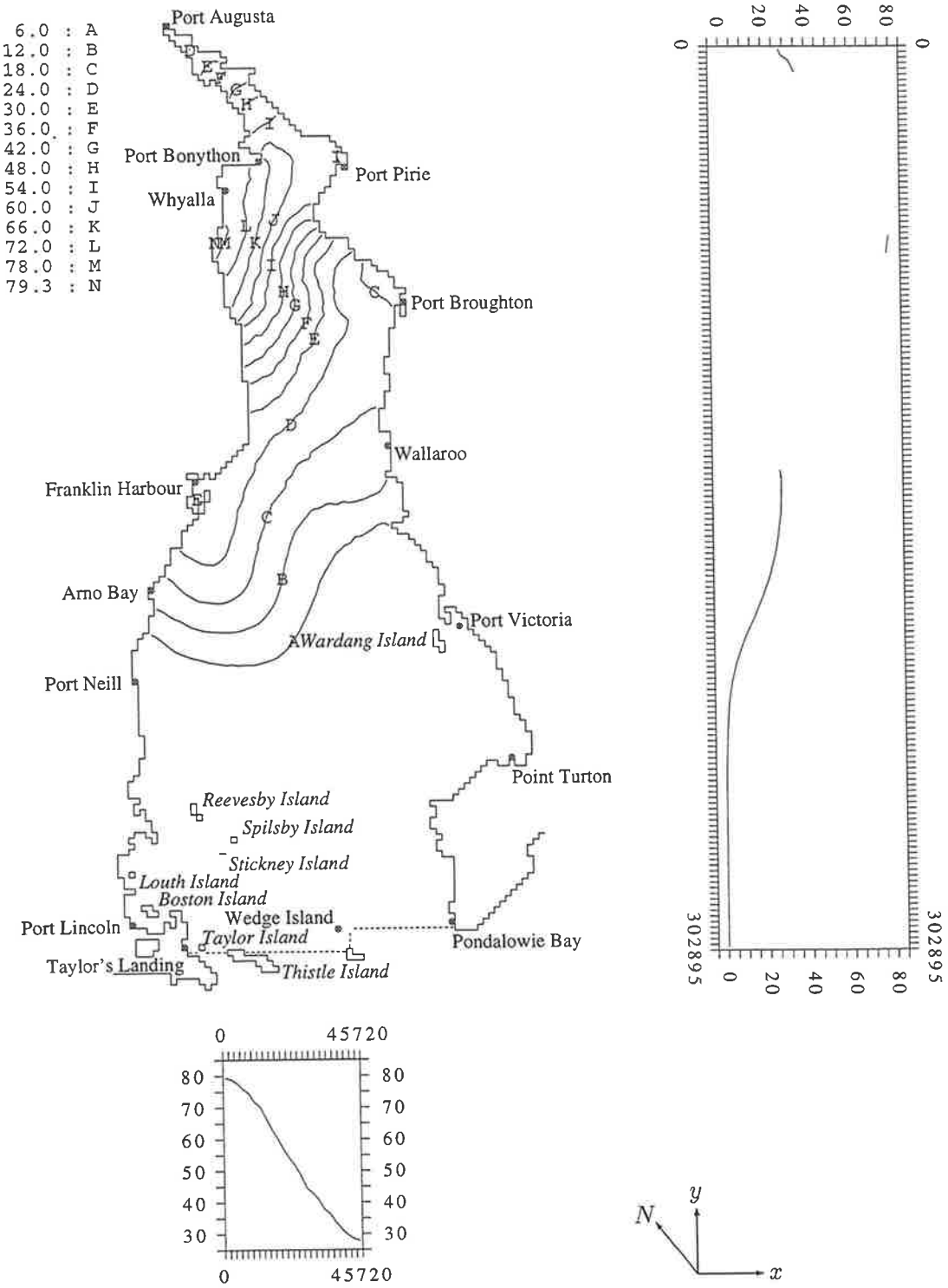

Figure 10.24: The 21:30 01/02/88–21:30 01/03/88 dispersion period simulation larval concentration (10^6 m^{-2}) level curves (top left), and y- (top right) and x- (bottom left) transects through N (south-west of Whyalla). The "average" initial condition was used. Tidal currents calculated with wind–stress were used. Tidal stations (crossed circles), islands (italics), and closed (solid lines) and open (dashed lines) boundaries are also shown.

The Dispersion Period Simulation Statistics for the Final Time–Step					
Dispersion Period	$\text{Max}\{+\tau\}$ ($10^6\,\text{m}^{-2}$)	$\text{Tot}\{+\tau\}$ ($10^6\,\text{m}^{-2}$)	$-\text{Tot}\{-\tau\}$ ($-10^6\,\text{m}^{-2}$)	Latitude (°S)	Longitude (°E)
21:30 15/12/87–21:30 13/01/88	8.33×10^1	6.70×10^4	2.20×10^{-6}	32°58.74′	137°36.84′
21:30 01/02/88–21:30 01/03/88	7.94×10^1	7.58×10^4	1.47×10^{-5}	33°07.74′	137°28.56′

Table 10.8: The final dispersion period simulation statistics for the final time–step. The tidal currents used in the two 29 d simulations were calculated with wind–stress.

The Dispersion Period Simulation Statistics Over All Time–Steps			
Dispersion Period	$\text{Max}\{+\tau\}$ ($10^6\,\text{m}^{-2}$)	$\text{Tot}\{+\tau\}$ ($10^6\,\text{m}^{-2}$)	$-\text{Tot}\{-\tau\}$ ($-10^6\,\text{m}^{-2}$)
21:30 15/12/87–21:30 13/01/88	4.16×10^2	1.64×10^8	1.18×10^0
21:30 01/02/88–21:30 01/03/88	4.19×10^2	1.82×10^8	5.01×10^1

Table 10.9: The dispersion period simulation statistics over all time–steps. The tidal currents used in the two 29 d simulations were calculated with wind–stress.

The mid-December peak spawning simulation resulted in a final larval maximum which is larger and further north than for the January/February simulation. Inspection of Tables 10.5 and 10.8 shows that these two locations correspond to the positions of the maxima of the simulations (of the January/February spawning peak) using the 1988 and "average" initial conditions (as discussed Section 10.2.2), respectively. The contours for both peak spawning simulations are similar in overall form, with some specific differences.

In upper Spencer Gulf, the initial maximum concentration was, in general, less diffused in the south-westerly direction for the mid-December peak spawning simulation (starting from a position south of Whyalla, near K in Figure 10.23) than for the January/February simulation (starting from a position south of Whyalla, near J in Figure 10.24). This can be seen from the relative positions of the contours labelled E–H on the left-hand northern coastline of these two figures. The different character of the shape of the concentration peaks, most apparent from the x-transects, is, however, more a product of the difference in positions of the maxima through which they were taken than of the concentrations in the northern Gulf region bounded by these locations.

In the lower Gulf, it can be seen that the initial larval concentration is diffused more in the southern direction by the currents of the January/February peak spawning dispersion period compared to those of the mid-December period. This can be appreciated by observing the relatively greater southerly protrusion of contours A–C in the open southern Gulf as well as in the western-coastal mid-Gulf in Figure 10.24 with respect to that in Figure 10.23.

The $\text{Max}\{+\tau\}$ measures in Table 10.8 confirm that the mid-December peak spawning period simulation produced a comparatively greater maximum concentration. The final and overall $\text{Tot}\{+\tau\}$ measures in both Tables 10.8 and 10.9 both show that the January/February peak spawning period simulation consistently resulted in greater numbers of predicted larvae. The greater height of, and larger area beneath, the transects in Figure 10.23 compared to those in Figure 10.24 do not, however, illustrate these points. As these transects were taken at different locations and also do not represent the *entire* biomass concentration, this apparent paradox is not surprising.

For the final but not the overall $-\text{Tot}\{-\tau\}$ measure, the January/February peak spawning period simulation produced comparatively more non-physical negative results. This point is less obvious in the figures—with the chosen transect axis scales—as these discarded spurious negative concentrations correspond to at most 2.8×10^{-5} % of the respective totals. When com-

pared to the January/February peak spawning period simulation, the mid-December simulation produced a peak of greater height, at a more northerly grid–point. This represents a stronger local concentration maximum at a location both relatively further towards the head of the Gulf, and away from the initial concentration peak location.

Tidal Circulations and Larval Dispersion

Tidal current residuals calculated at the near sea–surface and sea–bed depth–levels are shown in Figures 10.25 and 10.26, respectively, with those for the mid-December period shown in Figures 10.25(a) and 10.26(a) and those for the January/February period shown in Figures 10.25(b) and 10.26(b). The qualitative differences in the lower Gulf between the simulation results of the mid-December and January/February peak spawning periods can be explained in terms of the residuals shown in these figures.

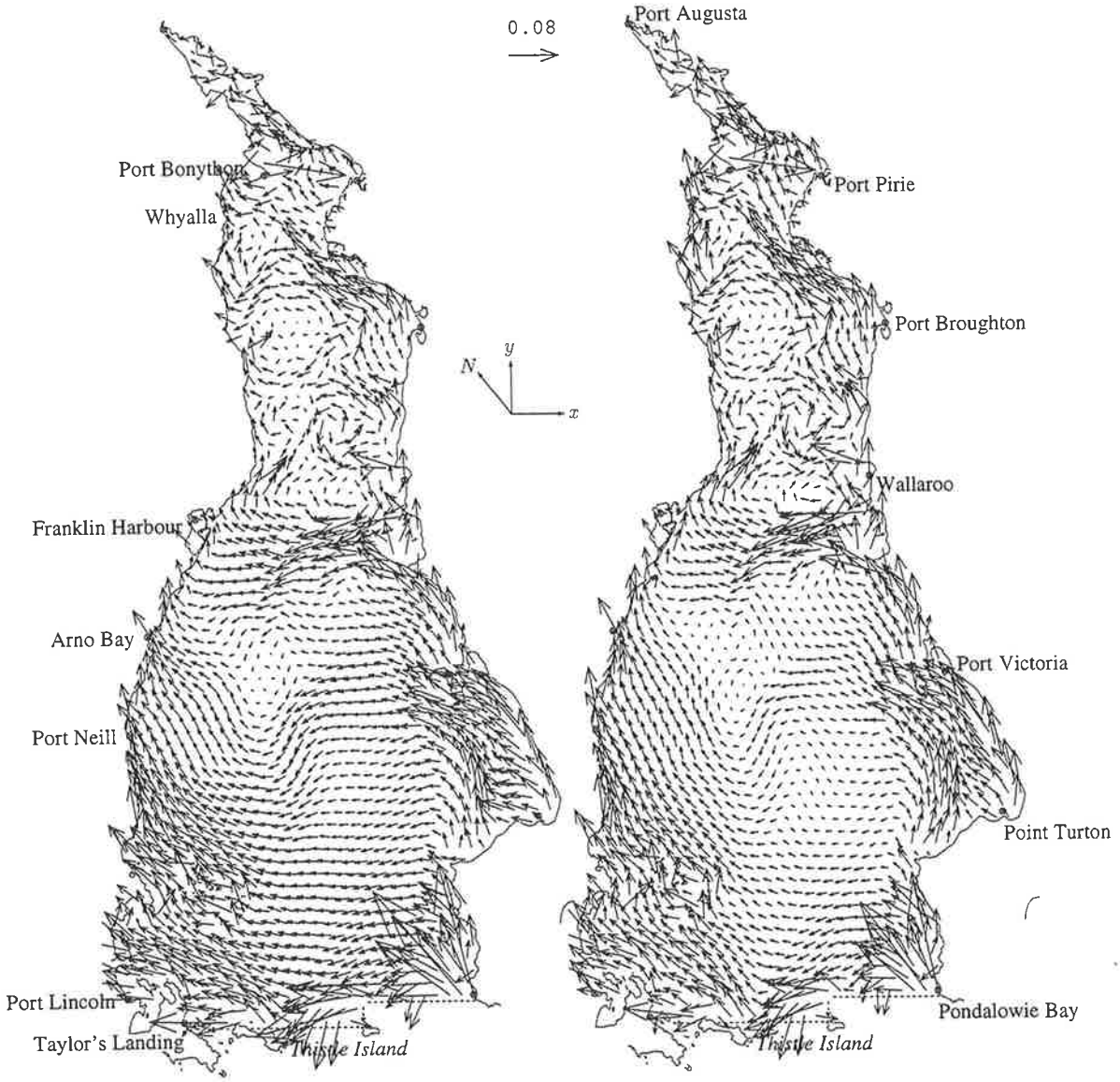

(a) 21:30 15/12/87–21:30 13/01/88 (b) 21:30 01/02/88–21:30 01/03/88

Figure 10.25: Spencer Gulf near sea–surface depth–level current residuals ($\mathrm{m\,s^{-1}}$) for the periods indicated, calculated with wind–stress. Vectors are plotted for every second computational element in both the x and y directions. Tidal stations (roman) and islands (italics) are named.

The lower Gulf sea–surface currents show a residual stream curving clockwise towards Port

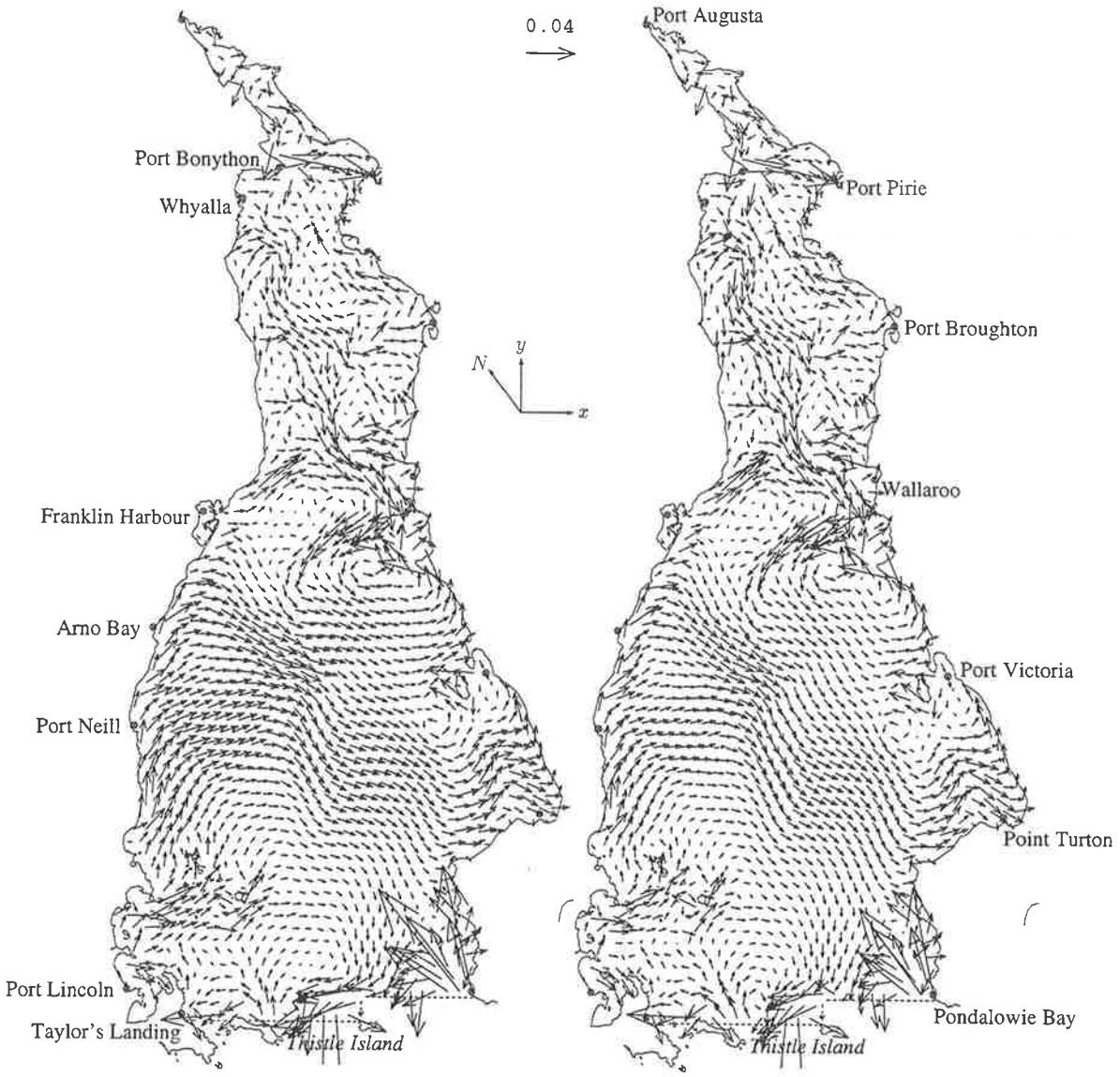

(a) 21:30 15/12/87–21:30 13/01/88

(b) 21:30 01/02/88–21:30 01/03/88

Figure 10.26: Spencer Gulf near sea–bed depth–level current residuals ($\mathrm{m\,s^{-1}}$) for the periods indicated, calculated with wind–stress. Vectors are plotted for every second computational element in both the x and y directions. Tidal stations (roman) and islands (italics) are named.

Neill from the mid-Gulf south-east offshore from this position, which is stronger during the mid-December period than during the January/February period. The existence of an area of relative residual current stagnation off Arno Bay is more noticeable in the January/February period residuals shown in Figure 10.25(b) than in those of the mid-December period shown in Figure 10.25(a). These two features, combined with the residual bed current stream meandering with equal strength southwards from the mid-Gulf south-east off shore of Arno Bay towards Point Turton, are proposed as a mechanism by which the southern Gulf concentration protrusion is more enhanced in the mid-Gulf for the January/February peak spawning simulation than in the mid-December simulation, but is less noticeably so as the left-hand coast is approached.

On the right-hand coast and further towards the head of the Gulf, the residual bed current stream from the mid-Gulf southwards towards Wallaroo and from there curving anticlockwise in a tidal eddy centred off a point south-west of Wallaroo have a relatively greater strength and radius, respectively, during the January/February period when compared to the mid-December period. A more significant residual sea–surface current stream north offshore from Port Victoria,

flowing right to left towards the stagnation zones off Port Neill is more pronounced in the mid-December period than in the January/February period. It is surmised that these features combine to result in the more southerly dispersion of larvae on the south-eastern coast of mid-Spencer Gulf, as discussed above.

Northern Gulf Circulations and Dispersion

In Figures 10.27 and 10.28, respectively, details of the residual near sea–surface depth–level and

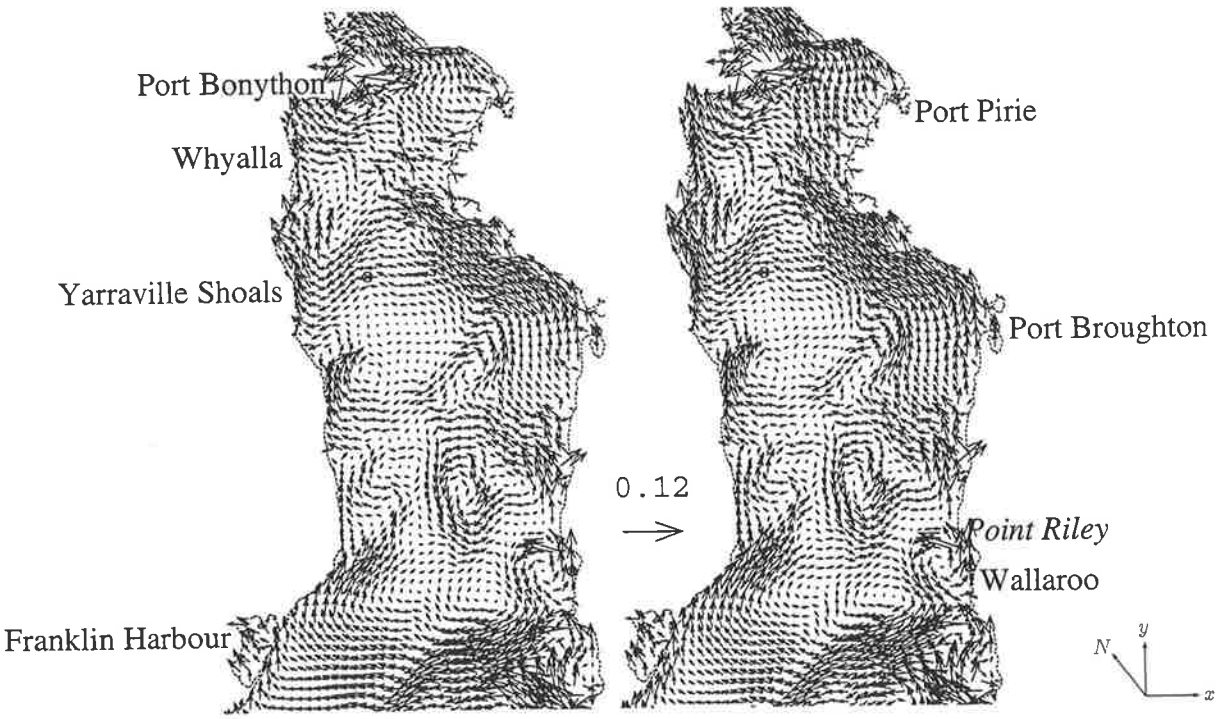

(a) 21:30 15/12/87–21:30 13/01/88 (b) 21:30 01/02/88–21:30 01/03/88

Figure 10.27: Mid-northern Spencer Gulf near sea–surface depth–level current residuals ($m\,s^{-1}$) for the 29 d periods indicated, calculated with wind–stress. Vectors are plotted for every computational element in both the x and y directions. Tidal stations (crossed circles) are shown.

near sea–bed depth–level currents in the northern Spencer Gulf region are plotted.

The near sea–surface depth–level residual currents show four main features. There are streams on the left hand coast turning clockwise into the two bays—between Yarraville Shoals and Whyalla (Cowleds Landing) and between Whyalla and Port Bonython (False Bay)—in which the final postlarval maxima for the February peak spawning and the December peak spawning simulations, respectively, are located. These two features are less apparent during the mid-December period (Figure 10.27(a)) than the January/February period (Figure 10.27(b)). On the right hand coast, there is another clockwise turning stream centred on the entrance to Port Pirie (Germein Bay). This feature is much less apparent during the mid-December period (Figure 10.27(a)) than the January/February period (Figure 10.27(b)). For both periods another stream turns anticlockwise around the narrowing part of northern Spencer Gulf past Port Broughton. For both periods this third stream continues its turn (through the location of the "average" initial condition maximum) to meet with the first, but also forks off to meet the second, although this is much less apparent during the mid-December period (Figure 10.27(a)) than the January/February period (Figure 10.27(b)).

The most predominant feature of the near sea–bed depth–level residual currents of Figure 10.28 is the stream meandering southwards from Port Bonython turning westwards towards the left-hand coast, then again southwards down the mid-northern mid-Gulf (through the loc-

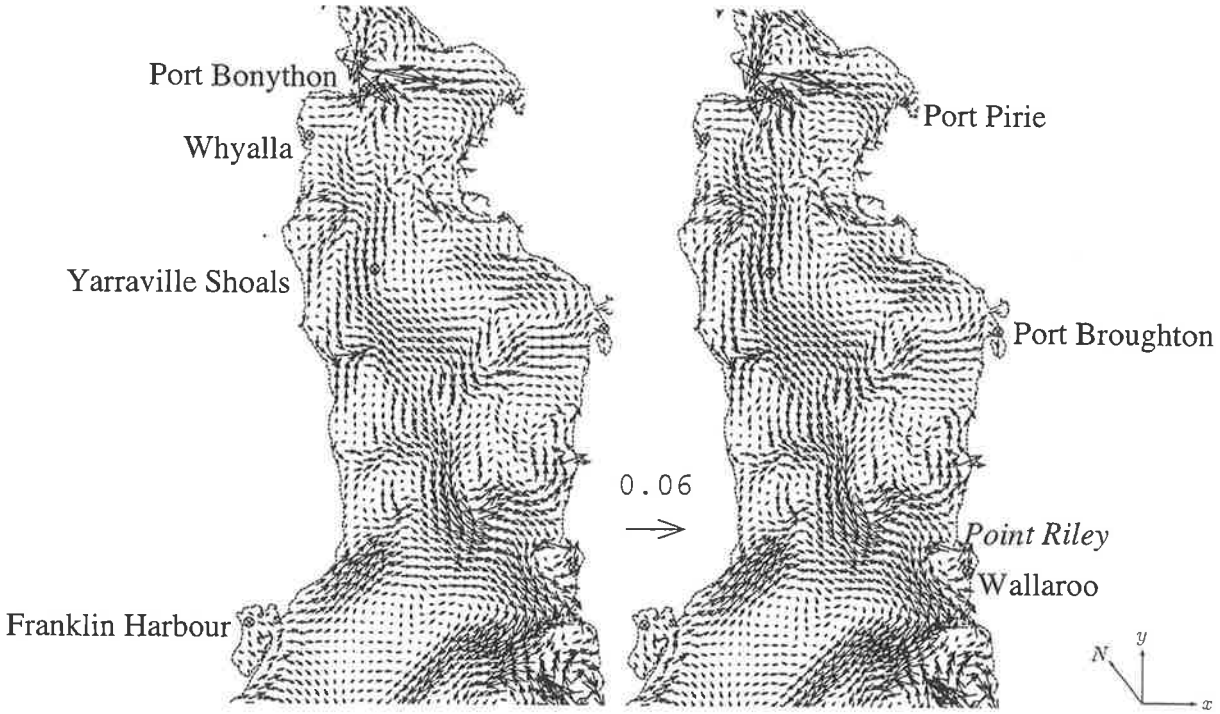

(a) 21:30 15/12/87–21:30 13/01/88 (b) 21:30 01/02/88–21:30 01/03/88

Figure 10.28: Mid-northern Spencer Gulf near sea–bed depth–level current residuals ($m\,s^{-1}$) for the 29 d periods indicated, calculated with wind–stress. Vectors are plotted for every computational element in both the x and y directions. Tidal stations (crossed circles) are shown.

ation of the "average" initial condition maximum), then westwards again towards Yarraville Shoals station.

The combined effect of these residual features—interacting particularly with the high concentrations in this area in the initial stages of the simulation—is surmised to be to transport larvae further south (due to the residual bed current differential) and thence westwards deeper into the bay of Cowleds Landing south-west of Whyalla (due to the residual surface current differentials) during the January/February period compared to the mid-December period. This is a plausible mechanism consistent with the final maximum postlarval locations in these two bays for the mid-December and January/February peak spawning simulations, and indeed those for the 1988, 1991–1994, and "average" initial condition simulations discussed in Section 2.1.5.

The meandering near sea–bed residual streams then turn, below Yarraville Shoals station, southwards once more and run past the two clockwise/anticlockwise residual eddy systems centred in the lower northern-Gulf. They then curve around the large residual eddy spanning the Gulf between Franklin Harbour and Wallaroo and head towards the southern-Gulf expanses. Other features of similar intensity are present in both sub-figures, but this particular feature is more apparent in the January/February period (Figure 10.28(b)) than the mid-December period (Figure 10.28(a)).

Tidal ellipses in the northern part of the Gulf, for both the mid-December and January/February peak spawning periods near both the sea–bed and sea–surface, are reproduced for the O_1, K_1, M_2, and S_2 tidal constituents in Figures 10.29, 10.30, 10.31, and 10.32, respectively. On close comparison of the near sea–surface ellipses of Figures 10.29(a) and 10.30(a) with those of Figures 10.29(b) and 10.30(b) and the near sea–bed ellipses of Figures 10.29(c) and 10.30(c) with those of Figures 10.29(d) and 10.30(d), it is evident that the diurnal constituent currents exhibit perceptibly greater lateral (x) component during the February period than during the December period. This trend is most pronounced towards the left-hand coast, particularly in the entrances to Port Pirie (Germein Bay) and Port Broughton. In all other respects, the

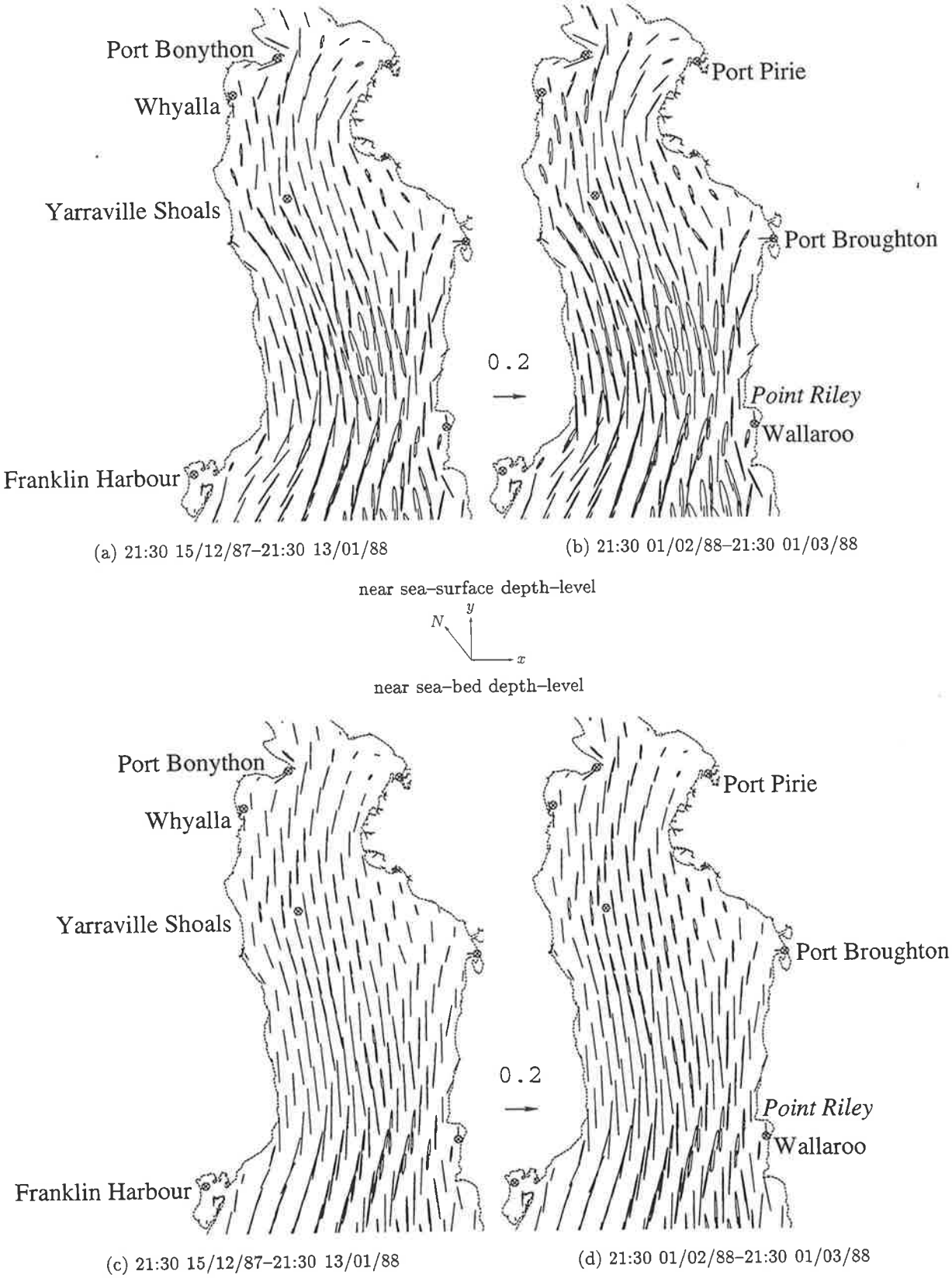

Figure 10.29: Mid-northern Spencer Gulf tidal ellipses ($m\,s^{-1}$) for the O_1 constituent during the 29 d periods indicated, calculated with wind–stress, and plotted at every third computational element in both the x and y directions. Tidal stations (crossed circles) are shown.

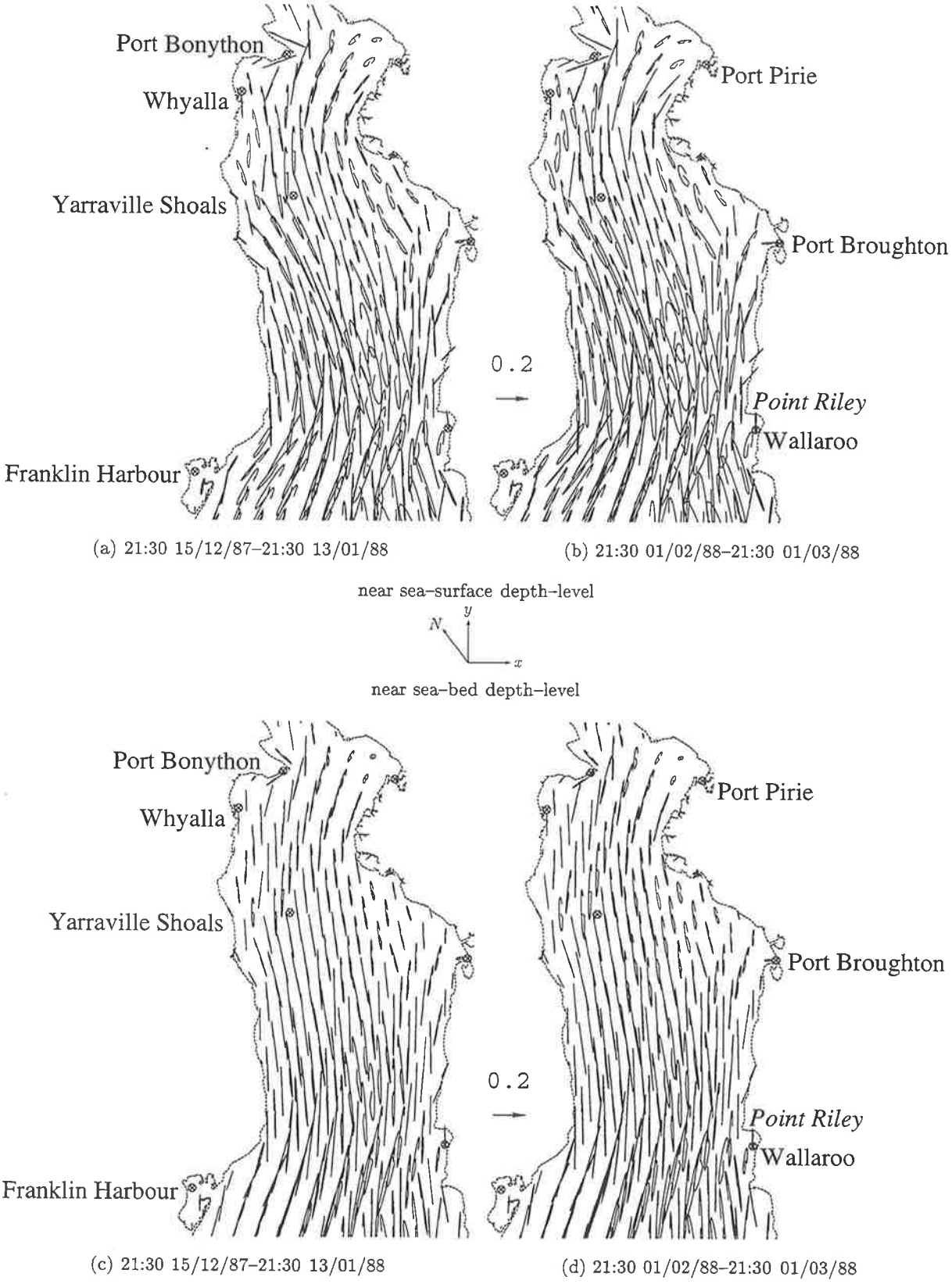

Figure 10.30: Mid-northern Spencer Gulf tidal ellipses ($m\,s^{-1}$) for the K_1 constituent during the 29 d periods indicated, calculated with wind–stress, and plotted at every third computational element in both the x and y directions. Tidal stations (crossed circles) are shown.

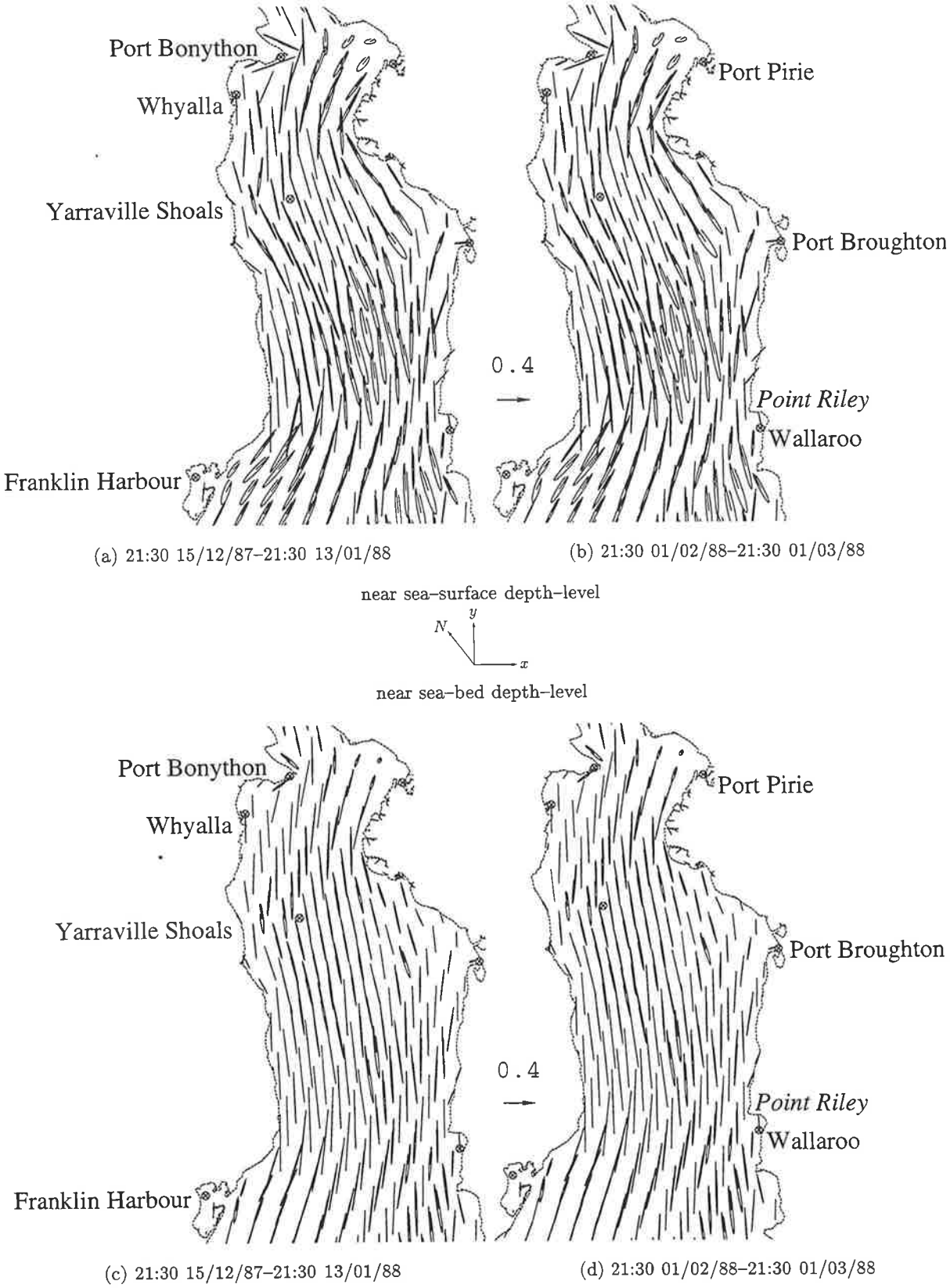

Figure 10.31: Mid-northern Spencer Gulf ellipses ($\mathrm{m\,s^{-1}}$) for the M_2 constituent during the 29 d periods indicated, calculated with wind–stress, and plotted at every third computational element in both the x and y directions. Tidal stations (crossed circles) are shown.

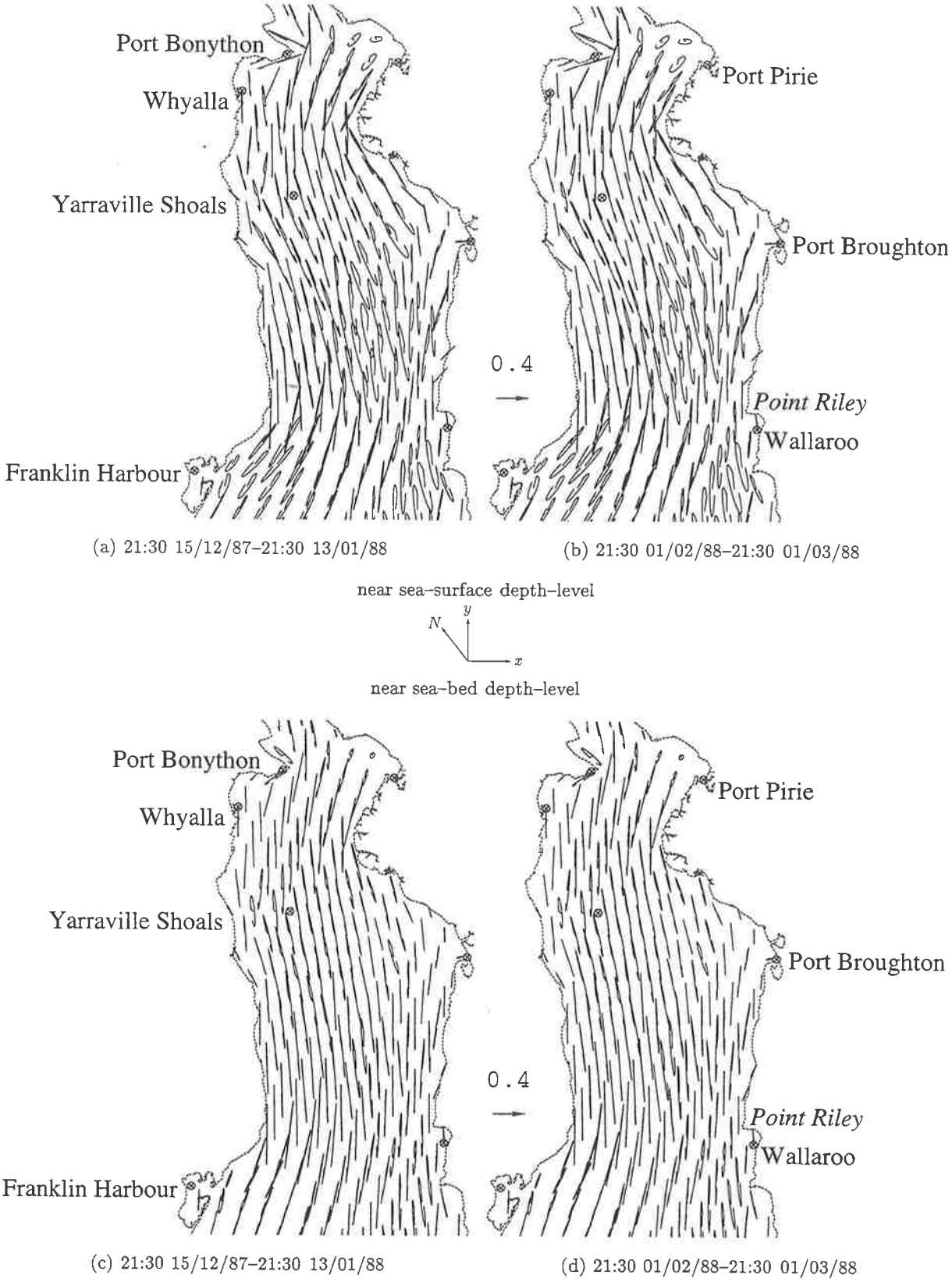

Figure 10.32: Mid-northern Spencer Gulf tidal ellipses ($m\,s^{-1}$) for the S_2 constituent during the 29 d periods indicated, calculated with wind–stress, and plotted at every third computational element in both the x and y directions. Tidal stations (crossed circles) are shown.

ellipses for the diurnal constituents are of extremely similar form.

The same can be said of the semi-diurnal current ellipses, where they are so similar in form that no perceptible difference in lateral component magnitude between the two periods was easily detected visually, for either the near sea–surface currents or the near sea–bed currents, even at scales of much greater enlargement than is reproduced here in Figures 10.31–10.32.

The extreme north-south orientation of the strong semi-diurnal currents and the comparatively more east-west orientation of the weaker diurnal currents, combined with the fact that this trend was more pronounced during the January/February than the mid-December period, would suggest greater lateral mixing in the former than in the latter. This hypothesis is somewhat supported by the greater east-west larval concentration spread in the vicinity above Port Broughton in the contours of Figure 10.24 with respect to those of Figure 10.23.

10.4.2 Variable Dispersion Periods

Representations of larval concentrations at simulation times between the initial larval "release" at 21:30 on the first day and the final postlarval "settlement" at 21:30 on the day 29 d after that day, for both the mid-December and the January/February spawning events, can be studied to provide further insight into the dynamics of larval dispersion in Spencer Gulf.

Time–series at individual computational elements over the entire simulation period show fine scale temporal dispersion dynamics, while transects along computational element groups at selected times during the simulation show general transport trends.

The reader is referred to Section 10.3 for details concerning the positions of the sites at which time–series stations and trend transects are defined.

Larval Time–Series

Time–series produced using linear interpolation of simulation results at all time–steps (i.e. every 20 min) in the week from 21:30 01/02/88 to 21:30 08/02/88 at SARDI sampling Stations 1–5 of Transect 1 are plotted in Figure 10.33.

The Transect 1 series at Station 1 (coarse dash), Station 2 (medium dash), and Station 5 (fine dash) in Figure 10.33(a) indicate a rapid increase in concentration from zero over the first few days, followed by a levelling off of this increase towards the end of the first week of simulations. This trend is less pronounced in the time–series of the more interior station (Station 2) than in that of the extreme western and eastern coastal stations (Stations 1 and 5, respectively).

The Transect 1 series at Station 3 (coarser dash), and Station 4 (finer dash) in Figure 10.33(b), however, indicate an equally pronounced decrease and increase, respectively, from non-zero concentrations over the first few days, followed by a levelling off of this towards the end of the first week of simulations.

These features illustrate the initial diffusion of the highly localised northern Gulf spawned larvae maximum, from the Gulf interior to the regions west and east towards each coast. Superimposed on these general trends can be seen the influence of the chiefly semi-diurnal nature of the tidal regime in Spencer Gulf on larval concentrations at the time–series sites, indicated by the "beats" apparent in the signals shown.

This beat phenomenon can be seen in Figure 10.34 to persist throughout the entire simulation period from 21:30 01/02/88 to 21:30 01/03/88 in the Transect 1 series at Station 2 (coarser dash), and Station 4 (finer dash). This figure also illustrates that the beats, often with local amplitude comparable to that of the month long time–series concentration range, can obscure overall trends—in this instance of initial rapid concentration increase from zero followed by gradual decline (Station 2), and of initial rapid concentration increase from non-zero followed by gradual decline (Station 4).

For this reason all time–series to follow are plotted using simulation results at times every 24 h from the initial larval release, thereby showing the trends in the absence of semi-diurnal

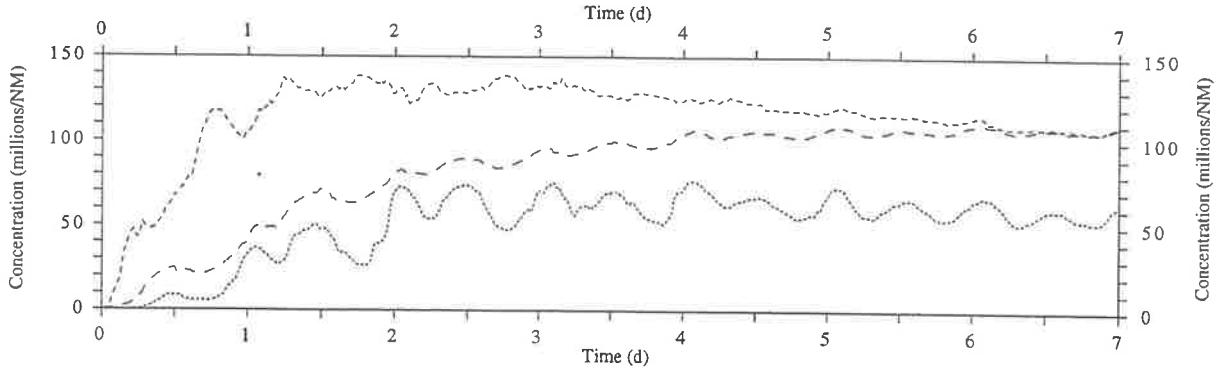

(a) Station 1 (coarse dash), Station 2 (medium dash), Station 5 (fine dash)

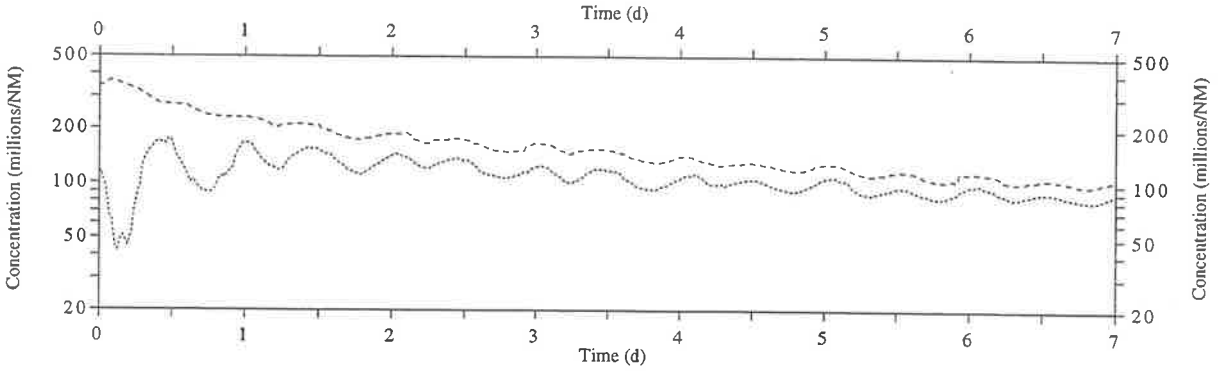

(b) Station 3 (coarser dash), Station 4 (finer dash)

Figure 10.33: Predicted concentration (10^6/nautical mile) time–series at SARDI larvae sample Transect 1 for the 7 d period of 21:30 01/02/88–21:30 08/03/88, with linear interpolation between each time–step (20 min).

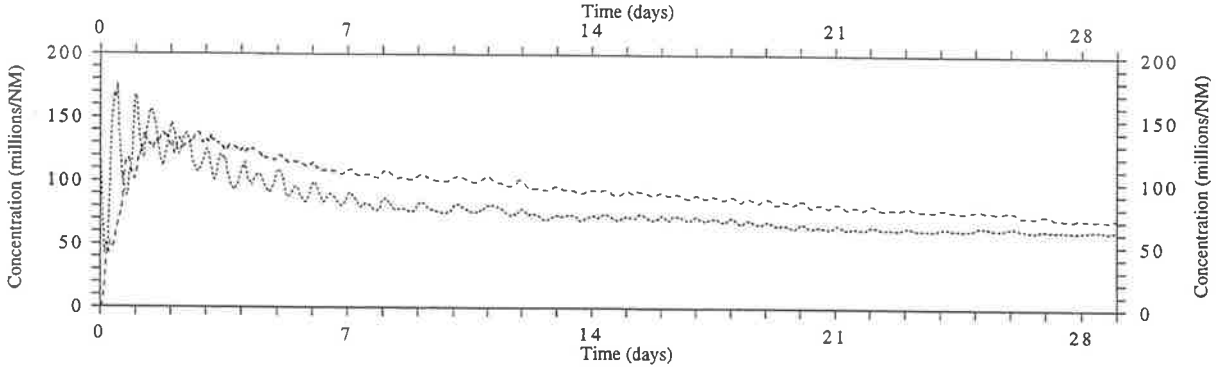

Figure 10.34: Predicted concentration (10^6/nautical mile) time–series at SARDI larvae sample Station 2 (coarser dash) and Station 4 (finer dash) of Transect 1 for the for the 29 d period of 21:30 01/02/88–21:30 01/03/88, with linear interpolation between each time–step (20 min).

period tidal effects. Time–series are plotted for the stations far west (Station 1), west (Station 2), midway (Station 3), east (Station 4), and far east (Station 5) along Transects 1–4, in Figures 10.35, 10.36, 10.37, 10.38, and 10.39, respectively. In these figures, time–series for the entire 29 d of both the mid-December (coarser dash) and the January/February (finer dash) simulations are plotted.

Figure 10.35 indicates an increase from zero in far west station larval abundance, with

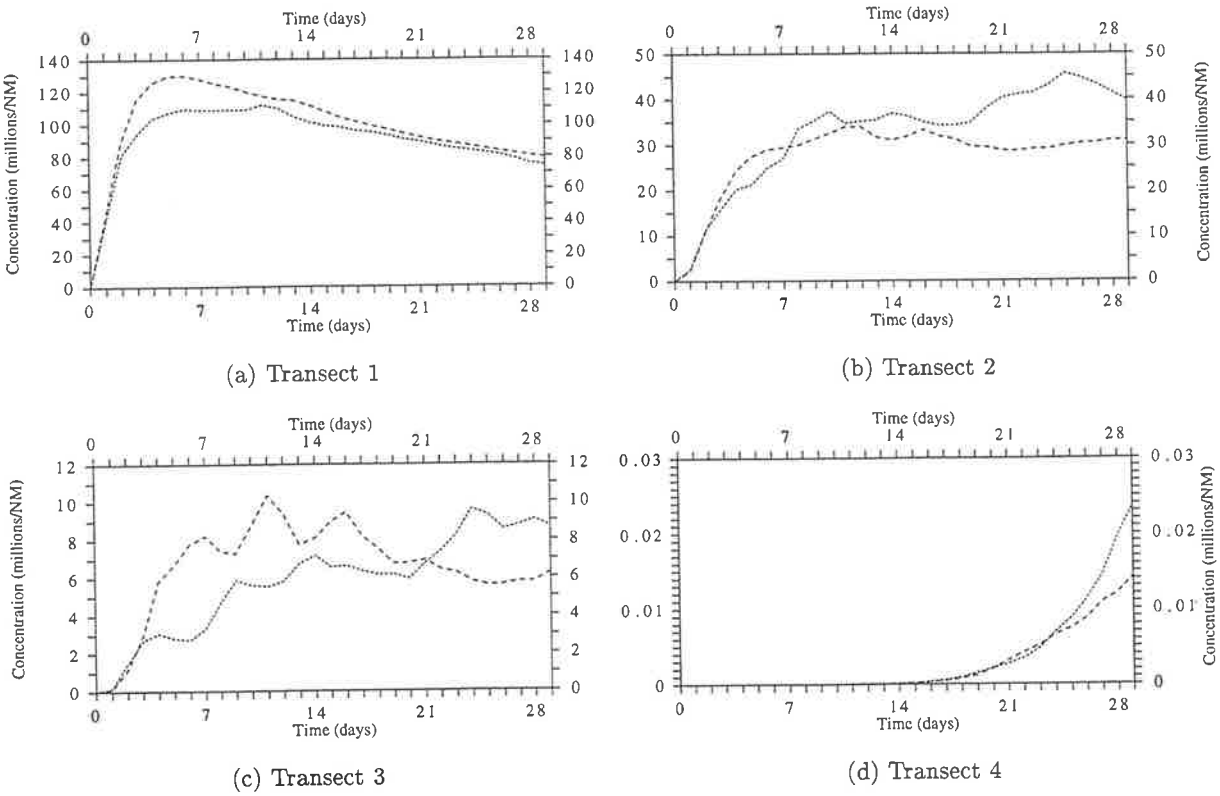

Figure 10.35: Predicted concentration (10^6/nautical mile) time–series at SARDI larvae sample Station 1 for the mid-December 1987 (coarser dash) and January/February 1988 (finer dash) simulations, with linear interpolation between each time–point (24 h).

later time–series behaviour of vastly different forms at each transect. In the upper-north (Figure 10.35(a)), an initial rapid increase in concentration gives way to a slow smooth decay with time. In the lower-north (Figure 10.35(b)), the increase is initially very rapid and then tapers off with time, with oscillations present. In the upper-south (Figure 10.35(c)), the overall trend is similar, but these oscillations are more pronounced. The oscillations for the mid-December (coarser dash) and the January/February (finer dash) simulations seem to be approximately out of phase and of half-weekly period, and are clearly more pronounced in the former than the latter. They thus may be indirectly related to meso-scale meteorological events effecting wind–stress and the resulting sea–surface and hence sea–bed currents at this station's location. In the lower-south (Figure 10.35(d)), the increase from zero is approximately exponential, and is only noticeable at the scale shown after approximately half way through the simulation.

There are similarities between the time–series at the far western stations of Figure 10.35 and those at the western stations of Figure 10.36. The general form in the upper-northern and lower-southern regions, at Transects 1 and 4 respectively, are similar (Figures 10.35(a) and 10.36(a), and Figures 10.35(d) and 10.36(d)). Both the western station lower-northern (Figure 10.36(b)) and upper-southern (Figure 10.36(c)) series, however, show overall decreases

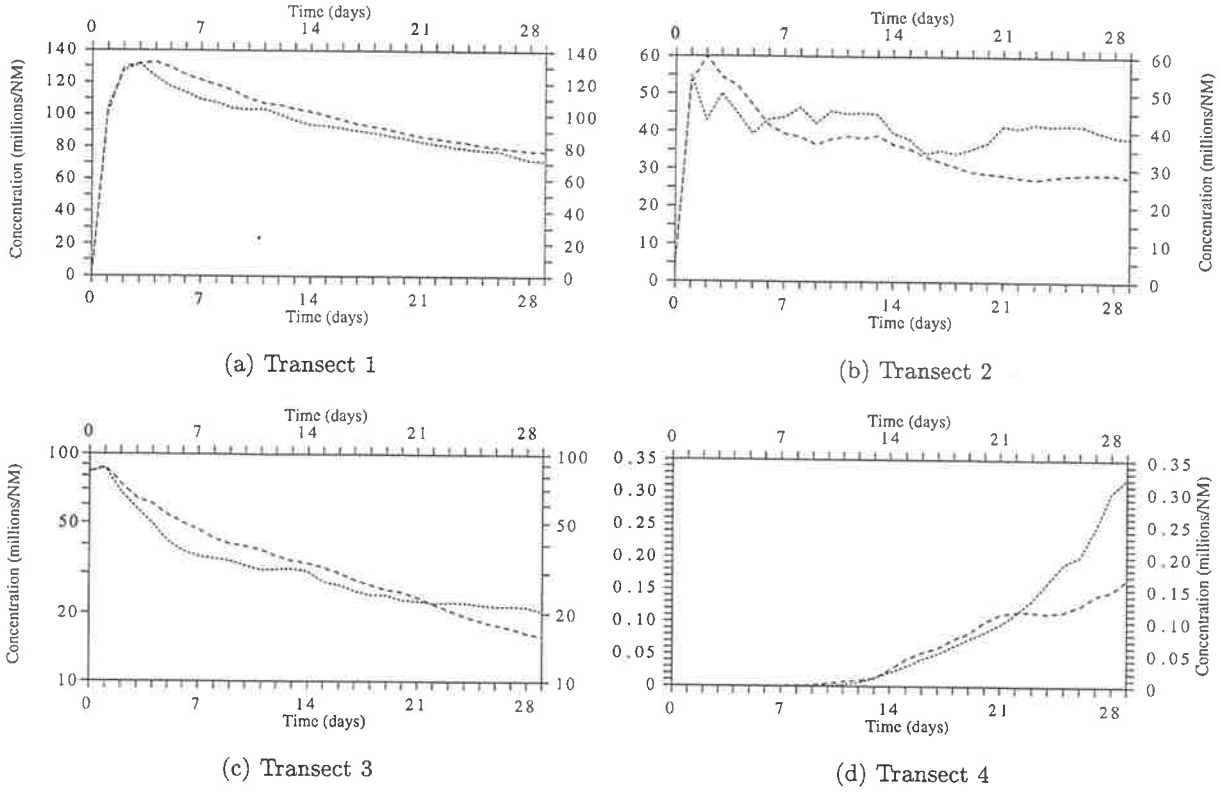

Figure 10.36: Predicted concentration (10^6/nautical mile) time–series at SARDI larvae sample Station 2 for the mid-December 1987 (coarser dash) and January/February 1988 (finer dash) simulations, with linear interpolation between each time–point (24 h).

during the simulation period, with the former starting with an initial rapid increase from zero (as the spawning peak is diffused from the interior towards the west coast) and the latter starting off with an initial rapid decrease from non-zero (as the spawning peak is diffused from the mid-Gulf both north and south towards the Gulf head and open boundary, respectively).

Figure 10.37 indicates, in both simulations, approximately exponential decay from the initially large local maxima in the mid-Gulf (Station 3) at locations in upper-northern (Transect 1), lower-northern (Transect 2), and upper-southern (Transect 3) Gulf, in Figures 10.37(a), 10.37(b), and 10.37(c), respectively. In the lower-southern mid-Gulf, an approximately linear increase from zero is indicated for both simulations in Figure 10.37(d).

Figures 10.38 and 10.39 show a greater difference between the two simulation periods than Figures 10.35–10.37. This can be seen most clearly from Figures 10.38(b) and 10.38(c) in which, apart from a short initial rapid concentration increase, clear trends are difficult to determine.

In Figures 10.39(b) and 10.39(c), however, a general pattern of larval concentration increase from zero, with this increase tapering off throughout the simulation, is well apparent. Equally apparent is the fact that the mid-December simulation results in fewer larvae predicted at these stations compared to the January/February simulation, after the first week of simulation.

An initial increase from zero, as a result of the significant spawned larvae concentration peak advection from the northern- and mid-Gulf towards the southern-Gulf expanses, can be seen in the series of Figures 10.38(d) and 10.39(d). The lower-southern Gulf transect (Transect 4) series at these stations (Stations 4 and 5), and in fact all stations, show the mid-December simulation results to increasingly deviate from those of the January/February simulation, with the latter increasingly predicting relatively greater larval numbers as one looks at stations from west to east across the transects.

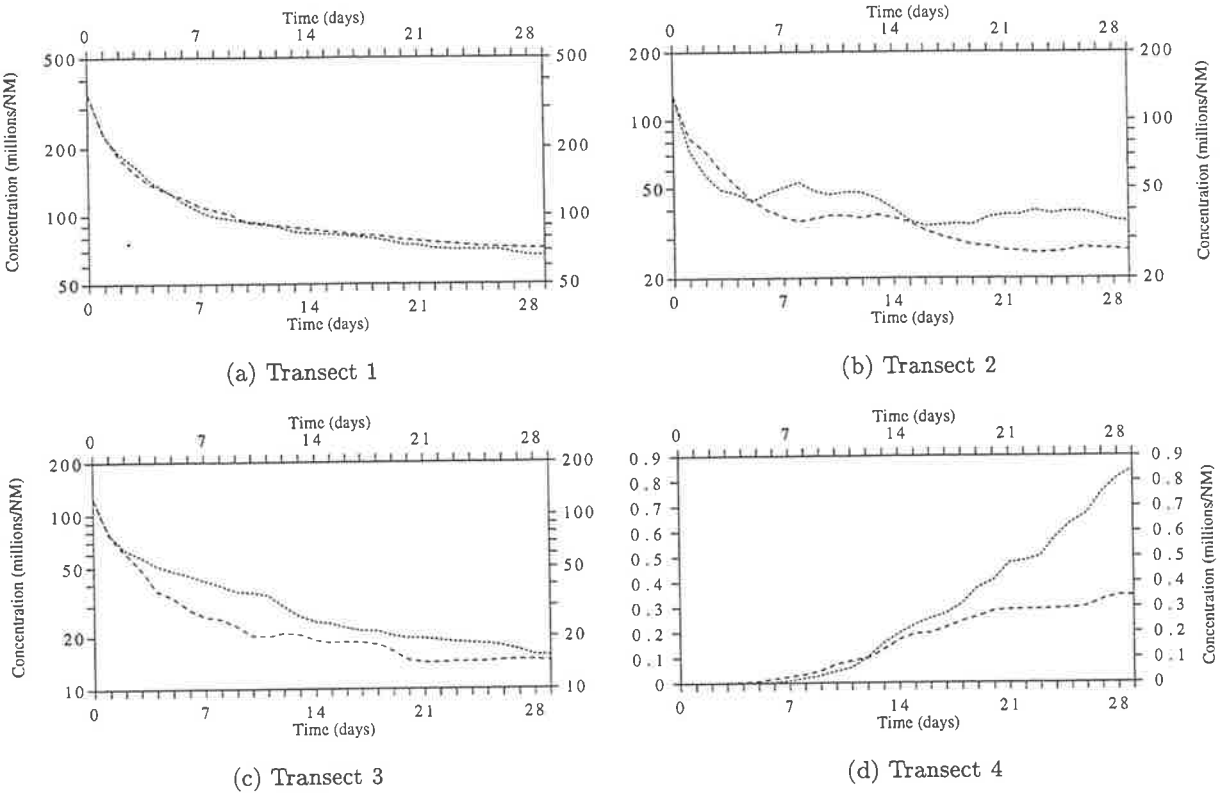

Figure 10.37: Predicted concentration (10^6/nautical mile) time–series at SARDI larvae sample Station 3 for the mid-December 1987 (coarser dash) and January/February 1988 (finer dash) simulations, with linear interpolation between each time–point (24 h).

In the upper-north (Transect 1) the two simulation time–series are, however, comparatively similar. An initial concentration increase from non-zero as a result of the spawned larvae peak diffusing from the mid-Gulf to towards the east coast, and then a decrease as northern Gulf mixing takes effect, can be seen in the series of Figure 10.38(a). A similar increase from zero, followed by a relatively constant signal can be seen in the series of Figure 10.39(a).

Carrick (1991) sampled six sites on each side of Spencer Gulf from 32° 40′ S to 33° 40′ S with sites interspersed by 10 NM. From the four samplings taken (November to early January) there was indication that settlement occurred at a low level in early December and increased to a higher level in late December and January (Carrick 1991, p. 6). On inspection of the figures, there may be modelled support for this qualitative conclusion based on preliminary field data analysis.

Consider the time–series predicted at Station 1 (Figure 10.35) and Station 5 (Figure 10.39) to approximate, respectively, the west coast and east coast settlement in the region sampled by Carrick (1991). Consider, also, the time–series predicted at Transect 1 (in Figures 10.35(a) and 10.39(a), respectively) and Transect 2 (in Figures 10.35(b) and 10.39(b), respectively) to approximate, respectively, the northern and southern extents of this region. Consider, further, the mid-December 1987 to mid-January 1988 dispersion period, indicated by the coarsely dashed curves of the figures, to approximate the November to early January samplings of Carrick (1991). The predicted series computed could be interpreted to lend support to the preliminary analysis conclusion, despite the many approximations required for this comparison. Since the Carrick (1991) raw data were not available, a more rigourous comparison of model predictions with field samplings was not possible.

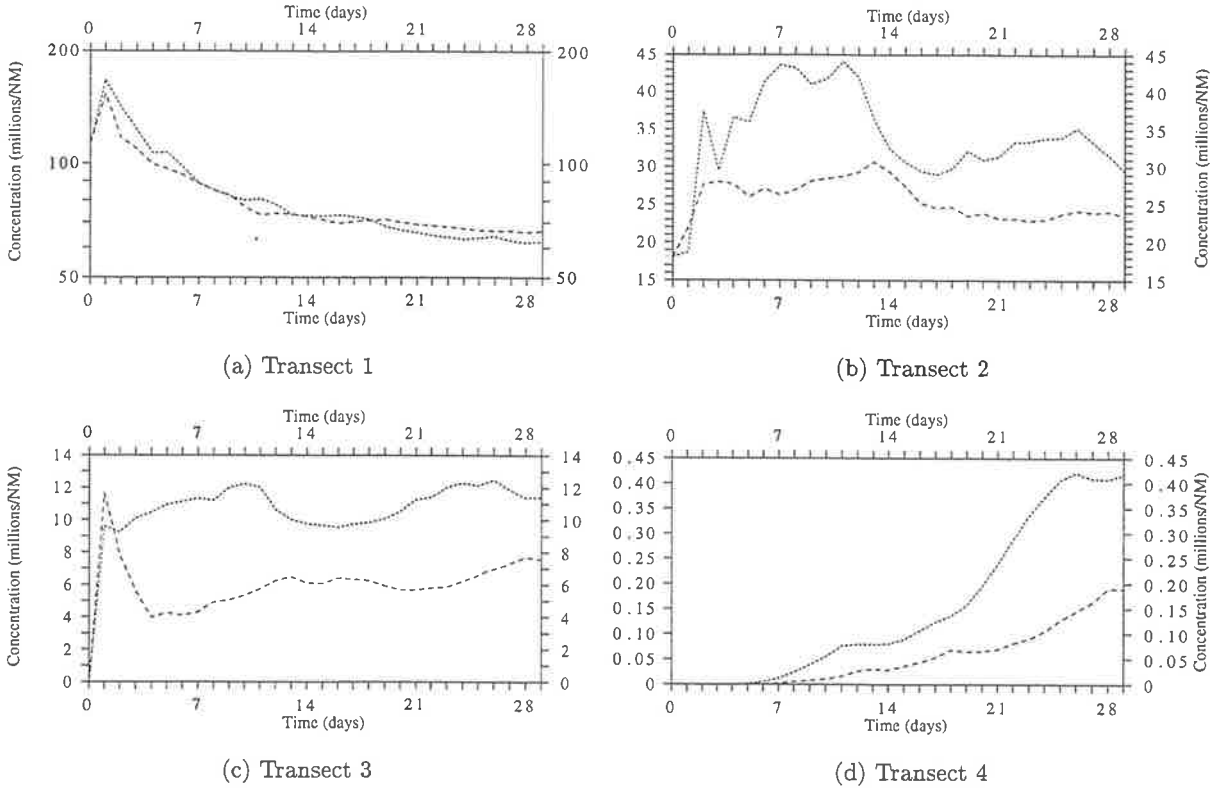

(a) Transect 1

(b) Transect 2

(c) Transect 3

(d) Transect 4

Figure 10.38: Predicted concentration (10^6/nautical mile) time–series at SARDI larvae sample Station 4 for the mid-December 1987 (coarser dash) and January/February 1988 (finer dash) simulations, with linear interpolation between each time–point (24 h).

10.4.3 Transect Trends

Figures 10.40 and 10.41 plot the initial egg and average of intermediate larval and of final postlarval concentrations from the mid-December (21:30 15/12/87 to 21:30 13/01/88) and the January/February (21:30 01/02/88 to 21:30 01/03/88) dispersion simulations. These figures indicate trends (solid lines) in the east-west and north-south direction, respectively. The concentrations (crossed points) for the initial egg (circles), average intermediate larval (squares), and average final postlarval (hexagons) time–points correspond to exactly 21:30 on the night of spawning, 09:30 on the morning of 14.5 d after spawning, and 21:30 on the night of 29 d after spawning, respectively.

East-West Transect Trends

The gradual diffusion of the initial concentration peaks in the upper-northern, lower-northern, and upper-southern Gulf can be seen in Figures 10.40(a), 10.40(b), and 10.40(c), for Transects 1, 2, and 3, respectively. Figure 10.40(d), however, illustrates gradual larval transport into the lower-southern Gulf from initially zero across the Gulf width there, to progressively greater effect, particularly in the mid-Gulf in this region.

The northern, middle, southern, and average means of Figures 10.40(e), 10.40(f), 10.40(g), and 10.40(h), respectively, indicate the general diffusion of the initial concentration peaks from the mid-Gulf regions in all of these areas, with a slight intermediate and final concentration peak towards, but not adjacent to, the west coast in all cases.

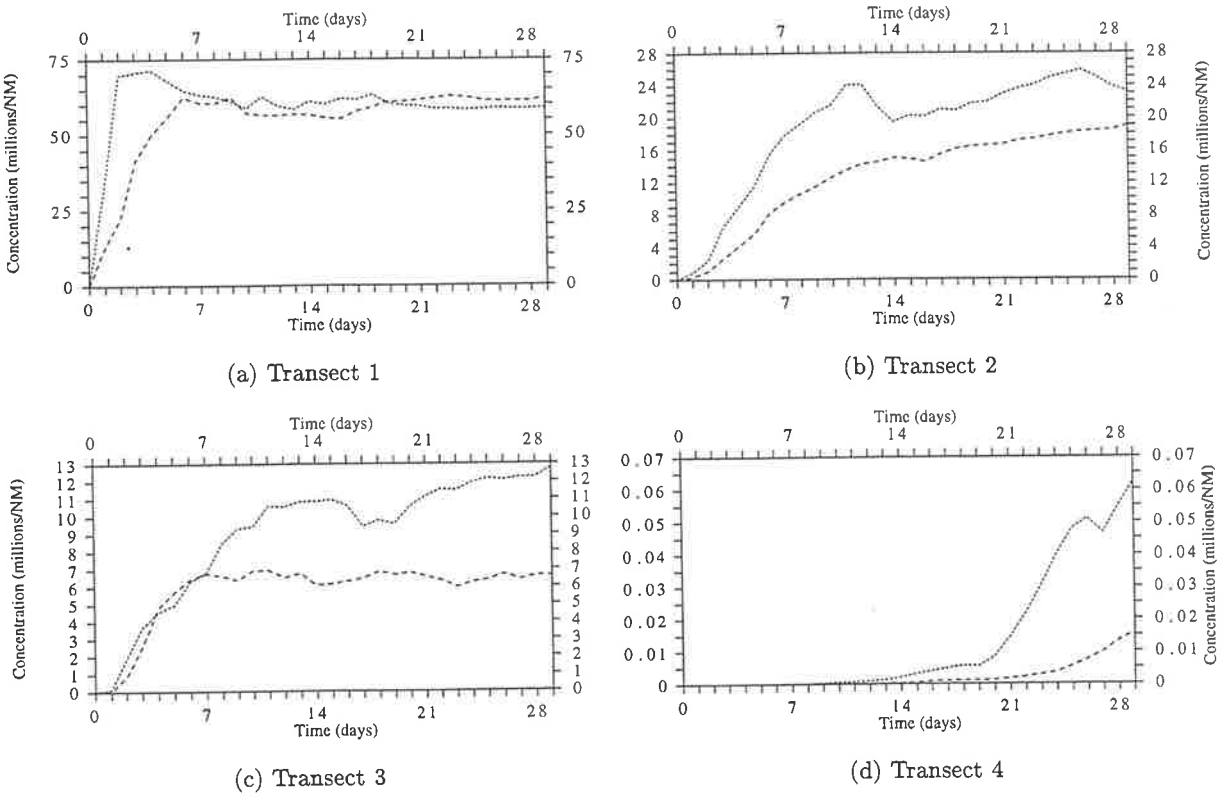

Figure 10.39: Predicted concentration (10^6/nautical mile) time–series at SARDI larvae sample Station 5 for the mid-December 1987 (coarser dash) and January/February 1988 (finer dash) simulations, with linear interpolation between each time–point (24 h).

North-South Transect Trends

Figure 10.41(a) shows larval transport into the originally barren west coast regions resulting in an intermediate peak which diminishes towards the simulation end, with this trend being less noticeable with increasing latitude south.

Figure 10.41(b) indicates larval transport from the upper-southern latitudes into the originally relatively barren northern-latitudes, for the regions towards, but not adjacent to, the west coast. As the simulation continues the upper-southern latitude peak diminishes, as does the northern latitude peak established soon after the original larval release.

Figure 10.41(c) indicates progressive diffusion of upper-northern and upper-southern latitude larval peaks in regions approximately midway between the west and east coasts. Figure 10.41(d) indicates progressive transport from upper-northern to more southern latitude larval peaks in the regions towards, but not adjacent to, the eastern coast. Both figures indicate that their trends are to a certain degree less pronounced as latitude increases south.

Figure 10.41(e) shows larval transport into the originally barren east coast regions resulting in an intermediate peak which continues to increase towards the simulation end, with this trend being less noticeable with increasing latitude south.

The average mean trends in Figure 10.41(f) indicate that simulations resulted in reduction of larval numbers at upper-northern and upper-southern stations, with this being more pronounced in the second and the first half of the simulation period, respectively. Lower-northern and lower-southern station concentrations are, on average, comparatively constant.

The mean western station (Stations 1 and 2) trend in Figure 10.41(g) has similar general characteristics to that for the western station (Station 2) in Figure 10.41(b), i.e. those of an upper-southern latitude peak progressively diffusing (northwards) and a northern-latitude peak

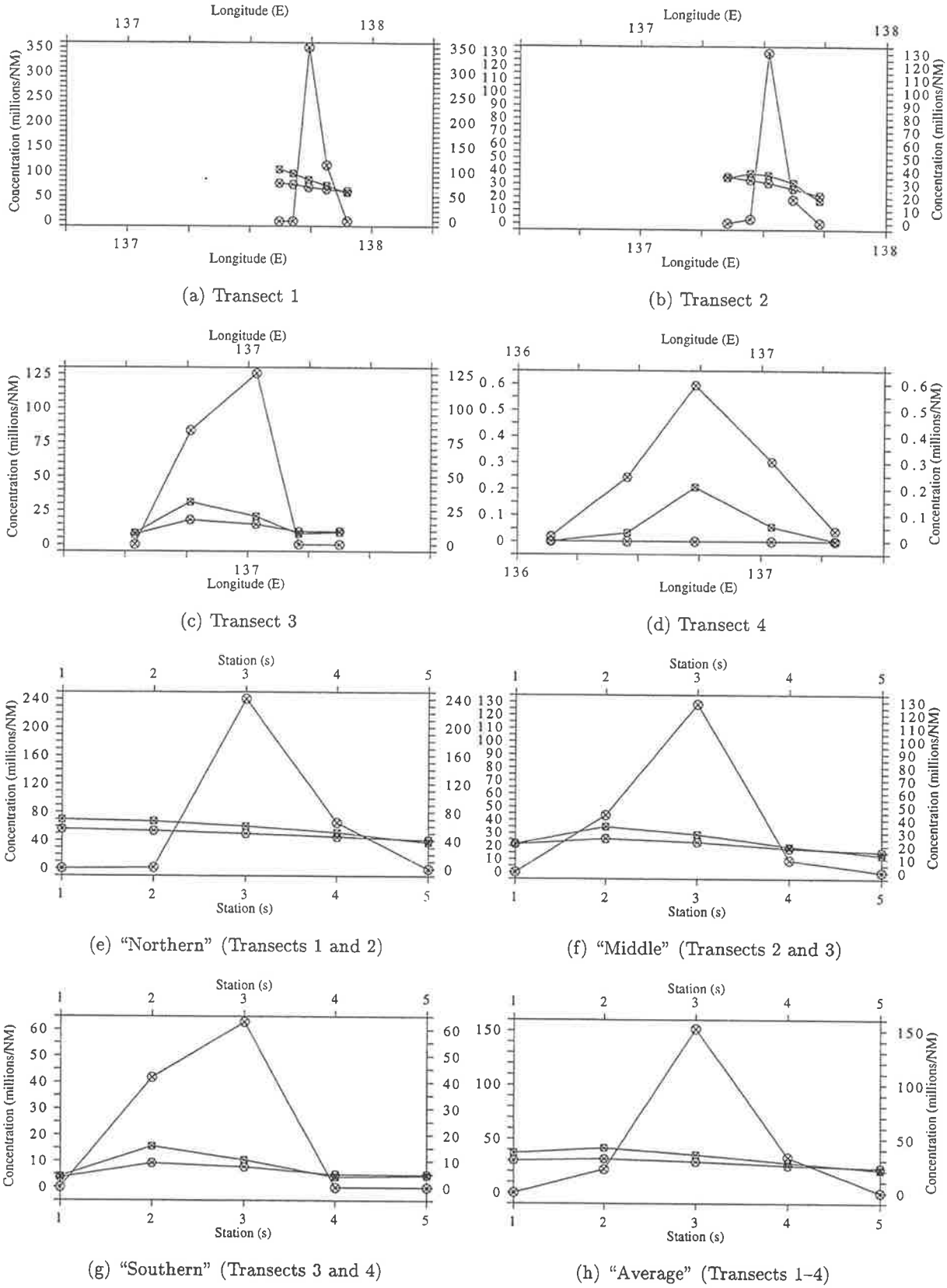

(a) Transect 1

(b) Transect 2

(c) Transect 3

(d) Transect 4

(e) "Northern" (Transects 1 and 2)

(f) "Middle" (Transects 2 and 3)

(g) "Southern" (Transects 3 and 4)

(h) "Average" (Transects 1–4)

Figure 10.40: The east-west trends and trend means at SARDI prawn larvae sample station locations (Longitude, °E; Station, s) for the initial (circles), intermediate (squares), and final (hexagons) average of mid-December 1987 and January/February 1988 larval concentrations (10^6/nautical mile).

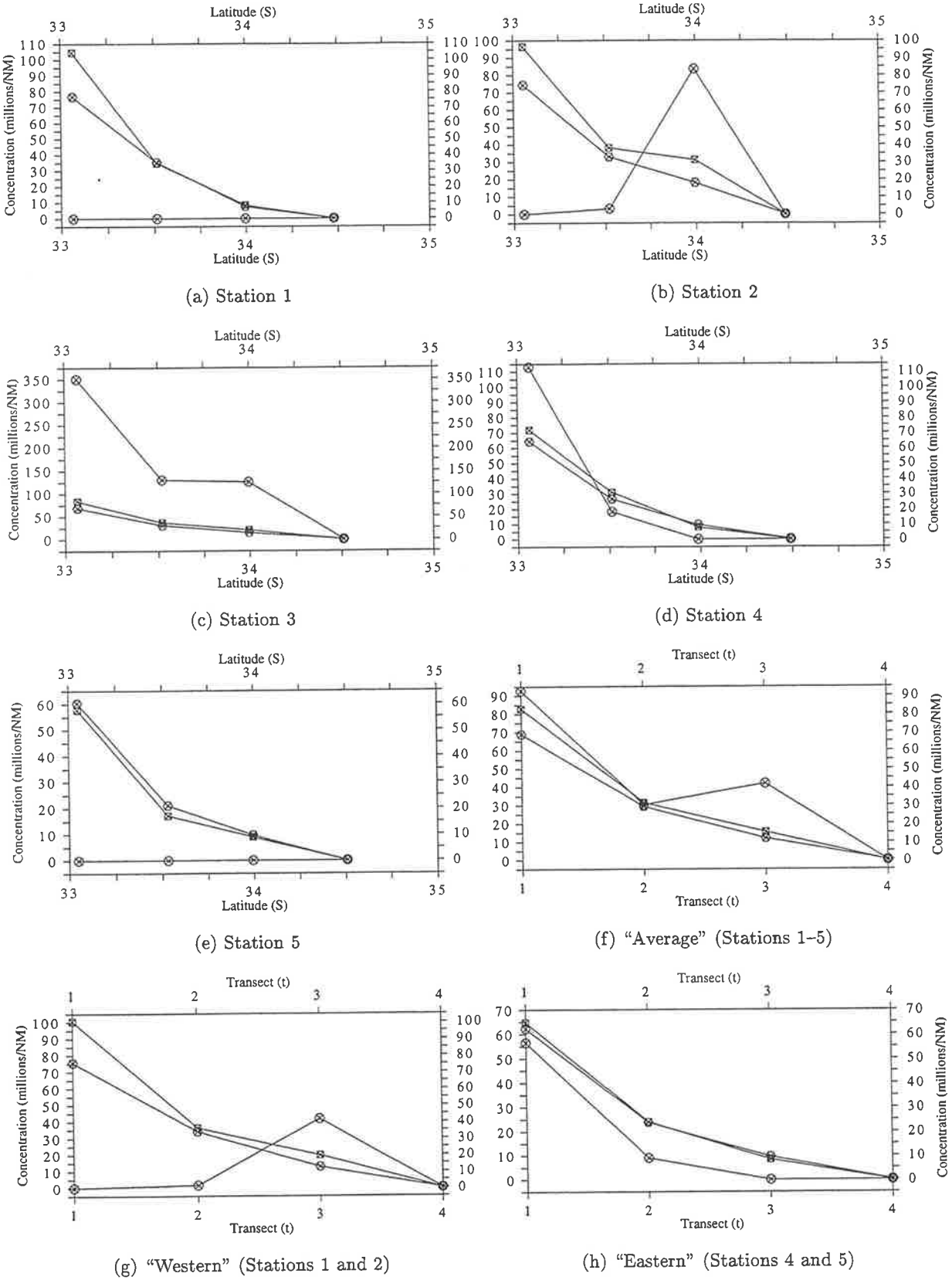

(a) Station 1

(b) Station 2

(c) Station 3

(d) Station 4

(e) Station 5

(f) "Average" (Stations 1–5)

(g) "Western" (Stations 1 and 2)

(h) "Eastern" (Stations 4 and 5)

Figure 10.41: The north-south trends and trend means at SARDI prawn larvae sample station locations (Latitude, °S; Transect, t) for the initial (circles), intermediate (squares), and final (hexagons) average of mid-December 1987 and January/February 1988 larval concentrations (10^6/nautical mile).

rapidly generating from a zero concentration and then also progressively diffusing (southwards).

The mean eastern station (Stations 4 and 5) trend in Figure 10.41(h) indicates significant larval transport during the first half of the simulation period into upper-northern, upper-southern, and lower-northern regions, with the magnitude of this transport increasing in this order. In the second half of the simulation period larvae are, somewhat less significantly, transported from the northern latitudes to the southern latitudes. Lower-southern station concentrations are, in the eastern regions, comparatively constant.

10.4.4 Conclusions

Numerical experiments were conducted with a number of prawn larvae dispersion period upper bounds and lower bounds. Concentration contours were plotted, indicating postlarval distributions corresponding to two larval dispersion periods. Time–series were plotted to indicate larval dispersion dynamics during two peak spawning periods. Concentration trends were plotted along east-west and north-south transects at the simulation start, middle, and end, to indicate bulk larval movements averaged over two peak spawning periods.

The differences and similarities between the model predictions of dispersion events over two time periods representing peak spawnings observed of *Penaeus latisulcatus* in Spencer Gulf were discussed. These discussions considered: larval time–series; initial, intermediate, and final larval concentration trends; and postlarval distributions as predicted by the dispersion model. They related these differences to the currents, during the appropriate time periods, as predicted by the tidal model. Comparisons of dispersion model predictions with field observation data were made, to a degree limited by the availability of those data. Within these limitations, model results were shown to correlate with field observations.

10.5 Summary

> I suspect that there is something wrong with our attitudes to working up and publishing primary data; and when the hideous cost of collecting the material is considered, we should, perhaps, be doing much better. While there may be concern about the data that are known to have been collected, one cannot help wondering how much has been collected about which nothing is known. One contribution that we could all make to the common cause is to check our data inventories, our cupboards, and our cellars. If there is real difficulty in publishing the original material, we should at least make sure that its existence is known (Harden Jones 1984, p. 7).

In this chapter, the sensitivity of the dispersion model output to its parameter input was investigated, since discrepancies between model results and field data can direct the modeller to include additional dynamics in the model equations or to alter the model parameter values (Wroblewski and Hofmann 1989, p. 91). Unfortunately field data, although they are purported to exist, were not available for such discrepancies to be determined in a quantitative manner. This situation supports the view that negative attitudes towards the publication of primary data are considered a serious hindrance towards advancing knowledge and understanding of migration (Harden Jones 1984, p. 1). The sensitivity analyses in this thesis were thus conducted in a qualitative rather than a quantitative manner.

The dispersion model predictions were found to be sensitive to the initial condition input to represent larval spawning, and the tidal currents input to represent advective processes. Since they were themselves predicted using a numerical tidal model, the sensitivity of these currents to pertinent tidal model input parameters was also investigated. The tidal model predictions were found to be sensitive to the wind–stress input to represent meteorological forcing, and the time–periods specified for the hydrodynamic, and hence larval dispersion, simulations. It should be noted, however, that the predictions of the combined model were found in Chapter 8

to be more dependent on the nature of the underlying numerical scheme used to approximate the advection and diffusion process, than any combination of input considered in this chapter.

Chapter 11

Conclusions and Recommendations

Present technological capability enables collection of biological data on time and space scales concurrent with physical data, so larval fluxes can be calculated. Assimilation of these data into an interdisciplinary model can be accomplished. Physical and biological model variables can be reinitialised with data and velocity fields updated during model execution, preventing a divergence between model simulations and observations due to computational restrictions (Wroblewski and Hofmann 1989, p. 91).

A similar divergence, due to inaccuracies in physical and biological model input *parameters* and underlying *formulations*, can also be used to good effect. It can allow for the model to be calibrated so as to determine those which result in the smallest obtainable divergence between simulation output and observational data. Unfortunately biological data, other than those quantifying *Penaeus latisulcatus* spawning events in Spencer Gulf, were not available within the time frame of this study. Thus, underlying formulations were not varied and input parameters were not changed, in any simulations, beyond those of the numerical schemes and sensitivity analyses, respectively, presented in this thesis.

On the other hand, models can fill in gaps in the database, i.e. interpolate between data points using a set of dynamical constraints (Wroblewski and Hofmann 1989, p. 91).

The larval dispersion model developed in this thesis was used primarily for this purpose. Results obtained using it, even without detailed comparison against observations, can provide information of biological and economic importance. For instance, the low *P. latisulcatus* concentrations predicted in the southern Gulf by all simulations indicate that recordings at larval sampling stations in these regions may not represent efficient allocation of SARDI field data collection resources.

11.1 The Biological Model

In the larval dispersion simulations reported in this thesis, no account was taken of physical environmental factors on larval settlement (and thus length of competent period), density and other effects on mortality (and thus length of precompetent period), or age, temperature, salinity or other space- and time-dependent phenomena on the length of time spent in the plankton by larvae. This was mainly due to the paucity of quantifiable data concerning these variables, and of their resulting effect on the length of the *P. latisulcatus* larval period in Spencer Gulf.

11.1.1 Observational Mortality Data

Detailed mortality data relevant to *P. latisulcatus* in Spencer Gulf was found to be lacking. Should mortality rates be well defined in the future, these could be incorporated into the larval dispersion model. The total of negative concentrations removed during the model "clipping" process could be incorporated into the mortality coefficient associated with larval dispersion, in order to artificially achieve at least partial conservation of total prawn larvae biomass. Since mortality was not incorporated in the prawn larvae dispersion model developed in this thesis,

and concentrations "clipped" in all simulations were shown to be very small compared to those predicted, this notion was not explored further.

11.1.2 Observational Spawning Data

Initial conditions were derived for individual spawning seasons, from egg production data obtained during sampling trawls conducted by SARDI research officers. Results of simulations using these individual initial conditions, and an average constructed from them, indicated that predictions were sensitive to the set of trawl sampling locations within each year as well as the data obtained at these locations. This sensitivity implies that spawning which occurs outside of the trawl regions, and is thus not represented in the initial conditions imposed, may affect *P. latisulcatus* distribution in Spencer Gulf in a way which cannot be determined by the larval dispersion model using the egg production data available.

All initial conditions imposed were instantaneous, in that larval concentrations were set at simulation commencement and no account was taken of the presumed "build-up" and "tail-off" before and after, respectively, the peak spawning periods. Simulations were, however, conducted in which predictions were made of larval dispersion following two known times of peak spawning. The peak spawning times themselves were approximations of those reported in the literature as being observed of *P. latisulcatus* in Spencer Gulf. In order to represent spawning events which are not instantaneous, field measurements are required to determine the larval release regime. The time, duration, and rate of spawning, once measured, could be represented mathematically in a continuous release spawning initial condition, possibly of a Gaussian nature.

11.1.3 Observational Dispersal Data

Larval concentration predictions of the dispersion model were presented in this thesis as time–series, at, and as trends, along, transects defined by the known locations of SARDI larval sampling sites. Unfortunately the larval concentration data themselves were not available for comparison with model predictions.

11.1.4 Observational Settlement Data

Surveys are required to determine settlement locations to a resolution greater than that of those cited from the literature in this thesis. These locations could be defined from direct field observations or deduced by indirect means.

The latter could involve the use of database and graphical information system (GIS) technology to determine the relative probability of successful *P. latisulcatus* settlement in regions of Spencer Gulf associated with particular combinations of water depth and quality, local salinity and vegetation, food abundance, etc. measures.

The former would require field sampling and postlarvae sorting to determine the approximate *P. latisulcatus* settlement regime (i.e. time, place, duration, rate) at specific Spencer Gulf locations. Four samplings in November to early January during one South Australian summer were, in fact, carried out by SARDI research officers at six sites on each side of the Gulf. Unfortunately these field data were not available for comparison with model predictions.

11.2 The Dispersion Model

Given observational data with which to compare predictions, quantitative error analyses could be carried out, and model input parameters calibrated to the former using the latter. The dispersion model itself could also be improved in other, more fundamental respects.

11.2.1 Three-Dimensional Dispersion Modelling

The most significant development of the larval dispersion model would be to extend it to full three-dimensionality. One approach taken could be to use an implicit and preferably unconditionally von Neumann stable and non-negative finite-difference method to solve for advection–diffusion in the vertical coordinate. Stability would thus be conserved, but computational resource requirements would increase significantly. The vertical velocity component computed by the tidal model could be incorporated with specified larval vertical migration velocities and vertical diffusion coefficients to simulate diel migration and spread in the water column. These velocity components and diffusion coefficients would, of course, be required to be parameterised so as to adequately represent observed vertical migration behaviour.

11.2.2 Eddy Diffusion Specification

Since these are calculated as part of the tidal model solution process, there is scope for time and/or space varying eddy diffusion coefficients to be determined by the hydrodynamic model for input to the dispersion model. The feasibility of this approach, however, has not been fully determined.

11.3 The Hydrodynamic Model

It is evident that the accuracy of an advection–diffusion model is limited by the accuracy of any hydrodynamic model which may be used to determine the advective velocities which are input to it. The accuracy of this model is in turn dependent on its own input, and underlying algorithms.

11.3.1 Fine Grid Spencer Gulf Model Validation

A direct comparison of predictions using the coarse grid Spencer Gulf model in Section 3.4 and the fine grid model in Chapter 6 should be the subject of future research. This would ideally be carried out in the same detail as the comparsion of the coarse grid model predictions with Spencer Gulf field observations in Bills (1991). It should consider tidal elevation, and depth-averaged and depth-dependent current velocity values.

11.3.2 Surface Wind Specification

Clearly data must be obtained for non-daylight hours at surface wind stations for the wind field to be determined—possibly by a higher-order surface fit using bicubic spline interpolation—from field measurements. It should be mentioned, however, that even the surface wind measurements discussed in this thesis were made on dry land. These were also taken at heights 10 m above the station elevations, and not at this elevation above MSL as required by the wind–stress specification used in the tidal model. Increased frictional effects over land must surely be taken into account, as well as effects due to local topography near the surface wind stations themselves. An accurate measurement-based wind field specification must then ideally be derived using wind data obtained from sea-based observations, of which there were none available from the BoM and are few known to the author for the region and time periods of interest.

The possibility of hindcasting a fine-resolution wind field using meteorological numerical models and pressure and temperature field forcing inputs to them, all supplied by the BoM, should be explored in future studies.

11.3.3 Tidal-Flats Representation

Simulations in this thesis predicted, in correlation with observations, that the majority of *P. latisulcatus* dispersion activity occurs in the northern regions of Spencer Gulf. These are known

to be shallow and prone to covering and uncovering periodically during the tidal cycle. This phenomenon can be simulated by the introduction of tidal-flats representation algorithms in the three-dimensional tidal model.

Such algorithms (Bills et al. 1993, 1994) have recently been developed for the three-dimensional model but are, as yet, unpublished. These were also not thoroughly tested at the time at which the numerical simulations discussed in the present work were carried out. Thus tidal-flats were not represented in the hydrodynamic modelling discussed in this thesis.

With tidal-flat covering and uncovering activities represented in the tidal model, one would also be required to represent these in the dispersion model. Algorithms by which larval concentration may be redistributed to covered regions from regions uncovering and/or represented as juveniles settling would need to be developed. The reflecting boundary condition of the present larval dispersion model with no partial settlement would clearly be inadequate.

11.3.4 Spherical Coordinate Representation

The present tidal, and hence dispersion, models were developed assuming orthogonal Cartesian coordinates. The error incurred by not employing a shell model of the relatively small Spencer Gulf region, derived assuming spherical coordinates, has been estimated to be insignificant (Bills 1991). Should the hydrodynamics of larger coastal regions be required to be simulated using a spherical coordinate tidal model, the dispersion model must also be modified accordingly.

11.3.5 Coastal Boundary Representation

The tidal model assumes an orthogonal rectangular grid in which impermeability is absolute normal to the coastline. The coastal boundary slip layer can be treated in a more physically and mathematically correct manner using the oblique boundary representation of I'Anson et al. (1994), Matthews (1995), Matthews and Noye (1996a, 1996b), and Matthews et al. (1995, 1996). This treatment had yet to be fully operational in the three-dimensional tidal model at the time at which the numerical simulations discussed in the present work were carried out. Had this treatment been used, the coastal boundary condition of the dispersion model must also have been modified accordingly.

11.4 Recruitment Forecasting

Accurate predictions of stock sizes should allow redirection of fishing effort. With penaeids the short duration of the life cycle only allows perhaps six months time to do this, instead of the six years which may be available in, e.g. a rock lobster industry. Any extension of this six months is time gained (Kirkegaard 1975, p. 58).

The larval dispersion model of Spencer Gulf developed in this thesis could be used to take advantage of the *Penaeus latisulcatus* life–cycle time lag. With support from adult population dynamics, and observational and statistical information on pertinent aspects of mature prawn behaviour, it is envisaged that models such as this could be used to enable real-time forecasting for the next adult season.

Chapter 12

Summary

> The interface between the environmental fluid and organisms is extensive. There is a long list of questions in planktonic community dynamics to which only an interdisciplinary blend of biology and fluid mechanics can provide the answers (Okubo 1986, p. 21).

It has been shown that many individual physical, behavioural, and environmental processes combine to affect the movement of larvae in the coastal environment. Physical processes such as advection and diffusion can be accurately modelled using theoretically proven mathematical and numerical techniques—in this instance finite-difference methods for the relevant tidal and transport equations, respectively—which are generally applicable in almost any specific region. Behavioural processes such as spawning, mortality, and diel vertical migration can be effectively modelled using a mathematically idealised representation, the appropriateness of which is primarily defined by the accepted biological and/or behavioural models and is secondarily constrained by the availability of data pertaining to the particular species, region, and period of interest. Environmental processes such as temporal and spatial variations in atmospheric pressure, sea–surface wind, and ambient light intensity can be adequately represented, provided that the data related to these processes are available on time and space scales appropriate to the species, region, and period of study, and at a level of accuracy commensurate to the underlying biological, mathematical, and numerical models.

The three broad types of processes interact with each other to affect the predicted dispersion of larvae in both a qualitative and quantitative manner. The success or failure of a total integrated model can only be determined through comparison with field measurements. The experimental design of the programmes by which these measurements are made can be influenced by the results of the models and visa versa. With this in mind, it is apparent that there is the possibility of feedback, not only between the processes being modelled, but between the simulated predictions output by the models and the measured data input to them.

It is only through close collaboration between the disciplines, organisations, and individuals interested in the problem of quantitative larvae dispersal prediction—each with their own knowledge, expertise, insight, and experience—that significant further advances can be achieved.

> With a conceptual basis established, we may proceed in a step-wise fashion towards building coupled physical-biological larval dispersal models capable of systematically synthesising the impact of a wide range of processes and their interactions. With this wider goal in mind, I have endeavoured in this [work] to clarify the interaction between the tides, which are the most pronounced, regular periodic phenomenon in the physical environment (and consequently the most predictable and best understood component of the physical system), with vertical migration, the most ubiquitous form of periodic behaviour in marine organisms (Hill 1995, p. 12).

Bibliography

Angel, M. V. (1984). The diel migrations and distributions within a mesopelagic community in the north east Atlantic. 3. Planktonic ostracods, a stable component in the community. *Progress in Oceanography 13*(3/4), 319–351.

Angel, M. V. (1989). Vertical profiles of pelagic communities in the vicinity of the Azores front and their implications to deep ocean ecology. *Progress in Oceanography 22*(1), 1–46.

Anonymous (1991, Aug). *$\mathcal{A}\mathcal{M}\mathcal{S}$-LaTeX Version 1.1: User's Guide.* Providence, Rhode Island: American Mathematical Society.

Anonymous (1994). Annual report 1994. Technical report, Spencer Gulf and West Coast Prawn Fishermen's Association Incorporated, Port Lincoln, South Australia.

Arakawa, A. and V. R. Lamb (1977). Computational design of the basic dynamical processes of the UCLA General Circulation Model. *Methods of Computational Physics 16*, 173–263.

Arnold, R. J. and B. J. Noye (1986). Open boundary conditions for a tidal and storm surge model of Bass Strait. In B. J. Noye and R. L. May (Eds.), *Computational Techniques and Applications: CTAC-85*, The University of Melbourne, Victoria, Australia, pp. 503–517. Elsevier Science Publishers B. V. (North-Holland), Amsterdam.

Barnes, R. D. (1986). *Invertebrate Zoology* (Fifth ed.). New York: Saunders College Publishing.

Bartsch, J., K. Brander, M. Heath, P. Munk, K. Richardson, and E. Svendsen (1989, Aug). Modelling the advection of herring larvae in the North Sea. *Nature 340*(6235), 632–636.

Batchelor, G. K. (1967). *An Introduction to Fluid Dynamics.* Cambridge, UK: Cambridge University Press.

Beard, D. A. and J. B. Nixon (1990, Oct). *DRAW: A Program for `vis603` Terminal Graphics and PostScript File Output* (First ed.). South Australia: Department of Applied Mathematics, The University of Adelaide. Simplifies plotting on: 1) vis603 terminals using screen graphics; 2) laser printers using the PostScript language.

Bills, P. J. (1991, Sep). *Barotropic Depth-Averaged and Three-Dimensional Tidal Programs for Shallow Seas.* Ph. D. thesis, The University of Adelaide, South Australia. Department of Applied Mathematics.

Bills, P. J. (1994). Personal Communications. Department of Applied Mathematics, The University of Adelaide, South Australia.

Bills, P. J., J. B. Nixon, and B. J. Noye (1993, Jul). Three-dimensional modelling of flow across tidal flats and sandbars. Paper presented by first author at the Computational Techniques and Applications Conference: CTAC-93. Australian National University, Canberra. Unpublished.

Bills, P. J., J. B. Nixon, and B. J. Noye (1994, Jul). Depth-averaged and three-dimensional modelling of flows across tidal flats and sandbars. Paper presented by first author at the Sixth Pacific Congress on Marine Science and Technology. James Cook University of North Queensland, Townsville, Australia. Unpublished.

Bills, P. J. and B. J. Noye (1984). Verification of a three-dimensional tidal model for coastal seas. In B. J. Noye and C. J. Fletcher (Eds.), *Computational Techniques and Applications: CTAC-83*, The University of Sydney, New South Wales, Australia, pp. 394–410. Elsevier Science Publishers B. V. (North-Holland), Amsterdam.

Bills, P. J. and B. J. Noye (1986). Tides of Spencer Gulf, South Australia. In B. J. Noye and R. L. May (Eds.), *Computational Techniques and Applications: CTAC-85*, The University of Melbourne, Victoria, Australia, pp. 519–531. Elsevier Science Publishers B. V. (North-Holland), Amsterdam.

Bills, P. J. and B. J. Noye (1987). An investigation of open boundary conditions for tidal models of shallow seas. In B. J. Noye (Ed.), *Numerical Modelling: Applications to Marine Systems*, Volume 145 of *North-Holland Mathematics Studies*, The University of Adelaide, South Australia, pp. 159–194. Elsevier Science Publishers B. V. (North-Holland), Amsterdam.

Bills, P. J. and B. J. Noye (1992). Model of a coastal sea with tidal flats. In B. J. Noye, B. R. Benjamin, and L. H. Colgan (Eds.), *Computational Techniques and Applications: CTAC-91*, The University of Adelaide, South Australia, pp. 117–126. Computational Mathematics Group, Australian Mathematical Society.

Black, K. P. (1989, Dec). Numerical simulation of steady and unsteady meso-scale eddies. In *Ninth Australasian Conference on Coastal and Ocean Engineering*, Number 89/20 in National Conference Publication, Australia, pp. 204–208. The Institution of Engineers.

Black, K. P. and S. L. Gay (1987, Aug). Eddy formation in unsteady flows. *Journal of Geophysical Research 92*(C9), 9514–9522.

Black, K. P., S. L. Gay, and J. C. Andrews (1990). Residence times of neutrally-buoyant matter such as larvae, sewage or nutrients on coral reefs. *Coral Reefs 9*(3), 105–114. Special Issue: *Acanthaster planci*.

Black, K. P. and P. J. Moran (1991, Jan). Influence of hydrodynamics on the passive dispersal and initial recruitment of larvae of *Acanthaster planci* (Echinodermata: Asteroidea) on the Great Barrier Reef. *Marine Ecology Progress Series 69*, 55–65.

Blumberg, A. F. and G. L. Mellor (1987). A description of a three-dimensional coastal ocean circulation model. In N. S. Heaps (Ed.), *Three-Dimensional Coastal Ocean Models*, Volume 4 of *Coastal and Estuarine Sciences*, pp. 1–16. Washington, DC: American Geophysical Union.

Bowden, K. F. (1964). Turbulence. *Oceanography and Marine Biology: An Annual Review 2*, 11–30.

Bowers, D. G. and G. W. Lennon (1987). Observations of stratified flow over a bottom gradient in a coastal sea. *Continental Shelf Research 7*(9), 1105–1121.

Bullock, D. A. (1975, Feb). The general water circulation of Spencer Gulf, South Australia, in the period February to May. *Transcripts of the Royal Society of South Australia 99*(1), 43–53.

Butler, A. J., A. M. Depers, S. C. McKillup, and D. P. Thomas (1975). The conservation of mangrove swamps in South Australia. Report, Nature Conservation Society of South Australia, Adelaide.

Bye, J. A. T. (1976). Physical oceanography of Gulf St. Vincent and Investigator Strait. In C. R. Twidale, M. J. Tyler, and B. P. Webb (Eds.), *Natural History of the Adelaide Region*, Chapter 11, pp. 143–160. Adelaide: Royal Society of South Australia.

Bye, J. A. T. (1981, Jun). Exchange processes for upper Spencer Gulf, South Australia. *Transcripts of the Royal Society of South Australia 105*(2), 59–66.

Bye, J. A. T. and J. A. Whitehead, Jr. (1975). A theoretical model of the flow in the mouth of Spencer Gulf, South Australia. *Estuarine and Coastal Marine Science 3*, 477–481.

Carreras, P. E. and A. N. Menéndez (1990). Mathematical simulation of pollutant dispersion. *Ecological Modelling 52*, 29–40.

Carrick, N. A. (1982). Spencer Gulf prawn fishery—Surveys increase our knowledge. *SAFIC 6*(4), 3–33. The magazine of the South Australian Department of Fisheries and the South Australian Fishing Industry Council.

Carrick, N. A. (1985, Jun/Jul). Management of the Spencer Gulf prawn fishery. *SAFIC 9*(3), 6–11. The magazine of the South Australian Department of Fisheries and the South Australian Fishing Industry Council.

Carrick, N. A. (1988). The role of the industry and fleet manipulation studies in the Spencer Gulf prawn fishery. *SAFIC 12*(4), 4–9. The magazine of the Fisheries Branch of the Department of Agriculture and Fisheries and the Australian Fishing Industry Council in South Australia.

Carrick, N. A. (1989). Personal Communications. Senior Prawn Biologist, South Australian Research and Development Institute.

Carrick, N. A. (1990). Personal Communications. Senior Prawn Biologist, South Australian Research and Development Institute.

Carrick, N. A. (1991). Key factors which affect prawn recruitment and implications to harvesting prawn stocks. Grant Application and Progress Report: Project 91/3, South Australian Research and Development Institute, West Beach, Adelaide. Funded by the Fisheries Research and Development Corporation.

Carrick, N. A. (1992a). Key factors which affect prawn recruitment and implications to harvesting prawn stocks. Application Renewal: Parts B–C, South Australian Research and Development Institute, West Beach, Adelaide. Funded by the Fisheries Research and Development Corporation.

Carrick, N. A. (1992b). Key factors which affect prawn recruitment and implications to harvesting prawn stocks. Progress Report: FRDC, 91/3, South Australian Research and Development Institute, West Beach, Adelaide. Funded by the Fisheries Research and Development Corporation.

Carrick, N. A. (1994). Personal Communications. Senior Prawn Biologist, South Australian Research and Development Institute.

Chaudhry, M. H., D. E. Cass, and J. E. Edinger (1983, May). Modelling of unsteady-flow water temperatures. *Journal of Hydraulic Engineering 109*(5), 657–669.

Church, J. A. and A. M. G. Forbes (1981). Non-linear model of the tides in the Gulf of Carpentaria. *Australian Journal of Marine and Freshwater Research 32*(5), 685–697.

Church, J. A. and A. M. G. Forbes (1983). Circulation in the Gulf of Carpentaria I. Direct observations of currents in the south-east corner of the Gulf of Carpentaria. *Australian Journal of Marine and Freshwater Research 34*(1), 1–10.

Connell Eddie & Associates (1981, Apr). Stony Point and Port Stanvac port facilities study. Technical report, SANTOS Ltd., North Adelaide, South Australia.

Cray Research, Inc. (1989, May). *UNICOS® Performance Utilities Reference Manual* (B ed.). Minnesota: Cray Research, Inc. Pub. No. SR-2040.

Cray Research, Inc. (1990a, Jun). *CF77^{TM} Compiling System, Volume 1: Fortran Reference Manual* (4.0 ed.). Minnesota: Cray Research, Inc. Pub. No. SR-3071.

Cray Research, Inc. (1990b, Jun). *CF77^{TM} Compiling System, Volume 4: Parallel Processing Guide* (4.0 ed.). Minnesota: Cray Research, Inc. Pub. No. SR-3074.

Cray Research, Inc. (1990c, Jan). *Designing for Speed: An Introduction to the Cray World of Computing* (1.2 ed.). Minnesota: Cray Research, Inc.

Crisp, D. J. (1978). Genetic consequences of different reproductive strategies in marine invertebrates. In B. Battaglia and J. A. Beardmore (Eds.), *Marine Organisms: Genetics, Ecology and Evolution*, pp. 257–273. New York: Plenum Press.

Daintith, J. and R. D. Nelson (1989). *The Penguin Dictionary of Mathematics.* London: Penguin Books.

Dall, W. (1985). A review of penaid prawn biological research in Australia. In P. C. Rothlisberg, B. J. Hill, and D. J. Staples (Eds.), *Second Australian National Prawn Seminar*, Kooralbyn, Queensland, pp. 11–21. NPS2, Cleveland, Queensland.

De Wolf, P. (1973, Apr). Ecological observations on the mechanisms of dispersal of barnacle larvae during planktonic life and settling. *Netherlands Journal of Sea Research 6*(1–2), 1–129.

Delbridge, A. and J. R. L. Bernard (Eds.) (1993). *The Macquarie Concise Dictionary* (Second ed.). Macquarie University, New South Wales: The Macquarie Library Pty. Ltd.

Dight, I. J., L. Bode, and M. K. James (1990a). Modelling the larval dispersal of *Acanthaster planci*: I. Large scale hydrodynamics, Cairns Section, Great Barrier Reef Marine Park. *Coral Reefs 9*(3), 115–123. Special Issue: *Acanthaster planci*.

Dight, I. J., L. Bode, and M. K. James (1990b). Modelling the larval dispersal of *Acanthaster planci*: II. Patterns of reef connectivity. *Coral Reefs 9*(3), 125–134. Special Issue: *Acanthaster planci*.

Domanski, P. (1984). The diel migrations and distributions within a mesopelagic community in the north east Atlantic. 8. A multivariate analysis of community structure. *Progress in Oceanography 13*(3/4), 491–511.

Doty, B. E. (1992, Jul 5). *Using the Grid Analysis Display System (GrADS)* (1.3.1 ed.). Department of Meteorology, University of Maryland: Centre for Ocean–Land–Atmosphere Interactions. doty@cola.iges.org.

Du Fort, E. C. and S. P. Frankel (1953). Stability conditions in the numerical treatment of parabolic differential equations. *Mathematical Tables and Other Aids to Computation 7*, 135–152.

Easton, A. K. (1970, May). *The Tides of the Continent of Australia.* Ph. D. thesis, The Flinders University of South Australia, Adelaide. Research Paper No. 37.

Easton, A. K. (1977, Jan). Selected programs for tidal analysis and prediction. Computing Report 9, Flinders Institute of Atmospheric and Marine Sciences, The Flinders University of South Australia.

Easton, A. K. (1978, Aug). A reappraisal of the tides in Spencer Gulf, South Australia. *Australian Journal of Marine and Freshwater Research 29*(4), 467–477.

Fairweather, P. G. (1991). Implications of 'supply–side' ecology for environmental assessment and management. *Trends in Ecology and Evolution 6*(2), 60–63. Reference Edition.

Flather, R. A. and N. S. Heaps (1975, Aug). Tidal computations for Morecombe Bay. *Geophysical Journal of the Royal Astronomical Society 42*(2), 489–517.

Forbes, A. M. G. and J. A. Church (1982). Water movements and the transport of prawn larvae in the Gulf of Carpentaria. Research report 1979–1981, CSIRO Marine Laboratories. Reprint No. 1357.

Forbes, A. M. G. and J. A. Church (1983). Circulation in the Gulf of Carpentaria II. Residual currents and mean sea level. *Australian Journal of Marine and Freshwater Research 34*(1), 11–22.

Fortier, L. and W. C. Leggett (1982). Fickian transport and the dispersal of fish larvae in estuaries. *Canadian Journal of Fisheries and Aquatic Sciences 39*, 1150–1163.

Fortier, L. and W. C. Leggett (1983, Oct). Vertical migrations and transport of larval fish in a partially mixed estuary. *Canadian Journal of Fisheries and Aquatic Sciences 40*(10), 1543–1555.

Forward Jr., R. B. (1988). Diel vertical migration: Zooplankton photobiology and behaviour. *Oceanography and Marine Biology: An Annual Review 26*, 361–393.

Gaines, S. D. and M. D. Bertness (1992, Dec). Dispersal of juveniles and variable recruitment in sessile marine species. *Nature 360*, 579–580.

Garrett, C. (1983, Nov). On the initial streakiness of a dispersing tracer in two- and three-dimensional turbulence. *Dynamics of Atmospheres and Oceans 7*(4), 265–277.

Gliwicz, M. Z. (1986, Apr). Predation and the evolution of vertical migration in zooplankton. *Nature 320*, 746–748.

Greenberg, D. A. (1983, May). Modeling the mean barotropic circulation in the Bay of Fundy and Gulf of Maine. *Journal of Physical Oceanography 13*(5), 886–904.

Gu, C. (1989, May). Rkpack and its applications: Fitting smoothing spline models. Technical Report 857, University of Wisconsin-Madison, Wisconsin. Department of Statistics.

Guvanasen, V. and R. E. Volker (1983, Mar–Apr). Numerical solutions for solute transport in unconfined aquifers. *International Journal for Numerical Methods in Fluids 3*(2), 103–123.

Hale, W. G. and J. P. Margham (1988). *Collins Dictionary of Mathematics*. Collins Reference. London: Collins.

Hannan, C. A. (1984, Sep). Planktonic larvae may act like passive particles in turbulent near-bottom flows. *Limnology and Oceanography 29*(5), 1108–1116. Notes.

Harden Jones, F. R. (1984). A view from the ocean. In J. D. McCleave, G. P. Arnold, J. J. Dodson, and W. H. Neill (Eds.), *Mechanisms of Migration in Fishes*, Volume 14 of *NATO Conference Series IV, Marine Sciences*, pp. 1–26. New York: Plenum Press.

Hays, G. C., C. A. Proctor, A. W. G. John, and A. J. Warner (1994). Interspecific differences in the diel vertical migration of marine copepods: The implications of size, colour, and morphology. *Limnology and Oceanography 39*(7), 1621–1629. Notes.

Hill, A. E. (1990, Jul). Pelagic dispersal of Norway lobster *Nephrops norvegicus* larvae examined using an advection-diffusion-mortality model. *Marine Ecology Progress Series 64*, 217–226.

Hill, A. E. (1991a, Feb). Advection-diffusion-mortality solutions for investigating pelagic larval dispersal. *Marine Ecology Progress Series 70*, 117–128.

Hill, A. E. (1991b). A mechanism for horizontal zooplankton transport by vertical migration in tidal currents. *Marine Biology 111*, 485–492.

Hill, A. E. (1991c, Aug). Vertical migration in tidal currents. *Marine Ecology Progress Series 75*, 39–54.

Hill, A. E. (1995). The kinematical principles governing horizontal transport induced by vertical migration in tidal flows. *Journal of the Marine Biological Association of the United Kingdom 75*, 3–13.

Hindmarsh, A. C., P. M. Gresho, and D. F. Griffiths (1984, Sep). The stability of explicit Euler time-integration for certain finite difference approximations of the multi-dimensional advection-diffusion equation. *International Journal for Numerical Methods in Fluids 4*(9), 853–897.

Holloway, P. E. (1974, Sep). Determination of eddy diffusion coefficients for northern Spencer Gulf. Cruise Report 4, The Flinders Institute for Atmospheric and Marine Sciences, The Flinders University of South Australia, Adelaide.

Holly, Jr., F. M. and J.-M. Usseglio-Polatera (1984, Jul). Dispersion simulation in two-dimensional tidal flow. *Journal of the Hydraulic Engineering 110*(7), 905–926.

I'Anson, K. (1989, Nov). A numerical model of the movement of prawn larvae in Spencer Gulf. Honours thesis, The University of Adelaide, South Australia. Department of Applied Mathematics.

I'Anson, K., B. J. Noye, and P. J. Bills (1994). Improved coastline representation in finite-difference tidal models. In D. Stewart, H. Gardner, and D. Singleton (Eds.), *Computational Techniques and Applications: CTAC-93*, Australian National University, Canberra, Australia, pp. 302–310. World Scientific, Singapore.

Jablonski, D. and R. A. Lutz (1983, Feb). Larval ecology of marine benthic invertebrates: Paleobiological implications. *Biological Reviews 58*, 21–89.

Jackson, G. A. and R. R. Strathmann (1981, Jul). Larval mortality from offshore mixing as a link between precompetent and competent periods of settlement. *The American Naturalist 118*(1), 16–26.

James, M. K. and J. P. Scandol (1992, Sep). Larval dispersal simulations: Correlation with the Crown-of-thorns starfish outbreaks database. *Australian Journal of Marine and Freshwater Research 43*(3), 569–582.

John, H.-C. (1984). Drift of larval fishes in the ocean: Results and problems from previous studies and a proposed field experiment. In J. D. McCleave, G. P. Arnold, J. J. Dodson, and W. H. Neill (Eds.), *Mechanisms of Migration in Fishes*, Volume 14 of *NATO Conference Series IV, Marine Sciences*, pp. 39–59. New York: Plenum Press.

Johnson, D. F. and K. W. Hess (1990). Numerical simulations of Blue Crab larval dispersal and recruitment. *Bulletin of Marine Science 46*(1), 195–213.

Jordan, T. F. and R. Baker, James (1980, Jul). Vertical structure of time-dependent flow dominated by friction in a well-mixed fluid. *Journal of Physical Oceanography 10*(7), 1091–1103.

Kimmerer, W. J. and A. D. McKinnon (1987, Nov). Zooplankton in a marine bay. II. Vertical migration to maintain horizontal distributions. *Marine Ecology Progress Series 41*, 53–60.

King, C. E. and M. R. Miracle (1995). Diel vertical migration by *Daphnia longispina* in a Spanish lake: Genetic sources of distributional variation. *Limnology and Oceanography 40*(2), 226–231.

King, M. G. (1976). The western king prawn, *Penaeus latisulcatus*, in South Australia. Background paper, South Australian Department of Agriculture and Fisheries.

King, M. G. (1980, Nov). The biology of the western king prawn *Penaeus latisulcatus* Kishinouye and aspects of the fishery in South Australia. Master's thesis, The University of Adelaide, South Australia. Department of Zoology.

Kirkegaard, I. (1975). Observations of penaeid larvae around Australia. In P. C. Young (Ed.), *First Australian National Prawn Seminar*, pp. 54–59. Australian Fisheries Council, Northern Fisheries Research Committee: Australian Government Publishing Service, Canberra.

Kumar, N. (1983, Jun). Unsteady flow against dispersion in finite porous media. *Journal of Hydrology 63*(3/4), 345–358.

Lamport, L. (1994, May). LaTeX—*A Document Preparation System—User's Guide and Reference Manual* (Second ed.). Reading, Massachusetts: Addison-Wesley Publishing Co., Inc.

Lapidus, L. and N. R. Amundson (1952, Nov). Mathematics of adsorption in beds. VI. The effect of longitudinal diffusion in ion exchange and chromatographic columns. *The Journal of Physical Chemistry 56*(8), 984–988.

Lax, P. D. and R. D. Richtmyer (1956, May). Survey of the stability of linear finite difference equations. *Communications on Pure and Applied Mathematics IX*(2), 267–293.

Lax, P. D. and B. Wendroff (1964, Aug). Difference schemes for hyperbolic equations with high order of accuracy. *Communications on Pure and Applied Mathematics XVII*(3), 381–398.

Leendertse, J. J. (1967). Aspects of a computational model for long-period water-wave propagation. Technical Report RM-5294-PR, The Rand Corporation, Santa Monica, California.

Leggett, W. C. (1984). Fish migrations in coastal and estuarine environments: A call for new approaches to the study of an old problem. In J. D. McCleave, G. P. Arnold, J. J. Dodson, and W. H. Neill (Eds.), *Mechanisms of Migration in Fishes*, Volume 14 of *NATO Conference Series IV, Marine Sciences*, pp. 159–178. New York: Plenum Press.

Leis, J. M. (1991). Vertical distribution of fish larvae in the Great Barrier Reef Lagoon, Australia. *Marine Biology 109*, 157–166.

Lennon, G. W. (1981, Jan). Physical oceanography. In *Draft Environmental Impact Statement for Port and Terminal Facilities at Stony Point, South Australia—Background Papers*, Volume 2, pp. 208–234. North Adelaide, South Australia: SANTOS Limited.

Lennon, G. W., D. G. Bowers, R. A. Nunes, B. D. Scott, M. Ali, J. Boyle, C. Wenju, M. Herzfeld, G. Johansson, S. Nield, P. Petrusevics, P. Stephenson, A. A. Suskin, and S. E. A. Wijffels (1987, Jun). Gravity currents and the release of salt from an inverse estuary. *Nature 327*(6124), 695–697.

Levesque, J. M. and J. W. Williamson (1988). *A Guidebook to Fortran on Supercomputers* (First ed.). San Diego: Academic Press.

Lewis, G. D. (1993). Personal Communications. Department of Applied Mathematics, The University of Adelaide, South Australia.

Lewis, G. D., B. J. Noye, and P. J. Bills (1996, Apr). Oil spill trajectory modelling in northern Spencer Gulf. In T. H. Aung (Ed.), *Proceedings of the Ocean and Atmosphere Pacific International Conference*, The Flinders University of South Australia, pp. 177–182. South Pacific Sea Level and Climate Monitoring Project: The National Tidal Facility.

Lewis, G. D., B. J. Noye, and P. L. Evans (1996). A comparison of finite difference and Lagrangian-stochastic methods for oil slick tracking. In R. L. May and A. K. Easton (Eds.), *Computational Techniques and Applications: CTAC-95*, Melbourne, Australia, pp. 471–478. Swinburne University of Technology: World Scientific, Singapore.

Matthews, K. (1995, Nov). *A Spherical Coordinate Tidal Model of the Great Australian Bight Using a New Coastal Boundary Representation.* Ph. D. thesis, The University of Adelaide, South Australia. Department of Applied Mathematics.

Matthews, K. and B. J. Noye (1996a). A depth-averaged tidal model of the Great Australian Bight. In R. L. May and A. K. Easton (Eds.), *Computational Techniques and Applications: CTAC-95*, Melbourne, Australia, pp. 533–540. Swinburne University of Technology: World Scientific, Singapore.

Matthews, K. and B. J. Noye (1996b, Apr). A three-dimensional tidal model of the Great Australian Bight. In T. H. Aung (Ed.), *Proceedings of the Ocean and Atmosphere Pacific International Conference*, The Flinders University of South Australia, pp. 207–212. South Pacific Sea Level and Climate Monitoring Project: The National Tidal Facility.

Matthews, K., B. J. Noye, and P. J. Bills (1995, Jun). Coastline representation in computational tidal models. In *Recent Advances in Marine Science and Technology '94*, Townsville, Australia, pp. 251–261. PACON International: James Cook University of North Queensland.

Matthews, K., B. J. Noye, and P. J. Bills (1996, Aug). A new method for numerical representation of the land-water boundary in lake circulation models. *Applied Mathematical Modelling 20*, 562–571.

McGurk, M. D. (1989, Jan). Advection, diffusion and mortality of Pacific herring larvae *Clupea harengus pallasi* in Bamfield Inlet, British Columbia. *Marine Ecology Progress Series 51*, 1–18.

McShane, P. E., K. P. Black, and M. G. Smith (1988). Recruitment processes in *Haliotis rubra* (Mollusca: Gastropoda) and regional hydrodynamics in southeastern Australia imply localized dispersal of larvae. *Journal of Experimental Marine Biology and Ecology 124*, 175–203.

Micklethwaite, D. (1991). Personal Communications. Supercomputer Consultant, Cray Research (Australia).

Miller, J. M., J. P. Reed, and L. J. Pietrafesa (1984). Patterns, mechanisms and approaches to the study of migrations of estuarine-dependent fish larvae and juveniles. In J. D. McCleave, G. P. Arnold, J. J. Dodson, and W. H. Neill (Eds.), *Mechanisms of Migration in Fishes*, Volume 14 of *NATO Conference Series IV, Marine Sciences*, pp. 209–225. New York: Plenum Press.

Minchinton, T. E. and R. E. Scheibling (1991, Oct). The influence of larval supply and settlement on the population structure of barnacles. *Ecology 72*(5), 1867–1879.

Mitchell, W. L., D. A. Beard, P. J. Bills, and B. J. Noye (1984). An application of a three-dimensional tidal model to the Gulf of Carpentaria. In B. J. Noye and C. J. Fletcher (Eds.), *Computational Techniques and Applications: CTAC-83*, The University of Sydney, New South Wales, Australia, pp. 411–424. Elsevier Science Publishers B. V. (North-Holland), Amsterdam.

Natural Systems Research Pty. Ltd. (1981, Jun). Liquids project oil spill trajectory study. Technical report, SANTOS Ltd., North Adelaide, South Australia. Final Report on the Stony Point Summer Investigations.

Nihoul, J. C. J. (1975). *Marine Systems Analysis*, Volume 10 of *Elsevier Oceanography Series*, pp. 3–40. Amsterdam: Elsevier Science Publishers B. V. (North-Holland).

Nixon, J. B. (1992). From minicomputer to supercomputer: A three-dimensional tidal model optimization. In B. J. Noye, B. R. Benjamin, and L. H. Colgan (Eds.), *Computational Techniques and Applications: CTAC-91*, The University of Adelaide, South Australia, pp. 355–364. Computational Mathematics Group, Australian Mathematical Society.

Nixon, J. B. (1993a, Jan 7). Modelling prawn larvae dispersion and settlement in Spencer Gulf—Management implications. Progress Report for Stage 1: 1/7/91–31/12/92, Department of Applied Mathematics, The University of Adelaide, South Australia. Funded by the Fisheries Research and Development Corporation.

Nixon, J. B. (1993b, Jul 27). Modelling prawn larvae dispersion and settlement in Spencer Gulf—Management implications. Progress Report for Stage 2: 1/1/93–30/6/93, Department of Applied Mathematics, The University of Adelaide, South Australia. Funded by the Fisheries Research and Development Corporation.

Nixon, J. B. (1994a, Jan 27). Modelling prawn larvae dispersion and settlement in Spencer Gulf—Management implications. Progress Report for Stage 3: 1/7/93–31/12/93, Department of Applied Mathematics, The University of Adelaide, South Australia. Funded by the Fisheries Research and Development Corporation.

Nixon, J. B. (1994b, Sep 2). Modelling prawn larvae dispersion and settlement in Spencer Gulf—Management implications. Progress Report for Stage 4: 1/1/94–30/6/94, Department of Applied Mathematics, The University of Adelaide, South Australia. Funded by the Fisheries Research and Development Corporation.

Nixon, J. B. (1995a, Mar 6). Modelling prawn larvae dispersion and settlement in Spencer Gulf—Management implications. Progress Report for Stage 5: 1/7/94–31/12/94, Department of Applied Mathematics, The University of Adelaide, South Australia. Funded by the Fisheries Research and Development Corporation.

Nixon, J. B. (1995b, Nov 20). Modelling prawn larvae dispersion and settlement in Spencer Gulf—Management implications. Progress Report for Stage 6: 1/1/95–30/6/95, Department of Applied Mathematics, The University of Adelaide, South Australia. Funded by the Fisheries Research and Development Corporation.

Nixon, J. B. (1995c, Nov 20). FINAL REPORT: Modelling prawn larvae dispersion and settlement in Spencer Gulf—Management implications: 91/004. Summary Report for period: 22/6/92–30/6/95, Department of Applied Mathematics, The University of Adelaide, South Australia. Funded by the Fisheries Research and Development Corporation.

Nixon, J. B. and B. J. Noye (1990). Implicit three-level finite difference methods for the one-dimensional constant coefficient advection-diffusion equation. In W. L. Hogarth and B. J. Noye (Eds.), *Computational Techniques and Applications: CTAC-89*, Griffith University, Brisbane, Queensland, Australia, pp. 341–348. Hemisphere Publishing Corp., New York.

Nixon, J. B. and B. J. Noye (1991). Explicit three-point three-level FDMs for the one-dimensional constant-coefficient advection-diffusion equation. *Computers and Mathematics with Applications 22*(11), 47–58.

Nixon, J. B. and B. J. Noye (1993a, Jan 7). Modelling prawn larvae dispersion and settlement in Spencer Gulf—Management implications. Application Renewal for Project 91/004, Department of Applied Mathematics, The University of Adelaide, South Australia. Funded by the Fisheries Research and Development Corporation. Completed.

Nixon, J. B. and B. J. Noye (1993b, Oct 16). Prawn larvae dispersion modelling. Presentation by both authors at the Spencer Gulf and West Coast Prawn Fishermen's Association Annual General Meeting. Terrace Hotel, Adelaide, South Australia.

Nixon, J. B. and B. J. Noye (1995, Jun). Prawn larvae dispersion modelling. In *Recent Advances in Marine Science and Technology '94*, Townsville, Australia, pp. 299–309. PACON International: James Cook University of North Queensland.

Nixon, J. B. and B. J. Noye (1996a, Feb 29). Modelling prawn larvae dispersion and settlement in Spencer Gulf—Management implications. Final Report for period: 22/6/92–30/6/95, Department of Applied Mathematics, The University of Adelaide, South Australia. Funded by the Fisheries Research and Development Corporation.

Nixon, J. B. and B. J. Noye (1996b, Apr). Prawn larvae dispersion modelling. In T. H. Aung (Ed.), *Proceedings of the Ocean and Atmosphere Pacific International Conference*, The Flinders University of South Australia, pp. 241–246. South Pacific Sea Level and Climate Monitoring Project: The National Tidal Facility.

Nixon, J. B. and B. J. Noye (1996c). Prawn larvae dispersion modelling. In R. L. May and A. K. Easton (Eds.), *Computational Techniques and Applications: CTAC-95*, Melbourne, Australia, pp. 587–594. Swinburne University of Technology: World Scientific, Singapore.

Noye, B. J. (1984a). Finite difference techniques for partial differential equations. In B. J. Noye (Ed.), *Computational Techniques for Differential Equations*, Volume 83 of *North-Holland Mathematics Studies*, pp. 95–354. Amsterdam: Elsevier Science Publishers B. V. (North-Holland).

Noye, B. J. (1984b). Physical processes and pollution in the waters of Spencer Gulf. *Marine Geology 61*, 197–220. Special Issue: "The Spencer Gulf Region".

Noye, B. J. (1986). Three-point two-level finite difference methods for the one-dimensional advection equation. In B. J. Noye and R. L. May (Eds.), *Computational Techniques and Applications: CTAC-85*, The University of Melbourne, Victoria, Australia, pp. 159–192. Elsevier Science Publishers B. V. (North-Holland), Amsterdam.

Noye, B. J. (1987a). Numerical methods for solving the transport equation. In B. J. Noye (Ed.), *Numerical Modelling: Applications to Marine Systems*, Volume 145 of *North-Holland Mathematics Studies*, The University of Adelaide, South Australia, pp. 195–229. Elsevier Science Publishers B. V. (North-Holland), Amsterdam.

Noye, B. J. (1987b). Time-splitting the one-dimensional transport equation. In B. J. Noye (Ed.), *Numerical Modelling: Applications to Marine Systems*, Volume 145 of *North-Holland Mathematics Studies*, The University of Adelaide, South Australia, pp. 271–295. Elsevier Science Publishers B. V. (North-Holland), Amsterdam.

Noye, B. J. (1988). Finite-difference methods for the one-dimensional transport equation. In B. J. Noye and C. J. Fletcher (Eds.), *Computational Techniques and Applications: CTAC-87*, The University of Sydney, New South Wales, Australia, pp. 539–562. Elsevier Science Publishers B. V. (North-Holland), Amsterdam.

Noye, B. J. (1990). Some explicit three-level finite-difference simulations of advection. *Mathematics and Computers in Simulation 32*(4), 359–372.

Noye, B. J. (1991a, Oct). A compact unconditionally stable finite-difference method for transient one-dimensional advection-diffusion. *Communications in Applied Numerical Methods 7*(7), 501–512.

Noye, B. J. (1991b). Some three-level finite difference methods for simulating advection in fluids. *Computers and Fluids 19*(1), 119–140.

Noye, B. J. and P. J. Bills (1992). A three-dimensional tidal model for shallow seas. In B. J. Noye, B. R. Benjamin, and L. H. Colgan (Eds.), *Computational Techniques and Applications: CTAC-91*, The University of Adelaide, South Australia, pp. 373–384. Computational Mathematics Group, Australian Mathematical Society.

Noye, B. J., P. J. Bills, K. I'Anson, and C. C. Wong (1992). Prediction of prawn larvae movement in a coastal sea. In B. J. Noye, B. R. Benjamin, and L. H. Colgan (Eds.), *Computational Techniques and Applications: CTAC-91*, The University of Adelaide, South Australia, pp. 385–392. Computational Mathematics Group, Australian Mathematical Society.

Noye, B. J., P. J. Bills, and G. D. Lewis (1994). Prediction of oil slick movement in northern Spencer Gulf. In D. Stewart, H. Gardner, and D. Singleton (Eds.), *Computational Techniques and Applications: CTAC-93*, Australian National University, Canberra, Australia, pp. 320–328. World Scientific, Singapore.

Noye, B. J. and K. J. Hayman (1986). Accurate finite difference methods for solving the advection-diffusion equation. In B. J. Noye and R. L. May (Eds.), *Computational Techniques and Applications: CTAC-85*, The University of Melbourne, Victoria, Australia, pp. 137–157. Elsevier Science Publishers B. V. (North-Holland), Amsterdam.

Noye, B. J. and K. J. Hayman (1994). New LOD and ADI methods for the two-dimensional diffusion equation. *International Journal of Computer Mathematics 51*, 215–228.

Noye, B. J., R. L. May, and M. D. Teubner (1981). Three-dimensional numerical model of tides in Spencer Gulf. *Ocean Management 6*, 137–147.

Noye, B. J., R. L. May, and M. D. Teubner (1982). A three dimensional tidal model for a shallow gulf. In B. J. Noye (Ed.), *Numerical Solutions of Partial Differential Equations*, The University of Melbourne, Victoria, Australia, pp. 417–436. Elsevier Science Publishers B. V. (North-Holland), Amsterdam.

Noye, B. J. and H. H. Tan (1989). Finite difference methods for solving the two-dimensional advection-diffusion equation. *International Journal for Numerical Methods in Fluids 9*, 75–98.

Noye, B. J. and K. C. S. Tronson (1978). Finite difference techniques applied to the simulation of tides and currents in gulfs. In B. J. Noye (Ed.), *Numerical Simulation of Fluid Motion*, Monash University, Melbourne, Australia, pp. 285–355. Elsevier Science Publishers B. V. (North-Holland), Amsterdam.

Nunes, R. A. and W. Lennon, Geoff (1986). Physical property distributions and seasonal trends in Spencer Gulf, South Australia: An inverse estuary. *Australian Journal of Marine and Freshwater Research 37*, 39–53.

O'Brien, G. G., M. A. Hyman, and S. Kaplan (1950). A study of the numerical solution of partial differential equations. *Journal of Mathematics and Physics XXIX*, 223–251.

Okubo, A. (1971). Oceanic diffusion diagrams. *Deep-Sea Research 18*, 789–802.

Okubo, A. (1976). Remarks on the use of 'diffusion diagrams' in modelling scale-dependent diffusion. *Deep-Sea Research 23*, 1213–1214.

Okubo, A. (1980). *Diffusion and Ecological Problems: Mathematical Models*, Volume 10 of *Lecture Notes in Biomathematics*. Berlin: Springer-Verlag.

Okubo, A. (1986, Apr). Planktonic micro-communities in the sea: Biofluid mechanical view. In A. Hastings (Ed.), *Lecture Notes in Biomathematics*, Volume 77 of *Community Ecology*, Chapter 2, pp. 13–24. Berlin: Springer-Verlag. A workshop held at Davis, California, April 1986.

Oliver, J. K., B. A. King, B. L. Willis, R. C. Babcock, and E. Wolanski (1992, Jul/Aug). Dispersal of coral larvae from a lagoonal reef—II. Comparisons between model predictions and observed concentrations. *Continental Shelf Research 12*(7/8), 873–889.

Orlanski, I. (1976). A simple boundary condition for unbounded hyperbolic flows. *Journal of Computational Physics 21*, 251–269.

Ozmidov, R. V. (1958). On the calculation of horizontal turbulent diffusion of the pollution patches in the sea. *Doklady Akademii Nauk SSSR 120*, 761–763.

Patashnik, O. (1988a, 8 Feb). *BibTEXing*. Stanford University. Documentation for general BibTEX users.

Patashnik, O. (1988b, 8 Feb). *Designing BibTEX Styles*. Stanford University. The part of BibTEX's documentation that's not meant for general users.

Penn, J. W. (1975). The influence of tidal cycles on the distributional pathway of *Penaeus latisulcatus* Kishinouye in Shark Bay, Western Australia. *Australian Journal of Marine and Freshwater Research 26*, 93–102.

Pitt, V. H. (Ed.) (1988). *The Penguin Dictionary of Physics*. London: Penguin Books.

Possingham, H. P. and J. Roughgarden (1990, Jun). Spatial population dynamics of a marine organism with a complex life cycle. *Ecology 71*(3), 973–985.

Power, J. H. (1984). Advection, diffusion, and drift migrations of larval fish. In J. D. McCleave, G. P. Arnold, J. J. Dodson, and W. H. Neill (Eds.), *Mechanisms of Migration in Fishes*, Volume 14 of *NATO Conference Series IV, Marine Sciences*, pp. 27–37. New York: Plenum Press.

Prandle, D. (1982, Nov). The vertical structure of tidal currents and other oscillatory flows. *Continental Shelf Research 1*(2), 191–207.

Provis, D. G. and G. W. Lennon (1983, Apr). Eddy viscosity and tidal cycles in a shallow sea. *Estuarine, Coastal and Shelf Science 16*(4), 351–361.

Pugh, D. T. (1987). *Tides, Surges and Mean-Sea Level*. Wiley.

Pugh, P. R. (1984). The diel migrations and distributions within a mesopelagic community in the north east Atlantic. 7. Siphonophores. *Progress in Oceanography 13*(3/4), 461–489.

Richards, S. A. (1995). Personal Communications.

Richards, S. A. (1996, Mar). *Mathematical Models of Zooplankton Dispersal*. Ph. D. thesis, The University of Adelaide, South Australia. Department of Applied Mathematics.

Richards, S. A. and B. J. Noye (1994). Solving the diffusion equation using adaptive mesh refinement. In D. Stewart, H. Gardner, and D. Singleton (Eds.), *Computational Techniques and Applications: CTAC-93*, Australian National University, Canberra, Australia, pp. 428–436. World Scientific, Singapore.

Richards, S. A., H. P. Possingham, and B. J. Noye (1995, Jun). Larval dispersion along a straight coast with tidal currents: Complex distribution patterns from a simple model. *Marine Ecology Progress Series 122*(1), 59–71.

Richards, S. A., H. P. Possingham, and B. J. Noye (1996). Diel vertical migration: Modelling light-mediated mechanisms. *Journal of Plankton Research*, 33. In press.

Richter, G. (1973). Field and laboratory observations on the diurnal vertical migration of marine gastropod larvae. *Netherlands Journal of Sea Research 7*, 126–134. 7th European Symposium on Marine Biology.

Ringelberg, J. (1995). Changes in light intensity and diel vertical migration: A comparison of marine and freshwater environments. *Journal of the Marine Biological Association of the United Kingdom 75*, 15–25.

Roe, H. S. J. (1984a). The diel migrations and distributions within a mesopelagic community in the north east Atlantic. 2. Vertical migrations and feeding of mysids and decapod crustacea. *Progress in Oceanography 13*(3/4), 269–318.

Roe, H. S. J. (1984b). The diel migrations and distributions within a mesopelagic community in the north east Atlantic. 4. The copepods. *Progress in Oceanography 13*(3/4), 353–388.

Roe, H. S. J., M. V. Angel, J. Badcock, P. Domanski, P. T. James, P. R. Pugh, and M. H. Thurston (1984). The diel migrations and distributions within a mesopelagic community in the north east Atlantic. 1. Introduction and sampling procedure. *Progress in Oceanography 13*(3/4), 245–268.

Roe, H. S. J. and J. Badcock (1984). The diel migrations and distributions within a mesopelagic community in the north east Atlantic. 5. Vertical migrations and feeding of fish. *Progress in Oceanography 13*(3/4), 389–424.

Roe, H. S. J., P. T. James, and M. H. Thurston (1984). The diel migrations and distributions within a mesopelagic community in the north east Atlantic. 6. Medusae, ctenophores, amphipods and euphausiids. *Progress in Oceanography 13*(3/4), 425–460.

Rokicki, T. (1993). *DVIPS: A TEX Driver* (5.495 ed.). Stanford University. FAX: (415) 327-3329, e-mail: `rokiki@cs.stanford.edu`.

Rothlisberg, P. C. (1982). Vertical migration and its effect on the dispersal of penaeid shrimp larvae in the Gulf of Carpentaria, Australia. *Fishery Bulletin 80*(3), 541–554.

Rothlisberg, P. C., J. A. Church, and A. M. G. Forbes (1983). Modelling the advection of vertically migrating shrimp larvae. *Journal of Marine Research 41*(3), 511–538.

Rothlisberg, P. C. and C. J. Jackson (1987). Larval ecology of penaeids of the Gulf of Carpentaria, Australia. II. Hydrographic environment of *Penaeus merguiensis*, *P. esculentus*, *P. semisulcatus* and *P. latisulcatus*, zoeae. *Australian Journal of Marine and Freshwater Research 38*(1), 19–28.

Rothlisberg, P. C., C. J. Jackson, and R. C. Pendrey (1985). Distribution and abundance of early penaeid larvae in the Gulf of Carpentaria, Australia. In P. C. Rothlisberg, B. J. Hill, and D. J. Staples (Eds.), *Second Australian National Prawn Seminar*, Kooralbyn, Queensland, pp. 23–30. NPS2, Cleveland, Queensland.

Rothlisberg, P. C., C. J. Jackson, and R. C. Pendrey (1987). Larval ecology of penaeids of the Gulf of Carpentaria, Australia. I. Assessing the reproductive activity of five species of *Penaeus* from the distribution and abundance of the zoeal stages. *Australian Journal of Marine and Freshwater Research 38*(1), 1–17.

Roughgarden, J., S. D. Gaines, and H. P. Possingham (1988, Sep). Recruitment dynamics in complex life cycles. *Science 241*(3), 1460–1466.

Royal Australian Survey Corps (1981, May). Map no. 2389. Hydrographic Service, Royal Australian Navy, Sydney. South Australia, St. Vincent and Spencer Gulfs.

Royal Australian Survey Corps (1982b, Apr). Map no. Aus 342. Hydrographic Service, Royal Australian Navy, Sydney. Australia—South Coast, South Australia, Streaky Bay to Whidbey Isles.

Royal Australian Survey Corps (1982a, Jan). Map no. Aus 778. Hydrographic Service, Royal Australian Navy, Sydney. Australia—South Coast, South Australia, Point Riley to Port Augusta.

Royal Australian Survey Corps (1984, Mar). Map no. 1008. Hydrographic Service, Royal Australian Navy, Sydney. Australia—South Coast, Backstairs Passage to Cape Martin.

Royal Australian Survey Corps (1989, Jul). Map no. Aus 777. Hydrographic Service, Royal Australian Navy, Sydney. Australia—South Coast, South Australia, Winceby Island to Point Riley.

Royal Australian Survey Corps (1990c, Nov). Map no. Aus 341. Hydrographic Service, Royal Australian Navy, Sydney. Australia—South Coast, South Australia, Twin Rocks to Streaky Bay.

Royal Australian Survey Corps (1990a, Oct). Map no. Aus 776. Hydrographic Service, Royal Australian Navy, Sydney. Australia—South Coast, South Australia, Williams Island to Winceby Island.

Royal Australian Survey Corps (1990b, Sep). Map no. Aus 781. Hydrographic Service, Royal Australian Navy, Sydney. Australia—South Coast, South Australia, Gulf of St. Vincent (Northern Portion).

Royal Australian Survey Corps (1991, May). Map no. Aus 343. Hydrographic Service, Royal Australian Navy, Sydney. Australia—South Coast, South Australia, Whidbey Island to Cape Du Coudic.

Royal Australian Survey Corps (1992, Nov). Map no. Aus 780. Hydrographic Office, Royal Australian Navy, Sydney. Australia—South Coast, Port Adelaide to Backstairs Passage.

Sale, P. F. (1990, Jan). Recruitment of marine species: Is the bandwagon rolling in the right direction? *Trends in Ecology and Evolution 5*(1), 25–27. Reference Edition.

SANTOS Limited (1981, Jul). Draft environmental impact statement for port and terminal facilities at Stony Point—South Australia. Technical report, Social and Ecological Assessment Pty. Ltd., North Adelaide, South Australia.

Scandol, J. P. and M. K. James (1992, Sep). Hydrodynamics and larval dispersal: A population model of *Acanthaster planci* on the Great Barrier Reef. *Australian Journal of Marine and Freshwater Research 43*(3), 583–596.

Schwiderski, E. W. (1980). On charting global ocean tides. *Reviews of Geophysics and Space Physics 18*, 243–268.

Shepherd, S. A. and R. C. Sprigg (1976). Substrates, sediments and subtidal ecology of Gulf St. Vincent and Investigator Strait. In C. R. Twidale, M. J. Tyler, and B. P. Webb (Eds.), *Natural History of the Adelaide Region*, Chapter 12, pp. 161–174. Adelaide: Royal Society of South Australia.

Smith, G. D. (1985). *Numerical Solution of Partial Differential Equations: Finite Difference Methods* (Third ed.). Oxford Applied Mathematics and Computing Science Series. Oxford: Clarendon Press.

Steedman, R. (1982). Review of Northern Spencer Gulf water circulation and dispersion. Report R117, Iron Triangle Study Group, South Australia.

Steinberg, C. R. (1983, Dec). Tidal exchanges at the mouth of Spencer Gulf, South Australia. Honours thesis, The Flinders University of South Australia, Adelaide, South Australia. School of Earth Sciences.

Sundqvist, H. and G. Veronis (1970). A simple finite-difference grid with non-constant intervals. *Tellus 1*, 26–31.

Teubner, M. D., P. E. Rasser, and B. J. Noye (1996). A systematic approach to calibrating hydrodynamic numerical models. In R. L. May and A. K. Easton (Eds.), *Computational Techniques and Applications: CTAC-95*, Melbourne, Australia, pp. 763–770. Swinburne University of Technology: World Scientific, Singapore.

Theisen, T. O. (1992). *ghostview—View PostScript documents using* `ghostscript` (1.4.1 ed.). Madison, Wisconsin: Department of Computer Sciences, University of Wisconsin-Madison. This is but a Unix `man` page.

Thomas, L. H. (1949). Elliptic problems in linear difference equations over a network. Technical report, Watson Scientific Computing Laboratory, Columbia University, New York.

Tronson, K. C. S. (1975). The hydraulics of the South Australian gulf system. Part 2: Resonances. *Australian Journal of Marine and Freshwater Research 26*, 363–374.

Uvarov, E. B. and A. Isaacs (1988). *The Penguin Dictionary of Science* (Sixth ed.). London: Penguin Books.

van Dam, G. C. (1982). Models of dispersion. In G. Kullenberg (Ed.), *Pollutant Transfer and Transport in the Sea*, Volume I, Chapter 2, pp. 91–160. Boca Raton, Florida: CRC Press, Inc.

Warming, R. F. and B. J. Hyett (1974, Feb). The modified equation approach to the stability and accuracy analysis of finite-difference methods. *Journal of Computational Physics 14*(2), 159–179.

Wichura, M. J. (1987, Sep). *The PiCTEX Manual* (1.1 ed.). Chicago, Illinois: The University of Chicago.

Wickins, J. F. (1976). Prawn biology and culture. *Oceanography and Marine Biology: An Annual Review 14*, 435–507.

Winstanley, R. H. (1975, May). Western king prawns caught in Victorian waters. *Australian Fisheries* (5), 16–17.

Wolanski, E. (1993). Facts and numerical artefacts in modelling the dispersal of crown-of-thorns starfish larvae in the Great Barrier Reef. *Australian Journal of Marine and Freshwater Research 44*(3), 427–436.

Wong, C. C. (1990, Oct). Numerical simulation of prawn larvae dispersal in Spencer Gulf. Honours thesis, The University of Adelaide, South Australia. Department of Applied Mathematics.

Wroblewski, J. S. and E. E. Hofmann (1989). U.S. Interdisciplinary modeling studies of coastal-offshore exchange processes: Past and future. *Progress in Oceanography 23*(2), 65–99.

Wu, J. (1982). Wind stress coefficients over sea surface from breeze to hurricane. *Journal of Geophysical Research 87*, 9704–9706.

Wu, J. (1990, Sep). Environmental factors affecting the survival and growth of the western king prawn, *Penaeus latisulcatus*, under aquaculture conditions in Spencer Gulf, South Australia. Master's thesis, The University of Adelaide, South Australia. Mawson Graduate Centre for Environmental Studies.

Zed, P. A. (1980, Aug). The biology of the western king prawn *Penaeus latisulcatus* Kishinouye 1900 in South Australia. Master's thesis, The University of Adelaide, South Australia. Department of Zoology.

Glossary of Notation

° : degree (unit)

- : dimensionless (notation)

! : factorial (notation)

! : FORTRAN comment delimiter (terminology)

% : percentage (notation)

^{c} : radian (unit)

1D : one-dimensional (abbreviation)

2D : two-dimensional (abbreviation)

3D : three-dimensional (abbreviation)

0 : Type 1 grid element—whose elevation grid–point lies on land (notation)

1 : Type 1 grid element—whose elevation grid–point lies on water within model (notation)

2 : Type 2 grid element—whose elevation grid–point lies on an open sea boundary (notation)

4 : Type 4 grid element—whose elevation grid–point lies on water outside model (notation)

1's : computational neighbourhood of Type 1 elements (notation)

0-1's : computational neighbourhood of Type 0 and 1 elements (notation)

0-1-2's : computational neighbourhood of Type 0, 1, and 2 elements (notation)

α : minimum absolute (or background) value for N_η ($\mathrm{m^2\,s^{-1}}$)

α : diffusion parameter ($\mathrm{m^2\,s^{-1}}$)

α_x, α_y : diffusion parameter in x and y direction, respectively ($\mathrm{m^2\,s^{-1}}$)

a : reduced horizontal eddy coefficient ($\mathrm{s^{-1}}$)

a_N, a_T : numerical and true wave amplitude, respectively ($\mathrm{m^{-2}}$)

$a_{m,b}$: tide–height amplitude of tidal constituent m at open boundary grid element b (m)

$A_{4/3}$: dissipation parameter associated with (7.6.1) ($\mathrm{m^{2/3}\,s^{-1}}$)

$A_{23/20}$: dissipation parameter associated with (7.6.5) ($\mathrm{m^{17/20}\,s^{-1}}$)

a : lower diagonal of tri-diagonal matrix passed to thomas subroutine (notation)

AD : advection–diffusion (abbreviation)

ADM : advection–diffusion–mortality (abbreviation)

AS : analytical solution (abbreviation)

β : constant used in quadratic formulation of vertical eddy viscosity coefficient (-)

b : index of open boundary grid element (notation)

b : one quarter of width of a tracer concentration field (m)

b_0 : one quarter of width of an initial Gaussian tracer concentration field (m)

`b` : centre diagonal of tri-diagonal matrix passed to `thomas` subroutine (notation)

BC : boundary condition (abbreviation)

BoM : Bureau of Meteorology (abbreviation)

BS : backward-space finite-difference approximation (abbreviation)

BT : backward-time finite-difference approximation (abbreviation)

c : radiated wave celerity at open boundary grid elements ($\mathrm{m\,s^{-1}}$)

c_{10} : sea–surface drag coefficient (-)

c : index of tidal constituent (notation)

c : Courant number (-)

c_x, c_y : Courant number in x and y direction, respectively (-)

$c_{\max}$: model maximum Courant number satisfying Courant–Friedrichs–Lewy condition (-)

C : number of tidal constituents c (notation)

C : depth-averaged concentration of larvae per unit volume ($\mathrm{m^{-3}}$)

$C_{q,p-q}$: equivalent partial differential equation truncation error coefficient (notation)

cm : centimetre (unit)

`c` : upper diagonal of tri-diagonal matrix passed to `thomas` subroutine (notation)

`cf77` : CRAY Y-MP UNICOS `FORTRAN` 77 compiler (terminology)

CFL : Courant–Friedrichs–Lewy (abbreviation)

CPU : central processor unit (abbreviation)

CRAY : vector supercomputer (terminology)

CS : centred-space finite-difference approximation (abbreviation)

CST : central standard time (Australian, $-9.5\,\mathrm{h}$ GMT) (abbreviation)

CT : centred-time finite-difference approximation (abbreviation)

`CALL` : `FORTRAN` reserved word (terminology)

`CDIR$` : `cf77` compiler directive reserved word (terminology)

`CFPP$` : `cf77` `FORTRAN` preprocessor reserved word (terminology)

CONTINUE : FORTRAN reserved word (terminology)

$\boldsymbol{d}$: right hand side vector of augmented matrix solved by thomas subroutine (notation)

d : day (unit)

d : vector of augmented matrix passed to thomas subroutine (notation)

DEC : Digital Equipment Corporation (abbreviation)

DEP : Department of Environment and Planning (abbreviation)

DF : Du Fort and Frankel (abbreviation)

ε : average tide–height amplitude and phase error, combined by means of expressing tide–height constants as a complex polar vector for all constituents at all calibration stations (m)

η : σ-transformation vertical coordinate mapping (-)

$\Delta\eta$: constant depth–level spacing (-)

η_k : transformed depth at level k, in terms of η coordinate (-)

$\Delta\eta_k$: dimensionless distance between η_k and η_{k+1} depth–levels (-)

η_p : modified equivalent partial differential equation truncation error coefficient (notation)

e : phase error (m)

e : transcendental number, exponential (-)

E : EPDE or MEPDE truncation error (notation)

E : east (notation)

E : east (abbreviation)

EAC : East Australian Current (abbreviation)

EIS : environmental impact statement (abbreviation)

E-W : east-west (abbreviation)

EPDE : equivalent partial differential equation (abbreviation)

ESS : sum of squares error (abbreviation)

ELSE : FORTRAN reserved word (terminology)

ELSEIF : FORTRAN reserved word (terminology)

ENDIF : FORTRAN reserved word (terminology)

.EQ. : FORTRAN reserved word (terminology)

f : Coriolis parameter (s^{-1})

f_i : Coriolis parameter at ζ grid–point of grid element i (s^{-1})

f_m : amplitude correction factor for constituent m (-)

$F(\eta)$: prescribed η-variation of vertical eddy viscosity coefficient (-)

F_z : z component of external body forces ($m\,s^{-2}$)

f66 : DEC VAX VMS **FORTRAN** 66 compiler (terminology)

f77 : Sun SPARC UNIX **FORTRAN** 77 compiler (terminology)

FDE : finite-difference equation (abbreviation)

FDM : finite-difference method (abbreviation)

FIAMS : The Flinders Institute for Atmospheric and Marine Sciences (abbreviation)

FRDC : Fisheries Research and Development Corporation (abbreviation)

FT : forward-time finite-difference approximation (abbreviation)

FTCS : forward-time centred-space (abbreviation)

FORTRAN : computer language (terminology)

γ_1 : minimum of prescribed vertical eddy viscosity function at sea–bed and sea–surface (-)

$\gamma_{m,b}$: tide–height phase of tidal constituent m at open boundary grid element b (°)

g : vertical acceleration due to gravity ($\mathrm{m\,s^{-2}}$)

G : von Neumann amplification factor ($\mathrm{m^{-2}}$)

GB : Gigabyte (abbreviation)

GCV : generalised cross validation (abbreviation)

GMT : Greenwich Meant Time (abbreviation)

GrADS : Grid Analysis Display System (abbreviation)

GIS : graphical information system (abbreviation)

GOTO : **FORTRAN** reserved word (terminology)

h : depth below mean sea level (m)

h_b : h-depth at ζ grid–point of boundary grid element b (m)

h_i : h-depth at ζ grid–point of grid element i (m)

$h_{\max}$: model maximum h-depth (m)

H : total depth (m)

H_b : H-depth at ζ grid–point of boundary grid element b (m)

H_i : H-depth at ζ grid–point point of grid element i (m)

H_i^n : H_i-depth at time–level n (m)

h : hour (unit)

hrs : hours (abbreviation)

$\imath$: $= \sqrt{-1}$ (notation)

i : maximum larval concentration y grid coordinate (notation)

i : index of a central horizontal grid element (notation)

$i_1 - 1$: index of element *above* and to *left* of element i (notation)

$i_1 + 1$: index of element *above* and to *right* of element i (notation)

i_{11} : index of element *above* element i_1 (notation)

i_1 : index of element *above* element i (notation)

$i - 1$: index of element to *left* of element i (notation)

$i + 1$: index of element to *right* of element i (notation)

$i_2 - 1$: index of element *below* and to *left* of element i (notation)

$i_2 + 1$: index of element *below* and to *right* of element i (notation)

i_{22} : index of element *below* element i_2 (notation)

i_2 : index of element *below* element i (notation)

$i + 2$: index of element to *right* of element $(i + 1)$ (notation)

I : number of ISLW to MSL correction iterations required (notation)

`i` : grid element **FORTRAN** index variable (notation)

I/O : input/output (abbreviation)

IC : initial condition (abbreviation)

ISD : Information Services Division (abbreviation)

ISLW : Indian Spring Low Water (abbreviation)

IF : **FORTRAN** reserved word (terminology)

j : maximum larval concentration x grid coordinate (notation)

j : index of present grid–line in x direction (notation)

J : number of grid–spacings in x direction (notation)

κ : parameter controlling depth–level concentration in Kappa method (-)

k : index of present grid–line in y direction (notation)

k : index of depth–level in vertical η-direction (notation)

K : number of grid–spacings in y direction (notation)

K : horizontal eddy diffusion coefficient ($m^2\,s^{-1}$)

$K_{4/3}$: horizontal eddy diffusion coefficient determined using (7.6.1) ($m^2\,s^{-1}$)

$K_{23/20}$: horizontal eddy diffusion coefficient determined using (7.6.5) ($m^2\,s^{-1}$)

K_h : horizontal eddy diffusion coefficient ($m^2\,s^{-1}$)

K_{Bye} : horizontal eddy diffusion coefficient determined by Bye (1981) ($m^2\,s^{-1}$)

K_{sg} : horizontal eddy diffusion coefficient determined for Spencer Gulf ($m^2\,s^{-1}$)

$\boldsymbol{K}$: depth-averaged diffusion tensor ($m^2\,s^{-1}$)

$K_{xx}, K_{xy}, K_{yx}, K_{yy}$: components of $\boldsymbol{K}$ tensor ($m^2\,s^{-1}$)

kg : kilogram (unit)

km : kilometre (unit)

kn : knot (unit)

k : depth–interval FORTRAN index variable (notation)

K_1 : luni-solar diurnal constituent, period 23.93 h (notation)

λ : larval loss through mortality per unit time (s^{-1})

$\mathcal{L}_\Delta$: finite-difference operator (notation)

LOD : locally one-dimensional (abbreviation)

LW : Lax and Wendroff (abbreviation)

μ : wave propagation characteristic relative wave speed (-)

μ : average tide–height amplitude error over all tidal constituents and calibration stations (m)

μ_c : average tide–height amplitude error for tidal constituent c over all calibration stations s (m)

$\mu^o_{c,s}$: observed tide–height amplitude of tidal constituent c at calibration station s (m)

$\mu^p_{c,s}$: predicted tide–height amplitude of tidal constituent c at calibration station s (m)

μ_m : phase correction for tidal constituent m (°)

m : index of tidal constituent (notation)

m : larval mortality rate (d^{-1})

M : number of dominant tidal constituents m (notation)

M : depth-averaged larval loss through mortality per unit time (s^{-1})

$\max\{q_n\}$: maximum of quantity q over all grid elements n (notation)

$\min\{p, q\}$: minimum of quantities p and q (notation)

M_2 : principal lunar constituent, period 12.42 h (notation)

m : metre (unit)

min : minute (unit)

mm : millimetre (unit)

mo : month (unit)

MB : Megabyte (abbreviation)

MEPDE : modified equivalent partial differential equation (abbreviation)

MFLOPS : millions of floating point operations per second (abbreviation)

MFTCS : "modified" forward-time centred-space (abbreviation)

MSL : mean sea level (abbreviation)

$\text{MSL}^{(i)}$: ith iterate of ISLW to MSL correction (notation)

$\text{MSL}_n^{(I)}$: depth of $\text{MSL}^{(I)}$ iterate at grid element n (m)

`make` : UNIX type operating system compilation command (terminology)

`makefile` : UNIX type operating system compilation file (terminology)

$\boldsymbol{n}$: outward vector normal to model coastline (notation)

n : coordinate of outward normal direction $\boldsymbol{n}$ (m)

n : index of grid–line in t direction (notation)

N_1, N_2 : number of Type 1 and Type 2 grid elements, respectively (notation)

N_x, N_y, N_z : eddy viscosity coefficient in x, y, and z direction, respectively ($\text{m}^2\,\text{s}^{-1}$)

N_λ : grid–spacings per wavelength (-)

N_1 : largest N_λ for which there is a wave propagation error of at least 1% (-)

N_η : transformed vertical eddy viscosity coefficient ($\text{m}^2\,\text{s}^{-1}$)

$N_{\max}$: maximum value of prescribed vertical eddy viscosity function ($\text{m}^2\,\text{s}^{-1}$)

N : north (notation)

N : Newton = $\text{kg}\,\text{m}\,\text{s}^{-1}$ (unit)

`ni` : number of grid elements i (notation)

`nk` : number of depth–intervals k (notation)

`nk` + 1 : number of depth–levels, including surface and bed levels (notation)

N : north (abbreviation)

NCC : National Climate Centre (abbreviation)

NCN : neighbourhood configuration number (abbreviation)

NE : north east (abbreviation)

NM : nautical mile (abbreviation)

NNE : north north east (abbreviation)

NNW : north north west (abbreviation)

N-S : north-south (abbreviation)

NTF : National Tidal Facility (abbreviation)

NW : north west (abbreviation)

`.NE.` : **FORTRAN** reserved word (terminology)

ω : depth-dependent velocity in η direction ($\text{m}\,\text{s}^{-1}$)

ω_i : ω-velocity at ζ grid–point of grid element i ($\text{m}\,\text{s}^{-1}$)

$\omega_{i,k}^n$: ω_i-velocity at depth–level k, time–level n ($\text{m}\,\text{s}^{-1}$)

ω^n : field of ω-velocity values at time–level n ($\mathrm{m\,s^{-1}}$)

ω_m : angular frequency of tidal constituent m ($^\circ\,\mathrm{s^{-1}}$)

$\omega^o_{c,s}$: observed phase of tidal constituent c at station s ($^\circ$)

$\omega^p_{c,s}$: predicted phase of tidal constituent c at station s ($^\circ$)

Ω : angular velocity of rotation for Earth ($\mathrm{s^{-1}}$)

$\mathrm{O}\{q\}$: of the order of q (notation)

$\mathrm{O_1}$: principal lunar diurnal constituent, period 25.82 h (notation)

`omega_calcn` : `ted` subroutine responsible for z velocity component calculation (terminology)

π : transcendental number, ratio of circle circumference to diameter (-)

ϕ : average phase error over all tidal constituents c and calibration stations s ($^\circ$)

ϕ_c : average phase error for tidal constituent c over all calibration stations s ($^\circ$)

$\phi^o_{c,s}$: observed phase of tidal constituent c at calibration station s ($^\circ$)

$\phi^p_{c,s}$: predicted phase of tidal constituent c at calibration station s ($^\circ$)

Φ : latitude north (negative in southern hemisphere) ($^\circ$)

p : Reynolds time-averaged pressure ($\mathrm{N\,m^{-2}}$)

p_a : Reynolds time-averaged atmospheric pressure ($\mathrm{N\,m^{-2}}$)

p_{a_i} : p_a at ζ grid–point of grid element i ($\mathrm{N\,m^{-2}}$)

$\mathrm{P_1}$: lunar diurnal constituent, period 24.07 h (notation)

PDE : partial differential equation (abbreviation)

PLI : preferred light intensity (abbreviation)

$q|_{z=z^*}$: quantity q evaluated at $z = z^*$ (notation)

$\boldsymbol{q}$: solution vector of augmented matrix solved by `thomas` subroutine (notation)

$\boldsymbol{Q}$: depth-dependent horizontal velocity matrix (notation)

`q` : velocity matrix returned by `thomas` subroutine (notation)

`qstore` : `ted` subroutine responsible for time–centring and windowing (terminology)

ρ : density of sea water ($\mathrm{kg\,m^{-3}}$)

ρ_a : density of air ($\mathrm{kg\,m^{-3}}$)

RPH : relative peak height (abbreviation)

RRC : relative rate of change (abbreviation)

`REAL` : `FORTRAN` reserved word (terminology)

σ_x^2, σ_y^2 : Gaussian distribution variance in x and y direction, respectively ($\mathrm{m^2}$)

$\Delta\sigma$: smallest resolvable tidal constituent speed difference ($^\circ\,\mathrm{h^{-1}}$)

s : index of tidal calibration station (notation)

s : diffusion number (-)

s_x, s_y : diffusion number in x and y direction, respectively (-)

S : number of tidal calibration stations s (-)

S_x, S_y : surface wind–stress in x and y direction, respectively ($\mathrm{kg\,m^{-1}\,s^{-2}}$)

s : second (unit)

S : south (notation)

S_2 : principal solar constituent, period 12.00 h (notation)

S : south (abbreviation)

SA : South Australia (abbreviation)

SARDI : South Australian Research and Development Institute (abbreviation)

SE : south east (abbreviation)

SG : Spencer Gulf (abbreviation)

SGWCPFA : Spencer Gulf and West Coast Prawn Fishermen's Association (abbreviation)

SPARC : scalar workstation (terminology)

SSE : south south east (abbreviation)

SSW : south south west (abbreviation)

SW : south west (abbreviation)

`SHORTLOOP` : `cf77` compiler directive (terminology)

$\hat{\tau}$: larval concentration ($\mathrm{m^{-2}}$)

τ : finite-difference approximation to $\hat{\tau}$ ($\mathrm{m^{-2}}$)

τ_j^n : approximation to $\hat{\tau}(x,t)$ at (j,n) grid–point ($\mathrm{m^{-2}}$)

$\tau_{j,k}^n$: approximation to $\hat{\tau}(x,y,t)$ at (j,k,n) grid–point ($\mathrm{m^{-2}}$)

t : temporal coordinate (s)

Δt : grid–spacing in t direction (s)

$\Delta t_{\max}$: model maximum Δt satisfying Courant–Friedrichs–Lewy condition (s)

T : final time at which solution is required (s)

$\boldsymbol{T}$: matrix inverted by `thomas` subroutine (notation)

T : true, with respect to north (notation)

`ted` : three-dimensional eddy viscosity tidal model (abbreviation)

`thomas` : `ted` subroutine responsible for matrix inversion (terminology)

`THEN` : `FORTRAN` reserved word (terminology)

u_{10} : x component of wind velocity recorded 10 m above mean sea level ($\mathrm{m\,s^{-1}}$)

$u_{10}|_i^n$: u_{10}-velocity at ζ grid–point of grid element i, time–level n ($\mathrm{m\,s^{-1}}$)

u : Reynolds time-averaged depth-dependent velocity in x direction ($\mathrm{m\,s^{-1}}$)

u_a : constant u-velocity ($\mathrm{m\,s^{-1}}$)

u_i : u-velocity at u grid–point of grid element i ($\mathrm{m\,s^{-1}}$)

$u_{i,k}^n$: u_i-velocity at depth–level k, time–level n ($\mathrm{m\,s^{-1}}$)

u^n : field of u-velocity values at time–level n ($\mathrm{m\,s^{-1}}$)

u_N : numerical wave speed ($\mathrm{m\,s^{-1}}$)

U : Reynolds time-averaged depth-averaged velocity in x direction ($\mathrm{m\,s^{-1}}$)

$U^\star(\eta)$: integral of u-velocity over interval $\eta^\star \in [0, \eta]$ ($\mathrm{m\,s^{-1}}$)

U_i^n : U-velocity at horizontal grid–point u_i at time–level n ($\mathrm{m\,s^{-1}}$)

U^n : field of U-velocity values at time–level n ($\mathrm{m\,s^{-1}}$)

UNICOS : CRAY Y-MP operating system (terminology)

UNIX : Sun SPARC operating system (terminology)

USA : United States of America (abbreviation)

`ucalcn` : `ted` subroutine responsible for x momentum component calculation (terminology)

`UNROLL` : UNICOS compiler directive (terminology)

v_{10} : y component of wind velocity recorded 10 m above MSL ($\mathrm{m\,s^{-1}}$)

$v_{10}|_i^n$: v_{10}-velocity at ζ grid–point of grid element i, time–level n ($\mathrm{m\,s^{-1}}$)

v : Reynolds time-averaged depth-dependent velocity in y direction ($\mathrm{m\,s^{-1}}$)

v_a : constant v-velocity ($\mathrm{m\,s^{-1}}$)

v_i : v-velocity at v grid–point of grid element i ($\mathrm{m\,s^{-1}}$)

$v_{i,k}^n$: v_i-velocity at depth–level k, time–level n ($\mathrm{m\,s^{-1}}$)

v^n : field of v-velocity values at time–level n ($\mathrm{m\,s^{-1}}$)

V : Reynolds time-averaged depth-averaged velocity in y direction ($\mathrm{m\,s^{-1}}$)

$V^\star(\eta)$: integral of v-velocity over interval $\eta^\star \in [0, \eta]$ ($\mathrm{m\,s^{-1}}$)

V_i^n : V-velocity at horizontal grid–point v_i at time–level n ($\mathrm{m\,s^{-1}}$)

V^n : field of V-velocity values at time–level n ($\mathrm{m\,s^{-1}}$)

$V_{0,m}$: total phase, relative to GMT, for a given tidal constituent, at start of epoch (°)

VAX : scalar minicomputer (terminology)

VMS : DEC VAX operating system (terminology)

`vcalcn` : `ted` subroutine responsible for y momentum component calculation (terminology)

w : Reynolds time-averaged depth-dependent velocity in z direction ($\mathrm{m\,s^{-1}}$)

w_i : w-velocity at ζ grid–point of grid element i ($\mathrm{m\,s^{-1}}$)

$w_{i,k}^n$: w_i-velocity at depth–level k, time–level n ($\mathrm{m\,s^{-1}}$)

w^n : field of w-velocity values at time–level n ($\mathrm{m\,s^{-1}}$)

wk : week (unit)

W : west (notation)

w : west (abbreviation)

x : distance from initial Gaussian tracer concentration field (m)

x : horizontal Cartesian spatial coordinate (m)

Δx : grid–spacing in x direction (m)

x_0 : x coordinate of initial Gaussian peak centre (m)

y : horizontal Cartesian spatial coordinate (m)

Δy : grid–spacing in y direction (m)

y_0 : y coordinate of initial Gaussian peak centre (m)

y : year (unit)

ζ : wave propagation characteristic amplitude response (-)

ζ : free surface elevation measured relative to mean sea level in positive z direction (m)

ζ_b : elevation at ζ grid–point of open boundary grid element b (m)

ζ_i : elevation at ζ grid–point of grid element i (m)

ζ_i^n : ζ_i-elevation at time–level n (m)

ζ^n : field of ζ-elevations at time–level n (m)

z : vertical Cartesian spatial coordinate (m)

Glossary of Terms

The definitions of the following terms were obtained from the works Barnes (1986), Daintith and Nelson (1989), Delbridge and Bernard (1993), Hale and Margham (1988), Pitt (1988), and Uvarov and Isaacs (1988), as well as many other sources cited in the text and listed in the Bibliography.

A

abyssal Referring to the bottom region of ocean basins.

anemometer Any instrument for measuring the rate of flow of a fluid.

annelid Member of the phylum Annelida, a group containing the segmented worms, e.g. earthworms, polychaete worms, and leeches.

arthropod Any of the Arthropoda, the phylum of segmented invertebrates, having jointed legs, as the insects, arachnids, crustaceans, and myriapods.

Acanthaster planci The crown of thorns starfish species.

Amphibolus antarctica A species of seagrass.

Amphibolus halophila A species of seagrass.

Avicennia marina A species of mangrove.

B

barotropic Wherein density can be represented as a function of only pressure.

benthic Bottom dwelling.

biomass The quantity of living matter contributed to a given habitat by one or several kinds of organism, and usually expressed as weight for unit area or volume.

Balanus cretatus A species of barnacle.

Balanus glandula A species of barnacle.

C

capelin A type of fish.

carapace The shield like piece of exoskeleton that covers at least part of the anterior dorsal surface of many arthropods.

chaeta A bristle-like structure, often chitinous. The structures are found particularly in annelid worms, where they occur as projections on most segments, and serve as anchors for that segment during locomotion.

chitin A polysaccharide containing nitrogen that has considerable strength because of its long fibrous molecules.

cohort A statistically significant size group.

competent period The "settlement delay period" of the planktic stage of planktotrophic species.

copepod Any minute free-living or parasitic crustacean of the subclass Copepoda. Copepods lack a carapace and are extremely common in both freshwater and marine plankton, where they constitute an important food source for larger animals such as fish.

crustacean Belonging to the Crustacea, a class of (chiefly aquatic) arthropods, including the lobsters, prawns, crabs, barnacles, slaters, etc., commonly having the body covered with a hard shell or crust.

cypris larva The larva of barnacles.

Clupea harengus An important (herring) food fish which occurs in enormous shoals in the North Sea and the North Atlantic.

Clupea harengus harengus A species of Atlantic herring.

Clupea harengus L. A species of North Sea herring.

Clupea harengus pallasi A species of Pacific herring.

Cyclops abyssorum A species of copepod.

D

decapod Any crustacean of the order Decapoda, including crabs, lobsters, crayfish, prawns, shrimps, etc., characterised by their five pairs of walking legs.

detritus Fragments of plant or animal remains.

diapycnal mixing Small-scale mixing across density surfaces.

diel Diurnal.

diurnal Daily.

E

echinoderm Any member of the phylum Echinodermata, including the sea urchins, starfish, brittle-stars, sea cucumbers, feather stars, and sea lilies. The phylum is characterised by a *pentaradiate structure* (a five-sided radial symmetry) and the presence of tube feet in most forms.

endogenous From within the body.

epibenthic Upon the bottom surface.

estuary Embayment at the junction of a river with the sea, typically containing water of low salinity (*brackish water*).

exogenous Originating from or due to external causes.

Eulerian approach A method of studying fluid motion in which one considers volume of elements at fixed points in space, across which material flows.

F

fecund Capable of producing offspring or fruit, vegetation, etc., in abundance.

filter feeding A type of suspension feeding in which particles (plankton and detritus) are filtered from a water current.

Fickian diffusion The rate of diffusion of matter across a plane is proportional to the negative of the rate of change of the concentration of the diffusing substance in the direction perpendicular to the plane.

Fick's law A law expressing the process of diffusion of liquids and solids in mathematical form. The mass of a dissolved substance crossing unit area of a plane of equal concentration in unit time is proportional to the concentration gradient. The constant of proportionality is called the Fickian diffusion coefficient.

G

gastropod Any of the Gastropoda, a class of molluscs comprising the snails, having a shell of a single valve, usually spirally coiled, and a ventral muscular foot on which they glide about.

geostrophic flow An unaccelerated, frictionless, horizontal flow, in which Coriolis acceleration balances pressure-gradient acceleration, causing flow parallel to the lines of constant pressure.

growth overfishing Fishing effort which significantly reduces the average size of individuals in the population.

H

herring A type of fish.

homogeneous Of uniform composition throughout.

hydrostatic Fluid in which the vertical acceleration of a fluid particle is negligible to the vertical forces acting upon it.

hydrostatic assumption The pressure at any level in the water column is due only to the weight of air above that level.

Halicarcinus A genus of crab.

Haliotis rubra A species of gastropod.

Heterozostera tasmanica A species of seagrass.

I

ichthyoplankton Fish plankton.

infauna Animals that live within bottom sediments.

intertidal Lying between the low and high tide levels.

invertebrate Not vertebrate; without a backbone.

isolume A contour of constant light intensity.

isopycnal mixing Stirring and mixing along density surfaces.

isotropic Having one or more properties that are the same in all directions.

J

juvenile Young.

K

knot A unit of speed equal to $1\,\mathrm{NM\,h^{-1}}$.

L

laminar flow The flow of a fluid that closely follows the shape of a streamlined surface without turbulence.

larva The young of any invertebrate animal.

Lagrangian method A method of studying fluid motion in which one considers volume of elements, i.e. "particles" which are carried along with the fluid, and across whose boundaries material does not flow.

M

mangroves Small tropical trees and shrubs adapted for living in the marine intertidal zone. Most highly developed in estuaries.

Mallotus villosus A species of capelin.

Mediomastus ambiseta A species of infaunal polychaete.

Monte–Carlo estimation The solution of a problem by sampling experiments.

N

natant Floating on water, as the leaf of an aquatic plant.

nauplius The typical crustacean larva which has a single eye, three pairs of limbs, and a rounded, transparent body.

nautical mile A unit of measurement of length, used in marine and aeronautical navigation, equal to $1,852\,\mathrm{m}$, originally defined as one minute of latitude.

Nephrops norvegicus A species of Norway Lobster.

O

overwintering The process of passing the winter.

P

pelagic Living, floating, or swimming above the water column.

phylum A primary division of the animal or vegetable kingdom, as the arthropods, the molluscs, the spermatophytes.

phytoplankton Microscopic algae suspended in that part of the water column of lakes and seas that is penetrated by light.

planktic A species which exists in the plankton for part of the larval life cycle.

plankton Organisms which live suspended in the water column but are unable to counter water currents because of small size or insufficient mobility.

planktotrophic Free-swimming, feeding larvae.

planktotrophic larvae Larvae that feed on other planktonic organisms.

polychaete Any marine annelid worm of the order Polychaeta, including both *errant* (moving) and *tubicolous* (mainly sedentary) forms. They are characterised by the presence of chaetae carried on *parapodia* (projections from the body) and in errant forms the head is well developed. The group includes Nereids (bristle worms such as the ragworm), tube worms, and fan worms.

precompetent period The growth and development period of the planktic stage of planktotrophic species.

protozoan Belonging to or pertaining to the phylum Protozoa, comprising animals consisting of one cell or of a colony of like or similar cells.

pycnocline A relative density or specific gravity discontinuity.

Penaeus esculentus A species of prawn.

Penaeus latisulcatus The western king prawn species.

Penaeus mergiensis A species of banana prawn.

Penaeus semisulcatus A species of prawn.

Posidonia australia A species of seagrass.

R

random walk A succession of movements along line segments where the direction and the length of each move is randomly determined.

recruitment To add a new cohort of young individuals to a population.

recruitment The transition from larval to juvenile phases.

recruitment The survival of juveniles for a period of time in the habitat in which they may survive to adulthood.

S

selective tidal stream transport Vertical migration with a period exactly matching the period of a sheared, oscillatory tidal current, resulting in long-term larval transport.

semi-diurnal Twice daily.

sessile Immobile, fixed in one position.

synodic period The minimum tidal signal length necessary to separate a pair of tidal constituents using harmonic analysis.

T

thermocline Density discontinuity in stratified fluids.

thermohaline current Those brought about by horizontal pressure gradients due to density variations caused by temperature and salinity differences.

V

vertical velocity shear The rate of change of velocity with depth.

Z

zoea The larva of crustacea.

zooplankton That part of the plankton made up of animal life.

Zostera mucronata A species of seagrass.